Biological and Medical Physics, Biomedical Engineering

Jan Ehrhardt
Cristian Lorenz *Editors*

4D Modeling and Estimation of Respiratory Motion for Radiation Therapy

Springer

Biological and Medical Physics, Biomedical Engineering

For further volumes:
http://www.springer.com/series/3740

The fields of biological and medical physics and biomedical engineering are broad, multidisciplinary and dynamic. They lie at the crossroads of frontier research in physics, biology, chemistry, and medicine. The Biological and Medical Physics, Biomedical Engineering Series is intended to be comprehensive, covering a broad range of topics important to the study of the physical, chemical and biological sciences. Its goal is to provide scientists and engineers with textbooks, monographs, and reference works to address the growing need for information.

Books in the series emphasize established and emergent areas of science including molecular, membrane, and mathematical biophysics; photosynthetic energy harvesting and conversion; information processing; physical principles of genetics; sensory communications; automata networks, neural networks, and cellular automata. Equally important will be coverage of applied aspects of biological and medical physics and biomedical engineering such as molecular electronic components and devices, biosensors, medicine, imaging, physical principles of renewable energy production, advanced prostheses, and environmental control and engineering.

Jan Ehrhardt · Cristian Lorenz
Editors

4D Modeling and Estimation of Respiratory Motion for Radiation Therapy

Springer

Editors
Jan Ehrhardt
Institut für Medizinische Informatik
Universität Lübeck
Lübeck
Germany

Cristian Lorenz
Department Digital Imaging
Philips Technologie GmbH
Forschungslaboratorien
Hamburg
Germany

ISSN 1618-7210
ISBN 978-3-642-36440-2 ISBN 978-3-642-36441-9 (eBook)
DOI 10.1007/978-3-642-36441-9
Springer Heidelberg New York Dordrecht London

Library of Congress Control Number: 2013939038

Printed on acid-free paper

Springer is part of Springer Science+Business Media (www.springer.com)

Foreword

It has never been safe to assume motion is absent in external beam radiotherapy, although this was common until recently. Body motion is intrinsically complex, often autonomous and not readily predictable in general. Autonomous organ motion, including the entire gut, heart, lungs, kidneys and ureters, bladder, uterus, and to some extent the entire bronchial and arterial trees are present in vivo. Voluntary motion further compounds the complexity of motion detection, tracking, prediction, and compensation.

Often we begin modeling efforts by assuming a system is linear and time invariant as an expedient to quickly reach a solution. Unfortunately, real world systems, even familiar and seemingly simple functions such as respiration, are not accurately predicted assuming linear and time invariance.

On the other hand, relaxing these assumptions imposes a high degree of complexity even under conditions of quiet and seemingly regular respiratory motion. To accommodate the variability of real respiration, it has been necessary to use high dimensional large deformation spatial time series methods with high complexity and computation demands.

The precision of radiotherapy to lesions in the thorax is limited by many factors, but respiratory motion has been the most difficult to overcome. Although respiration is a normal physiological function required for life, it is notoriously difficult to model and predict, especially in any given individual patient. Simply assuming that organs and the tumor target are fixed limits therapy delivery to the target or exposes adjacent normal tissues to overexposure and undue risk. The spatial time series of even normal respiration is oversimplified with 2D projection imaging, so 3D spatial image sequences are required with sufficient temporal resolution to track excursions of all major structures.

The principal benefit from real-time imaging of respiratory motion with CT systems that enable motion sampling, characterization, and compensation is greater precision in treatment delivery.

Pioneering work has been done by investigators worldwide in an effort to capture, model, predict, and apply detailed spatial knowledge of large-scale deformations in real time to remove the major constraint on precision radiotherapy

delivery imposed by respiration. This effort has yielded impressive results when compared with the simplistic models and approaches of even a decade ago.

The major contributors from groups around the world have joined to author this volume with innovative and robust solutions that apply state-of-the-art computational anatomy methods to characterize and provide the basis for solving the respiratory motion problem of radiotherapy.

The solution consists of several key enabling components: sufficient imaging detail and temporal resolution to acquire snapshots of anatomic structures in real time, followed by modeling of steady-state and variable motion, augmented by registration methods, and variability modeling needed to fully realize 4D radiotherapy in the presence of unconstrained respiration.

To say that this is a major advance in biomedical image processing understates the real achievements where longstanding assumptions of limited or no motion can be relaxed to provide an accurate and precise estimate of where each target and surrounding normal tissue element lies, so they can be tracked and the lesion ameliorated.

Chicago, November 2012 Michael W. Vannier

Contents

Contributors

Ryan E. Amelon Department of Biomedical Engineering, The University of Iowa, Iowa, IA, USA, e-mail: ryan-amelon@uiowa.edu

Kunlin Cao Biomedical Image Analysis Laboratory, GE Global Research Center, Niskayuna, NY, USA, e-mail: kunlincao@gmail.com

Gary E. Christensen Department of Electrical and Computer Engineering and the Department of Radiation Oncology, The University of Iowa, Iowa, IA, USA, e-mail: gary-christensen@uiowa.edu

Max Dahele Department of Radiation Oncology, VU University Medical Center, Amsterdam, The Netherlands, e-mail: m.dahele@vumc.nl

Kai Ding Department of Radiation Oncology, Johns Hopkins University, Baltimore, MD, USA, e-mail: kding1@jhmi.edu

Kaifang Du Department of Biomedical Engineering, The University of Iowa, Iowa, IA, USA, e-mail: kaifang-du@uiowa.edu

Jan Ehrhardt Institute of Medical Informatics, University of Lübeck, Lübeck, Germany, e-mail: ehrhardt@imi.uni-luebeck.de

Sven Kabus Philips Research Laboratories, Hamburg, Germany, e-mail: sven.kabus@philips.com

Paul Keall School of Medicine, University of Sydney, Sydney, Australia, e-mail: paul.keall@sydney.edu.au

Tobias Klinder Philips Research Laboratories, Hamburg, Germany, e-mail: tobias.klinder@philips.com

Cristian Lorenz Philips Research Laboratories, Hamburg, Germany, e-mail: cristian.lorenz@philips.com

Daniel Low UCLA Radiation Oncology, Los Angeles, CA, USA, e-mail: DLow@mednet.ucla.edu

Jamie McClelland Centre for Medical Image Computing, Department of Medical Physics and Bioengineering, University College London, London, UK, e-mail: j.mcclelland@ucl.ac.uk

Keelin Murphy Image Sciences Institute, University Medical Center Utrecht, Utrecht, The Netherlands, e-mail: keelin@isi.uu.nl

Tinsu Pan M.D. Anderson Cancer Center, Houston, TX, USA, e-mail: TPan@mdanderson.org

Madhavan L. Raghavan Department of Biomedical Engineering, The University of Iowa, Iowa, IA, USA, e-mail: ml-raghavan@uiowa.edu

Joseph M. Reinhardt Department of Biomedical Engineering, The University of Iowa, Iowa, IA, USA, e-mail: joe-reinhardt@uiowa.edu

Simon Rit Université de Lyon, CREATIS CNRS UMR5220, Inserm U1044, INSA-Lyon, Université Lyon 1, Centre Léon Bérard, Lyon, France, e-mail: simon.rit@creatis.insa-lyon.fr

David Sarrut Université de Lyon, CREATIS CNRS UMR5220, Inserm U1044, INSA-Lyon, Université Lyon 1, Centre Léon Bérard, Lyon, France, e-mail: David.Sarrut@creatis.insa-lyon.fr

Surseh Senan Department of Radiation Oncology, VU University Medical Center, Amsterdam, The Netherlands, e-mail: s.senan@vumc.nl

Jan-Jakob Sonke Department of Radiation Oncology, The Netherlands Cancer Institute, Amsterdam, The Netherlands, e-mail: j.sonke@nki.nl

Yelin Suh Department of Radiation Oncology, Stanford University, Stanford, CA, USA, e-mail: ysuh@stanford.edu

Jef Vandemeulebroucke Department of Electronics and Informatics (ETRO), Vrije Universiteit Brussel, Brussels, Belgium, e-mail: jefvdmb@gmail.com

Michael Vannier The University of Chicago Medicine, 5841 S. Maryland Avenue, MC 2026, Chicago, IL 60637, USA, e-mail: mvannier@radiology.bsd.uchicago.edu

Sastry Vedam Department of Radiation Physics, University of Texas M. D. Anderson Cancer Center, Houston, TX, USA, e-mail: svedam@mdanderson.org

Jens von Berg Philips Research Laboratories, Hamburg, Germany, e-mail: jens.von.berg@philips.com

René Werner University Medical Center Hamburg-Eppendorf, Hamburg, Germany, e-mail: r.werner@uke.de

Tokihiro Yamamoto Department of Radiation Oncology, Stanford University, Stanford, CA, USA, e-mail: Tokihiro@stanford.edu

Acronyms

1D	One-dimensional
2D	Two-dimensional
3D	Three-dimensional
4D	Four-dimensional
AAPC	Autoadaptive phase-correlation
AAPM	American Association of Physicists in Medicine
ADI	Anisotropy deformation index
AIP	Average intensity projections
ANT	Advanced Normalization Tools
AP	Anterior–posterior
ARMA	Auto regressive moving average
ASD-POCS	Adaptive Steepest Descent Projection Onto Convex Sets
ASTRO	American Society of Therapeutic Radiology and Oncology
BC	Boundary condition
BFGS	Broyden–Fletcher–Goldfarb–Shannon
BHCT	Breath-hold computed tomography
BREP	Boundary representation
BVP	Boundary value problem
CA	Computational Anatomy
CACT	Coronary artery computed tomography
CBCT	Cone beam computed tomography
CD	Centerline distance
CG	Conjugate gradient
CPU	Central processing unit
CR	Correlation ratio
CRT	Conformal radiation therapy
CT	Computed tomography
CTV	Clinical target volume
DC	Dice coefficient
DFP	Davidon–Fletcher–Powell
DI	Distortion index
DIR	Deformable image registration

DMLC	Dynamic multi-leaf collimator
DRR	Digitally computed radiograph
DoG	Difference of Gaussian
DSA	Difference of specific air volume change
DSC	Data sufficiency condition
DT	Difference of tissue volume
DTS	Digital tomosynthesis
DVF	Deformation vector field
EBS	Elastic body spline
EE	End expiration
EI	End inspiration
EMPIRE10	Evaluation of Methods for Pulmonary Image Registration (MICCAI 2010)
EORTC	European Organisation for the Research and Treatment of Cancer
EPID	Electronic portal imaging device
EXACT'09	Extraction of airways from CT (MICCAI 2009)
FDK	Feldkamp, Davis and Kress
FEM	Finite element methods
FFD	Free-form deformation
FOV	Field of view
FPE	Fissure positioning error
FRC	Functional residual capacity
FSR	Full-scan reconstruction
GD	Gradient descent
GPU	Graphical processing unit
GTV	Gross tumor volume
HSR	Half-scan reconstruction
HU	Hounsfield unit
IB-DIR	Intensity-based deformable image registration
ICC	Inverse consistency constraint
ICP	Iterative closest point
IGRT	Image-guided radiotherapy
IMRT	Intensity modulated radiation therapy
ITK	Insight Segmentation and Registration Toolkit
ITV	Internal target volume
JC	Jaccard coefficient
KDE	Kernel density approximation
LBFGS	Limited memory Broyden–Fletcher–Goldfarb–Shannon
LCC	Linear correlation coefficient
LDDMM	Large deformation diffeomorphic metric mapping
LLL	Left lower lobe
LM	Levenberg-Marquardt
LOLA11	Lobe and Lung Analysis (MICCAI 2011)
LR	Left-right
LTI	Linear and time invariant

LUL	Left upper lobe
MCAT	Mathematical cardiac torso phantom
MCL	Multi-leaf collimator
MI	Mutual information
MICCAI	Medical Image Computing and Computer Assisted Intervention
MIDRAS	Multi-Institutional Deformable Registration Accuracy Study
MIP	Maximum intensity projections
MIRD	Medical Internal Radiation Dosimetry phantom
MKB	McKinnon–Bates
MRI	Magnetic resonance imaging
MSCT	Multislice computed tomography
n-SIFT	n-dimensional Scale-Invariant Feature Transform
NCAT	NURBS-based cardiac-torso phantom
NMI	Normalized mutual information
NSCLC	Non-small-cell lung cancer
NTCP	Normal tissue complication probability
NURBS	Non-uniform rational B-spline
OAR	Organ at risk
OD	Orthogonal displacement projection
ORNL	Oak Ridge National Laboratory
PCA	Principal component analysis
PCR	Principal component regression
PDE	Partial differential equations
PET	Positron emission tomography
PICCS	Prior Image Constrained Compressed Sensing
POPI	Point-validated pixel-based breathing thorax model
PTV	Planning target volume
PV	Partial volume
QA	Quality assurance
QN	Quasi-Newton
RLL	Right lower lobe
RML	Right middle lobe
ROI	Region of interest
RPM	Real-time position management
RT	Radiation therapy
RTDD	Radiation treatment dose distribution
RTP	Radiotherapy treatment planning
RUL	Right upper lobe
SACJ	Specific air volume change by corrected Jacobian
SAD	Sum of absolute differences
SAI	Specific air volume change by intensity change
SAJ	Specific air volume change by specific volume change
SART	Simultaneous Algebraic Reconstruction Technique
SBRT	Stereotactic body radiotherapy
SI	Superior–inferior

SIFT	Scale-Invariant Feature Transform
SNR	Signal-to-noise ratio
SPECT	Single photon emission computed tomography
SRO	Simultaneously read-out
SSCT	Single slice computed tomography
SSD	Sum of squared differences
SSTVD	Sum of squared tissue volume difference
SSVMD	Sum of squared vesselness measure difference
STE	Spatio-temporal error
SURF	Speed-up robust features
SVD	Singular value decomposition
TCP	Tumor control probability
TLC	Total lung capacity
TO	Target overlap
TRE	Target registration error
VESSEL12	Vessel Segmentation in the Lung (MICCAI 2012)
VM	Vesselness measure
VMAT	Volumetric modulated arc therapy
VO	Volumetric overlap
XCAT	Extended NURBS-based cardiac-torso phantom
Xe-CT	Xenon-enhanced computed tomography

Chapter 1
Introduction to 4D Motion Modeling and 4D Radiotherapy

Paul Keall, Tokihiro Yamamoto and Yelin Suh

Abstract The fusion of the fast growing fields of imaging science, imaging hardware, and computational modeling, together with a broad interest in learning more about respiratory anatomy and physiology, has led to major advances in the scientific understanding and clinical applications of 4D motion modeling and radiotherapy. The advent of respiratory correlated, or '4D' CT imaging has opened up applications in ventilation imaging, radiation oncology and beyond. In radiation oncology in particular, 4D CT is used in clinical practice by over 60 % of US cancer centers, growing ≈7 % per year. In this chapter we give discuss the history and growth of 4D CT, describe the variability in respiratory motion, and state both the applications and limitations of 4D CT imaging.

1.1 Introduction

Four-dimensional (4D) radiotherapy started to emerge in the early 2000s. An American Society of Radiation Oncology (ASTRO) panel on *Time: the* 4th *Dimension in Radiotherapy* at the 2003 annual meeting defined 4D radiotherapy as "the explicit inclusion of the temporal changes during the imaging, planning and delivery of radiotherapy". The definitions were further refined as: [35]

- **4D thoracic computed tomography (CT) imaging**: The acquisition of a sequence of CT image sets over consecutive segments of a breathing cycle

P. Keall (✉)
School of Medicine, University of Sydney, Sydney, Australia
e-mail: paul.keall@sydney.edu.au

P. Keall · T. Yamamoto · Y. Suh
Department of Radiation Oncology, Stanford University, Stanford, USA

Y. Suh
Department of Radiation Oncology, MD Anderson Cancer Center, Houston, USA

J. Ehrhardt and C. Lorenz (eds.), *4D Modeling and Estimation of Respiratory Motion for Radiation Therapy*, Biological and Medical Physics, Biomedical Engineering,
DOI: 10.1007/978-3-642-36441-9_1,

- **4D treatment planning**: Designing treatment plans on CT image sets obtained for each segment of the breathing cycle
- **4D treatment delivery**: Continuous delivery of the designed 4D treatment plan throughout the entire breathing cycle

Each of these areas have been substantially researched and developed in the intervening years, with key areas of motion estimation and modeling, deformable registration, and applications of these methods well beyond those originally envisaged such as lung ventilation imaging. Also, the limitations of existing hardware and software have been identified, with further refinements suggested and implemented. This book gives a detailed state-of-the-art insight into 4D CT image acquisition, 4D motion estimation and modeling, and 4D radiotherapy.

1.2 Brief History of 4D CT

A key driver in 4D motion modeling and radiotherapy has been the development and widespread implementation of the more correctly termed respiratory correlated CT but more commonly termed 4D CT. The phenomenal growth of the technology is shown in Fig. 1.1. From its first inception and commercial availability in 2002–03 there has been a steady 7 % annual growth in the clinical implementation of this technology. In 2009 44 % of US cancer centers [71] used 4D CT; it is estimated that over 60 % of centers use this technology now. At Stanford University 4D CT is in routine use for planning lung, pancreas, liver and breast cancer treatments, with over 1000 scans estimated to have been acquired in the single institution.

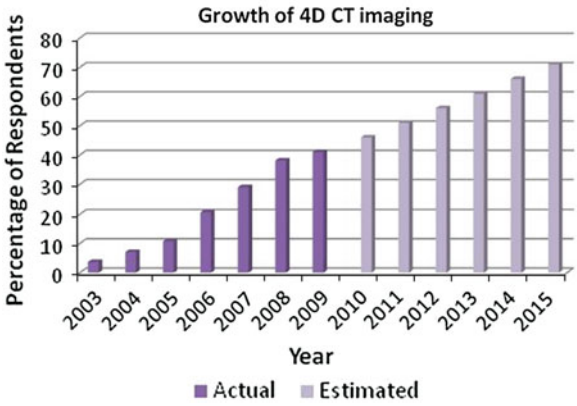

Fig. 1.1 The growth of the clinical implementation of 4D CT with time based on a survey of US radiation oncologists (394 respondents) [71]. Survey data courtesy of Drs. Daniel Simpson and Loren Mell, UC San Diego

Table 1.1 History of the development of 4D thoracic CT acquisition from 2003–2006

Development	Year	First author
Multislice cine	2003	Low [46]
Single slice helical	2003	Ford [19], Vedam [81]
Multislice cine (commercial)	2003	Pan [57]
Cone beam (benchtop)	2003	Taguchi [79]
Multislice helical	2004	Keall [38]
Multislice cine PET/CT	2004	Nehmeh [53, 54]
Cone beam (clinical)	2005	Sonke [73]
Applications outside radiation oncology	2005–2006	Guerrero [27, 28] and Low [47]

A summary of the early history of 4D CT developments is shown in Table 1.1. Despite the first 4D thoracic CT articles dating back only to 2003, there has been an intense clinical and commercial interest in this new technology, and the number of systems and clinical implementation of 4D CT are fast growing. The initial developments of 4D thoracic CT were on single slice scanners published in 2003 with the first commercial implementation on a multislice scanner available in the same year. 4D CT is now available from all major CT vendors. Four-dimensional cone-beam CT (CBCT) [73] and 4D PET/CT are currently active areas of development.

1.3 Respiratory Motion Statistics

During medical imaging and therapy procedures motion in the thorax and abdomen is predominantly caused by breathing, and therefore it is worth briefly reviewing respiratory motion statistics. Organs in the thoracic and abdominal regions move due to respiration. Patients' respiration may vary, resulting in variations in the organ motion. Figure 1.2 shows an example of the variations in tumor positions, respiratory baseline, and respiratory patterns over time. The respiration-induced organ motion and the extent and degree of its variations are acknowledged in the literature. Table 1.2 summarizes the literature of the respiration-induced organ motion. A few guidelines for the respiration-induced organ motion are:

- Organs translate, rotate, and deform due to respiration.
- Significant variations have been observed in the extent, phase, direction, regularity, and linearity of the respiration-induced organ motion
- The motion variations result in wide variations in tumor positions, tumor positions relative to critical structures, tumor motion hysteresis, respiratory baseline, and respiratory patterns, from cycle to cycle, from fraction to fraction, and from patient to patient.
- The motion can be from 0 to 5 cm for free breathing, and averages $\sim$0.5 cm for lung tumors and $\sim$1 cm for liver and pancreas tumors
- For lungs, the greatest motion is generally in the superior-inferior direction, whereas the least motion is in the left-right direction, and the motion tends to increase from the upper lobes to the lower lobes of the lungs.

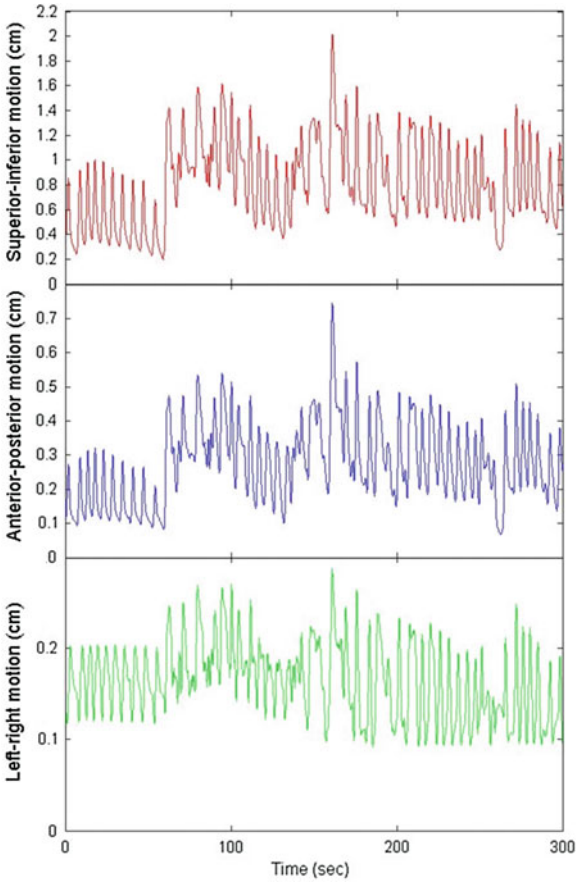

Fig. 1.2 Tumor motion variations over time in three dimensions observed during stereotactic body radiotherapy in Cyberknife Synchrony [77]: there are significant variations in tumor positions, respiratory baseline, and respiratory patterns

Chapter 4 is further expanding on the biophysics and on the possibility of computational modeling of pulmonary motion.

1.4 Methods for 4D Thoracic CT Imaging

An example of 4D CT scan acquisition is shown in Fig. 1.3. 4D CT image acquisition involves, firstly, the real-time recording of a respiratory signal simultaneously with over-sampled CT image acquisition. Over-sampling by re-imaging the same anatomy at different respiratory positions, typically by a factor of 8–15, is performed in order to obtain sufficient number of CT slices over a given longitudinal width so that there

Table 1.2 Literature summary of respiration-induced motion of organs in the thoracic and abdominal regions in three dimensions: mean extent (minimum-maximum) in millimeters. This is a summary and an update of Tables I and II in The American Association of Physicists in Medicine Task Group 76 [37]

Literature	Sites	Direction		
		Superior-inferior (mm)	Anterior-posterior (mm)	Left-posterior (mm)
Barnes et al. [5]	Lung, lower lobe	18.5 (9–32)	-	-
	Lung, middle/upper lobe	7.5 (2–11)	-	-
Bryan et al. [6]	Pancreas, shallow respiration	20 (0–35)	-	-
Case et al. [7]	Liver	8.0 (0.1–18.8)	4.3 (0.1–12.1)	1.8 (0.1–7)
Chen et al. [9]	Lung	(0–50)	-	-
Davies et al. [11]	Diaphragm, shallow respiration	12 (7–28)	-	-
	Diaphragm, deep respiration	43 (25–57)	-	-
	Kidney, shallow respiration	11 (5–16)	-	-
	Liver, shallow respiration	10 (5–17)	-	-
	Liver, deep respiration	37 (21–57)	-	-
Ekberg et al. [15]	Lung	3.9 (0–12)	2.4 (0–5)	2.4 (0–5)
Engelsman et al. [16]	Lung, lower lobe	(2–9)	-	-
	Lung, middle/upper lobe	(2–6)	-	-
Erridge et al. [17]	Lung	12.5 (6–34)	9.4 (5–22)	7.3 (3–12)
Ford et al. [20]	Diaphragm, shallow respiration	20 (13–31)	-	-
Giraud et al. [24]	Diaphragm, deep respiration	35 (3–95)	-	-
Grills et al. [25]	Lung	(2–30)	(0–10)	(0–6)
Hanley et al. [30]	Lung	12 (1–20)	5 (0–13)	1 (0–1)
Harauz et al. [31]	Liver, shallow respiration	14	-	-
Korin et al. [41]	Diaphragm, shallow respiration	13	-	-
	Diaphragm, deep respiration	39	-	-
Murphy et al. [51]	Lung	7 (2–15)	-	-
Plathow et al. [59]	Lung, lower lobe	9.5 (4.5–16.4)	6.1 (2.5–9.8)	6.0 (2.9–9.8)
	Lung, middle lobe	7.2 (4.3–10.2)	4.3 (1.9–7.5)	4.3 (1.5–7.1)
	Lung, upper lobe	4.3 (2.6–7.1)	2.8 (1.2–5.1)	3.4 (1.3–5.3)

(continued)

Table 1.2 (continued)

Literature	Sites	Direction		
		Superior-inferior (mm)	Anterior-posterior (mm)	Left-posterior (mm)
Redmond et al. [60]	Lung	6.7	2.9	2.1
Ross et al. [64]	Lung, lower lobe	-	1 (0–4)	10.5 (0–13)
	Lung, middle lobe	-	0	9 (0–16)
	Lung, upper lobe	-	1 (0–5)	1 (0–3)
Seppenwoolde et al. [67]	Lung	5.8 (0–25)	2.5 (0–8)	1.5 (0–3)
Shimizu et al. [68]	Lung	-	6.4 (2–24)	-
Sixel et al. [72]	Lung	(0–13)	(0–5)	(0–4)
Stevens et al. [74]	Lung	4.5 (0–22)	-	-
Suh et al. [77]	Lung	4.8 (0.2*-14.4)	-	-
Suramo et al. [78]	Kidney, shallow respiration	19 (10–40)	-	-
	Kidney, deep respiration	40 (20–70)	-	-
	Liver, shallow respiration	25 (10–40)	-	-
	Liver, deep respiration	55 (30–80)	-	-
	Pancreas, shallow respiration	20 (10–30)	-	-
	Pancreas, deep respiration	43 (20–80)	-	-
Wade [83]	Diaphragm, shallow respiration	17	-	-
	Diaphragm, deep respiration	101	-	-
Weiss et al. [84]	Diaphragm, shallow respiration	13 ± 5	-	-
	Liver, shallow respiration	13 ± 5	-	-

This is a summary and an update of Tables I and II in The American Association of Physicists in Medicine Task Group 76 [37]

are enough images to achieve respiratory sorting with acceptable spatial accuracy. Over-sampled images from the CT dataset are sorted into several bins based on the information obtained from the respiratory signal. Such a sorting procedure results in the classification of the over-sampled images into several respiratory-sorted image bins, such as end-exhale, mid-inhale etc. A complete set of image bins acquired over a respiratory cycle constitutes a 4DCT dataset. Typically 8–15 respiratory bins are used. Further details and alternative a pproaches for 4DCT image acquisitions are given in Chaps. 2 and 3 of this book.

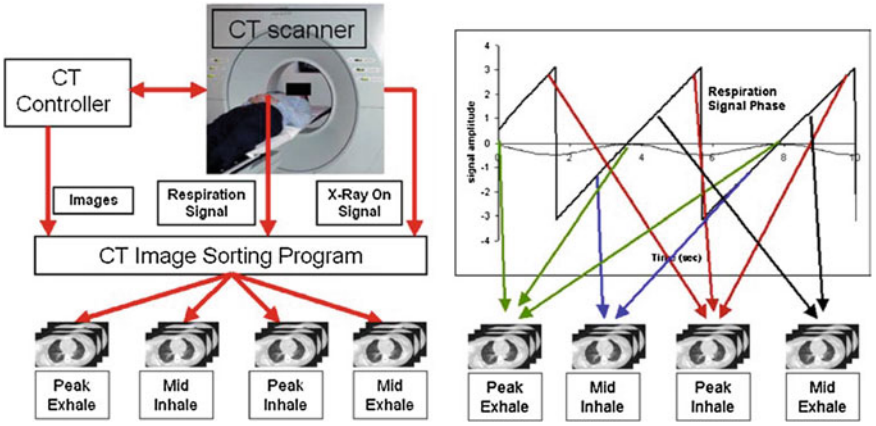

Fig. 1.3 An example of the basics of 4D CT image acquisition. The 4D CT sorting process: the CT images, breathing tracking signal and 'X-Ray ON' signal form the input data stream. The breathing cycle is divided into distinct bins (for example, peak exhale, mid inhale, peak inhale, mid exhale). Images are sorted into these image bins depending on the phase or displacement of the respiratory cycle in which they are acquired, yielding a 4D CT dataset. From Vedam et al. [81]. Further details on 4D CT image acquisitions are given in Chaps. 2 and 3 of this book

1.5 Respiratory Motion Estimation and Analysis

4D CT image data provides a rich source of information about pulmonary motion which is, however, not trivial to exploit for the benefit of radiation therapy. A tumor may be interactively tracked by defining landmarks in a set of CT images. To do this for several tumors is already cumbersome and very time consuming. Assessing breathing motion properties of the whole lungs, however, renders impossible without suitable image processing algorithms. Deformable image registration algorithms as discussed in Chaps. 5–8 play a crucial role in this context. They deliver whole lung motion vector fields that allow following an arbitrary tissue element through the breathing cycle. Based on this information, not only tumor motion can be assessed, but also further physiologically relevant lung properties like the local expansion and contraction of lung parenchyma (local ventilation).

Non rigid image registration can also be used to adjust the treatment plan in case of organ motion, to avoid completely anew organ contouring. The motion may have occurred between two radiation fractions or within, e.g. due to breathing motion.

While 4D CT imaging is well suited to assess pulmonary motion, it is not always available when needed, especially not during the actual treatment sessions. Therefore the idea has been followed to create patient specific motion models based on 4D CT image data. In combination with breathing motion surrogates, which can be measured during radiation therapy, these models can be used to estimate the location and velocity of an arbitrary lung tissue element during treatment. Suitable surrogates can be body motion visible from outside the body, e.g., chest wall and

abdominal motion, but also internal motion, e.g., diaphragm motion as imaged using an on-board X-ray imaging device. Methods to generate breathing motion models, how to correlate them with breathing surrogates, are introduced in Chaps. 9 and 10.

1.6 4D CT Artifacts

Despite the potential and clinical applications of 4D CT, there are several limitations, such as the increased acquisition time (by an additional 2–10 min depending on the scanner configuration), additional post-processing time and additional radiation dose as the same anatomy is imaged several times at different respiratory states. However, a major limitation of current 4D CT technology are the imaging artifacts due to irregular breathing. The prevalence of artifacts, as well as ongoing methods to improve these artifacts are discussed below.

1.6.1 Quantification of Artifact Frequency and Magnitude

Typically there are temporal variations in patient breathing patterns, which lead to mismatches in the respiratory phases or displacements between two adjacent couch positions (data segments) in a 4D CT scan. These variations could manifest as artifacts in the coronal 4D CT images for the current retrospective phase-based sorting methods [1, 14, 18, 26, 44, 48, 52, 56, 58, 62, 63, 90]. 4D CT artifacts can be classified into four types: blurring, duplicate structure, overlapping structure, and incomplete structure as shown in Fig. 1.4. The blurring artifact occurs within a couch position, when the organ motion exceeds the temporal resolution of scanning due to the finite gantry rotation time. In contrast, all the other artifacts occur at an interface between two adjacent couch positions due to a difference in respiratory states. We manually quantified the frequency and magnitude of artifacts in 50 consecutive cine 4D CT images created by retrospective phase-based sorting, and found an alarming result, i.e., 45 of 50 patients (90 %) had at least one artifact (except blurring) with a mean magnitude of 11.6 mm (range, 4.4–56.0 mm) in the diaphragm or heart [90]. Statistical analysis revealed that the patients with artifacts had a significantly larger motion variability between respiratory cycles compared to the patients without artifacts ($p = 0.02$). Furthermore, the magnitude of artifact in the diaphragm was found to be weakly, but significantly correlated with the abdominal displacement difference (surface mismatch) between two adjacent couch positions ($R = 0.34$, $p < 0.01$, see also Fig. 1.5). These results indicate a need for improved respiratory reproducibility and/or significant improvements in 4D CT methods.

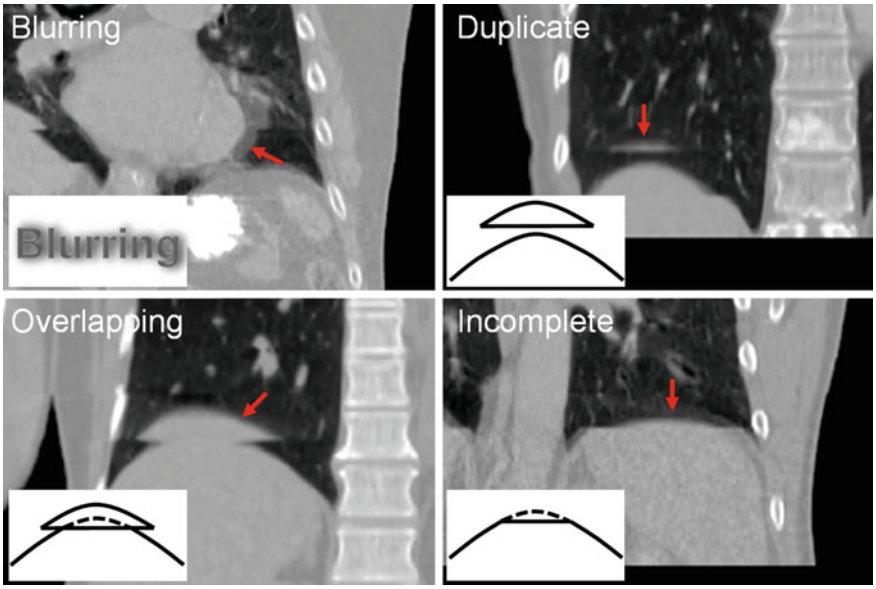

Fig. 1.4 Example 4D CT images with artifacts: blurring, duplicate structure, overlapping structure, and incomplete structure. Schematic diagrams of respective types of artifacts are also shown. Corresponding artifacts are indicated by *red arrows*. From Yamamoto et al. [90]

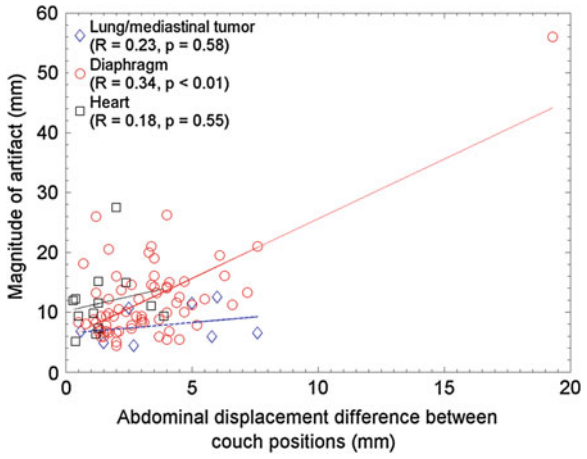

Fig. 1.5 Abdominal displacement difference between two adjacent couch positions (data segments) versus absolute magnitude of artifacts in tumor, diaphragm and heart. From Yamamoto et al. [90]

1.6.2 Artifact Reduction Methods

Many methods have been proposed to reduce 4D CT artifacts. These methods can be divided into four categories: (1) audiovisual biofeedback, (2) respiration-synchronized acquisition, (3) improved sorting and (4) post-processing. The first two methods try to improve the acquisition of CT slices used to create a 4D data set, while the other two try to improve a 4D data set from the acquired CT slices. These four categories are described in detail below.

1.6.2.1 Audiovisual Biofeedback

Audiovisual biofeedback to guide patient breathing has been demonstrated to improve the respiratory regularity for healthy volunteers [45, 55, 82] and patients [21–23, 40, 55, 75]. Venkat et al. demonstrated significant reductions in the root mean square variations by 55 % for displacement, and by 75 % for period ($p < 0.01$) in a ten-volunteer study [82]. Therefore, audiovisual biofeedback is expected to reduce 4D CT artifacts by minimizing the mismatches in the respiratory phases or displacements between two adjacent couch positions. Some patients may not show any improvement because of poor pulmonary function or other reasons. Currently a clinical study has been ongoing at Stanford to test the hypothesis that audiovisual biofeedback significantly reduces 4D CT artifacts.

1.6.2.2 Respiration-Synchronized Acquisition

Respiration-synchronized acquisition methods have been developed to gate the 4D CT acquisition based on pre-determined tolerances of the respiratory state (i.e., displacement, phase or velocity) and real-time monitoring of the respiratory signal [39, 42]. Gating ensures that CT data from irregular breathing patterns, which cause artifacts, are not acquired. Recently Langner and Keall compared 4D CT images simulated with the respiration-synchronized methods and the retrospective phase-based sorting, and demonstrated 50 % smaller magnitude of 4D CT artifacts for the respiration-synchronized methods compared to the retrospective sorting [43]. Moreover the respiration-synchronized methods reduce the imaging dose by approximately 50 % by eliminating unnecessary oversampling, however prolongs the acquisition time 20–100 % [43].

1.6.2.3 Improved Sorting

Several investigators showed that using the respiratory signal displacement rather than the respiratory signal phase resulted in better quality 4D CT images [1, 18, 48, 52, 58, 62]. Lu et al. demonstrated better performance of displacement-based sorting

than phase-based sorting for 33 of 35 patients and equally well for two patients [48]. However, irregular breathing patterns lead to gaps in the coronal images where there are no CT slices with a corresponding displacement. Displacement versus phase-based gating is further discussed in Chap. 3.

Although most 4D CT sorting methods depend on external respiratory signals such as the Varian Real-time Position Management (RPM) system, the correlation between the external signal and internal anatomy motion may be weak. Recently Li et al. have developed a sorting method based on internal anatomic features and demonstrated that the resulting 4D CT images had fewer artifacts than the images sorted by the RPM signal for a patient with a moderate correlation between the internal motion and external signal [44].

1.6.2.4 Post-processing

Several post-processing methods have been proposed to create interpolated 4D CT images at pre-defined respiratory states by deformable image registration (DIR) [14, 65, 85]. Ehrhardt et al. developed an optical flow-based interpolation method and found better image quality for 39 of 40 data sets compared to the current method, where the nearest available segments were used [14]. The post-processing methods would also provide the images with smoother transitions throughout a respiratory cycle, however requires a heavy computational burden and a well-validated DIR technique.

1.7 4D CT Applications 1: Radiation Therapy

Despite the limitations of 4D CT imaging including artifacts and higher imaging dose, as shown in Fig. 1.1 there has been a rapid uptake of 4D CT within the radiation oncology community. There are many current and potential applications of 4D CT. A number of practical and clinical issues of the 4D technology in radiation therapy are discussed in Chap. 11, including a comparison of imaging techniques to detect tumor and organ motion, and strategies to incorporate 4D imaging into radiotherapy planning and treatment. A primary goal is to improve the image quality, and large artifacts (larger than those from 4D imaging) associated with conventional 3D imaging of the thorax. This allows improved confidence in the tumor delineation for treatment planning. A comparison of 3D and 4D CT imaging of the same patient is shown in Fig. 1.6.

Another important application of 4D CT is to quantify tumor motion, from which an appropriate management strategy can be determined. The European Organisation for Research and Treatment of Cancer guidelines [66] recommend that “An assessment of 3D tumor mobility is essential for treatment planning and delivery in lung cancer”. The AAPM Task Group on Respiratory Motion Management [37] recommended that explicit respiratory motion management should be considered if motion

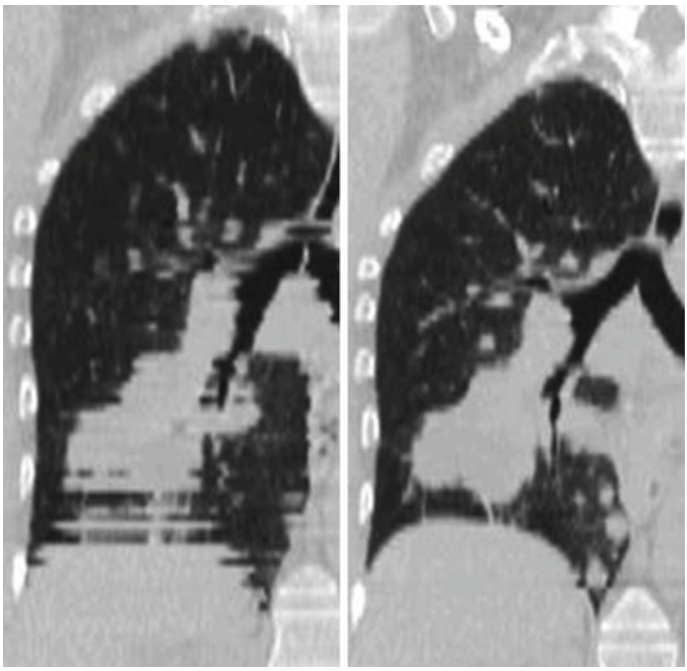

Fig. 1.6 3D (*left*) and 4D (*right*) images from the same patient [36]. A lung tumor is clearly visible in the 4D CT image. In the 3D image, artifacts in the tumor and liver can be clearly seen. These image artifacts reduce the confidence of tumor delineation for treatment planning, leading to larger safety margins needed for the radiotherapy beams

of 5 mm or more is observed for conventional radiotherapy. Stricter guidelines for stereotactic body radiotherapy should be observed.

When 4D CT is used in treatment planning, the additional 8–15 fold increase in data needs to be accounted for. With the recent FDA-approval of DIR algorithms which can map anatomy between different respiratory phases, then subsets of the anatomy, such as contours and dose absorbed can also be transferred or propagated between phases. A generic process of using 4D CT data is shown in Fig. 1.7. There is currently a wide variation in practice in how 4D CT information is currently used, and also depends on the motion management strategy used (discussed further below).

If explicit motion management strategies are warranted for treatment delivery then there are three main treatment strategies that can be used, motion inclusive, gating or tracking (see Chap. 11 for a detailed discussion). In motion inclusive planning, typically the tumor volume observed including the entire motion range is used to define the target, after which addition margins are used to account for additional uncertainties in the radiotherapy process. During treatment delivery the beam is on continuously throughout the breathing cycle. For gating, the tumor from one or a few respiratory bins is used to determine the target, and the beam delivery is synchronized to have the beam on during the same respiratory bins and off throughout the rest of

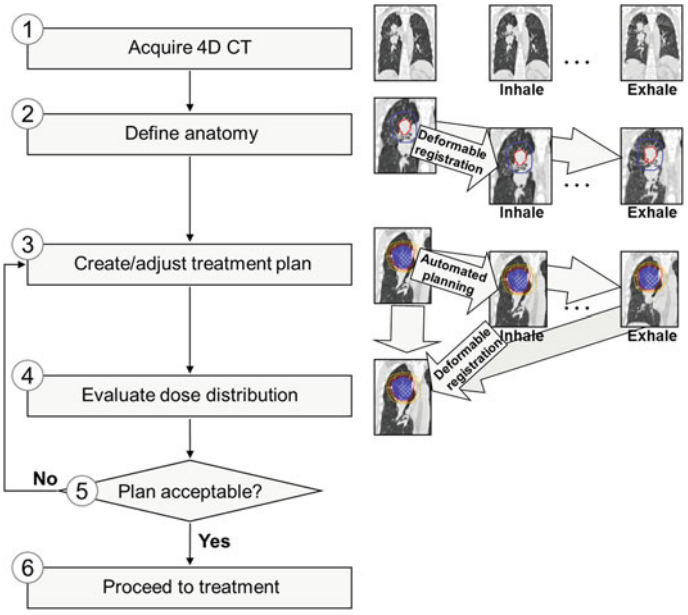

Fig. 1.7 A generic radiation therapy treatment planning workflow utilizing 4D CT data

the delivery. For tracking, the beam delivery is continuously adjusted to be aligned with the position of the moving tumor.

Gating or tracking techniques require knowledge about the internal target motion, however, it can be difficult to image the internal motion during treatment. An alternative strategy is to acquire a respiratory surrogate signal during treatment, e.g. by spirometry or by measuring the displacement of the patient's abdomen or chest using optical devices, and to correlate these surrogate signals to the internal motion by a previously defined correspondence model. Such correspondence models built from patient-specific 4D images are introduced and discussed in Chap. 9 of this book.

The accuracy and precision of gated or tracked radiation delivery depends on the ability of the system to adapt to the constantly changing target position. The latency of the Linear accelerator systems cause the need for prediction techniques (discussed in Chap. 12) to estimate the target position in advance.

The use of 4D cone beam CT [73] immediately prior to treatment delivery opens up capabilities to improve patient alignment, verify the original motion model, build an updated correspondence model and perform replanning based on the more recent 4D anatomic estimate. The use of 4D cone beam CT in image guided radiation therapy is reviewed in Chap. 14.

1.8 4D CT Applications 2: Ventilation Imaging

In this section, we shortly discuss a new and fascinating application of motion estimation algorithms: the computation of lung ventilation from 4D CT images. Ventilation is an index of lung function and can be useful in radiation therapy planning or for the investigation of pulmonary diseases. A in-depth discussion can be found in Chap. 13 of this book.

1.8.1 Rationale

Recently 4D CT images or CT images with different respiratory phases have been used to estimate pulmonary ventilation by DIR [8, 10, 27, 28, 33, 61, 87]. Ventilation images could be used for functional avoidance in lung cancer radiotherapy [88, 91], investigating the radiation response of pulmonary function [12], and would also further our understanding of pathophysiological characteristics of pulmonary diseases including chronic obstructive pulmonary disease (COPD) and asthma. There are several techniques for ventilation imaging which includes nuclear medicine imaging (the current clinical standard of care) [4, 76], hyperpolarized gas magnetic resonance (MR) imaging [3, 34], and Xe-CT imaging [29, 50, 80]. These techniques have drawbacks such as low resolution, high cost, long scan time, and/or low accessibility from radiotherapy centers. The 4D CT ventilation can be considered as 'free' information for lung cancer radiotherapy patients, because 4D CT scans are now in routine use for treatment planning purposes at many centers, and ventilation computation involves only image processing. Moreover, 4D CT ventilation imaging has higher resolution, lower cost, shorter scan time, and higher accessibility than existing methods.

1.8.2 Ventilation Imaging Methods

Ventilation images can be created from 4D CT images in two steps, by (1) the spatial mapping of different respiratory phases of 4D CT images using DIR, and (2) quantitative analysis of the resultant displacement vector fields for computing the ventilation metric (see Fig. 1.8). Guerrero et al. at M. D. Anderson Cancer Centre have originally developed this method using paired breath-hold CT images [28]. They used DIR to map the peak-exhale CT image to the peak-inhale image, and calculated the change in the air fraction per voxel as a metric of regional ventilation based on the theory proposed by Simon [69]. To date several investigators have used this method with some modifications, i.e., M. D. Anderson [8, 27, 91], the University of Iowa [12, 13, 61], Henry Ford [92], and a collaborative group between Stanford University and Philips Research Europe [33, 86–88].

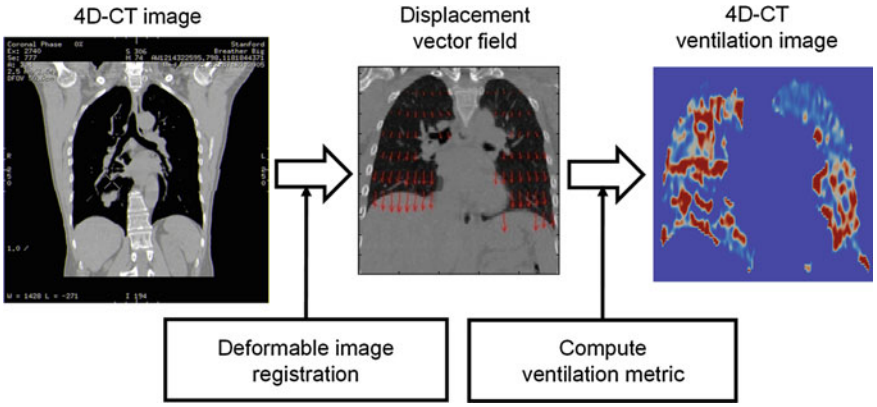

Fig. 1.8 Schematic diagram for creating a 4D CT ventilation image through deformable image registration and quantitative analysis of the resultant displacement vector field for computing the ventilation metric

There are various DIR algorithms and two classes of ventilation metric that can be used for 4D CT ventilation imaging. Recently we quantified the variability of the 4D CT ventilation to DIR algorithms and metrics for 12 patients [89]. We have compared four different 4D CT ventilation images computed with the four different combinations of two DIR algorithms: volumetric (DIR^{vol}) and surface-based (DIR^{sur}) that are fundamentally different from each other, and two ventilation metrics: Hounsfield unit (HU)-change (V_{HU}) [8, 13, 27, 28, 33, 86, 87, 89] and Jacobian determinant of deformation (V_{Jac}) [8, 13, 33, 61, 86, 87, 89] that are the only two proposed classes of metric. A detailed definition and derivation of these metrics is given in Chap. 13. The voxel-based correlation coefficients of $V_{\text{HU}}^{\text{vol}}$ (reference) with $V_{\text{HU}}^{\text{sur}}$, $V_{\text{Jac}}^{\text{vol}}$ and $V_{\text{Jac}}^{\text{sur}}$ were 0.79 ± 0.05, 0.37 ± 0.11 and 0.31 ± 0.11 respectively, indicating that the metric introduced large variability in the images than the DIR algorithm. Castillo et al. also observed spatial differences between the V_{HU} and V_{Jac} images with low Dice similarity coefficients (average, <0.5) for the highest and lowest functional lung regions [8]. These results indicate that careful physiologic validation to determine the appropriate DIR algorithm and metric is needed prior to its applications.

1.8.3 Validation of 4D CT Ventilation Imaging

There have been limited studies on validation of 4D CT ventilation imaging. Reinhardt et al. investigated its physiologic accuracy for the first time by comparing V_{Jac} to the Xe-CT ventilation in five anesthetized sheep, and demonstrated reasonably high correlations (average, $R^2 = 0.73$) [61]. More recently, Ding et al. further investigated three metrics: V_{HU}, V_{Jac} and a metric combining these two (corrected V_{Jac}) by comparison with the Xe-CT ventilation in three anesthetized sheep [13].

They found that the corrected V_{Jac} consistently showed stronger correlations with Xe-CT than V_{Jac} in all sheep, and V_{Jac} consistently showed stronger correlations than V_{HU}. For the human subjects, Yamamoto et al. investigated the physiologic accuracy of 4D CT ventilation imaging for the first time by correlating ventilation with emphysema in 12 patients [86]. They showed that V_{HU} resulted in significantly lower ventilation in emphysematous lung regions (i.e., known low signal regions) than in non-emphysematous regions (i.e., known high signal regions), however V_{Jac} resulted in non-significant differences. This result indicates that V_{HU} has the potential to achieve the high physiologic accuracy. Recently Castillo et al. [8] and Yamamoto et al. [87] quantified the physiologic accuracy of 4D CT ventilation imaging by comparison with the SPECT ventilation in thoracic cancer patients. Castillo et al. demonstrated significantly higher Dice similarity coefficients between V_{HU} and the SPECT ventilation than those between V_{Jac} and SPECT ($p < 10^{-4}$), while Yamamoto et al. demonstrated a higher correlation with V_{Jac} than V_{HU}. These conflicting results on the physiologic accuracy could be in part due to limitations of the reference ventilation data used in each study, i.e., Xe-CT or SPECT. For Xe-CT, there are several major limitations in the Xe-CT method including moderate solubility of Xe in blood, and much greater density and viscosity than air, which could introduce uncertainties as described by Simon [70]. For SPECT, both Castillo et al. [8] and Yamamoto et al. [87] used technetium-99m-labeled diethylenetriamine pentaacetate (^{99m}Tc-DTPA) aerosols which are significantly deposited in central airways for COPD patients [49]. Central deposition limits the uniform penetration of aerosol particles to periphery, yielding non-representative SPECT ventilation [2, 32]. Further studies are necessary to validate the physiologic accuracy of 4D CT ventilation imaging.

1.9 Summary

4D motion modeling and 4D radiotherapy have quickly evolved to play a central role in the management of cancer patients with thoracic and abdominal malignancies. The development has spawned a number of evolving research areas, and applications of motion modeling outside of radiation therapy into other areas of respiratory medicine. Given the growth and possibilities the future of 4D motion modeling and 4D radiotherapy is very exciting. Enjoy the rest of the book!

Acknowledgments The authors wish to thank Julie Baz for her formatting and always valuable critique. PJK acknowledges financial support of the Australian NHMRC Australia Fellowship and US NIH/NCI grants P01CA116602 and R01CA93626. Thanks to Drs. Daniel Simpson and Loren Mell, UC San Diego, for providing the raw data for Fig. 1.1.

References

1. Abdelnour, A.F., Nehmeh, S.A., Pan, T., Humm, J.L., Vernon, P., Schoder, H., Rosenzweig, K.E., Mageras, G.S., Yorke, E., Larson, S.M., Erdi, Y.E.: Phase and amplitude binning for 4D-CT imaging. Phys. Med. Biol. **52**(12), 3515–3529 (2007)

2. Agnew, J.E., Francis, R.A., Pavia, D., Clarke, S.W.: Quantitative comparison of 99Tcm-aerosol and 81Krm ventilation images. Clin. Phys. Physiol. Meas. **3**(1), 21–30 (1982)
3. Albert, M.S., Cates, G.D., Driehuys, B., Happer, W., Saam, B., Springer, C.S.J., Wishnia, A.: Biological magnetic resonance imaging using laser-polarized 129Xe. Nature **370**(6486), 199–201 (1994)
4. Alderson, P.O., Line, B.R.: Scintigraphic evaluation of regional pulmonary ventilation. Semin. Nucl. Med. **10**(3), 218–242 (1980)
5. Barnes, E.A., Murray, B.R., Robinson, D.M., Underwood, L.J., Hanson, J., Roa, W.H.: Dosimetric evaluation of lung tumor immobilization using breath hold at deep inspiration. Int. J. Radiat. Oncol. Biol. Phys. **50**(4), 1091–1098 (2001)
6. Bryan, P.J., Custar, S., Haaga, J.R., Balsara, V.: Respiratory movement of the pancreas: an ultrasonic study. J. Ultrasound. Med. **3**(7), 317–320 (1984)
7. Case, R.B., Moseley, D.J., Sonke, J.J., Eccles, C.L., Dinniwell, R.E., Kim, J., Bezjak, A., Milosevic, M., Brock, K.K., Dawson, L.A.: Interfraction and intrafraction changes in amplitude of breathing motion in stereotactic liver radiotherapy. Int. J. Radiat. Oncol. Biol. Phys. **77**(3), 918–925 (2010)
8. Castillo, R., Castillo, E., Martinez, J., Guerrero, T.: Ventilation from four-dimensional computed tomography: density versus jacobian methods. Phys. Med. Biol. **55**(16), 4661–4685 (2010)
9. Chen, Q.S., Weinhous, M.S., Deibel, F.C., Ciezki, J.P., Macklis, R.M.: Fluoroscopic study of tumor motion due to breathing: facilitating precise radiation therapy for lung cancer patients. Med. Phys. **28**(9), 1850–1856 (2001)
10. Christensen, G.E., Song, J.H., Lu, W., El Naqa, I., Low, D.A.: Tracking lung tissue motion and expansion/compression with inverse consistent image registration and spirometry. Med. Phys. **34**(6), 2155–2163 (2007)
11. Davies, S.C., Hill, A.L., Holmes, R.B., Halliwell, M., Jackson, P.C.: Ultrasound quantitation of respiratory organ motion in the upper abdomen. Br. J. Radiol. **67**(803), 1096–1102 (1994)
12. Ding, K., Bayouth, J.E., Buatti, J.M., Christensen, G.E., Reinhardt, J.M.: CT4D-based measurement of changes in pulmonary function following a course of radiation therapy. Med. Phys. **37**(3), 1261–1272 (2010)
13. Ding, K., Cao, K., Amelon, R.E., Christensen, G.E., Raghavan, M.L., Reinhardt, J.M.: Comparison of intensity- and jacobian-based estimates of lung regional ventilation. Proceedings of the Third International Workshop on Pulmonary Image Analysis, MICCAI 2010, pp. 49–60 (2010)
14. Ehrhardt, J., Werner, R., Saring, D., Frenzel, T., Lu, W., Low, D., Handels, H.: An optical flow based method for improved reconstruction of 4D CT data sets acquired during free breathing. Med. Phys. **34**(2), 711–721 (2007)
15. Ekberg, L., Holmberg, O., Wittgren, L., Bjelkengren, G., Landberg, T.: What margins should be added to the clinical target volume in radiotherapy treatment planning for lung cancer? Radiother. Oncol. **48**, 71–77 (1998)
16. Engelsman, M., Damen, E.M., Jaeger, K.D., van Ingen, K.M., Mijnheer, B.J.: The effect of breathing and set-up errors on the cumulative dose to a lung tumor. Radiother. Oncol. **60**(1), 95–105 (2001)
17. Erridge, S.C., Seppenwoolde, Y., Muller, S.H., van Herk, M., Jaeger, K.D., Belderbos, J.S., Boersma, L.J., Lebesque, J.V.: Portal imaging to assess set-up errors, tumor motion and tumor shrinkage during conformal radiotherapy of non-small cell lung cancer. Radiother. Oncol. **66**, 75–85 (2003)
18. Fitzpatrick, M.J., Starkschall, G., Antolak, J.A., Fu, J., Shukla, H., Keall, P.J., Klahr, P., Mohan, R.: Displacement-based binning of time-dependent computed tomography image data sets. Med. Phys. **33**(1), 235–246 (2006)
19. Ford, E.C., Mageras, G.S., Yorke, E., Ling, C.C.: Respiration-correlated spiral ct: a method of measuring respiratory-induced anatomic motion for radiation treatment planning. Med. Phys. **30**(1), 88–97 (2003)

20. Ford, E.C., Mageras, G.S., Yorke, E., Rosenzweig, K.E., Wagman, R., Ling, C.C.: Evaluation of respiratory movement during gated radiotherapy using film and electronic portal imaging. Int. J. Radiat. Oncol. Biol. Phys. **52**(2), 522–531 (2002)
21. George, R., Chung, T.D., Vedam, S.S., Ramakrishnan, V., Mohan, R., Weiss, E., Keall, P.J.: Audio-visual biofeedback for respiratory-gated radiotherapy: impact of audio instruction and audio-visual biofeedback on respiratory-gated radiotherapy. Int. J. Radiat. Oncol. Biol. Phys. **65**(3), 924–933 (2006)
22. George, R., Ramakrishnan, V., Siebers, J.V., Chung, T.D., Keall, P.J.: Investigation of patient, tumour and treatment variables affecting residual motion for respiratory-gated radiotherapy. Phys. Med. Biol. **51**(20), 5305–5319 (2006)
23. George, R., Vedam, S.S., Chung, T.D., Ramakrishnan, V., Keall, P.J.: The application of the sinusoidal model to lung cancer patient respiratory motion. Med. Phys. **32**(9), 2850–2861 (2005)
24. Giraud, P., Rycke, Y.D., Dubray, B., Helfre, S., Voican, D., Guo, L., Rosenwald, J.C., Keraudy, K., Housset, M., Touboul, E., Cosset, J.M.: Conformal radiotherapy (CRT) planning for lung cancer: analysis of intrathoracic organ motion during extreme phases of breathing. Int. J. Radiat. Oncol. Biol. Phys. **51**(4), 1081–1092 (2001)
25. Grills, I.S., Yan, D., Martinez, A.A., Vicini, F.A., Wong, J.W., Kestin, L.L.: Potential for reduced toxicity and dose escalation in the treatment of inoperable non-small-cell lung cancer: a comparison of intensity-modulated radiation therapy (IMRT), 3D conformal radiation, and elective nodal irradiation. Int. J. Radiat. Oncol. Biol. Phys. **57**(3), 875–890 (2003)
26. Guckenberger, M., Weininger, M., Wilbert, J., Richter, A., Baier, K., Krieger, T., Polat, B., Flentje, M.: Influence of retrospective sorting on image quality in respiratory correlated computed tomography. Radiother. Oncol. **85**(2), 223–231 (2007)
27. Guerrero, T., Sanders, K., Castillo, E., Zhang, Y., Bidaut, L., Pan, T., Komaki, R.: Dynamic ventilation imaging from four-dimensional computed tomography. Phys. Med. Biol. **51**(4), 777–791 (2006)
28. Guerrero, T., Sanders, K., Noyola-Martinez, J., Castillo, E., Zhang, Y., Tapia, R., Guerra, R., Borghero, Y., Komaki, R.: Quantification of regional ventilation from treatment planning CT. Int. J. Radiat. Oncol. Biol. Phys. **62**(3), 630–634 (2005)
29. Gur, D., Drayer, B.P., Borovetz, H.S., Griffith, B.P., Hardesty, R.L., Wolfson, S.K.: Dynamic computed tomography of the lung: regional ventilation measurements. J. Comput. Assist. Tomogr. **3**(6), 749–753 (1979)
30. Hanley, J., Debois, M.M., Mah, D., Mageras, G.S., Raben, A., Rosenzweig, K., Mychalczak, B., Schwartz, L.H., Gloeggler, P.J., Lutz, W., Ling, C.C., Leibel, S.A., Fuks, Z., Kutcher, G.J.: Deep inspiration breath-hold technique for lung tumors: the potential value of target immobilization and reduced lung density in dose escalation. Int. J. Radiat. Oncol. Biol. Phys. **45**(3), 603–611 (1999)
31. Harauz, G., Bronskill, M.J.: Comparison of the liver's respiratory motion in the supine and upright positions: concise communication. J. Nucl. Med. **20**(7), 733–735 (1979)
32. Jogi, J., Jonson, B., Ekberg, M., Bajc, M.: Ventilation-perfusion SPECT with 99mTc-DTPA versus technegas: a head-to-head study in obstructive and nonobstructive disease. J. Nucl. Med. **51**(5), 735–741 (2010)
33. Kabus, S., von Berg, J., Yamamoto, T., Opfer, R., Keall, P.J.: Lung ventilation estimation based on 4D-CT imaging. Proceedings of the First International Workshop on Pulmonary Image Analysis, MICCAI 2008, pp. 73–81 (2008)
34. Kauczor, H., Surkau, R., Roberts, T.: MRI using hyperpolarized noble gases. Eur. Radiol. **8**(5), 820–827 (1998)
35. Keall, P.: 4-dimensional computed tomography imaging and treatment planning. Semin. Radiat. Oncol. **14**(1), 81–90 (2004)
36. Keall, P.J., Kini, V.R., Vedam, S.S., Mohan, R.: Potential radiotherapy improvements with respiratory gating. Australas. Phys. Eng. Sci. Med. **25**(1), 1–6 (2002)
37. Keall, P.J., Mageras, G.S., Balter, J.M., Emery, R.S., Forster, K.M., Jiang, S.B., Kapatoes, J.M., Low, D.A., Murphy, M.J., Murray, B.R., Ramsey, C.R., van Herk, M.B., Vedam, S.S., Wong,

J.W., Yorke, E.: The management of respiratory motion in radiation oncology report of AAPM task group 76. Med. Phys. **33**, 3874–3900 (2006)
38. Keall, P.J., Starkschall, G., Shukla, H., Forster, K.M., Ortiz, V., Stevens, C.W., Vedam, S.S., George, R., Guerrero, T., Mohan, R.: Acquiring 4D thoracic CT scans using a multislice helical method. Phys. Med. Biol. **49**(10), 2053–2067 (2004)
39. Keall, P.J., Vedam, S.S., George, R., Williamson, J.F.: Respiratory regularity gated 4D CT acquisition: concepts and proof of principle. Australas. Phys. Eng. Sci. Med. **30**(3), 211–220 (2007)
40. Kini, V.R., Vedam, S.S., Keall, P.J., Patil, S., Chen, C., Mohan, R.: Patient training in respiratory-gated radiotherapy. Med. Dosim. **28**(1), 7–11 (2003)
41. Korin, H.W., Ehman, R.L., Riederer, S.J., Felmlee, J.P., Grimm, R.C.: Respiratory kinematics of the upper abdominal organs: a quantitative study. Magn. Reson. Med. **23**(1), 172–178 (1992)
42. Langner, U.W., Keall, P.J.: Prospective displacement and velocity-based cine 4D CT. Med. Phys. **35**(10), 4501–4512 (2008)
43. Langner, U.W., Keall, P.J.: Quantification of artifact reduction with real-time cine four-dimensional computed tomography acquisition methods. Int. J. Radiat. Oncol. Biol. Phys. **76**(4), 1242–1250 (2010)
44. Li, R., Lewis, J.H., Cervino, L.I., Jiang, S.B.: 4D CT sorting based on patient internal anatomy. Phys. Med. Biol. **54**(15), 4821–4833 (2009)
45. Lim, S., Park, S.H., Ahn, S.D., Suh, Y., Shin, S.S., Lee, S.W., Kim, J.H., Choi, E.K., Yi, B.Y., Kwon, S.I., Kim, S., Jeung, T.S.: Guiding curve based on the normal breathing as monitored by thermocouple for regular breathing. Med. Phys. **34**(11), 4514–4518 (2007)
46. Low, D.A., Nystrom, M., Kalinin, E., Parikh, P., Dempsey, J.F., Bradley, J.D., Mutic, S., Wahab, S.H., Islam, T., Christensen, G., Politte, D.G., Whiting, B.R.: A method for the reconstruction of four-dimensional synchronized CT scans acquired during free breathing. Med. Phys. **30**(6), 1254–1263 (2003)
47. Low, D.A., Parikh, P.J., Lu, W., Dempsey, J.F., Wahab, S.H., Hubenschmidt, J.P., Nystrom, M.M., Handoko, M., Bradley, J.D.: Novel breathing motion model for radiotherapy. Int. J. Radiat. Oncol. Biol. Phys. **63**(3), 921–929 (2005)
48. Lu, W., Parikh, P.J., Hubenschmidt, J.P., Bradley, J.D., Low, D.A.: A comparison between amplitude sorting and phase-angle sorting using external respiratory measurement for 4D CT. Med. Phys. **33**(8), 2964–2974 (2006)
49. Magnant, J., Vecellio, L., de Monte, M., Grimbert, D., Valat, C., Boissinot, E., Guilloteau, D., Lemarie, E., Diot, P.: Comparative analysis of different scintigraphic approaches to assess pulmonary ventilation. J. Aerosol. Med. **19**(2), 148–159 (2006)
50. Marcucci, C., Nyhan, D., Simon, B.A.: Distribution of pulmonary ventilation using Xe-enhanced computed tomography in prone and supine dogs. J. Appl. Physiol. **90**(2), 421–430 (2001)
51. Murphy, M.J., Martin, D., Whyte, R., Hai, J., Ozhasoglu, C., Le, Q.T.: The effectiveness of breath-holding to stabilize lung and pancreas tumors during radiosurgery. Int. J. Radiat. Oncol. Biol. Phys. **53**(2), 475–482 (2002)
52. Mutaf, Y.D., Antolak, J.A., Brinkmann, D.H.: The impact of temporal inaccuracies on CT4D image quality. Med. Phys. **34**(5), 1615–1622 (2007)
53. Nehmeh, S.A., Erdi, Y.E., Pan, T., Pevsner, A., Rosenzweig, K.E., Yorke, E., Mageras, G.S., Schoder, H., Vernon, P., Squire, O., Mostafavi, H., Larson, S.M., Humm, J.L.: Four-dimensional (4D) PET/CT imaging of the thorax. Med. Phys. **31**(12), 3179–3186 (2004)
54. Nehmeh, S.A., Erdi, Y.E., Pan, T., Yorke, E., Mageras, G.S., Rosenzweig, K.E., Schoder, H., Mostafavi, H., Squire, O., Pevsner, A., Larson, S.M., Humm, J.L.: Quantitation of respiratory motion during 4D-PET/CT acquisition. Med. Phys. **31**(6), 1333–1338 (2004)
55. Neicu, T., Berbeco, R., Wolfgang, J., Jiang, S.B.: Synchronized moving aperture radiation therapy (SMART): improvement of breathing pattern reproducibility using respiratory coaching. Phys. Med. Biol. **51**(3), 617–636 (2006)

56. Olsen, J.R., Lu, W., Hubenschmidt, J.P., Nystrom, M.M., Klahr, P., Bradley, J.D., Low, D.A., Parikh, P.J.: Effect of novel amplitude/phase binning algorithm on commercial four-dimensional computed tomography quality. Int. J. Radiat. Oncol. Biol. Phys. **70**(1), 243–252 (2008)
57. Pan, T., Lee, T.Y., Rietzel, E., Chen, G.T.: 4D-CT imaging of a volume influenced by respiratory motion on multi-slice CT. Med. Phys. **31**(2), 333–340 (2004)
58. Pan, T., Sun, X., Luo, D.: Improvement of the cine-CT based 4D-CT imaging. Med. Phys. **34**(11), 4499–4503 (2007)
59. Plathow, C., Ley, S., Fink, C., Puderbach, M., Hosch, W., Schmahl, A., Debus, J., Kauczor, H.U.: Analysis of intrathoracic tumor mobility during whole breathing cycle by dynamic MRI. Int. J. Radiat. Oncol. Biol. Phys. **59**(4), 952–959 (2004)
60. Redmond, K.J., Song, D.Y., Fox, J.L., Zhou, J., Rosenzweig, C.N., Ford, E.: Respiratory motion changes of lung tumors over the course of radiation therapy based on respiration-correlated four-dimensional computed tomography scans. Int. J. Radiat. Oncol. Biol. Phys. **75**(5), 1605–1612 (2009)
61. Reinhardt, J.M., Ding, K., Cao, K., Christensen, G.E., Hoffman, E.A., Bodas, S.V.: Registration-based estimates of local lung tissue expansion compared to xenon CT measures of specific ventilation. Med. Image Anal. **12**(6), 752–763 (2008)
62. Rietzel, E., Chen, G.T.: Improving retrospective sorting of 4D computed tomography data. Med. Phys. **33**(2), 377–379 (2006)
63. Rietzel, E., Pan, T., Chen, G.T.: Four-dimensional computed tomography: image formation and clinical protocol. Med. Phys. **32**(4), 874–889 (2005)
64. Ross, C.S., Hussey, D.H., Pennington, E.C., Stanford, W., Doornbos, J.F.: Analysis of movement of intrathoracic neoplasms using ultrafast computerized tomography. Int. J. Radiat. Oncol. Biol. Phys. **18**(3), 671–677 (1990)
65. Schreibmann, E., Chen, G.T., Xing, L.: Image interpolation in 4D CT using a BSpline deformable registration model. Int. J. Radiat. Oncol. Biol. Phys. **64**(5), 1537–1550 (2006)
66. Senan, S., De Ruysscher, D., Giraud, P., Mirimanoff, R., Budach, V.: On behalf of the radiotherapy group of the European Organization for research and treatment of cancer: literature-based recommendations for treatment planning and execution in high-dose radiotherapy for lung cancer. Radiother. Oncol. **71**(2), 139–146 (2004)
67. Seppenwoolde, Y., Shirato, H., Kitamura, K., Shimizu, S., van Herk, M., Lebesque, J.V., Miyasaka, K.: Precise and real-time measurement of 3D tumor motion in lung due to breathing and heartbeat, measured during radiotherapy. Int. J. Radiat. Oncol. Biol. Phys. **53**(4), 822–834 (2002)
68. Shimizu, S., Shirato, H., Ogura, S., Akita-Dosaka, H., Kitamura, K., Nishioka, T., Kagei, K., Nishimura, M., Miyasaka, K.: Detection of lung tumor movement in real-time tumor-tracking radiotherapy. Int. J. Radiat. Oncol. Biol. Phys. **51**(2), 304–310 (2001)
69. Simon, B.A.: Non-invasive imaging of regional lung function using X-ray computed tomography. J. Clin. Monit. Comput. **16**(5–6), 433–442 (2000)
70. Simon, B.A.: Regional ventilation and lung mechanics using X-ray CT. Acad. Radiol. **12**(11), 1414–1422 (2005)
71. Simpson, D.R., Lawson, J.D., Nath, S.K., Rose, B.S., Mundt, A.J., Mell, L.K.: Utilization of advanced imaging technologies for target delineation in radiation oncology. J. Am. Coll. Radiol. **6**(12), 876–883 (2009)
72. Sixel, K.E., Ruschin, M., Tirona, R., Cheung, P.C.: Digital fluoroscopy to quantify lung tumor motion: potential for patient-specific planning target volumes. Int. J. Radiat. Oncol. Biol. Phys. **57**(3), 717–723 (2003)
73. Sonke, J., Zijp, L., Remeijer, P., Van Herk, M.: Respiratory correlated cone beam CT. Med. Phys. **32**(4), 1176–1186 (2005)
74. Stevens, C.W., Munden, R.F., Forster, K.M., Kelly, J.F., Liao, Z., Starkschall, G., Tucker, S., Komaki, R.: Respiratory-driven lung tumor motion is independent of tumor size, tumor location, and pulmonary function. Int. J. Radiat. Oncol. Biol. Phys. **51**(1), 62–68 (2001)

75. Stock, M., Kontrisova, K., Dieckmann, K., Bogner, J., Poetter, R., Georg, D.: Development and application of a real-time monitoring and feedback system for deep inspiration breath hold based on external marker tracking. Med. Phys. **33**(8), 2868–2877 (2006)
76. Suga, K.: Technical and analytical advances in pulmonary ventilation SPECT with Xenon-133 gas and Tc-99m-technegas. Ann. Nucl. Med. **16**(5), 303–310 (2002)
77. Suh, Y., Dieterich, S., Cho, B., Keall, P.J.: An analysis of thoracic and abdominal tumour motion for stereotactic body radiotherapy patients. Phys. Med. Biol. **53**, 3623–3640 (2008)
78. Suramo, I., Paivansalo, M., Myllyla, V.: Cranio-caudal movements of the liver, pancreas and kidneys in respiration. Acta Radiol. Diagn. (Stockh) **25**(2), 129–131 (1984)
79. Taguchi, K.: Temporal resolution and the evaluation of candidate algorithms for four-dimensional CT. Med Phys **30**(4), 640–50 (2003)
80. Tajik, J.K., Chon, D., Won, C., Tran, B.Q., Hoffman, E.A.: Subsecond multisection CT of regional pulmonary ventilation. Acad. Radiol. **9**(2), 130–146 (2002)
81. Vedam, S.S., Keall, P.J., Kini, V.R., Mostafavi, H., Shukla, H.P., Mohan, R.: Acquiring a four-dimensional computed tomography dataset using an external respiratory signal. Phys. Med. Biol. **48**(1), 45–62 (2003)
82. Venkat, R.B., Sawant, A., Suh, Y., George, R., Keall, P.J.: Development and preliminary evaluation of a prototype audiovisual biofeedback device incorporating a patient-specific guiding waveform. Phys. Med. Biol. **53**, N197–N208 (2008)
83. Wade, O.: Movement of the thoracic cage and diaphragm in respiration. J. Physiol. **124**, 193–212 (1954)
84. Weiss, P.H., Baker, J.M., Potchen, E.J.: Assessment of hepatic respiratory excursion. J. Nucl. Med. **13**(10), 758–759 (1972)
85. Xu, S., Taylor, R.H., Fichtinger, G., Cleary, K.: Lung deformation estimation and four-dimensional CT lung reconstruction. Acad. Radiol. **13**(9), 1082–1092 (2006)
86. Yamamoto, T., Kabus, S., von Berg, J., Klinder, T., Blaffert, T., Lorenz, C., Keall, P.J.: Physiological validation of 4D-CT-based ventilation imaging in patients with chronic obstructive pulmonary disease (COPD). Med. Phys. **36**(6), 2821 (Abstract) (2009)
87. Yamamoto, T., Kabus, S., von Berg, J., Lorenz, C., Goris, M.L., Loo B. W., J., Keall, P.J.: Evaluation of four-dimensional (4D) computed tomography (CT) pulmonary ventilation imaging by comparison with single photon emission computed tomography (SPECT) scans for a lung cancer patient. Proceedings of the Third International Workshop on Pulmonary Image Analysis, MICCAI 2010, pp. 117–128 (2010)
88. Yamamoto, T., Kabus, S., von Berg, J., Lorenz, C., Keall, P.J.: Impact of four-dimensional computed tomography pulmonary ventilation imaging-based functional avoidance for lung cancer radiotherapy. Int. J. Radiat Oncol. Biol. Phys. **79**(1), 279–288 (2011)
89. Yamamoto, T., Kabus, S., Klinder, T., Lorenz, C., von Berg, J., Keall, P.J.: Sensitivity of 4D-CT pulmonary ventilation imaging to deformable image registration algorithms and metrics. Med. Phys. **37**(6), 3424 (Abstract) (2010)
90. Yamamoto, T., Langner, U., Loo, B.W.J., Shen, J., Keall, P.J.: Retrospective analysis of artifacts in four-dimensional CT images of 50 abdominal and thoracic radiotherapy patients. Int. J. Radiat. Oncol. Biol. Phys. **72**(4), 1250–1258 (2008)
91. Yaremko, B.P., Guerrero, T.M., Noyola-Martinez, J., Guerra, R., Lege, D.G., Nguyen, L.T., Balter, P.A., Cox, J.D., Komaki, R.: Reduction of normal lung irradiation in locally advanced non-small-cell lung cancer patients, using ventilation images for functional avoidance. Int. J. Radiat. Oncol. Biol. Phys. **68**(2), 562–571 (2007)
92. Zhong, H., Fragoso, M., Patel, S., Ajlouni, M., Movsas, B., Chetty, I.: A method to evaluate region-specific pulmonary function using 4D CT images for lung cancer patients undergoing radiation therapy. Med. Phys. **36**(6), 2762 (Abstract) (2009)

Part I
4D Image Acquisition

Chapter 2
Helical 4D CT and Comparison with Cine 4D CT

Tinsu Pan

Abstract 4D CT was one of the most important developments in radiation oncology in the last decade. Its early development in single slice CT and commercialization in multi-slice CT has radically changed our practice in radiation treatment of lung cancer, and has enabled the stereotactic radiosurgery of early stage lung cancer. In this chapter, we will document the history of 4D CT development, detail the data sufficiency condition governing the 4D CT data collection; present the design of the commercial helical 4D CTs from Philips and Siemens; compare the differences between the helical 4D CT and the GE cine 4D CT in data acquisition, slice thickness, acquisition time and work flow; review the respiratory monitoring devices; and understand the causes of image artifacts in 4D CT.

2.1 Introduction

Helical computed tomography (CT) was first introduced by Kalender et al. in 1990 [10] on a single-slice CT (SSCT) scanner. It allows data to be taken while the table is in translation. Prior to that, CT data was obtained in the axial mode whereby the table was stationary during data acquisition. The helical SSCT was not practical to clinical 4D CT imaging because of its limited detector coverage and slow gantry rotation of more than 1 s per revolution. It was not until multi-slice CT (MSCT) introduced in 1998 did 4D CT imaging become feasible. With the large detector coverage of more than 1 cm, a single CT rotation in a MSCT scanner could produce more than 4 slices of 2.5 mm images, leading to 3–6 times faster in scanning speed than the SSCT. Almost as significant as the development of MSCT was the introduction of gantry rotation of 0.5 s and less, which enabled cardiac CT imaging of the coronary arteries. Cardiac CT dominated most of the MSCT development in the last

T. Pan(✉)
M.D. Anderson Cancer Center, Houston, TX, USA
e-mail: TPan@mdanderson.org

J. Ehrhardt and C. Lorenz (eds.), *4D Modeling and Estimation of Respiratory Motion for Radiation Therapy*, Biological and Medical Physics, Biomedical Engineering,
DOI: 10.1007/978-3-642-36441-9_2,

decade, culminating in high spatial resolution of less than 0.5 mm and high temporal resolution of less than 200 ms. Today, 64-slice CT has become popular in diagnostic imaging and is into radiation oncology. The scanner with the largest detector coverage at present is Aquillion One 320-slice CT scanner (Toshiba America Medical Systems, Tustin, CA), with the coverage of 16 cm per gantry rotation [4, 19]. It has been shown that the 320-slice MSCT can help characterize the tumor motion more accurately than a 16-slice MSCT in a phantom study [3]. Its clinical application on 4D CT is promising. The scanner with the highest temporal resolution (<100 ms) is the Somatom Definition dual-source CT scanner [5] (Siemens Medical Solutions USA, Malvern, PA). Cardiac CT is a non-invasive clinical procedure to image the coronary arteries and was the first 4-dimensional CT (4D CT) application.

The first applications of 4D CT imaging of the lung tumor subject to the respiratory motion were first published by Vedam et al. [20] and Ford et al. [7] on the AcQSIM SSCT scanner (Philips Medical Systems, Andover, MA). The smallest pitch on this scanner was 0.5, which is defined as the table travel per rotation divided by the width of the x-ray beam on the rotation axis. A slow gantry rotation cycle of 1.5 s was used to slow down the table speed to meet the data sufficiency condition [17]. However, the table speed in this design was still too fast for 4D CT and resulted in gaps between images. Also the long acquisition time of up to 7 min due to the limited coverage of the SSCT scanner was not well suited to the clinical application of 4D CT.

The first clinical use of 4D CT was made by commercialization of the cine 4D CT (first announced at the AAPM 2002 Annual Meeting in Montreal, Canada) on the LightSpeed MSCT scanner (GE Healthcare, Waukesha, WI) [17]. The cine 4D CT utilized the cine CT scan capability already available on the LightSpeed CT scanner, which can scan at the same slice location for multiple gantry rotations. It does not require any hardware or software modification on the LightSpeed CT scanner, and it only needs an image sorting software, which correlates the same phase of CT images across the multiple table positions to a single phase of 4D CT images. The GE LightSpeed CT allows for a large coverage of cine CT scan up to over 30 cm in a single scan setup, convenient for the application of cine 4D CT. Radiation dose in the thorax application of 4D CT is generally less than 50 mGy. Low et al. [3] proposed a similar cine 4D CT technique on a Siemens Somatom 4-slice CT using a spirometer to record the respiratory signal. In their approach, each cine CT scan of 1 cm coverage requires a new scan setup [15, 16]. It takes 15 scans of 0.5 s (7.5 s total x-ray on time) per position to scan over one respiratory cycle of data. There was an inter-scan delay of 0.25 s between two 0.5 s scans. In total, 11.25 s per step was needed by taking into account the inter-scan delay time. A scanning pause of about 2 min after 7 scans was required for the user to reprogram another sequence of 7 scans. Although this approach could achieve 4D CT, it was not very practical for a large coverage of over 30 cm due to an inconvenience of setting up the scan protocol.

Both Phillips and Siemens later adopted a low-pitch helical CT scanning mode from cardiac CT for their 4D CT design [11]. This design was commercialized in 2006 on the MSCT scanners of at least 16 slices. In comparison, all the LightSpeed MSCT scanners of 4 slices and up, which have the cine CT scan capability that allows for a large coverage of the thorax in a simple protocol setup, were applicable for 4D CT.

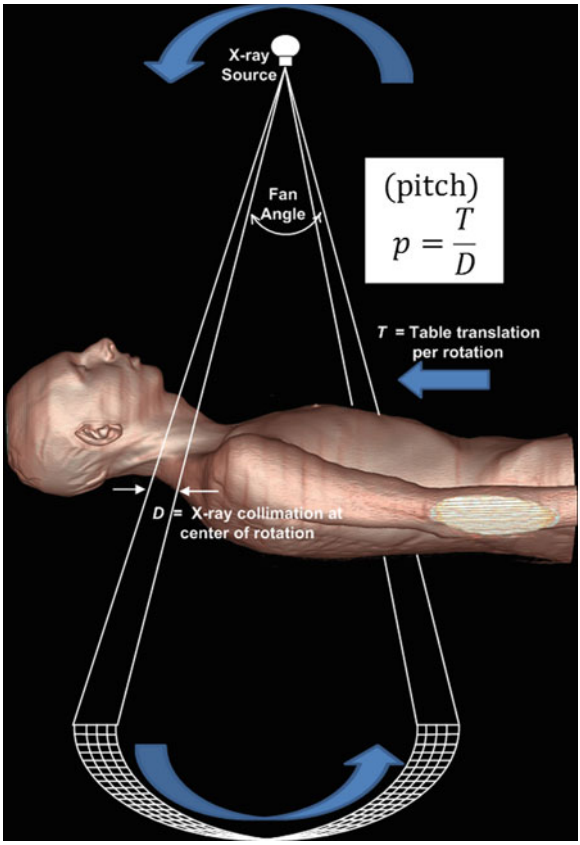

Fig. 2.1 Illustration of a helical CT scan with four active detector rows and its pitch definition

We will detail the data sufficiency condition governing the 4D CT data collection; present the design of the commercial helical 4D CTs from Philips and Siemens; compare the differences between the helical 4D CT and the cine 4D CT in data acquisition, slice thickness, acquisition time and work flow; review the respiratory monitoring devices in 4D CT; and understand the causes of image artifacts in 4D CT.

2.2 Helical 4D CT Data Acquisition

The challenge in 4D CT imaging is to capture a complete breathing cycle of the lung motion in CT imaging. Since no CT detector is able to cover the whole lungs, and the conventional scan speeds for diagnostic CT and cardiac CT imaging are still too fast for 4D CT of the lungs. Special care has to be taken to ensure the scanner parameters such as pitch value, gantry rotation speed, table speed or table translation

per rotation, and detector configuration are suitable for 4D CT imaging. Figure 2.1 is an illustration of a helical CT system. An X-ray source sends out a cone-like radiation field illuminating a multi-row detector. It is characterized by the in-plane fan angle of about 60° and the x-ray collimation (the active detector width) at the center of rotation. Since the patient table is moving while the CT gantry is rotating, the illumination field follows a spiral course in a patient centric coordinate system. Table motion and gantry rotation speed have to be selected in a way that (i) each volume element in the lungs is covered in the X-ray cone-beam for at least a whole breathing cycle. In the following, the interplay between detector aperture, gantry rotation, table motion and breathing frequency is discussed in Sect. 2.2.1. Section 2.2.2 explains the influence of detector configuration settings, and Sect. 2.2.3 the correlation between scan settings and image resolution. The breathing phase selection and respective differences between cine and helical 4D CT is discussed in Sect. 2.4. Finally, an overview on commercial helical CT systems, and respiratory monitoring devices is given in Sects. 2.5 and 2.6, respectively.

2.2.1 Data Sufficiency Condition (DSC)

To achieve 4D CT imaging of an object in the presence of respiratory motion, one must acquire data at each location for the duration of at least one breath cycle plus the duration needed to acquire sufficient projections for one image reconstruction. This is the data sufficiency condition (DSC) for 4D CT imaging [16]. The time needed to acquire one image is equal to one gantry rotation cycle for full-scan reconstruction (FSR) or $\frac{1}{2}$ of a gantry rotation cycle plus fan-angle for half-scan reconstruction (HSR) [18], which is 180° plus about 60°, amounting to roughly $\frac{2}{3}$ gantry rotations. Additional data acquisition is needed because it takes at least $\frac{2}{3}$ of a gantry rotation cycle in CT for reconstruction of an image and to ensure that there are images at both ends of a complete breath cycle. This additional data acquisition is not necessary for projection x-ray imaging such as fluoroscopy in which each projection is an image by itself [13]. Two acquisition modes, helical and cine, can be used to realize the 4D CT imaging. A helical CT scan acquires data when the table translates at a constant speed programmed by a pitch factor p, which is defined as the table travel per rotation divided by the width of the x-ray beam projected onto the rotation axis (Fig. 2.1).

To satisfy the DSC with FSR, the pitch values

$$p \leq \frac{T_g}{T_b + T_g}, \tag{2.1}$$

and with HSR

$$p \leq \frac{T_g}{T_b + \frac{2}{3}T_g} \tag{2.2}$$

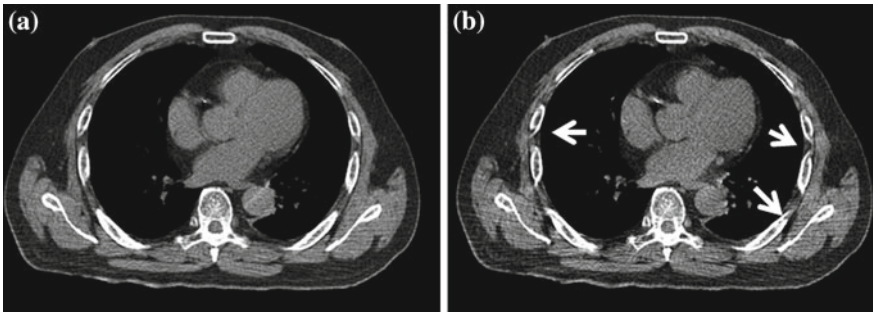

Fig. 2.2 Images reconstructed with the full scan reconstruction (FSR) with 360° of CT data in (**a**) and the half scan reconstruction (HSR) with 240° of CT data in (**b**). The *arrows* indicate artifacts coming out of HSR. The image of FSR is also less noisy than the image of HSR because FSR has more projection data in the image reconstruction than HSR

where T_g and T_b are the durations of the gantry rotation cycle and the breath cycle, respectively. Let us examine the formula for FSR. If the breath cycle T_b is the same as the T_g, then after one T_g (e.g., $T_b = T_g = 4\,\text{s}$), the detector moves in and out of the x-ray beam in exactly one T_b. Taking into account of the extra acquisition of T_g for one image reconstruction, $p = 0.5$. If the breath cycle T_b is 4 times of T_g (i.e., $T_b = 4\,\text{s}$, $T_g = 1\,\text{s}$), then $p = 0.2$. Typically $T_b = 4\,\text{s}$ and $T_g = 0.5\,\text{s}$ and $p = 0.11$, almost the same gantry rotation cycle as the typical pitch factor of 0.1 or less in the helical 4D CT in Tables 2.1 and 2.2. Similar reasoning can be applied to Eq. (2.2) for HSR.

Although HSR is used in cardiac CT for better temporal resolution, FSR is typically used in 4D CT because FSR gives rise to fewer image artifacts between 25 and 50 cm reconstruction field of view (FOV) than HSR (Fig. 2.2). The FOV with HSR is typically less than 25 cm only to cover the heart. The FOV for radiation therapy simulation is at least 50 cm. Since FSR uses more data in the image reconstruction than HSR, its image will also be less noisy. One very important observation of the pitch value selection is that the longer the breath cycle T_b or the shorter the gantry rotation cycle T_g is, the smaller the pitch factor p becomes. In diagnostic CT imaging with patient breath-hold and without gating, p is about 1, which is 10 times faster than in a helical 4D CT scan with respiratory gating!

2.2.2 Data Acquisition Modes

A MSCT can be characterized by the number of data channels that can be simultaneously read-out (SRO) in the patient table direction. This number of SRO is also frequently referred to as the number of slices in MSCT. A MSCT with a higher number of SRO typically means a newer MSCT that can scan the same coverage faster. To acquire the cine 4D CT data with GE scanners, the numbers of SRO data channels

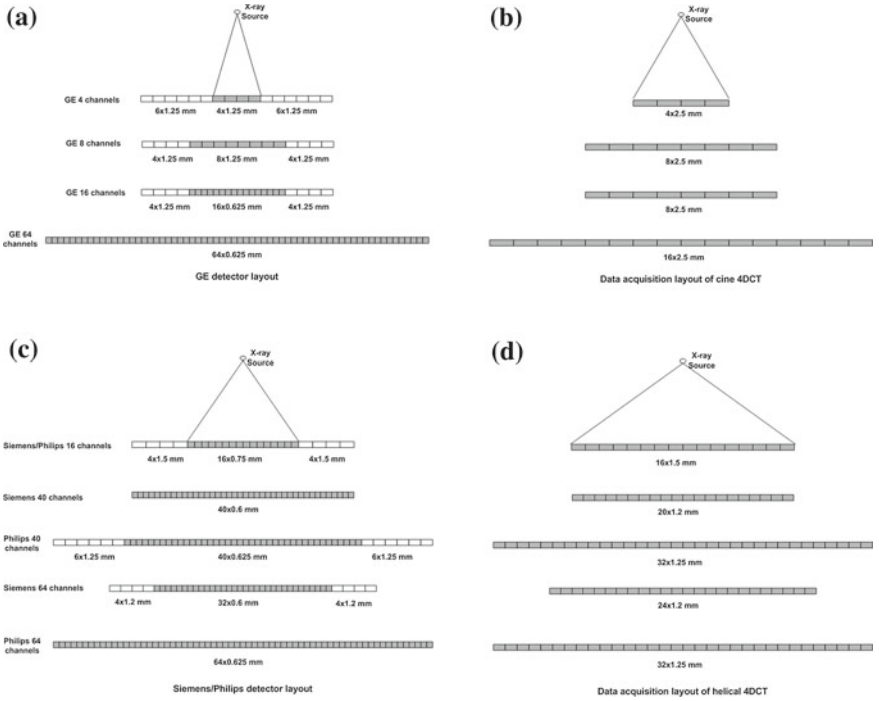

Fig. 2.3 (a) GE detector layout for 4, 8, 16 and 64 data channels. The *shaded regions* illustrate the data channels that can be simultaneously read-out. (b) Data acquisition layout of GE 4D CT for various numbers of data channels. Each 2.5 mm datum is combined from two to four data channels of 1.25 or 0.625 mm. The speed of cine 4D CT acquisitions is the same for both 8 and 16 data channels, which utilizes 2 cm (8 × 2.5 mm) detector coverage. (c) Siemens/Philips detector layout of 16, 20, 40, and 64 data channels. Siemens 40 and 64-channel scanners (marked with *asterisk* *) based on the 20 and 32-channel detectors, respectively, utilize the technology of z-flying focal spot to fast switch between two focal spots at each projection angle to achieve the effect of 40 and 64 data channels, respectively. Note that the physical detector sizes of 40 and 64-channel are 2.4 and 2.88 cm, respectively. Philips 64-channel has the detector size of 4 cm, identical to GE 64-channel. (d) Data acquisition layout of Siemens/Philips helical 4D CT for various data channels. The detector coverage of 4 cm is the same for the Philips 40 and 64 channels. The detector coverage of 2.4 cm is the same for the Siemens 16, 20 and 40 channels

are 4, 8, 16 and 64 (Fig. 2.3a). To acquire the helical 4D CT data with Siemens or Philips scanners, the numbers of SRO data channels are 16, 20, 40, and 64 (Fig. 2.3c). The reason that helical 4D CT started at 16-slice was because Siemens/Philips only introduced the low pitch helical CT scan ($p = 0.1$) in their 16-slice and up CT scanners. This practice is typical in commercial CT that a new feature is only introduced in newer CT scanners, which was 16-slice at the time.

The number of physical data channels on a MSCT is at least the number of data channels of SRO. Both GE's 4 and 8 channels have 16 physical detectors. For GE's 16 and 64 channels, there are 24 and 64, detectors, respectively. During data acquisition, the cine 4D CT utilizes the data acquisition modes of 4 × 2.5, 8 × 2.5, 8 × 2.5 and

16 × 2.5 mm on GE's 4, 8, 16 and 64-slice CTs, respectively (Fig. 2.3b) to produce the images of slice thickness 2.5 mm for treatment planning. Combination of smaller data channels to 2.5 mm slice is conducted in data acquisition. A 16-slice CT may not have a significant advantage over an 8-slice CT in terms of acquisition speed for the cine 4D CT because the detector size is at the maximum of 2 cm for both the 8- and 16-slice GE CT.

In helical 4D CT data acquisition, the raw data before helical data interpolation are smaller than 1.5 mm (Fig. 2.3d). For the 16-slice, the mode of data acquisition is 16 × 1.5 mm. For the Siemens 20/40-slice, it is 20 × 1.2 mm. For the Philips 40/64-slice, it is 32 × 1.25 mm. Siemens 16, 20 and 40-slice CTs have the same detector coverage of 2.4 cm. Therefore, the speed of helical 4D CT is the same for the Siemens 16, 20 and 40-slice CTs. The Siemens 40 and 64-slice scanners use the z flying-focal spot to fast-switch the focal spot between two positions to double-sample each angle of projection data to achieve the effect of 40 and 64-slice data even though their detector channels are 20 and 32, respectively [6]. The detector size of 16, 20 and 40-slice Siemens CTs is 2.4 cm, and it is 2.88 cm for the 64-slice Siemens CT. The Philips 40 and 64-slice CTs have 4 cm detector coverage, and their data acquisition is at 32 × 1.25 mm for the helical 4D CT, which will shorten the acquisition time for their large coverage. It is important to note that slice broadening of 180 % in the low-pitch helical 4D CT prevents the smallest data element in data acquisition to be greater than 1.5 mm.

2.2.3 Image Location, Slice Thickness, and Scan Time

Helical 4D CT scan data allow for CT image reconstruction at any location by permitting data interpolation between two neighboring detector elements (Fig. 2.4), whereas cine 4D CT scan data allow for reconstructions only at the scan position. When using 4D CT to scan patients with lung cancer, it is important to have a complete coverage of the lungs for tumor delineation and dose calculation. The flexibility of image reconstruction at any location is not important as long as the images of uniformly spaced slices can be reconstructed to create a 4D volume. Typical image slice thicknesses in radiation treatment planning are 2–3 mm. There is a penalty from data interpolation in helical 4D CT as it widens the slice sensitivity profile, a measure of the slice thickness of the CT image. It is important to use thin slice collimation of 16 × 1.50 mm in helical 4D CT on a 16-slice MSCT scanner because data interpolation will widen the slice thickness to almost 2.7 mm (that is, the 1.5 mm slice will be thickened to 1.8 times its original width). Similarly, this means that if the detector configuration is 8 × 2.50 mm, the slice thickness will become 4.5 mm in helical 4D CT. Same 8 × 2.50 mm collimation in cine 4D CT will generate the slices of 2.5 mm because no data interpolation is in the cine CT image reconstruction. In diagnostic imaging, data interpolation causes only about 20 % widening when the pitch is greater than 0.5; the amount of widening reaches 180 % when the pitch is less than 0.2 (Fig. 2.5). To better understand this, we can take two independent slices

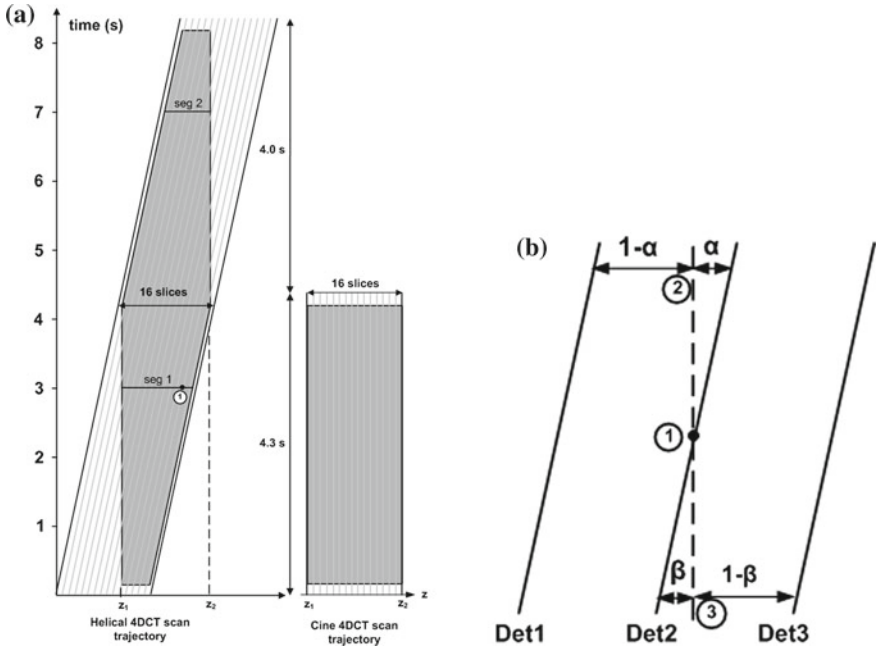

Fig. 2.4 Illustration of the concept that data interpolation widens the slice thickness. The scanning trajectories of helical and cine 4D CTs for a breath cycle of 4 s are shown in (**a**). The data in both "seg1" and "seg2" correspond to the same phase of the cycle. Data interpolation of the helical CT data around point 1 in "seg 1" is illustrated in (b). Note that 240° worth of CT data is needed for image reconstruction with HSR. The two *grey regions* in (**a**) indicate the 4D CT data between the two locations of z_1 and z_2. To scan only one breath cycle of 4D CT data, helical acquisition needs to scan for 8.3 s, whereas cine acquisition only needs 4.3 s, assuming the gantry rotation cycle $T_g = 0.5$ s. Helical CT data interpolation is illustrated in ((b). There is only one data point from Det2 ("Det" stands for detector) for data point 1 (no interpolation is needed); two data points of Det1 and Det2 are weighted by (1-α) and α for data point 2; and two data points of Det2 and Det3 are weighted by β and (1-β) for data point 3. The location of the reconstructed image is at the *dashed line*

of 2.5 mm at two neighboring locations in cine 4D CT and interpolate for an image located equidistant to the two slices; in such a case, interpolation would assign 50 % weight to each image, and the composite image will become a 5.0 mm slice (resulting in 200 % broadening of the slice thickness). Image reconstruction at pitch values of less than 0.1 in helical 4D CT significantly thickens the CT images as shown in Fig. 2.4. Once the pitch factor p becomes 0, helical CT interpolation is no longer needed and the helical 4D CT becomes cine 4D CT. That is the reason that the typical detector configuration in a 16-slice MSCT is 16×1.50 mm to keep the slice thickness <3 mm.

If the breath cycle is 4 s and the fan angle of the CT detector arc is 60°, and the gantry rotation cycle is 0.5 s, a cine 4D CT acquisition will take 4.3 s and a helical 4D CT acquisition 8.3 s to cover 2 cm on a 16-slice MSCT scanner (Fig. 2.4). The 8.3 s

was from 4 s breath cycle, 0.3 s of 60° arc and additional 4 s to allow for a complete breath cycle at the location of interest between z_1 and z_2. The longer acquisition time needed for helical 4D CT is due to the additional time needed for the table to translate to acquire the data over one respiratory cycle. Since the 4D CT acquisition for the lung cancer patient typically covers the whole lung, this overhead in the helical 4D CT acquisition is not significant. It contributes to a small amount of extra time required for acquisition and a small amount of extra radiation exposure to the patient. Overall, helical 4D CT is faster than cine 4D CT for imaging the thorax because in cine 4D CT the table will be paused to allow the table to move to the next position; the accumulated pause time lengthens the overall acquisition time required for cine 4D CT, making helical 4D CT a faster 4D CT. The speed up (in favor of helical 4D CT) and extra radiation (in favor of cine 4D CT) are both very small.

2.3 Workflow and Phase Selection Accuracy

The clinical workflow of helical 4D CT is illustrated in Fig. 2.6a. Once the pitch factor is determined on the basis of either Table 2.1 or 2.2, collections of the helical 4D CT data and the respiratory signal have to proceed simultaneously. Reconstruction of the helical 4D CT images will not start until completion of the scan and after the respiratory signal can be examined for accurate identification of the end-inspiration phases. This process allows for the reconstruction of 4D CT images at the specified phases in the helical 4D CT scan. Helical 4D CT tends to be slower than cine 4D CT in processing because the reconstruction is performed after (1) completion of the low-pitch helical CT scan and (2) verification of the end-inspiration phases in the respiratory signal. A suggestion to start image reconstruction before completion of data acquisition is possible. However, any change of image selection will likely result in additional image reconstruction. Because of these factors, multiple phases of helical 4D CT may not be available several minutes after the patient leaves the 4D CT acquisition session.

The clinical workflow of step and shoot cine 4D CT is illustrated in Fig. 2.6b. Data processing is generally faster for cine 4D CT than helical 4D CT to generate the 4D CT images. Once the average duration of the respiratory signal has been determined, the cine scan duration per location is set to the average duration plus 1 s. This additional 1 s is recommended in case the patient's breath cycle becomes longer during data acquisition. Image reconstruction starts immediately when there is enough data for one image to be reconstructed. The time interval between two CT image reconstructions should be less than T_g. For example, if $T_g = 0.5$ s, then the interval can be set at 0.25 s for 50 % data sharing between two image reconstructions to generate more images for data correlation with the respiratory signal, whose end-inspiration phases can be checked independently from the cine CT data collection. Increase of data sharing is to increase data sampling in cine 4D CT for data correlation so that the image selection will have a better chance of getting the images at the targeted phases. Because image reconstruction is performed independently from

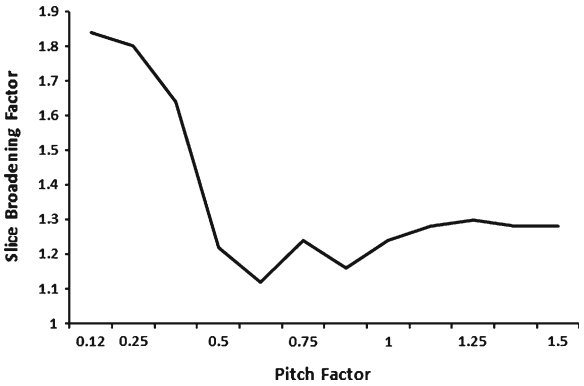

Fig. 2.5 The measured slice broadening factor in terms of full width half maximum over a range of pitch factors. When helical 4D CT is operated at a pitch of 0.1 or less, the thickness of the CT slice increases. For example, collimation of 16 × 1.5 mm will generate 2.7 mm-thick slices (calculated by multiplying the 1.5 mm collimation width by a factor of 1.8 to account for the effect of the low pitch)

acquisition of the respiratory signal, more accurate correlation of the CT images to a particular phase of the breathing cycle is possible when two successive image reconstructions share more data or the time interval between two images is much shorter than T_g.

In general, phase selection accuracy is better with helical 4D CT than with cine 4D CT because the reconstruction of a particular phase is determined before image reconstruction in helical 4D CT, but not in cine 4D CT. Figure 2.7 illustrates this point. In cine 4D CT, the reconstructed images may not correspond to the specified phases of 0, 10, 20, . . . , 90 %. However, the impact is not significant due to the fact that 4D CT is primarily used to depict the extent of tumor motion and that each CT image itself can cover more than 10 % of a respiratory cycle. For example a CT image reconstruction from 0.5 s of data is 12.5 % of a 4-s breath cycle and 10 % of a 5-s cycle. A difference of several percentages in image selection in the cine 4D CT will not degrade the utility of cine 4D CT. For a long respiratory cycle (exaggerated as a 10-s respiratory cycle in Fig. 2.7), helical 4D CT may result in less sampling of the 4D CT images than cine 4D CT would and therefore may not fully capture the extent of tumor motion depicted in the maximum intensity projection images [17]. It may be advisable to increase the number of phases in image reconstruction in helical 4D CT to improve the inclusion of the tumor motion so that the full extent of tumor motion will be included.

One important quality control measure that must be undertaken in 4D CT is to ensure that identification of the end-inspiration phases by the respiratory monitoring device is accurate. If phase calculation or identification is not accurate, both helical and cine 4D CTs will generate erroneous data, not representative of the 4D CT data. One example of this is illustrated in Fig. 2.8. Some end-inspiration phases in (a) were incorrectly identified or missing. The correct identification of the phases is shown in

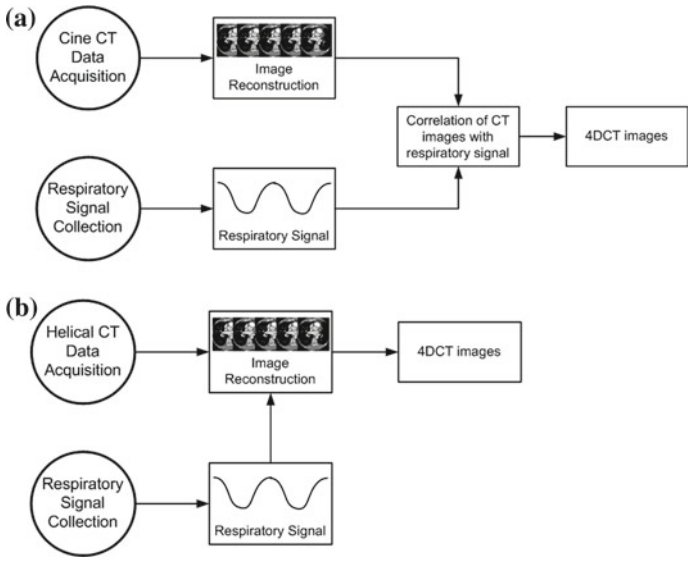

Fig. 2.6 (a) Helical 4D CT needs the respiratory signal to direct its image reconstruction. (b) Cine 4D CT does not need the respiratory signal for image reconstruction. The 4D CT images are generated on the basis of correlation between the cine CT images and the respiratory signal. The specific phases of the breathing cycle can only be approximated in the 4D CT images. In general, cine 4D CT generates 4D CT images more quickly than helical 4D CT

(b). This step of ensuring accurate identification of end-inspiration phases is critical and should be checked in every 4D CT data processing.

2.4 Commercial Helical 4D CT Systems

Philips and Siemens offer helical 4D CT. Both implementations were derived from the low-pitch helical CT scan of cardiac CT, which has pitch values p of 0.2–0.3 for a targeted heart rate of about 60 beats per minute. By lowering p to 0.1 or less, and replacing the electrocardiographic monitor with a respiratory monitor, the helical 4D CT for imaging the thorax under the condition of respiratory motion of 10–20 cycles per minute (corresponding to a 3- to 6-s respiratory cycle) becomes possible. The slower the respiratory motion, the smaller the pitch value p has to be to meet the DSC and to avoid under-sampling in helical 4D CT. An example of under-sampling is shown in Fig. 2.3c.

The pitch values p of the Philips CT scanners [2] and calculated values by Eq. (2.1) for the breathing cycles of 3–6 s and gantry rotations of 0.44 and 0.5 s for FSR are listed in Table 2.1. Both values match closely. When the gantry rotation time changes from 0.5 to 0.44 s, pitch values p become smaller because the shorter gantry rotation

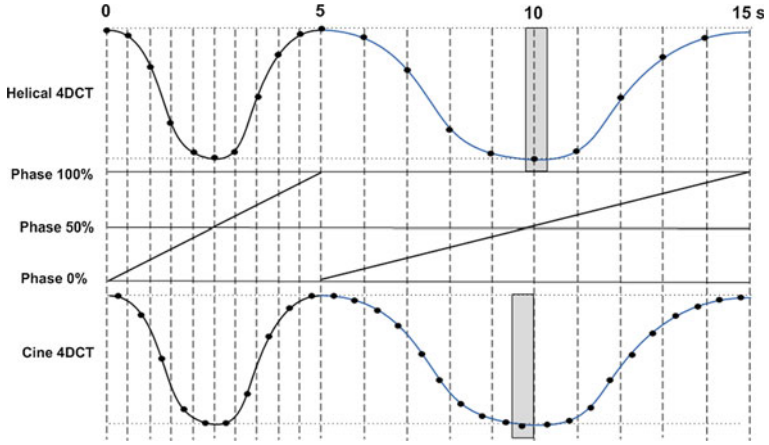

Fig. 2.7 Comparison of helical 4D CT and cine 4D CT in data acquisition and image reconstruction. Two respiratory cycles of 5 and 10 s are shown side by side, and the end-inspiration phase of each cycle is identified at the peak of each cycle. The 10 phases of the helical 4D CT images are reconstructed at the phases of 0–90 % in an increment of 10 %, or at the *vertical dashed lines*. Each *solid circle* indicates a reconstructed image. The two *gray regions* indicate the 0.5 s duration of data used in image reconstruction. In cine 4D CT, the images are reconstructed at 0.5-s intervals (assuming a gantry rotation cycle $T_g = 0.5$ s), which may not correspond to the exact positions of the 10 % phase increments denoted by the *vertical dashed lines*. At the time of data correlation with the respiratory signal, each cine CT image will be assigned to the closest phase and then all the images are combined to make up the 10 phases of the cine 4D CT images. Unlike cine 4D CT, Helical 4D CT can reconstruct the images at the exact respiratory phases. However, given a slower respiratory cycle such as the 10-s cycle, cine 4D CT reconstructs more images than helical 4D CT, resulting in more complete coverage of the tumor motion than in helical 4D CT

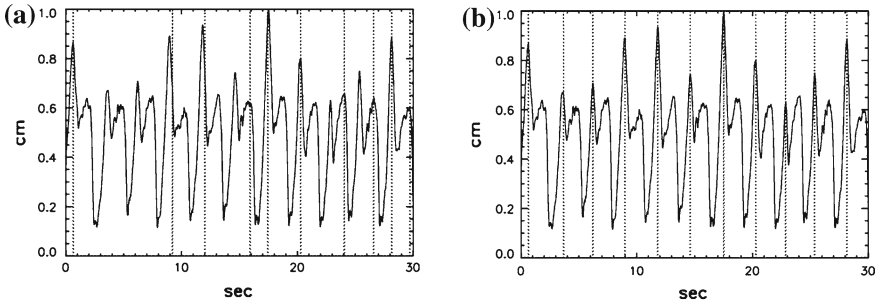

Fig. 2.8 **a** An example of a respiratory signal over 30 s with an inaccurate identification of the end-inspiration phases, marked by *dotted vertical lines*. **b** is the accurate identification of the end-inspiration phases

time allows the scanner to cover a larger volume for the same duration at the same pitch, which may cause the scanner to scan too fast and violate the data sufficiency condition. Equation (2.1) can be used to calculate the gantry rotation cycles and the breath cycle durations other than those listed in Table 2.1.

Table 2.1 Pitch values p for the Philips CT scanner and calculated values from Eq. (2.1) at the given gantry rotation cycles T_g and breath cycles of 3–6 s

	Phillips' design		Calculated values with FSR	
T_b	p @ $T_g = 0.5$	p @ $T_g = 0.44$	p@ $T_g = 0.5$	p @ $T_g = 0.44$
3	0.15	0.12	0.14	0.13
4	0.11	0.1	0.11	0.1
5	0.09	0.08	0.09	0.08
6	0.075	0.065	0.077	0.068

Table 2.2 Pitch values p for the Siemens CT scanner and calculated values from Eq. (2.1) at given gantry rotation cycles T_g and breath cycles of 3–6 s

	Siemens design		Calculated values with FSR	
T_b	p @ $T_g = 0.5$	p@$T_g = 1.0$	p @ $T_g = 0.5$	p @ $T_g = 1.0$
3	0.1	N/A	0.14	0.25
4	0.1	N/A	0.11	0.20
5	0.1	N/A	0.09	0.17
6	N/A	0.1	0.077	0.14

The Siemens pitch values [1] and theoretical values are listed in Table 2.2. This scanner uses a single pitch value of 0.1 and two gantry rotation cycles of 0.5 and 1.0 s [9]. Since the pitch values p stay the same, the gantry rotation time has to be increased with the duration of the breath cycle. This design is different from that of the Philips CT scanner, whose pitch value becomes smaller when the breath cycle becomes longer. In the Siemens design, a longer gantry rotation cycle of 1.0 s is required to slow down the scan speed to accommodate for a breath cycle of more than 6 s with the same pitch value of 0.1. One disadvantage in this design is that each CT image will have a temporal resolution of 1 s for FSR and 0.5 s for HSR. Longer breath cycles tend to have a longer duration of expiration than shorter cycles do. A decrease of the temporal resolution will increase image blurring in the CT image, particularly for the images acquired in the transition of the end-expiration phase to the end-inspiration phase, which tends to have the largest motion during respiration.

2.5 Respiratory Monitoring Devices

4D CT needs the timing information of the end-inspiration phase to guide its image reconstruction in helical 4D CT or image correlation in cine 4D CT. Many respiratory monitoring devices have been suggested [13]. The range of phases between two end-inspiration phases is denoted as 100 %. The phase is linearly increased from one end-inspiration phase to the next end-inspiration phase. One alternative is to select end-expiration phase as 50 %, and to linearly increase from 0 to 50 % and from 50 to 100 %. However, this may cause a smaller maximum-intensity-projection volume

Fig. 2.9 Respiratory monitoring devices used in 4D CT. (a) Two reflective markers on a plastic box and an infrared camera from Varian; (b) A pressure sensor from Anzai; and (c) Air bellow and pressure sensor from Philips

for tumor contouring [21]. Spirometer was used to measure the lung volume in inhale and exhale for the respiratory signal to correlate with the cine CT images for 4D CT [15]. The spirometer measurement is highly dependent on patient cooperation and, may not be reproducible. We will cover the three respiratory recording/monitoring devices adopted in the commercial 4D CT.

The most popular device for recording and monitoring the respiratory signal in 4D CT is the Real-time Position Management (RPM) respiratory gating system (Varian Medical Systems, Palo Alto, CA). The camera and the reflector box are shown in Fig. 2.9a. The system consists of multiple infrared emitting diodes, an infrared camera, a plastic box with two or six infrared reflective markers, and the optical tracing software and computer. The infrared emitting diodes are mounted on the camera, which receive the reflected infrared signal from the reflective markers on a plastic box sitting on top of the patient's abdomen between the umbilicus and xiphoid process. The RPM device can measure the patient's respiratory pattern and range of motion and displays them as a waveform. It can also send out triggers to enable prospective gating of CT. The plastic box, which is the only thing touching the patient, is almost radiation translucent, and the RPM can be integrated with some linear accelerators which use the device to turn the treatment beam on and off when the patient's breathing amplitude falls into the range of treatment. However, if the patient's abdomen or chest does not have a flat surface to allow the plastic box to sit on, placing the plastic box to the camera at the right angle may not be straightforward. The RPM system has been integrated in the GE and Philips 4D CTs.

Another device is the AZ-733V pressure sensor device (Anzai Medical Corporation, Tokyo, Japan) for recording the respiratory signal, respiratory gating and triggering. The system is comprised of chest/abdominal belt, pressure transducer (Fig. 2.9b), sensor port, Wave Deck (signal processing box), laptop PC with connecting cables and a trolley cart for storage and transport of the system. The pressure sensor can be easily attached to a patient with a Velcro belt. Measurement of the breathing signal is relative because the output of the pressure sensor is dependent on the tightness the Velcro belt fastened around the patient's chest or abdomen. One disadvantage of this system is that the sensor is radiopaque and can induce metallic artifacts. Placement of the sensor outside of the treatment field can avoid the metallic

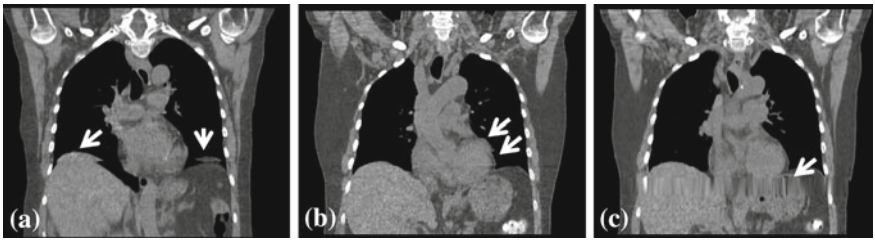

Fig. 2.10 4D CT artifacts due to (a) irregular respiration (b) misregistration in the cardiac region, not accounted for in 4D CT and (c) undersampling of a prolonged breathing cycle

artifacts. The AZ-733V system is integrated in the Siemens 4D CT. It has been shown that there is a high correlation between the AZ-733V and RPM [14].

A third device also used in 4D CT is the air bellow (Fig. 2.9c), which is an elastic belt positioned around the abdomen that expands and contracts with the respiratory motion [12].The device contains a pressure transducer, which converts the pressure waveform to a voltage signal, which is then digitalized and transmitted to the CT scanner. Using a respiratory bellow to monitor the breathing state has also been applied to CT-guided intervention procedure and MR imaging.

2.6 Image Artifacts

The basic assumption of 4D CT is that the respiratory motion is reproducible throughout the data acquisition and the duration of data acquisition at any location is at least one breath cycle plus the duration for one image reconstruction, which is one or 2/3 of a CT gantry rotation. Anything deviating from this assumption can induce artifacts manifested as (1) irregular respiratory motion, (2) misregistration at the cardiac region as the heart beating is not taken into account in 4D CT, and (3) missing data if the scan at a location is less than one breath cycle due to an under-estimate of the patient's breath cycle duration. As a result, a higher helical pitch p set in the Philips helical 4D or a faster CT gantry rotation set in the Siemens helical 4D, or a shorter cine scan duration set in GE cine 4D could introduce artifacts [8]. Figure 2.10 shows an example of these three types of artifacts.

2.7 Conclusions and Future Directions

4D CT was an important development for imaging the tumors subject to the respiratory motion for radiation therapy. Its development was very closely tied to the MSCT technology, commercialized in 1998. Helical 4D CT was adopted by Siemens and Philips and commercialized in 2006, and cine 4D CT was developed by GE and

commercialized in 2003. Both helical and cine 4D CT scans need to meet the requirement of data sufficiency condition to ensure there is at least one respiratory cycle of data at each location. Unlike cine 4D CT, helical 4D CT tends to result in thicker slices due to data interpolation and a longer workflow because image reconstruction cannot start until the respiratory signal of the helical 4D CT scan has been completely acquired. Commercial helical 4D CT can be performed by MSCT scanners of 16-slice or up, while cine 4D CT can be done using MSCT scanners with 4-slice or up. Three popular respiratory recording and monitoring devices are the optical device of RPM from Varian, the pressure sensor from Anzai and the air bellow pressure sensor from Philips. To ensure a complete depiction of tumor motion, one should obtain at least 10 phases of 4D CT images in helical 4D CT, in particular for patients with the breath cycle duration of more than 6 s. A very important quality control step in 4D CT is to ensure accuracy in identifying the end-inspiration phases of the respiratory signal because inaccurate identification of the end-inspiration phases will cause 4D CT to generate incorrect data.

For the future development, the capability of 4D CT to cope with the irregular respiration is critical, and deserves the attention of the research community. On the other hand, it may not be possible to demand an artifact free 4D CT due to the irregular respiration when 4D CT is applied on the patient population associated with the lung disease which manifests itself as coughing and irregular respiration.

References

1. Somatom Sensation Open Reference Manual, pp. 159–177
2. Quick Steps for Retrospective Spiral Respiratory Correlated Imaging with Varian RPM (2007). For the Brilliance CT Big Bore v2.2.2 system and the Brilliance 16–64 v2.2.5
3. Coolens, C., Bracken, J., Driscoll, B., Hope, A., Jaffray, D.: Dynamic volume versus respiratory correlated 4DCT for motion assessment in radiation therapy simulation. Med. Phys. **39**(5), 2669–2681 (2012)
4. Dewey, M., Zimmermann, E., Laule, M., Rutsch, W., Hamm, B.: Three-vessel coronary artery disease examined with 320-slice computed tomography coronary angiography. Eur. Heart J. **29**(13), 1669 (2008)
5. Flohr, T.G., McCollough, C.H., Bruder, H., Petersilka, M., Gruber, K., Suss, C., Grasruck, M., Stierstorfer, K., Krauss, B., Raupach, R., Primak, A.N., Kuttner, A., Achenbach, S., Becker, C., Kopp, A., Ohnesorge, B.M.: First performance evaluation of a dual-source CT (DSCT) system. Eur. Radiol. **16**(2), 256–268 (2006)
6. Flohr, T.G., Stierstorfer, K., Ulzheimer, S., Bruder, H., Primak, A.N., McCollough, C.H.: Image reconstruction and image quality evaluation for a 64-slice CT scanner with z-flying focal spot. Med. Phys. **32**(8), 2536–2547 (2005)
7. Ford, E.C., Mageras, G.S., Yorke, E., Ling, C.C.: Respiration-correlated spiral CT: a method of measuring respiratory-induced anatomic motion for radiation treatment planning. Med. Phys. **30**(1), 88–97 (2003)
8. Han, D., Bayouth, J., Bhatia, S., Sonka, M., Wu, X.: Characterization and identification of spatial artifacts during 4D-CT imaging. Med. Phys. **38**(4), 2074–2087 (2011)
9. Hurkmans, C.W., van Lieshout, M., Schuring, D., van Heumen, M.J., Cuijpers, J.P., Lagerwaard, F.J., Widder, J., van der Heide, U.A., Senan, S.: Quality assurance of 4D-CT scan

techniques in multicenter phase III trial of surgery versus stereotactic radiotherapy (radiosurgery or surgery for operable early stage (stage 1A) non-small-cell lung cancer [ROSEL] study). Int. J. Radiat. Oncol. Biol. Phys. **80**(3), 918–927 (2011)
10. Kalender, W.A., Seissler, W., Klotz, E., Vock, P.: Spiral volumetric CT with single-breath-hold technique, continuous transport, and continuous scanner rotation. Radiology **176**(1), 181–183 (1990)
11. Keall, P.J., Starkschall, G., Shukla, H., Forster, K.M., Ortiz, V., Stevens, C.W., Vedam, S.S., George, R., Guerrero, T., Mohan, R.: Acquiring 4D thoracic CT scans using a multislice helical method. Phys. Med. Biol. **49**(10), 2053–2067 (2004)
12. Klahr, P., Subramanian, P., Yanof, J.H.: Respiratory-correlated multislice CT for radiation therapy planning: imaging and visualization methods. Medicamundi **49**(3), 34–37 (2005)
13. Kubo, H.D., Hill, B.C.: Respiration gated radiotherapy treatment: a technical study. Phys. Med. Biol. **41**(1), 83–91 (1996)
14. Li, X.A., Stepaniak, C., Gore, E.: Technical and dosimetric aspects of respiratory gating using a pressure-sensor motion monitoring system. Med. Phys. **33**(1), 145–154 (2006)
15. Low, D.A., Nystrom, M., Kalinin, E., Parikh, P., Dempsey, J.F., Bradley, J.D., Mutic, S., Wahab, S.H., Islam, T., Christensen, G., Politte, D.G., Whiting, B.R.: A method for the reconstruction of four-dimensional synchronized CT scans acquired during free breathing. Med. Phys. **30**(6), 1254–1263 (2003)
16. Pan, T.: Comparison of helical and cine acquisitions for 4D-CT imaging with multislice CT. Med. Phys. **32**(2), 627–634 (2005)
17. Pan, T., Lee, T.Y., Rietzel, E., Chen, G.T.: 4D-CT imaging of a volume influenced by respiratory motion on multi-slice CT. Med. Phys. **31**(2), 333–340 (2004)
18. Parker, D.L.: Optimal short scan convolution reconstruction for fanbeam CT. Med. Phys. **9**(2), 254–257 (1982)
19. Siebert, E., Bohner, G., Dewey, M., Masuhr, F., Hoffmann, K.T., Mews, J., Engelken, F., Bauknecht, H.C., Diekmann, S., Klingebiel, R.: 320-slice CT neuroimaging: initial clinical experience and image quality evaluation. Br. J. Radiol. **82**(979), 561–570 (2009)
20. Vedam, S.S., Keall, P.J., Kini, V.R., Mostafavi, H., Shukla, H.P., Mohan, R.: Acquiring a four-dimensional computed tomography dataset using an external respiratory signal. Phys. Med. Biol. **48**(1), 45–62 (2003)
21. Zamora, D.A., Riegel, A.C., Sun, X., Balter, P., Starkschall, G., Mawlawi, O., Pan, T.: Thoracic target volume delineation using various maximum-intensity projection computed tomography image sets for radiotherapy treatment planning. Med. Phys. **37**(11), 5811–5820 (2010)

Chapter 3
Acquiring 4D Thoracic CT Scans Using Ciné CT Acquisition

Daniel Low

Abstract One method for acquiring 4D thoracic CT scans is to use ciné acquisition. Ciné acquisition is conducted by rotating the gantry and acquiring x-ray projections while keeping the couch stationary. After a complete rotation, a single set of CT slices, the number corresponding to the number of CT detector rows, is produced. The rotation period is typically sub second so each image set corresponds to a single point in time. The ciné image acquisition is repeated for at least one breathing cycle to acquire images throughout the breathing cycle. Once the images are acquired at a single couch position, the couch is moved to the abutting position and the acquisition is repeated. Post-processing of the images sets typically resorts the sets into breathing phases, stacking images from a specific phase to produce a thoracic CT scan at that phase. Benefits of the ciné acquisition protocol include, the ability to precisely identify the phase with respect to the acquired image, the ability to resort images after reconstruction, and the ability to acquire images over arbitrarily long times and for arbitrarily many images (within dose constraints).

3.1 Introduction

One of the uses of CT scan acquisition is to obtain images that can be used to model human breathing motion. CT scans are relatively fast; modern scanners can acquire images in less than 0.4 s, and around 0.2 s if fewer than 360° of projections are required. This speed reduces breathing motion artifacts that occur when scanner rotation periods are more than 1 s.

There are two basic modes of CT scanning. By far, the most common is helical CT (the subject of Chap. 2), whereby the CT scanner rotates as the couch moves with a uniform speed. The radiation beam central axis traces a helix through the patient

D. Low
UCLA Radiation Oncology, Los Angeles, CA, USA
e-mail: DLow@mednet.ucla.edu

J. Ehrhardt and C. Lorenz (eds.), *4D Modeling and Estimation of Respiratory Motion for Radiation Therapy*, Biological and Medical Physics, Biomedical Engineering,
DOI: 10.1007/978-3-642-36441-9_3,

as the projection data are acquired. This method is the most efficient method for acquiring CT data. The couch can be moved more than the width of the collimated beam during each rotation (pitch >1) which, when coupled with a fast rotation rate and large longitudinal coverage, makes helical scanning extremely fast; CT scans of the thorax can be acquired within two seconds with modern scanners.

The couch motion for helical scanning is typically constrained to be constant; once the parameters of pitch, field size, and rotation rate are selected, the couch speed is fixed. While this is not a problem for standard scanning, it provides a significant constraint for 4D imaging. In order to acquire useful breathing modeling data, CT data need to be acquired during at least one breath. Breathing periods are approximately 5 s, so the minimum time that any one region of tissue needs to be imaged is 5 s. While the CT scanner rotation rate can be slowed down to guarantee that each portion of the patient is being imaged for 5 s, such slow acquisition will lead to breathing motion artifacts. The CT scan rotation period needs to be less than 0.5 s to avoid these artifacts. Rather than slow rotation rate, most helical CT scanning protocols reduce the pitch, slowing the couch and acquiring multiple images at each location within the patient. The protocols are designed such that each portion of the patient is scanned for a period of at least 5 s [3, 7].

While helical scanning is the dominant acquisition mode and a 4D helical scanning solution has been found and implemented for most commercial systems, helical scanning has some significant limitations. First, the minimum pitch for CT scanners is approximately 0.15, which when combined with a rotation rate of 0.5 s, leads to a total amount of time that any one location is scanned of 0.5/0.06 s = 8.33 s. This amount of time is greater than the breathing period for most patients, which means that for most patients and most times, CT images will be scanned throughout the breathing cycle for the whole patient. Many patients have irregular breathing cycles and some take pauses in their breathing. The CT scanner cannot pause a helical CT acquisition, so image artifacts will occur if the patient breathing pauses for more than a few seconds. Figure 3.1 shows examples from Lu et al. [6] of breathing patterns that have such irregularities.

3.2 Benefits of Ciné CT

Ciné acquisition, in contrast to helical acquisition, is conducted with a stationary couch. The CT scanner rotates and acquires projection data over a longitudinal span that nearly matches the radiation field length. The length of this span depends on the detector layout and is usually between 2 and 4 cm (see Sect. 2.2.2). The number of acquisitions per couch position is programmed in advance and the CT rotation time determines the temporal resolution of the scan. The number of scans multiplied by the scan period is the minimum amount of time that scans can be acquired for, but pauses between scans can be programmed to lengthen the effective scan time to assure that at least one breathing period occurs at each couch position. In fact, the

amount of time can easily be stretched to multiple breathing periods to reduce the chance that no motion data are acquired because of breathing irregularities.

Ciné CT acquisition provides many benefits over helical acquisition. Principally, the number of scans is selectable and not constrained by couch speed limitations. Prospective gating is also possible with ciné-CT [4]. Ciné-CT protocols can be programmed to be started by an external trigger, set for example to specific phases of the breathing cycle. Sophisticated analysis of the breathing cycle could be conducted to assure that only images that will provide the required breathing motion data will be acquired, reducing the radiation dose to the patient and improving the usability of the CT scan data.

CT images are reconstructed using x-ray projections from up to 360°. In helical multislice CT, the projection angles also include an out-of-plane angle. Ideally these projections would be acquired over a limited period of time. In order to minimize image noise, however, when reconstructing an image at a specific breathing phase, manufacturers utilize each projection acquired during a time consistent with that breathing phase. The projections may therefore be acquired during different breaths. If the user wants to use the commercial sorting algorithm to reconstruct images, there is no problem, but if the user wants to control the specific timepoints from which projection data are taken, this process is not useful. An advantage of ciné CT is that the projections used to acquire the CT data are acquired only during the gantry rotation time for the specific ciné acquisition. This allows the user to precisely control the timepoints at which the data are acquired for subsequent reconstructions. Pat et al. [7] compared data sufficiency conditions for helical and ciné acquisitions using a 20 cm coverage, 4 s breathing cycle, half-scan reconstruction. He found that the helical acquisition benefited from more rapid scan time (by 10 %) than the ciné acquisition. The helical slice sensitivity profile was 1.8 times broader than the ciné profile and required an additional breathing cycle of scanning at the beginning and end of the scan to assure adequate sampling at the ends of the scans. The ciné scans also delivered between 4 and 8 % less dose than the helical acquisition.

Table 3.1 shows a summary of the comparison between helical and ciné acquisitions.

Table 3.1 Summary of the comparison between helical and ciné acquisition

	Ciné	Helical
Temporal resolution	++	+
Temporal control (knowing when image data were acquired)	++	–
Spatial resolution (blurring)	++	+
Ability to prospectively gate	++	–
Image artifacts	–	+
Ability to manage irregular breathing	+	–
Ability to do amplitude based sorting	++	++
Acquisition flexibility	++	–
Cone beam artifacts (assuming fan-beam ciné reconstruction)	–	++

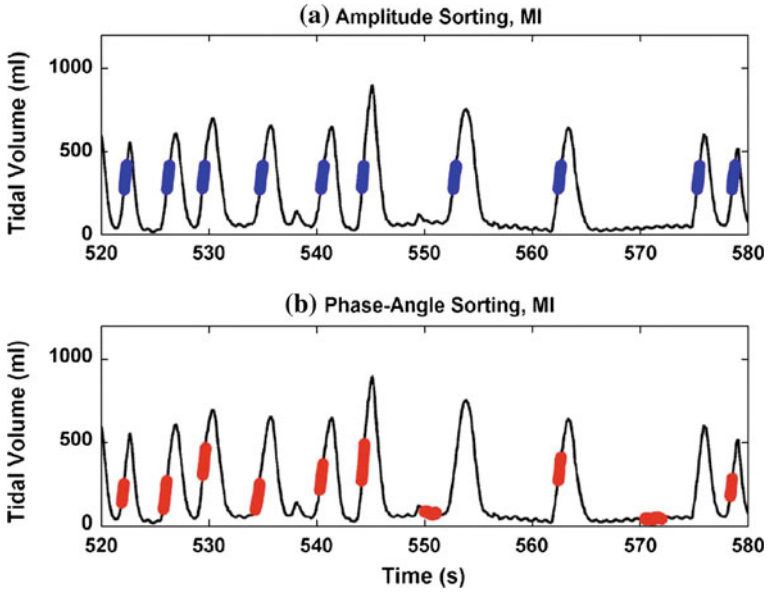

Fig. 3.1 Example of irregular breathing waveforms highlighting that breathing patterns can pause for times approaching 10 s. Figure is from Lu et al. [6]

3.3 Development of Volumetric CT Using Ciné CT Scans

Ciné CT scan acquisition yields a series of CT slice scans (collections), each acquired at different times and breathing phases. Between 10 and 25 repeated CT scans are acquired per table position before the table is moved to the next position, and this process is repeated until the entire volume of interest is scanned. The process of generating useful 4D CT images that encompass the organs of interest involves the building of 3D CT images at different breathing phases using the acquired ciné images.

There are two current approaches to generate 4D CT images from ciné CT acquisitions and a breathing surrogate measured at acquisition time. They are termed amplitude-based sorting and phase-based sorting. Figure 3.2 shows an example of the amplitude-based process as described by Low et al. [5]. They selected the tidal volume measured with spirometry as the method for describing the breathing cycle. To create a 3D CT image at a specific tidal volume, they selected the ciné scans that were obtained at each couch position with a tidal volume closest to the desired volume. The result was a full 3D CT that represented the patient geometry as though the patient had been scanned at that tidal volume. This process could be repeated for any tidal volume for which there was sufficient scan data.

General Electric used a phase-based approach with their commercial ciné 4D CT scanners [8, 10]. Figure 3.3 shows the process that GE uses to acquire their

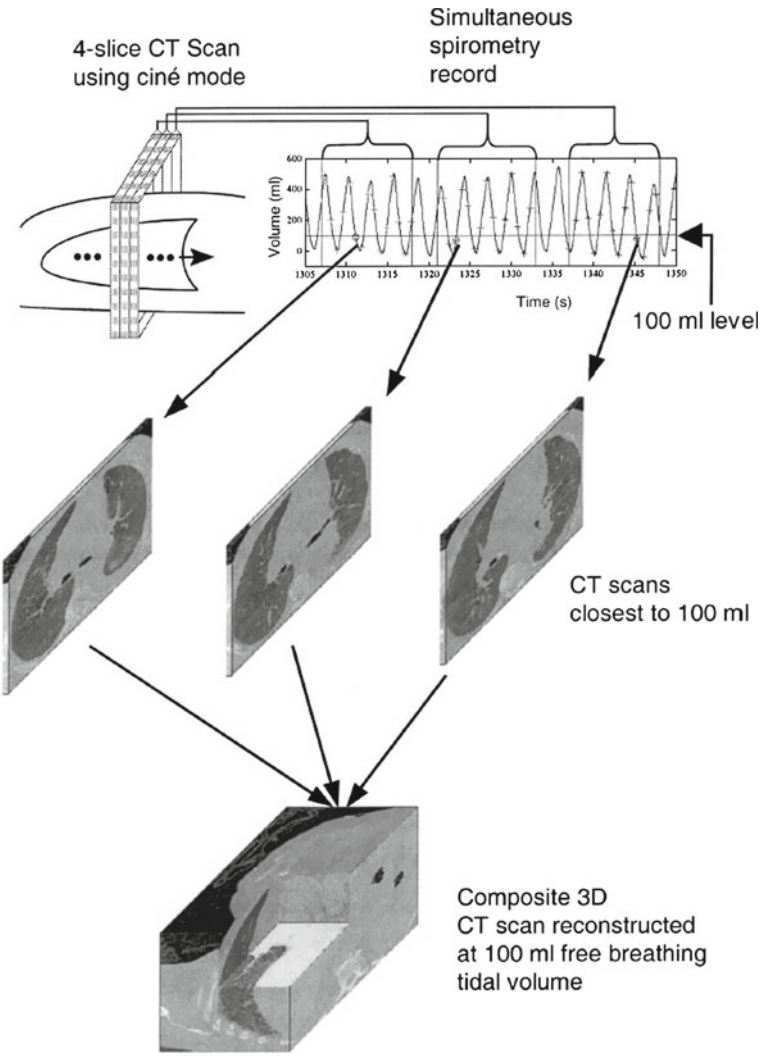

Fig. 3.2 Process for building a 3D CT scan from sequentially acquired ciné CT image datasets. In each couch position, a number of ciné images are acquired. The image is from Low et al. [5]

4D CT scans. The scans are acquired at the same time as a breathing surrogate is measured. The breathing cycles are divided in phases that are equal in time between inhalations. The images acquired in each phase are collected for each table position to form single-phase CT images, similar to what is done in Fig. 3.2 for breathing amplitude gating.

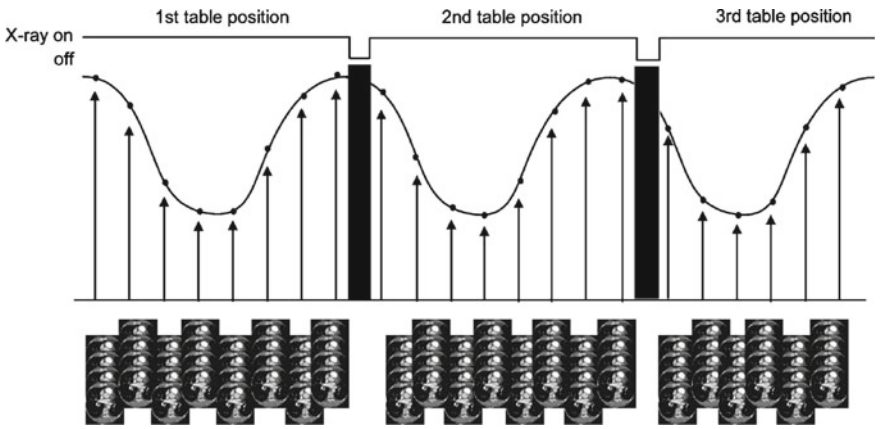

Fig. 3.3 Phase-based reconstruction of 4D CT scans using a commercial phase-based sequence. The figure is from Pan et al. [8]

3.3.1 Amplitude and Phase-Angle Sorting

CT manufacturers have long provided robust cardiac gating acquisition and sorting tools. This is because the cardiac cycle is straightforwardly measurable and temporally stable. Typically, CT scans required well monitoring the cardiac cycle and the x-ray projections are resorted according to the cardiac phase, which is defined as the relative time between equivalent points in the cardiac cycle. Because of the stability of the cardiac cycle, this approach has been extremely successful. Figure 3.4 shows an outstanding surface rendered image of the heart from Wijesekera et al. [11]. In contrast, Fig. 3.5 shows an example of retrospectively phase-based sorted 4D CT acquired using a ciné protocol [4]. Artifacts are present at the dome of the diaphragm and tumor volume and shape (below the cross-hairs in each of the four images) are altered from phase to phase making it difficult to delineate correctly. Such artifacts are common because breathing is less reproducible than cardiac motion, and both approaches to sorting respiratory-gated CT scans are affected from this motion variability.

3.3.1.1 Phase-Angle Sorting

In phase-angle gating, the breathing cycle is assumed to be reproducible in time; each breath is assumed to have the same characteristics as other breaths. A specific phase is selected as the start of respiration. The time between then and the time at which that same phase is next reached is a single breathing period. The breathing cycle is subdivided as a fraction of the time between those phases. For example, if the breathing cycle is begun at peak exhalation, and the time to the peak inhalation is

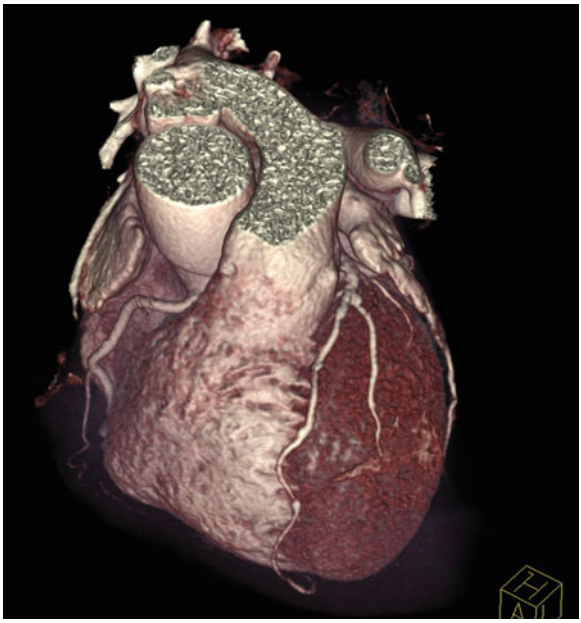

Fig. 3.4 Surface rendered image of the heart acquired using cardiac gated CT. The figure is from [11].

40 % of the total breathing period, peak inhalation is said to occur at the 40 % phase. Often, phases are described in terms of angles with 360° between successive breaths.

Phase angle sorting is effective for regular breathing patients. The patient's breathing amplitude is consistent, so their internal anatomy will reproducibly located in the same place during the same phase angle. When breathing is irregular, however, the algorithm breaks down. For example, if a deep breath is followed immediately by a shallow breath, the peak inhalation phase will be identified in both breaths and be considered equivalent. The phase angle sorting algorithm will collect image data from both of those breaths at the same phase and include them in an image that is representative of inhalation. Clearly, the internal anatomy will be positioned differently for the deep and shallow breaths. Because of the similarity between phase angle respiratory sorting and cardiac sorting, this algorithm was the first to be commercially implemented because of the significant effort that imaging vendors had already invested in cardiac imaging.

Seppenwolde et al. [9] reported in 2002 their breathing motion model which was based on the phase angle approach. They had reviewed a series of fluoroscopic video images of implanted fiducial markers in a large number of lung cancer patients. The motion of the markers appeared either straight or took an elliptical pattern. They parameterized the motion into components that were aligned to the motion ellipses. Their model provided flexibility such that it could accommodate both straight and elliptical motion. For example, in Fig. 3.6, two examples are shown, one with straight

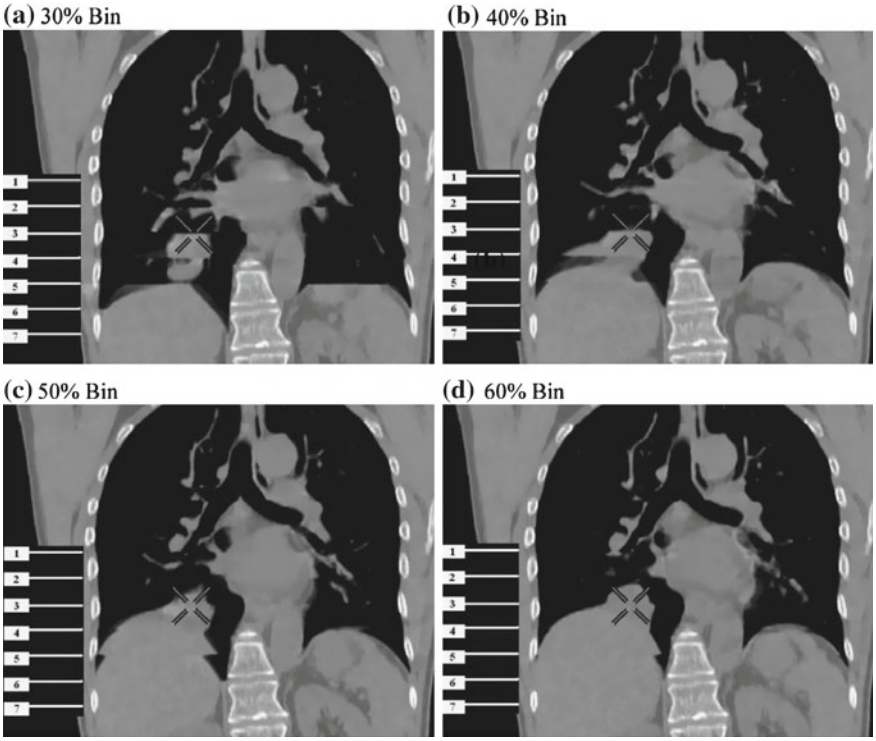

Fig. 3.5 Examples of artifacts in ciné CT caused by irregular breathing and retrospective sorting (image taken from [4]). The *numbered lines* on each image represent the detector span for different couch positions (2 cm in this case). The cross-hairs provide a common reference point in each image

and one with elliptical motion. As can be seen by the figure, the development of elliptical motion comes from a phase difference between the two directional components. While this technique worked well for regular breathing, it failed to allow the modeler to manage irregular breathing. Figure 3.7 compares modeled motion to measured motion in the craniocaudal direction for two patients. Figure 3.7a represents a regular breather and shows the model was able to accurately describe breathing motion. Figure 3.7b shows an irregular breather, in this case defined as a breathing pattern with a variable frequency. The model, having fixed frequency, phase, and amplitude is unable to manage variations in any of these quantities.

3.3.1.2 Amplitude-Based Sorting

In contrast to phase angle sorting, amplitude-based sorting assumes that internal anatomical positions of tissues are functions of the depth of breathing rather than the fraction of time between successive breaths. Irregularity in breathing amplitude

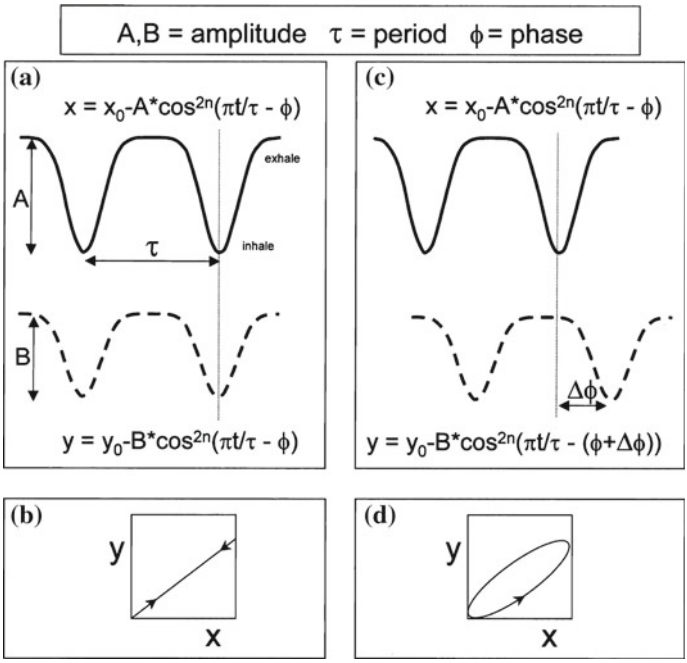

Fig. 3.6 Breathing tissue motion model proposed by Seppenwolde et al. [9]. The model describes embedded radiopaque marker locations as periodic functions in time

or frequency is straightforwardly managed by amplitude sorting. Images acquired during irregular breathing incur fewer artifacts when using amplitude sorting than phase angle sorting. The main issue with amplitude-based sorting is that it does not distinguish between inhaling and exhaling, so that a specific amplitude during mid-inhalation and mid-exhalation will be treated the same. This makes it impossible to model hysteresis motion with strict amplitude-based approaches. However, the greatest component of motion is not due to hysteresis but due to the expansion and contraction of lungs during inhalation and exhalation, respectively.

Lu et al. [6], examined phase angle and amplitude based sorting and its relation to irregular breathing. They reconstructed 3-D image data sets for 12 breathing phases for 40 patients, computing the air content, defined as the integrated amount of air in the lungs based on the CT scan and using air content as a surrogate for tumor position. They correlated breathing phase and amplitude to air content and determined the correlation residual. In most cases, amplitude sorting resulted in a smaller residual than phase angle sorting. When tidal volume was used as the comparator, the variation was always less for amplitude than phase angle gating. Figure 3.1 shows an example from Lu et al. [6] that explains the differences between amplitude and phase-angle sorting for an irregular breathing patient. The times that are consistent with a specific part of the breathing cycle, in this case the definition of mid-inspiration, are

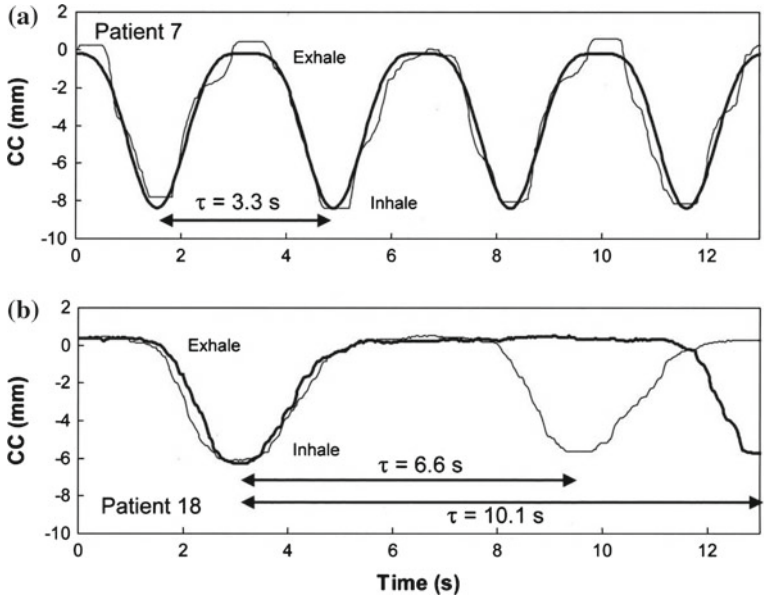

Fig. 3.7 Example of breathing motion model results from Seppenwoolde et al. [9] for (**a**) a regular-breathing patient and (**b**) irregular breathing patient (defined here as a patient with a variable breathing period). The model works well when the breathing frequency, amplitude, and phase are stable, but breaks down if any of these three factors change

highlighted in the figure. The selected times correspond to the point in time where projection data would be used to reconstruct a mid-inspiration image. In the amplitude sorted case (Fig. 3.1a), those points in time are identified when the patient's tidal volume was between 250 and 450 mL. In contrast, Fig. 3.1b shows mid-inspiration times when phase-based sorting is used. In this example, mid-inspiration was defined as halfway in time between maximum expiration and maximum inspiration. When examining the amplitudes during these times, times where the phase-based sorting algorithm would select projection data, it is clear that not all of the times correspond to a physiologically reasonable definition of mid-inspiration.

3.4 Challenges with Ciné CT

3.4.1 Cone-Beam Artefacts in Ciné CT

Single slice CT projections can be approximated as being one-dimensional. The finite longitudinal dimension causes volume averaging. Multislice CT scanners, on the other hand have longitudinally diverging beams. The projecting rays of even a

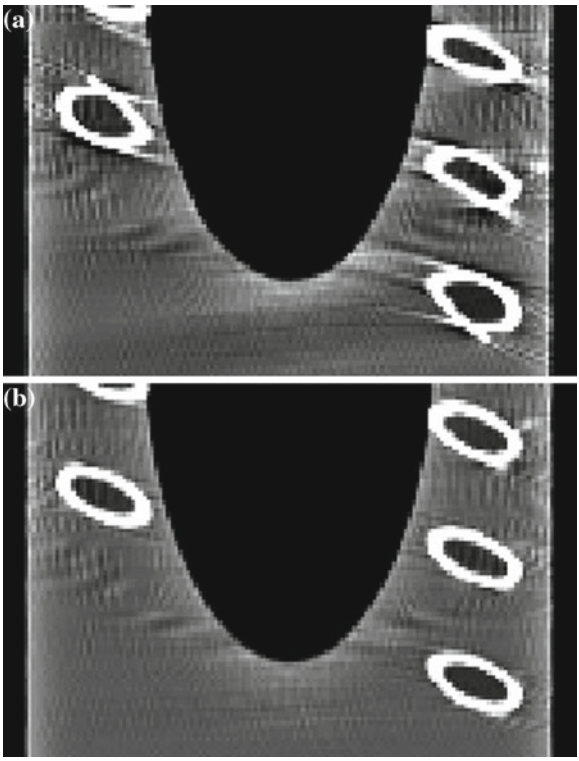

Fig. 3.8 Example of cone-beam artifacts in multisclice CT scanners. **a** This image was reconstructed using fan-beam reconstruction. **b** This image was reconstructed using cone-beam reconstruction. Images are from Barrett and Keat [1]

4-slice CT scanner are not parallel to the plane of rotation for the first and fourth slice. Images can be reconstructed assuming that the rays for each slice lie in parallel planes and for a 4-slice CT scanner this approximation does not cause significant image artifacts.

As the number of slices increases, and specifically the out-of-plane angle of the rays increases, the images start to contain cone-beam artifacts. Figure 3.8 shows an example of scans of a chest phantom acquired using a 16-slice CT scanner [1]. Figure 3.8a, b were reconstructed using fan-beam reconstruction and cone-beam reconstruction, respectively. The chest phantom includes synthesized ribs that provide high contrast surfaces with which to evaluate the artifacts. The ribs in the fan-beam reconstructed images contain clear artifacts in spite of the fact that the scanner used to acquire these images was only 16 slice (there are 356 slice scanners available). The artifacts disappear when cone-beam reconstruction is used.

Manufacturers of CT scanners often do not reconstruct ciné images using cone-beam algorithms. Cone-beam algorithms remove the artifacts by using projections that would otherwise be associated with more-off axis slices. This reduces

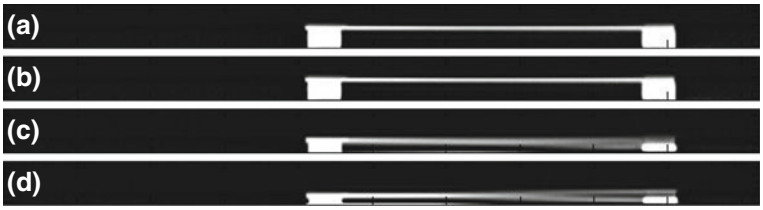

Fig. 3.9 Coronal CT images of a cylindrical acrylic rod of 3 mm diameter illustrating the blurring and doubling cone-beam CT artifact. The entire 500 mm FOV of the scanner is displayed. **a** Rod placed at Z = 1 mm relative to the center of field of view. **b** Rod placed at Z = 3.6 mm. **c** Rod placed at Z = 6 mm. **d** Rod placed at Z = 8.4 mm

the reconstruction volume such that it is no longer equal to the number of slices multiplied by the slice width. Acquisition of abutting ciné CT volumes would require overlapping of the radiation fields, which manufacturers are reluctant to do. Cone-beam artifacts become worse as the cone-beam angle increases.

An example of the impact of cone beam artifacts is shown in Fig. 3.9. A 3 mm diameter cylindrical acrylic rod was scanned using a 64 slice CT scanner with a 4 cm coverage. The acrylic rod was placed to intercept the central detectors and was oriented in the transverse plane. A single scan was acquired and then the rod was moved and scanned a total of three times, each time at a greater and greater distance from the central axis plane. When the rod was placed near the edge of the field of view in both the axial (8.4 mm) and longitudinal directions, the image of the rod was split by at least 5 mm. This implies that soft tissue structures such as vessels, bronchial branches, and nodules would exhibit similar splitting near the field edge. Figure 3.10 shows intensity profiles taken in a longitudinal direction through the images of the acrylic rod when the rod was 8.4 mm from the central plane. The profiles are identified by their distance from the central axis. The variation in the imaged shape of the cylindrical rod is evident in the profiles. When the rod is near the CT scanner central axis, the profile is nearly Gaussian in shape. At approximately 8 cm from central axis and extending to the edge of the field, the shape of the profile changes from a single peak to a double peak, consistent with the image shown in Fig. 3.9d.

The cone-beam artifacts do not appear to affect clinical use of lung CT scans. The structures that are impacted are the small vessels and bronchi, which are typically not the subject of contouring or segmentation. Motion artifacts are usually present in these CT scans and some of the cone-beam artifacts may have been misinterpreted as motion artifacts. The challenge with having these artifacts present in the images comes when the images are being used with automated segmentation. Systematic artifacts that make the tissues appear differently depending on which detector row they intersect will make registration difficult because the registration algorithms expect the structures to have consistent shapes no matter where they are imaged.

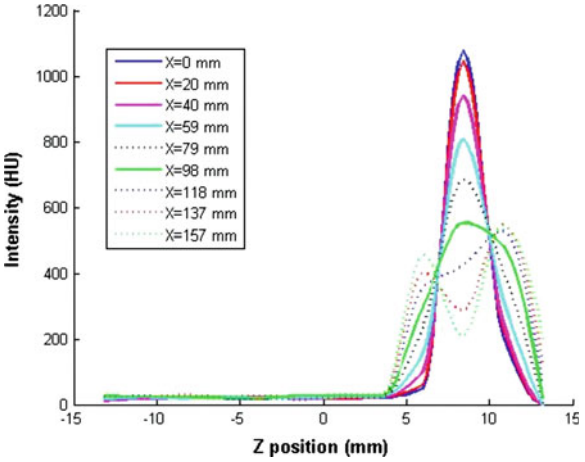

Fig. 3.10 Longitudinal profiles of the image of the acrylic rod at various sagittal slices (as indicated in the legend). The rod was placed horizontally in an axial plane Z = 8.4 mm relative to the center of the FOV. The profiles have been interpolated from the raw pixel values using cubic interpolation

3.4.2 Abutment Challenges

An important step in developing breathing models is mapping the breathing motion. Ciné CT scans have the advantage that the time of acquisition is accurately known so the specific breathing phase associated with the scan data can also be accurately determined. This allows researchers in breathing motion modeling to assign breathing phases. However, in all cases, some form of image registration is required to map the motion of the lung tumor or normal lung to provide the raw data for a breathing model.

Tissue registration, specifically deformable image registration is challenging for ciné CT acquired image data. If the user intends to build a volumetric CT at a specific breathing phase, misregistration artifacts will occur at the abutment regions between neighboring ciné acquisitions. These are caused by the use of images that were acquired at slightly different breathing phases so the lung tissues do not match exactly at the abutments. Image registration algorithms are ill-suited to manage such tissue discontinuities. One way of managing this is to deformable register images to a common breathing phase and then stack them to form a single volumetric image dataset that corresponds to that phase. This was proposed by Ehrhardt et al. [2]. They used tidal volume as the method of describing the breathing cycle and interpolated pairs of ciné images to a selected tidal volume. The two sets of ciné images that were closest to the desired tidal volume, one larger and one smaller, were used. The full image registration using optical flow defined motion vectors between images and the resulting image was interpolated to the appropriate tidal volume. Figure 3.11 shows an example of the interpolation process. The diaphragm dome shows the amount of

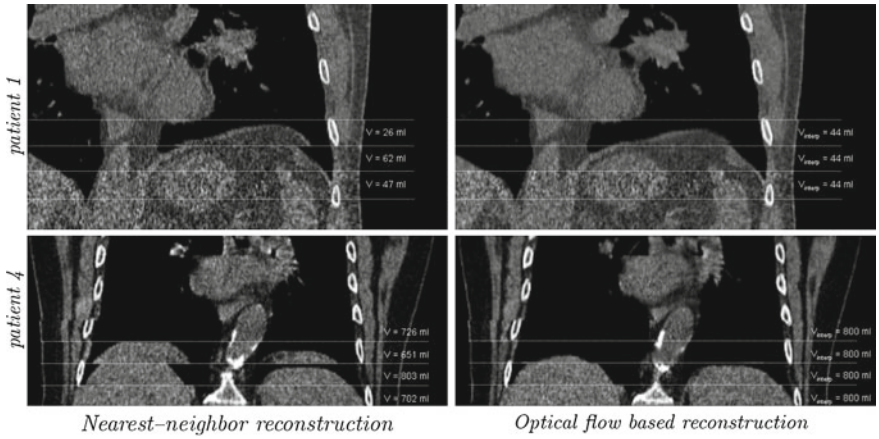

Fig. 3.11 Examples of the impact of interpolating to a common breathing phase (in this case 44 and 800 ml tidal volumes) on the image abutment quality for ciné CT scanning. Figure from Ehrhardt et al. [2].

misregistration when nearest neighbor tidal volumes are used. Using optical flow interpolation the misregistration artifact becomes much smaller.

3.5 Future of Respiratory Sorting

Even when employing amplitude-based sorting, and managing the variation in breathing amplitude, the breathing amplitude variations still have an impact in the quality of the resulting CT scans as well as the interpretation of the scans. For example, as shown in Fig. 3.1, there is a single breath near the time point of 545 s that is deeper than the remaining breaths. The internal lung tissues presumably moved to locations that differed from the rest of the breaths shown in Fig. 3.1. Treatment plans conducted using amplitude-based sorting would not likely have the feedback to know that the patient takes an occasional deep breath. Therefore, some feedback to provide the planner with an understanding of motion outside of that which is provided by the images would be extremely useful.

Figure 3.12 shows the breathing pattern for a regular breathing patient as well as a differential histogram that shows the relative time that the patient spent at each amplitude. The breathing histogram can be used firstly to identify meaningful definitions of peak inhalation and exhalation. Rather than select the two points in time that have the maximum and minimum breathing extent, a more useful definition would be based on the ability to generate an amplitude based CT scan with only minor artifacts. The minimum amplitude for which a useful CT scan can be constructed is typically the 5th percentile. Similarly, an amplitude for which a CT scan can reliably be constructed at inhalation is often the 85th percentile. The histogram shows both

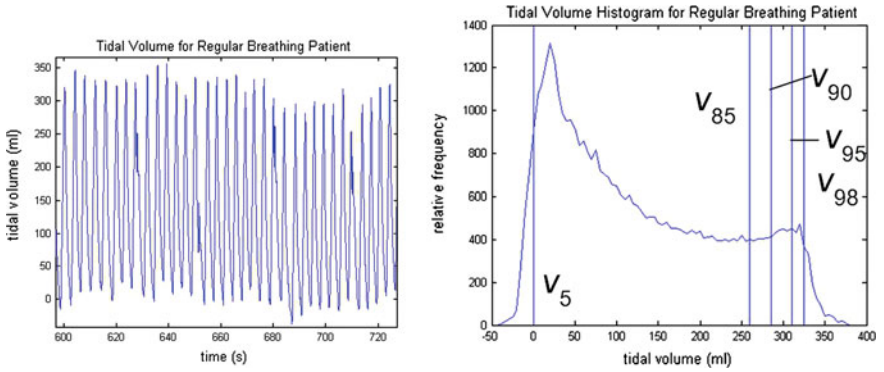

Fig. 3.12 **a** Breathing pattern for a regularly breathing patient. **b** The histogram corresponding to the breathing pattern shown in **a**. The tidal volume percentiles are shown for reference

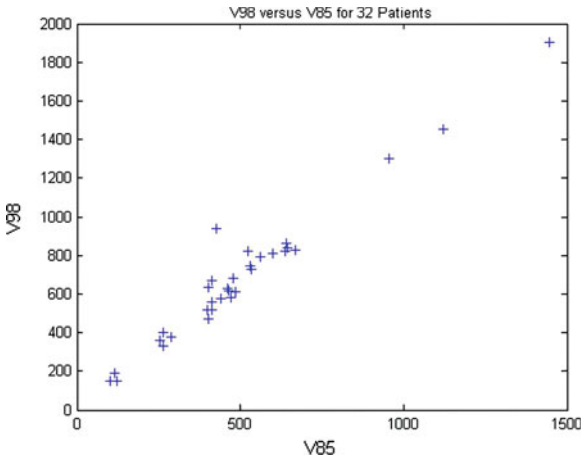

Fig. 3.13 Comparison of two tidal volumes that could correspond to inhalation for a cohort of 32 patients. V_{85}, is often the tidal volume whereby a reliable CT scan can be reconstructed while V_{98} is useful as a metric for deeper inhalation. Linear regression shows that the relationship between the two is 1.39 ± 0.19

of these values. However, constructing images at the fifth and 85th percentiles to signify exhalation and inhalation, respectively, ignores the 20 % of time that the patient spends outside of those amplitudes. Therefore, the treatment planner is unaware of how much they should extrapolate the motion they see on the reconstructed CT scans to encompass more of the actual motion envelope.

Figure 3.13 shows the relationship between the 98th percentile and the 85th percentile (relative to the 5th percentile) for 32 patients. The relationship is remarkably linear and has a slope of 1.39 ± 0.19. The difference between the 98th percentile and 85th percentile is obviously 13 %, which means that a breathing motion envelope generated using the 85th percentile image should be extrapolated by 40 % in order to

expand the fraction of time that the envelope represents from 80 to 93 %. This type of information would be extremely useful for treatment planners to allow them to more accurately understand the impact of gating decisions as well as the development of internal target volumes to encompass tumors. At this point in time, while the data necessary to provide this information to treatment planners is readily available from the 4DCT acquisition, it is neither analyzed nor provided.

References

1. Barrett, J.F., Keat, N.: Artifacts in CT: recognition and avoidance. Radiographics **24**(6), 1679–1691 (2004)
2. Ehrhardt, J., Werner, R., Säring, D., Frenzel, T., Lu, W., Low, D., Handels, H.: An optical flow based method for improved reconstruction of 4D CT data sets acquired during free breathing. Med Phys **34**(2), 711–721 (2007)
3. Ford, E.C., Mageras, G.S., Yorke, E., Ling, C.C.: Respiration-correlated spiral CT: a method of measuring respiratory-induced anatomic motion for radiation treatment planning. Med Phys **30**(1), 88–97 (2003)
4. Langner, U.W., Keall, P.J.: Prospective displacement and velocity-based cine 4D CT. Med Phys **35**(10), 4501–4512 (2008)
5. Low, D.A., Nystrom, M., Kalinin, E., Parikh, P., Dempsey, J.F., Bradley, J.D., Mutic, S., Wahab, S.H., Islam, T., Christensen, G., Politte, D.G., Whiting, B.R.: A method for the reconstruction of four-dimensional synchronized CT scans acquired during free breathing. Med Phys **30**(6), 1254–1263 (2003)
6. Lu, W., Parikh, P.J., Hubenschmidt, J.P., Bradley, J.D., Low, D.A.: A comparison between amplitude sorting and phase-angle sorting using external respiratory measurements for 4D CT. Med Phys **33**(8), 2964–2974 (2006)
7. Pan, T.: Comparison of helical and cine acquisitions for 4D-CTimaging with multislice ct. Med Phys **32**(2), 627–34 (2005)
8. Pan, T., Lee, T.Y., Rietzel, E., Chen, G.T.Y.: 4D-CT imaging of a volume influenced by respiratory motion on multi-slice ct. Med Phys **31**(2), 333–40 (2004)
9. Seppenwoolde, Y., Shirato, H., Kitamura, K., Shimizu, S., vanHerk, M., Lebesque, J.V., Miyasaka, K.: Precise and real-time measurement of 3D tumor motion in lung due to breathing and heartbeat, measured during radiotherapy. Int J Radiat Oncol Biol Phys **53**(4), 822–834 (2002)
10. Underberg, R.W.M., Lagerwaard, F.J., Cuijpers, J.P., Slotman, B.J., van Sörnsen de Koste, J.R., Senan, S.: Four-dimensional CT scans for treatment planning in stereotactic radiotherapy for stage I lung cancer. Int J Radiat Oncol Biol Phys **60**(4), 1283–1290 (2004)
11. Wijesekera, N.T., Duncan, M.K., Padley, S.P.G.: X-ray computed tomography of the heart. Br Med Bull **93**, 49–67 (2010)

Part II
Motion Estimation and Modeling

Chapter 4
Biophysical Modeling of Respiratory Organ Motion

René Werner

Abstract Methods to estimate respiratory organ motion can be divided into two groups: biophysical modeling and image registration. In image registration, motion fields are directly extracted from 4D (= 3D + t) image sequences, often without concerning knowledge about anatomy and physiology in detail. In contrast, biophysical approaches aim at identification of anatomical and physiological aspects of breathing dynamics that are to be modeled. In the context of radiation therapy, biophysical modeling of respiratory organ motion commonly refers to the framework of continuum mechanics and elasticity theory, respectively. Underlying ideas and corresponding boundary value problems of those approaches are described in this chapter, along with a brief comparison to image registration-based motion field estimation.

4.1 Introduction

Approaches for estimation of respiratory organ motion in 4D image sequences can be divided into two main types: image registration and biophysical modeling [32, 56, 62]. Image registration aims at estimating motion fields by directly extracting them from the 4D image sequences, commonly by maximizing similarity measures between the individual 3D frames of the image sequences; knowledge about breathing physiology and physical properties of organs are (usually) not taken into account [25, 32]. In contrast, biophysical modeling means to identify aspects of the physiological processes and to describe them within a physics-based mathematical formulation. These approaches are also often referred to as biomechanical or biophysics-based (image) registration [4, 11, 44] and so contrasted to other types of image registration such as intensity- or feature-based. In addition, biophysical models

R. Werner
University Medical Center Hamburg-Eppendorf, Hamburg, Germany
e-mail: r.werner@uke.de

J. Ehrhardt and C. Lorenz (eds.), *4D Modeling and Estimation of Respiratory Motion for Radiation Therapy*, Biological and Medical Physics, Biomedical Engineering,
DOI: 10.1007/978-3-642-36441-9_4,

are often directly associated with Finite Element Methods (FEM) because FEM are frequently applied to solve the problem formulation derived during the modeling process (usually partial differential equations, PDEs), especially for approaches within the framework of continuum mechanics. Strictly speaking, it should be noted that synonymous use of the terms FEM-based and biophysical modeling is misleading because FEM represent only a technique, amongst others, to numerically solve PDE systems. Therefore, subsequently only the term of biophysical motion modeling is used.

Biophysical modeling of breathing mechanics initiated long before the introduction of modern 4D imaging devices (see [29, 37] and references therein as examples). A diversity of approaches can be found in the literature and the spatial scales range from microscopic (e.g. analysis and simulation of alveolar structures in the lungs) to global ranges. Multi-scale models are also being developed, cf. the lung physiome project [16], but in the context of radiation therapy, only large scale models are commonly applied. These are models that assess macroscopic structure behavior and interactions [9]. Underlying techniques cover, for example, *mass-spring models*, in which organs are described by a set of distributed masses connected by springs [9, 30], or more generally *particle systems*, where the organ is represented by a collection of particles [18, 28]. For mass-spring models, the system behavior is mainly characterized by the spring parameters and applied external forces; using particle systems, organ deformation is controlled by specified physical particle properties, assumed interaction potentials and the external forces. Although these techniques tend to be intuitive and computationally efficient, they are not necessarily accurate. The behavior of mass-spring models, for instance, is described to be dependent on the topology of the springs and masses [20]. Further, proper values for the spring constants/particle properties are not always easy to derive and say little about the material being modeled [20, 40]. Therefore, the most prominent model formulations refer directly to the framework of continuum mechanics, and predominantly elasticity theory. The main ideas of these approaches are described and exemplified in this chapter.

The chapter is therefore organized as follows: First, models that focus on motion of a single organ are described, with the lungs and the liver as examples (Sect. 4.2). Extensions of the single organ models to provide motion estimation for several anatomical structures are presented in Sect. 4.3. In the last section, comparison studies of biophysical modeling approaches and image registration-based motion field estimation are briefly reflected. We close with conclusions on potential benefits by combining the two worlds.

To describe the modeling ideas and corresponding boundary value problems, it is referred to the notation of elasticity theory. The main terms are summarized in Table 4.1, but please refer to corresponding textbooks like [10, 63] for detailed explanations and derivations.

Table 4.1 Notation of continuum mechanics/elasticity theory used in this chapter, mainly following the notation introduced in [10]

Γ_i	Undeformed/initial organ geometry for breathing phase i
$\partial\Gamma_i$	Surface of Γ_i
$\boldsymbol{n}$	Outer-pointing normal to the surface $\partial\Gamma_i$
φ	Injective and orientation preserving transformation $\varphi = \mathbf{1} + \boldsymbol{u}$ of organ Γ_i
$\mathbf{1}$	Identity map
$\boldsymbol{u}$	Displacement field parameterizing the transformation φ. Typically, $\boldsymbol{u} = \left(u_x, u_y, u_z\right)^T$ represents the sought motion field estimation
$\hat{\boldsymbol{u}}$	Prescribed displacements for $\boldsymbol{x} \in \partial\Gamma_i$ (Dirichlet boundary conditions)
$\boldsymbol{\varepsilon}$	Linear or infinitesimal strain tensor
$\boldsymbol{E}$	Green-St.Venant (Green-Lagrange, Lagrange) strain tensor
$\boldsymbol{e}$	Eulerian-Almansi strain tensor
$\boldsymbol{\sigma}$	Cauchy or true stress tensor
$\boldsymbol{S}$	First Piola-Kirchhoff stress tensor
$\boldsymbol{\Sigma}$	Second Piola-Kirchhoff stress tensor
W	Strain energy function. Used to define the stress–strain relation for hyperelastic materials
λ	First Lamé parameter; no physical interpretation
μ	Second Lamé parameter, shear modulus; measure for the resistance to volume preserving shear deformations, ratio of shear stress to shear strain
Y	Young's modulus; relative material stiffness within the elastic range, defined as ratio of uniaxial (tensile) stress to uniaxial (tensile) strain
ν	Poisson's ratio; measure of the compressibility, defined as ratio of relative transverse contraction to relative longitudinal stretching
$\boldsymbol{f}$	Density of external body forces (e.g. gravity)
$\tilde{(\cdot)}$	$\tilde{(\cdot)}$ indicates that the term refers to the deformed organ geometry. Example: Γ_i represents the undeformed organ geometry for breathing phase i, whilst $\tilde{\Gamma}_i = \varphi\left(\Gamma_i\right)$ describes its deformed state

4.2 Single Organ Motion as a Problem of Elasticity Theory

Modeling respiratory organ motion using elasticity theory is motivated by the view that organ movements can be described as elastic body deformations. Current literature on single organ modeling focuses primarily on two structures: the lungs as the central organ for breathing, and the liver as the largest abdominal organ.

4.2.1 Modeling Macroscopic Lung Motion

Modeling and simulation studies regarding lung elasticity can be found already in the 1970s (and most likely before) [38, 59]. The pioneer studies were based on only simplified lung shape-like geometry definitions due to the lack of modern (4D) tomographic imaging devices and limited computational power. The ideas can often be considered to be the ground of current biophysical breathing motion modeling

attempts, but the models were rarely intended or suited to be used in radiation therapy context. This section therefore focuses on state-of-the-art approaches motivated by that application.

These approaches usually aim at explicit modeling of the process of lung ventilation. Conditions of lung deflation tend to be more sophisticated from the perspective of modeling (key words: passive process, retraction forces), and so the majority of the studies focuses rather on lung inflation than deflation. In the next paragraph, the physiological principles of inflation are briefly described first. Following, the modeling ideas are explained and the corresponding boundary value problems defined.

4.2.1.1 Background: Thoracic Anatomy and the Physiology of Lung Inflation

Anatomically, each lung is surrounded by a pleura sac, which is made up of two layers: parietal pleura and visceral pleura (Fig. 4.1). The parietal pleura is adherent to the internal surface of the thoracic cavity, the diaphragm, and the mediastinum. The visceral pleura covers the outer surface of the lungs. Both layers join at the root of the lung, which is the point of entry of the pulmonary vasculature, nerves, and airways into the lung. The space enclosed by the pleurae is the pleural cavity. It is filled with an incompressible fluid and subject to the so-called (intra-)pleural pressure, which is generally negative (relative to the atmospheric pressure) [27].

In lung inflation, the breathing muscles (diaphragm, outer intercostal muscles) contract and the thoracic cavity expands. As a consequence, the intrapleural pressure takes larger negative values. This, in turn, forces parietal and visceral pleura to keep contact and finally the lungs to follow the expansion of the thoracic cavity. Driven by diaphragmatic breathing, the lung deformation occurs predominantly in superior-inferior direction and so—due to the liquid in the pleural gap—the visceral

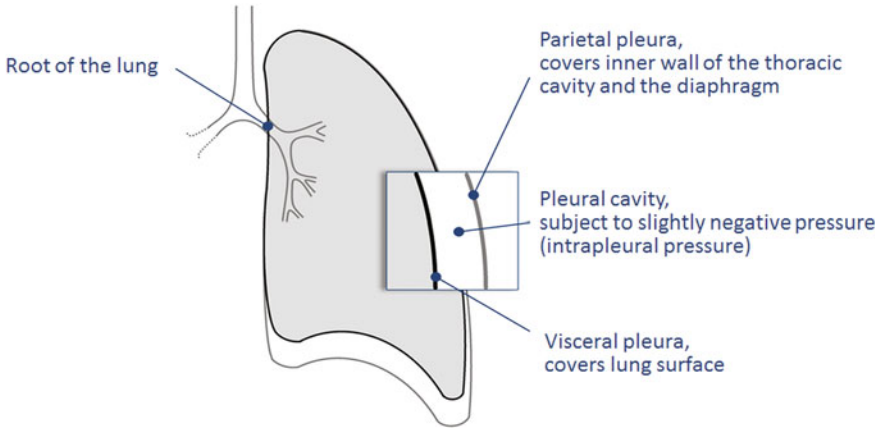

Fig. 4.1 Illustration of the anatomical terminology

pleura slides down the parietal pleura. This behavior is the starting point of most current modeling approaches.

4.2.1.2 Lung Inflation as Elastic Boundary Value Problem

Despite detailed anatomical knowledge of the lungs: The majority of current studies on modeling macroscopic lung behavior approximate lung tissue to be homogeneous and isotropic [1, 6, 52, 55, 56, 62]. Inner lung structures like the bronchial tree and pulmonary vessels are ignored, each of which having in principle different elastic properties [3, 56]. Then, given the lung at its undeformed state (subsequently assumed to be end expiration, EE) and described by a closed and connected subset Γ_{EE} of $\mathbb{R}^3$, the sought injective and orientation preserving deformation is denoted by $\varphi : \Gamma_{\mathrm{EE}} \to \mathbb{R}^3$, which is parameterized by a displacement field (= motion field estimation) $\boldsymbol{u} : \Gamma_{\mathrm{EE}} \to \mathbb{R}^3$ and $\varphi = \mathbf{1} + \boldsymbol{u}$.

Further, inertia effects are also usually neglected and a quasi-static formulation is employed [25, 51]. This can be seen as being motivated by assuming breathing frequencies to be only low and, consequently, the lungs to remain in quasi-static equilibrium—which, in turn, allows for an easier model formulation because the notations of elastostatics can be applied.

Starting with these approximations and simplifying assumptions, elastic boundary value problems (BVPs) are defined to determine the transformation or the displacement field within elasticity theory, including the specification of the governing equations described in the following: kinematic equations (strain-displacement relationship), constitutive equations (material properties), the equations of equilibrium, and appropriate boundary conditions.

Kinematic Equations (Strain-Displacement Relationship)

The kinematic equations describe the relationship between the displacements, interpreted as movements of the continuum or organ particles, and the resulting changes of the particle configuration, characterized by the regional distribution of strain tensors. The principle concept of strain is to measure how much a given displacement $\boldsymbol{u}$ differs locally from a rigid body displacement. Strain tensor formulations are usually expressed in terms of the displacement gradient $\nabla \boldsymbol{u}$, defined by

$$\nabla \boldsymbol{u} = \begin{pmatrix} \frac{\partial u_x}{\partial x} & \frac{\partial u_x}{\partial y} & \frac{\partial u_x}{\partial z} \\ \frac{\partial u_y}{\partial x} & \frac{\partial u_y}{\partial y} & \frac{\partial u_y}{\partial z} \\ \frac{\partial u_z}{\partial x} & \frac{\partial u_z}{\partial y} & \frac{\partial u_z}{\partial z} \end{pmatrix} \tag{4.1}$$

with u_x, u_y and u_z being the components of $\boldsymbol{u}$. In classical mechanics, different strain tensor formulations are in use, with the following being most common in the given context.[1]

- **Infinitesimal Strain Tensor**. The (Cauchy's) infinitesimal or linear strain tensor is composed of the linear (normal) strain along x, y, and z axes,

$$\varepsilon_x = \frac{\partial u_x}{\partial x}, \quad \varepsilon_x = \frac{\partial u_y}{\partial y}, \quad \varepsilon_x = \frac{\partial u_z}{\partial z},$$

and the (engineering) shear strain components,

$$\gamma_{xy} = \frac{\partial u_x}{\partial y} + \frac{\partial u_y}{\partial x}, \ \gamma_{yz} = \frac{\partial u_y}{\partial z} + \frac{\partial u_z}{\partial y}, \ \gamma_{xz} = \frac{\partial u_x}{\partial z} + \frac{\partial u_z}{\partial x},$$

which describe the angular change at any point between two lines crossing this point before and after deformation. They are combined, resulting in the symmetric tensor

$$\boldsymbol{\varepsilon} = \begin{pmatrix} \varepsilon_x & \frac{\gamma_{xy}}{2} & \frac{\gamma_{xz}}{2} \\ \frac{\gamma_{yx}}{2} & \varepsilon_y & \frac{\gamma_{yz}}{2} \\ \frac{\gamma_{zx}}{2} & \frac{\gamma_{zy}}{2} & \varepsilon_z \end{pmatrix} = \frac{1}{2}\left(\nabla \boldsymbol{u}^T + \nabla \boldsymbol{u}\right). \tag{4.2}$$

Note that the infinitesimal strain tensor is an approximate measure, assuming the first derivatives of the components being so small that higher order terms (squares, products of partial derivatives) are negligible [8, 10]. If larger shape changes are to be expected (i.e. undeformed and deformed configurations are assumed to be substantially different), strain tensors of finite strain theory (also called large deformation or large displacement theory) are applied.

- **Green-St.Venant Strain Tensor**. Within finite strain theory, the Green-St.Venant Strain Tensor (also known as Green or Lagrangian finite strain tensor) measures the strain with respect to the undeformed geometry. It is defined by

$$\boldsymbol{E} = \frac{1}{2}\left(\nabla \boldsymbol{u}^T + \nabla \boldsymbol{u} + \nabla \boldsymbol{u}^T \nabla \boldsymbol{u}\right). \tag{4.3}$$

and therefore introduces a non-linear strain-displacement relationship. As before, the off-diagonal elements of $\boldsymbol{E}$ can be referred to as shear strains, the diagonal elements as normal strains, and it becomes obvious that Eq. 4.2 represents a

[1] Please note that the following explicit definition of the specific tensors aims at a complete description of current model formulations. Further, the tensors offer starting points for a detailed analysis of estimated motion fields from a biophysical perspective; related aspects will be demonstrated in Sect. 3.4. The definition could, however, deter readers not familiar with continuum mechanics. These could skip the next passages and continue reading with, e.g., the description of the constitutive equations or boundary conditions without loosing the central thread of the chapter.

linearization of Eq. 4.3; for further detailed descriptions of the underlying physical motivation and corresponding derivations please refer to, e.g., [8, 10].

- **Eulerian-Almansi Strain Tensor**. The counterpart of the Green-St.Venant Strain Tensor within finite strain problem settings, but defined with reference to the deformed configuration, is given by the Almansi or Eulerian (finite) strain tensor,

$$\boldsymbol{e} = \frac{1}{2}\left(\nabla\tilde{\boldsymbol{u}}^T + \nabla\tilde{\boldsymbol{u}} - \nabla\tilde{\boldsymbol{u}}^T\nabla\tilde{\boldsymbol{u}}\right). \tag{4.4}$$

  Thereby and hereinafter, $\tilde{(\cdot)}$ indicates that the corresponding term (here: $\tilde{\boldsymbol{u}}$) refers to the deformed geometry.

Focusing on respiratory lung motion, occurring displacements are generally considered to be too large to assume that changes in geometry do not influence the (local) lung behavior [52]. Thus, most modeling approaches assume geometrical non-linearity/a non-linear strain-displacement relation; they make use of finite strain theory and corresponding strain tensors.

Constitutive Equations (Material Properties)

The constitutive equations relate stresses to the imposed strains and therefore determine the actual behavior of the modeled media. Stresses can be interpreted as internal forces (force exerted per unit area) arising under the impact of the applied external forces. They are measured using stress tensors. Similar to the above paragraph different variants exist and are used in the given context:

- **Cauchy Stress Tensor**. The Cauchy or true stress tensor $\boldsymbol{\sigma} : \tilde{\Gamma}_{\mathrm{EE}} \rightarrow \mathbb{R}^{3\times3}$ is defined with respect to the deformed geometry $\tilde{\Gamma}_{\mathrm{EE}} = \varphi(\Gamma_{\mathrm{EE}})$, i.e. it relates forces to areas in the deformed configuration. To define $\boldsymbol{\sigma}$, consider a small cube in the object of interest with the normals of the cube faces being oriented along the canonical unit vectors $\boldsymbol{e}_x, \boldsymbol{e}_y, \boldsymbol{e}_z$ of $\mathbb{R}^3$. Let further $\boldsymbol{T}^{(\boldsymbol{e}_i)}$ be the stress vector acting on the face with its normal being oriented along $\boldsymbol{e}_i$. Then, the Cauchy stress tensor is given by

$$\boldsymbol{\sigma} = \left(\boldsymbol{T}^{(\boldsymbol{e}_x)}, \boldsymbol{T}^{(\boldsymbol{e}_y)}, \boldsymbol{T}^{(\boldsymbol{e}_z)}\right)^T = \begin{pmatrix} \sigma_{xx} & \sigma_{xy} & \sigma_{xz} \\ \sigma_{yx} & \sigma_{yy} & \sigma_{yz} \\ \sigma_{zx} & \sigma_{zy} & \sigma_{zz} \end{pmatrix}. \tag{4.5}$$

  Similar to the strain tensors, the diagonal elements are referred to as normal stresses and the off-diagonal elements as shear stresses. The stress components are positive, if they act in positive direction of the coordinate axes.

- **First and Second Piola-Kirchhoff Stress Tensors**. The first and second Piola-Kirchhoff stress tensors $\boldsymbol{S} : \Gamma_{\mathrm{EE}} \rightarrow \mathbb{R}^{3\times3}$ and $\boldsymbol{\Sigma} : \Gamma_{\mathrm{EE}} \rightarrow \mathbb{R}^{3\times3}$ are defined with respect to the undeformed geometry. The first Piola-Kirchhoff or Lagrangian stress

tensor links forces in the deformed and areas in the undeformed configuration. Its relation to the Cauchy stress tensor is given by

$$\boldsymbol{S} = \det(\nabla\varphi)\boldsymbol{\sigma}\nabla\varphi^{-T} \tag{4.6}$$

with $\nabla\varphi = \mathbf{1} + \nabla\boldsymbol{u}$ being the Jacobian matrix of the transformation φ.
The second Piola-Kirchhoff stress tensor relates forces and areas in the initial configuration. Its relationship to $\boldsymbol{S}$ is given by

$$\boldsymbol{\Sigma} = \nabla\varphi^{-1}\boldsymbol{S}. \tag{4.7}$$

Note that for infinitesimal deformations, $\boldsymbol{\sigma}$, $\boldsymbol{S}$ and $\boldsymbol{\Sigma}$ are identical; the specification whether the stress is measured with respect to the undeformed or deformed geometry is only necessary in finite strain theory [8]. However, as mentioned before, the use of finite strain theory is currently the standard approach in modeling respiratory lung motion and constitutive equations are usually formulated using the second Piola-Kirchhoff stress tensor [26, 35, 55, 56], which features a computationally favorable symmetric structure.

No consensus exists, however, about the correct formulation of the constitutive equations for lung motion modeling in detail. For the majority of material property parameters it is at least impractical to experimentally measure the values, and so only a limited number of studies can be found about the measurement of mechanical properties of lung tissue [1]. And even for existing experiments and measurements, it remains widely unclear how far reported parameter values are suitable for dimensioning elastic constants during modeling. While experiments are mainly conducted in vitro, the actual in vivo behavior may, e.g., be influenced by other processes than contraction of the breathing muscles, for instance by tissue perfusion. As aggravating aspects, lung tissue properties are also affected by various factors such as age [34], lung parenchyma distortion [21], or tissue location [61]. This makes the formulation of constitutive equations difficult—especially when aiming at precise and patient-specific motion modeling. Currently, usually hyperelastic material models are chosen. Hyperelastic materials can be defined as represented by a stress-strain relation that is determined by a strain energy density function W so that $\boldsymbol{\Sigma}(\boldsymbol{E}) = \frac{\partial W}{\partial \boldsymbol{E}}$ (cf. [8, 63]). Thus, it is guaranteed that the stress state depends only on the instantaneous strain state and is independent of history or rate of loading [10]. Doing so, most modeling approaches can be classified into two groups:

- **St. Venant-Kirchhoff material model**. The St. Venant-Kirchhoff material model is the probably most common of the hyperelastic models. It holds for isotropic materials and features a linear stress-strain relationship:

$$\boldsymbol{\Sigma}(\boldsymbol{E}) = \lambda\,\mathrm{tr}(\boldsymbol{E})\,\mathbf{1} + 2\mu\boldsymbol{E}. \tag{4.8}$$

Table 4.2 Literature values for Young's modulus Y and Poisson's ratio ν applied in lung motion modeling studies using the St. Venant-Kirchhoff material model

Reference	Young's modulus Y (kPa)	Poisson's ratio ν
Al-Mayah et al. [1]	7.8	0.43
Al-Mayah et al. [5, 6]	3.74	0.35–0.499
Al-Mayah et al. [4]	3.74	0.4
Brock et al. [15]	5.0	0.45
Nakao et al. [39]	10	0.25
Sundaram et al. [49]	0.1	0.2
Villard et al. [52]	0.823	0.25–0.35
West et al. [59]	0.25	0.3
Werner et al. [56]	0.1–10	0.2–0.45
Zhang et al. [62]	4.0	0.35

$\lambda > 0$ and $\mu > 0$ are called the Lamé constants. Other pairs of elastic constants could be used instead, e.g. Young's modulus[2] $Y > 0$ and Poisson's ratio $0 < \nu < 0.5$. The constants can be converted by

$$Y = \frac{\mu\,(3\lambda + 2\mu)}{\lambda + \mu} \quad \text{and} \quad \nu = \frac{\lambda}{2\,(\lambda + \mu)}. \tag{4.9}$$

- **Experimentally motivated material models**. Zeng et al. conducted an experimental investigation of human lung material properties based on ex vivo lung tissue specimen (specimen tested within 48 h after death) [61]. The measurements yield a non-linear stress-strain relationship, which could be fitted by a theoretically derived strain potential per unit volume (cf. [27, 61] for details):

$$\begin{aligned} W = \frac{1}{2}c \Big(& \exp\left(a_1 E_{11}^2 + a_2 E_{22}^2 + 2a_4 E_{11} E_{22}\right) \\ & + \exp\left(a_1 E_{11}^2 + a_2 E_{33}^2 + 2a_4 E_{11} E_{33}\right) \\ & + \exp\left(a_1 E_{33}^2 + a_2 E_{22}^2 + 2a_4 E_{33} E_{22}\right)\Big). \end{aligned} \tag{4.10}$$

The mean values of c, a_1, a_2, and a_4 were found to be 11.8 g/cm, 0.43, 0.56, and 0.32. E_{ij} refers to the components of the Green-St. Venant strain tensor.

Examples of use of the St. Venant-Kirchhoff material model are given in [9, 49, 51, 52, 55, 56, 62]. Applied values of the elastic constants differ, though; an overview is given in Table 4.2; most values were chosen heuristically due to the lack of experimental data. Further, Baudet et al. proposed to define a patient-specific Young's modulus value adopting measurements of the patient's compliances and initial lung volumes [9, 52]. The compliance C represents the ratio of air volume

[2] Young's modulus is often also denoted by E, which in the current case would lead to confusion when referring to the Green-St. Venant strain tensor.

variation and the variation of air pressure. Under simplifying assumptions, C can be linked to the elastic constants by $\frac{V_i}{C} = \frac{Y}{3(1-2\nu)}$ with V_i as the initial lung volume [9].

As the second approach, the experimental measurements of Zeng et al. were used in the studies by Eom et al., in which the strain potential of Eq. 4.10 was applied [25, 26], and by Al-Mayah et al., who fitted the test data by a Marlow form strain energy density function [1, 3, 4, 6].

Equations of Static Equilibrium

Finally, a state of static equilibrium is sought, i.e. the net force acting on the deformed lungs has to be zero. Let therefore $\tilde{f}$ denote the density of body forces (N/m^3) acting on the volume elements of $\tilde{\Gamma}_{\mathrm{EE}}$ and $\boldsymbol{T}^{(\tilde{\boldsymbol{n}})}$ be the stress vector acting on the deformed lung boundary $\partial\tilde{\Gamma}_{\mathrm{EE}}$ (N/m^2; see also Eq. 4.5) with $\tilde{\boldsymbol{n}}$ as the outer-pointing normal. Then, equilibrium means that

$$\int_{\tilde{\Gamma}_{\mathrm{EE}}} \tilde{\boldsymbol{f}}\, d\tilde{\boldsymbol{x}} + \int_{\partial\tilde{\Gamma}_{\mathrm{EE}}} \boldsymbol{T}^{(\tilde{\boldsymbol{n}})} d\tilde{\boldsymbol{a}} = 0.$$

With $\boldsymbol{T}^{(\tilde{\boldsymbol{n}})} = \boldsymbol{\sigma}^T \tilde{\boldsymbol{n}}$, $\boldsymbol{\sigma}^T = \boldsymbol{\sigma}$, and Gauss' theorem, the equation reduces to

$$-\tilde{\boldsymbol{\nabla}} \cdot \boldsymbol{\sigma} = \tilde{\boldsymbol{f}} \tag{4.11}$$

in the case of elastostatics and with respect to the deformed geometry. The corresponding equation, but referring to the undeformed geometry instead (here: using the second Piola-Kirchhoff stress tensor), would read as

$$-\boldsymbol{\nabla} \cdot \{(\mathbf{1} + \boldsymbol{\nabla u})\, \boldsymbol{\Sigma}\, (\boldsymbol{E}\, (\boldsymbol{u}))\} = \boldsymbol{f} \tag{4.12}$$

with $\boldsymbol{f} = \det(\boldsymbol{\nabla}\varphi)\, \tilde{\boldsymbol{f}}$. The term $\boldsymbol{A}(\boldsymbol{u}) = -\boldsymbol{\nabla} \cdot \{(\mathbf{1} + \boldsymbol{\nabla u})\, \boldsymbol{\Sigma}\, (\boldsymbol{E}\, (\boldsymbol{u}))\}$ is sometimes referred to as the operator of non-linear elasticity. Considering Eqs. 4.11 and 4.12, it should be noted that for the majority of current modeling approaches any volume forces such as gravity effects etc. are simplistically neglected (i.e. $\tilde{\boldsymbol{f}} = \boldsymbol{f} = 0$).

Boundary Conditions

The BVP further requires appropriate boundary conditions to be defined. For modeling lung ventilation, mainly two boundary condition concepts can be found in literature (see Fig. 4.2 for illustration).

The first one incorporates a *precomputation of surface displacements*, i.e. lung boundary displacements are determined prior to the actual biophysical modeling. They are applied as displacement or Dirichlet boundary conditions for the entire lung surface,

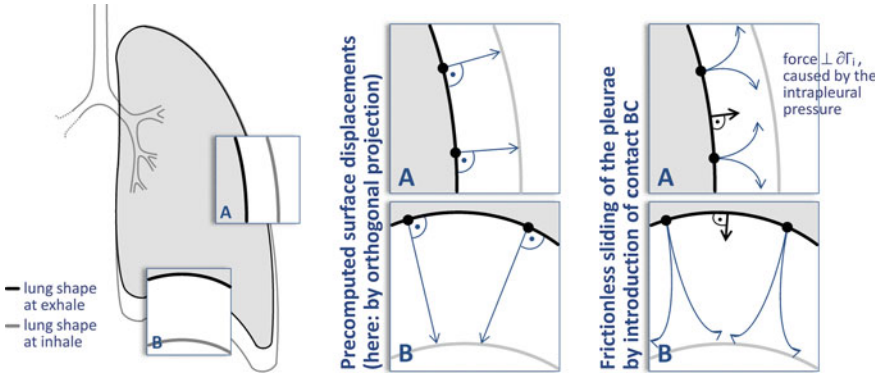

Fig. 4.2 Illustration of two boundary condition (BC) concepts commonly applied for biophysical modeling of lung ventilation. The first approach is to precompute lung surface displacements prior to the actual biophysical modeling process (here: by orthogonal projection). The displacements are then specified as Dirichlet BC. The second approach is motivated by the physiological behavior of the pleurae during breathing. Although forces applied to the lung boundary are along the surface normal (simulating the effect of the intrapleural pressure), the motion of the lung surface points is not limited to movements perpendicular to the surface. Instead, the points are allowed to slide along a limiting geometry (here: lung surface at an intended final breathing phase)

$$\forall \boldsymbol{x} \in \partial \Gamma_{\mathrm{EE}} : \ \boldsymbol{u}(\boldsymbol{x}) = \hat{\boldsymbol{u}}(\boldsymbol{x}), \tag{4.13}$$

with $\hat{\boldsymbol{u}}$ as the prescribed surface displacements.

If this concept is applied, then modeling aims primarily at the generation of plausible inner lung displacement fields. Obviously, plausibility and accuracy of the estimated fields (at least near lung borders) depend on the quality of the precomputed lung surface displacements. The displacements are either prescribed by making a (heuristic) guess of their values [39], or—using 4D image information—they are extracted by using algorithms for matching lung surfaces representing the lung shapes at different breathing phases. Methods proposed are a surface matching by orthogonal projection [15] (also known as orthogonal displacements, OD; cf. [22]) and the extraction of corresponding information from motion fields estimated by intensity-based non-linear registration [35].

The second concept is directly related to the physiology of lung inflation and aims at simulating the sliding motion of the pleurae by *specification of contact conditions*. Conventional Dirichlet boundary conditions are usually prescribed only for the area of the root of the lung, which is assumed to be fixed [23, 25, 39, 55, 56, 62]. The lung expansion caused by the change of the intrapleural pressure is modeled by a uniform negative pressure $p_{\mathrm{intrapleural}}$ acting on the remaining lung surface [9, 23, 51, 52, 55, 56]. The expansion is limited by a rigid geometry representing the cavity or the lung shape at an intended final state of breathing, e.g. end inspiration (EI). Contact between the expanded lung and the limiting geometry is commonly modeled as frictionless [7, 23, 25, 26, 51, 52, 55, 56, 62], which can be expressed by Signorini

conditions [31]:

$$(g \geq 0) \quad \wedge \quad (p_{\text{contact}} \leq 0) \quad \wedge \quad (p_{\text{contact}} \cdot g = 0)\,. \tag{4.14}$$

g measures the distance between the deformed initial lung surface and the limiting geometry and p_{contact} denotes a contact pressure. Equation 4.14 means that in the case of contact ($g = 0$) or penetration ($g < 0$), and only then, a contact pressure is introduced that acts against penetration of lung and limiting geometry. Intrapleural and contact pressure define the stress boundary conditions,

$$\boldsymbol{\sigma}\,(\tilde{\boldsymbol{x}})\,\tilde{\boldsymbol{n}} = \left(p_{\text{intrapleural}} + p_{\text{contact}}\right)\tilde{\boldsymbol{n}}. \tag{4.15}$$

The concept of sliding contact BC for simulation of the pleurae behavior was also adopted to model lung deflation [7]. In this case, the deformation of Γ_{EI} would be assumed to be caused by the intrapleural pressure taking smaller negative values (again, relative to atmospheric pressure) and to be limited by Γ_{EE}. It should further be noted that approaches for dimensioning the intrapleural pressure differ: In [55, 56], the magnitude of $p_{\text{intrapleural}}$ was increased gradually until the deformed lung shape nearly matches the limiting cavity. In contrast, Villard et al. proposed to dimension the pressure for correct inflating based on the compliance recoil law with the compliance being measured for the specific patient [52] and Eom et al. extracted pressure amplitudes for different breathing phases from measured P-V curves, representing the relationship between lung volume and transpulmonary pressure (= difference between alveolar and intrapleural pressure) [26].

Al-Mayah et al. additionally noted that frictionless contact might be a simplifying model for the pleurae behavior as the viscosity of the liquid in the pleural cavity plus surface asperities may restrict them from sliding. Based on experimental measurements [36] they therefore integrated Coloumb friction (i.e. friction that is independent of sliding velocity; here: friction coefficients of 0.1 and 0.2) into the contact BC [5, 6].

4.2.1.3 Beyond Homogeneity: Integration of Inner-Lung Structures

4D image analysis has shown that larger lung tumors affect local lung dynamics and deformation patterns [42, 58]. This may be caused by different elastic properties of tumorous tissue in comparison to healthy lung tissue [56], and so some approaches were proposed to distinguish between them (e.g. Ref. [6]: lung tissue properties were modeled according to the measurements in [61], whilst the tumor was assumed to be a St. Venant-Kirchhoff material stiffer than normal lung tissue). Additional effects of lung tissue heterogeneity on the modeling accuracy were investigated in [3, 7], where the bronchial tree geometry was integrated into the lung model and assigned with material properties other than for the lungs (bronchi as St. Venant-Kirchhoff material, Young's modulus between 0.01 and 18 MPa).

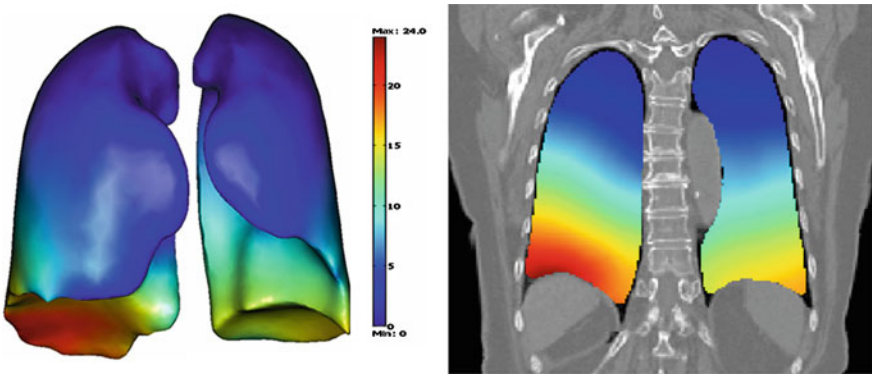

Fig. 4.3 Color-coded visualization of lung motion as estimated by a biophysical modeling approach with frictionless contact BC. *Left* motion vector magnitude for lung surface points [range from 0 (*blue*) to 24 mm (*red*)]; *right* inner lung motion vectors, superimposed to a coronal CT slice (color coding as before). Illustration from [54]

4.2.1.4 Implementation and Assessment of Modeling Accuracy

The boundary value problems defined during the modeling process are—as mentioned before—commonly solved by Finite Element Methods. The usual work flow starts with the segmentation of the structures of interest, followed by a generation of appropriate FE meshes. Finally, the actual FE analysis takes place. Both free and commercially available FEM packages are applied ([1, 3–7]: FE preprocessing using Hypermesh and Hypermorph,[3] FE analysis using Abaqus[4]; [23, 52]: Code-aster[5]; [55, 56]: Comsol Multiphysics[6]; [62]: Ansys[7]; [49]: implementation using the Insight Segmentation and Registration Toolkit, ITK[8]).

For illustration of the estimated fields and plausibility tests, often magnitudes of the displacement vectors are visualized color-coded (Fig. 4.3). A quantitative analysis of the modeling accuracy is usually based on inner lung landmarks, such as bifurcations of bronchi or the vessel tree, which are annotated in the image data underlying the modeling process (cf. Chap. 8). Resulting target registration errors (TRE) and integral statements of different studies are summarized in Table 4.3.

Thereby, the modeling accuracy is shown to be improved by replacing a linear stress-strain function by experimentally measured non-linear relationships [1, 5, 6]. However, the effect of material properties and elastic constants on the prediction quality is not obvious and depends on, for instance, the definition and implementation

[3] Altair Engineering, http://www.altair.com.

[4] Dassault Systemes Simulia Corp., http://www.simulia.com.

[5] http://www.code-aster.org.

[6] Comsol AB, http://www.comsol.com.

[7] Ansys inc., http://www.ansys.com.

[8] Kitware, http://www.itk.org.

Table 4.3 Ranges of patient-specific target registration errors (TRE) and integral statements of studies for biophysical modeling of lung motion

Reference	TRE (mm)	Modeling approach/statement
Brock et al. [15]	4.4 ± 2.0[a]	St. Venant-Kirchhoff material model, lung surface displacements precomputed by center of gravity alignment in AP and LR, plus subsequent orthogonal surface projection (OD)
Li et al. [35]	2.9–4.4	No sliding contact BC; surface displacements precomputed by fluid-like intensity-based non-linear registration
Didier et al. [22]	3.1–6.2	St. Venant-Kirchhoff material model, lung surface displacements precomputed by OD
	2.1–5.2	Frictionless sliding contact BC
Werner et al. [56]	2.4–5.1	St. Venant-Kirchhoff material model, frictionless sliding contact BC
		Modeling accuracy decreases for patients with larger lung tumors and near large tumors
Al-Mayah et al. [1, 5, 6]	n/a	Motion prediction errors in SI decrease by using material properties based on Zeng et al. [61] instead of St. Venant-Kirchhoff material model. (Frictionless) Sliding contact BC further reduce SI errors (3.3–0.9 mm)
Eom et al. [26]	2.0–4.5[b]	Material properties based on Zeng et al. [61], frictionless contact BC
Al-Mayah et al. [6]	n/a	Frictionless sliding BC yield better motion prediction than with Coulomb friction
Al-Mayah et al. [7]	2.7–2.8[c]	Integration of the bronchial tree into the model has no significant effect on modeling accuracy
Al-Mayah et al. [4]	2.8 ± 1.7	No significant TRE differences between a linear and a non-linear constitutive model, if frictionless sliding BC are applied

BC boundary conditions, *EE* end expiration, *EI* end inspiration, *AP* anterior-posterior, *LR* left-right, *SI* superior-inferior. Note that the studies are based on different data sets; direct comparison of the TRE values is therefore difficult

[a]Reported as part of a multi-organ modeling study. TRE is a mean for liver and lung

[b]TRE values for estimated motion between EE and EI. Values for other breathing phases are of similar order

[c]TRE increasing for high values of Young's modulus for the bronchial tree

details of the boundary conditions. In [56], to give an example, the impact of different values for Young's modulus and Poisson's ratio was found to be small with respect to the estimated motion fields. In contrast, Poisson's ratio was observed to be important in [52]. Both studies applied the St. Venant-Kirchoff material model, but the dimensioning of the intrapleural pressure to force lung expansion was different.

A wide consensus exists that incorporation of the pleural sliding behavior by contact conditions improves plausibility and accuracy of the models (cf. Fig. 4.4): With precomputed surface displacements, systematic directional errors were observed [15] and larger TRE values were reported [1, 5, 6, 22] than for sliding contact BC.

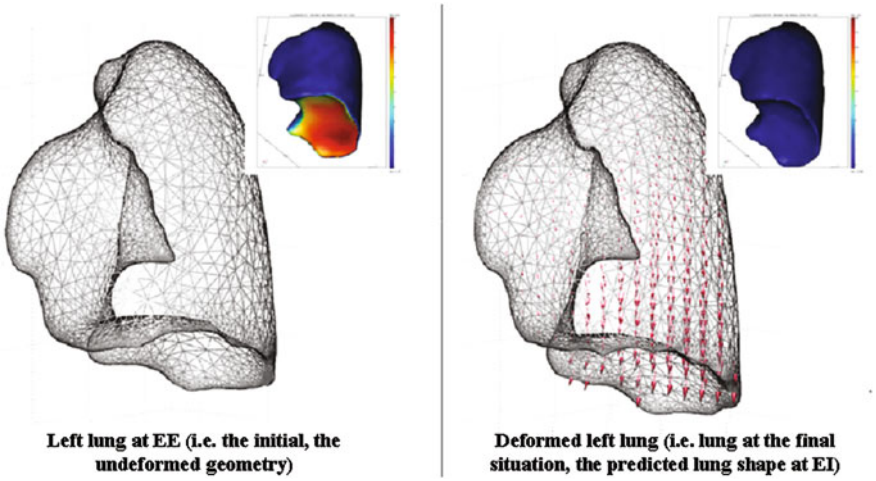

Fig. 4.4 Surface mesh for a left lung at end-expiration (EE; *left*) and simulated end-inspiration (EI; *right*). Arrows indicate the direction of motion. The small figures in the right upper corners represent the distance between EE and EI surfaces before and after simulation (*red* distance $\geq$20 mm; *blue* no distance). It can be seen that using frictionless contact BC larger motion vectors can be found in areas of initially small surface distances of EE and EI geometries [55]

However, neither the experimentally motivated Coulomb friction model for the sliding movements [5, 6] nor an integration of the bronchial tree as separate structure [3, 7] further improved the modeling accuracy. Thus, the assumption of homogeneous lung tissue plus appropriately defined boundary conditions seems to be a good first order approximation for modeling respiratory lung motion.

4.2.2 Liver Motion

Techniques for *patient-specific biophysical modeling of respiratory liver motion* using the framework of continuum mechanics are similar to those for lung motion. Corresponding publications are (currently) mostly associated with the research group of K. Brock (Princess Margaret Hospital, Toronto, Canada; Refs. [2, 13–15, 41]), who implemented biophysical liver motion estimation within the multi-organ deformable registration platform *MORFEUS*; cf. Sect. 4.3.1. Liver tissue was usually—and simplistically—assumed to be homogeneous and isotropic, with a linear stress-strain relationship. Applied values of the elastic constants were 7.8 kPa for Young's modulus Y and between 0.3 and 0.45 for Poisson's ratio μ. The choice was motivated by experimental measurements [33], but considering also discussions in related disciplines (e.g. image-guided liver surgery [17, 19]) it becomes obvious that—similar to lung tissue modeling—appropriate moduli values are controversial.

Contrary to lung motion estimation, (at least) in earlier studies a small deformation framework was used for modeling liver motion [14]. Thus, in terms of elasticity

theory notation the strain-displacement relationship can be linearized based on the assumption of only small shape changes and expressed by the linearized strain tensor (cf. Eq. 4.2). Further given a linear stress-strain relationship, the equilibrium equations in terms of the displacements are then given by the Cauchy-Navier equations of elastostatics,

$$-\mu \boldsymbol{\Delta u} - (\mu + \lambda)\, \boldsymbol{\nabla} (\boldsymbol{\nabla} \cdot \boldsymbol{u}) = \boldsymbol{f}. \tag{4.16}$$

Again, body forces are usually neglected (i.e. $\boldsymbol{f} = 0$).

Other studies integrated geometrical non-linearity into the model [2]; in that case, the derivation of the equations for liver motion estimation is similar to that for lung motion presented in Sect. 4.2.2.

The boundary condition concept predominantly used for modeling liver motion is to precompute the displacements of the liver surface and to adopt them as Dirichlet boundary conditions. Displacements are determined by, e.g., orthogonal displacement projection (OD) after center of gravity alignment of liver segmentations in the images, which form the basis of the modeling process (mainly images at EE and EI) [13, 15, 41]. Recently, Al-Mayah et al. proposed applying frictionless sliding contact boundary conditions as well for modeling liver motion [2]. Similar to lung motion modeling, the choice is explained by the foundations of anatomy and physiology: The liver has no fixed relationship to the skin and surrounding organs during breathing, and so its movements are mainly driven by the (sliding) contact characteristics with neighboring organs.

Solving the defined boundary value problems again by Finite Element Methods and FEM packages, respectively, modeling accuracy in terms of a landmark based TRE was reported to be in the order of 4 mm for the OD boundary conditions (cf. [13, 15]; slice thickness of the corresponding MR images was 3–5 mm). Based on 4D CT images, Al-Mayah et al. showed that the (directional) modeling errors can be reduced by incorporation of liver sliding characteristics [2].

Extending the capabilities of patient-specific modeling, Nguyen et al. described first steps towards the development of a *biophysical motivated liver (motion) population model* [41]. Liver segmentations (here: at exhale as reference breathing phase) of the patients of the considered population were rigidly aligned and subsequently combined by a logical OR-function. This population liver shape model is used for generation of a triangle surface mesh, which is registered to corresponding patient-specific liver models by the OD-based biophysical small deformation model described above (see [15] for details). The resulting population-patient specific exhale liver (shape) model is applied to estimate the motion field between exhale and inhale using again the OD-based small deformation model. The procedures then provide a series of population-patient specific models with corresponding surface points. A mean motion model is subsequently generated by averaging the surface point motion vectors obtained for the different patients. Using the surface displacements as Dirichlet boundary conditions, the governing equations for solving for the inner liver displacements would be the same as for the patient-specific modeling approaches. An example of mean liver surface motion patterns is visualized in Fig. 4.5.

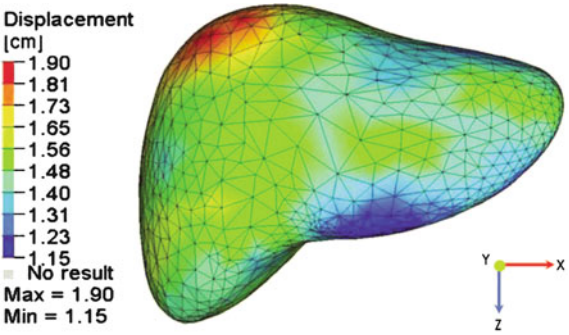

Fig. 4.5 Color-coded visualization of respiratory liver motion, extracted from a biophysically motivated population model that was built up from 10 liver CT images at end-inspiration and end-expiration. Image from [41]

4.3 Multi-Organ Modeling Approaches

4.3.1 Straight-Forward Extension of Single- to Multi-Organ Models

The biophysical single organ modeling approaches of Sect. 4.2 can be extended in a straight-forward way to multi-organ models. Brock et al. generalized the small deformation liver motion model of Sect. 4.2.2 to cover movements of several thoracic and abdominal organs (*MORFEUS* platform, see [13, 15]). They distinguished between implicit and explicit deformation of organs. The boundary conditions (here: displacement BC, determined by orthogonal surface projection) were only applied to organs featuring a detectable and consistent boundary representation in the image data; the organs were deformed explicitly during a subsequent FE solving procedure. Other organs of interest were only implicitly deformed by explicitly deforming neighboring organs. In [15], as an example, abdominal and thoracic MRI data at EE and EI served as image basis, and respiratory movements of lungs, liver, spleen, and the external were modeled explicitly, whilst breast, stomach, and kidney motion were considered implicitly. Modeling accuracy for implicitly deformed organs was in the same order as for the explicitly modeled structures (TRE of explicitly modeled organs: 4.4 ± 2.0 mm; TRE of implicitly modeled organs: 2.4 ± 1.8 mm).

The integration of the bronchial tree or lung tumors into lung motion models as described in Sect. 4.2.1 can also be considered as a similar multi-organ or multi-structure approach. Here, the lungs are explicitly, and the inner-lung structures are implicitly deformed. The same idea was proposed for liver motion modeling and accounting for specific elastic properties of liver tumors [13].

It should be noted that the straight-forward extension to multi-organ models is neither limited to the small-deformation setting used in [15], nor to a specific boundary condition concept. However, the problem of assigning appropriate material properties becomes more complicated with the increasing number of structures. Similar to single organ models, the choice of the elastic constant values is usually motivated by reported experimental data, but these do not necessarily yield best

modeling accuracy, and so it was also proposed to determine material properties "after a patient population optimization," i.e. to dimension them heuristically (empirically) instead. In [15], this led for the stomach to a larger value of Young's Modulus than measured (500 kPa; measured: 1–100 kPa).

4.3.2 Going Further Towards Realistic Biomechanics: Incorporation of Rib Cage and Diaphragm Kinematics

Almost all modeling approaches described before focused on modeling soft tissue deformation based on image data acquired at (at least) two different breathing phases of the same scanning session and corresponding segmentations of the organs to be explicitly modeled. However, respiratory motion shows intra- and interfractional variations [48, 53], which cannot be assessed—and are not addressed—by those models. One way to do so would be statistical modeling of organ motion (see Sect. 4.2). Another approach was presented by Didier et al., who suggested driving the biophysical (lung) models directly by simulated actions of the breathing muscles, i.e. the diaphragm and the intercostal muscles/the rib cage, instead of using the lung shape at a final state of breathing as a helping structure limiting the organ deformation [22, 23, 43].

For simulation of the rib cage kinematics, a particular rigid transformation was precomputed based on a patient's 4D CT data set; transformation parameters were extracted using three rib points (one point near rib head, one in the middle of the rib, and the last just before the cartilage part) [22]. These parameters were later applied (as displacement boundary conditions) to unseen data with only one respiratory state available [43]. Finally, it is intended to deduce rib cage motion from thorax skin motion detected by, e.g., optical markers [23]. Motivated by anatomy, the diaphragm model was composed of central tendon and a peripheral part. The peripheral part represented muscle fibers that are connected to ribs. Diaphragm contraction was then simulated by cranio-caudal forces applied to the muscular part of the diaphragm [43], and it was eventually intended to deduce its motion or the forces by external parameters such as air flow [23]. The widened thoracic cavity allowed the lungs to expand due to an applied negative pressure; this part of the model corresponds to Sect. 4.2.1 with frictionless sliding boundary conditions with other structures being implicitly deformed. Constitutive equations for the different tissues were assumed to be linear, and the elastic constants were reported to be dimensioned based on literature values (please refer to [43] and references therein).

The basic modeling idea is illustrated in Fig. 4.6. By definition of different muscle actions, the method allows to model different breathing maneuvers of the patient and to estimate associated motion fields. No detailed quantitative validation of modeling accuracy of the modeling approach is given so far, but preliminary results "seem to be very promising" [23].

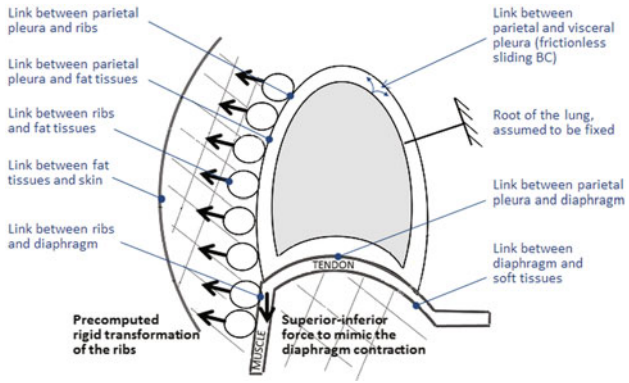

Elastic properties of modeled structures:

	Y [MPa]	μ
Lungs	$700 \cdot 10^{-6}$	0.3
Ribs and vertebrae	5000	0.3
Fat and soft tissues	3	0.4
Skin	3	0.4
Diaphragm muscle	5.32	0.3
Diaphragm tendon	10	0.3

Fig. 4.6 Illustration of the multi-organ modeling approach proposed in [43]. The deformation of the different structures is driven by simulated rib cage and diaphragm actions. To mimic diaphragm contraction, a superior-inferior force is applied to the muscle part of the diaphragm, which is attached to the rib cage. For each rib, a rigid transformation is precomputed and used to define displacement boundary conditions (BC). The resulting widening of the thoracic cavity forces the lungs to expand due to an applied negative pressure in the pleural cavity. A contact between the pleurae is modeled by frictionless sliding BC. All other structures are rigidly linked to each other, but feature different deformation behavior due to the assigned material properties (see Table on the *right*). The figure was adapted from [43]

4.4 Comparison to Image Registration: The Benefit of Biophysical Modeling

4.4.1 Comparison Studies

The cited studies prove that, in general, biophysical approaches can be successfully applied for 4D organ motion estimation. The reported quantitative evaluation results should nevertheless always be interpreted within the given context: The underlying image data have different spatial resolution, image quality varies, and TRE values—if given—are based on different landmark sets. An objective assessment and valuation of the modeling accuracy can only be achieved by cross comparison of different approaches for motion estimation using the same image data and evaluation criteria.

Based on 4D CT image data of lung tumor patients, Sarrut et al. and Werner et al. showed that for lung motion estimation intensity-based image registration remains superior in terms of accuracy [45, 57]. Moreover, in a multi-institution study (MIDRAS), the *MORFEUS* approach was only ranked 19th out of 21 participants regarding the TRE for lung motion estimation [12]. The superior performance of intensity-based image registration is understandable as the registration approaches—in contrast to the biophysical models—account for all patient-specific inner-organ image information about fissures, bronchi and vessel tree, enabling a more precise matching of those structures [50].

The potential of biophysical modeling approaches becomes clear when considering that only little image information is required (usually organ surfaces) to obtain acceptable results. In challenging conditions, if only sparse image information are available (e.g. PET imaging, cross modality motion estimation), this may become advantageous because the models fully exploit the physical prior knowledge of the problem [50, 62]. In the MIDRAS study, as an example, the *MORFEUS* approach ranked 1st out of three participants for matching of liver MRI data (slice thickness 7 mm) and contrast CT data of the same patient; the other two approaches were intensity-based registration techniques.

4.4.2 Combining Both Worlds

A strict separation of biophysical modeling and image registration approaches might, however, be unnecessarily restrictive. Anatomical and physiological aspects considered by biophysical modeling approaches can often serve as indication of potential improvement for image registration techniques if applied to specific anatomical sites. A common example is the use of lung segmentations to separate the motion field estimation inside the lungs from the estimation for the background in order to cope with the discontinuities in lung and chest wall motion [57, 60]. This can be seen as analogue to the sliding contact BC introduced in Sect. 4.2.1 [50]. As a further example, Schmidt-Richberg et al. introduced decoupled diffusion regularization in normal and tangential direction to allow for the sliding motion of lung and liver surfaces [46, 47]. Incorporation of these biophysically inspired mechanisms were reported to improve the modeling accuracy and the plausibility of the estimated motion fields. Furthermore, biophysical priors could be used to differentiate processing of several anatomical structures, e.g. by assigning specific regularization schemes that reflect the physical and material properties of the structures [50].

Inversely, biophysical modeling approaches could benefit by rendering the models more patient-specific by, e.g., integration of further image information. Current biophysical models usually stop with extracting geometrical information from the patient's image data, but several studies reported that diseases could affect tissue properties and motion patterns, respectively [24, 42, 56]. In a clinical context, such information and images reflecting them should be available. The influence of those factors and their integration into the biophysical modeling process should be studied—e.g. by taking into account the entire image information as it is done in classical registration-based motion estimation.

References

1. Al-Mayah, A., Moseley, J., Brock, K.K.: Contact surface and material nonlinearity modeling of human lungs. Phys. Med. Biol. **53**(1), 305–317 (2008)

2. Al-Mayah, A., Moseley, J., Velec, M., Brock, K.: Deformable modeling of human liver with contact surface. In: Science and Technology for Humanity (TIC-STH), 2009 IEEE Toronto International Conference, pp. 137–140. Toronto (2009)
3. Al-Mayah, A., Moseley, J., Velec, M., Brock, K.: Effect of heterogeneous material of the lung on deformable image registration. In: Miga, M.I., Wong, K.H. (eds.) SPIE Medical Imaging 2009: Visualization, Image-Guided Procedures, and Modeling, Proc. SPIE, vol. 7261, pp. 72, 610V–2–8 (2009)
4. Al-Mayah, A., Moseley, J., Velec, M., Brock, K.: Toward efficient biomechanical-based deformable image registration of lungs for image-guided radiotherapy. Phys. Med. Biol. **56**(15), 4701–4713 (2011)
5. Al-Mayah, A., Moseley, J., Velec, M., Brock, K.K.: Effect of friction and material compressibility on deformable modeling of human lung. In: Bello, F., Edwards, E. (eds.) International Symposium on Computational Models for Biomedical Simulation—ISBMS 2008, LNCS, vol. 5104, pp. 98–106. Springer, London (2008)
6. Al-Mayah, A., Moseley, J., Velec, M., Brock, K.K.: Sliding characteristic and material compressibility of human lung: parametric study and verification. Med. Phys. **36**(10), 4625–4633 (2009)
7. Al-Mayah, A., Moseley, J., Velec, M., Hunter, S., Brock, K.K.: Deformable image registration of heterogeneous human lung incorporating the bronchial tree. Med. Phys. **37**(9), 4560–4571 (2010)
8. Banks, H.T., Hu, S., Kenz, Z.R.: A brief review of elasticity and viscoelasticity for solids. Adv. Appl. Math. Mech. **3**(1), 1–51 (2011)
9. Baudet, V., Villard, P.F., Jaillet, F., Beuve, M., Shariat, B.: Towards accurate tumour tracking in lungs. In: IV '03: Proceedings of the Seventh International Conference on Information Visualization, pp. 338–343. IEEE Computer Society, Washington, DC, USA (2003)
10. Bower, A.F.: Applied Mechanics of Solids. CRC Press, Boca Raton (2010)
11. Brock, K.K.: Image registration in intensity-modulated, image-guided and stereotactic body radiation therapy. Front. Radiat. Ther. Oncol. **40**, 94–115 (2007)
12. Brock, K.K.: Deformable Registration Accuracy Consortium:Results of a multi-institution deformable registration accuracy study (MIDRAS). Int. J. Radiat. Oncol. Biol. Phys. **76**(2), 583–596 (2010)
13. Brock, K.K., Dawson, L.A., Sharpe, M.B., Moseley, D.J., Jaffray, D.A.: Feasibility of a novel deformable image registration technique to facilitate classification, targeting, and monitoring of tumor and normal tissue. Int. J. Radiat. Oncol. Biol. Phys. **64**(4), 1245–1254 (2006)
14. Brock, K.K., Hollister, S.J., Dawson, L.A., Balter, J.M.: Technical note: creating a four-dimensional model of the liver using finite element analysis. Med. Phys. **29**(7), 1403–1405 (2002)
15. Brock, K.K., Sharpe, M.B., Dawson, L.A., Kim, S.M., Jaffray, D.A.: Accuracy of finite element model-based multi-organ deformable image registration. Med. Phys. **32**(6), 1647–1659 (2005)
16. Burrowes, K.S., Swan, A.J., Warren, N.J., Tawhai, M.H.: Towards a virtual lung: multi-scale, multi-physics modelling of the pulmonary system. Phil. Trans. A Math. Phys. Eng. Sci. **366**(1879), 3247–3263 (2008)
17. Cash, D.M., Miga, M.I., Sinha, T.K., Galloway, R.L., Chapman, W.C.: Compensating for intraoperative soft-tissue deformations using incomplete surface data and finite elements. IEEE Trans. Med. Imaging **24**(11), 1479–1491 (2005)
18. Chhatkuli, S., Koshizuka, S., Uesaka, M.: Dynamic tracking of lung deformation during breathing by using particle method. Modelling and Simulation in Engineering Article ID 19307, pp. 7 (2009)
19. Clements, L.W., Dumpuri, P., Chapman, W.C., Galloway, R.L., Miga, M.I.: Atlas-based method for model updating in image-guided liver surgery. In: Cleary, K.R., Miga, M.I. (eds.) SPIE Medical Imaging 2007: Visualization and Image-Guided Procedures, Proc. SPIE, vol. 6509, pp. 650, 917–1–12 (2007)
20. Delingette, H.: Towards realistic soft tissue modeling in medical simulation. Proc. IEEE **86**(3), 512–523 (1998) (Special Issue on Surgery Simulation)

21. Denny, E., Schroter, R.C.: A model of non-uniform lung parenchyma distortion. J. Biomech. **39**(4), 652–663 (2006)
22. Didier, A.L., Villard, P.F., Bayle, J.Y., Beuve, M., Shariat, B.: Breathing thorax simulation based on pleura physiology and rib kinematics. In: MEDIVIS'07: Proceedings of the International Conference on Medical Information Visualisation—BioMedical Visualisation, pp. 35–42. IEEE Computer Society, Washington, DC, USA (2007)
23. Didier, A.L., Villard, P.F., Saade, J., Moreau, J.M., Beuve, M., Shariat, B.: A chest wall model based on rib kinematics. In: Banissi, E., et al. (eds.) VIZ '09: Proceedings of the Second International Conference in Visualisation, pp. 159–164. IEEE Computer Society, Barcelona (2009)
24. Ehrhardt, J., Werner, R., Schmidt-Richberg, A., Handels, H.: Prediction of respiratory motion using a statistical 4D mean motion model. In: Brown, M., de Bruijne, M., van Ginneken, B., Kiraly, A., Kuhnigk, J.M., Lorenz, C., McClealland, J.R., Mori, K., Reeves, A., Reinhardt, J. (eds.) The Second Annual Workshop on Pulmonary Image Analysis, pp. 3–14. London (2009)
25. Eom, J., Shi, C., Xu, G.X., De, S., et al.: Modeling respiratory motion for cancer radiation therapy based on patient-specific 4DCT data. In: Yang, G.Z. (ed.) Medical Image Computing and Computer-Assisted Intervention, MICCAI 2009, LNCS, vol. 5762, pp. 348–355. Great Britain, London (2009)
26. Eom, J., Xu, X.G., De, S.: Predictive modeling of lung motion over the entire respiratory cycle using measured pressure-volume data, 4DCT images, and finite-element analysis. Med. Phys. **37**(8), 4389–4400 (2010)
27. Fung, Y.: Biomechanics: Motion, Flow, Stress, and Growth. Springer, Heidelberg (1990)
28. Jaillet, F., Amrani, M., Beuve, M.: Tracking of target motion using physically based modelling of organs. Radiother. Oncol. **73**(Suppl 2), S73–S76 (2004)
29. Jodat, R.W., Horgan, J.D., Lange, R.L.: Simulation of respiratory mechanics. Biophys. J. **6**(6), 773–785 (1966)
30. Kaye, J., Primiano, F.P., Metaxas, D.: Anatomical and physiological simulation for respiratory mechanics. J. Image. Guid. Surg. **1**(3), 164–171 (1995)
31. Kikuchi, N., Oden, J.T.: Contact Problems in Elasticity: A Study of Variational Inequalities and Finite Element Methods. SIAM, Philadelphia (1988)
32. Klinder, T., Lorenz, C., Ostermann, J.: Free-breathing intra- and intersubject respiratory motion capturing, modeling, and prediction. In: Pluim, J.P.W., Dawant, B.M. (eds.) SPIE Medical Imaging 2009: Image Processing, Proc. SPIE, vol. 7259, pp. 72,590T–1–11 (2009)
33. Kruse, S.A., Smith, J.A., Lawrence, A.J., Dresner, M.A., Manduca, A., Greenleaf, J.F., Ehman, R.L.: Tissue characterization using magnetic resonance elastography: preliminary results. Phys. Med. Biol. **45**(6), 1579–1590 (2000)
34. Lai-Fook, S.J., Hyatt, R.E.: Effects of age on elastic moduli of human lungs. J. Appl. Physiol. **89**(1), 163–168 (2000)
35. Li, P., Malsch, U., Bendl, R.: Combination of intensity-based image registration with 3D simulation in radiation therapy. Phys. Med. Biol. **53**(17), 4621–4637 (2008)
36. Loring, S.H., Brown, R.E., Gouldstone, A., Butler, J.P.: Lubrication regimes in mesothelial sliding. J. Biomech. **38**(12), 2390–2396 (2005)
37. Mead, J.: Mechanical properties of lungs. Physiol. Rev. **41**(2), 281–330 (1961)
38. Mead, J., Takishima, T., Leith, D.: Stress distribution in lungs: a model of pulmonary elasticity. J. Appl. Physiol. **28**(5), 596–608 (1970)
39. Nakao, M., Kawashima, A., Kokubo, M., Minato, K.: Simulating lung tumor motion for dynamic tumor-tracking irradiation. In: 2007 IEEE Nuclear Science Symposium Conference Record, pp. 4549–4551. IEEE Computer Society (2007)
40. Nealen, A., Müller, M., Keiser, R., Boxerman, E., Carlson, M.: Physically based deformable models in computer graphics. Comput. Graph. Forum **4**, 809–836 (2006)
41. Nguyen, T.N., Moseley, J.L., Dawson, L.A., Jaffray, D.A., Brock, K.K.: Adapting liver motion models using a navigator channel technique. Med. Phys. **36**(4), 1061–1073 (2009)
42. Plathow, C., Fink, C., Ley, S., Puderbach, M., Eichinger, M., Zuna, I., Schmähl, A., Kauczor, H.U.: Measurement of tumor diameter-dependent mobility of lung tumors by dynamic MRI. Radiother. Oncol. **73**(3), 349–354 (2004)

43. Saadé, J., Didier, A.L., Villard, P.F., Buttin, R., Moreau, J.M., Beuve, M., Shariat, B.: A preliminary study for a biomechanical model of the respiratory system. In: Engineering and Computational Sciences for Medical Imaging in Oncology, VISAPP (2010)
44. Sarrut, D.: Deformable registration for image-guided radiation therapy. Z. Med. Phys. **16**(4), 285–297 (2006)
45. Sarrut, D., Delhay, B., Villard, P.F., Boldea, V., Beuve, M., Clarysse, P.: A comparison framework for breathing motion estimation methods from 4-d imaging. IEEE Trans. Med. Imaging **26**(12), 1636–1648 (2007)
46. Schmidt-Richberg, A., Ehrhardt, J., Werner, R., Handels, H.: Direction-dependent regularization for improved estimation of liver and lung motion in 4D image data. In: Dawant, B.M., Haynor, D. (eds.) SPIE Medical Imaging 2010: Image Processing, Proc. SPIE, vol. 7623, pp. 76,232Y–1–8 (2010)
47. Schmidt-Richberg, A., Werner, R., Handels, H., Ehrhardt, J.: Estimation of slipping organ motion by registration with direction-dependent regularization. Med. Image Anal. **16**(1), 150–159 (2012)
48. Sonke, J.J., Lebesque, J., van Herk, M.: Variability of four-dimensional computed tomography patient models. Int. J. Radiat. Oncol. Biol. Phys. **70**(2), 590–598 (2008)
49. Sundaram, T.A., Gee, J.C.: Towards a model of lung biomechanics: pulmonary kinematics via registration of serial lung images. Med. Image Anal. **9**(6), 524–537 (2005)
50. Vandemeulebroucke, J.: Lung motion modelling and estimation for image guided radiation therapy. Ph.D. thesis, L'Institut National des Sciences Appliqu'ees de Lyon (2010)
51. Villard, P.F., Beuve, M., Shariat, B., Baudet, V., Jaillet, F.: Lung mesh generation to simulate breathing motion with a finite element method. In: IV '04: Proceedings of the Information Visualisation, Eighth International Conference, pp. 194–199. IEEE Computer Society, Washington, DC, USA (2004)
52. Villard, P.F., Beuve, M., Shariat, B., Baudet, V., Jaillet, F.: Simulation of lung behaviour with finite elements: Influence of bio-mechanical parameters. In: MEDIVIS '05: Proceedings of the International Conference on Medical Information Visualisation—BioMedical Visualisation, pp. 9–14. IEEE Computer Society, Washington, DC, USA (2005)
53. von Siebenthal, M., Székely, G., Gamper, U., Boesiger, P., Lomax, A., Cattin, P.: 4D MR imaging of respiratory organ motion and its variability. Phys. Med. Biol. **52**(6), 1547–1564 (2007)
54. Werner, R., Ehrhardt, J., Handels, H.: Modeling of respiratory lung motion as a contact problem of elasticity theory. In: 2nd European COMSOL-Conference on Multiphysics, Simulation. Hannover (2008)
55. Werner, R., Ehrhardt, J., Schmidt, R., Handels, H.: Modeling respiratory lung motion—a biophysical approach using finite element methods. In: Hu, X.P., Clough, A.V. (eds.) SPIE Medical Imaging 2008: Physiology, Function, and Structure from Medical Images, Proc. SPIE, vol. 6916, pp. 69,160N–1–11 (2008)
56. Werner, R., Ehrhardt, J., Schmidt, R., Handels, H.: Patient-specific finite element modeling of respiratory lung motion using 4D CT image data. Med. Phys. **36**(5), 1500–1511 (2009)
57. Werner, R., Ehrhardt, J., Schmidt, R., Handels, H.: Validation and comparison of a biophysical modeling approach and non-linear registration for estimation of lung motion fields in thoracic 4D CT data. In: Pluim, J.P.W., Dawant, B.M. (eds.) SPIE Medical Imaging 2009: Image Processing, Proc. SPIE, vol. 7259, pp. 7259U–1–8 (2009)
58. Werner, R., Ehrhardt, J., Schmidt-Richberg, A., Heiss, A., Handels, H.: Estimation of motion fields by non-linear registration for local lung motion analysis in 4D CT image data. Int. J. Comput. Assist. Radiol. Surg. **5**(6), 595–605 (2010)
59. West, J.B., Matthews, F.L.: Stresses, strains, and surface pressures in the lung caused by its weight. J. Appl. Physiol. **32**(3), 332–345 (1972)
60. Wu, Z., Rietzel, E., Boldea, V., Sarrut, D., Sharp, G.C.: Evaluation of deformable registration of patient lung 4DCT with subanatomical region segmentations. Med. Phys. **35**(2), 775–781 (2008)

61. Zeng, Y.J., Yager, D., Fung, Y.C.: Measurement of the mechanical properties of the human lung tissue. J. Biomech. Eng. **109**(2), 169–174 (1987)
62. Zhang, T., Orton, N.P., Mackie, T.R., Paliwal, B.R.: Technical note: a novel boundary condition using contact elements for finite element based deformable image registration. Med. Phys. **31**(9), 2412–2415 (2004)
63. Zienkiewicz, O.C., Taylor, R.L.: The Finite Element Method for Solid and Structural Mechanics. Elsevier Butterworth-Heinemann, Burlington (2005) (sixth edition)

Chapter 5
Feature-Based Registration Techniques

Cristian Lorenz, Tobias Klinder and Jens von Berg

Abstract In contrast to intensity-based image registration, where a similarity measure is typically evaluated at each voxel location, feature-based registration works on a sparse set of image locations. Therefore, it needs an explicit step of interpolation to supply a dense deformation field. In this chapter, the application of feature-based registration to pulmonary image registration as well as hybrid methods, combining feature-based with intensity-based registration, is discussed. In contrast to pure feature based registration methods, hybrid methods are increasingly proposed in the pulmonary context and have the potential to out-perform purely intensity based registration methods. Available approaches will be classified along the categories *feature type*, *correspondence definition*, and *interpolation type* to finally achieve a dense deformation field.

5.1 Introduction

Probably the most intuitive approach to find a suitable transformation bringing two images into the same frame of reference, is by means of a set of corresponding points. In principle, they could be defined manually. But since we want to define a non-rigid registration, needing perhaps hundreds or thousands of points for a decent deformation field, we will concentrate on automated procedures. We will discuss how suitable *feature* points can be found, how point correspondence in two images can be established, and how a transformation can finally be estimated. Still, we have a sparse point set in mind, associated with a specific feature, be it a vessel bifurcation or a characteristic gray value structure. This is in contrast to the so called *intensity based registration* which will be discussed in Chaps. 6 and 7. Intensity based image registration treats typically each image location equally. For every grid position or voxel in a source image, the corresponding location in a target image is found

C. Lorenz (✉) · T. Klinder · J. von Berg
Philips Research Laboratories, Hamburg, Germany
e-mail: cristian.lorenz@philips.com

J. Ehrhardt and C. Lorenz (eds.), *4D Modeling and Estimation of Respiratory Motion for Radiation Therapy*, Biological and Medical Physics, Biomedical Engineering,
DOI: 10.1007/978-3-642-36441-9_5,

by evaluating a suitable intensity based similarity measure. Most medical images, however, contain more or less homogeneous regions with no or little gray value contrast. This makes the above task of finding correspondence an ill-posed problem. It is commonly solved by either applying explicit smoothness constraints to the deformation field or by exploiting implicit smoothness introduced by the specific parameterization of the deformation field. In effect, the behavior of an intensity-based registration is mainly characterized by matching image regions with suitable contrast and performing an implicit or explicit interpolation in between.
The *feature-based* registration, however, explicitly attempts to register only highly structured image regions and to obtain a dense deformation field by interpolating the resulting sparse deformation vector field. A considerable variety of methods has been proposed, differing in feature type, and how feature correspondence is established. In addition, hybrid methods have been proposed, combining feature-based and intensity-based registration.
We classify feature-based registration algorithms based on the following categories:

- **Feature type**, which includes feature dimension (point, line, surface) and feature characterization (e.g. bifurcation-point, vessel-centerline, ridge-line of a surface, or other intensity patterns)
- **Feature correspondence definition** (e.g. anatomical labeling, 3D Shape Context, current-based, shaped-constrained deformable models)
- **Interpolation type** for generating dense deformation fields.

Consequently, the rest of this chapter is organized along these categories. Feature-based registration was very frequently used to estimate rigid or affine transformations. Here, we focus on non-linear transformations, for which feature-based registration was pioneered for the purpose of brain registration. In the context of a comparison of algorithms for pulmonary image registration, performed at a satellite workshop of the 13th International Conference on Medical Image Computing and Computer Assisted Intervention (MICCAI 2010), actually none of the high-ranking methods was a purely feature-based method. However, a few of them, including the winner [19] of the online-contest, were hybrid methods, combining intensity with feature-based registration. The feature part of those hybrid methods will also be discussed in this chapter. Table 5.1 contains an overview of feature-based and hybrid non-rigid registration approaches for pulmonary applications. In this chapter, we focus on feature-based registration for lung motion estimation and not on the registration of surrounding structures, such as vertebrae and ribs, for which we only give the work of Matsopoulus (item 2 in Table 5.1) as an example. The authors attempt here to achieve a registration of the lung region of interest independent of the breathing phase.
Feature-based registration approaches can provide a natural way to treat motion field discontinuities, for example at the lung pleura, by separate registration of feature sub-sets, e.g., pulmonary structures and ribs. This is similar to a regionally restricted intensity-based registration, but does not require an accurate region segmentation. The problem, however, how to interpolate a dense motion field for the full image domain persists.

Table 5.1 Classification of feature-based registration for pulmonary applications

	Author	Year	Feature	Correspondence	Interpolation
1	C.V. Stewart et al. [32]	2004	Points, lines, and surfaces	Modified ICP	B-spline-based
2	G.K. Matsopoulos et al. [28]	2005	Points: vertebrae, ribs, shoulder	Self organizing maps	RBF (shifted log)
3	M. Urschler and H. Bischof [33]	2005	Surface: lung surface	Shape context	TPS
4	A. Hilsmann et al. [21]	2007	Points: vessel tree bifurcations	Shape context	TPS
5	T. Klinder et al. [24]	2008	Surfaces: lung surf. and inner structures	Shape constrained deformation	TPS
6	Y. Huang et al. [22]	2009	Points, and lines: bronchial tree, bifurcation points	Hufman code	TPS and Demons
7	V. Gorbunova et al. [17]	2009	Lines, surfaces: vessel tree, lung surface	Currents-based registration	Gaussian kernel diffeomorphic matching
8	K. Cao et al. [6]	2010	Lines: vessel tree	Via hybrid registration	Via hybrid registration
9	D. Loecks et al. [25]	2010	Points: vessel bifurcations	Local and global correspondence model	Via hybrid registration
10	X. Han [19]	2010	Points: Förstner operator	SURF descriptor	Via hybrid registration

5.2 Feature Types

Feature-based registration does not necessarily mean that a point-wise correspondence between landmarks is established, meaning that at the landmark position all degrees of freedom (DOF) for the deformation field are removed. By registration of line-like features such as vessels or bronchial branches only DOF across the line are removed. This leaves one DOF along the line. Similarly, surfaces like the pleura or the lung fissures locally remove only one DOF and leave two DOF on the surface. However, even in the case of line or surface features, often in a successive step, a virtual point-to-point correspondence is established with suitable mapping approaches, such as the iterative closest point (ICP) or related algorithms [3, 12]. Features may be determined as anatomical objects, or by their gray value structure, independent from the anatomy. Examples are, e.g., a bronchial or vascular bifurcation point, or a point with high gray value variability in all three spatial directions.

5.2.1 Anatomical Features

If an anatomical feature can be identified in both images as a unique anatomical landmark, the correspondence problem becomes trivial. In addition, anatomical features are easy to handle in interactive definition or correction schemes. For the registration of the thorax, anatomical objects surrounding the lungs, such as vertebrae and ribs can be used if an independence from the breathing phase is [28] intended. For the estimation of pulmonary motion, however, the surface of the lungs, fissures, bronchial and vascular tree can be used.

Regarding the lung surface, it can be assumed that the motion of it, can to some extent serve as a predictor of the internal lung motion. This is especially the case in the region around the diaphragm. Furthermore, most of the intensity based registration algorithms need as input a delineation of the lungs in order to properly handle the motion discontinuities at the lung borders. While automated lung segmentation is a fairly easy task (at least in the absence of gross pathologies), it is less straight forward to establish anatomical correspondence on the lung surface. In Sects. 5.3.4, 5.3.5, and 5.3.6 approaches to solve the correspondence problem for the lung surface will be discussed.

Further candidates are bronchi and blood vessels. The distal portions of bronchial and vascular trees in the lungs are inaccessible for anatomical identification due to inter-patient variability, the obscuring influences of noise and image artifacts, and the sheer amount of structures such as small branches or bifurcations. Still, these structures can be detected and used as input for feature-based registration.

A weak feature influence within a hybrid registration method was introduced by Cao et al. [6], by adding a 'vesselness'-based [13] similarity measure. With weak in this context we mean that no explicit point-to-point correspondence is established. The approach increases the probability that vessels are registered to vessels, without the need to establish explicit correspondence between the vessel trees to be matched. The additional similarity measure follows Frangi's proposal of using the Eigenvalues of the Hessian matrix to extract curvi-linear image structures in 2D and 3D images. The approach is on the borderline between feature based and intensity based registration. It can be argued that just an additional similarity measure is introduced in an intensity based registration algorithm and that no explicit correspondences are established. On the other hand, image regions are treated differently, depending on the appearance of vessel-like features. Loeckx et al., again in the context of a hybrid registration approach, determined a set of corresponding vessel bifurcation points in fixed and moving image and used them in an additional similarity measure [25]. In a pre-processing step, a set of bifurcations points is generated in both images using a threshold-based segmentation and sub-sequent skeletonization of the pulmonary vessel tree. In addition, the correspondence between the bifurcation points in both images is established (see Sect. 5.3). During the iterations of the hybrid registration, the Euclidean distance between bifurcation points in the fixed image and transformed corresponding points in the moving image is used in addition to a mutual information-based similarity measure.

5.2.2 Gray Value Structure Features

In contrast to anatomically motivated features, it is also possible to search for gray value structures that are on the one hand characteristic enough to allow a good localization and that on the other hand provide a better lung coverage in the distal regions of bronchial and vascular tree. A standard approach for this idea is the analysis of the gradient structure of a small image region, as given by an averaged structure tensor. The structure tensor is the tensor product of the image gradient ∇I with itself. The Eigenvalues of the averaged structure tensor $C = \overline{\nabla I \, (\nabla I)^T}$ are characteristic for the type of structure in the covered region as depicted in Fig. 5.1. Three Eigenvalues that are large in magnitude are required for a characteristic landmark, because this indicates intensity variation in all directions. Consequently, a variety of formulas based on the product of the Eigenvalues of C as given by the determinant, by the sum of the Eigenvalues as given by the trace of C have been proposed as feature point detectors (see [20] for an overview and comparison). Han [19] determined local maxima of the structure tensor-based Förstner operator $det(C)/trace(C^{adj})$ [20] as feature points and established point correspondence using SURF descriptors [1] (see Sect. 5.3). In a hybrid registration setup, the quadratic distance between the resulting feature-based transformation field and the current estimated transformation field was used in addition to a mutual information and a curvature penalizing term during the hybrid registration iterations.

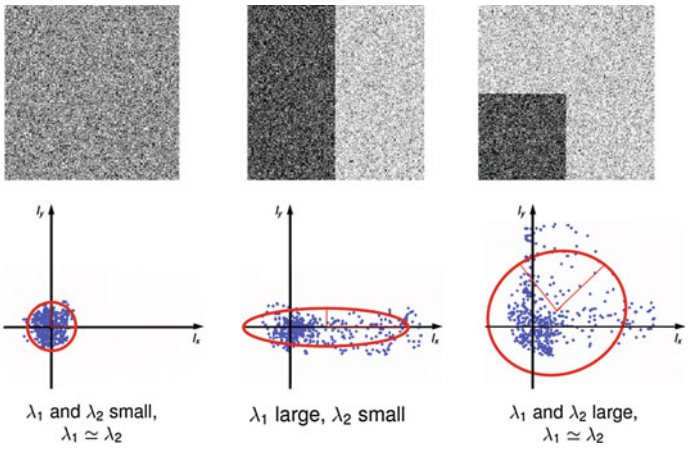

Fig. 5.1 Illustration of the structure tensor for three artificial 2D cases with (i) no predominant (*left*), (ii) one predominant (*middle*), and (iii) two predominant (*right*) gradient directions. The Eigenvectors and values λ_i of the structure tensor can be interpreted as direction and length of the principal axes of an ellipsoid fitted to the distribution. Figure from Goldlücke [16]

5.3 Feature Correspondence

In the case of unique anatomical landmarks, the feature correspondence is trivially given. If this is not the case, correspondence has to be either explicitly established in an additional processing step or implicitly, e.g., by combining the feature-based procedure with an intensity-based registration into a hybrid registration approach. Often, even for named line or surface features, where correspondence of the whole anatomical structure is given, a point-wise correspondence between point sets distributed on the pair of lines or surfaces is established. The main approaches for establishing correspondence are described in the following.

5.3.1 Iterative Closest Point and Modifications

The iterative closest point (ICP) was initially presented by Besl in [3]. Its main idea is to establish a correspondence between two point clouds P and X by performing the following four steps (i) compute for each $\mathbf{p}_i \in P$ the closest point from X, (ii) compute a transformation to match P to X, (iii) apply the transformation to all points in P, (iv) repeat (i)–(iii) until convergence. Initially, it was assumed that the transformation between the two point clouds could be described by a rigid transformation so that step (iii) could be found in a closed form solution. It has to be noted that X does not necessarily have to be a discrete point cloud but could also be a line or surface. Various extensions have been presented to allow non-rigid transformations between the two point clouds (see e.g., [12]). Although the ICP states a very standard algorithm for finding a correspondence between two point sets as it is fast and accurate in many cases, it is a method minimizing a non-convex cost function, and thus it lacks in terms of robustness w.r.t. the initial transformation because of local minima. Furthermore, the computation time is proportional to the number of points, which can be prohibitive when registering two large sets of points. For that reason, many approaches exist addressing robustness, e.g., using a random sampling of points at each iteration, bidirectional distance measurements, remove outliers, or introducing probabilities, and speed, e.g., using k-d trees and/or closest point caching. However, even with latest modifications, robustness and speed are still critical when applying the ICP.

5.3.2 Shape-Based Descriptors

The 'Robust Tree Registration' approach described by Loeckx et al. [25] uses the distance between corresponding vessel tree bifurcation points as an additional similarity measure in a hybrid registration approach. Correspondence is established by means of internal distances between any pair of points. Two distance measures, namely Euclidean and Geodesic distance (shortest path along the tree skeleton) are used

separately. Using a Gaussian distribution model, a distance-based matching probability $P(C_{(i,j).(k,l)})$ is calculated for the occurrence $C_{(i,j).(k,l)}$, that two point-pairs $g_{1,ij}$ and $g_{2,kl}$ found in fixed and moving image respectively, do match.

$$P(C_{(i,j).(k,l)}) = \frac{1}{\sqrt{2\pi\sigma^2}} exp\left(-\frac{\left\|g_{1,ij}, g_{2,kl}\right\|^2}{\sigma^2}\right) \tag{5.1}$$

By marginalization, matching probabilities for any two points in fixed and moving image can be found:

$$P(C_{i,k}) = \sum_j \sum_l P(C_{(i,j).(k,l)}) = m_{G,ik} \tag{5.2}$$

The authors calculate Geodesic $m_{G,ik}$ and Euclidean $m_{E,ik}$ probabilities according to (5.2) and additionally a gray value-based correspondence probabilitiy (see next sub-Sect.). The product of the three is used to finally establish hard correspondences between feature points in fixed and moving image.

5.3.3 Gray Value Descriptors

The 'Robust Tree Registration' approach by Loeckx et al. [25], mentioned in the previous section, uses the gray value-based *'n-dimensional Scale-Invariant Feature Transform'* (*n-SIFT*) descriptor [8] in addition to a shape-based descriptor. The *n-SIFT* descriptor is an extension of the 2-dimensional SIFT descriptor introduced by Lowe [27]. The SIFT approach addresses feature localization as well as feature description. For feature localization, a resolution (scale) pyramid of Gaussian blurred images is created. 'Difference-of-Gaussian' (DoG) images are created by subtracting images of neighboring scales. Feature points are selected as local maxima (in space and scale) in the DoG images. The local orientation is determined based on a gradient orientation histogram around the feature point (see Fig. 5.2 for illustration). The described procedure delivers localization, orientation and scale of a feature point. The final feature description adds information about the local neighborhood of the feature point. First, the image gradient magnitudes and orientations are sampled around the feature point. To achieve orientation invariance, the gradient orientations are rotated relative to the feature point orientation. In order to avoid discontinuities of the descriptor for even small position changes and to give less emphasis to gradients that are far from the feature point, a Gaussian weighting function is used to assign a weight to the magnitude of each sample point. The weighted gradient magnitudes are collected block-wise in orientation histograms. The final descriptor is a vector containing the values of all the orientation histogram entries. In [25], the orientation histogram-based feature descriptor is taken instead of the DoG-based point selection to determine the correspondence between bifurcations in fixed and moving image.

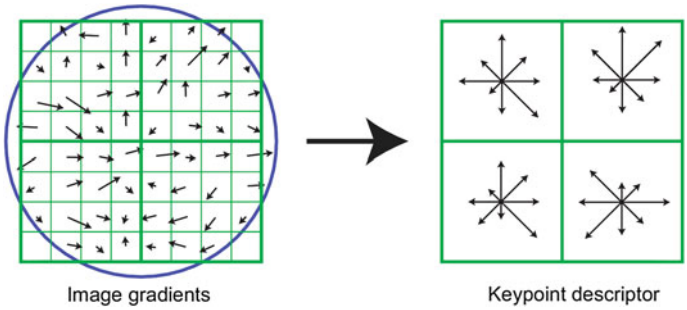

Fig. 5.2 Depiction of the gradient histogram based keypoint descriptor of the SIFT approach [27]. Image gradients (*left*) are weighted by a Gaussian window (*blue circle*) and are accumulated into orientation histograms summarizing the content of a subregion (*right*). The *arrow* length depicts the sum of the gradient magnitudes of the respective directional bin. The figure shows the case of a 2×2 descriptor array computed from an 8×8 set of samples. Figure from Lowe [27]

A cubic volume around each bifurcation is partitioned into 64 blocks and the gradient information is captured in a 60 bin histogram resulting in a 3840 dimensional feature vector. The feature descriptors are used in a probabilistic framework with the probability of correspondence between two bifurcations i and k modeled as Gaussian function:

$$P(i,k) \sim e^{-\|f_i - f_k\|^2}. \tag{5.3}$$

With f_i and f_k being the feature descriptor vector for bifurcation i and k, and $\|\|$ being the magnitude of the difference vector.

The so-called *SURF* features, for 'Speed-Up Robust Features' [1] follow a similar line of thinking. In order to speed up the computation, *SURF* features are based on 'Integral Images' instead of a resolution pyramid of smoothed images. 'Integral Images' give for each pixel position the sum (integral) of image intensities of the image block spanned between image origin and pixel position. They allow the fast computation of approximated blurred derivatives using box-filters. Instead of local maxima of the DoG as in the case of *SIFT*, an approximated determinant of the Hessian matrix is used as detector of blob-like structures to localize feature points. The *SURF* descriptor captures information of the local neighborhood using first order Haar wavelets (see, e.g., [9]) responses, which again can be computed efficiently using the Integral Image. As in the *SIFT* case, image information is captured block wise around the feature point. Denoting the wavelet response in x, y, and z-direction with d_x, d_y, and d_z respectively, the feature descriptor for the ith block is given by the sum of responses within the block:

$$v_i = \left(\sum d_x, \sum d_y, \sum d_z, \sum |d_x|, \sum |d_y|, \sum |d_z|\right) \tag{5.4}$$

The feature descriptors for all blocks are concatenated to produce the total feature descriptor. The *SURF* descriptor was used by Han [19], however for feature points

selected using the Förstner operator (see Sect. 5.2.2). Han used 64 blocks covering a cubic region, resulting in a 384 dimensional feature vector. Correspondences between feature points in fixed and moving image were found using nearest neighbors in the feature space. The inventors of the *SURF* descriptor claim that it combines high quality in terms of repeatability, distinctiveness, and robustness, with high computational performance. For application to pulmonary CT images this is supported by the fact that Han had won the online 'EMPIRE' registration contest within the MICCAI 2010 Workshop 'Medical Image Analysis For The Clinic—A Grand Challenge' [34] while having presented one of the fastest solutions with approx. 10 min computation time per case. It is, however, difficult to determine the portion of success that related to using the *SURF*, since Han used a hybrid approach and further information concerning the contribution of the individual parts of the approach is not available.

5.3.4 Shape Context

The 2D shape context as a regional descriptor of shape was introduced by Belongie et al. [2]. Assume a 2D shape is described by the set of its contour points. Then the idea of the Shape Context is to characterize a location on the contour by assessing in which view directions and in which distance other points on the contour appear. In order to do so, a log-polar histogram is positioned at a reference point on the objects contour and the number of remaining contour points is counted per histogram bin which gives a feature vector representing the shape at the reference point. The 3D shape context [14] is a straightforward extension of the 2D shape context being a 3D spherical histogram H_i in which the displacement vectors from the reference point p_i to the other points are counted. With K denoting the number of bins in the shape context histogram, Urschler and Bischof [33] use a cost function of the form

$$C\left(p_i, p_j\right) = \frac{1}{2}\sum_{k=1}^{K}\frac{\left[h_i(k) - h_j(k)\right]^2}{h_i(k) + h_j(k)} \tag{5.5}$$

to assess whether a point p_i on one shape instance of the lung surface corresponds to a point p_j on another shape instance. The same idea can be applied to a point set representing the centerlines of a tree structure. This allows to establish correspondence between branching points of vessel trees [21] or bronchial trees [5].

5.3.5 Shape Constrained Deformation

The key idea of shape constrained deformation to establish feature correspondence is to adapt a triangulated surface mesh from one image to the other. During the iterative adaptation, an external force attracts the mesh vertices to image features, while an internal force regularizes the attraction by preserving similarity. The topology remains unchanged. The sparse motion field is then derived from the displacement

of corresponding vertices. In contrast to other techniques for feature correspondence, the shape constrained deformation as well as the Shape Context, take into account the topology of the underlying structure and does not treat the feature points as an unconnected set.

5.3.5.1 Lung Surface Generation

The shape constrained deformation relies on the definition of a triangulated surface mesh in one image. In order to not only determine the deformation on the outer surface of the organ, internal structures should also be covered by the surface. In the context of motion field estimation of the lungs, *patient-specific* triangulated surfaces of the lungs are automatically generated in one image which contain most parts of the vessel tree and tumor surfaces. After applying a lung segmentation, all other structures besides the lungs are removed and a triangulation is applied after thresholding the segmented image. Triangulation is thereby performed using marching cubes [26]. Finally, the mesh is post-processed by applying several mesh operations to obtain a smooth surface with a certain amount of triangles, as shown in Fig. 5.3.

5.3.5.2 Mesh Adaptation

Shape-constrained deformation was proposed in [36] and applied for motion estimation in [24, 35]. Using a physical metaphor, the vertex configuration $\mathbf{v}$ that minimizes the following functional of summed energies is computed in each iteration

$$E(\mathbf{v}) = E_{\text{ext}}(\mathbf{v}) + \alpha E_{\text{int}}(\mathbf{v}). \tag{5.6}$$

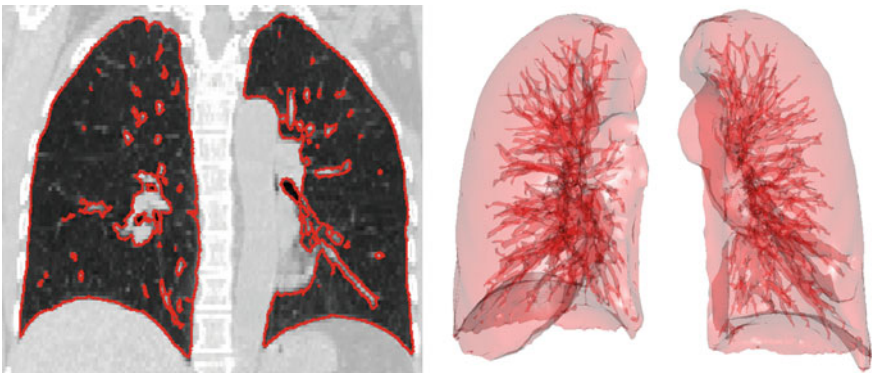

Fig. 5.3 Surface mesh capturing the transition from lung parenchyma to the lungs wall and to lung internal structures, such as vessels and bronchi. The mesh is shown in a coronal cut-plane (*left*) and as surface rendering (*right*). Shape constrained deformation allows to track the mesh through the breathing cycle, keeping mesh vertices at anatomically corresponding points

The parameter α balances the influence of both energy terms.

The external energy drives the mesh towards detected candidates by performing a feature search in a local neighborhood around the surface. Feature search is realized in a discrete manner by searching via a predefined sample pattern. For each barycenter of a triangle $\hat{\mathbf{x}}_i$, feature search is carried out in the direction of its normal $\mathbf{n}_i$

$$\mathbf{c}_j = j\delta\mathbf{n}_i \quad \text{with} \quad j = -l, \ldots, l, \tag{5.7}$$

which results in $(2l + 1)$ discrete sampling points $\mathbf{c}_j$, with a distance of δ. At every sampling point $\mathbf{x}_i^j = \hat{\mathbf{x}}_i + \mathbf{c}_j$, a feature function is evaluated and finally the target point is chosen best combining the feature value $F(.)$ and the distance $j\delta$ to the barycenter of the triangle

$$\mathbf{x}_i^{\text{target}} = \min_{\mathbf{x}_i^j \,|\, j=-l,\ldots,l} \left\{ Dj^2\delta^2 - F(\mathbf{x}_i^j) \right\} \tag{5.8}$$

with the weighting factor D.

With the detected target points $\mathbf{x}_i^{\text{target}}$, the external energy is given in a quadratic form as

$$E_{\text{ext}}(\mathbf{v}) = \sum_i w_i \left(\frac{\nabla I(\mathbf{x}_i^{\text{target}}) \nabla I(\mathbf{x}_i^{\text{target}})^T}{\left\| \nabla I(\mathbf{x}_i^{\text{target}}) \right\|^2} (\mathbf{x}_i^{\text{target}} - \mathbf{M}_i\mathbf{v}) \right)^2, \tag{5.9}$$

where $\mathbf{M}_i$ expresses the vertices $\mathbf{v}$ in terms of triangle centers and w_i is a weighting factor. The projection of $(\mathbf{x}_i^{\text{target}} - \mathbf{M}_i\mathbf{v})$ onto the image gradient at the target position $\nabla I(\mathbf{x}_i^{\text{target}})$ makes the energy invariant to movements of the triangle within the object tangent plane, thus preventing the triangle from becoming stuck at the target position. The weights w_i in Eq. (5.9) can be chosen according to the feature value of the target points to give the most promising points the largest influence during mesh reconfiguration.

Attraction of the mesh vertices to image features is accomplished by evaluating a certain feature function given as:

$$F(\mathbf{x}_i^j) = s \cdot \mathbf{n}_i^T \nabla I(\mathbf{x}_i^j) \frac{e^{\frac{\left\| \nabla I(\mathbf{x}_i^j) \right\|}{g_{\max}}}}{1 + \frac{\left\| \nabla I(\mathbf{x}_i^j) \right\|}{g_{\max}} e^{\frac{\left\| \nabla I(\mathbf{x}_i^j) \right\|}{g_{\max}}}}, \tag{5.10}$$

where the parameter $s \in \{1, -1\}$ accounts for the gradient direction, and $\mathbf{n}_i$ is the normal of the triangle for which the feature search is carried out. The gradient response is bounded by some threshold $g_{\max}$.

In order to distinguish between edges with similar feature responses further image quantities, as e.g., gray value statistics along the edge, have to be considered. For

Table 5.2 Registration accuracy for 5 publicly available image pairs at end of exhale and inhale breathing phase [7]

		Case 1	Case 2	Case 3	Case 4	Case 5
Without	$\mu \pm \sigma$	3.89 ± 2.78	4.34 ± 3.90	6.94 ± 4.05	9.83 ± 4.86	7.47 ± 5.51
registration	max	10.90	17.69	16.55	20.25	24.77
SCD	$\mu \pm \sigma$	1.01 ± 0.55	1.10 ± 0.53	1.33 ± 0.79	1.62 ± 1.16	1.70 ± 1.30
	max	3.42	3.47	5.19	12.39	16.54
Currents	$\mu \pm \sigma$	1.44 ± 0.72	1.72 ± 1.38	2.97 ± 2.96	3.30 ± 2.61	3.52 ± 2.91
FEIR	$\mu \pm \sigma$	1.02 ± 0.50	1.04 ± 0.50	1.44 ± 0.94	1.60 ± 1.32	1.67 ± 1.53
	max	2.77	3.40	7.31	13.26	15.92

The target registration error (TRE) for 300 manually placed landmarks, also provided by the study is presented. The Table lists mean, max, and std. dev. values of the TRE in mm resulting from two feature-based registration techniques: *Shape constrained deformation* (SCD, see Sect. 5.3.5), and *Currents* (see Sect. 5.3.6), and one intensity based registration technique: *Fast elastic image registration* (FEIR [23]). SCD and FEIR result in very similar TREs. The Currents based approach results in slightly higher values.

this reason, rejection intervals can be defined so that the feature will not be evaluated if certain image quantities, q^k, violate some learned criteria

$$\tilde{F}(\mathbf{x}_i^j) = \begin{cases} F(\mathbf{x}_i^j) : q^k \in [q^k_{\min}, q^k_{\max}] & \text{for all } q^k \text{ in } S \\ 0 \quad\quad\;\; : q^k \notin [q^k_{\min}, q^k_{\max}] & \text{for some } q^k \text{ in } S \end{cases}, \tag{5.11}$$

where S is the set of considered quantities.

Penalizing a deviation of the model's shape regularizes the image forces acting on it, and decreases the attraction to false image features. The internal energy

$$E_{\text{int}}(\mathbf{v}) = \sum_{j \in V} \sum_{k \in N(j)} ((\mathbf{v}_j - \mathbf{v}_k) - (\mathcal{T}_{\text{int}}[\mathbf{m}_j] - \mathcal{T}_{\text{int}}[\mathbf{m}_k]))^2 \tag{5.12}$$

preserves the shape similarity of all adapted vertices $\mathbf{v}_j$ to the model vertices $\mathbf{m}_j$, with $N(j)$ being the set of neighbors of the vertex with index j. Deviations from the initial model are penalized by calculating the vector difference between neighboring vertices of the adapted mesh and the corresponding vertices of the shape model undergoing a geometric transformation $\mathcal{T}_{\text{int}}[.]$. Depending on the desired flexibility of the underlying shape prior, similarity transformations or affine transformations are typically chosen. In each case, the geometric transformation is determined prior to the calculation of Eq. (5.12) in a closed form solution based on the point correspondences between adapted and model vertices.

Table 5.2 shows the target registration error (TRE) for 5 publicly available inhale/exhale image pairs [7] in comparison to the Currents based approach, discussed in the next chapter, and to an intensity based image registration approach [23].

5.3.6 Currents-Based Registration

Another approach, using so called currents, to circumvent explicit correspondences was used by Gorbunova et al. in [17]. The basic idea is to represent shapes as sets of vectors: Tangential vectors in the case of curvi-linear shapes and normal vectors in the case of *surfaces* (see [11] and references therein). The *current* associated with a surface is defined as the flux of a probing vector field ω through the surface S:

$$S(\omega) = \int_S \omega(\mathbf{x})^t (\mathbf{u} \times \mathbf{v})(\mathbf{x}) d\sigma(\mathbf{x}) \tag{5.13}$$

where $(\mathbf{u}, \mathbf{v})$ is a local basis of its tangent plane at $\mathbf{x}$, $(\mathbf{u} \times \mathbf{v})(\mathbf{x})$ being the surface normal at $\mathbf{x}$ and $d\sigma(\mathbf{x})$ the area element of the surface. Similarly, the current associated with a curvi-linear structure L is defined as the path-integral of a probing vector field ω along the curve:

$$L(\omega) = \int_L \omega(\mathbf{x})^t \tau(\mathbf{x}) \mathbf{dx} \tag{5.14}$$

with $\tau(\mathbf{x})$ being the tangent of the curve at $\mathbf{x}$. Figure 5.4 depicts the currents representing a pulmonary vessel tree. We adhere to the notation of the authors of [11] by using the same letters L and S for the geometrical structure and their associated currents. So currents are a mapping of the space of vector fields ω to the space of real numbers $\mathbb{R}$. This provides the basis to define a similarity measure in the context of the registration of curves, surfaces, or sets of them. Simplified, to register the surfaces S_1 and S_2, the idea is to evaluate the flux integral Eq. (5.13) through S_1 using a probing vector field constructed from S_2 and vice versa. To be able to do this efficiently, the vector fields ω are represented as an integral (or sum in the discrete case) of reproducing Gaussian kernels $K^W(\mathbf{x}, \mathbf{y}) = exp(- \parallel \mathbf{x} - \mathbf{y} \parallel^2 \lambda_w^2)$. $\mathbf{x}, \mathbf{y}$ are the positions and λ_W the width of the kernel. Given a vector β at position $\mathbf{y}$, the

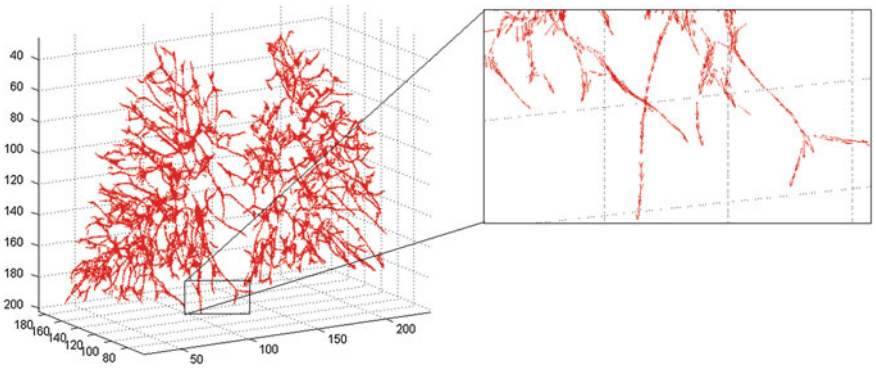

Fig. 5.4 Currents corresponding to pulmonary vessel centerlines. Figure from Gorbunova et al. [17]

corresponding vector field is given by $\omega(\mathbf{x}) = K^W(\mathbf{x}, \mathbf{y})\beta$, the vector field of a set of local vectors is the superposition of the individual contributions. Representing curves and surfaces as piecewise linear structures (e.g. as polygons, or triangular meshes, respectively), each element (a straight line element, or a triangle, respectively) gives rise to a reproducing kernel positioned at the center of that element. In the formalism above, the distance between two curves or two surfaces can be calculated without the need for establishing point-wise correspondence between the two structures. This is achieved by a distance metric using a kernel-based inner product of currents:

$$\langle L, L^{'} \rangle = \sum_{i=1}^{n} \sum_{j=1}^{m} (\tau_i)^t K^W(\mathbf{c}_i, \mathbf{c}_j^{'}) \tau_j^{'}, \tag{5.15}$$

where L and $L^{'}$ are the two curves to be matched, with a number of n and m line-elements, and with tangential vectors τ_i and $\tau_j^{'}$, and centers $\mathbf{c}_i$ and $\mathbf{c}_j^{'}$ respectively. So the term $(\tau_i)^t K^W(\mathbf{c}_i, \mathbf{c}_j^{'})\tau_j^{'}$ measures the match of tangential vectors of the line elements. The distance between the two curves L and $L^{'}$ is then

$$d^2(L, L^{'}) = \| L^{'} - L \|^2 = \| L \|^2 + \| L^{'} \|^2 - 2\langle L, L^{'} \rangle, \tag{5.16}$$

with the norm of a current L, $\| L \|$ being defined as the supremum path integral of any regular vector field. The registration of the curves L and $L^{'}$ is performed in the framework of large deformation diffeomorphic matching [15] with a cost function combining the distance for line, and surface features, and a regularization term advancing smoothness of the resulting transformation field. Currents-based registration of lung images has been recently introduced. Results reported so far (see 5.2) do not completely reach the accuracy of intensity-based registration, but possibly the advantages of the approach have not been completely exploited yet. Recently, a hybrid registration approach using currents has been presented [18].

5.4 Interpolation

Finally, to be able to obtain deformation vectors between feature points, an interpolation of the sparsely given deformation field is required. In the following sub-Sections a selection of proposed methods will be discussed.

5.4.1 B-Splines

B-spline-based approaches are very efficient when a sparse set of deformation vectors defined on a Cartesian grid shall be interpolated, see e.g. Rueckert et al. [31].

McClelland used B-spline interpolation to create a 4D motion model in [29]. Since in our case, feature points are virtually always irregularly distributed and since B-spline-based interpolation is described in some detail in Chap. 6.2.1, we omit a description here.

5.4.2 Radial Basis Functions

Radial basis functions perform an interpolation of the sparse and possibly irregularly defined deformation by expressing the deformation as a linear combination of the sparse deformation weighted by some kernel. One common way to perform the interpolation is by using thin-plate splines (TPS) [4]. The TPS approach is physically motivated by a thin metal plate which will take the overall shape in which it is least bent given the deformation at some locations. The approach can be generalized to arbitrary dimensions d and degrees of smoothness in terms of the order m of derivatives of the associated functional to be minimized [30]. For the physically motivated case of minimal bending energy, we have $m = 2$. The radial basis functions $U(\mathbf{x}, \mathbf{p})$ associated to the respective choice of d and m are

$$U(\mathbf{x}, \mathbf{p}) \sim \begin{cases} |\mathbf{x} - \mathbf{p}|^{2m-d} \, ln|\mathbf{x} - \mathbf{p}|, & \text{if } (2m - d) \text{ is an even positive integer} \\ |\mathbf{x} - \mathbf{p}|^{2m-d}, & \text{otherwise} \end{cases} \tag{5.17}$$

In contrast to TPS, elastic-body splines (EBS) [10] use a more sophisticated physical model derived from the Navier partial differential equations for a homogeneous isotropic elastic body subjected to loads (forces)

$$\mathbf{f}(\mathbf{x}) = \mu \nabla^2 \mathbf{u}(\mathbf{x}) + (\lambda + \mu) \nabla (\nabla \cdot \mathbf{u}(\mathbf{x})) \tag{5.18}$$

where $\mathbf{u}(\mathbf{x})$ is the displacement of a point, ∇^2 denote the Laplacian and ∇ the gradient, $\nabla \cdot \mathbf{u}(\mathbf{x})$ is the divergence and $\mathbf{f}(\mathbf{x})$ is the force field. Typically, for the three-dimensional case, the radial kernel for the EBS that defines the force field is chosen as $r(\mathbf{x}) = (x + y + z)^{\frac{1}{2}}$. The Lamé coefficients λ and μ allow to describe the physical properties of the elastic material. Both TPS and EBS lead to an equation of the type

$$\mathbf{d}(\mathbf{x}) = \sum_i \mathbf{U}(\mathbf{x}, \mathbf{p}_i)\mathbf{c}_i + \mathbf{A}\mathbf{x} + \mathbf{b} \tag{5.19}$$

expressing the deformation vector $\mathbf{d}$ with an affine part $\mathbf{A}\mathbf{x} + \mathbf{b}$ and a weighted sum of radial basis functions $U(\mathbf{x}, \mathbf{p}_i)$. Weights $\mathbf{c}_i$ are determined using the condition that Eq. (5.19) is fulfilled for all point-pairs $\mathbf{p}_i$ and $\mathbf{q}_i$ in fixed and moving image, respectively. This condition leads with $\mathbf{d}_i = \mathbf{q}_i - \mathbf{p}_i$ to a linear equation system which can be solved with standard approaches, such as the Singular Value Decomposition. In case of EBS, equations are coupled with respect to space coordinates. The TPS equations, associated with displacements along one coordinate axis, are independent.

Therefore, the computational effort for EBS is higher limiting the use of EBS. For many applications, TPS provide a sufficient model and can be computed with reasonable computational effort and they are thus the method of choice. However, as the radial basis function-based interpolation is defined as a linear combination of the sparse deformation weighted by some kernel, the deformation at one location $\mathbf{x}$ is influenced by *all* given displacement vectors of the sparse deformation field, i.e., in other words the impact of some displacement vectors of the sparse deformation field is not only local but global. Thus, as all displacement vectors of the sparse deformation field have to be considered, the radial based interpolation can result in high computational costs once the number of given displacement vectors becomes large.

5.4.3 Nearest Neighbour Interpolation

The idea of a K nearest neighbour (KNN) interpolation is to find the dense deformation by taking the K nearest locations with sparse motion vectors $\mathbf{u}_k$ for a given position $\mathbf{x}$ and then calculate the deformation as

$$\mathbf{u}_\mathbf{x} = \frac{1}{\sum_{k=1}^{K} w_k} \sum_{k=1}^{K} w_k \mathbf{u}_k \tag{5.20}$$

where $\mathbf{u}_\mathbf{x}$ is the deformation vector at position $\mathbf{x}$ and w_k is a weighting factor. If w_k is equal to one, then the mean is calculated. However, the w_k can also be defined to be distance dependant, so that $\mathbf{u}_k$ that belong to locations that lie further away from $\mathbf{x}$ have less influence. In contrast to other interpolation schemes, the KNN interpolation does not assume a physical model. Especially, when a large number of sparse locations is given, computation of, e.g., radial basis function-based interpolation, can be computationally very expensive. However, the problem of KNN is that the interpolation is not smooth which can lead to a locally implausible deformation field and, e.g., Gaussian-smoothing is needed to overcome this limitation. Comparing lung motion fields interpolated motion fields using TPS and KNN interpolation, showed that TPS provided a higher landmark accuracy [35].

References

1. Bay, H., Ess, A., Tuytelaars, T., Van Gool, L.: Speeded-up robust features (surf). Comput. Vis. Image Underst. **110**, 346–359 (2008)
2. Belongie, S., Malik, J., Puzicha, J.: Shape matching and object recognition using shape contexts. IEEE Trans. Pattern Anal. Mach. Intell. **24**(4), 509522 (2002)
3. Besl, P.J., McKay, N.D.: A method for registration of 3-d shapes. IEEE Trans. Pattern Anal. Mach. Intell. **14**, 239–256 (1992)

4. Bookstein, F.: Principal warps: thin-plate splines and the decomposition of deformations. IEEE Trans. Pattern Anal. Mach. Intell. **11**(6), 567–585 (1989)
5. Buelow, T., Lorenz, C., Wiemker, R., Honko, J.: Point based methods for automatic bronchial tree matching and labelling In: Proceedings of SPIE Conference on Medical Imaging: Physiology and Function from Medical Images, vol. 6143, pp. O1430. San Diego (2006)
6. Cao, K., Du, K., Ding, K., Reinhardt, J.M., Christensen, G.E.: Regularized nonrigid registration of lung ct images by preserving tissue volume and vesselness measure. In: van Ginneken, B. Murphy, K., Heimann, T., Pekar, V., Deng, X. (eds.) MICCAI2010 Workshop: Medical Image Analysis For The Clinic–A Grand Challenge, pp. 43–54. CreateSpace (2010)
7. Castillo, R., Castillo, E., Guerra, R., Johnson, V.E., McPhail, T., Garg, A.K., Guerrero, T.: A framework for evaluation of deformable image registration spatial accuracy using large landmark point sets. Phys. Med. Biol. **54**(7), 18491870 (2009)
8. Cheung, W., Hamarneh, G.: n-sift: n-dimensional scale invariant feature transform. IEEE Trans. Image Process. **18**, 2012–2021 (2009)
9. Chui, C.K.: An Introduction to Wavelets. Academic Press, San Diego (1992)
10. Davis, M., Khotanzad, A., Flamig, D., Harms, S.: A physics-based coordinate transformation for 3-d image matching. IEEE Trans. Med. Imaging **16**(3), 317–328 (1997)
11. Durrleman, S., Pennec, X., Trouvé, A., Thompson, P., Ayache, N.: Inferring brain variability from diffeomorphic deformations of currents: an integrative approach. Med. Image Anal. **12**(5), 626–637 (2008)
12. Feldmar, J., Declerck, J., Malandain, G., Ayache, N.: Extension of the icp algorithm to nonrigid intensity-based registration of 3d volumes. Comput. Vis. Image Und. **66**(2), 193–206 (1997)
13. Frangi, A.F., Niessen, W.J., Vincken, K.L., Viergever, M.A.: Muliscale vessel enhancement filtering. In: Medical Image Computing and Computer-Assisted Intervention (MICCAI 1998). Lecture Notes in Computer Science **1496**, 130–137 (1998)
14. Frome, A., Huber, D., Kollure, R., Bülow, T., Malik, J.: Recognizing objects in range data using regional point descriptors. In: Proceedings of ECCV, pp. 533540 (2004)
15. Glaunes, J., Qiu, A., Miller, M.I., Younes, L.: Large deformation diffeomorphic metric curve mapping. Int. J. Comput. Vis. **80**(3), 317–336 (2008)
16. Goldlücke, B.: The Structure Tensor of an Image. In: Lecture: Introduction to Image Processing on the GPU, Heidelberg Collaboratory for Image Processing. http://hci.iwr.uni-heidelberg.de/Staff/bgoldlue/cuda_ss_2012/cuda_ss_2012_01_structure_tensor.pdf (2012)
17. Gorbunova, V., Durrleman, S., Lo, P., Pennec, X., de Bruijne, M.: Curve- and surface-based registration of lung CT images via Currents. In: Proceedings of Second International Workshop on Pulmonary Image Processing, MICCAI, pp. 15–25. London (2009)
18. Gorbunova, V., Durrleman, S., Lo, P., Pennec, X., de Bruijne, M.: Lung CT registration combining intensity, curves and surfaces. In: IEEE International Symposium on Biomedical Imaging: From Nano to Macro, 2010, pp. 340–343 (2010)
19. Han, X.: Feature-constrained nonlinear registration of lung ct images. In: van Ginneken, B., Murphy, K., Heimann, T., Pekar, V., Deng, X. (eds.) MICCAI2010 Workshop: Medical Image Analysis For The Clinic–A Grand Challenge, pp. 63–72. CreateSpace (2010)
20. Hartkens, T., Rohr, K., Stiehl, H.S.: Evaluation of 3d operators for the detection of anatomical point landmarks in MR and CT images. Comput. Vis. Image Und. **86**(2), 118–136 (2002)
21. Hilsman, A., Vik, T., Kaus, M., Franks, K., Bissonette, J.P., Purdie, T., Beziak, A., Aach, T.: Deformable 4D CT lung registration with vessel bifurcations. In: Proceedings of International Conference of Computer Assisted Radiology and Surgery (CARS 2007). Berlin, Germany (2007)
22. Huang, Y., Feng, H., Zhao, P., Tong, T., Li, C.: Automatic landmark detection and norid registration of intra-subject lung CT images. In: International Conference on Information Science and, Engineering, pp. 3605–3608 (2009)
23. Kabus, S., Lorenz, C. : Fast elastic image registration. In: van Ginneken, B., Murphy, K., Heimann, T., Pekar, V., Deng, X. (eds.) MICCAI2010 Workshop: Medical Image Analysis For The Clinic–A Grand Challenge, pp. 81–89. CreateSpace (2010)

24. Klinder, T., Lorenz, C., von Berg, J., Renisch, S., Blaffert, T., Ostermann, J.: 4DCT image-based lung motion field extraction and analysis. In: Proceedings of SPIE Conference on Medical Imaging: Image Processing, vol. 6914, pp. 69, 141L–1-11 (2008)
25. Loeckx, D., Smeets, D., Keustermans, J., Hermans, J., Maes, F., Vandermeulen, D., Suetens, P.: 3d lung registration using splineMIRIT and robust tree registration (RTR). In: B. van Ginneken, K. Murphy, T. Heimann, V. Pekar, X. Deng (eds.) MICCAI2010 Workshop: Medical Image Analysis For The Clinic—A Grand Challenge, pp. 109–117. CreateSpace (2010)
26. Lorensen, W., Cline, H.: Marching cubes: a high resolution 3D surface construction algorithm. Comput. Graph. **21**, 163–169 (1987)
27. Lowe, D.G.: Distinctive image features from scale-invariant keypoints. Int. J. Comput. Vis. **60**, 91–110 (2004)
28. Matsopoulos, G.K., Mouravliansky, N.A., Asvestas, P.A., Delibasis, K.K., Kouloulias, V.: Thoracic non-rigid registration combining self-organizing maps and radial basis functions. Med. Image Anal. **9**(3), 237–254 (2005)
29. McClelland, J.R., Blackall, J.M., Tarte, S., Chandler, A.C., Hughes, S., Ahmad, S., Landau, D.B., Hawkes, D.J.: A continuous 4d motion model from multiple respiratory cycles for use in lung radiotherapy. Med. Phys. **33**(9), 3348–3358 (2006)
30. Rohr, K., Stiehl, H., Sprengel, R., Buzug, T., Weese, J., Kuhn, M.: Landmark-based elastic registration using approximating thin-plate splines. IEEE Trans. Med. Imaging **20**(6), 526–534 (2001)
31. Rueckert, D., Sonoda, L.I., Hayes, C., Hill, D.L.G., Leach, M.O., Hawkes, D.J.: Non-rigid registration using free-form deformations: application to breast mr images. IEEE Trans. Med. Imaging **18**(8), 712–721 (1999)
32. Stewart, C.V., Lee, Y.L., Tsai, C.L.: An uncertainty-driven hybrid of intensity-based and feature-based registration with application to retinal and lung CT images. In: Medical Image Computing and Computer-Assisted Intervention (MICCAI 2004). Lecture Notes in Computer Science **3216**, 870–877 (2004)
33. Urschler, M., Bischof, H.: Assessing breathing motion by shape matching of lung and diaphragm surfaces. In: Proceedings of SPIE Conference on Medical Imaging: Physiology and Function from Multidimensional Images, vol. 5746, pp. 440–452. San Diego (2005)
34. van Ginneken, B., Murphy, K., Heimann, T., Pekar, V., Deng, X. (eds.): MICCAI2010 Workshop: Medical Image Analysis for the Clinic—A Grand Challenge. CreateSpace (2010)
35. von Berg, J., Barschdorf, H., Blaffert, T., Kabus, S., Lorenz, C.: Surface based cardiac and respiratory motion extraction for pulmonary structures from multi-phase CT. In: Proceedings of SPIE Conference on Medical Imaging: Physiology and Function from Medical Images, vol. 6511, pp. 65, 110Y1-11 (2007)
36. Weese, J., Kaus, M., Lorenz, C., Lobregt, S., Truyen, R., Pekar, V.: Shape constrained deformable models for 3D medical image segmentation. In: Proceedings of Image Processing in Medical Imaging (IPMI), pp. 380–387. Springer (2001)

Chapter 6
Intensity-Based Deformable Registration: Introduction and Overview

David Sarrut, Jef Vandemeulebroucke and Simon Rit

Abstract The purpose of this chapter is to give an introduction to intensity-based deformable image registration and present a brief overview of the state-of-the-art. First, we lay out the basic principles of deformable registration. Next, the key components of the registration framework are discussed in detail and two popular algorithms for deformable registration are described as an example. We review past studies on respiratory motion estimation for radiotherapy. Finally, we briefly list useful open-source software packages and available image and validation data sets for deformable registration of the thorax.

6.1 Principles of Intensity-Based Deformable Registration

6.1.1 Introduction

Deformable image registration (DIR) is a fundamental image processing tool that is widely used for the analysis of medical images. Its use in the field of radiation therapy is relatively recent and in constant progress: over 150 full-length papers can be retrieved on *PubMed*, about a third of which appeared in 2011 (Fig. 6.1). The application of DIR in the field of radiotherapy is usually related to estimating

D. Sarrut (✉) · S. Rit
Université de Lyon, CREATIS, CNRS UMR5220, Inserm U1044, INSA-Lyon, Université Lyon 1, Centre Léon BérardLyon, France
e-mail: David.Sarrut@creatis.insa-lyon.fr

J. Vandemeulebroucke
iMinds, Department of Future Media and Imaging, Gaston Crommenlaan 8 (box 102), B-9050 Ghent, Belgium

J. Vandemeulebroucke
Vrije Universiteit Brussel, Department of Electronics and InformaticsPleinlaan 2, B-1050 Brussels, Belgium

J. Ehrhardt and C. Lorenz (eds.), *4D Modeling and Estimation of Respiratory Motion for Radiation Therapy*, Biological and Medical Physics, Biomedical Engineering,
DOI: 10.1007/978-3-642-36441-9_6,

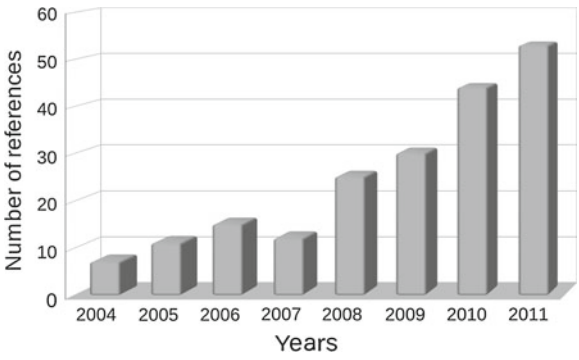

Fig. 6.1 Number of full-length papers by year available on PubMed dealing with deformable registration for radiation therapy. The numbers documented correspond to the hits of a search with terms "deformable registration" and "radiotherapy" (and related terms such as "radiation therapy", "non-rigid registration", "non-linear registration", etc.)

anatomical changes that occur from one treatment fraction to another, or during fractions. In particular, respiration—an important source of intrafraction motion in the thorax and upper abdomen—has been studied extensively. DIR is considered a key enabling tool for 4D radiation therapy [29].

Registration is the task of retrieving the unknown spatial transformation that puts two images in correspondence, by aligning the imaged objects. For deformable image registration, the mapping can be spatially varying, and is usually locally or semi-locally defined. Intensity-based DIR (IB-DIR) consists in considering the pixel intensity values to retrieve that mapping, in contrast to other approaches such as biophysical modeling (see Chap. 4) or surface- and landmark-based registration techniques (see Chap. 5). No preprocessing involving image segmentation or feature extraction is generally required and only the intensity distributions of the images are used.

The difficulty of deformable registration is twofold. First of all, the problem is ill-posed. A problem is said to be well-posed when a solution exists, is unique, and depends continuously on the initial data. A problem is ill-posed when it fails to satisfy at least one of these criteria. As a consequence, it is important to incorporate prior knowledge about the sought transformation in the registration framework, limiting the search space to physically or physiologically plausible solutions. Several approaches have been proposed to do so, and we will present some general mechanisms in the following sections. Methods specifically developed for images of the thorax are discussed in Chap. 7.

A second issue of DIR is that there is no standardized means for evaluating the accuracy of the result. On real patient images, establishing a reference is a tedious and time-consuming task, and the validation obtained is partial and only locally valid due to the large amount of degrees of freedom. Despite numerous recent efforts, evaluation of DIR remains challenging. Validation of DIR will be extensively discussed in Chap. 8.

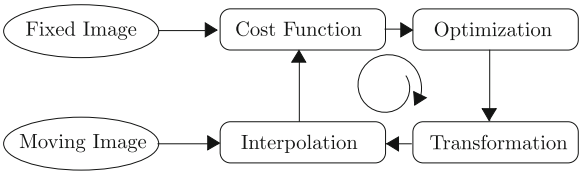

Fig. 6.2 A general registration framework indicating the main components of the iterative registration procedure. Following Ibanez et al. [25]

6.1.2 General Framework

Registration is commonly formulated as an optimization problem which aims at finding the spatial transformation $\boldsymbol{T}$, that minimizes a cost function over a *fixed* image $I_A : \Omega_A \rightarrow \mathbb{R}$ and a *moving* image $I_B : \Omega_B \rightarrow \mathbb{R}$ with $\Omega_A, \Omega_B \subset \mathbb{R}^3$, given the coordinate transformation $\boldsymbol{T}$ (see Eq. (6.1)).

$$\hat{\boldsymbol{T}} = \arg\min_{\boldsymbol{T}} F(I_A, I_B, \boldsymbol{T}) \tag{6.1}$$

Equation (6.1) can usually not be solved directly, but an estimate of the optimal transformation is obtained through an iterative optimization process.

A general framework of the registration procedure is presented in Fig. 6.2. Assume the procedure is started with an initial transformation. The latter can be applied to the moving image, effectively mapping it to the coordinate space of the fixed image. The result of the cost function can be computed, expressing the fitness of the current mapping. The optimizer can then propose a new set of transformation parameters based on this measure in an attempt to improve the matching, and the iteration loop is repeated until convergence.

It is important to note that registration takes place in physical space. As images are generally available as discrete representations, computing the fitness value between a fixed image and a transformed moving image will require evaluating the moving image at non-grid positions using interpolation. Commonly used interpolation schemes include nearest neighbor interpolation, linear interpolation and B-spline interpolation [33]. Interpolation will not be discussed further. The remaining registration components will be described in detail in the following sections.

6.1.3 Transformation

The term transformation is used here to refer to the mathematical expression of the spatial mapping between the coordinate spaces of the images. It is defined by the parametrization used to represent the deformation and subsequently determines the search space over which the optimization is to be performed. The transformation

is one of the components that allows to enforce a transformation model, in which deformations are favored that respect certain mathematical or physical laws, or mimic some particular physiological behavior (see Holden et al. [24] for an excellent review on transformation models).

By convention, the transformation is defined as mapping points from the coordinate space of the fixed image to coordinate space of the moving image, i.e. the position $\boldsymbol{x}$ in the image I_A is mapped to a corresponding position $\boldsymbol{T}(\boldsymbol{x}) = \boldsymbol{x}'$ in image I_B. Observe that by retrieving the intensities of the moving image at the transformed grid positions of the fixed image—using interpolation, one effectively warps the moving image to the coordinate space of fixed image.

Based on the support of the underlying functions, roughly three groups of parametrizations can be distinguished to represent a deformable transformation: global, semi-local and local. Global representations include transformations expressed using harmonic functions or global polynomials, such as thin plate splines or radial basis functions. Semi-local transformations are expressed using functions with a compact support, such as wavelets and B-splines. They tend to be more suited for representing highly localized deformation, in addition to being advantageous during optimization because of their reduced complexity. Local parametrizations are typically dense vector fields, in which a vector is used for representing the displacement of a single voxel.

6.1.4 Similarity Measure

The cost function F should quantify the fitness of a transformation between two images. The cost function usually represents a compromise between image similarity and deformation regularity, e.g.

$$F = \alpha S(I_A, I_B, \boldsymbol{T}) + (1 - \alpha)R(\boldsymbol{T}), \tag{6.2}$$

in which S is a dissimilarity metric which evaluates the correspondence between the image intensity distributions in a predefined metric space, given the transformation. R is a regularization term favoring certain properties in the transformation and will be discussed in Sect. 6.1.5.

Based on the nature of the dissimilarity metric S, we can make a distinction between feature-based and intensity-based approaches, or hybrid approaches that are a combination of both. Feature-based approaches rely on the matching of landmarks, segmentations or other features extracted from the images prior to registration, and are the subject of Chap. 5.

6.1.4.1 Theoretical Background of Intensity-Based Similarity Measures

Intensity-based similarity between two images is quantified by measuring a link between the intensity distributions of the image pair. The underlying assumption is that this link will become stronger when images are well registered, and inversely will become weaker as the quality of the registration decreases. The link should exist because images are acquired from the same physical structure using two different devices or at two different times, or from the corresponding structure belonging to different subjects.

The link is evaluated through the concept of *dependency*. The intensity distributions are said to be dependent when a variation in one distribution leads to variation in the other. Note that dependence does not mean causality. The term *correlation* is generally used when the relationship is reciprocal. If there is no link, intensity distributions are *independent*, whereas if the knowledge of one distribution allows to perfectly predict the second, the link is said to be *functional*; i.e. there exists a function $\mathcal{T}$ allowing to map a grey-level from one distribution to a grey-level of the other; i.e. $\mathcal{T}(a) = b$. Again, note that this relationship is not necessarily reciprocal.

The concept of *variation* plays an important role in the evaluation of the dependency. Dependency is often regarded as the reduction of the variation of a distribution caused by the knowledge of the other. Different definitions of the type of variation lead to different measures. We can therefore define the term intensity-based similarity measure in the following way: it is a function that measures a type of dependency between the distributions of the intensities that characterize the images.

6.1.4.2 Joint Histogram

The majority of the existing intensity-based similarity measures can be computed (even though it is not always necessary) from the same mathematical object called the joint histogram. It is essentially a 2D matrix $p^T_{A,B}$, that summarizes the statistical link between the intensity distributions of the images for a given transformation. $p^T_{A,B}(a, b)$ represents the probability of having the intensity a in the image I_A and b in image I_B at the same spatial location, for a given transformation $\boldsymbol{T}$.

In practice, it is computed by looping over all pixel positions $\boldsymbol{x}$ in the image I_A and looking at the corresponding $\boldsymbol{T}(\boldsymbol{x}) = \boldsymbol{x}'$ position in image I_B. As we are dealing with discrete images, interpolation is required and several methods can be used to deal with non-integer pixel positions. Conventional approaches involve nearest neighbor interpolation, linear interpolation and partial volume [37].

The process is illustrated for two dimensional images in Fig. 6.3. Suppose $a = I_A(\boldsymbol{x})$ and $\boldsymbol{x}_3$ is the nearest pixel position of $\boldsymbol{T}(\boldsymbol{x})$ in I_B with $b = I_B(\boldsymbol{x}_3)$ the intensity in I_B. For nearest neighbor interpolation, the joint intensity matrix $h^T_{A,B}$ is updated by $h^T_{A,B}(a, b) += 1$. Using a linear interpolation approach, the intensity is first interpolated, $c = \sum_i w_i I_B(\boldsymbol{x}_i)$, and used to update the histogram $h^T_{A,B}(a, c) += 1$. Using the partial volume approach, the histogram is updated

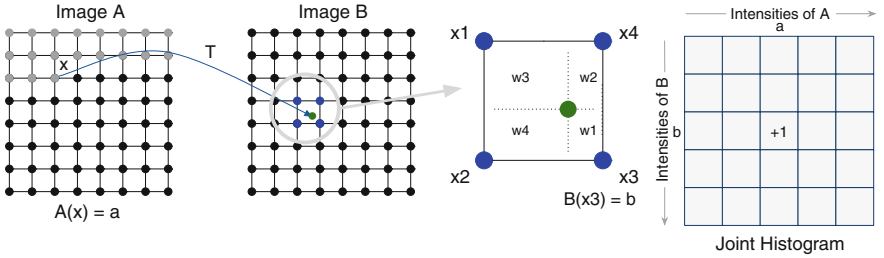

Fig. 6.3 2D illustration of the joint histogram updating process

for four intensities $I_B(\boldsymbol{x}_i) = b_i$, with $h^T_{A,B}(a, b_i) += w_i$, which tends to give smoother histograms. The computed frequencies of joint intensities are normalized to the number of overlapping voxels N, resulting in the joint probabilities $p^T_{A,B}(a, b) = h^T_{A,B}(a, b)/N$.

Following the previous description, the size of the joint histogram matrix would be $N_A \times N_B$ with N_A and N_B the number of different intensities in I_A and I_B. In practice however, this would lead to large matrix sizes, which is why intensities are usually grouped into bins to reduce the size and enhance the statistics of the joint histogram.

For motion estimation of thoracic CT images, the two measures that have been frequently used are the sum of squared differences and mutual information, and we will focus on them first.

6.1.4.3 Sum of Squared Differences

The main advantage of computing the sum of squared differences (SSD) lies in its simplicity. It consists in summing the quadratic differences between the image intensities, voxel by voxel. The SSD can be computed from the joint histogram, $SSD(I_A, I_B) = \sum_{a,b}(a-b)^2 \times p^T_{A,B}(a, b)$, but it is more efficient to not explicitly compute the joint histogram. Usually, the result is averaged over the amount of voxels N of the current overlap between the images $\Omega^T_{A,B}$, to avoid favoring transformations that minimize the overlap,

$$SSD(I_A, I_B) = \frac{1}{N} \sum_{\boldsymbol{x} \in \Omega^T_{A,B}} \Big(I_A(\boldsymbol{x}) - I_B\big(\boldsymbol{T}(\boldsymbol{x})\big) \Big)^2, \tag{6.3}$$

in which we assumed an interpolation scheme for evaluating $I_B(\boldsymbol{T}(\boldsymbol{x}))$. It allows an easy expression of the derivatives and it is fast to compute. However, it assumes that the intensity distributions are similar in the two images and this assumption is violated when considering expiration to inspiration registration, due to the changes in lung density.

Variants have been proposed, aimed at taking into account this lung density change. For example, Yin et al. [80] proposed to use the sum of squared tissue volume difference (SSTVD) to account for the preservation of the tissue mass of the lungs during respiration. Alternatively, pre-processing of the images has been proposed [57]. Similarity measures developed specifically for the lung are described in Chap. 7.

6.1.4.4 Mutual Information

Another measure that has been extensively used is the mutual information (MI) [37, 46, 74]

$$MI(I_A, I_B) = \sum_a \sum_b \left(p^T_{A,B}(a,b) \ln \frac{p^T_{A,B}(a,b)}{p_A(a)p_B(b)} \right), \tag{6.4}$$

with $p_A(a)$ and $p_B(b)$ the probability of intensity a in image I_A, and b in image I_B, and $p^T_{A,B}(a,b)$ the joint probability for a given $\boldsymbol{T}$ as described earlier.

The underlying idea is to measure the statistical dependence between the distributions of intensities of the two images. The link is quantified by an entropy measure. The entropy of a distribution $H(I_A) = -\sum_a p_A(a) \ln p_A(a)$ is a logarithmic measure of the density of states and can be considered as a measure of the uncertainty of the distribution: entropy is zero when one state is certain ($p_A(a) = 1$) and is maximal when all events have the same probability.

Given an intensity distribution, the mutual information can be interpreted as the decrease of uncertainty (or gain of information) brought by the knowledge of the second distribution ($MI(I_A, I_B) = H(I_B) - H(I_B|I_A)$). It can also be viewed as a distance between two 2D distributions: the current one composed of the joint image intensity probability given the current transformation ($p^T_{A,B}(a,b)$), and the one corresponding to the case where there is a total independence of the two distributions ($p_A(a) \times p_A(b)$). The further the joint probability from the total independence, the better the registration. The distance measure is called the Kullback-Leibler distance. A variant, the normalized mutual information (NMI) [65], normalizes the measure with respect to the image overlap and has shown to be less sensitive to changes in overlap.

6.1.4.5 Other Similarity Measures

Other conventional measures for mono-modal image registration are the sum of absolute differences (SAD), or the linear correlation coefficient (LCC) which measures the of a linear relationship between the intensity distributions and is also widely used for registration of thoracic CT [82, 84]. For multi-modal cases, the correlation

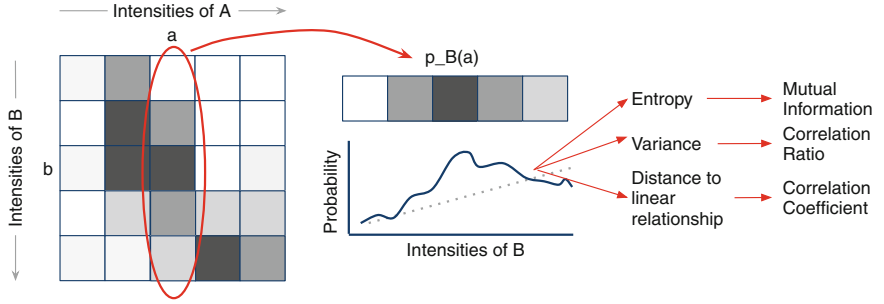

Fig. 6.4 Illustration of three different ways to measure uncertainty in the partial intensity probability distribution of intensity a in A: $P_B(a)$

ratio (CR) [50] measures the strength of the dependency using the variance of the distributions.

Figure 6.4 illustrates three cases, where the variation in I_B knowing a in I_A is measured in three different ways. LCC considers that the function $\mathcal{T}$ between the intensity distributions is a linear function.This is a stronger assumption on the link between the image intensities than in the case of CR and MI, which assume a functional relation and statistical dependence, respectively. MI considers the intensities like labels and thus any pairwise inversion of labels leads to the same value. CR is not a symmetric measure ($CR(I_A, I_B) \neq CR(I_B, I_A)$) and one image must be chosen as the one which potentially *explains the other image more*. MI and LCC are symmetric measures.

Deformable 2D-3D registration between CT and CBCT images is an emerging field of interest and measures have been proposed, specifically designed for this purpose. These include entropy of difference images, gradient correlation and pattern intensity. A review can be found in [38].

6.1.5 Regularization

In this section, we focus on the second term in Eq. (6.2). $R(\boldsymbol{T})$ represents a regularization mechanism that penalizes undesirable properties of the transformation $\boldsymbol{T}$. Generally, regularizations are defined using an energy function and computed directly from the deformation field and independently of the image intensities. It constitutes an important tool to enforce a transformation model to the sought deformation, and incorporate prior knowledge into the registration framework. R is often chosen to favor spatially smooth solutions, but any mathematical or physical property can be penalized, provided a penalty can be devised.

It is advantageous to consider the transformation $\boldsymbol{T}$ as the sum of the identity transformation and a displacement function $\boldsymbol{u}$, i.e.

$$\boldsymbol{T}(\boldsymbol{x}) = \boldsymbol{x} + \boldsymbol{u}(\boldsymbol{x}), \tag{6.5}$$

as most regularization energies will only be affected by the displacement.

The linear elastic energy is commonly used for registration [14]:

$$R(\boldsymbol{T}) = \int_{\Omega} \sum_{i=1}^{3}\sum_{j=1}^{3} \lambda \frac{\partial u_i(\boldsymbol{x})}{\partial x_i}\frac{\partial u_j(\boldsymbol{x})}{\partial x_j} + \frac{\mu}{2}\left(\frac{\partial u_i(\boldsymbol{x})}{\partial x_j} + \frac{\partial u_j(\boldsymbol{x})}{\partial x_i}\right)^2 d\boldsymbol{x}. \tag{6.6}$$

It is based on the physical equations of the deforming material, assuming that the relationship between strain and stress is linear. Viscous fluid energy [1, 2, 5] has the same equations as the linear elastic energy, but computed for the velocity field (the increment in each iteration to the transformation) instead of the deformation field.

The membrane or Laplacian energy,

$$R(\boldsymbol{T}) = \int_{\Omega} \sum_{i}^{3}\sum_{j}^{3} \left(\frac{\partial u_i(\boldsymbol{x})}{\partial x_j}\right)^2 d\boldsymbol{x}, \tag{6.7}$$

can be considered as a simplification of the linear elastic energy where the cross-directional effects are ignored.

Bi-harmonic energy [4],

$$R(\boldsymbol{T}) = \int_{\Omega} \sum_{i}^{3}\sum_{j}^{3} \left(\frac{\partial^2 u_i(\boldsymbol{x})}{\partial x_i x_j}\right)^2 d\boldsymbol{x}\,, \tag{6.8}$$

also known as bending energy or second-order Tikhonov stabilizer, is another popular regularization energy which penalizes non-affine transformations. Note that this quantity is the 3D counterpart of the 2D bending energy of a thin plate of metal. Thin-plate splines commonly used in feature-based registration approaches (see Sect. 5.4.2) correspond to an exact solution of this energy minimization.

Several authors proposed regularizations based on the Jacobian $J = \det(\nabla \boldsymbol{T})$ [32, 51], including:

$$R(\boldsymbol{T}) = \int_{\Omega} \exp\left(-\alpha \det(\nabla \boldsymbol{T})\right) d\boldsymbol{x}, \tag{6.9}$$

$$R(\boldsymbol{T}) = \int_{\Omega} \log\left(\det(\nabla \boldsymbol{T})\right) d\boldsymbol{x} \tag{6.10}$$

The Jacobian is used to enforce the computed transformations to be incompressible [51] or to penalize locally non-invertible functions [32], respectively.

Non-isotropic energies have also been proposed [42, 52, 59]. These approaches consist in modifying the intensity of the regularization according to image content.

Typically, it allows to reduce smoothness across image gradients or to limit the smoothness according to normal or tangential directions at organs boundaries.

Two important mathematical properties of the transformation should be mentioned. The first is inverse consistency [26], which is studied in Chap. 7. The second enforces the transformation to be a diffeomorphism, that is a one-to-one, smooth and continuous mapping with derivatives that are invertible. Such transformations maintain the topology and guarantee that connected regions of an image remain connected [14].

Vercauteren et al. [72] proposed a modification of the Demons method (see Sect. 6.2.2) to constrain the deformation to be diffeomorphic. Similarly, for transformations represented by free-form deformations using cubic B-splines (see Sect. 6.2.1), constraints were devised to ensure a diffeomorphic mapping [13]. This can be done by limiting control point displacements, which guarantee that the transformation is locally injective over the whole domain. For example, with 20 mm control point spacing, the maximum control point displacement is 8 mm. Larger deformations can be retrieved using a hierarchical transformation pyramid [53].

Several other regularizations have been proposed in the literature. Readers should refer to Cachier et al. [8] who reports that numerous regularization energies are based on the same small set of differential quadratic forms. No regularizations have been shown to be superior to the others. The optimal choice will depend on the application. Hybrid approaches in which regularization is adapted according to image regions may be an interesting approach to better take into account the non-homogeneous nature of biological tissues, thus linking conventional intensity-based DIR with biophysical modeling approaches as discussed in Sect. 4.4.2.

6.1.6 Optimization

6.1.6.1 Optimization as a Search Strategy

As stated before, DIR is essentially an optimization problem. The goal of an optimization algorithm is to find the parameters for which a function reaches an optimum (minimum or maximum). In the following, we will assume that an optimal value corresponds to a minimum. In the registration framework, the objective function F is a combination of a similarity measure and a regularization penalty, and the parameters to be found are those used to represent the sought transformation T.

An optimization algorithm defines a search strategy to find the function's minimum by iteratively evaluating the function and exploring the search space. This search space is defined by the parametrization of the transformation and has as many dimensions as the number of parameters, each point of this space representing a potential solution to the registration. Each function evaluation corresponds to the computation of the objective function, for a given set of parameter values. The goal is not only to find the minimum, but also to do it fast by minimizing the number of

function evaluations. In practice, the search cannot be exhaustive because of the size of the search space.

We focus on deterministic optimization strategies, but other approaches such as stochastic-based optimizations exist. Stochastic-based optimizations have been studied for rigid or affine registration [9], potentially providing more robust results, but, to our knowledge, no proposition has been made for deformable registration. Somewhat related is the method proposed by Staring et al. [64]. They still use a deterministic optimization approach (a gradient descent approach), but compute the cost function with a stochastically chosen subsets of voxels, renewed at each iteration. Such an approach allows to significantly decrease the computation time per iteration. This is similar to the approach followed by Wells et al. [74] for computing the mutual information.

6.1.6.2 Types of Optimization Strategies

An optimization procedure consists in building a series of points $\boldsymbol{p}_k$ in the search space, each $\boldsymbol{p}_k$ being a vector of parameters representing a potential transformation $\boldsymbol{T}$, such that $F(\boldsymbol{p}_{k+1}) < F(\boldsymbol{p}_k)$. A predefined stopping criteria will determine when the procedure can be terminated. For example, a tolerance on the cost function value can be used to stop the optimization when the improvement made with respect to the previous iteration is below a threshold ($F(\boldsymbol{p}_k) - F(\boldsymbol{p}_{k+1}) < \epsilon$). Similarly, the algorithm can be halted when the incremental changes in the parameter values become smaller than the desired precision.

An iteration consists in determining a new search point $\boldsymbol{p}_{k+1}$ from the current one $\boldsymbol{p}_k$. Methods generally rely on determining a descent direction $\boldsymbol{d}_k$, such that $\boldsymbol{p}_{k+1} = \boldsymbol{p}_k + \alpha_k \boldsymbol{d}_k$. Finding the correct α_k corresponds to a 1D line-search, and proposing a new direction $\boldsymbol{d}_k$ depends on the type of algorithm. Common approaches include:

- Gradient descent (GD) $\boldsymbol{d}_k = -\tau \nabla F(\boldsymbol{p}_k)$. Advance following the direction and magnitude of the negative gradient scaled by a learning rate τ. Variants exist in which the learning rate reduces over the course of the algorithm.
- Conjugate gradient (CG) $\boldsymbol{d}_k = -\nabla F(\boldsymbol{p}_k) + \beta_k \boldsymbol{d}_{k-1}$. Where β_k can be computed using different methods. For example, Fletcher & Reeves: $\beta_k = \frac{\boldsymbol{g}_k^T \cdot \boldsymbol{g}_k}{\boldsymbol{g}_{k-1}^T \cdot \boldsymbol{g}_{k-1}} = \frac{||\boldsymbol{g}_k||^2}{||\boldsymbol{g}_{k-1}||^2}$ or Polak & Ribiere: $\beta_k = \frac{(\boldsymbol{g}_k - \boldsymbol{g}_{k-1})^T \cdot \boldsymbol{g}_k}{\boldsymbol{g}_{k-1}^T \cdot \boldsymbol{g}_{k-1}}$, with $\boldsymbol{g}_k = \nabla F(\boldsymbol{p}_k)$.
- Newton (N) $\boldsymbol{d}_k = -H^{-1}(\boldsymbol{p}_k) \cdot \nabla F(\boldsymbol{p}_k)$, with $H(\boldsymbol{p}_k) = \nabla^2 F(\boldsymbol{p}_k)$ the Hessian.
- Quasi-Newton (QN) $\boldsymbol{d}_k = -A_k^{-1} \cdot \nabla F(\boldsymbol{p}_k)$, with A_k^{-1} an approximation of the inverse of the Hessian at iteration k. The approximation A_k^{-1} can be updated each iteration based on A_{k-1}^{-1} and $\nabla F(\boldsymbol{p}_k)$. Several update methods exist, including Davidon-Fletcher-Powell (DFP) or the widely used Broyden-Fletcher-Goldfarb-Shannon (BFGS). The latter is a variant of the former and was empirically found to be superior. Equations can be found in [47].

- Limited-memory BFGS (LBFGS) Limited memory Broyden-Fletcher-Goldfarb-Shannon is a variation of the QN-BFGS approach [7, 43], where only a certain number of vector corrections are maintained to a diagonal estimate of A_k^{-1}. It allows to reduce time and memory requirements [31].
- Levenberg-Marquardt (LM) is a method that varies continuously from a Gradient Descent (GD), when far from the solution, to a Quasi-Newton (QN) scheme when approaching convergence.

More details can be found in [31, 47]. Most of theses methods are available in the ITK framework (www.itk.org).

6.1.6.3 Initialization and Multi-Resolution

The high-dimensional search space of deformable registration problems represent several challenges for an optimization strategy. There are often multiple minima within the parameter space, and registration can fail if the optimization converges to the wrong one. Depending on the specifics of the application, the global minimum might not even correspond to the sought transformation.

One way to handle this, is to start the algorithm within the capture range of the correct minimum, that is within that part of the search space where the algorithm is most likely to converge to the correct optimum. In practice this means one must ensure proper initialisation in order to improve the robustness of the optimization. When possible, deformable registration should start from an alignment given by prior rigid or affine registration.

Another mechanism that improves robustness is to progressively increase the level of detail in the input images using a multi-resolution approach. Images are first registered at low resolution, and the estimated transformation is used as a starting point for registration at a higher resolution. Most transformations also allow to progressively increase the number of transformation parameters to be estimated, and a similar hierarchical approach can be employed, in which transformations with higher dimensionality can be initialized using estimates obtained from a smaller search space.

6.2 Popular Algorithms of Deformable Image Registration

6.2.1 Free-Form Deformations Using Cubic B-Splines

Deformable registration using a parametric transformation composed of free-form deformations (FFD) based on cubic B-splines, in combination with an intensity-based similarity metric was originally proposed by Rueckert et al. [54]. B-splines are piecewise polynomials of degree r (tri-cubic splines are often used, $r = 3$), with interesting mathematical properties: compact support, continuous $(r - 1)th$

derivatives, etc. The FFD is a uniform mesh of control points (sometimes referred to as knots). The number of control points times the image dimension determines the number of parameters used to describe the transformation, and the number of parameters to be optimized.

The transformation along each dimension k at a given pixel position $\boldsymbol{x}$ is modeled as

$$T_k(\boldsymbol{x}) = x_k + \sum_{i}^{(r+1)^d} c_i \beta_i^r(\boldsymbol{x}), \tag{6.11}$$

with d the image dimension, c_i the B-spline coefficients, i the index of the control points in the support region of size $(r+1)^d$. $\beta_i^r(\boldsymbol{x}) = \prod_j^d \beta^r(p_{ij} - x_j)$ is the tensor product of β^r, the B-spline basis functions of degree r, i is the index of a control point with coordinate p_{ij}, x_j is the jth coordinate of $\boldsymbol{x}$. The basic function is a polynomial of degree r and is recursively obtained by convolving the rectangle function β^0, r times with itself. An analytic expression can also be obtained by applying the recursive Cox-de Boor formula [58]. More details on B-splines properties can be found in [68].

For a given position $\boldsymbol{x}$, $(r+1)^d$ different tensor products are computed, one for each control point with non-zero weight at $\boldsymbol{x}$. B-splines are separable, i.e. the components of the transformation can be processed independently. Another interesting advantage is that it can be extended to other image dimensions. In practice, 3D is of course most common, but 2D or 4D applications have also been proposed [32]. When dealing with 4D transformations, other constraints can be added such as temporal continuity and periodicity.

The originally proposed algorithm [54] used NMI (see Sect. 6.1.4.4) as a similarity measure, bending energy for regularization and a gradient descent optimization strategy. However, one of the main advantages of the parametric FFD approach is that it fits the general registration framework perfectly, allowing registration components to be interchanged and tuned to the application.

An important practical parameter of the transformation is the control point spacing, which is generally several times greater than the image spacing. Low control point spacing allows to represent finer deformations but the number of parameters, and consequently the complexity of the optimization, increases rapidly. To reduce computation times, several authors have proposed accelerated implementations using GPU [40, 61, 63] or, less efficiently, optimized CPU methods [58].

6.2.2 The Demons Algorithm

Another widely used approach consists in representing the transformation with a dense deformation vector field

$$\boldsymbol{T}(\boldsymbol{x}) = \boldsymbol{x} + \boldsymbol{u}(\boldsymbol{x}), \tag{6.12}$$

considering up to one vector per voxel. When used with linear interpolation, it is equivalent to using a B-spline FFD of degree $r = 1$, the B-spline coefficients thus simply representing the displacement vectors $\boldsymbol{u}(\boldsymbol{x})$.

Probably one of the most popular methods using these dense vector fields is the so called Demons method, initially proposed by Thirion [67]. In summary, the algorithm consists of an iterative procedure composed of two steps. The first step aims at defining an active force at each voxel

$$\nabla D_{SSD}(\boldsymbol{x}, \boldsymbol{u}) = \frac{I_A(\boldsymbol{x}) - I_B(\boldsymbol{x} + \boldsymbol{u}(\boldsymbol{x}))}{||\nabla I_A(\boldsymbol{x})||^2 + \alpha^2 (I_A(\boldsymbol{x}) - I_B(\boldsymbol{x} + \boldsymbol{u}(\boldsymbol{x})))^2} \nabla I_A(\boldsymbol{x}). \tag{6.13}$$

This force is directed in the opposite direction of the image gradient, with a magnitude proportional to the grey-level difference between the two images. Note that Eq. (6.13) is a slightly modified expression proposed by Pennec et al. [45], which allows to limit the local displacement at each iteration using an additional parameter α, improving stability of the algorithm for small gradient values.

The second step is a Gaussian smoothing of the vector field that results from applying this force to the current deformation

$$\boldsymbol{u}_{i+1}(\boldsymbol{x}) = G_\sigma \left(\nabla D_{SSD}(\boldsymbol{x}, \boldsymbol{u}_i) \circ \boldsymbol{u}_i(\boldsymbol{x}) \right), \tag{6.14}$$

with

$$G_\sigma(\boldsymbol{x}) = \frac{1}{\sqrt{2\pi}\sigma} e^{-\frac{\|\boldsymbol{x}\|^2}{2\sigma^2}}. \tag{6.15}$$

This two step procedure is iterated till convergence, and was shown [8, 45] to be an approximation of a second order gradient descent of the SSD (see Sect. 6.1.4).

Demons and variants have been extensively used for deformable registration in thoracic CT images [2, 56, 72]. The main advantage is the simplicity of the algorithm, and the low computational cost. The fact that the algorithm is implicitly related to the SSD similarity measure however, limits its use to mono-modal registration problems.

6.3 Overview of Respiratory Motion Estimation Based on IB-DIR

In this section, we present a short overview of studies on respiratory motion estimation based on IB-DIR methods. Their popularity can be explained by the recent developments in imaging technologies, improving accessibility to rapid or respiratory-correlated CT images (4D CT). Others modalities include breath-hold CT scans (BHCT) acquired at different breathing states, cone-beam CT images and 4D MRI.

The Fig. 6.5 presents an excerpt of published studies on lung motion modeling based on IB-DIR methods. We stress the reader here that there is abundant literature on the subject and we do not pretend to be exhaustive. In order to highlight some

tendencies over the years, we summarized the main registration components that were used in terms of similarity measure, transformation type, regularization scheme and optimization strategy (Fig. 6.6).

Over the years, methodological advances have been proposed. Regarding the metrics, several approaches have been proposed to take into account the change in density of the lung during respiration (APLDM [57], SSTVD [80], CCLG [11]), even if conventional MI is still used. Others have proposed to include constraints that reinforce anatomical correspondence (vessels) in the metric.

For the transformations, some global consistency and invertibility constraints have been proposed to limit the search space of the optimization. In order to circumvent over-smoothing in case of sliding motion, several authors proposed to separately register each region [48, 69, 77]. Alternatively, locally non-isotropic regularization with respect to a prior segmentation also allows to take into account the sliding problem [16, 59]. Clearly, all *prior knowledge* that is available could be inserted into the registration process in order to make it more robust.

Another important aspect is that *implementation does matter*. Authors using similar (even though not strictly equivalent) registration methods, obtain large differences in terms of accuracy and speed. Nonetheless, large comparative registration challenges [41] have shown that the overall accuracy obtained for CT images of the lung is around 1–2 mm, which is acceptable for radiotherapy applications. The next challenges should be robustness of the algorithms and real time computation.

6.4 Open-Source Software and Data Sets

The following list is a snapshot of existing open-source software related to deformable image registration.

- **ITK**: large library for image segmentation and registration, http://www.itk.org/
- **Elastix**: based on ITK, focused on deformable image registration http://elastix.isi.uu.nl [30]
- **Plastimatch**: GPU implementation of FFD using B-splines, and the demons algorithm http://plastimatch.org/ [62]
- **Niftyreg**: GPU implementation of FFD using B-splines http://sourceforge.net/projects/niftyreg/files/latest/download [40]
- **B-LUT**: fast B-spline interpolation http://www.creatis.insa-lyon.fr/rio/b-lut [58]
- **ANTS**: for brain and image mapping http://www.picsl.upenn.edu/ANTS/
- **VV**: visualization of Deformable Vector Field (DVF) and 4D images http://vv.creatis.insa-lyon.fr [49, 60]
- **DROP**:http://www.mrf-registration.net/deformable/index.html [21]

Similarly, here is a list of validation data sets (see also Chap. 8):

- **EMPIRE10**: lung registration challenge http://empire10.isi.uu.nl/ [41]
- **Dir-Lab**: 4D CT and landmarks http://www.dir-lab.com [12]

Ref	Year	Metric	Transformation	Regularization, penalty	Optimization	Data	Comment
[20] Fan et al	2001	SSD	NP	OFC + anisotropic smoothness + divergence free	GD	BH	
[75] Weruaga et al	2003	CC + SID	Parametric	Adapted from snake	Fitting and filtering	BH	
[34] Li et al	2003	Consistent SSD	TPS	Consistency constraint	GD (alternate with landmark)	BH	
[36] Lu et al	2004	SSD	NP	FB	Gauss-Seidel finite difference	BH	
[23] Guerrero et al	2004	SSD	NP	FB	GD	BH	
[28] Kaus et al	2004	SSD	B-Spline	no	LM	4DCT	
[15] Coselmon et al	2004	MI	TPS	no	Iterative with control points	BH	Lung mask
[81] Zeng et al	2004	SSD	B-Spline	Derivative smoothness penalties	LM	Synthetic 2D/3D	
[56] Sarrut et al	2005	Demons	NP	Gaussian	GD	BH	
[66] Sundaram et al	2005	NCC	NP	LE (fluid)	GD	MRI 2D	
[57] Sarrut et al	2006	Demons+APLDM	NP	Gaussian and LE	GD	BH	
[39] McClelland et al	2006	MI	B-Spline	ST	GD	4DCT cine	Spatio-temporal
[48] Rietzel et al	2006	MI	B-Spline	no	GD	4DCT	Sliding
[82] Zeng et al	2007	SSD + NLCC	B-Spline	Spatial and temporal motion roughness penalty	CG	2D/3D	
[35] Li et al	2007	SSD	B-Spline	no	LBFSG	CT, 4DCBCT	
[73] Von Siebenthal et al.	2007	SSD	B-Spline	no	GD	4D MR	
[78] Yang et al	2008	SSD	NP	OFC + Inverse consistency (ICE)	GD	4D CT	
[77] Wu et al	2008	SSD	NP, B-Spline	Gaussian	GD, LBFGS	4D CT	Sliding
[3] Boldea et al	2008	Demons	NP	Gaussian	GD	4D CT	Euler/Langragian
[44] Noe et al	2008	H&S and C&K	NP	OFC	GD	4D CT, CBCT	GPU
[76] Wolthaus et al	2008	Phase-based SSD	NP	OFC ; adaptive filter for sliding	Analytical solution	4D CT	sliding
[84] Zhao et al	2009	NCC	NP	no	Nelder–Mead	4D CT ciné	5D Lung motion model
[19] Ehrhardt et al	2009	Demons (symmetric)	NP	FB diffeomorphic	Diffusive regularization (GD)	4D CT	
[59] Schmidt-Richberg et al	2009	Demons	NP	FB + DDR	GD	4D CT	sliding
[55] Ruppertshofen et al.	2009	SSD	NP	LE	CG	4D CT	non uniform grid
[80] Yin et al	2009	SSTVD	B-Spline	BC	LBFGS	BH	
[18] Ding et al	2009	SSTVD	B-Spline	BC	LBFGS	BH	lobe by lobe
[11] Castillo et al	2009	CCLG	NP	FB	CG	4D CT	
[17] Ding et al	2010	MI	B-Spline	Local rigidity penality	SGD	follow up CT	
[22] Gu et al	2010	Demons and variants	NP	Gaussian, inverse	GD	4D CT	GPU
[10] Castillo et al	2010	CCLG	Cubic polynomial	FB	LM	4D CT	Spatio-temporal
[70] Vandemeulebroucke et al	2011	SSD	B-Spline	ST	LBFGS	4D CT	Spatio-temporal, sliding

Fig. 6.5 Some published studies on lung motion modeling based on IB-DIR methods

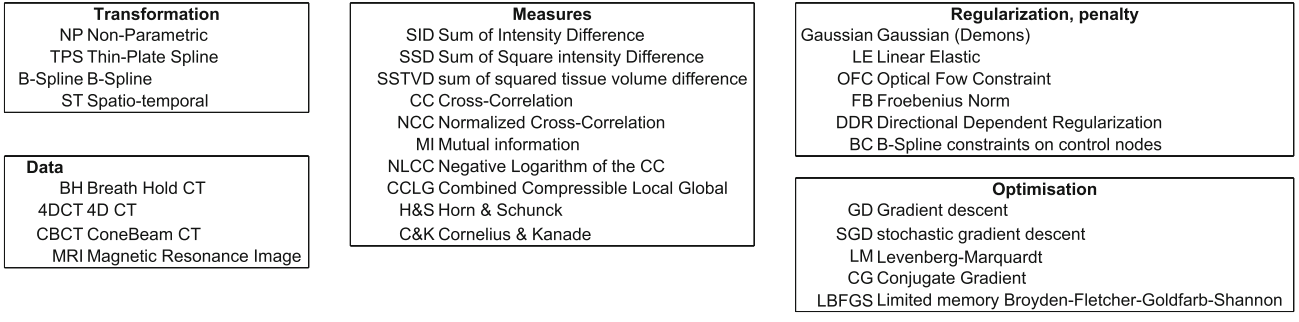

Fig. 6.6 Legend of the Fig. 6.5

- **MIDRAS**: 4D CT [6] (data not directly available)
- **POPI**: 4D CT images, DVF and landmarks http://www.creatis.insa-lyon.fr/rio/popi-model [71]

References

1. Boldea, V., Sarrut, D., Carrie, C.: Comparison of 3D dense deformable registration methods for breath-hold reproducibility study in radiotherapy. In: SPIE Medical Imaging: Visualization, Image-Guided Procedures, and Display, vol. 5747, pp. 222–230 (2005)
2. Boldea, V., Sarrut, D., Clippe, S.: Lung deformation estimation with non-rigid registration for radiotherapy treatment. In: International Conference on Medical Image Computing and Computer-Assisted Intervention (MICCAI), vol. 2878, pp. 770–777 (2003)
3. Boldea, V., Sharp, G.C., Jiang, S.B., Sarrut, D.: 4D-CT lung motion estimation with deformable registration: quantification of motion nonlinearity and hysteresis. Med. Phys. **35**(3), 1008 (2008)
4. Bookstein, F.: Principal warps: thin-plate splines and the decomposition of deformations. IEEE Trans. Pattern Anal. Mach. Intell. **11**(6), 567–585 (2002)
5. Bro-Nielsen, M., Gramkow, C.: Fast fluid registration of medical images. In: Visualization in Biomedical Computing, pp. 265–276. Springer, Berlin (1996)
6. Brock, K.K.: Results of a multi-institution deformable registration accuracy study (MIDRAS). Int. J. Radiat. Oncol. Biol. Phys. **76**(2), 583–596 (2010)
7. Byrd, R., Lu, P., Nocedal, J., Zhu, C.: A limited memory algorithm for bound constrained optimization. SIAM J. Sci. Comput. **16**(5), 1190–1208 (1995)
8. Cachier, P., Ayache, N.: Isotropic energies, filters and splines for vector field regularization. J. Math. Imaging Vis. **20**, 251–265 (2004)
9. Capek, K.: Optimisation strategies applied to global similarity based image registration methods. In: International Conferences in Central Europe on Computer Graphics, Visualization and Computer Vision (WSCG), vol. 2, pp. 369–374, Plzen, Czech Republic (1999)
10. Castillo, E., Castillo, R., Martinez, J., Shenoy, M., Guerrero, T.: Four-dimensional deformable image registration using trajectory modeling. Phys. Med. Biol. **55**(1), 305–327 (2010)
11. Castillo, E., Castillo, R., Zhang, Y., Guerrero, T.: Compressible image registration for thoracic computed tomography images. J. Med. Biol. Eng. **29**(5) (2009)
12. Castillo, R., Castillo, E., Guerra, R., Johnson, V.E., McPhail, T., Garg, A.K., Guerrero, T.: A framework for evaluation of deformable image registration spatial accuracy using large landmark point sets. Phys. Med. Biol. **54**(7), 1849–1870 (2009)
13. Choi, Y., Lee, S.: Local injectivity conditions of 2D and 3D uniform cubic B-spline functions. In: Proceedings of the Seventh Pacific Conference on Computer Graphics and Applications, 1999, vol. 62, pp. 302–311 (1999)
14. Christensen, G., Johnson, H.: Consistent image registration. IEEE Trans. Med. Imaging **20**(7), 568–582 (2001)
15. Coselmon, M.M., Balter, J.M., McShan, D.L., Kessler, M.L.: Mutual information based CT registration of the lung at exhale and inhale breathing states using thin-plate splines. Med. Phys. **31**(11), 2942 (2004)
16. Delmon, V., Rit, S., Pinho, R., Sarrut, D.: Direction dependent B-splines decomposition for the registration of sliding objects. In: MICCAI (Medical Image Computing and Computer-Assisted Intervention); Four International Workshop on Pulmonary Image, Analysis, pp. 45–55 (2011)
17. Ding, K., Bayouth, J.E., Buatti, J.M., Christensen, G.E., Reinhardt, J.M.: 4DCT-based measurement of changes in pulmonary function following a course of radiation therapy. Med. Phys. **37**(3), 1261 (2010)
18. Ding, K., Yin, Y., Cao, K., Christensen, G., Lin, C., Hoffman, E., Reinhardt, J.: Evaluation of lobar biomechanics during respiration using image registration. In: Medical Image Computing and Computer-Assisted Intervention—MICCAI, 2009, pp. 739–746 (2009)

19. Ehrhardt, J., Werner, R., SchmidtRichberg, A., Handels, H., SchmidtRichberg, A.: Prediction of respiratory motion using a statistical 4D mean motion model. In: Second International Worskshop on Pulmonary Image Processing, pp. 3–14 (2009)
20. Fan, L.: Evaluation and application of 3D lung warping and registration model using HRCT images. In: Proceedings of SPIE, pp. 234–243 (2001)
21. Glocker, B., Komodakis, N., Tziritas, G., Navab, N., Paragios, N.: Dense image registration through MRFs and efficient linear programming. Med. Image Anal. **12**(6), 731–741 (2008)
22. Gu, X., Pan, H., Liang, Y., Castillo, R., Yang, D., Choi, D., Castillo, E., Majumdar, A., Guerrero, T., Jiang, S.B.: Implementation and evaluation of various demons deformable image registration algorithms on a GPU. Phys. Med. Biol. **55**(1), 207–219 (2010)
23. Guerrero, T., Zhang, G., Huang, T.C., Lin, K.P.: Intrathoracic tumour motion estimation from CT imaging using the 3D optical flow method. Phys. Med. Biol. **49**(17), 4147–4161 (2004)
24. Holden, M.: A review of geometric transformations for nonrigid body registration. IEEE Trans. Med. Imaging **27**(1), 111–128 (2008)
25. Ibanez, L., Schroeder, W., Ng, L., Cates, J., Insight consortium: the ITK software guide. Technical report, pp. 1–3 (2005)
26. Johnson, H., Christensen, G.: Consistent landmark and intensity-based image registration. IEEE Trans. Med. Imaging **21**(5), 450–461 (2002)
27. Kabus, S., Klinder, T., Murphy, K., Van Ginneken, B., Van Lorenz, C., Pluim, J.P.W., Lorenz, C.: Evaluation of 4D-CT lung registration. In: Medical Image Computing and Computer-Assisted Intervention, vol. 12(Pt 1), pp. 747–754 (2009)
28. Kaus, M., Netsch, T., Kabus, S., Pekar, V., McNutt, T., Fischer, B.: Estimation of organ motion from 4D CT for 4D radiation therapy planning of lung cancer. In: Medical Image Computing and Computer-Assisted Intervention, MICCAI 2004, vol. 3217, pp. 1017–1024. Springer, Berlin (2004)
29. Keall, P.: 4-dimensional computed tomography imaging and treatment planning. Semin. Radiat. Oncol. **14**(1), 81–90 (2004)
30. Klein, S., Staring, M., Murphy, K., Viergever, M.A., Pluim, J.P.W.: Elastix: a toolbox for intensity-based medical image registration. IEEE Trans. Med. Imaging **29**(1), 196–205 (2010)
31. Klein, S., Staring, M., Pluim, J.P.W.: Evaluation of optimization methods for nonrigid medical image registration using mutual information and B-splines **16**, 2879–2890 (2007)
32. Kybic, J., Unser, M.: Multidimensional elastic registration of images using splines. In: Proceedings of International Conference on Image Processing, 2000, vol. 2, pp. 455–458 (2000)
33. Lehmann, T.M., Gönner, C., Spitzer, K.: Survey: interpolation methods in medical image processing. IEEE Trans. Med. Imaging **18**(11), 1049–1075 (1999)
34. Li, B., Christensen, G.G.E.G., Homan, E., McLennan, G., Reinhardt, J.M.J., Hoffman, E.A.: Establishing a normative atlas of the human lung: intersubject warping and registration of volumetric CT images. Acad. Radiol. **10**(3), 255–265 (2003)
35. Li, T., Koong, A., Xing, L.: Enhanced 4D cone-beam CT with inter-phase motion model. Med. Phys. **34**(9), 3688 (2007)
36. Lu, W., Chen, M., Olivera, G., Ruchala, K.J., Mackie, T.: Fast free-form deformable registration via calculus of variations. Phys. Med. Biol. **49**(14), 3067 (2004)
37. Maes, F., Collignon, A., Vandermeulen, D., Marchal, G., Suetens, P.: Multimodality image registration by maximization of mutual information. IEEE Trans. Med. Imaging **16**(2), 187–198 (1997)
38. Markelj, P., Tomazevic, D., Likar, B., Pernus, F.: A review of 3D/2D registration methods for image-guided interventions. Med. Image Anal. **16**(3), 642–661 (2010)
39. Mcclelland, J.R., Blackall, J., Tarte, S., Chandler, A., S: A continuous 4D motion model from multiple respiratory cycles for use in lung radiotherapy. Med. Phys. 333348 (2006)
40. Modat, M., Ridgway, G.R., Taylor, Z.A., Lehmann, M., Barnes, J., Hawkes, D.J., Fox, N.C., Ourselin, S.: Fast free-form deformation using graphics processing units. Comput. Methods Programs Biomed. **98**(3), 278–284 (2010)
41. Murphy, K., van Ginneken, B., Reinhardt, J.M., et al.: Evaluation of registration methods on thoracic CT: the EMPIRE10 challenge. IEEE Trans. Med. Imaging **30**(11), 1901–1920 (2011)

42. Nagel, H., Enkelmann, W.: An investigation of smoothness constraints for the estimation of displacement vector fields from image sequences. IEEE Trans. Pattern Anal. Mach. Intell. **8**(5), 565–593 (1986)
43. Nocedal, J.: Updating quasi-Newton matrices with limited storage. Math. comput. **35**(151), 773–782 (1980)
44. Noe, K.O., Tanderup, K., Lindegaard, J.C., Grau, C., Sørensen, T.S.: GPU accelerated viscous-fluid deformable registration for radiotherapy. Stud. Health Technol. Inform. **132**, 327–332 (2008)
45. Pennec, X., Cachier, P.: Understanding the demon's algorithm: 3D non-rigid registration by gradient descent. In: MICCAI (Medical Image Computing and Computer-Assisted Intervention), pp. 597–606 (1999)
46. Pluim, J.P.W., Maintz, J., Viergever, M.A.: Mutual-information-based registration of medical images: a survey. IEEE Trans. Med. Imaging **22**(8), 986–1004 (2003)
47. Press, W.H., Flannery, B.P., Teukolsky, S.A., Vetterling, W.T.: Numerical recipes in C: the art of scientific computing. Comput. Math. Appl. **19**(7), 100 (1990)
48. Rietzel, E., Chen, G.T.Y.: Deformable registration of 4D computed tomography data. Med. Phys. **33**(11), 4423 (2006)
49. Rit, S., Pinho, R., Delmon, V., Pech, M., Bouilhol, G., Schaerer, J., Navalpakkam, B., Vandemeulebroucke, J., Seroul, P., Sarrut, D.: VV, a 4D slicer. In: MICCAI Conference International Workshop on Pulmonary Image Analysis (2011)
50. Roche, A., Malandain, G., Ayache, N., N: Unifying maximum likelihood approaches in medical image registration. Int. J. Imaging Syst. Technol. **11**(1), 71–80 (2000)
51. Rohlfing Jr, T., C.M., Bluemke, D., Jacobs, M.: Volume-preserving nonrigid registration of MR breast images using free-form deformation with an incompressibility constraint. IEEE Trans. Med. Imaging **22**(6), 730–741 (2003)
52. Ruan, D., Esedoglu, S., Fessler, J.: Discriminative sliding preserving regularization in medical image registration. In: Proceedings of the Sixth IEEE international conference on Symposium on Biomedical Imaging: From Nano to Macro, pp. 430–433. IEEE Press, Piscataway (2009)
53. Rueckert, D., Aljabar, P., Heckemann, R.A., Hajnal, J.V., Hammers, A.: Diffeomorphic registration using B-splines. In: International Conference on Medical Image Computing and Computer-Assisted Intervention—LNCS 4191, vol. 9(Pt 2), pp. 702–709 (2006)
54. Rueckert, D., Sonoda, L., Hayes, C., Hill, D., Leach, M.: Nonrigid registration using free-form deformations: application to breast MR images. IEEE Trans. Med. Imaging **18**(8), 712–721 (1999)
55. Ruppertshofen, H., Kabus, S., Fischer, B.: Image Registration using Tensor Grids for Lung Ventilation Studies: Bildverarbeitung für die Medizin, vol. 6, pp. 117–121 (2009)
56. Sarrut, D., Boldea, V., Ayadi, M., Badel, J., Ginestet, C., Clippe, S.: Nonrigid registration method to assess reproducibility of breath-holding with ABC in lung cancer. Int. J. Radiat. Oncol. Biol. Phys. **61**(2), 594–607 (2005)
57. Sarrut, D., Boldea, V., Miguet, S., Ginestet, C.: Simulation of four-dimensional CT images from deformable registration between inhale and exhale breath-hold CT scans. Med. Phys. **33**(3), 605 (2006)
58. Sarrut, D., Vandemeulebroucke, J.: B-LUT: fast and low memory B-spline image interpolation. Comput. Methods Programs Biomed. **99**, 172–178 (2010)
59. Schmidt-Richberg, A., Ehrhardt, J., Werner, R., Handels, H., Schmidt-Richberg, A.: Slipping objects in image registration: improved motion field estimation with direction-dependent regularization. In: International Conference on Medical Image Computing and Computer-Assisted Intervention (MICCAI), vol. 12(Pt 1), pp. 755–62 (2009)
60. Seroul, P., Sarrut, D.: VV: a viewer for the evaluation of 4D image registration. MIDAS J., 1–8 (2008). http://hdl.handle.net/10380/1458
61. Shackleford, J.a., Kandasamy, N., Sharp, G.C.: On developing B-spline registration algorithms for multi-core processors. Phys. Med. Biol. **55**(21), 6329–6351 (2010)
62. Shackleford, J.A., Kandasamy, N., Sharp, G.C.: On developing B-spline registration algorithms for multi-core processors. Phys. Med. Biol. **55**(21), 6329–6351 (2010)

63. Sharp, G.C., Kandasamy, N., Singh, H., Folkert, M.: GPU-based streaming architectures for fast cone-beam CT image reconstruction and demons deformable registration. Phys. Med. Biol. **52**(19), 5771 (2007)
64. Staring, M., Klein, S., Pluim, J.P.W.: A rigidity penalty term for nonrigid registration. Med. Phys. **34**(11), 4098 (2007)
65. Studholme, C., Hill, D., Hawkes, D.: Others: an overlap invariant entropy measure of 3D medical image alignment. Pattern Recogn. **32**(1), 71–86 (1999)
66. Sundaram, T., Gee, J.: Towards a model of lung biomechanics: pulmonary kinematics via registration of serial lung images. Med. Image Anal. **9**(6), 524–537 (2005)
67. Thirion, J.: Image matching as a diffusion process: an analogy with Maxwell's demons. Med. Image Anal. **2**(3), 243–260 (1998)
68. Unser, M., Aldroubi, A., Eden, M.: B-spline signal processing: Part I theory. IEEE Trans. Signal Process. **41**(2), 821–833 (1993)
69. Vandemeulebroucke, J., Bernard, O., Rit, S., Kybic, J., Clarysse, P., Sarrut, D.: Automated segmentation of a motion mask to preserve sliding motion in deformable registration of thoracic CT. Med. Phys. **39**(2), 1006 (2012)
70. Vandemeulebroucke, J., Rit, S., Kybic, J., Clarysse, P., Sarrut, D.: Spatiotemporal motion estimation for respiratory-correlated imaging of the lungs. Med. Phys. **38**(1), 166 (2011)
71. Vandemeulebroucke, J., Sarrut, D., Clarysse, P.: The POPI-model, a point-validated pixel-based breathing thorax model. In: XVth International Conference on the use of Computers in Radiation Therapy (ICCR), pp. 1–8. Toronto, Canada (2007)
72. Vercauteren, T., Pennec, X., Perchant, A., Ayache, N.: Diffeomorphic demons: efficient non-parametric image registration. Neuroimage **45**(1), S61–S72 (2009)
73. von Siebenthal, M., Székely, G., Gamper, U., Boesiger, P., Lomax, A., Cattin, P.: 4D MR imaging of respiratory organ motion and its variability. Phys. Med. Biol. **52**(6), 1547–1564 (2007)
74. Wells 3rd, W., Viola, P., Atsumi, H., Nakajima, S., Kikinis, R.: Multi-modal volume registration by maximization of mutual information. Med. Image Anal. **1**(1), 35–51 (1996)
75. Weruaga, L., Morales, J., Nunez, L., Verdu, R.: Estimating volumetric motion in human thorax with parametric matching constraints. IEEE Trans. Med. Imaging **22**(6), 766–772 (2003)
76. Wolthaus, J.W.H., Sonke, J.J., van Herk, M., Belderbos, J.S.A., Rossi, M.M.G., Lebesque, J.V., Damen, E.M.F.: Comparison of different strategies to use four-dimensional computed tomography in treatment planning for lung cancer patients. Int. J. Radiat. Oncol. Biol. Phys. **70**(4), 1229–1238 (2008)
77. Wu, Z., Rietzel, E., Boldea, V., Sarrut, D., Sharp, G.C.: Evaluation of deformable registration of patient lung 4DCT with subanatomical region segmentations. Med. Phys. **35**, 775 (2008)
78. Yang, D., Li, H., Low, D., Deasy, J.O., El Naqa, I.M.: A fast inverse consistent deformable image registration method based on symmetric optical flow computation. Phys. Med. Biol. **53**(21), 6143–6165 (2008)
79. Yang, D., Lu, W., Low, D., Deasy, J.O., Hope, A.J., El Naqa, I.M.: 4D-CT motion estimation using deformable image registration and 5D respiratory motion modeling. Med. Phys. **35**(10), 4577 (2008)
80. Yin, Y., Hoffman, E., Lin, C.: Mass preserving nonrigid registration of CT lung images using cubic B-spline. Med. Phys. **36**(9), 4213–4222 (2009)
81. Zeng, R., Fessler, J.A., Balter, J.M.: Respiratory motion estimation from slowly rotating x-ray projections: theory and simulation. Med. Phys. **32**(4), 984 (2005)
82. Zeng, R., Fessler, J.J.A., Balter, J.M.: Estimating 3-D respiratory motion from orbiting views by tomographic image registration. IEEE Trans. Med. Imaging **26**(2), 153–163 (2007)

83. Zhang, Q., Pevsner, A., Hertanto, A., Hu, Y.C., Rosenzweig, K.E., Ling, C.C., Mageras, G.S.: A patient-specific respiratory model of anatomical motion for radiation treatment planning. Med. Phys. **34**(12), 4772 (2007)
84. Zhao, T., Lu, W., Yang, D., Mutic, S., Noel, C.E., Parikh, P.J., Bradley, J.D., Low, D.A.: Characterization of free breathing patterns with 5D lung motion model. Med. Phys. **36**(11), 5183 (2009)

Chapter 7
Intensity-Based Registration for Lung Motion Estimation

Kunlin Cao, Kai Ding, Ryan E. Amelon, Kaifang Du, Joseph M. Reinhardt, Madhavan L. Raghavan and Gary E. Christensen

Abstract Image registration plays an important role within pulmonary image analysis. The task of registration is to find the spatial mapping that brings two images into alignment. Registration algorithms designed for matching 4D lung scans or two 3D scans acquired at different inflation levels can catch the temporal changes in position and shape of the region of interest. Accurate registration is critical to post-analysis of lung mechanics and motion estimation. In this chapter, we discuss lung-specific adaptations of intensity-based registration methods for 3D/4D lung images and review approaches for assessing registration accuracy. Then we introduce methods for estimating tissue motion and studying lung mechanics. Finally, we discuss methods for assessing and quantifying specific volume change, specific ventilation, strain/ stretch information and lobar sliding.

7.1 Introduction

Image registration can be used to determine a spatial mapping that matches images collected at different time points, or using different imaging modalities. It has been widely used in radiotherapy for various applications, such as in motion studies, dose accumulation/composite, dose response evaluation, adaptive planning, auto contouring etc. for various radiotherapy treatment sites such as brain, lung, head neck, prostate, and cervix. In motion studies, image registration has been used to evalu-

K. Cao (✉)
Biomedical Image Analysis Laboratory, GE Global Research Center, Niskayuna, NY, USA
e-mail: kunlincao@gmail.com

K. Ding · R. E. Amelon · K. Du · J. M. Reinhardt · M. L. Raghavan
Department of Biomedical Engineering, The University of Iowa, Iowa City, IA, USA

G. E. Christensen
Department of Electrical and Computer, The University of Iowa, Iowa City, IA, USA
e-mail: gary-christensen@uiowa.edu

J. Ehrhardt and C. Lorenz (eds.), *4D Modeling and Estimation of Respiratory Motion for Radiation Therapy*, Biological and Medical Physics, Biomedical Engineering,
DOI: 10.1007/978-3-642-36441-9_7,

ate the internal target volume (ITV) which encompasses the clinical target volume (CTV) and internal margin (IM) to account for the variation in size, shape and position, e.g. filling of bladder and movements of respiration [54]. In auto contouring, the contours drawn by physicians on the initial data set can be propagated to the data set of interest after image registration is performed to define the gross tumor volume (GTV) or the organs at risk (OAR) [95]. Such image pair can be intra-modality images such as 4D CT images or inter-modality images such as the images of PET-CT image and planning CT image. In addition to the primary contours drawn by the physicians, the OARs can also be defined as atlas from population so that they can be propagated to any new patient data set when the contour task is required. The auto contour greatly reduced the total treatment planning time and allows for the potential fast same day simulation, planning and treatment clinical work flow [34]. Similarly, in the dose accumulation/composite, instead of propagating the contours, the planning dose from previous treatments can be propagated to the later treatment scans so that the total planning dose can be accumulated for further dose response evaluation or adaptive planning [100].

In lung cancer radiotherapy, image registration is a key tool as one seeks to link images across modalities, across time, or between lung volumes in the use of pulmonary investigations [39, 46, 58, 60], due to the inherent motion of the respiratory system. For example, registration can be used to determine the spatial locations of corresponding voxels in a sequence of pulmonary scans, as discussed in Chap. 6. The computed correspondences immediately yield the displacement fields corresponding with the motion of the lung between a pair of images. Using the image registration, the auto contouring, dose accumulation/composite, adaptive planning tools etc. as introduced above can be built upon. Furthermore, because of the lung tissue's mechanical property during expansion and contraction is highly related to its ventilation function, the image registration has also been extended to the functional lung imaging as discussed in Chap. 13.

Chapters 2 and 3 introduced different methods for 4D thoracic CT image acquisition. Imaging allows non-invasive study of lung behavior and image registration has been used to examine lung mechanics and pulmonary functions [31, 43, 74]. Some groups have utilized non-invasive imaging and image registration techniques to examine the linkage between estimates of regional lung expansion and local lung ventilation [26, 32, 42–44, 74, 88, 89, 102]. Guerrero et al. used two CT images, acquired at different lung inflations, and optical flow image registration to estimate regional ventilation to identify functioning versus non-functioning lung tissue for radiotherapy treatment planning [43, 44]. Sundaram and Gee used serial magnetic resonance imaging to quantify lung kinematics in statically acquired sagittal cross-sections of the lung at different inflations [88, 89]. Using non-linear image registration, they estimated a dense displacement field from one image to the other, and from the displacement field they computed regional lung strain. Christensen et al. used consistent image registration to match images across cine-CT sequences, and estimate rates of local tissue expansion and contraction [26]. Their measurements matched well with spirometry data. Reinhardt et al. used image registration to match lung CT volumes across different levels of inflation [32, 74]. They calculated local

specific volume changes as an index of regional ventilation, and compared specific volume change to xenon-CT based estimates of regional ventilation in sheep. Gorbunova et al. developed a weight preserving image registration method for monitoring disease progression [42]. Yin et al. proposed a new similarity cost preserving the lung tissue volume, and compared the new cost function driven registration method with SSD driven registration in the estimation of regional lung function [102].

Local lung expansion can be estimated by using registration to match images acquired at different levels of inflation. Tissue expansion (and thus, specific volume change) can be estimated by calculating the Jacobian determinant of the transformation field derived by image registration [74]. The tissue strain tensor can also be calculated from the transformation field. Since both the Jacobian matrix and the strain tensor are formed using partial derivatives of the transformation field, it is important that the underlying registration transformation model be well-behaved with respect to these derivatives if the functional and mechanical results obtained are to be useful.

7.2 Intensity-Based Registration

The goal of registration is to find the spatial mapping that will bring the moving image into alignment with the fixed image. Many image registration algorithms have been proposed and various features such as landmarks, contours, surfaces and volumes have been utilized to manually, semi-automatically or automatically define correspondences between two images [39, 59, 60]. Chapters 5 and 6 introduced feature-based and intensity-based registration techniques. The input data to the registration process is usually two images; one is defined as the moving or template image I_1, and the other is defined as the fixed or target image I_2. The transform defines how points from the moving image I_1 are mapping to their corresponding points in the fixed image I_2. In three dimensional space, let $\boldsymbol{x} = (x, y, z)^T$ define a voxel coordinate in the image domain of the fixed image I_2. The transformation $\boldsymbol{T}$ is a (3×1) vector-valued function defined on the voxel lattice of fixed image, and $\boldsymbol{T}(\boldsymbol{x})$ gives the corresponding location in moving image to the point $\boldsymbol{x}$. The cost function represents the similarity measure of how well the fixed image is matched by a warped moving image. The optimizer is used to optimize the similarity criterion over search space defined by transformation parameters.

4D image registrations have been developed for spatial and temporal motion estimation in a 4D image sequence. 4D CT images are given as a sequence of 3D images representing different respiratory phases in the breathing cycle as discussed in Chaps. 2 and 3. Typical values are 10 phases from 0 to 90 % phase at 10 % intervals, where 0 % represents maximum inhale and 50 % approximately maximum exhalation. Most registration approaches use a pairwise registration paradigm, including the reference-strategy which registers each phase to a chosen reference phase (e.g. the end of expiration), and the consecutive-strategy which describes deformations respect to the neighboring time point. Figure 7.1 depicts the reference-strategy with the 50 % image as reference. For a voxel localization $\boldsymbol{x}$ in the reference phase, the

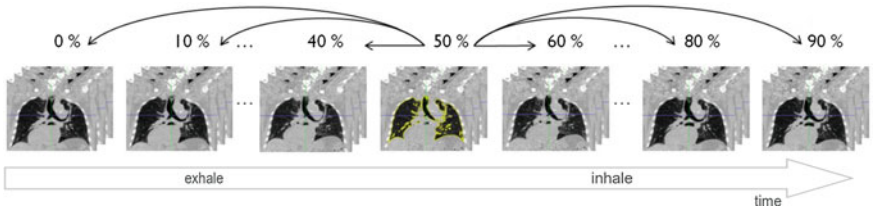

Fig. 7.1 Registration scheme for motion field extraction of a 4D CT data set using the reference-strategy. Each phase of the 4D CT image is registered with a chosen reference phase (e.g. the end of expiration) (figure adapted from [57])

corresponding localization in the rest of the phases is given by the computed transformation, and in this way, the trajectory of a point is easily defined. Using the consecutive strategy, transformations have to be concatenated to compute a trajectory, whereby interpolation errors may be introduced.

In addition to pair-wise methods, groupwise strategies have been developed which simultaneously align multiple phases in a 4D image sequence. In these approaches, all the phase images in a 4D data set are input into the registration algorithm without assigning fixed or moving image [16, 62, 93, 99]. In this chapter, we introduce lung motion estimation from pair-wise registration between images acquired at different inflation levels.

7.2.1 Preprocessing

Many registration techniques for lung CT images require image preprocessing steps. Common preprocessing operations include downsampling large datasets, extracting region of interest (ROI), and initial pre-aligning images. As the CT imaging techniques improve, it is now possible to image lung structures with high spatial resolution, and thus produce large CT datasets. In many cases, downsampling is needed to resize the original data and to improve the registration efficiency and robustness. A further common preprocessing step is an initial alignment to roughly catch the translation, rotation, and scaling between two images, i.e. by an affine pre-registration.

One of the major challenges for registration methods in lung motion estimation is the occurrence of sliding motion between the visceral and parietal pleura (see Sect. 4.2.1) and between the individual lung lobes [4, 12, 33]. Sliding motion contradicts common regularization models applied to avoid discontinuities like gaps or foldings in the computed transformation. To cope with sliding motion, many registration methods utilize a lung segmentation mask to restrict registration to the inside of the lung. In the inter-institutional study Evaluation of Methods for Pulmonary Image Registration (EMPIRE10) [66], 16 out of 20 participating methods applied masking in at least on step of the algorithm. Due to the large density difference between the

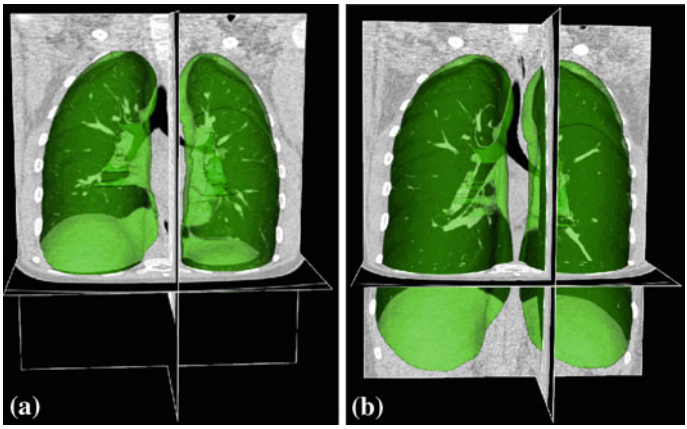

Fig. 7.2 Pulmonary CT images acquired at breath-hold (**a**) maximum exhale and (**b**) maximum inhale with renderings of the lung segmentations (*green* objects)

air-filled lungs and surrounding tissue, robust automatic algorithms exist for lung segmentation in CT images [52]. Figure 7.2 gives an illustration of pulmonary CT images with renderings of the lung segmentations. Image pair was acquired during breath-holds near functional residual capacity (maximum exhale) and total lung capacity (maximum inhale). Although first approaches for automatic segmentation of lung lobes exist [76, 92], lobe segmentation remains challenging because of imperceptible fissures in 4D CT images. Performing registration in the region of interest may help improve registration accuracy and efficiency, but registration is limited to the object (lung or lobe) and provides no information about other image regions. Recently, novel regularization approaches has been presented to explicitly model the sliding motion along organ boundaries (see Sect. 7.2.3.3).

7.2.2 Similarity Criteria

Intensity-based registration utilizes the intensity information of two images to measure how well they are aligned. It takes advantage of the strong contrast between the lung parenchyma and the chest wall, and between the parenchyma and the blood vessels and larger airways. To solve the intensity-based image registration problem, it is usually assumed that intensities of corresponding voxels are related to each other in some way. Many criteria to construct the intensity relationship between corresponding points have been suggested for aligning two images, as discussed in Chap. 6. Cost functions such as mean square difference (MSD), correlation coefficient, mutual information, pattern intensity, and gradient correlation are routinely used for image registration [50, 72].

7.2.2.1 Sum of Squared Difference (SSD)

A simple and common similarity function is the sum of squared difference (SSD), which measures the intensity difference at corresponding points between two images. Mathematically, it is defined by

$$C_{\text{SSD}} = \int_{\Omega} [I_2(\boldsymbol{x}) - I_1(\boldsymbol{T}(\boldsymbol{x}))]^2 \, d\boldsymbol{x}, \tag{7.1}$$

where I_1 and I_2 are the moving and fixed images, respectively. Ω denotes the union of lung regions in fixed image and deformed moving image. The underlying assumption of SSD is that the image intensity at corresponding points between two images should be similar. This is true when registering images of the same modality. In such cases, if the images are perfectly mapped, the corresponding intensities should be identical, which means the same underlying structure has the same intensity value in the two images.

However, considering the change in CT intensity as air inspired and expired during the respiratory cycle, the grayscale range are different within the lung region in two CT images acquired at different inflation levels. To balance this grayscale range difference, normalization of the intensities are needed. For example, a histogram matching procedure [98] can be used before SSD registration to modify the histogram of moving image so that it is similar to that of fixed image. Figure 7.3

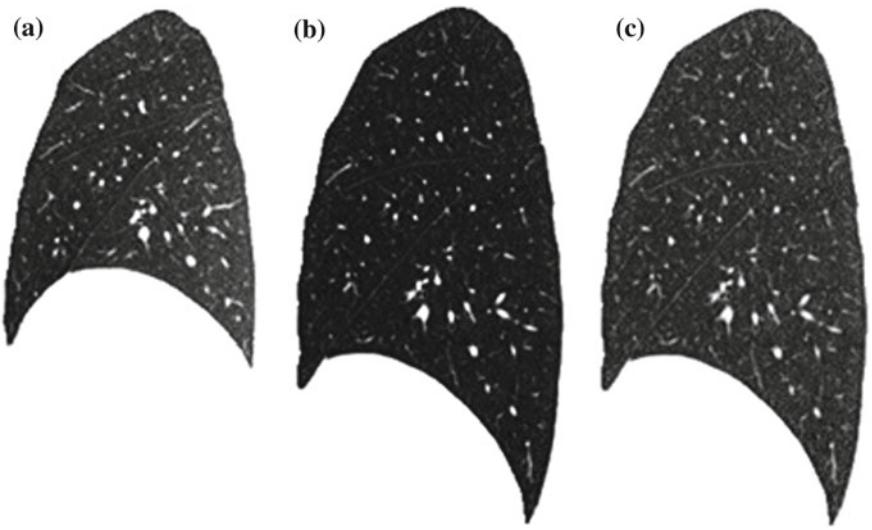

Fig. 7.3 Illustration of histogram matching before SSD registration between breath-hold maximum exhale and maximum inhale images from a human subject. **a** A sagittal slice from maximum exhale. **b** A sagittal slice from maximum inhale. **c** The sagittal slice of **b** after histogram modification so that its grayscale range is similar to that of **a**

gives an illustration of histogram matching before SSD registration between a pair of images acquired at breath-hold maximum exhale and maximum inhale from a human subject. Alternative approaches use a-priori knowledge about density changes in the lungs to preprocess images before the registration [81]. Please note that intensity normalization is only needed for SSD similarity function discussed here. It is not necessary for the similarity functions discussed below.

7.2.2.2 Similarity Functions for Multi-Modal Registration

As mentioned above, CT intensity is a measure of tissue density and therefore changes as the tissue density changes during inflation and deflation. The registration problem under this circumstance is similar to the multi-modality image registration, where similarity functions based on correlation coefficients (CC) [7, 48] or on mutual information (MI) [27, 61, 91, 94] are well suited and widely used. In the EMPIRE10 study for lung registration [66], 10 out of 20 participants used multi-modal similarity metrics based on CC or MI.

The local normalized cross-correlation (NCC) between two images I_1 and I_2 assumes a linear dependency between the image intensities and is defined by

$$C_{\mathrm{NCC}} = \frac{1}{|\Omega|} \sum_{\boldsymbol{x} \in \Omega} \frac{\sum_{\boldsymbol{x}_i} \left(I_2(\boldsymbol{x}_i) - \mu_{I_2(\boldsymbol{x})}\right) \left(I_1 \circ \boldsymbol{T}(\boldsymbol{x}_i) - \mu_{I_1 \circ \boldsymbol{T}(\boldsymbol{x})}\right)}{\sqrt{\sum_{\boldsymbol{x}_i} \left(I_2(\boldsymbol{x}_i) - \mu_{I_2(\boldsymbol{x})}\right)^2} \sqrt{\sum_{\boldsymbol{x}_i} \left(I_1 \circ \boldsymbol{T}(\boldsymbol{x}_i) - \mu_{I_1 \circ \boldsymbol{T}(\boldsymbol{x})}\right)^2}}, \tag{7.2}$$

where $\boldsymbol{x}_i \in \mathcal{N}(\boldsymbol{x})$ iterates through a neighborhood of voxel $\boldsymbol{x}$ and μ is the mean value within this neighborhood.

Mutual information expresses the amount of information that one image contains about the other one. Analogous to the Kullback-Leibler measure, the negative mutual information cost of two images is defined as [61, 91]

$$C_{\mathrm{MI}} = -\sum_i \sum_j p(i, j) \log \frac{p(i, j)}{p_{I_1 \circ \boldsymbol{T}}(i) p_{I_2}(j)}, \tag{7.3}$$

where $p(i, j)$ is the joint intensity distribution of transformed moving image $I_1 \circ \boldsymbol{T}$ and fixed image I_2; $p_{I_1 \circ \boldsymbol{T}}(i)$ and $p_{I_2}(j)$ are their marginal distributions, respectively. The histogram bins of $I_1 \circ \boldsymbol{T}$ and I_2 are indexed by i and j. Misregistration results in a decrease in the mutual information, and thus, increases the similarity cost C_{MI}. Note that the MI metric does not assume a linear relationship between the intensities of the two images (see Sect. 6.1.4.5 too). Multi-modal metrics omit the need of intensity normalization in lung registration, but the computational effort of these measures is increased compared to SSD.

7.2.2.3 Sum of Squared Tissue Volume Difference (SSTVD)

Beside the widely used standard similarity functions for mono- or multi-modal registration, a number of lung-specific similarity metrics have been developed recently.

A recently developed similarity function, the sum of squared tissue volume difference (SSTVD) [42, 102], accounts for the variation of intensity in the lung CT images during respiration. This similarity criterion minimizes the local difference of tissue volume inside the lungs scanned at different pressure levels. This criterion is based on the assumption that the tissue volume is constant between inhale and exhale.[1]

Assume that lung is a mixture of two materials: air and tissue/blood (non-air). Then the Hounsfield units (HU) in lung CT images is a function of tissue and air content. From the HU of CT lung images, the regional tissue volume and air volume can be estimate following the air-tissue mixture model by Hoffman et al. [49]. Let $v(\boldsymbol{x})$ be the volume element at location $\boldsymbol{x}$. Then the tissue volume $V(\boldsymbol{x})$ within the volume element can be estimated as

$$V(\boldsymbol{x}) = v(\boldsymbol{x})\frac{HU(\boldsymbol{x}) - HU_{air}}{HU_{tissue} - HU_{air}} = v(\boldsymbol{x})\beta(I(\boldsymbol{x})), \tag{7.4}$$

where we assume that $HU_{air} = -1000$ and $HU_{tissue} = 0$. Let $v_1(\boldsymbol{T}(\boldsymbol{x}))$ and $v_2(\boldsymbol{x})$ be the anatomically corresponding volume elements, and $V_1(\boldsymbol{T}(\boldsymbol{x}))$ and $V_2(\boldsymbol{x})$ be the tissue volumes within anatomically corresponding volume elements, respectively. Then the intensity similarity function SSTVD is defined as [101, 102]

$$\begin{aligned} C_{\text{SSTVD}} &= \int_{\Omega} [V_2(\boldsymbol{x}) - V_1(\boldsymbol{T}(\boldsymbol{x}))]^2 \, d\boldsymbol{x} \\ &= \int_{\Omega} [v_2(\boldsymbol{x})\beta(I_2(\boldsymbol{x})) - v_1(\boldsymbol{T}(\boldsymbol{x}))\beta(I_1(\boldsymbol{T}(\boldsymbol{x})))]^2 \, d\boldsymbol{x}. \end{aligned} \tag{7.5}$$

The Jacobian determinant (often simply called the Jacobian) of a transformation $J(\boldsymbol{T})$ estimates the local volume changes resulted from mapping an image through the deformation [10, 21, 25]. In 3D space, let $\boldsymbol{T}(x, y, z) = [T_x(x, y, z), T_y(x, y, z), T_z(x, y, z)]^T$ be the vector-valued transformation which deforms the moving image I_1 to the fixed image I_2. The Jacobian of the transformation $J(\boldsymbol{T}(x, y, z))$ at location $(x, y, z)^T$ is defined as

$$J(\boldsymbol{T}(x, y, z)) = \begin{vmatrix} \frac{\partial T_x(x,y,z)}{\partial x} & \frac{\partial T_x(x,y,z)}{\partial y} & \frac{\partial T_x(x,y,z)}{\partial z} \\ \frac{\partial T_y(x,y,z)}{\partial x} & \frac{\partial T_y(x,y,z)}{\partial y} & \frac{\partial T_y(x,y,z)}{\partial z} \\ \frac{\partial T_z(x,y,z)}{\partial x} & \frac{\partial T_z(x,y,z)}{\partial y} & \frac{\partial T_z(x,y,z)}{\partial z} \end{vmatrix}. \tag{7.6}$$

[1] However, we need to mention that this is not fully true due to the increased blood volume through inhalation [43].

Thus, the tissue volumes in image I_1 and I_2 are related by $v_1(\boldsymbol{T}(\boldsymbol{x})) = v_2(\boldsymbol{x}) \cdot J(\boldsymbol{T}(\boldsymbol{x}))$, and Eq. (7.5) can be rewritten as

$$C_{\mathrm{SSTVD}} = \int_{\Omega} \{v_2(\boldsymbol{x}) [\beta(I_2(\boldsymbol{x})) - J(\boldsymbol{T}(\boldsymbol{x}))\beta(I_1(\boldsymbol{T}(\boldsymbol{x})))]\}^2 \, d\boldsymbol{x}. \tag{7.7}$$

An alternative approach based on the assumption that the total mass (tissue volume) of the lung is conserved was proposed by Castillo et al. [17], named "combined compressible local-global optical flow" (CCLG). The main idea of this approach is to substitute the conservation of mass equation for the constant intensity assumption in the classical optical flow formulation of Horn and Schunk [51].

7.2.2.4 Sum of Squared Vesselness Measure Difference (SSVMD)

Feature information extracted from the intensity image is important to help guide the image registration process. During the respiration cycle, blood vessels keep their tubular shapes and tree structures. Therefore, the spatial and shape information of blood vessels can be utilized to help improve the registration accuracy. Blood vessels have larger HU values than that of parenchyma tissues. The intensity difference between parenchyma and blood vessels can effectively help intensity-based registration. However, as the blood vessel branches, the diameter of vessel becomes smaller and smaller. The small blood vessels are difficult to see because of their low intensity contrast. Therefore, grayscale information of the small vessels give almost no contribution to similarity functions directly based on intensity. In order to better utilize the information of blood vessel locations, the vesselness measure (VM) computed from intensity image can be used.

The vesselness measure is based on analyses of eigenvalues of the Hessian matrix of the image intensity. These eigenvalues can be used to indicate the shape of the underlying object. In 3D lung CT images, tubular structures such as blood vessels (bright) are associated with one negligible eigenvalue and two similar non-zero negative eigenvalues [40]. Ordering eigenvalues of a Hessian matrix by magnitude $|\lambda_1| \leq |\lambda_2| \leq |\lambda_3|$, the Frangi's vesselness function [40] is defined as

$$F(\lambda) = \begin{cases} \left(1 - e^{-\frac{R_A^2}{2\alpha^2}}\right) \cdot e^{\frac{-R_B^2}{2\beta^2}} \cdot \left(1 - e^{-\frac{S^2}{2\gamma^2}}\right) & \text{if } \lambda_2 < 0 \text{ and } \lambda_3 < 0 \\ 0 & \text{otherwise} \end{cases} \tag{7.8}$$

with

$$R_A = \frac{|\lambda_2|}{|\lambda_3|}, \quad R_B = \frac{|\lambda_1|}{\sqrt{|\lambda_2 \lambda_3|}}, \quad S = \sqrt{\lambda_1^2 + \lambda_2^2 + \lambda_3^2}, \tag{7.9}$$

where R_A distinguishes between plate-like and tubular structures, R_B accounts for the deviation from a blob-like structure, and S differentiates between tubular structure

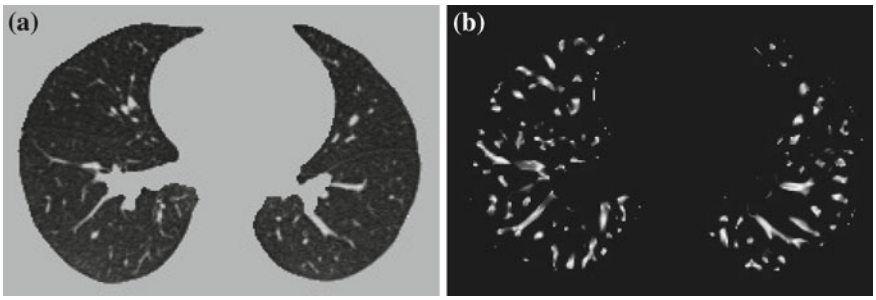

Fig. 7.4 The vesselness images calculated from lung CT grayscale images. **a** A transverse slice of breath-hold maximum exhale data. **b** The vesselness measure of slice in **a**. Vesselness measure is computed in multiscale analysis and rescaled to [0, 1]

and noise. α, β, γ control the sensitivity of the vesselness measure. In lung CT images, an example parameter setting is $\alpha = 0.5$, $\beta = 0.5$, and $\gamma = 5$.

The Hessian matrix is computed by convolving the intensity image with second and cross derivatives of the Gaussian function. For a multiscale analysis, the response of the vesselness filter will achieve the maximum at a scale which approximately matches the size of vessels to detect. Therefore, the final vesselness measure is estimated by computing Eq. (7.8) for a range of scales and selecting the maximum response: $F = \max_{\sigma_{min} \leq \sigma \leq \sigma_{max}} F(\lambda)$. Here σ is the standard deviation of the Gaussian function [36].

The vesselness image is rescaled to [0, 1] and can be considered as a probability-like estimate of vesselness features. Larger vesselness value indicates the underlying object is more likely to be a vessel structure, as shown in Fig. 7.4. The sum of squared vesselness measure difference (SSVMD) is designed to match similar vesselness patterns in two images. Given $F_1(\boldsymbol{x})$ and $F_2(\boldsymbol{x})$ as the vesselness measures of images I_1 and I_2 at location $\boldsymbol{x}$ respectively, the vesselness cost function is formed as [13, 14]

$$C_{\text{SSVMD}} = \int_{\Omega} [F_2(\boldsymbol{x}) - F_1(\boldsymbol{T}(\boldsymbol{x}))]^2 \, . \tag{7.10}$$

Mismatch from vessel to tissue structures will result a larger SSVMD cost. This similarity metric can be used together with any other intensity-based volumetric metrics to help guide the registration process and improve matching accuracy.

7.2.3 Transformation Constraints

Enforcing constraints on the transformation helps to generate more meaningful registration results. In general, the computed transformation should be smooth and maintain the topology of the transformed images. Furthermore, the registration

method should be symmetric, and should produce the same correspondences between two images independent of the choice of fixed and moving images.

7.2.3.1 Regularization Constraints

Continuum mechanical models such as linear elasticity [22, 23] and viscous fluid [22, 24] can be used to regularize the transformations. For example, linear-elastic constraint of the form

$$C_{\text{ELA}} = \int_{\Omega} ||L\boldsymbol{u}(\boldsymbol{x})||^2 d\boldsymbol{x}, \tag{7.11}$$

can be used to regularize the displacement fields where

$$\boldsymbol{u}(\boldsymbol{x}) = \boldsymbol{T}(\boldsymbol{x}) - \boldsymbol{x}. \tag{7.12}$$

The linear elasticity operator L has the form of $L\boldsymbol{u}(\boldsymbol{x}) = -\alpha\nabla^2\boldsymbol{u}(\boldsymbol{x}) - \beta\nabla(\nabla\cdot\boldsymbol{u}(\boldsymbol{x})) + \gamma\boldsymbol{u}(\boldsymbol{x})$ where $\nabla = \left[\frac{\partial}{\partial x}, \frac{\partial}{\partial y}, \frac{\partial}{\partial z}\right]$ and $\nabla^2 = \nabla\cdot\nabla = \left[\frac{\partial^2}{\partial x^2} + \frac{\partial^2}{\partial y^2} + \frac{\partial^2}{\partial z^2}\right]$. In general, L can be any nonsingular linear differential operator [63], e.g. a Laplacian regularization constrain is given by

$$C_{\text{LAP}} = \int_{\Omega} ||\nabla^2\boldsymbol{u}(\boldsymbol{x})||^2 d\boldsymbol{x}. \tag{7.13}$$

Further regularization terms are discussed in Sect. 6.1.5.

The purpose of the regularization constraints are to constrain the transformation to obey the laws of continuum mechanics and ensure it maintains the topology of two images. Using a linear differential operator as defined in Eq. (7.11) can help to smooth the transformation, and to eliminate abrupt changes in the displacement fields. However, it can not prevent the transformation from folding onto itself, i.e. destroying the topology of the images under transformation [25].

To help maintain desirable properties of the moving and fixed images during deformation, another regularization example can be a constraint that prevents the Jacobian of transformations from going to zero or infinity. The Jacobian is a measurement to estimate the pointwise expansion and contraction during the deformation (see Sect. 7.2.2.3). A constraint that penalizes small and large Jacobian is given by [21]

$$C_{\text{Jac}}(\boldsymbol{T}) = \int_{\Omega} \left[(J(\boldsymbol{T}(\boldsymbol{x})))^2 + \left(\frac{1}{J(\boldsymbol{T}(\boldsymbol{x}))}\right)^2 \right] d\boldsymbol{x}. \tag{7.14}$$

Further examples of regularization constraints that penalize large and small Jacobians can be found in Sect. 6.1.5, and Ashburner et al. [6].

7.2.3.2 Inverse Consistency Constraint

In order to find better correspondence mapping and reduce pairwise registration error, one method is to jointly estimate the forward and reverse transformations between two images while minimizing the inverse consistent error.

Define forward transformation $\boldsymbol{T}$ deforms I_1 to I_2 and the reverse transformation $\boldsymbol{G}$ deform I_2 to I_1. A meaningful map between two anatomical images should be one-to-one, i.e. each point in image I_1 is mapped to only one point in image I_2 and vice versa. However, many unidirectional image registration techniques have the problem that their similarity cost function does not uniquely determine the correspondence between two images. The reason is that the local minima of similarity cost functions cause the estimated forward mapping $\boldsymbol{T}$ to be different from the inverse of the estimated reverse mapping $\boldsymbol{G}^{-1}$. To overcome correspondence ambiguities, transformations $\boldsymbol{T}$ and $\boldsymbol{G}$ can be jointly estimated. Ideally, $\boldsymbol{T}$ and $\boldsymbol{G}$ should be inverses of one another, i.e. $\boldsymbol{T} = \boldsymbol{G}^{-1}$. In order to couple the estimation of $\boldsymbol{T}$ and $\boldsymbol{G}$ together, an inverse consistency constraint (ICC) [21] is imposed as

$$C_{\text{ICC}} = \int_{\Omega} ||\boldsymbol{T}(\boldsymbol{x}) - \boldsymbol{G}^{-1}(\boldsymbol{x})||^2 d\boldsymbol{x}. + \int_{\Omega} ||\boldsymbol{G}(\boldsymbol{x}) - \boldsymbol{T}^{-1}(\boldsymbol{x})||^2 d\boldsymbol{x}. \tag{7.15}$$

The constraint is minimized and the corresponding transformations are said to be inverse-consistent if $\boldsymbol{T} = \boldsymbol{G}^{-1}$.

7.2.3.3 Sliding Preserving Regularization

The physiological characteristics of the lung motion imply discontinuities between the motion of lung and rib cage contradicting common regularization schemes. As discussed in Sect. 7.2.1, most lung-specific registration algorithms address this problem using lung segmentation masks.

Recently, novel regularization approaches were presented to explicitly model the sliding motion along organ boundaries. Ruan et al. [78] uses a regularization that preserves large shear values to allow for sliding motion. Schmidt-Richberg et al. [83] addressed sliding motion by a direction-dependent regularization at organ boundaries extending the common diffusion registration by distinguishing between normal- and tangential-directed motion. The idea of direction-dependent regularization was adopted in other publications, too [30, 71].

7.2.4 Parameterization, Optimization and Multi-Resolution Scheme

7.2.4.1 Transformation Parameterization

The transformation model defines how one image can be deformed to match another. It can be a simple rigid or affine transformation, or a non-linear transformation such

as the spline-based registrations [90], elastic models [9], fluid models [19], finite element (FE) models [38], etc. The lung is composed of non-homogenous, soft tissue, interlaced by branching networks of airways, arteries, and veins. Lung tissue expansion varies within in the lung depending on body orientation, the direction of gravitation forces, the pattern of airway and vessel branching, disease conditions, and other factors. Since lung expansion is non-uniform, non-linear transformation models are needed to track tissue expansion across changes in lung volume.

To represent the locally varying geometric distortions, the transformation can be represented through different forms. There are three common parameterizations used for intensity-based registration methods of lung CT. The first type of transformation is based on B-splines, as introduced in Sect. 6.2.1. B-splines [79] are well suited for shape modeling and are efficient to capture the local nonrigid motion between two images. Considering the computational efficiency and accuracy requirement, the cubic B-Spline based parameterization is commonly chosen to represent the transformation. In the EMPIRE10 study 10 out of 20 algorithms used a B-Spline parametrization as transformation model [66]. Other basis functions such as thin-plate splines(TPS) [8], Fourier series [5], elastic body spline(EBS) [29] can also be used to parameterize the deformation.

The second type of transformation is dense deformable vector field (DVF), which is introduced in Sect. 6.2.2. The DVF is a non-parametric model representing the deformation by displacement vectors $\boldsymbol{u}(\boldsymbol{x})$ for each voxel location. The transformation is then given by $\boldsymbol{T}(\boldsymbol{x}) = \boldsymbol{x} + \boldsymbol{u}(\boldsymbol{x})$.

In the third type, the transformation is represented by a velocity field $\boldsymbol{v} : \Omega \to \mathbb{R}^d$ in order to ensure that the transformation is diffeomorphic. Diffeomorphisms define a globally one-to-one smooth and continuous mapping, and therefore, preserve topology and are suitable for the study of pulmonary kinematics. Given a time-dependent velocity field $\boldsymbol{v} : \Omega \times [0, 1] \to \mathbb{R}^d$, one defines the ordinary differential equation (ODE): $\partial_t \boldsymbol{\phi}(\boldsymbol{x}, t) = \boldsymbol{v}(\boldsymbol{\phi}(\boldsymbol{x}, t), t)$, with $\boldsymbol{\phi}(\boldsymbol{x}, 0) = \boldsymbol{x}$. For sufficient smooth $\boldsymbol{v}$ and fixed t, e.g. $t = 1$, the solution $\boldsymbol{T}(\boldsymbol{x}) = \boldsymbol{\phi}(\boldsymbol{x}, 1)$ of this ODE is known to be a diffeomorphism on Ω [103]. Diffeomorphic registration algorithms are discussed in more detail in Sect. 10.4.2. Several approaches use diffeomorphic registration methods to model lung motions [28, 35, 41, 82, 86].

7.2.4.2 Optimization

Most registration algorithms employ standard optimization techniques to the optimal transformation, as discussed in Chap. 6. There are several existing methods in numerical analysis such as the partial differential equation (PDE) solvers to solve the elastic and fluid transformation, gradient descent, conjugate gradient method, Newton, Quasi-Newton, LBFGS, etc [56, 68, 69, 73]. One efficient optimization method is a limited-memory, quasi-Newton minimization method with bounds (L-BFGS-B) [11, 104]. It is well suited for optimization with a high dimensional parameter space. In addition, this algorithm allows bound constraints on the independent variables. For example, if the transformation are represented using B-splines, then the bound

constraints can be applied on B-spline coefficients so that it is sufficient to guarantee the local injectivity (one-to-one property) of transformation [18], i.e. the transformation maintains the topology of two images. According to the analysis from Choi and Lee [18], the displacement fields are locally injective all over the domain if B-Spline coefficients satisfy the condition that $c_x \leq \delta_x/K, c_y \leq \delta_y/K, c_z \leq \delta_z/K$, where c_x, c_y, c_z are B-Spline coefficients, $\delta_x, \delta_y, \delta_z$ are B-Spline grid sizes along each direction, and K is a constant approximately equal to 2.479772335.

7.2.4.3 Multi-Resolution Scheme

In order to improve speed, accuracy and robustness of registration algorithms, a spatial multiresolution procedure from coarse to fine is often used. The basic idea of multiresolution is that registration is first performed at a coarse scale where the images have much fewer pixels, which is fast and can help eliminate local minima. The resulting spatial mapping from the coarse scale is then used to initialize registration at the next finer scale. This process is repeated until registration is performed at the finest scale.

7.3 Registration Accuracy Assessment

Validation and evaluation of image registration accuracy is an important task to quantify the performance of registration algorithms. Due to the absence of a 'gold standard' to judge a registration algorithm, various evaluation methods are needed to validate the performance of image registration with respect to different properties of transformations. Focusing on lung image registration, the following image features and information can be used to measure registration accuracy:

- Features extracted from image, such as landmarks, airway and vessel trees, fissures, and object volumes;
- Transformation properties, such as zero singularities and inverse consistency properties;
- Additional information that is not used in the registration data, such as ventilation map estimated from Xenon-CT image;

All the features and image information mentioned above provide different perspectives for registration accuracy measurement. Additional validation methods to measure registration accuracy can be found in Chap. 8.

7.3.1 Evaluation Methods Used in the EMPIRE10 Challenge

Researchers usually test their algorithms on their own data, which varies widely. To make a fair comparison of different methodologies, EMPIRE10 challenge (Evaluation

of Registration Methods on Thoracic CT) was designed to evaluate the performance of different lung registration algorithms on the same set of 30 thoracic CT pairs.

All the registration results were evaluated in four aspects: (1) alignment of the lung boundaries, (2) alignment of the major fissures, (3) alignment of correspondence of annotated point pairs, (4) analysis of singularities in the deformation field. We will shortly discuss these validation methods, full details can be found in [66].

7.3.1.1 Landmark Matching Accuracy

Landmarks are point features of an object. Anatomical landmarks have biological meaning. Intra-subject images of the lung contain identifiable landmarks such as airway-tree and vascular-tree branch points. An example of the landmark distribution is shown in Fig. 7.5 with the assistance of a semi-automatic system [67]. The Euclidean distance between registration-predicted landmark position and its true position is defined as landmark error.

In the EMPIRE10 study, landmarks were generated semi-automatically by three independent experts.

7.3.1.2 Fissure Alignment Distance

The human lungs are divided into five independent compartments which are called lobes. Lobar fissures are the division between adjacent lung lobes. The lobes can

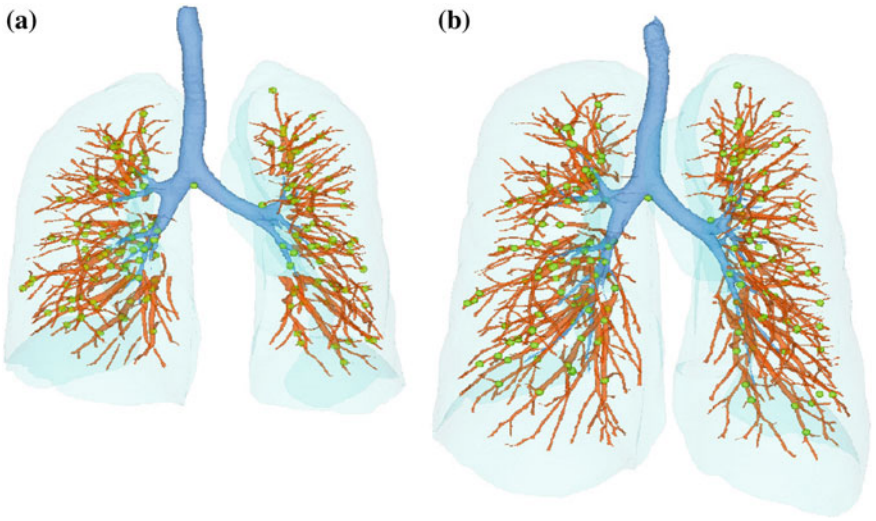

Fig. 7.5 Distribution of landmarks (*green* points) selected at vessel-tree branch points on breath-hold (**a**) maximum exhale, and (**b**) maximum inhale scans from one human subject

be segmented [92] and the fissures represent important physical boundaries within the lungs. Therefore, alignment of fissures is an important evaluation category. The statistics of fissure positioning error (FPE) can be used to evaluate the fissure alignment. The FPE is defined as the minimum distance between a point on the deformed fissure and the closest point on the corresponding target fissure. Mathematically, this metric can be stated as

$$FPE(\boldsymbol{x}) = \min_{\boldsymbol{y} \in F_2} d(\boldsymbol{x}, \boldsymbol{T}(\boldsymbol{y})) \tag{7.16}$$

for a given point $\boldsymbol{x}$ in F_1, where F_1 (F_2, resp.) is the set of all points in the fissure in image I_1 (I_2, resp.) and $d(\cdot)$ defines the Euclidean distance.

7.3.1.3 Relative Overlap of Lung Segmentations

The relative overlap (RO) is used to measure how well the corresponding parenchymal regions of interest agree with each other. The RO metric is given by

$$RO(S_1 \circ \boldsymbol{T}, S_2) = \frac{|(S_1 \circ \boldsymbol{T}) \cap S_2|}{|(S_1 \circ \boldsymbol{T}) \cup S_2|} \tag{7.17}$$

where S_1 and S_2 are corresponding regions of interest in images I_1 and I_2, respectively. $S_1 \circ \boldsymbol{T}$ corresponds to a segmentation transformed from image I_1 to I_2. The relative overlap of segmentations can be evaluated on the whole parenchyma region, or subvolumes of left lung, right lung, or even on the lobe level whenever the segmentations are available.

7.3.1.4 Validation on Transformation Properties

Good matching accuracy on the feature locations does not guarantee that regions away from the features are correctly aligned. In order to reveal how well a transformation preserves the topology between two images during the deformation, the Jacobian determinant of the transformation field derived by image registration can be used for singularity assessment.

The Jacobian determinant J at a given point gives important information about the behavior of transformation $\boldsymbol{T}$ at that point. If the Jacobian value at $\boldsymbol{x}$ is zero, then $\boldsymbol{T}$ is not invertible near $\boldsymbol{x}$. A negative Jacobian indicates $\boldsymbol{T}$ reverses orientation, which folds the domain [20, 25]. A positive Jacobian means the transformation $\boldsymbol{T}$ preserves orientation near $\boldsymbol{x}$. These indications of Jacobian are listed in Eq. (7.18).

$$\begin{cases} J > 0, \text{preserve orientation} \begin{cases} J > 1, \text{local expansion} \\ J = 1, \text{no deformation} \\ 0 < J < 1, \text{local contraction} \end{cases} \\ J = 0, \text{non-injective} \\ J < 0, \text{reverse orientation} \end{cases} \tag{7.18}$$

The Jacobian evaluates the quality of transformations by measuring how well the transformation preserves topology. For lung registration, a meaningful and physically plausible deformation within a continuous region should be diffeomorphic, and thus contains no singularities ($J \leq 0$).

Other measures of transformation properties can be defined, e.g. the inverse consistency error (see Sect. 8.1). It measures the consistency between a forward transformation and a reverse transformation between two images. Ideally, composing the forward and reverse transformations together should produce the identity map when there is no inverse consistency error.

7.3.1.5 Registration Algorithms for Lung Motion Estimation

The EMPIRE10 competition included a wide variety of registration algorithms (transformation models, similarity measures, etc.). Most algorithms used lung-specific preprocessing (masking, histogram-matching, etc.), but beside this, only a selection of algorithms were tailored towards thoracic CT applications. A conclusion of the EMPIRE10 study was *"[..] generic algorithms which were not tailored for this data performed extremely well and many different approaches to registration were shown to be successful."* [66]. Accurate registration of lung CT images is possible, as shown by an average TRE of less than 1 mm for the top six algorithms in this study. Another important result was that landmark matching accuracy provided the most useful reference for distinguishing between registration algorithm results.

In the following, we review some of the registration algorithms that participated in this study: Song et al. proposed the algorithm which includes affine transformation and different diffeomorphic transformation by maximizing cross correlation between images [86]. Han proposed a hybrid feature-constrained deformable registration method. The features are detected based on robust 3D SIFT descriptors, and then a mutual information based registration is used to match those features. The feature correspondences are used to guide an intensity-based deformable image registration which maximizes the mutual information and minimize the normalized sum of squared differences between images [47]. Ruhaak et al. presented a variational approach which drives the registration towards exact lung boundary matching. They used the normalized gradient field to measure the distance focusing on image edges instead of intensities, and a curvature regularizer is applied to penalize the second order derivatives and yields smooth solutions [80]. Muenzing et al. developed a novel regularization model incorporates information from two different knowledge sources: anatomical aspect and statistical aspect in which the regularization is

considered as a machine learning problem. Predominant anatomical structures are extracted and used to model the ROI as composition of anatomical objects. And finally, a link function is formulated to combine the two pieces of information [65]. Modat et al. proposed the NiftyReg package which contains a global and a local registration algorithm [64]. A block-matching technique is used in the global registration, as proposed by Ourselin et al. [70]. The Free-Form Deformation (FFD) algorithm is used in the local registration stage to maximize the normalized mutual information. Staring et al. proposed the algorithm including a combination of an affine as well as non-rigid transformations by maximizing the normalized correlation coefficient, which is implemented in elastix [87]. Schmidt-Richberg et al. developed a robust registration approach which consists of an affine alignment, a shape-based adjustment of lung surfaces and an intensity-based diffeomorphic image registration. The algorithm has been optimized for the registration of lung CT data [82]. Cao et al. developed a nonrigid registration method to preserve both parenchymal tissue volume and vesselness measure. The transformation is regularized and its local injectivity is guaranteed [15]. Kabus et al. proposed a fast elastic registration algorithm that can be used in a multi-resolution setting. It is initialized by an affine pre-registration of the lungs followed by simultaneously minimizing of the similarity measure calculated as the sum of squared differences as well as the regularizing term based on the Navier-Lame equation [55]. The elastic regularizer assumes the lung tissue can be characterized as an elastic and compressible material. All these methods achieved good results in the evaluation challenge.

7.3.2 Validation Using Additional Information

7.3.2.1 Correlation Between Lung Expansion and Xe-CT Estimates of Specific Ventilation

Anatomical reference can usually provide features such as landmarks at the regions with high contrast which can be recognized by either human observer or computer algorithms. However, they are not be able to assess registration accuracy at the regions where no high contrast landmarks are available. Registration results in estimate of the regional specific ventilation (regional lung function). By comparing it with functional information, such as the xenon-CT based estimate of the regional specific ventilation, it is possible to assess the registration accuracy using lung function.

Previous studies have shown that the degree of regional lung expansion is directly related to specific ventilation (sV) [74]. A good registration should produce a deformation map (Jacobian map) which has high correlation with Xe-CT estimates of ventilation map.

An example of Jacobian map derived from registering CT images between positive end-expiratory pressure (PEEP) 10 cm H_2O and 25 cm H_2O for one sheep subject, and its sV measures resulted from Xe-CT image analysis [45, 85] are shown on a transverse slice in Fig. 7.6a, b. The correlation between ventilation map and Jacobian

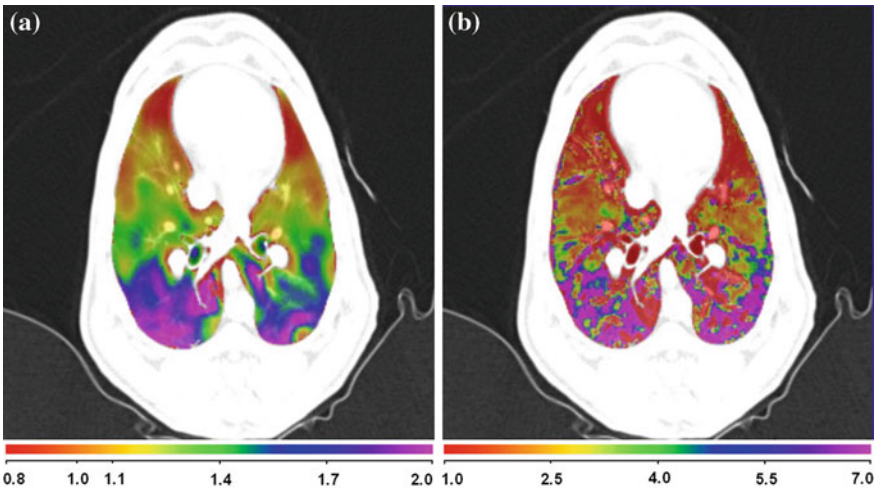

Fig. 7.6 Color-coded maps overlaid on a transverse slice showing (**a**) the Jacobian of transformation between PEEP 10 cm H_2O and 25 cm H_2O for one sheep subject, and (**b**) the corresponding specific ventilation (1/min) from the Xe-CT analysis. *Blue and purple* regions show larger deformation in **a** and higher ventilation in **b**, while *red and orange* regions show smaller deformation in **a** and lower ventilation in **b**

map can be utilized to validate the registration results. A higher correlation indicates a better registration. As shown in Fig. 7.6, both sV and Jacobian maps show a similar ventral to dorsal gradient. High specific ventilation should correspond with large tissue expansion.

7.4 Application: Assessment of Lung Biomechanics

CT imaging of the lungs provides a new opportunity for assessment of lung function by non-rigid image registration of a pair of scans at different inflation levels. After finding out the transforms and correspondence for each voxel between two images, we are ready for motion estimation and mechanical analysis in a regional level. Post-analysis of the registration results reflects the mechanical properties of local lung tissue. The computed measurements from dense displacement fields can be used to estimate regional tissue motion, analyze regional pulmonary function and help diagnose lung diseases.

Measurements resulting from image registration reveal details of local tissue deformation patterns. Tissue motion can be quantified by parameters and index maps from:

- Displacement field analysis, quantifying the magnitude and direction of local tissue movement;

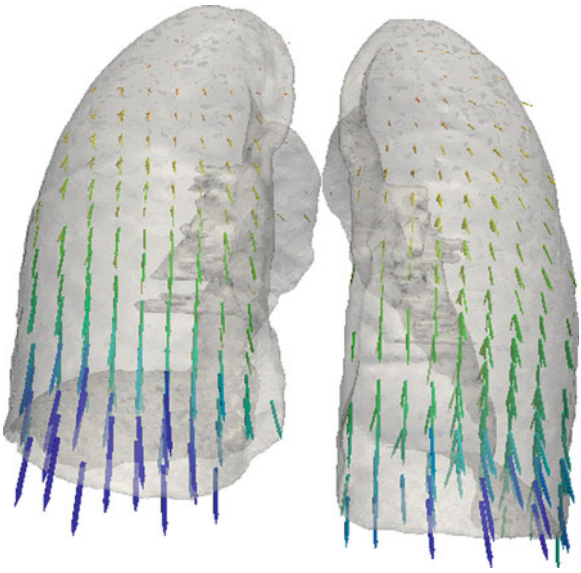

Fig. 7.7 3D displacement from breath-hold maximum exhale to maximum inhale for one human subject

- Specific volume change and ventilation analysis, quantifying specific volume and specific air volume change through the deformation;
- Strain analysis, quantifying the major deformation magnitude and direction;
- Anisotropic deformation analysis, quantifying regional deformation patterns;
- Shear stretch analysis, quantifying the lobar sliding.

7.4.1 Displacement Vector Field

The displacement fields can be directly used to assess the magnitude and direction of local volume movement. Figure 7.7 shows a 3D displacement filed computed from two 3D CT data sets, acquired at breath-hold maximum exhale and breath-hold maximum inhale. The two 3D CT images are registered using a Laplacian regularization and a combination of the squared tissue volume difference (SSTVD) and the squared vesselness measure difference (SSVMD) as distance measure (see Sects. 7.2.2.3, 7.2.2.4, and 7.2.3.1). The vector field gives the direction of tissue motion, and the length of vectors reflects the motion magnitude. Notice that regions near the diaphragm have larger tissue motions, and are moving downwards.

Figure 7.8 demonstrates how tissue movement may be tracked during respiratory cycles using 4DCT data. The 4DCT data sets were acquired using a Siemens Biograph 40-slice CT scanner operating in helical mode, and reconstructed at 0 %, 20 %, 40 %,

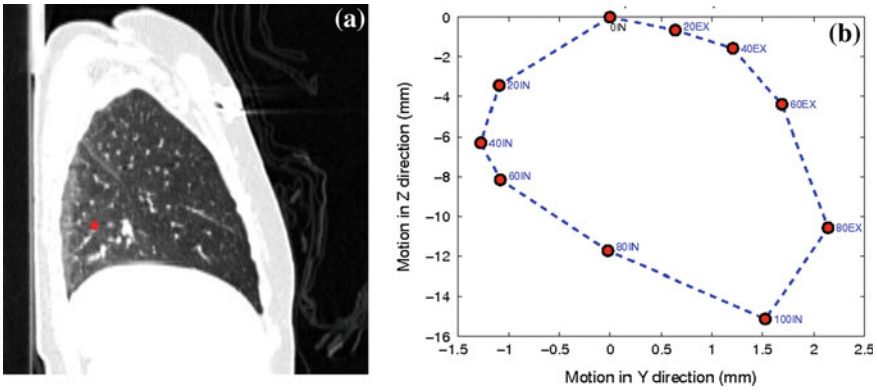

Fig. 7.8 Tissue ROI trajectory in 4DCT for one human subject. **a** ROI position in the sagittal slice. **b** ROI movement trajectory during the respiratory cycle

60 %, 80 %, 100 % during inspiration (noted as 0IN, 20IN, 40IN, 60IN, 80IN, 100IN), and 80 %, 60 %, 40 %, 20 % during expiration (noted as 80EX, 60EX, 40EX, 20EX). Again, a Laplacian regularization and C_{SSTVD} combined with C_{SSVMD} were used for the registration of the images acquired at different inflation levels. The tissue ROI is noted in Fig. 7.8a, and its motion is shown in the Y (dorsal-to-ventral) direction and Z (base-to-apex) direction in Fig. 7.8b. The motion of the ROI mainly occurred in the Z direction, and moved around 15 mm from 0IN to 100IN. During inspiration, its movement along Z direction in each interval was quite uniform (around 3 mm in each of the five intervals). During expiration, its backwards movement was much faster from 100IN to 80EX, and from 80EX to 60EX intervals (totally around 11 mm in the two intervals), while in the rest three intervals it only moved around 4 mm to its original position.

7.4.2 Specific Volume Change

Different measures can be defined to quantify lung tissue deformation patterns. Specific volume change (*sVol*) measures the volume change of local structure under deformation, and regions of local expansion or contraction can be identified. The most intuitive way to calculate *sVol* is derived through the Jacobian determinant of the transformation $J(\boldsymbol{T})$. Using a Lagrangian reference frame, a Jacobian value of one corresponds to zero expansion or contraction. Local tissue expansion corresponds to a Jacobian greater than one and local tissue contraction corresponds to a Jacobian less than one. These indications of Jacobian are listed in Eq. (7.18).

As derived in Sect. 13.2 the specific volume change can be expressed as

$$sVol = J(\boldsymbol{T}(\boldsymbol{x})) - 1. \tag{7.19}$$

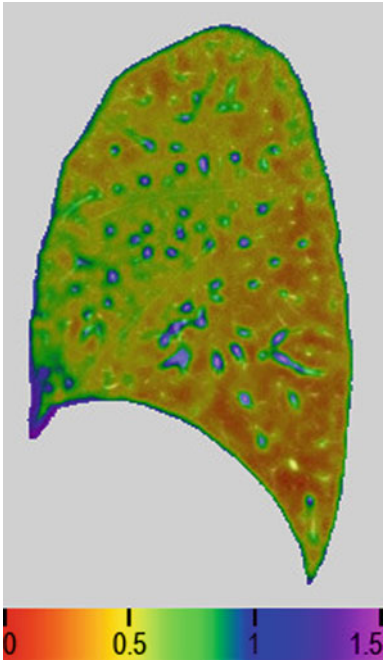

Fig. 7.9 The Jacobian map showing local volume deformation in exhalation stage from one human subject. Local tissue expansion corresponds to a Jacobian greater than one and local tissue contraction corresponds to a Jacobian less than one

Note that *sVol* is linearly related to the Jacobian and therefore it is possible to use the Jacobian measurement to reflect the specific volume change.

In Fig. 7.9, the specific volume change maps reflected by Jacobian show local volume deformation during exhalation stage. Since the CT images were acquired with subjects in the supine orientation, the more dependent region of lung is the dorsal region since it is closest to the direction of the force of gravity. Thus, there is more ventilation in the dorsal region. The maps also reflect the fact that vessels have little deformation during respiratory cycles while lung tissues and airways deform a lot.

7.4.3 Specific Ventilation

Specific ventilation measures the specific air volume change, and can be calculated from the intensity information of corresponding regions. More details about specific ventilation can be found in Chap. 13. The lung density is represented by CT grayscale in Hounsfield units (HU), which is defined such that the HU of water and air are 0 and -1000, respectively. Since the lung density decreases as it inflates with air, changes in the lung CT density during inflation can also be used to quantify regional mechanical properties. Therefore, given CT images of a lung region at two different pressures,

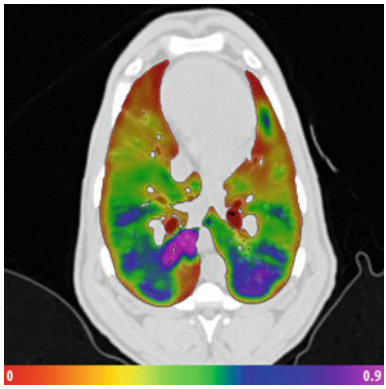

Fig. 7.10 Color-coded maps showing specific ventilation computed from images pair acquired at PEEP 10 cm H_2O and 15 cm H_2O for one sheep subject

it is possible to estimate the regional air volume change based on the HU values at corresponding regions. Assuming that the fraction of air in a region located at $\boldsymbol{x}$ is given by $F_{air}(\boldsymbol{x}) = -I(\boldsymbol{x})/1000$, where I is the intensity function of a image, the specific ventilation sV can be calculated by [84]

$$sV = 1000 \frac{I_1(\boldsymbol{T}(\boldsymbol{x})) - I_2(\boldsymbol{x})}{I_2(\boldsymbol{x})(1000 + I_1(\boldsymbol{T}(\boldsymbol{x})))}. \tag{7.20}$$

A derivation of this equation and more details about specific ventilation can be found in Chap. 13.

Figure 7.10 shows an example specific ventilation map computed from images pair acquired at positive end-expiratory pressure (PEEP) of 10 cm H_2O and 15 cm H_2O for one sheep subject. During this experiment, the sheep was anesthetized, mechanically ventilated, and CT scans covering the thorax were acquired at 0, 5, 10, 15, 20, and 25 cm H_2O airway pressures. The consistent image registration method [21] was used to register the sheep data with different airway pressures. An obvious dorsal to ventral gradient is noticed from the sV map. This agrees with well known physiology that subjects positioned in the supine posture have more ventilation in the dorsal region.

7.4.4 Strain Tensors

In classical mechanics, deformation of structures is characterized by the regional distribution of a strain or stretch tensor. Some of the most common strain tensors, such as Linear strain tensor, Green-St. Venant strain tensor, and Eulerian-Almansi strain tensor are discussed in Chap. 4.

These strain tensors can be computed from the deformation field and used to analyze the stress caused by the geometrical deformation of the lung. In there most

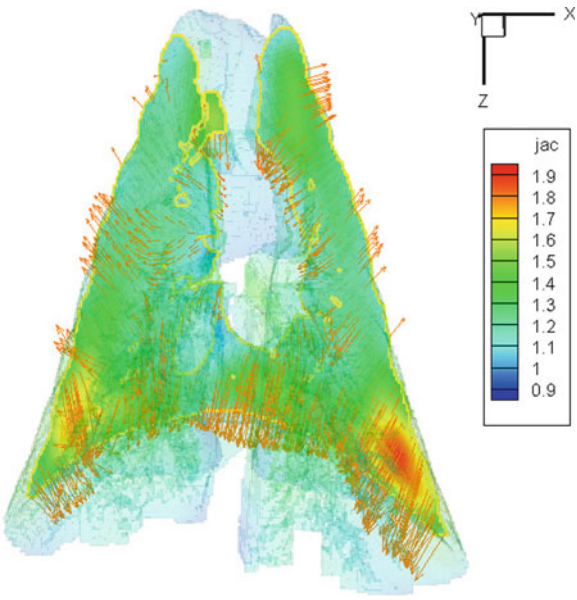

Fig. 7.11 Maximal principal direction of transformation mapping images from PEEP 0 cm H_2O to PEEP 10 cm H_2O for one sheep subject. The vector magnitude represents the maximal principal strain, and the colored contour expresses the Jacobian

general form, the strain tensors are real symmetric matrices. Through singular value decomposition (SVD), they can be represented as a set of orthogonal eigenvectors, along which there is no shear, but only expansion or compression. These eigenvalues and eigenvectors are denoted as principal strains and principal directions. The maximal eigenvalue for each tensor is defined as maximal principal strain, and its corresponding eigenvector is called maximal principal direction. The principal strains and directions provide valuable information on preferential directionalities in deformation.

Figure 7.11 illustrates the maximal principal direction, maximal principal strain, and Jacobian together on coronal slice for one sheep subject when deforming images from PEEP 0 cm H_2O to PEEP 10 cm H_2O. Strain tensors provide complementary information to the Jacobian for analyzing lung tissue expansion. The regions near diaphragm have larger maximal principal strain. The maximal principal strain on the lung boundaries are towards the chest wall.

Figure 7.12 shows maps of the maximal principal strain from linear strain, Green strain, and Eulerian strain tensors. Although they are of different ranges, regional patterns are similar among all three strain measures. The regions near lung boundaries and near the heart has larger maximal principal strains, while the dorsal regions have less maximal principal strains.

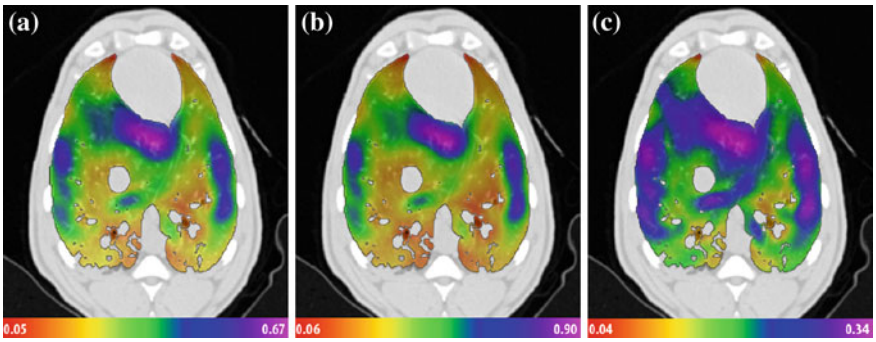

Fig. 7.12 Maximal principal strain from (**a**) linear strain, (**b**) Green strain, and (**c**) Eulerian strain tensors on a transverse slice of deformed image from PEEP 0 cm H_2O to PEEP 10 cm H_2O for one sheep subject

7.4.5 Anisotropy Analysis

Regional deformation of the lung during inspiration and expiration is more than just volume change. Volume change may also have orientational preference anisotropy of deformation [77, 97]. For instance, regions closest to the diaphragm are likely to experience more volume change in the vertical orientation. And regions closest to the heart may be more constrained from expanding normal to the heart. Volume change and deformation anisotropy are independent quantities as a region may undergo no volume change but still have deformed significantly, such as the case that the lengthening in one orientation is compensated by contraction along another orientation. Therefore, without orientational preference, regional volume change alone is not enough to characterize lung deformation.

7.4.5.1 Regional Stretch

In continuum mechanics, the deformation gradient tensor $\mathbf{F}$ is the same as the Jacobian matrix $\mathbf{J}$ of the transformation, which describes the continuum deformation from point-wise displacements, and it can be decomposed into stretch and rotation components:

$$\mathbf{F} = \mathbf{J} = \begin{bmatrix} 1 + \frac{\partial u_x}{\partial x} & \frac{\partial u_x}{\partial y} & \frac{\partial u_x}{\partial z} \\ \frac{\partial u_y}{\partial x} & 1 + \frac{\partial u_y}{\partial y} & \frac{\partial u_y}{\partial z} \\ \frac{\partial u_z}{\partial x} & \frac{\partial u_z}{\partial y} & 1 + \frac{\partial u_z}{\partial z} \end{bmatrix} = \mathbf{RU}, \tag{7.21}$$

where the $\mathbf{U}$ is the right stretch tensor and $\mathbf{R}$ is an orthogonal rotation tensor.

The Cauchy-Green deformation tensor is defined as

$$\mathbf{C} = \mathbf{F}^T\mathbf{F} = \mathbf{U}^T\mathbf{R}^T\mathbf{RU} = \mathbf{U}^T\mathbf{U}. \tag{7.22}$$

In order to obtain stretch information **U** from this equation, it is first necessary to evaluate the principal directions of **C**, denoted here by the eigenvector N_1, N_2 and N_3 and their corresponding eigenvalues λ_1^2, λ_2^2 and λ_3^2. Therefore, after eigendecomposition and taking the square root of the eigenvalues of **C**, we can get the eigenvalues of **U**: λ_1, λ_2 and λ_3 (ordered as $\lambda_1 > \lambda_2 > \lambda_3$). The eigenvalues of **U** are defined as principal stretches and calculated as

$$\lambda_i = \sqrt{eigenvalues\ of\ \mathbf{C}}. \tag{7.23}$$

7.4.5.2 Distortion Index (DI)

The ratio of the length in the direction of maximal stretch over the length in the direction of minimal stretch is defined as distortion index (DI)

$$DI = \frac{\lambda_1}{\lambda_3}. \tag{7.24}$$

The DI value is always larger or equal to 1. A big DI value indicates an anisotropic expansion, while a DI values approximately 1 represents an isotropic expansion.

Figure 7.13 gives an example of maps showing Jacobian, principal linear strain and distortion index from PEEP 0 cm H_2O to PEEP 10 cm H_2O registration for one sheep subject. Comparison between Jacobian and principal strain together with the distortion index (DI) map can reflect more lung tissue deformation information. For the region near the aorta in the left lung (black rectangular region), the Jacobian is large while the principal strain is relatively small. This illustrates that this region experienced an isotropic expansion, shown as red in the DI map (small DI value approximately 1) . For the region near the heart (red rectangular region), the Jacobian is near 1 while its principal strain is large. This illustrates that region

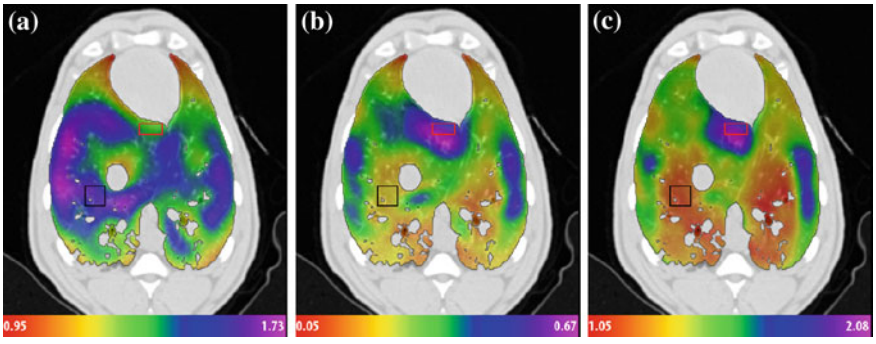

Fig. 7.13 Lung expansion measures resulted from registration. **a** Jacobian, **b** principal linear strain, and **c** anisotropic deformation index on a transverse slice of deformed image from PEEP 0 cm H_2O to PEEP 10 cm H_2O for one sheep subject

experienced an anisotropic expansion, shown as purple in the DI map (larger DI value approximately 2). This anisotropic expansion may be caused by the blocking of the heart. Regional deformation is significantly anisotropic at the posterior end of lungs, but more isotropic at the anterior end.

Amelon et al. [3] has proposed another method to quantify the magnitude of anisotropy by defining the anisotropy deformation index (ADI)

$$ADI = \sqrt{\left(\frac{\lambda_1 - \lambda_2}{\lambda_2}\right)^2 + \left(\frac{\lambda_2 - \lambda_3}{\lambda_3}\right)^2}. \tag{7.25}$$

It takes the three stretch factors into consideration, and thus has better discriminability among different anisotropy deformation patterns. This ADI calculation ranges from 0 to ∞ where 0 indicates perfectly isotropic deformation.

7.4.6 Quantification of Lobar Sliding

The lung is divided into five lobes, three in the right lung and two in the left lung. It is thought that the lobes slide with respect to each other during breathing to reduce parenchymal distortion avoiding high stress concentrations [53]. Almost all methods of assessing lung function treat the lung as a single continuum, such as image registration [26, 44, 75, 88] or finite element simulation [1, 2, 37, 96], and fail to fully account for the discontinuity in the displacement field at the lobar fissures. The impact of neglecting discontinuities at the fissures is not understood as the degree of sliding in the lobes is relatively unaddressed in literature. There is value in quantifying the amount of lobar sliding if not for the sole purpose of analyzing its influence on current methods of assessing lung function.

Ding et al. quantified lobar sliding from lobe-by-lobe CT image registration by interpolating the displacement field on either side of the fissure to the fissure surface [33]. The difference in the displacement field represents the degree of sliding. Up to 20 mm of sliding was observed in the ventral portions of the fissure, increasing from nearly no sliding near carina. However, due to complexities in the algorithm only the left lung was considered since it contains only a single fissure. Other groups have also noted discontinuities in the displacement field along the fissures. For example, Cai et al. used grid-tagged MRI to obtain a displacement field within the lung [12]. They clearly demonstrate a discontinuity in the displacement field along fissure surfaces and note that discontinuities can be up to 20 mm.

Another approach to quantify lobar sliding is based on a finite element analysis of the displacement field using the previous defined stretch tensor $\mathbf{U}$ [4]. A discontinuity in the displacement field will manifest itself as a region of elevated shear. If the amount of shear created due to sliding is much greater than the shear created by parenchymal distortion then shear can be considered a good indicator of relative sliding. Since large strain theory is used, we consider the shear components of the

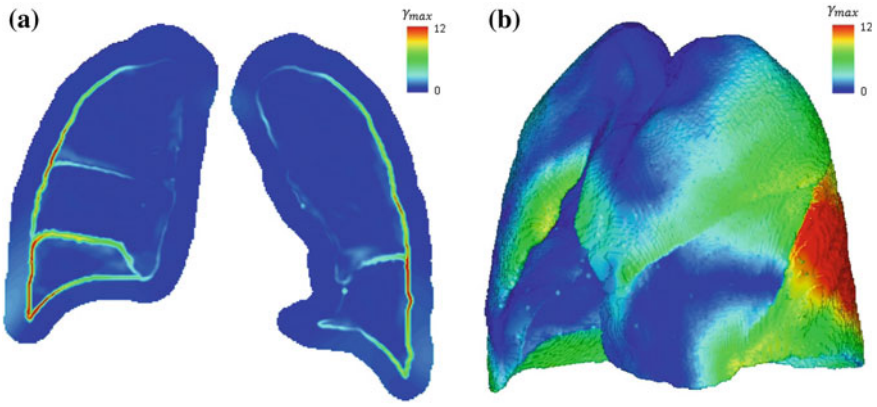

Fig. 7.14 Distribution of maximum shear from breath-hold maximum exhale to maximum inhale for one human subject. **a** 2D view on a coronal slice, with lung and chest wall regions included. **b** 3D view within the lung region

stretch tensor **U**. The eigenvalues of **U** define the stretch in the principal directions of **U** (see Eq. (7.22) and Sect. 7.4.5.1). It can be shown that the maximum shear component (denoted γ_{max}) at a point is half the difference between the maximum principal stretch and minimum principal stretch. Consider that $\lambda_1 > \lambda_2 > \lambda_3$, the maximum shear is defined as

$$\gamma_{max} = \frac{\lambda_1 - \lambda_3}{2}. \tag{7.26}$$

Figure 7.14 gives an example of maximum shear distribution from breath-hold maximum exhale to maximum inhale for one normal human subject. Figure 7.14a shows the distribution of maximum shear on a coronal slice. To obtain the image, each lobe and the chest wall are segmented and independently registered. The resulting displacement fields are then added to form a single image. In doing this, the discontinuity at the lobar boundaries is properly accounted for as no information outside of the respective lobe is included in the registration. Note that large sliding magnitudes are observed on the outer lung surface and lobar fissures. The sliding magnitude dissipates when moving medially along the fissure between the right upper lobe and right middle lobe. Figure 7.14b shows the 3D distribution of maximum shear within the lung region. Higher shear stretch (higher sliding) is observed in the dorsal region, while less sliding is observed near the carina.

7.5 Summary

Image registration can be used to determine the spatial locations of corresponding voxels in a sequence of pulmonary scans. The computed correspondences yield the displacement fields corresponding with the motion of the lung between a pair

of images. In this chapter, we discussed a method of intensity-based registration designed to match lung images. Since image registration is inherently an ill-posed problem due to the fact that determining the unknown the displacements merely from the images is an underdetermined problem, it is necessary to validate registration methods in the context of physiologically plausible results. We provided several methods for validating lung registration performance. Accurate registrations can represent the underlying anatomical and physiological changes of lung tissue, and thus make post-analysis on motion estimation and lung mechanics meaningful. We also provided a systematic study of image registration based measurements of the regional lung mechanics and motion patterns. Local volume change, major deformation magnitude and direction, anisotropy deformation pattern, and shear stretch on lobar fissures and lung surface against chest wall were discussed. These measurements enable estimation of tissue motion and assessment of lung function at a regional level.

References

1. Al-Mayah, A., Moseley, J., Velec, M., Brock, K.K.: Sliding characteristic and material compressibility of human lung: parametric study and verification. Med. Phys. **36**(10), 4625–4633 (2009)
2. Al-Mayah, A., Moseley, J., Velec, M., Hunter, S., Brock, K.: Deformable image registration of heterogeneous human lung incorporating the bronchial tree. Med. Phys. **37**(9), 4560–4571 (2010)
3. Amelon, R., Cao, K., Ding, K., Christensen, G.E., Reinhardt, J.M., Raghavan, M.L.: Three-dimensional characterization of regional lung deformation. J. Biomech. **44**(13), 2489–2495 (2011)
4. Amelon, R., Cao, K., Reinhardt, J.M., Christensen, G.E., Raghavan, M.: Estimation of lung lobar sliding using image registration. Proc. SPIE 8317, 83171H (2012).
5. Amit, Y.: A non-linear variational problem for image matching. SIAM J. Sci. Comput. **15**(1), 207–224 (1994)
6. Ashburner, J., Andersson, J., Friston, K.: High-dimensional image registration using symmetric priors. NeuroImage **9**, 619–628 (1999)
7. Avants, B.B., Tustison, N.J., Song, G., Cook, P.A., Klein, A., Gee, J.C.: A reproducible evaluation of ANTs similarity metric performance in brain image registration. NeuroImage **54**(3), 2033–2044 (2011)
8. Bookstein, F.L.: Principal warps: thin-plate splines and the decomposition of deformations. IEEE Trans. Pattern Anal. Mach. Intell. **11**(6), 567–585 (1989)
9. Broit, C.: Optimal registration of deformed images. Ph.D. Thesis, University of Pennsylvania, Philadelphia, PA, USA (1981)
10. Buck, R.C.: Advanced Calculus, 3rd edn. McGraw-Hill, St. Louis (1978)
11. Byrd, R.H., Lu, P., Nocedal, J., Zhu, C.: A limited memory algorithm for bound constrained optimization. SIAM J. Sci. Comput. **16**(5), 1190–1208 (1995)
12. Cai, J., Sheng, K., Benedict, S.H., Read, P.W., Larner, J.M., Mugler, J.P., III, de Lange, E.E., Cates, G.D., Jr., Miller, G.W.: Dynamic MRI of grid-tagged hyperpolarized Helium-3 for the assessment of lung motion during breathing. Int. J. Radiat. Oncol. Biol. Phys. **75**(1), 276–284 (2009)
13. Cao, K., Ding, K., Christense, G.E., Reinhardt, J.M.: Tissue volume and vesselness measure preserving nonrigid registration of lung CT images. Proc. SPIE **7623**, 762309 (2010)

14. Cao, K., Ding, K., Christensen, G.E., Raghavan, M.L., Amelon, R.E., Reinhardt, J.M.: Unifying vascular information in intensity-based nonrigid lung CT registration. In: 4th International Workshop on Biomedical Image Registration, LCNS 6204, pp. 1–12. Springer, Berlin (2010)
15. Cao, K., Du, K., Ding, K., Reinhardt, J.M., Christensen, G.E.: Regularized nonrigid registration of lung CT images by preserving tissue volume and vesselness measure. In: Grand Challenges in Medical Image Analysis (2010)
16. Castillo, E., Castillo, R., Martinez, J., Shenoy, M., Guerrero, T.: Four-dimensional deformable image registration using trajectory modeling. Phys. Med. Biol. **55**(1), 305 (2010)
17. Castillo, E., Castillo, R., Zhang, Y., Guerrero, T.: Compressible image registration for thoracic computed tomography images. J. Med. Biol. Eng. **29**(5), 222-233 (2009)
18. Choi, Y., Lee, S.: Injectivity conditions of 2D and 3D uniform cubic B-spline functions. Graph. Models **62**(6), 411–427 (2000)
19. Christensen, G.E.: Deformable shape models for anatomy. Ph.D. Thesis, Department of Electrical Engineering, Sever Institute of Technology, Washington University, St. Louis, MO 63130 (1994)
20. Christensen, G.E.: Consistent linear-elastic transformations for image matching. In: Kuba, A., Samal, M. (eds.) Information Processing in Medical Imaging, LCNS 1613, pp. 224–237. Springer, Berlin (1999)
21. Christensen, G.E., Johnson, H.J.: Consistent image registration. IEEE Trans. Med. Imaging **20**(7), 568–582 (2001)
22. Christensen, G.E., Joshi, S.C., Miller, M.I.: Volumetric transformation of brain anatomy. IEEE Trans. Med. Imaging **16**(6), 864–877 (1997)
23. Christensen, G.E., Rabbitt, R.D., Miller, M.I.: 3D brain mapping using a deformable neuroanatomy. Phys. Med. Biol. **39**, 609–618 (1994)
24. Christensen, G.E., Rabbitt, R.D., Miller, M.I.: Deformable templates using large deformation kinematics. IEEE Trans. Image Proc. **5**(10), 1435–1447 (1996)
25. Christensen, G.E., Rabbitt, R.D., Miller, M.I., Joshi, S., Grenander, U., Coogan, T., Essen, D.V.: Topological properties of smooth anatomic maps. In: Bizais, Y., Braillot, C., Paola, R.D. (eds.) Information Processing in Medical Imaging, vol. 3, pp. 101–112. Kluwer Academic, Boston (1995)
26. Christensen, G.E., Song, J.H., Lu, W., Naqa, I.E., Low, D.A.: Tracking lung tissue motion and expansion/compression with inverse consistent image registration and spirometry. Med. Phys. **34**(6), 2155–2165 (2007)
27. Collignon, A., Maes, F., Delaere, D., Vandermeulen, D., Suetens, P., Marchal, G.: Automated multi-modality image registration based on information theory. In: Bizais, Y., Braillot, C., Paola, R.D. (eds.) Information Processing in Medical Imaging, vol. 3, pp. 263–274. Kluwer Academic, Boston (1995)
28. Cook, T.S., Tustison, N., Biederer, J., Tetzlaff, R., Gee, J.: How do registration parameters affect quantitation of lung kinematics? In: Proceedings of the 10th International Conference on Medical Image Computing and Computer-Assisted Intervention—MICCAI'07, vol. Part I, pp. 817–824. Springer, Berlin (2007)
29. Davis, M.H., Khotanzad, A., Flamig, D.P., Harms, S.E.: Elastic body splines: a physics based approach to coordinate transformation in medical image matching. In: Proceedings of the Eighth Annual IEEE Symposium on Computer-Based Medical Systems, CBMS '95, pp. 81–88. IEEE Computer Society, Washington, DC, USA (1995)
30. Delmon, V., Rit, S., Pinho, R., Sarrut, D.: Direction dependent B-splines decomposition for the registration of sliding objects. In: Proceedings of the Fourth International Workshop on Pulmonary Image Analysis, pp. 45–55, Toronto, Canada (2011)
31. Ding, K., Bayouth, J.E., Buatti, J.M., Christensen, G.E., Reinhardt, J.M.: 4DCT-based measurement of changes in pulmonary function following a course of radiation therapy. Med. Phys. **37**(3), 1261–1272 (2010)
32. Ding, K., Cao, K., Christensen, G.E., Hoffman, E.A., Reinhardt, J.M.: Registration-based regional lung mechanical analysis: retrospectively reconstructed dynamic imaging versus static breath-hold image acquisition. In: Proceedings of SPIE Conference on Medical Imaging, vol. 7262, p. 72620D (2009)

33. Ding, K., Yin, Y., Cao, K., Christensen, G.E., Lin, C.L., Hoffman, E.A., Reinhardt, J.M.: Evaluation of lobar biomechanics during respiration using image registration. In: Proceedings of International Conference on Medical Image Computing and Computer-Assisted Intervention 2009, vol. 5761, pp. 739–746 (2009)
34. Dunlap, N., McIntosh, A., Sheng, K., Yang, W., Turner, B., Shoushtari, A., Sheehan, J., Jones, D.R., Lu, W., Ruchala, K., Olivera, G., Parnell, D., Larner, J.L., Benedict, S.H., Read, P.W.: Helical tomotherapy-based STAT stereotactic body radiation therapy: dosimetric evaluation for a real-time SBRT treatment planning and delivery program. Med. Dosim. **35**(4), 312–319 (2010)
35. Ehrhardt, J., Werner, R., Schmidt-Richberg, A., Handels, H.: Statistical modeling of 4D respiratory lung motion using diffeomorphic image registration. IEEE Trans. Med. Imaging **30**(2), 251–265 (2011) (in press)
36. Enquobahrie, A., Ibanez, L., Bullitt, E., Aylward, S.: Vessel enhancing diffusion filter. Insight J (2007)
37. Eom, J., Shi, C., Xu, X., De, S.: Modeling respiratory motion for cancer radiation therapy based on patient-specific 4DCT data. In: Medical Imaging Computing and Computer Assisted Intervention, Lecture Notes in Computer Science, vol. 12, pp. 348–355 (2009)
38. Ferrant, M., Warfield, S.K., Nabavi, A., Jolesz, F.A., Kikinis, R.: Registration of 3D intraoperative MR images of the brain using a finite element biomechanical model. In: MICCAI '00: Proceedings of the Third International Conference on Medical Image Computing and Computer-Assisted Intervention, pp. 19–28. Springer, London (2000)
39. Fitzpatrick, J., Hill, D., Maurer, C.: Image registration. In: Sonka, M., Fitzpatrick, J. (eds.) Handbook of Medical Imaging, vol. 2, chap. 8, pp. 447–513. SPIE Press, San Diego (2000)
40. Frangi, A.F., Niessen, W.J., Vincken, K.L., Viergever, M.A.: Multiscale vessel enhancement filtering. In: MICCAI, vol. 1496, pp. 130–137 (1998)
41. Gee, J.C., Sundaram, T., Hasegawa, I., Uematsu, H., Hatabu, H.: Characterization of regional pulmonary mechanics from serial MRI data. In: Proceedings of the 5th International Conference on Medical Image Computing and Computer-Assisted Intervention-Part I, MICCAI '02, pp. 762–769. Springer, London (2002)
42. Gorbunova, V., Lo, P., Ashraf, H., Dirksen, A., Nielsen, M., de Bruijne, M.: Weight preserving image registration for monitoring disease progression in lung CT. In: MICCAI, vol. 5242, pp. 863–870 (2008)
43. Guerrero, T., Sanders, K., Castillo, E., Zhang, Y., Bidaut, L., Pan, T., Komaki, R.: Dynamic ventilation imaging from four-dimensional computed tomography. Phys. Med. Biol. **51**(4), 777–791 (2006)
44. Guerrero, T., Sanders, K., Noyola-Martinez, J., Castillo, E., Zhang, Y., Tapia, R., Guerra, R., Borghero, Y., Komaki, R.: Quantification of regional ventilation from treatment planning CT. Int. J. Radiat. Oncol. Biol. Phys. **62**(3), 630–634 (2005)
45. Guo, J., Fuld, M.K., Alford, S.K., Reinhardt, J.M., Hoffman, E.A.: Pulmonary analysis software suite 9.0: Integrating quantitative measures of function with structural analyses. In: First International Workshop on Pulmonary Image Analysis, pp. 283–292, New York (2008)
46. Hajnal, J.V.: Medical Image Registration (Biomedical Engineering), 1st edn. CRC Press, Cambridge (2001)
47. Han, X.: Feature-constrained nonlinear registration of lung CT images. In: Grand Challenges in Medical Image Analysis (2010)
48. Hermosillo, G., Chefd'Hotel, C., Faugeras, O.: Variational methods for multimodal image matching. Int. J. Comput. Vision **50**, 329–343 (2002)
49. Hoffman, E.A., Ritman, E.L.: Effect of body orientation on regional lung expansion in dog and sloth. J. Appl. Physiol. **59**(2), 481–491 (1985)
50. Holden, M., Hill, D., Denton, E., Jarosz, J., Cox, T., Rohlfing, T., Goodey, J., Hawkes, D.: Voxel similarity measures for 3-D serial MR brain image registration. IEEE Trans. Med. Imaging **19**, 94–102 (2000)
51. Horn, B.K., Schunck, B.G.: Determining Optical Flow. Artif. Intell. **17**, 185–203 (1981)

52. Hu, S., Hoffman, E.A., Reinhardt, J.M.: Automatic lung segmentation for accurate quantitation of volumetric X-ray CT images. IEEE Trans. Med. Imaging **20**, 490–498 (2001)
53. Hubmayr, R.D., Rodarte, J.R., Walters, B.J., Tonelli, F.M.: Regional ventilation during spontaneous breathing and mechanical ventilation in dogs. J. Appl. Physiol. **63**(6), 2467–2475 (1987)
54. ICRU Report: Prescribing, recording and reporting photon beam therapy. ICRU, Bethesda, MD (1999). Supplement to ICRU report 50
55. Kabus, S., Lorenz, C.: Fast elastic image registration. In: Grand Challenges in Medical Image Analysis (2010)
56. Klein, S., Staring, M., Pluim, J.P.: Evaluation of optimization methods for nonrigid medical image registration using mutual information and B-splines. IEEE Trans. Image Process. **16**(12), 2879–2890 (2007)
57. Klinder, T., Lorenz, C., Ostermann, J.: Free-breathing intra- and intersubject respiratory motion capturing, modeling, and prediction. In: SPIE Medical Imaging 2009: Image Processing, vol. 7259 (2009)
58. Knowlton, R.: Clinical applications of image registration, Handbook of Medical Imaging, pp. 613–621. Academic Press, Orlando (2000)
59. Lester, H., Arridge, S.: A survey of hierarchical non-linear medical image registration. Med. Image Anal. **32**(1), 129–149 (1999)
60. Maintz, J., Viergever, M.: A survey of medical image registration. Med. Image Anal. **2**(1), 1–36 (1998)
61. Mattes, D., Haynor, D., Vesselle, H., Lewellen, T., Eubank, W.: PET-CT image registration in the chest using free-form deformations. IEEE Trans. Med. Imaging **22**(1), 120–128 (2003)
62. Metz, C., Klein, S., Schaap, M., van Walsum, T., Niessen, W.: Nonrigid registration of dynamic medical imaging data using nD + tB-splines and a groupwise optimization approach. Med. Image Anal. **15**(2), 238–249 (2011)
63. Miller, M.I., Banerjee, A., Christensen, G.E., Joshi, S.C., Khaneja, N., Grenander, U., Matejic, L.: Statistical methods in computational anatomy. Stat. Methods Med. Res. **6**, 267–299 (1997)
64. Modat, M., McClelland, J., Ourselin, S.: Lung registration using the Niftyreg package. In: Grand Challenges in Medical Image Analysis (2010)
65. Muenzing, S.E.A., van Ginneken, B., Pluim, J.P.W.: Knowledge driven regularization of the deformation field for PDE based non-rigid registration algorithms. In: Grand Challenges in Medical Image Analysis (2010)
66. Murphy, K., van Ginneken, B., Reinhardt, J.M., et al.: Evaluation of registration methods on thoracic CT: the EMPIRE10 challenge. IEEE Trans. Med. Imaging **30**(11), 1901–1920 (2011)
67. Murphy, K., van Ginneken, B., Pluim, J., Klein, S., Staring, M.: Semi-automatic reference standard construction for quantitative evaluation of lung CT registration. In: MICCAI, vol. 5242, pp. 1006–1013 (2008)
68. Nocedal, J.: Updating quasi-Newton matrices with limited storage. Math. Comput. **35**(151), 773–782 (1980)
69. Nocedal, J., Wright, S.J. (eds.): Numerical Optimization. Springer, New York (1999)
70. Ourselin, S., Roche, A., Subsol, G., Pennec, X., Ayache, N.: Reconstructing a 3D Structure from Serial Histological Sections. Image Vision Comput. **19**(1–2), 25–31 (2000)
71. Pace, D., Enquobahrie, A., Yang, H., Aylward, S., Niethammer, M.: Deformable image registration of sliding organs using anisotropic diffusive regularization. In: IEEE International Symposium on Biomedical Imaging: From Nano to Macro, 2011, pp. 407–413 (2011)
72. Penney, G., Weese, J., Little, J., Desmedt, P., Hill, D., Hawkes, D.: A comparison of similarity measures for use in 2-d-3-d medical image registration. IEEE Trans. Med. Imaging **17**, 586–595 (1998)
73. Press, W.H., Teukolsky, S.A., Vetterling, W.T., Flannery, B.P.: Numerical recipes in C: the art of scientific computing, 2nd edn. Cambridge University Press, New York (1992)
74. Reinhardt, J.M., Ding, K., Cao, K., Christensen, G.E., Hoffman, E.A., Bodas, S.V.: Registration-based estimates of local lung tissue expansion compared to xenon-CT measures of specific ventilation. Med. Image Anal. **12**(6), 752–763 (2008)

75. Reinhardt, J.M., Ding, K., Cao, K., Christensen, G.E., Hoffman, E.A., Bodas, S.V.: Registration-based estimates of local lung tissue expansion compared to xenon CT measures of specific ventilation. Med. Image Anal. **12**(6), 752–763 (2008)
76. Rikxoort, E.M., Prokop, M., Hoop, B., Viergever, M.A., Pluim, J.P., Ginneken, B.: Automatic segmentation of the pulmonary lobes from fissures, airways, and lung borders: evaluation of robustness against missing data. In: Proceedings of the 12th International Conference on Medical Image Computing and Computer-Assisted Intervention: Part I, MICCAI '09, pp. 263–271. Springer, Berlin (2009)
77. Rodarte, J.R., Hubmayr, R.D., Stamenovic, D., Walters, B.J.: Regional lung strain in dogs during deflation from total lung capacity. J. Appl. Physiol. **58**(1), 164–172 (1985)
78. Ruan, D., Esedoglu, S., Fessler, J.: Discriminative sliding preserving regularization in medical image registration. In: IEEE International Symposium on Biomedical Imaging: From Nano to Macro, 2009. ISBI '09, pp. 430–433 (2009)
79. Rueckert, D., Sonoda, L., Hayes, C., Hill, D., Leach, M., Hawkes, D.: Nonrigid registration using free-form deformations: application to breast MR images. IEEE Trans. Med. Imaging **18**(8), 712–721 (1999)
80. Ruhaak, J., Heldmann, S.: Variational lung registration with explicit boundary alignment. In: Grand Challenges in Medical Image Analysis (2010)
81. Sarrut, D., Boldea, V., Miguet, S., Ginestet, C.: Simulation of four-dimensional CT images from deformable registration between inhale and exhale breath-hold CT scans. Med. Phys. **33**(3), 605–617 (2006)
82. Schmidt-Richberg, A., Ehrhardt, J., Werner, R., Handels, H.: Diffeomorphic diffusion registration of lung CT images. In: Grand Challenges in Medical Image Analysis (2010)
83. Schmidt-Richberg, A., Werner, R., Handels, H., Ehrhardt, J.: Estimation of slipping organ motion by registration with direction-dependent regularization. Med. Image Anal. **16**(1), 150–159 (2012)
84. Simon, B.: Non-invasive imaging of regional lung function using X-ray computed tomography. J. Clin. Monit. Comput. **16**(5–6), 433–442 (2000)
85. Simon, B.A., Marcucci, C.: Parameter estimation and confidence intervals for Xe-CT ventilation studies: a Monte Carlo approach. JAP **84**(2), 709–716 (1998)
86. Song, G., Tustison, N., Avants, B., Gee, J.C.: Lung ct image registration using diffeomorphic transformation models. In: Grand Challenges in Medical Image Analysis (2010)
87. Staring, M., Klein, S., Reiber, J.H.C., Niessen, W.J., Stoel, B.C.: Pulmonary image registration with elastix using a standard intensity-based algorithm. In: Grand Challenges in Medical Image Analysis (2010)
88. Sundaram, T.A., Gee, J.C.: Towards a model of lung biomechanics: pulmonary kinematics via registration of serial lung images. Med. Image Anal. **9**(6), 524–537 (2005)
89. Sundaram, T.A., Gee, J.C.: Quantitative comparison of registration-based lung motion estimates from whole-lung mr images and corresponding two-dimensional slices. In: Proceedings of ISMRM 15th Meeting, p. 3039 (2007)
90. Szeliski, R., Coughlan, J.: Spline-based image registration. Int. J. Comput. Vision **22**(3), 199–218 (1997)
91. Thevenaz, P., Unser, M.: Spline pyramids for inter-modal image registration using mutual information. In. Proc. SPIE **3169**, 236–247 (1997)
92. Ukil, S., Reinhardt, J.M.: Anatomy-guided lung lobar surface detection in X-ray CT images. IEEE Trans. Med. Imaging **28**(2), 202–214 (2009)
93. Vandemeulebroucke, J., Rit, S., Kybic, J., Clarysse, P., Sarrut, D.: Spatiotemporal motion estimation for respiratory-correlated imaging of the lungs. Med. Phys. **38**(1), 166–178 (2011)
94. Viola, P., III, Wells, M.W.: Alignment by maximization of mutual information. Int. J. Comput. Vision **24**(2), 137–154 (1997)
95. Wang, H., Garden, A.S., Zhang, L., Wei, X., Ahamad, A., Kuban, D.A., Komaki, R., O'Daniel, J., Zhang, Y., Mohan, R., Dong, L.: Performance evaluation of automatic anatomy segmentation algorithm on repeat or four-dimensional computed tomography images using deformable image registration method. Int. J. Radiat. Oncol. Biol. Phys. **72**(1), 210–219 (2008)

96. Werner, R., Ehrhardt, J., Schmidt, R., Handels, H.: Patient-specific finite element modeling of respiratory lung motion using 4D CT image data. Med. Phys. **36**(5), 1500–1511 (2009)
97. West, J.B., Matthews, F.L.: Stress, strain, and surface pressures in the lung caused by its weight. J. Appl. Physiol. **32**(3), 332–345 (1972)
98. Wikipedia: Histogram matching. Hypertext Document. http://en.wikipedia.org/wiki/Histogram_matching
99. Wu, G., Wang, Q., Lian, J., Shen, D.: Estimating the 4d respiratory lung motion by spatiotemporal registration and building super-resolution image. In: Proceedings of the 14th International Conference on Medical Image Computing and Computer-Assisted Intervention—vol. Part I, MICCAI'11, pp. 532–539 (2011)
100. Yang, D., Brame, S., Naqa, I.E., Aditya, A., Wu, Y., Goddu, S.M., Mutic, S., Deasy, J.O., Low, D.A.: Technical note: DIRART—a software suite for deformable image registration and adaptive radiotherapy research. Med. Phys. **38**(1), 67–77 (2011)
101. Yin, Y., Hoffman, E.A., Lin, C.L.: Local tissue-weight-based nonrigid registration of lung images with application to regional ventilation. In: Hu, X.P., Clough, A.V. (eds.) SPIE Medical Imaging 2009: Biomedical Applications in Molecular, Structural, and Functional Imaging, vol. 7262, p. 72620C, Lake Buena Vista, FL (2009)
102. Yin, Y., Hoffman, E.A., Lin, C.L.: Mass preserving non-rigid registration of CT lung images using cubic B-spline. Med. Phys. **36**(9), 4213–4222 (2009)
103. Younes, L., Arrate, F., Miller, M.I.: Evolutions equations in computational anatomy. NeuroImage **45**(1 Suppl), S40–S50 (2009)
104. Zhu, C., Byrd, R.H., Lu, P., Nocedal, J.: Algorithm 778: L-BFGS-B: Fortran subroutines for large-scale bound-constrained optimization. ACM Trans. Math. Softw. **23**(4), 550–560 (1997)

Chapter 8
Validation and Comparison of Approaches to Respiratory Motion Estimation

Sven Kabus, Tobias Klinder, Keelin Murphy, René Werner and David Sarrut

Abstract The accuracy of respiratory motion estimation has a direct impact on the success of clinical applications such as diagnosis, as well as planning, delivery, and assessment of therapy for lung or other thoracic diseases. While rigid registration is well suited to validation and has reached a mature state in clinical applications, for non-rigid registration no gold-standard exists. This chapter investigates the validation of non-rigid registration accuracy with a focus on lung motion. The central questions addressed in this chapter are (1) how to measure registration accuracy, (2) how to generate ground-truth for validation, and (3) how to interpret accuracy assessment results.

8.1 Lack of a Gold-Standard in Non-Rigid Image Registration

Respiratory motion estimation is a topic receiving much attention in medical imaging. For clinical applications such as diagnosis as well as better planning, delivery, and assessment of therapy for lung or liver diseases, estimation of and compensation for motion is indispensable and its accuracy has direct impact on the success of the clinical applications.

S. Kabus (✉) · T. Klinder
Philips Research Laboratories, Hamburg, Germany
e-mail: sven.kabus@philips.com

K. Murphy
Image Sciences Institute, University Medical Center Utrecht, Utrecht, The Netherlands

R. Werner
University Medical Center Hamburg-Eppendorf, Hamburg, Germany

D. Sarrut
Université de Lyon, CREATIS, CNRS UMR5220, Inserm U1044, INSA-Lyon, Université Lyon 1, Centre Léon Bérard, Lyon, France

J. Ehrhardt and C. Lorenz (eds.), *4D Modeling and Estimation of Respiratory Motion for Radiation Therapy*, Biological and Medical Physics, Biomedical Engineering,
DOI: 10.1007/978-3-642-36441-9_8,

As detailed in the previous chapters of this book, respiratory motion estimation and compensation require non-rigid registration of CT thorax data typically acquired in a dynamic protocol as for respiratory-gated 4D scans. In each case, a voxel-wise computation of respiratory motion between different respiratory states is needed. However, while rigid registration is well suited for validation [1] and has come to a mature state in clinical applications, for non-rigid registration no gold-standard exists. Moreover, a discrepancy between the maturity of non-rigid registration in the image processing community and its dissemination in clinical workstations can be observed, indicating a lack of acceptance of the technique that can only be overcome by establishing commonly accepted validation metrics and procedures. This chapter therefore investigates current approaches for the validation of non-rigid registration when applied to motion estimation, focusing particularly on lung motion.

A necessary criterion for a successful registration is the alignment of visible image structures, often converted into an inspection of the residuum (i.e., the subtraction of the aligned data) where mis-aligned image structures show up. However, the absence of any structure in the residuum image does not guarantee that the non-rigid registration was successful, since the residuum is invariant to the deformation of image regions with homogeneous intensities. Even for image regions containing structures such as lung vessels an increased similarity of the aligned data (determined by a correlation coefficient for example) does not always imply an increased registration accuracy [2]. Furthermore, a registration scheme allowing for a very flexible alignment tends to result in an almost perfect residuum but suffers from implausible deformations and consequently from decreased accuracy. Additional evaluation criteria are therefore indispensable.

The most obvious method is probably to identify corresponding positions of anatomical structures in the images to be compared. For example, in lung data such features are usually anatomical points located on lung structures with adequate image contrast like vessel bifurcations, fissures and pleura, or the boundary of a potential tumor. To provide additional information, point positions can also be extended to line structures such as the centerlines of the bronchial tree defined at different respiratory states, and surface structures and volumes define objects like the lung fissures or target regions (e.g. masses) and organs at risk in radiotherapy. In each case, after applying the registration result, a *validation metric* such as a landmark-based registration error, or a line or surface alignment error is computed to measure registration accuracy quantitatively.

The validation metrics described so far focus on *morphological* structures but not on the physical and physiological plausibility of the entire deformation. A physically implausible result such as local folding in the deformation can be detected by analysis of the local volume change [3] as a simple example for *functional* validation. Another validation metric based on the entire deformation vector field measures the sensitivity of the registration result to the order of the input data (consistency metric). For a clinical application, the computed structural correspondence is certainly expected to be the same when aligning a follow-up scan with a baseline scan or vice versa (i.e., a consistent mapping). Moving from conventional diagnostic CT data to respiratory-gated CT data (4D-CT), anatomical positions can be tracked over (respiratory) time

leading to motion trajectories. Since 4D-CT data usually suffer from lower spatial resolution and higher noise levels due to reduced radiation dose, and, in addition, often contain motion-induced artifacts [4] due to irregular patient breathing during image acquisition, the use of motion trajectories in combination with a breathing model for validation is beneficial.

A reliable ground-truth is essential to make use of any type of validation metric. However, there are many different types of ground-truth. Whereas morphological validation metrics such as landmark-, centerline- and overlap-based metrics require corresponding lists of annotated voxel positions, functional validation metrics rest upon underlying models, e.g. a certain breathing model for trajectory analysis or the positive Jacobian map as minimum requirement for a physiologically plausible tissue deformation. While in the past published validation studies [3, 5–7] have often been based on a limited number of registration algorithms and/or on proprietary datasets (typically with different imaging parameters such as dose or voxel resolution) there is an increasing trend towards multi-institutional validation studies. Recently, there have been two examples in the field of respiratory motion estimation. The Multi-Institutional Deformable Registration Accuracy Study (MIDRAS) [8] was motivated by the use of registration schemes for improved radiation therapy planning and therefore selected CT and MRI data showing the lungs, the liver and the prostate, while the Evaluation of Methods for Pulmonary Image REgistration 2010 (EMPIRE10) challenge [9], organized in conjunction with the Grand Challenge workshop[1] at MICCAI 2010, provided a public platform for comparison of registration algorithms applied to thoracic CT data. Based on the selected datasets, the participants calculated deformation vector fields and submitted them to the organizational teams for independent evaluation. Evaluation was, dependent on the study, performed considering anatomical landmarks, lung boundary alignment, fissure alignment, and the presence of deformation field singularities. Furthermore, the DIR-lab of the University of Texas M. D. Anderson Cancer Center[2] and the Léon Bérard Cancer Center together with the CREATIS-LRMN CNRS Research lab (POPI-model)[3] provide a series of freely available 4D-CT and exhale-inhale CT image data along with landmark lists for the validation and comparison of non-linear registration algorithms [2, 10].

Common to these studies and databases is the potentially exhausting task of generating ground-truth. The manual selection of landmarks, for example, is time-consuming and landmark locations are prone to uncertainties due to intra- and inter-observer variability and approaches for (semi-)automation are therefore desirable; finally, an interpretation of validation metric results also needs to be addressed since each validation metric poses only a single necessary condition.

Taking into account the above mentioned two principal types of validation metrics, their ability to identify characteristics of individual registration schemes and the issues of ground-truth generation, this chapter is divided into the description of

[1] http://www.grand-challenge.org/index.php/MICCAI_2010_Workshop

[2] http://www.dir-lab.com

[3] http://www.creatis.insa-lyon.fr/rio/popi-model

morphological validation criteria and of functional validation criteria. Each section then discusses the specific validation criterion in detail, including metric definitions, available ground-truth and the interpretation of corresponding results.

8.2 Morphological Validation Criteria

Morphological validation is currently the state-of-the-art in estimating the accuracy of registration results. Validation metrics defined in zero-dimensional space (e.g. landmarks) or higher spaces (e.g. tree structures or tumor surfaces) are frequently used and well understood. This section describes the validation metrics and the considered anatomical structures in the order of their dimensionality. Each subsection then describes how registration accuracy can be measured, what possibilities exist to generate ground-truth, and how to interpret the results when comparing multiple registration schemes.

8.2.1 Landmarks

8.2.1.1 Validation Metrics

Landmarks are usually understood as being characteristic anatomical points, which can therefore be considered as being zero-dimensional features and leading to validation metrics defined in zero-dimensional space, respectively. Typical landmark candidates are, as described in Sect. 8.1, salient bifurcations of the bronchial tree (lungs), specific branches of vessel trees (lungs, liver), or calcified nodules [5, 8, 11, 12], cf. Fig. 8.1.

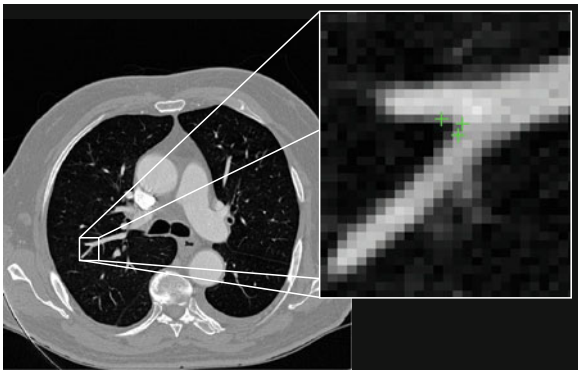

Fig. 8.1 Example of a landmark in a lung CT data set, selected by three medical experts. It can be seen that manual landmark selection and subsequent quantitative registration evaluation suffers from interobserver variability of landmark identification

For evaluation purposes, a (usually relatively sparse) set of landmarks is identified within each of the images A and B to register. For a single landmark $\boldsymbol{x}_A$ within the discrete domain of image A, Ω_A, and a spatial transformation $\boldsymbol{T}$ mapping Ω_A onto Ω_B, the standard validation metric is the Euclidean distance between the mapped landmark position $\boldsymbol{x}_B^{[pred]} = \boldsymbol{T}(\boldsymbol{x}_A)$ after registration and the position $\boldsymbol{x}_B^{[actual]}$ in Ω_B that is anatomically corresponding to landmark $\boldsymbol{x}_A$. In literature, this metric

$$\mathrm{TRE}(\boldsymbol{x}_A) = \left\| \boldsymbol{x}_B^{[pred]} - \boldsymbol{x}_B^{[actual]} \right\|_2 \tag{8.1}$$

is also often referred to as landmark-based, point, or target registration error [2, 13], and to summarize the error distribution for a set of landmarks, the mean error, the standard deviation, the maximum error and/or error quantiles are commonly considered.

Whilst landmark-based registration errors as defined above represent (in the sense of a metric) absolute, non-negative error values, over- or underestimation of respiratory motion along a certain direction can also be identified using landmark sets. Therefore let the direction of interest being represented by a unit vector $\boldsymbol{e_a}$ along a vector $\boldsymbol{a}$; then, directional errors and over/underestimation can be deduced from the projections of the misalignments $\left(\boldsymbol{x}_B^{[pred]} - \boldsymbol{x}_B^{[actual]}\right)$ onto $\boldsymbol{e}_a$.

8.2.1.2 Ground-Truth Generation

Ground-truth for evaluating the landmark-based registration error is commonly generated by annotating corresponding landmarks within the images to register manually and is usually carried out by 'medical experts' (radiologists, medical students, etc.). The manual selection of such points is, however, time-consuming and landmark locations are prone to uncertainties due to intra- and interobserver variability concerning exact point selection [5, 12] (cf. Fig. 8.1), for instance caused by low image resolution or partial volume effects. In the case of lung CT registration, landmark identification additionally suffers from low contrast in near-to-pleura regions, which often leads to very limited landmark sets grouped around the mediastinum [3]. To serve as reliable ground-truth, the landmarks should preferably consist of a well-distributed set of verifiable anatomical correspondences throughout the image region of interest (e.g. the lungs) and be large enough in number to enable meaningful statistical analysis. The required number of landmarks can be assessed by a posteriori statistical sample size calculation [2]. The number may vary for individual data sets and motion estimation approaches, but it has been reported to be even more than 1000 anatomical point pairs [2] and so efforts have been made to (partially) automate identification of landmark sets.

One such algorithm is described in [11, 14], here serving as an example. The algorithm starts with automatic detection of landmarks in an image A. A so-called distinctiveness term is defined to quantify the distinctiveness of a voxel within its local neighborhood. The distinctiveness term combines both differential properties

(gradient magnitude) and intensity characteristics to quantify the suitability of the voxel as a landmark candidate. Good distribution throughout the region of interest is ensured by forcing a minimum Euclidean distance between the landmark candidates. In a second step, the interactive landmark transfer to the image B to be aligned with image A by registration is supported by computing and progressively refining a thin-plate-splines transformation based on user-annotated landmark correspondences. After manually transferring an adequate number of landmarks, the transformation can be applied to guide the user to find correspondences for the remaining landmarks or even be used to transfer the landmarks fully automatically.

The algorithm has recently been applied for a number of registration evaluation studies [3, 9, 15], but it is only one example for construction of a landmark-based ground-truth. For instance, reviving earlier works on landmark detection [16] it has been suggested to incorporate curvature-based operators for distinctiveness calculation [17] or to consider Shannon entropy instead [18]. Furthermore, template matching methods have been applied for landmark transfer in order to fully automate the evaluation process [17, 19]; however, especially automating the landmark transfer can be controversial [2]. The transfer represents, by definition, a (point-based) registration problem. Thus, a (semi-)automatic landmark transfer may lead to biased evaluation if the registration method to evaluate and the landmark transfer methods are similar in some sense (for example if they maximize the same similarity measure).

8.2.1.3 Validation in Practice

The usage of landmarks is the most popular method of validation of non-linear registration. As well as the validation studies mentioned above and the described publicly accessible 4D-CT databases, numerous research articles have used anatomical landmark sets denoted by experts.

However, the actual size of the landmark sets varies from small numbers of about 20 landmark positions to large sets of 1500 positions, cf., e.g. [2, 20]. Naturally, the larger the number of landmarks, the better the estimation of accuracy is likely to be (cf. requirements for ground-truth generation described above). For a simple illustration beyond pure statistical computations, consider a lung with a volume of 4 l together with a set of 20 landmark positions. In this example, each cube of lung parenchyma with edge length 58 mm contains one landmark on average. Increasing the set of landmarks to 100 or even to 1500, the edge length of this cube reduces to 34 mm and 14 mm, respectively. A landmark spacing of a size of 14 mm undoubtedly allows for registration accuracy estimation on a coarse scale but not on a finer scale when taking into account the distinctive inhomogeneity of lung parenchyma.

Another critical point is the requirement of the landmarks to represent a well-distributed set over the structure/region of interest. If landmarks are placed on the bifurcations of major blood vessels as shown exemplarily in Fig. 8.2, left, they are concentrated around the mediastinum which has a number of disadvantages: (1) this type of ground-truth does not allow for accurate estimation in regions near to the pleura or diaphragm where registration accuracy is typically worse; (2) the stiffness

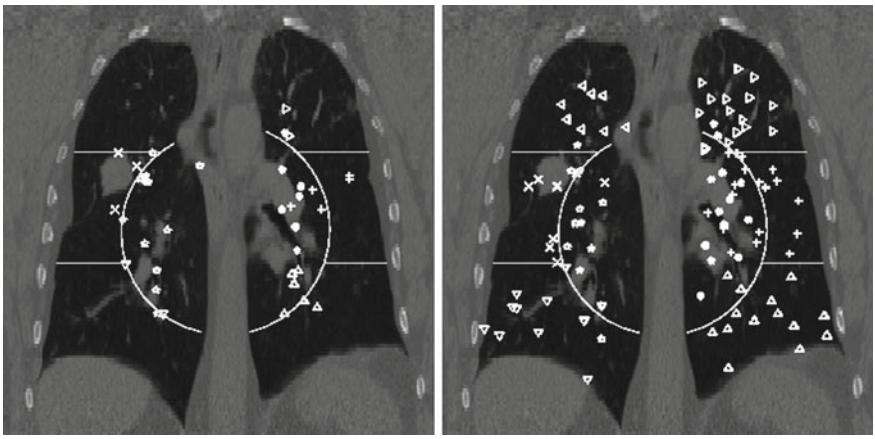

Fig. 8.2 Region definition and landmark positions shown in a coronal projection for a landmark set as commonly used in the literature (*left*) and for a well-dispersed landmark set (*right*). For improved visualization each region is given a unique landmark symbol

of the lungs is highest in the surroundings of the major bronchial tree—reducing the local motion and meaning that the registration task is most difficult elsewhere; (3) major bifurcations are clearly visible to a human observer but also to the majority of registration schemes—unlike the hardly detectable low-contrast structures near to the pleura. The importance of the requirement of a good distribution of the landmarks in the region of interest is demonstrated in [3]. The authors compared landmark-based registration error as obtained for two landmark sets, one set as commonly used in the literature (cf. POPI-model), the other set well-distributed throughout the lung volume (shown in Fig. 8.2). A collection of six popular methods including surface- and volume-based as well as parametric and non-parametric methods was investigated. From each of these algorithms, a deformation vector field was extracted and used to transform the landmarks from both sets. While the mean landmark-based registration error on both landmark sets differs only slightly, a region-based analysis reveals smaller errors in apical regions but also a significantly higher error in the lower right lung (Fig. 8.3) and therefore a dependency of the landmark-based registration error on the distribution of landmarks. This dependency is observed for each of the six registration schemes.

Conclusion: Landmarks are a popular and intuitive method of registration validation. Both a large number of corresponding positions and a good distribution of the points throughout the organ of interest are crucial for reliable registration accuracy assessment. However, landmarks estimate registration accuracy only at selected locations and additional validation metrics are beneficial to provide deeper insight.

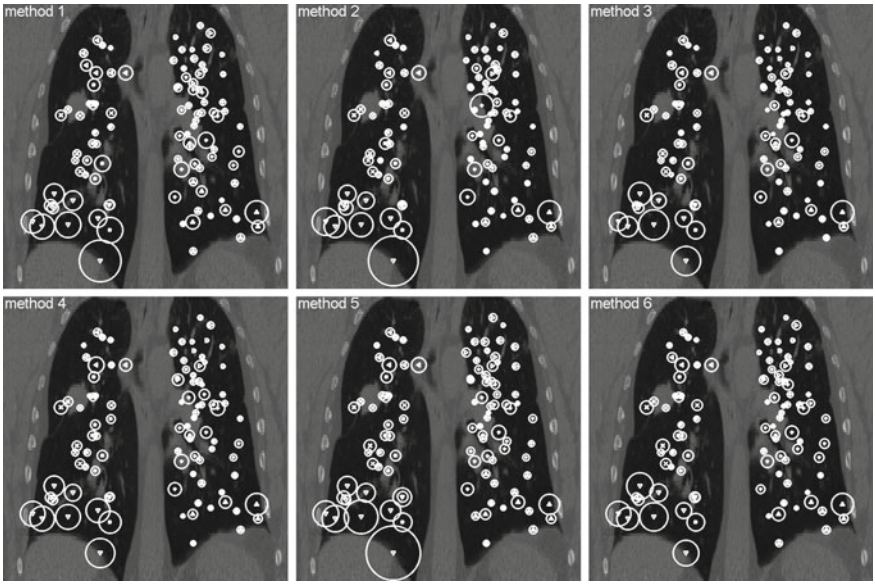

Fig. 8.3 Landmark-based registration error, shown proportional to the spheres' diameters after registration by six different algorithms. Note the different errors in apical regions and lower right lung indicating the need for a well-dispersed set of landmarks

8.2.2 Line-Like Anatomical Structures

8.2.2.1 Validation Metrics

Landmarks focus on prominent points which are in most cases bifurcations of airways or the vessel tree. In order to extend the evaluation, validation metrics for line-like anatomical structures analyze he registration accuracy not only at discrete positions, but take the properties of the structure (e.g. vessel or airway) into account. For example, significant changes in curvature, folding along a branch, or implausible changes in branch length are interesting properties that can not be captured by landmarks. In the following, it is assumed that for both images a segmentation of the airways and/or vessels is given. Furthermore, the individual branches are labelled, so that for each branch in one image, the corresponding part in the other image is known. From the segmentation, a centerline representation can be derived and the branching points can be extracted.

Now, consider a given set of centerline points defined between two branch points of consecutive branching generations. An adequate interpolation scheme can be chosen to represent the point set as a continuous curve with a parametrization as a function $\alpha(t)$ with $t \in [0, 1]$. The corresponding curve described by a function β can be derived in the other image as well. Having two continuous corresponding line segments allows the definition of a variety of distance measures.

As an example, the registration accuracy along the centerline can be evaluated as the difference between corresponding points that have the same value of the parametrization constant as

$$D_1^i(t) = ||T(\boldsymbol{c}_{\alpha(t)}^{i,A}) - \boldsymbol{c}_{\beta(t)}^{i,B}||_2\,, \tag{8.2}$$

where i defines the branch index and $T(\boldsymbol{c}_{\alpha(t)}^{i,A})$ is the transformed centerline belonging to the ith branch defined in image A. Note that this measure is sensitive to a change in the length of the centerline. As the structures considered in the lungs can be assumed to preserve their absolute length during respiration, this sensitivity might be desirable.

Alternatively, it is also possible to evaluate the distance by finding the closest point on the corresponding other centerline as

$$D_2^i(t_A) = \min_{t_B \in [0,1]} ||T(\boldsymbol{c}_{\alpha(t_A)}^{i,A}) - \boldsymbol{c}_{\beta(t_B)}^{i,B}||_2\,. \tag{8.3}$$

Based on the centerline representation, other measures can be evaluated that consider line properties of the transformed centerline, for example local curvature, to detect implausible deformations. However, so far metrics for line-like structures have rarely been applied, mainly because segmentation and labelling of the considered structures is difficult to achieve.

8.2.2.2 Ground-Truth Generation

Examples that can be considered for line-like structures are airways and vessels. In each case the ground-truth generation relies on a segmentation and a labelling. However, manual segmentation and labelling is very time-consuming and from a practical point of view not always possible. Although a variety of automatic segmentation algorithms exists, failure especially in the case of pathologies or low image resolution, which is the case in 4D-CT, is likely to occur. A reliable ground-truth may be most efficiently obtained by applying an automatic segmentation first which is then inspected and manually corrected.

Both airways and blood vessels form dense tubular structures, but typically differ in appearance in a CT image. Thus, most approaches that take into account the tubular characteristic of the structure to be segmented can be often applied for both airways and vessels by simply changing the appearance parameters.

Many existing algorithms for airway and vessel segmentation are based on region growing [21]. However, in areas where the contrast is low, for example due to resolution and noise, leakage is observed. One possibility to circumvent this problem is by means of explosion control, for example by introducing certain rules derived from anatomical knowledge [22], or using template tracking based methods [23, 24]. For a recent overview on vessel segmentation techniques see [25] as well as algorithms

described within challenges on vessel segmentation in the lung (VESSEL12)[4] and on airway extraction (EXACT09, [26]).[5]

For matching of both airways and vessels, different approaches have been proposed [27, 28]. However, as the methods have been used on different data sets, it is not clear which is currently the method of choice.

8.2.2.3 Validation in Practice

Validation based on labelled airways or vessels as introduced in Sect. 8.2.2.1 has, to our knowledge, not been published so far. While a considerable amount of work has been done on automatic segmentation as well as on matching of both airways and vessels, little of this information has been used for registration evaluation. This might be due to the fact that even with the help of automatic segmentation algorithms, generating a reliable ground-truth would require the verification of the obtained segmentations which is still very difficult and time-consuming. Furthermore, automatic extraction of both airways and vessels is still difficult on 4D-CT with low resolution and severe pathologies.

Conclusion: Compared to the use of landmarks that evaluate the registration accuracy at distinct locations, metrics described here can be used to measure the registration accuracy along a line-like structure. These measures have the potential to provide additional valuable insight into the registration, for example by detecting folding of a branch or change in branch length, etc. Nevertheless, measurements based on line-like structures have not been used so far because of the difficulties of obtaining a reliable ground-truth.

8.2.3 Surface Structures and Volumes

8.2.3.1 Validation Metrics

Estimating the registration accuracy for anatomical structures like the lungs, the lobes and the fissures leads to validation metrics for surface structures and volumes. The segmentations of a corresponding anatomical surface area or volume in two images A and B are denoted as voxel sets S_A and S_B, respectively, with the transformed voxel set denoted as $\tilde{S}_A$ (cf. Fig. 8.4).

One common measure for evaluation of the registration accuracy using surface structures such as the outer lung boundaries or the fissures is the average surface distance. For each voxel $\boldsymbol{x}_B$ contained in S_B, the closest voxel $\boldsymbol{x}_A$ in $\tilde{S}_A$ is determined and the Euclidean distance between them is calculated as

[4] http://vessel12.grand-challenge.org

[5] http://image.diku.dk/exact

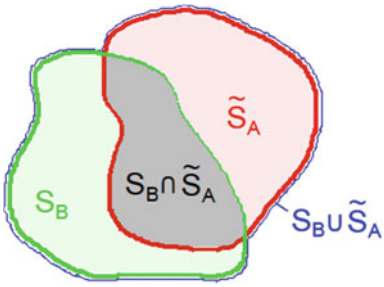

Fig. 8.4 Illustration of union and intersection between two volumes

$$d(\boldsymbol{x}_B, \tilde{S}_A) = \min_{\boldsymbol{x}_A \in \tilde{S}_A} \|\boldsymbol{x}_B - \boldsymbol{x}_A\|_2 \,. \tag{8.4}$$

To ensure symmetry, the error $d(\boldsymbol{x}_A, S_B)$ at each voxel in $\tilde{S}_A$ is also calculated and finally the average overall error is computed.

For the calculation of the volumetric overlap between two voxel sets several methods exist [29–32] where the most frequently used are

- *Dice coefficient* (DC) [33] which is also called volume overlap index [34]

$$\mathrm{DC} = \frac{2(|S_B \cap \tilde{S}_A|)}{|S_B| + |\tilde{S}_A|} \,, \tag{8.5}$$

- *Jaccard coefficient* (JC) or *volumetric overlap* (VO) [35]

$$\mathrm{JC} = \mathrm{VO} = \frac{|S_B \cap \tilde{S}_A|}{|S_B \cup \tilde{S}_A|} \,, \tag{8.6}$$

  which can also be alternatively calculated as [36]

$$\mathrm{JC} = \frac{|S_B| + |\tilde{S}_A|}{|S_B \cup \tilde{S}_A|} - 1 \,, \tag{8.7}$$

- *target overlap* (TO)

$$\mathrm{TO} = \frac{|S_B \cap \tilde{S}_A|}{|S_B|} \,. \tag{8.8}$$

8.2.3.2 Ground-Truth Generation

Ground-truth generation for surface structures and volumes requires the segmentation of the respective objects of interest. For the purpose of evaluation of lung motion estimation, the most relevant structures are (i) lungs, (ii) lung lobes and fissures

and (iii) potential tumors. Manual segmentation of those structures is usually very time-consuming. Thus, ground-truth generation that results from semi-automatic or automatic segmentation algorithms which are inspected and manually corrected is much more feasible from a practical point of view.

For the segmentation of the lungs, automatic approaches have been presented ranging from voxel-based segmentation methods [37] to multi-atlas registration [38]. Voxel-based methods are based on the assumption that, for normal lung parenchyma, there is a large difference in attenuation between the lung parenchyma and the surrounding tissue. While those methods have low computational time, they fail especially in the case of pathological lungs or image artifacts. Other methods that involve prior knowledge give potentially better results on pathological cases but have a significant increase in runtime. Further algorithms are described within a challenge on lobe and lung analysis (LOLA11).[6]

Fissure segmentation has been recently described in [39, 40] and extensions have been presented to deal with incomplete fissures or cases where the fissures are hardly visible [41]. Interactive methods [42] allow for correction of a given automatic segmentation result or manual segmentation from scratch.

In the context of radiotherapy planning and treatment, evaluating the correctness of tumor motion estimation is of major importance. For ground-truth generation, a variety of methods for semi-automatic and automatic tumor segmentation exists including vessel removal and pleural surface removal [43].

8.2.3.3 Validation in Practice

Volumetric overlap measures are well established and often applied to evaluate the results of an automatic segmentation [38]. However, especially in the case of large volumes, surface distance metrics are probably more relevant as there can still be quite large errors near the boundaries even though large parts of the volumes are overlapping.

For the registration methods from Fig. 8.3, a careful inspection of the pleura revealed good alignment with no significant inter-method variation. This observation is supported by the EMPIRE10 challenge [9] where 12 (26) out of 34 methods matched more than 99.99 % (99.9 %) of pleura-adjacent voxels correctly to either the interior or the exterior of the lung boundary.

Unlike the lung boundaries, the fissures are of much lower contrast in CT and thus more challenging to align in particular for larger motion amplitudes. In the EMPIRE10 challenge 2 (20) out of 34 methods matched more than 99.9 % (99 %) of fissure-adjacent voxels to the correct lung lobe. Registration of fissures is examplarily shown in Fig. 8.5. For visual inspection, the fissure of the left lung (marked by green plus signs) as extracted from the reference image (shown top left) is overlayed onto the transformed template images from three of the six registration methods under consideration. Although none of the methods employs dedicated knowledge about

[6] http://www.lola11.com

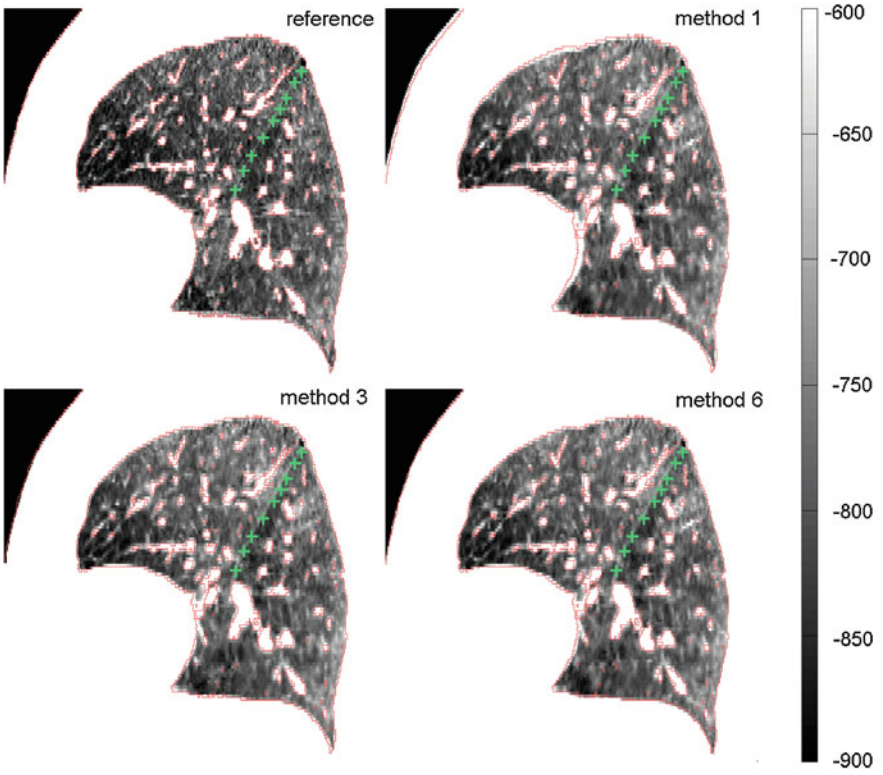

Fig. 8.5 Sagittal view of reference image (*top left*) and transformed template images after registration with different registration algorithms. *Green plus signs* and *red contours* indicate fissure and −650 HU iso-contour and are extracted from the reference image. Their overlay onto the transformed template images allow for visual inspection of fissure and vessel alignment

the fissures (e.g. by detecting them first), the fissures are roughly matched with a misalignment of only one to two voxels. Taking into account their low contrast, it can be assumed that matching of the fissures is assisted by high contrast surrounding vessel structures guiding the algorithm towards the desired deformation result (cf. Fig. 8.5 where the iso-contour is defined at −650 HU in the reference image and overlayed onto each transformed template image).

For both lung boundaries and fissures, it should be noted that surface-based metrics do not evaluate the motion in the tangential direction. At the lung boundary slipping occurs along the rib-lung interface, while sliding motion can also occur along the fissures which are built up of two tissue layers with lubricant fluid in-between. Evaluation of this sliding effect is not captured by the surface-based metrics.

While for both the lung boundary as well as the fissures, the individual methods seemed to have very similar performance results, inter-method differences exist that can be highlighted, for example, by comparing residual images. The residual image is

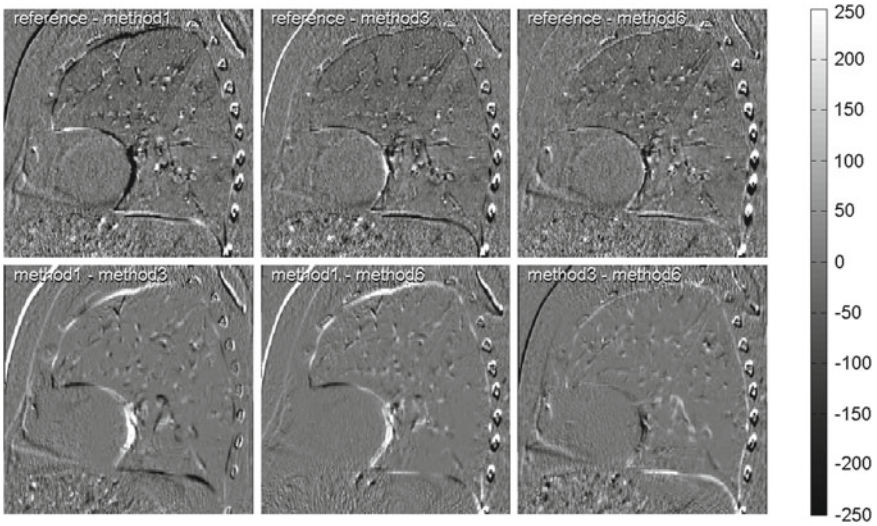

Fig. 8.6 Same view as in Fig. 8.5 but with residuals (*top row*) and subtraction of residuals (*bottom row*) depicted

defined as the subtraction of a transformed template image from the reference image (cf. Fig. 8.6, top row). Misaligned image structures show up whereas well-aligned structures cancel out after subtraction (given the same imaging protocol). It can therefore serve as a rough indicator of successful registration. Optimizing a registration result on the basis of the residual image will provide very little regularization of the deformation. Registration accuracy, however, does not necessarily improve with decreased regularization and is, moreover, often worsened since image noise starts to dominate the computed deformation.

Figure 8.6, bottom row, displays the residual images after subtraction from each other. These secondary residuals highlight image regions being differently deformed by the three registration methods under consideration. Moreover, secondary residuals are less impacted by differences in SNR or parenchymal densities between reference and template image since both the minuend and the subtrahend are interpolated from the template image. For the investigated case pleura and pleura-adjacent vessels are more similarly transformed by methods 3 and 6 than by 1 and 3 or 1 and 6. On the other hand, methods 1 and 6 better agree for vessel structures near to the fissure.

Conclusion: Both surface-based as well as volume-based metrics are well established methods to evaluate the overlap of two structures. While the methods can be used to provide a first indication of the quality of a registration method, detailed analysis of the transformation is limited. Most prominently, in the case of lung boundaries and fissures surfaces, sliding motion that occurs in tangential direction along the boundary is not captured by surface-based metrics. Furthermore, as surface-based metrics evaluate the overall overlap (lung volume overlap) or registration accuracy

at distinct structures (fissures), detailed information about particular regions or far away from the considered structures is difficult to derive as demonstrated in Fig. 8.6.

8.3 Functional Validation Criteria

In the previous section, a number of morphological validation criteria are described. Among these are anatomical landmarks measuring the correspondence of point positions and surface structures measuring the alignment of lung boundaries or lung fissures. All these criteria, however, focus on certain anatomical structures. As soon as the anatomy under investigation is aligned, from a morphological point of view it is irrelevant if and how other regions are transformed. Functional validation criteria can fill this gap by adding prior knowledge in terms of assumptions on the functional behaviour of the lung tissue.

The following subsection revisits landmarks but now considered in the context of (respiratory-gated) 4D datasets where they define a motion trajectory over time. Another class of validation metrics is based on the deformation vector field (DVF). Contrary to morphological validation criteria, ground-truth data does not exist for these metrics, thus careful interpretation of the results is required.

8.3.1 Trajectory Analysis

8.3.1.1 Validation Metrics

Landmark-based evaluation relies on a set of independent point positions, corresponding to anatomical features. When dealing with respiratory-gated 4D thoracic datasets, each point is expected to follow a cyclic trajectory and additional prior knowledge can be used on this trajectory. Such prior information is important for deriving robust and efficient algorithms but can serve also in the validation process.

The conventional approach for the registration of 4D-CT datasets is to compute a set of DVFs—either between a designated reference phase and all remaining phases or between any adjacent respiratory phases. An alternative is to register the designated reference phase with the entire 4D dataset (sometimes referred to as group-wise registration). This is equivalent to estimating motion trajectories of individual point positions and can be called spatio-temporal registration.

In this context, it can be interesting to generalize the landmark-based registration error to take into account the time spent at the main phases of a trajectory. For example, an error metric could take into account that more time is spent at the end-inspiration and end-expiration phases than between these extremes and therefore be designed to reflect the decreased likelihood for motion-induced image artifacts. In other words, estimation of errors at an intermediate phase of the cycle should have lower weight than errors at extreme phases. According to known prior 1D

breathing models, such as the one proposed by [44], locally defined material points move along their trajectories at variable speeds (determined by the derivative of the globally defined lung volume curve). One such metric is called spatio-temporal error (STE) [12] and is defined by

$$STE_{t_a,t_b}(L_1, L_2) = \frac{1}{t_b - t_a} \int_{t_a}^{t_b} ||L_1(s(t)) - L_2(s(t))||_2 \tag{8.9}$$

where L_1 and L_2 are two parametric trajectories (each of which defines the set of the different locations of a material point during its motion), $s(t)$ the normalized curvilinear abscissa of the trajectory according to a prior breathing model to take into account the relative breathing velocity. This abscissa is a function of time and denotes the curve length travelled between initial time t_a and time t. However, in practice, such methods have not been shown to be more effective or more robust than conventional landmark-based registration error in evaluating registration accuracy.

8.3.1.2 Validation in Practice

To our knowledge, few studies analyze respiratory motion estimation in terms of point trajectories. Sets of 4D landmark points sets were used to test the adequacy of some trajectory model. In [45] the authors proposed a 4D local trajectory model for thoracic 4D-CT, where trajectories were modeled with cubic polynomials through the expiratory phases (neither cyclic nor inspiratory phase was included). For the validation, experts were asked to select corresponding anatomical points in expiratory phases with the help of a dedicated GUI named Assisted Point Registration of Internal Landmarks (APRIL) [6].

In [46], projection sequences of cone-beam images were used to analyse craniocaudal positions of the diaphragm over time. A database of motion was obtained and used to assess the validity of several trajectory models. Validation of respiratory motion estimation on 4D-CT was then performed with sets of about 100 expert-selected corresponding points by temporal frame, using a semi-automatic software [11] (see Fig. 8.7 for an illustration of such trajectories). The mean distance between the experts' annotations was 0.5 mm (0.9 mm standard deviation).

In practice, two main issues are encountered. Firstly, the manual (even semi-automatic) definition of landmarks across the 4D dataset is very time-consuming. In addition, an alarmingly high number of acquisitions contain motion-induced artifacts, mainly due to irregular patient breathing during image acquisition. In the case of artifacts, the image information can be considered locally invalid, as it does not correspond to the patient anatomy. Clinical use of the estimated motion fields requires them to be as close to the unknown reality as possible. A patient-specific, spatio-temporal deformation model could assist in reducing sensitivity to local image irregularities and render the motion estimate more plausible and potentially more representative of the patient's breathing motion under these challenging circumstances. In [46], robustness of registration methods was illustrated and compared by

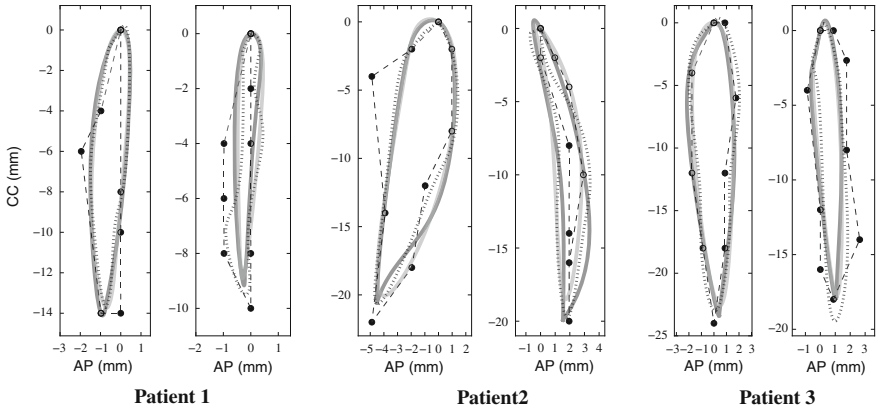

Fig. 8.7 (from [47]). Example landmarks with large displacements projected onto the sagittal plane: manually identified landmark positions are plotted together with trajectories obtained using three different trajectory models (shown using *black*, *gray* and *dashed lines*)

introducing artificial artifacts in 4D-CT. Qualitative evaluation was performed visually on images with real artifacts. From this very limited dataset, it seems that the addition of temporal information improves the robustness of the registration.

Conclusion: To validate the robustness of a registration method remains challenging, but taking into account the temporal dimension by means of point trajectories may be useful.

8.3.2 Deformation Vector Field Analysis

8.3.2.1 Validation Metrics

This paragraph describes validation metrics based on the deformation vector field (DVF) $\boldsymbol{T}$ mapping the discrete domain of an image A onto that of an image B, $\boldsymbol{T} : \Omega_A \rightarrow \Omega_B$.

One such validation metric employs the asymmetric nature of image registration[7]. A natural assumption is that independent of the order of the input images, the resulting transformations are inverse to each other. More specifically, defining $\boldsymbol{T}_{A\rightarrow B}$ as the spatial transformation after registration with A as the reference image and $\boldsymbol{T}_{B\rightarrow A}$ as that with B as the reference image, for an ideal registration $\tilde{\boldsymbol{x}}_A := \boldsymbol{T}_{B\rightarrow A}\left(\boldsymbol{T}_{A\rightarrow B}\left(\boldsymbol{x}_A\right)\right)$ is equal to $\boldsymbol{x}_A$ for all voxels of image A. More generally, in the case of n images with computed pairwise transformations $\boldsymbol{T}_{A_1\rightarrow A_2}, \boldsymbol{T}_{A_2\rightarrow A_3}$,

[7] Symmetric registration approaches are independent of the order of input images while asymmetric approaches are not. Naturally, a validation metric based on a specific criterion is not designed for approaches already relying on the same criterion.

$\ldots \boldsymbol{T}_{A_{n-1}\to A_n}, \boldsymbol{T}_{A_n\to A_1}$ let $\tilde{\boldsymbol{T}}$ denote the concatenation of all transformations,

$$\tilde{\boldsymbol{T}} := \boldsymbol{T}_{A_n\to A_1} \circ \boldsymbol{T}_{A_1\to A_2} \circ \ldots \circ \boldsymbol{T}_{A_{n-1}\to A_n} \ . \tag{8.10}$$

The n-consistency metric [48] is then defined as

$$C(\boldsymbol{x}_A) := \|\tilde{\boldsymbol{T}}(\boldsymbol{x}_A) - \boldsymbol{x}_A\|_2 \ , \quad \boldsymbol{x}_A \in \Omega_A \ . \tag{8.11}$$

It is common to consider mean and standard deviation as well as the maximum of the consistency map C.

A second DVF-based validation metric investigates the local volume change at every voxel position. In particular, it measures how much an infinitesimally small region around a voxel is contracting or expanding. For applications involving respiratory motion, large contractions of parenchymal tissue can occur. Taking a contraction beyond its physically possible limit, however, it can occur that two anatomical positions different from each other are mapped onto the same anatomical position, resulting in a loss of image information. This property is often described as the limit to folding, non-invertibility, non-bijectivity or non-diffeomorphism. For registration tasks containing pathologies, e.g. registration of a pre-operative planning image with an image taken after tumor resection, a locally folding DVF can be reasonable. However, respiratory motion estimation in this chapter assumes the absence of intervention related tissue loss. Therefore, any occurences of folding indicate a local registration failure. This is measured by calculation of the Jacobian map $\det(\nabla \boldsymbol{T}_{A\to B}(\boldsymbol{x}_A))$. Folding is defined as

$$F := \{\boldsymbol{x}_A \in \Omega_A \mid \det(\nabla \boldsymbol{T}_{A\to B}(\boldsymbol{x}_A)) \leq 0\} \ . \tag{8.12}$$

8.3.2.2 Validation in Practice

Since ground-truth is not available, necessary conditions for registration accuracy, so-called indications, can be considered. For the following discussion, the comparison study [3] cited in previous subsections is referenced again.

Firstly, for registration methods with both forward and backward DVFs available, the 2-consistency metric is computed. Since none of the registration methods under consideration is consistent by definition, measuring the consistency error is a suitable indicator of how independent the registration result is from the image input order. Figure 8.8, top row, as well as quantitative evaluation (details are described in [3]) indicate different consistency errors for methods 1, 3, 4 and 6.

Next, the Jacobian map is computed, a metric which is often used as a surrogate for local lung ventilation estimation. Since each DVF considered here is defined in the end-inspiration domain, a contraction is generally expected. A comparison of the various methods (cf. Fig. 8.8, bottom row) revealed large differences: whereas methods 1, 3 and 6 show a relatively homogeneous contraction, the remaining

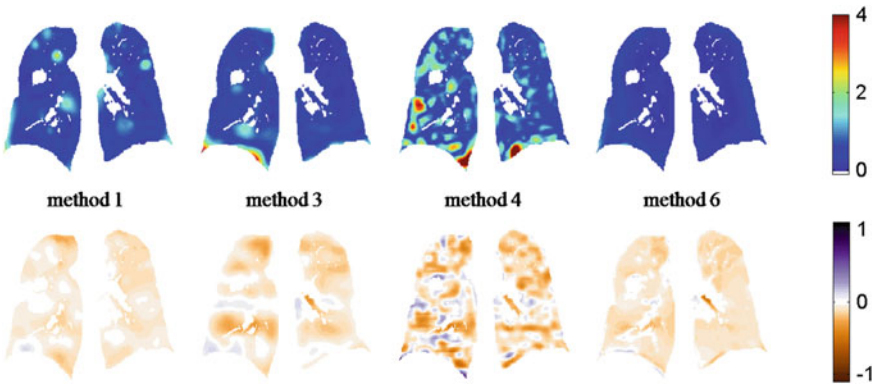

Fig. 8.8 2-consistency metric (*top*) and Jacobian map (*bottom*) for coronal views after registration with different registration algorithms. The consistency error as the amplitude of the geometrical discrepancy between forward and backward registration is given in mm. The Jacobian map estimates local lung ventilation: positive (negative) values indicate local expansion (contraction)

methods result in heterogeneous contraction-expansion patterns, methods 2 and 5 even show severe foldings [3]. Folding in the spatial domain is equivalent to partial loss of image information and should therefore be avoided. However, even without folding, heterogeneous contraction-expansion patterns are less plausible from a physiological point of view. Lungs in healthy condition are expected to be equally ventilated throughout with two exceptions: (1) gravity can impact both parenchymal density and ventilation resulting in a ventral-dorsal gradient [49, 50], (2) inertia can cause the lower lung regions to be more ventilated at intermediate respiratory phases when using dynamic acquisition protocols (as in respiratory-gated 4D-CT for example) rather than breath-hold imaging.

Lung diseases such as emphysema or fibrosis can cause ventilation of a certain lung region to be poor or even absent. Diseases showing (partially) obstructed airways can lead to an abnormal local level of synchrony since air flow entering a lung compartment with obstructed airways is slowed down and therefore continues to fill this compartment after the rest of the lung has stopped inhalation and switched to exhalation [51]. Such diseases can explain a heterogeneous level of contraction between end-inspiration state and end-expiration state but not a mix between contraction and expansion. On this basis, an experienced radiologist rated the result from method 6 (Fig. 8.8, last column) as the most plausible one, followed by method 1 (Fig. 8.8, first column).

Conclusion: Ground-truth in a strict sense does not exist for DVF-based validation metrics. Metrics such as consistency or the Jacobian map serve as necessary conditions for registration accuracy, thus they are indicators only. Registration methods with similar accuracy measured by morphological metrics can differ significantly for DVF-based metrics illustrating out the inadequacy of landmark- or surface-based

validation alone. Use of the Jacobian map to define lung ventilation is an important measure of functional validation.

8.3.3 Beyond Pure Deformation

Functional criteria from the previous section such as the consistency metric and the Jacobian map were demonstrated to add further information to the validation space. This can increase plausibility of the registration result and highlight previously unseen variations among different registration methods. A fully-automated evaluation of the Jacobian map is, however, difficult to establish: regions undergoing folding can, without any doubt, be classified as local registration failure. But what about regions compressed to 30 % or even to 10 % of their original volume, for example? Without dedicated knowledge of parenchymal elasticity in general and the specific patient status in particular, it is certainly not possible to rate this level of compression. Likewise, the radiologist's preference for a homogenoeus contraction as shown in Fig. 8.8 can not be automatically achieved.

One possible way to deal with the limitations of the Jacobian map for automatic validation is to link it to the voxel-specific tissue density. From a functional perspective, the lungs are comprised of tissue structures ranging from stiff to elastic. In CT imaging, higher densities are usually associated with stiff structures (e.g., bronchial walls or larger vessels) whereas low densities result from lung parenchyma consisting of alveoli and capillary vessels. In fact, due to the partial volume effect almost all voxels represent a mixture of stiff and elastic structures. During breathing, air can inflate or deflate the lungs, thus leading to a change in volume of lung parenchyma indicated by a change in local density. Generally, the change is proportional to the

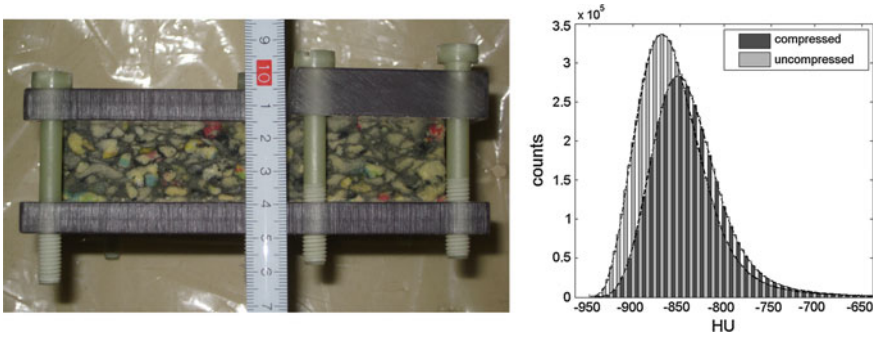

Fig. 8.9 Phantom composed of foam pieces with size ranging from about 1 mm to more than 10 mm. A sensory analysis reveals the single pieces to be of individual elasticity. The composite foam is mounted between two plates of acrylic glass with the upper plate splitted into two parts. Screws are used to fix the upper plate parts to the lower plate. On the *left*, the phantom is displayed in compressed state ("axial" view), on the *right*, intensity histograms after CT acquisition are shown

fraction of air. A change in volume of a certain structure, however, requires the structure to be elastic. Thus, elasticity is proportional to the fraction of air as well.

A recent study [52] investigated the voxel-wise calculated correlation between the Jacobian map and tissue density based entities such as the SAI measure (Eq. 13.17). However, the reported resulting correlation is not sufficient for use as a validation metric yet. Possible sources of errors include image noise, image artifacts, registration errors and inhomogeneous changes in the blood distribution during respiration. It should also be noted that lung diseases may change elasticity locally with possible impact on the relationship between expected parenchymal elasticity and air fraction. For instance, lung regions affected by emphysema or fibrosis are characterized by decreased compliance of the lung tissue [53] resulting in reduced ventilation and loss of elasticity. To rule out any possibility of impact from unknown pathologies, a compressible CT phantom with spatially varying elasticity (see Fig. 8.9) has been chosen [54] to investigate the relation between parenchymal elasticity and air fraction for functional validation.

The phantom is scanned twice ($0.33 \times 0.33 \times 0.45\,\mathrm{mm}^3$, further details are described in [54]), once in the uncompressed state and once in a compressed state (see Fig. 8.10a, b for exemplary slices). A histogram analysis (Fig. 8.9, right) reveals that, as for the lungs, the density in the compressed state is higher than in the uncompressed state.

For illustration and comparison, two registration methods are chosen: (1) one with a spatially constant elasticity constraint and (2) one with a spatially varying elasticity constraint. The two methods result in a similar landmark accuracy (50 well-dispersed landmarks; TRE given as mean $\pm$ std (max) [mm]) of $0.28 \pm 0.13(0.72)$ and $0.33 \pm 0.14(0.76)$, respectively. The Jacobian maps (cf. Sect. 8.3.2.1) shown in Fig. 8.10c reveal mostly contracting regions but also expanding regions occuring with a spatially constant elasticity constraint as depicted by regions color-coded in blue. Recalling that the phantom was exposed to overall contraction, expanding regions would be physically unrealistic.

Registration accuracy is now functionally analysed by relating the Jacobian map voxel-wise with the HU densities. Relating these two entitites is achieved by means of joint histograms. Since the relationship depends on the applied compression level, for each level of relative compression (relC) a normalized joint histogram is computed. Finally, to combine the information from the different compression levels, from each histogram a median graph is extracted. The collection of graphs shown in an ensemble plot (Fig. 8.11) now describes the reaction of a material with a certain HU value to individually applied compression forces. The differences between the spatially constant elasticity constraint (shown left) and the spatially varying constraint (shown right) underline the impact of the elasticity constraint on the registration result: the constant elasticity setting results in a graph ensemble with implausible positive Jacobian values for voxels with higher intensity. The positive values are directly linked to the expanding regions visible in Fig. 8.10c. On the contrary, for the spatially varying constraint no part of the phantom has been expanded.

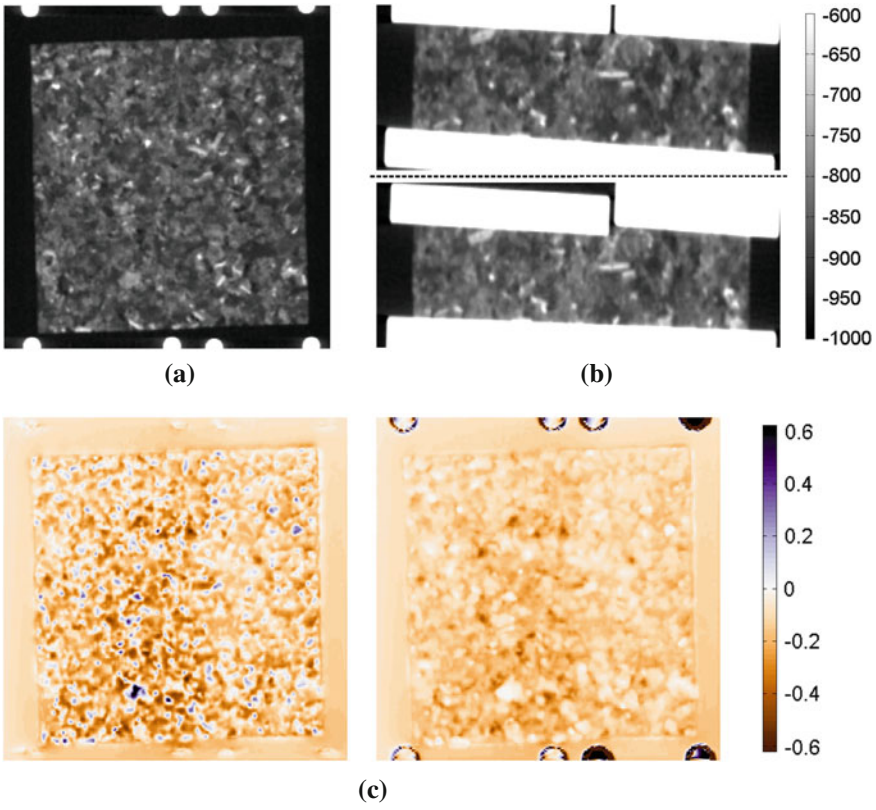

Fig. 8.10 **a** Mid coronal slice of CT phantom in uncompressed state. **b** Mid axial slice in uncompressed (*top*) and compressed state (*bottom*). **c** Jacobian maps (same slice as for (**a**)) for spatially constant elasticity constraint (*left*) and for spatially varying elasticity constraint (*right*)

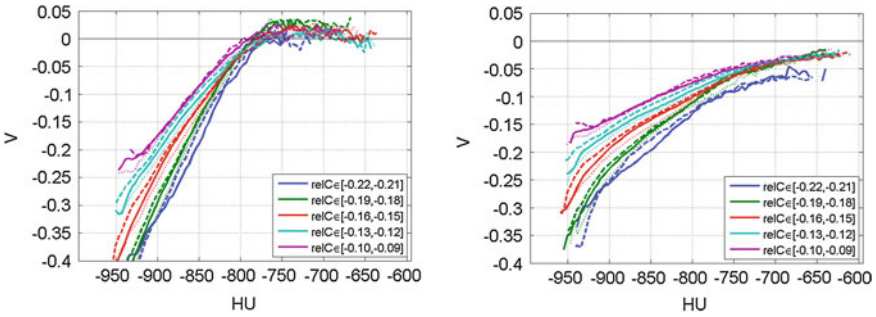

Fig. 8.11 Ensemble plots derived from normalized joint histograms (see text for explanation) for spatially constant elasticity constraint (*left*) and for spatially varying elasticity constraint (*right*)

Conclusion: It has been shown that landmark-based registration error is not sufficient to validate the deformations of an elastic body under compression. Moreover, validation based solely on this error may lead to a tuning of registration methods towards high flexibility but less physiologically plausible deformations. This experiment, which was carried out under laboratory conditions (no patient induced artifacts, high image dose) supports another recent study [3] where different registration schemes showed partially implausible contraction-expansion patterns but resulted in similar landmark-based registration errors.

Functional validation is exemplarily demonstrated by relating the Jacobian map voxel-wise with HU densities. Validation is no longer restricted to analysis of high contrast anatomical structures, but has been extended to include assessment of image regions with homogeneous intensities.

References

1. West, J., Fitzpatrick, J., Wang, M., Dawant, B., et al.: Comparison and evaluation of retrospective intermodality brain image registration techniques. J. Comput. Assist. Tomogr. **21**(4), 554–566 (1997)
2. Castillo, R., Castillo, E., Guerra, R., Johnson, V., McPhail, T., Garg, A., Guerrero, T.: A framework for evaluation of deformable image registration spatial accuracy using large landmark point sets. Phys. Med. Biol. **54**, 1849–1870 (2009)
3. Kabus, S., Klinder, T., Murphy, K., van Ginneken, B., Lorenz, C., Pluim, J.P.W.: Evaluation of 4D-CT lung registration. In: MICCAI, vol. 5761, pp. 747–54 (2009)
4. Yamamoto, T., Langner, U., Loo, B.W., Shen, J., Keall, P.J.: Retrospective analysis of artifacts in four-dimensional CT images of 50 abdominal and thoracic radiotherapy patients. Int. J. Radiat. Oncol. Biol. Phys. **72**(4), 1250–1258 (2008)
5. Werner, R., Ehrhardt, J., Schmidt-Richberg, A., Handels, H.: Validation and comparison of a biophysical modeling approach and non-linear registration for estimation of lung motion fields in thoracic 4D CT data. In: Reinhardt, J., Pluim, J. (eds.) Proceedings of SPIE Medical Imaging, vol. 7259, pp. 0U1–0U8 (2009)
6. Castillo, E., Castillo, R., Zhang, Y., Guerrero, T.: Compressible image registration for thoracic computed tomography images. J. Med. Biol. Eng. **29**, 222–233 (2009)
7. Glocker, B., Komodakis, N., Tziritas, G., Navab, N., Paragios, N.: Dense image registration through MRFs and efficient linear programming. Med. Image Anal. **12**, 731–741 (2008)
8. Brock, K.: Deformable registration accuracy consortium: results of a multi-institution deformable registration accuracy study (MIDRAS). Int. J. Radiat. Oncol. Biol. Phys. **76**(2), 583–596 (2010)
9. Murphy, K., van Ginneken, B., Reinhardt, J.M., et al.: Evaluation of registration methods on thoracic CT: the EMPIRE10 challenge. IEEE Trans. Med. Imaging **30**(11), 1901–1920 (2011)
10. Vandemeulebroucke, J., Sarrut, D., Clarysse, P.: The POPI-model, a point-validated pixel-based breathing thorax model. In: ICCR (2007)
11. Murphy, K., Pluim, J., van Rikxoort, E., de Jong, P., de Hoop, B., Gietema, H., Mets, O., de Bruijne, M., Lo, P., Prokop, M., van Ginneken, B.: Toward automatic regional analysis of pulmonary function using inspiration and expiration thoracic CT. Med. Phys. **39**(3), 1650–1662 (2012)
12. Sarrut, D., Delhay, B., Villard, P.F., Boldea, V., Beuve, M., Clarysse, P.: A comparison framework for breathing motion estimation methods from 4-D imaging. IEEE Trans. Med. Imaging **26**(12), 1636–1648 (2007)

13. Werner, R., Ehrhardt, J., Schmidt-Richberg, A., Heiss, A., Handels, H.: Estimation of motion fields by non-linear registration for local lung motion analysis in 4D CT image data. Int. J. Comput. Assist. Radiol. Surg. **5**(6), 595–605 (2010)
14. Murphy, K., van Ginneken, B., Klein, S., Staring, M., de Hoop, B.J., Viergever, M.A., Pluim, J.P.W.: Semi-automatic construction of reference standards for evaluation of image registration. Med. Image Anal. **15**(1), 71–84 (2011)
15. Klein, S., Staring, M., Murphy, K., Viergever, M.A., Pluim, J.P.W.: Elastix: a toolbox for intensity-based medical image registration. IEEE Trans. Med. Imaging **29**(1), 196–205 (2010)
16. Hartkens, T., Rohr, K., Stiehl, H.S.: Evaluation of 3D operators for the detection of anatomical point landmarks in MR and CT images. Comput. Vis. Image Underst. **86**, 118–136 (2002)
17. Werner, R., Wolf, J.C., Ehrhardt, J., Schmidt-Richberg, A., Handels, H.: Automatische Landmarkendetektion und -übertragung zur Evaluation der Registrierung von thorakalen CT-Daten. In: Deserno, T., Handels, H., Meinzer, H., Tolxdorff, T. (eds.) Bildverarbeitung für die Medizin 2010, Informatik aktuell, pp. 31–35. Springer, Heidelberg (2010)
18. Berlinger, K., Roth, M., Sauer, O., Vences, L., Schweikard, A.: Fully automatic detection of corresponding anatomical landmarks in volume scans of different respiratory state. Med. Phys. **33**(6), 1569–1572 (2006)
19. Likar, B., Pernus, F.: Automatic extraction of corresponding points for the registration of medical images. Med. Phys. **26**(8), 1678–1686 (1999)
20. Vik, T., Kabus, S., von Berg, J., Ens, K., Dries, S., Klinder, T., Lorenz, C.: Validation and comparison of registration methods for free-breathing 4D lung CT. In: Proceedings of SPIE Medical Imaging, vol. 6914, pp. 69,142P–1–69,142P–10 (2008)
21. Wan, S.Y., Higgins, W.: Symmetric region growing. IEEE Trans. Image Process. **12**(9), 1007–1015 (2003)
22. Schlathölter, T., Lorenz, C., Carlsen, I.C., Renisch, S., Deschamps, T.: Simultaneous segmentation and tree reconstruction of the airways for virtual bronchoscopy. In: Proceedings of SPIE Medical Imaging, vol. 2, pp. 103–113 (2002)
23. Schaap, M., Smal, I., Metz, C., van Walsum, T., Niessen, W.: Bayesian tracking of elongated structures in 3d images. In: Proceedings of Information Processing in Medical Imaging (IPMI), vol. 4584, pp. 74–85 (2007)
24. Friman, O., Hindennach, M., Kühnel, C., Peitgen, H.O.: Multiple hypothesis template tracking of small 3D vessel structures. Med. Image Anal. **14**(2), 160–171 (2010)
25. Lesage, D., Angelini, E., Bloch, I., Funka-Lea, G.: A review of 3D vessel lumen segmentation techniques: models, features and extraction schemes. Med. Image Anal. **13**, 819–845 (2009)
26. Lo, P., van Ginneken, B., Reinhardt, J., de Bruijne, M.: Extraction of airways from CT (EXACT'09). IEEE Trans. Med. Imaging **31**(11), 2093–2107 (2012)
27. Tschirren, J., McLennan, G., Palagyi, K., Hoffman, E., Sonka, M.: Matching and anatomical labeling of human airway tree. IEEE Trans. Med. Imaging **24**(12), 1540–1547 (2005)
28. Bülow, T., Lorenz, C., Wiemker, R., Honko, J.: Point based methods for automatic bronchial tree matching and labeling. In: Proceedings of SPIE Medical Imaging, vol. 6143 (2006)
29. Bouix, S., Martin-Fernandez, M., Ungar, L., Nakamura, M., Koo, M.S., McCarley, R.W., Shenton, M.E.: On evaluating brain tissue classifiers without a ground truth. NeuroImage **36**(4), 1207–1224 (2007)
30. Harris, E.J., Donovan, E.M., Yarnold, J.R., Coles, C.E., Evans, P.M.: Characterization of target volume changes during breast radiotherapy using implanted fiducial markers and portal imaging. Int. J. Radiat. Oncol. Biol. Phys. **73**(3), 958–966 (2009)
31. Hanna, G.G.: Hounsell, a.R., O'Sullivan, J.M.: Geometrical analysis of radiotherapy target volume delineation: a systematic review of reported comparison methods. Clin. Oncol. (R. Coll. Radiol.) **22**(7), 515–525 (2010)
32. Crum, W., Camara, O., Hill, D.: Generalized overlap measures for evaluation and validation in medical image analysis. IEEE Trans. Med. Imaging **25**(11), 1451–1461 (2006)
33. Dice, L.R.: Measures of the amount of ecologic association between species. Ecology **26**(3), 297 (1945)

34. Louie, A.V., Rodrigues, G., Olsthoorn, J., Palma, D., Yu, E., Yaremko, B., Ahmad, B., Aivas, I., Gaede, S.: Inter-observer and intra-observer reliability for lung cancer target volume delineation in the 4D-CT era. Radiother. Oncol. **95**(2), 166–171 (2010)
35. Jaccard, P.: Étude comparative de la distribution florale dans une portion des Alpes et des Jura. Bulletin del la Société Vaudoise des Sciences Naturelles **37**, 547–579 (1901)
36. Tralins, K.S., Douglas, J.G., Stelzer, K.J., Mankoff, D.A., Silbergeld, D.L., Rostomily, R.C., Hummel, S., Scharnhorst, J., Krohn, K.A., Spence, A.M., Rostomilly, R.: Volumetric analysis of 18F-FDG PET in glioblastoma multiforme: prognostic information and possible role in definition of target volumes in radiation dose escalation. J. Nucl. Med. **43**(12), 1667–1673 (2002)
37. Hu, S., Hoffman, E., Reinhardt, J.: Automatic lung segmentation for accurate quantitation of volumetric X-ray CT images. IEEE Trans. Med. Imaging **20**(6), 490–499 (2001)
38. van Rikxoort, E., de Hoop, B., Viergever, M., Prokop, M., van Ginneken, B.: Automatic lung segmentation from thoracic computed tomography scans using a hybrid approach with error detection. Med. Phys. **36**(7), 2934–2947 (2009)
39. van Rikxoort, E., van Ginneken, B., Klik, M., Prokop, M.: Supervised enhancement filters: application to fissure detection in chest CT scans. IEEE Trans. Med. Imaging **27**(1), 1–10 (2008)
40. Ukil, S., Reinhardt, J.: Anatomy-guided lung lobe segmentation in X-ray CT images. IEEE Trans. Med. Imaging **28**(2), 202–214 (2009)
41. van Rikxoort, E., Prokop, M., de Hoop, B., Viergever, M., Pluim, J.P.W., van Ginneken, B.: Automatic segmentation of pulmonary lobes robust against incomplete fissures. IEEE Trans. Med. Imaging **29**(6), 1286–1296 (2010)
42. Lassen, B., Kuhnigk, J.M., van Rikxoort, E., Peitgen, H.O.: Interactive lung lobe segmentation and correction in tomographic images. In: Proceedings of SPIE Medical Imaging, vol. 79631S, pp. 79, 631S–1–11 (2011)
43. Reeves, A., Chan, A., Yankelevitz, D., Henschke, C., Kressler, B., Kostis, W.: On measuring the change in size of pulmonary nodules. IEEE Trans. Med. Imaging **25**(4), 435–450 (2006)
44. Lujan, A., Larsen, E., Balter, J., Ten Haken, R.: A method for incorporating organ motion due to breathing into 3D dose calculations. Med. Phys. **26**(5), 715–720 (1999)
45. Castillo, E., Castillo, R., Martinez, J., Shenoy, M., Guerrero, T.: Four-dimensional deformable image registration using trajectory modeling. Phys. Med. Biol. **55**(1), 305–327 (2010)
46. Vandemeulebroucke, J., Rit, S., Kybic, J., Clarysse, P., Sarrut, D.: Spatiotemporal motion estimation for respiratory-correlated imaging of the lungs. Med. Phys. **38**(1), 166 (2011)
47. Vandemeulebroucke, J., Bernard, O., Rit, S., Kybic, J., Clarysse, P., Sarrut, D.: Automated segmentation of a motion mask to preserve sliding motion in deformable registration of thoracic CT. Med. Phys. **39**(2), 1006 (2012)
48. Christensen, G., Johnson, H.: Consistent image registration. IEEE Trans. Med. Imaging **20**(7), 568–582 (2001)
49. Kabus, S., Lorenz, C.: Fast elastic image registration. In: Grand Challenges in Medical Image Analysis, pp. 81–89 (2010)
50. Ding, K., Cao, K., Amelon, R., Christensen, G., Raghavan, M., Reinhardt, J.: Comparison of intensity- and jacobian-based estimates of lung regional ventilation. In: Proceedings of Third International Workshop on Pulmonary Image Analysis, pp. 49–60 (2010)
51. West, J.: Respiratory Physiology: The Essentials. Lippincott Williams & Wilkins, Philadelphia (2008)
52. Yamamoto, T., Kabus, S., Klinder, T., Lorenz, C., Loo, B., Keall, P.: Four-dimensional computed tomography pulmonary ventilation images vary with deformable image registration algorithms and metrics. Med. Phys. **38**(3), 1348–1358 (2011)
53. Pratt, P.: Pulmonary Pathology, chap. Emphysema and Chronic Airways Disease, pp. 651–69. Springer, New York (1988)
54. Kabus, S., Klinder, T., von Berg, J., Lorenz, C.: Functional non-rigid registration validation: a CT phantom study. In: Fischer, B., Dawant, B., Lorenz, C. (eds.) WBIR, Springer, vol. 6204, pp. 116–127 (2010)

Part III
Modeling of Motion Variability

Chapter 9
Estimating Internal Respiratory Motion from Respiratory Surrogate Signals Using Correspondence Models

Jamie McClelland

Abstract It is often difficult or impossible to directly monitor the respiratory motion of the tumour and other internal anatomy during RT treatment. Implanted markers can be used, but this involves an invasive procedure and has a number of other associated risks and problems. An alternative option is to use a correspondence model. This models the relationship between a respiratory surrogate signal(s), such as spirometry or the displacement of the skin surface, and the motion of the internal anatomy. Such a model allows the internal motion to be estimated from the surrogate signal(s), which can be easily monitored during RT treatment. The correspondence model is constructed prior to RT treatment. Imaging data is simultaneously acquired with the surrogate signal(s), and the internal motion is measured from the imaging data, e.g. using deformable image registration. A correspondence model is then fit relating the internal motion to the surrogate signal(s). This can then be used during treatment to estimate the internal motion from the surrogate signal(s). This chapter reviews the most popular correspondence models that have been used in the literature, as well as the different surrogate signals, types of imaging data used to measure the internal motion, and fitting methods used to fit the correspondence model to the data.

9.1 Introduction

The previous chapters have described how to acquire 4D CT images of the patient prior to treatment (cf. Part I) and how to estimate and model the respiratory motion from these images using bio-mechanical models or deformable image registration (cf. Part II). This information about the respiratory motion can be very useful for planning RT treatments, e.g. to define appropriate targets and margins that encompass the tumour motion, and to account for motion in dose calculations (cf. Chap. 11).

J. McClelland (✉)
Centre for Medical Image Computing, Department of Medical Physics and Bioengineering, University College London, London, UK
e-mail: j.mcclelland@ucl.ac.uk

J. Ehrhardt and C. Lorenz (eds.), *4D Modeling and Estimation of Respiratory Motion for Radiation Therapy*, Biological and Medical Physics, Biomedical Engineering,
DOI: 10.1007/978-3-642-36441-9_9,

However, if the respiratory motion can be monitored during treatment then there is the possibility of actively modifying the treatment to compensate for the respiratory motion, e.g. gated or tracked treatments (cf. Sects. 11.5 and 11.6). During gated treatment the radiotherapy beam is switched off when the tumour moves outside the target region (e.g. as the patient breathes in), and switched back on when it returns within the target region [4]. This effectively reduces the motion of the tumour but increases the treatment time. Tracked treatments attempt to make the radiotherapy beam follow the tumour motion, effectively reducing the motion of the tumour without increasing treatment time. There are two main approaches that have been proposed for tracked treatments: using a robotically mounted LINAC [57], and moving the leaves of a dynamic multi-leaf collimator (MLC) so that the collimated radiotherapy beam follows the tumour [49]. Both gated and tracked treatments can potentially compensate for respiratory motion, so they can use a smaller target volume as it does not need to encompass the tumour motion which can reduce the dose to the surrounding healthy tissue.

One of the main challenges with actively modifying the treatments is that it can be very difficult to image the tumour motion during treatment. Some lung tumours may be visible using x-ray imaging from certain angles, but generally it is very difficult to accurately identify the tumour. The only current practical solution to this problem is to use implanted markers. However, this involves an invasive procedure to implant the markers and there are a number of other potential problems including the possibility of marker migration [50, 62]. Also, markers are usually only implanted in or close to the tumour so only provide information on the tumour motion. While this is the most important information for guiding gated or tracked treatments, knowing how the rest of the anatomy is moving may be important for ensuring that dose limits to organs at risk are not exceeded.

Instead of attempting to directly image the motion of the tumour and other internal anatomy during treatment, a correspondence model can be used [47]. This models the relationship between the motion of the internal anatomy and a respiratory surrogate signal, such as spirometry or the displacement of the skin surface, which can be easily measured during treatment. Figures 9.1 and 9.2 illustrate the concept of a correspondence model. Prior to treatment imaging data is acquired simultaneously with one or more respiratory surrogate signals. The internal motion is measured from the imaging data and then a correspondence model is fitted which relates the internal motion to the respiratory surrogate signal(s) (cf. Fig. 9.1). The surrogate signal can then be monitored during treatment and used to estimate the motion of the internal anatomy and to guide gated or tracked treatments (cf. Fig. 9.2).

Correspondence models have also been proposed for other applications including motion compensated image reconstruction in Cone-Beam CT (CBCT) [37, 54, 69] (cf. Sect. 14.5) and Positron Emission Tomography (PET) [38] and for other image guided interventions such as High Intensity Focussed Ultrasound (HIFU) and cardiac catheterisation. For example, to perform motion compensated CBCT reconstruction a correspondence model can be built from 4D CT, which relates the motion of the anatomy to the displacement of the diaphragm. When the CBCT data is acquired the diaphragm motion can be measured from each individual projection.

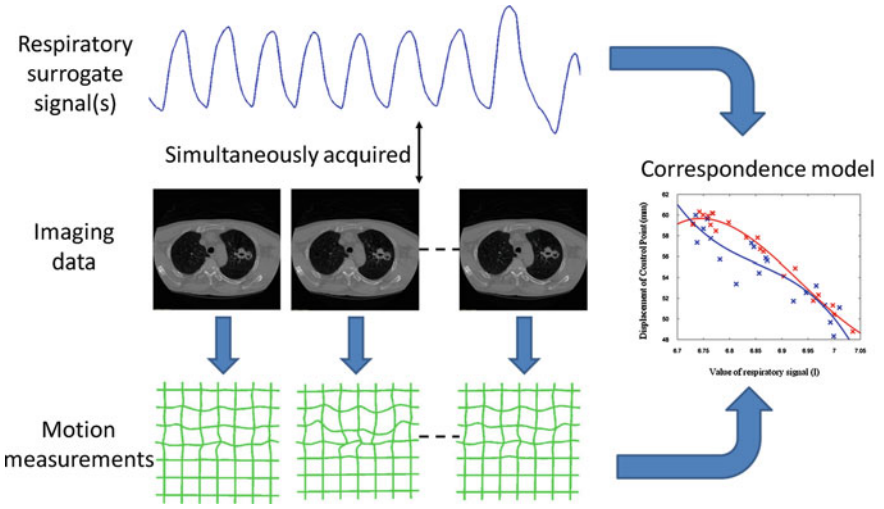

Fig. 9.1 An illustration of how a correspondence model is typically built. Prior to treatment one or more respiratory surrogate signals are acquired simultaneously with imaging data. The motion of the internal anatomy is measured from the imaging data, e.g. using deformable image registration. A correspondence model is then fit which approximates the relationship between the internal motion and the surrogate signal(s)

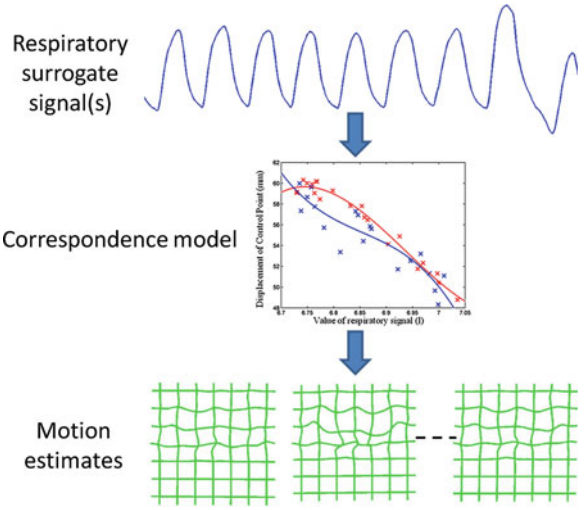

Fig. 9.2 An illustration of how a correspondence model is typically used. During RT treatment the respiratory surrogate signal(s) can be easily measured. The correspondence model can then be used to estimate the internal motion corresponding to the measured surrogate signal(s). These motion estimates could then be used to guide gated or tracked treatments

The correspondence model can then be used to estimate the motion for each projection, enabling a motion compensated reconstruction to be performed. A recent review paper [47] which covers all aspects of using correspondence models to estimate respiratory motion includes a description of the various different applications that have used such models.

Establishing accurate and robust correspondence models can be very challenging and is still very much an open area of research. Issues such as hysteresis, where the tumour follows a different path during inhalation and exhalation, and phase offsets between the tumour motion and the surrogate motion, may mean that a simple linear correlation between the surrogate signal and the tumour motion is insufficient to accurately predict the tumour motion [1, 2, 8, 16, 24, 28, 34, 39, 53]. Another problem is that it is well known that there can be breath to breath variations (inter-cycle variation) in the respiratory motion, both during a single fraction of treatment (intra-faction variation) and between fractions of treatment (inter-fraction variation) [24, 48]. Therefore the correspondence models need to account for or adapt to the variations in the respiratory motion.

The rest of the chapter is arranged as follows: Sect. 9.2 will review different respiratory surrogate signals that have been used for correspondence model in the literature; Sect. 9.3 will review different methods used to image the internal motion and different representations of the motion used for correspondence models; Sect. 9.4 will review the correspondence models that have been used in the literature; Sect. 9.4.2 will review methods of fitting the correspondence models to the data; and Sect. 9.5 will discuss some of the issues raised by the previous sections and the problems that still need to be overcome before the correspondence models can enter widespread clinical use.

9.2 Respiratory Surrogate Signals

Many different respiratory surrogate signals have been used for correspondence models. This section will give a brief overview of some of the most common surrogate signals that have been used in the literature. Note, surrogate signals are also used in 4D CT reconstruction to sort the imaging data into coherent volumes (cf. Part I).

Spirometers are used to measure the volume (or flow) of air being inhaled and exhaled by the patient. Spirometry is a popular choice of respiratory surrogate signal [24, 27, 41–43, 68, 71] as the signal is physiologically related to the respiratory motion and has historically been used for assessing respiratory performance and patterns [3]. However, it has been reported that some patients can have difficulty tolerating spirometry for long periods of time [24], and that spirometry measurements can be subject to time dependent drifts of the end-exhale and end-inhale values due to escaping air and instrumentation errors [24, 27, 43]. One solution to this problem is to use another ‘drift-free’ surrogate signal to correct for the drifts [43].

Another popular choice of respiratory surrogate signal is to measure the displacement of the patient’s chest or abdomen. This is often done using one or

more Infra-Red (IR) markers which are tracked optically [2, 8–15, 21, 23, 25, 37, 38, 43, 45, 46, 49, 57–60, 64, 66], and there are a number of commercial system that use this technology: e.g. the Real-Time Position Management (RPM) system (Varian, Palo Alto, California, USA), the Cyberknife (Accuray, Sunnyvale, California, USA), and the ExacTrac system (Brainlab, Feldkirchen, Germany). Other methods of tracking the displacement of the chest or abdomen include electromagnetic tracking systems [24], laser tracking systems [4, 28, 55, 61], and respiratory belts which go around the patient's chest or abdomen and stretch with respiration, e.g. the Anzai respiratory gating system (Siemens, Erlangen, Germany).

Another option for measuring the displacement of the chest and abdomen is to acquire a 3D representation of the patient's skin surface over the chest and abdomen. This has been done using stereo imaging techniques (e.g the Align RT system, Vision RT, London, UK) [26, 27, 44, 48], and the use of time of flight cameras has also been proposed [17]. For building the correspondence models the skin surface can be extracted from CT [15, 17, 19, 35, 45, 46] or MR volumes [20], although another method will be required to monitor the surface during treatment. The displacement at different points on the surface or over different areas of the surface can be followed and used as surrogate signals [15, 17, 19, 20]. Alternatively, a single, global, surrogate signal can be produced by calculating the volume underneath the skin surface [44, 48], which has been shown to produce a similar signal to that acquired from a spirometer but without the signal drift that can affect spirometry [27, 35].

Surrogate signals measured from the internal anatomy have also been proposed in the literature. Such signals may be more closely related to the motion of the tumour and other internal anatomy, but are much more challenging to measure during RT treatment. The motion of one or more points on the diaphragm can be used as surrogate signals [5–7, 32, 33, 54, 69, 70]. During treatment diaphragm position could be followed using x-ray imaging (although imaging dose could be a factor) [6, 7] or using ultrasound imaging [67]. It has also been proposed that the lung surface could be used as a surrogate signal [40], although it is not clear how the full lung surface would be detected during RT treatment delivery.

It should be noted that a number of correspondence models use derived surrogate signals as well as the measured surrogate signals. These include processing the surrogate signal to calculate the respiratory phase, a time-delayed copy of the surrogate signal, and the temporal derivative of the surrogate signal. Using respiratory phase can be useful for modelling hysteresis, but if respiratory phase is used on its own then it is not possible to model any inter-cycle variation. Using the time derivative of a surrogate signal, or a time delayed copy of the surrogate signal, in conjunction with the original signal can enable the modelling of hysteresis and some degree of inter-cycle variation.

Some authors have proposed using full 2D images of the internal anatomy (e.g. CBCT projection data) as surrogate data [36, 65]. When using full images as the surrogate data, the direct relationship between the surrogate data and the internal motion is not modelled. Rather, an 'in-direct' correspondence model is used to estimate the internal motion from the surrogate data (cf. Sect. 9.4.3).

9.3 Internal Motion Data

9.3.1 Imaging the Internal Motion

This section will describe the different imaging modalities that have been used in the literature for imaging the internal respiratory motion. Some papers image the respiratory motion and construct the correspondence models at the same time as planning the RT treatment, i.e. several days before the treatment. Other papers image the respiratory motion just prior to treatment with the patient setup ready for treatment. This means that a new model can be built for each fraction of treatment and can help account for inter-fraction variations in the respiratory motion (cf. Sect. 9.5). Figure 9.3 shows examples of the different types of imaging data that have been used to image the motion of the internal anatomy.

Dynamic x-ray imaging (such as fluoroscopy) has been used to image the internal respiratory motion [1, 4, 6, 7, 9–11, 14, 24, 25, 28, 29, 44, 55, 57–61, 64, 66] (cf. Fig. 9.3a). Its main advantages are that it can be easily acquired just prior to or during RT treatment and can be acquired with a very high temporal resolution so that the images can be considered free of motion artefacts. However, as noted in the introduction to this chapter, it can be very difficult to detect the tumour in x-ray images due to it being occluded by high intensity structures such as bones or the mediastinum. One solution is to implant small radio-opaque markers into or close to the tumour in order to follow its motion [4, 9–11, 14, 25, 28, 29, 55, 57, 58, 61, 64].

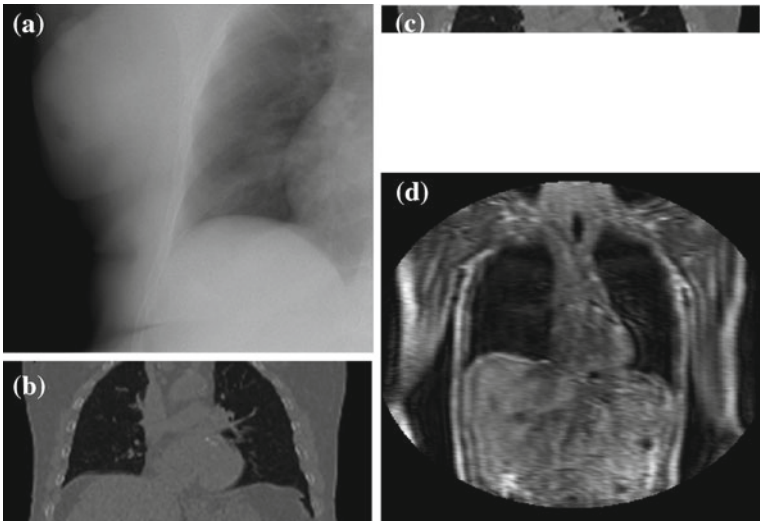

Fig. 9.3 Examples of the different types of imaging data that have been used to image the respiratory motion of the internal anatomy. **a** An x-ray projection image, **b** a 4D CT volume, **c** a Cine CT volume, **d** a dynamic MRI volume (acquisition time approx 250 ms for the full volume)

These markers are easily detectable in the x-ray images and can be automatically tracked, but have a number of drawbacks including an invasive procedure to implant them and the possibility of them moving away from their intended locations [50, 62]. Therefore developing methods to automatically determine the tumour motion from x-ray images without using implanted markers is an active area of research [44, 60]. As x-rays produce 2D projection images two simultaneous x-ray images from different directions are generally required to track the 3D motion. Another option that has been proposed is to use a series of x-ray images acquired with the source and detector rotating around the patient, i.e. the raw projections images from a cone-beam CT acquisition (cf. Chap. 14). The model can then be fit to all of the x-ray images simultaneously, allowing the full 3D motion to be modelled [44].

CT imaging has been widely used in the literature to image the internal respiratory motion. It provides information on the full 3D motion and deformation of the anatomy, enabling 3D deformable registrations to be performed. Many studies have used 4D CT datasets as described in Part I to image the respiratory motion during free breathing [2, 15–19, 32, 33, 36–38, 40, 54, 65, 69, 70] (cf. Fig. 9.3b). These are popular as they provide images over the full region of interest. However, they are formed by combining data acquired from several different respiratory cycles, and are based on the assumption that the respiratory motion will be the same from one respiratory cycle to the next. Breath-to-breath variations in the respiratory motion will cause artefacts in the 4D CT volumes (cf. Sect. 1.5.1 and Sect. 2.5). This also means that 4D CT volumes are not appropriate for studying and modelling the short term breath-to-breath variations in the respiratory motion.

To overcome this problem some studies have used Cine CT data [8, 12, 21, 23, 41, 42, 45, 46, 48, 49, 68, 71] (cf. Fig. 9.3c) which is essentially the unsorted data used to construct cine 4D CT volumes (cf. Chap. 2). This means that the field of view and number of slices in the superior-inferior direction is limited by the size of the CT detector. Many scanners used clinically only have 12 or 16 slices covering approximately 2-2.5 cm. Some recently developed scanners can have a much larger detector giving greater coverage and many more slices [51], although these are still not generally large enough to cover the whole region of interest for RT planning. Therefore, if motion estimates are required for the whole region of interest it may be necessary to build multiple correspondence models and to combine the results from these models [45, 46, 48, 49, 68]. Cine CT data may be acquired at the same location over more than one respiratory cycle, giving information on the breath-to-breath variations that occur.

MRI data has also been used for constructing correspondence models [5, 20, 34, 39, 53] (cf. Fig. 9.3d). MRI has the advantage that it does not deliver any radiation dose to the patient, potentially allowing much more data to be acquired so as to study both the intra- and inter-fraction variation, and enabling volunteer studies. It is possible to acquire 3D MR volumes of a large region of interest (e.g. the lungs) at a temporal resolution fast enough to image the respiratory motion (0.5 s per image), although the spatial resolution and image quality is poor compared to 4D CT making accurate image registration much more challenging [5, 20].

9.3.2 Representing the Internal Motion Data

Some papers just model the motion of one or a small number of points of interest. In a clinical setting the point of interest would usually correspond to the tumour. Some papers manually determine the motion of the point of interest but most papers use an automatic method such as template tracking (e.g. [41]). Other correspondence models estimate the motion over an entire region of interest. In these cases image registration is often used to determine the motion from the imaging data. Affine registrations have been used [5], although deformable registrations are more common as these can account for the local deformations that occur during respiration. Several different deformable registration algorithms have been used in the literature, including B-spline (e.g. [46]), demons (e.g. [36]), optical flow/diffusion (e.g. [70]), fluid (e.g. [40]), and surface based registrations (e.g. [33]). For more information on the different registration algorithms please see Part II.

All correspondence models in the literature essentially represent the internal motion data using a motion vector, $\mathbf{m} = \left[m_1, m_2, \ldots, m_{N_m}\right]^T$, where there are N_m values representing the internal motion. In some cases the elements of the motion vector correspond to the motion of one or more anatomical points. These could be a point of interest such as the tumour [1, 2, 6–11, 13, 14, 24, 25, 28, 29, 34, 39, 41, 42, 44, 55, 57–61, 64, 71], or they could be points defining the surface of an organ [5, 32, 33]. The actual values used could correspond to the absolute position of the points (in some predefined coordinate system) or the displacement of the points relative to a reference position [33]. Some papers only model the 1D motion (usually in the SI direction) of the anatomical points, so $\mathbf{m} = \left[x_1, x_2, \ldots, x_{N_p}\right]^T$ where x_n is the motion of the nth point and N_p is the number of anatomical points. In this case $N_m = N_p$. Some papers model the 2D motion of the anatomical points so $\mathbf{m} = \left[x_1, y_1, x_2, \ldots, x_{N_p}, y_{N_p}\right]^T$ and $N_m = 2N_p$, and some papers model the full 3D motion of the points so $\mathbf{m} = \left[x_1, y_1, z_1, x_2, \ldots, x_{N_p}, y_{N_p}, z_{N_p}\right]^T$ and $N_m = 3N_p$, where x_n is the motion of the nth point in the x direction, y_n is the motion of the nth point in the y direction, and z_n is the motion of the nth point in the z direction.

Other representations of the motion have also been used in the literature. The motion vector could represent a deformation field [15, 17, 19, 36–38, 40, 54, 65, 68–70], where each element of $\mathbf{m}$ corresponds to the motion of a voxel in a particular direction, and N_m equals 3 times the number of voxels in the volume. The motion vector could represent a velocity field that defines a diffeomorphic transformation [21, 23], where each element of $\mathbf{m}$ corresponds to the velocity at a voxel in a particular direction, and N_m again equals 3 times the number of voxels in the volume. Or the motion vector could represent a control point grid defining a B-spline transformation [12, 18, 20, 45, 46, 48, 49], where each element of $\mathbf{m}$ corresponds to the displacement of one of the control points in one direction and N_m equals 3 times the number of control points that define the B-spline transformation. The size of the motion vector, N_m, will depend on the motion representation being used. It will be small if only one or a few points of interest are being modelled, it could be several thousand if

points defining an organ surface are being modelled, it could be many thousand if a B-spline control point grid is being modelled, or it could be millions if a deformation or velocity field is being modelled.

9.4 Correspondence Models

9.4.1 Types of Model

This section will describe some of the different correspondence models that have been used to relate the internal motion to respiratory surrogate signals. Table 9.1 summarises the different correspondence models that have been used in the literature. Figure 9.4 illustrates the different motion trajectories that can be modelled by the more popular types of correspondence models in Table 9.1.

9.4.1.1 Linear Models

As can be seen in Table 9.1, linear correspondence models are by far the most common in the literature. These model the motion as a linear combination of surrogate signals:

$$\mathbf{m} = \mathbf{Cs} + \mathbf{C_0} \tag{9.1}$$

Table 9.1 Summary of the different types of correspondence models used in the literature

Type	Details	Examples
Linear	1 surrogate signal	[1, 2, 6–9, 11, 16, 24, 25, 28, 34, 39, 53, 55, 57–61]
	2 or more surrogate signals	[6, 7, 10, 13–15, 17, 19, 20, 29, 32, 33, 40–42, 44, 48, 55, 68–71]
Piece-wise linear	1 surrogate signal	[21, 23]
	Using respiratory phase as surrogate signal	[54]
Polynomial	1 surrogate signal	[13, 25, 45, 55]
	With separate inhalation and exhalation	[5, 13, 14, 25, 48, 61, 64]
	2 surrogate signals	[55, 64]
B-spline	Using respiratory phase as surrogate signal	[12, 45, 46, 48, 49]
	2 or more surrogate signals	[18]
Others	Fourier series	[45]
	Neural networks	[29, 64]
	Fuzzy logic	[64]
	Support vector regression	[13, 14]

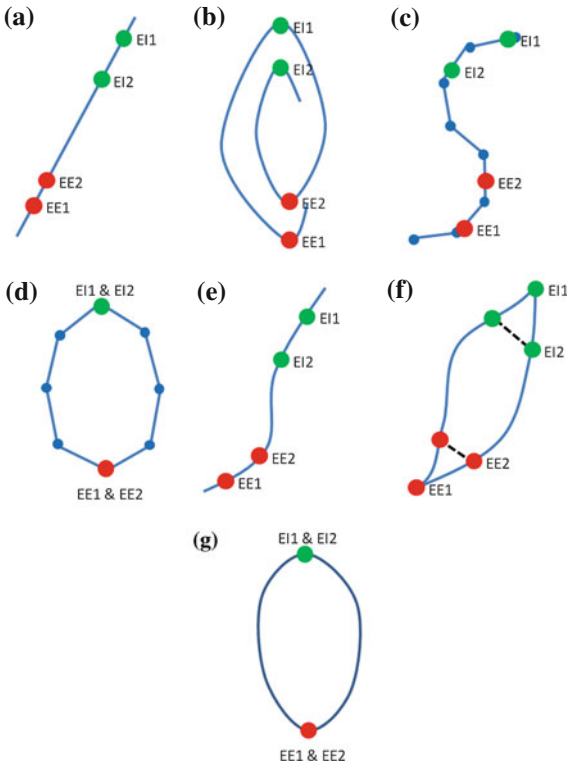

Fig. 9.4 Examples of the different motion trajectories that can be produced by the different types of correspondence model. The points corresponding to end-exhalation (*red circles*) and end-inhalation (*green circles*) from two breath cycles are marked (EE1, EI1, EE2, EI2). **a** A linear correspondence model using one surrogate signal constrains the motion to follow a straight line during every breath cycle. The estimated motion may move a different distance along the line during each breath, depending on how deep the breathing is (i.e. EE1 $\neq$ EE2 and EI1 $\neq$ EI2). **b** A linear (or other) correspondence model that uses two or more surrogate signals can model complex motion including hysteresis (a different trajectory during inhalation and exhalation) and inter-cycle variation (EE1 $\neq$ EE2 and EI1 $\neq$ EI2). **c** A piece-wise linear model produces a motion trajectory that is made up of several straight line segments. The *blue circles* correspond to known motion measurements made from the imaging data. As with the linear model, the estimated motion is constrained to follow the same path during every breath, but may move a different distance along the path depending on how deeply the individual is breathing. **d** If the surrogate signal used for the piece-wise linear model is a derived respiratory phase signal rather than the actual measured surrogate signal then the line segments will form a loop shaped trajectory. In this case the estimated motion will go around the same loop during every breath cycle. This means that hysteresis can be modelled, but inter-cycle variation cannot (i.e. EE1 = EE2 and EI1 = EI2). **e** A polynomial correspondence model also constrains the motion to follow the same path during every breath, but now the path is a curve rather than one or more straight lines. **f** In order to model hysteresis some authors have proposed using two polynomial models, one for inhalation and one for exhalation. While this does allow hysteresis to be modelled it may result in discontinuous motion estimates when switching between the two models, as shown at EE2 and EI2. **g** Using respiratory phase as the surrogate signal and a periodic B-spline correspondence model gives a similar trajectory to using phase with a piece-wise linear model, but the trajectory is now a smooth curve rather than being composed of a number of straight line segments

where $\mathbf{m}$ is the vector of motion estimates (see Sect. 9.3.2), $\mathbf{s}$ is a vector of surrogate signals (i.e. $\mathbf{s} = \left[s_1, s_2, \ldots, s_{N_s}\right]^T$ where s_n is the nth surrogate signal and there are N_s surrogate signals, some of which may be derived surrogate signals), $\mathbf{C}$ is a $N_m \times N_s$ matrix of linear coefficients, and $\mathbf{C_0}$ is a N_m element vector of constant terms.

Several papers use a linear model with just a single surrogate signal (i.e. $N_s = 1$), which is therefore a simple linear correlation between the surrogate signal and the motion. This constrains the motion to follow a straight line during each breath (cf. Fig. 9.4a). Such a model was first proposed for RT related applications by Schweikard et al. [57] for guiding tracked RT treatment using the Cyberknife (Accuray, Sunnyvale, California, USA). Although such a model may not be very realistic, it has been shown to be sufficiently accurate in some circumstances, and is used clinically in the Cyberknife system to treat some patients [25, 61].

There have been a number of studies assessing how different factors can affect the correlation between the surrogate signal and the motion [1, 2, 8, 16, 24, 28, 34, 39, 53], e.g. the surrogate signal used [24], the type of breathing the patient is performing (deep or shallow, using their ribs or using their diaphragm) [34, 53], and over what time scales the linear correlations are valid [24]. These studies have had mixed results. In some circumstances a simple linear correlation can approximate the respiratory motion relatively well over a short time frame, but in other circumstances, such as when there is significant hysteresis, a simple 1-D linear correlation is not sufficient.

Other papers have used linear models of two or more (sometimes many more) surrogate signals (i.e. $N_s > 1$). When there are only two signals these usually comprise one measured surrogate signal and one derived surrogate signal, either a time delayed signal or the temporal derivative (e.g. [41]). When more signals are used they are often multiple measured surrogate signals from different parts of the anatomy (e.g. [32]), although sometimes they will use multiple measured and multiple derived signals (e.g. [20]), and sometimes just a single measured signal with multiple derived signals (i.e. a number of time delayed signals with a different length delay for each signal, e.g. [29]). Sometimes the different signals may be highly correlated with each other, e.g. when the signals represent points on the surface of an organ, and this can make the models susceptible to over-fitting [32, 33]. However, the models are very flexible and can potentially model complex motion including both hysteresis and inter-cycle variation (cf. Fig. 9.4b). Linear models using multiple surrogate signals were first proposed for RT related applications by Low et al. [41].

One way to model more complex motion with only a single surrogate signal is to use a piece-wise linear model [21, 23, 37, 38, 54]. In this case the motion has been measured from several images (e.g. using deformable image registration), each of which corresponds to a different surrogate signal value. These motion measurements are linearly interpolated to estimate the motion at other surrogate signal values where data has not been acquired. Such models allow the motion to follow more complex paths than a simple straight line, but as with any model using a single surrogate signal, they are limited in the variation they can model. A piece-wise linear model that

relates the motion to the measured surrogate signal [21, 23] cannot model hysteresis but can model some limited inter-cycle variation. The motion will always follow the same trajectory during each breath, but can move a different distance along this trajectory depending on how deeply the patient is breathing (cf. Fig. 9.4c). A piece-wise linear model that relates the motion to respiratory phase [37, 38, 54] can model hysteresis but cannot model any inter-cycle variation (cf. Fig. 9.4d). Furthermore, a piece-wise linear model cannot extrapolate outside the range of surrogate signal values used to build the model.

9.4.1.2 Polynomial Models

Polynomial correspondence models have also been widely used. These estimate the motion as a polynomial function of the surrogate signal(s). The equation for a polynomial correspondence model using a single scalar surrogate signal, s_1, is:

$$\mathbf{m} = \sum_{i=0}^{p} \mathbf{C}_i \, s_1^i \tag{9.2}$$

and the equation for a polynomial model using two scalar surrogate signals, s_1 and s_2, is:

$$\mathbf{m} = \sum_{i=0}^{p} \sum_{j=0}^{n-i} \mathbf{C}_{i,\,j} \, s_1^i s_2^j \tag{9.3}$$

where $\mathbf{C}_i$ and $\mathbf{C}_{i,j}$ are vectors of polynomial coefficients and p is the order of the polynomial. Such models are usually second or third order polynomials. Higher orders polynomials have been investigated [45], but they are more likely to over-fit the data and lead to very large extrapolation errors. Polynomial models were first proposed for RT related applications by Blackall et al. [5].

Polynomial models are usually used with a single scalar surrogate signal, but they have also been used with respiratory phase [45], and with two surrogate signals (the second being a precursor of the first) [55, 64]. As with the linear models, if a single surrogate is used the motion is constrained to follow the same trajectory during each breath, although it can move a different distance along this trajectory. However, unlike the linear models the trajectory is no longer constrained to be a straight line (cf. Fig. 9.4e). As polynomial models can be susceptible to large extrapolation errors some papers revert to using a linear model when estimating the motion for values of the surrogate signal that are outside the range used to build the model [13, 14, 61, 64].

A polynomial model of a single surrogate signal cannot model hysteresis as the motion is constrained to follow the same path during inhalation and exhalation. Therefore some papers fit two separate polynomial models, one to the data from inhalation and one to the data from exhalation, as first proposed in Blackall

et al. [5]. This allows hysteresis to be modelled but can result in discontinuities in the motion estimates when switching from inhalation to exhalation (cf. Fig. 9.4f). To try and minimise the discontinuities some papers 'blend together' the polynomial models and a linear model in the regions corresponding to end-exhale and end-inhale, creating a smooth transition from one model to the other and allowing the linear model to be used when extrapolation is required [13, 14].

9.4.1.3 B-Spline Models

B-spline correspondence models have also been proposed to relate the surrogate signal(s) and the motion. These are usually used with a single derived surrogate signal representing respiratory phase, so a 1D B-spline is used. One paper [18] has proposed using both a derived respiratory phase signal and the actual measured signal so uses a two dimensional B-spline.

As the internal motion is related to respiratory phase, ϑ, most of the papers have modified the standard B-spline function so as to make it periodic (or cyclic), so that there are no discontinuities between one breath cycle and the next:

$$\mathbf{m} = \sum_{i=0}^{3} \mathbf{C}_{i+k \bmod N} B_i(j) \tag{9.4}$$

where $j = \frac{\vartheta}{\delta} - \lfloor \frac{\vartheta}{\delta} \rfloor$, $k = \lfloor \frac{\vartheta}{\delta} \rfloor - 1$, ϑ is the respiratory phase (between 0 and 100 %), B_i is the ith B-spline basis function (see Sect. 6.1.2.1 or [56]), $\mathbf{C}_0, \ldots, \mathbf{C}_N$ are vectors of B-spline control points (with N_m elements), N is the number of control points, and δ is the control point spacing ($\delta = \frac{100\%}{N}$). Note, although the equation does directly relate the estimated motion to a measured surrogate signal, the values of the B-spline basis functions B_i depend on the value of the respiratory phase, ϑ, which is derived from the measured surrogate signal.

Periodic B-spline correspondence models were first proposed for RT related applications by McClelland et al. [45, 46]. A 1D periodic B-spline correspondence model constrains the motion to follow a loop shaped trajectory. This means that hysteresis can be modelled, but inter-cycle variation cannot be modelled (cf. Fig. 9.4g). The 2D B-spline model can potentially model inter-cycle variation and hysteresis, but as there are many more model parameters to fit there is a much higher risk of over-fitting the data.

9.4.1.4 Others

Other correspondence models have also been proposed in the literature, including models based on Fourier series [45], neural networks [29, 64], fuzzy logic [64], and support vector regression [13, 14]. However, these models have not been widely used

in the literature so they will not be covered in detail here. Interested readers should refer to the papers referenced above for more detail on these methods.

9.4.2 Fitting the Correspondence Models

A number of different methods and techniques have been used to fit the correspondence models to the data. This section will describe some of the more widely used methods.

To fit a correspondence model the motion of the internal anatomy and the surrogate signals must both be simultaneously sampled a number of times. Each sample will usually represent a specific timepoint, although is some papers they represent an entire breath cycle [32, 33]. The motion of the internal anatomy at each sample, t, is represented by the motion vector $\mathbf{m}_t = \left[m_{1,\,t}, m_{2,\,t}, \ldots, m_{N_m,\,t}\right]^T$, where there are N_m values representing the internal motion (e.g. N_m is 3 times the number of voxels if the motion is represented as a deformation field, cf. Sect. 9.3.2). The surrogate signals at each sample, t, are represented by another vector $\mathbf{s}_t = \left[s_{1,\,t},\ s_{2,\,t}, \ldots,\ s_{N_s,\,t}\right]^T$, where there are N_s surrogate signals. All of the samples of the motion data can be then concatenated into a matrix, $\mathbf{M} = \left[\mathbf{m}_1, \mathbf{m}_2, \ldots, \mathbf{m}_{N_t}\right]$ and samples of the surrogate signal can be concatenated into another matrix, $\mathbf{S} = \left[\mathbf{s}_1, \mathbf{s}_2, \ldots, \mathbf{s}_{N_t}\right]$ where N_t is the number of training samples, i.e. the number of timepoints that the internal motion has been imaged (or the number of breath cycles imaged). N_t is typically 8 or 10 if 4D CT has been used to image the internal motion (one sample for each 4D CT image), but may be more if a different modality (e.g. x-ray imaging) has been used.

9.4.2.1 Linear Least Squares

By far the most commonly used method is linear least squares [5, 9–14, 25, 41, 42, 45, 46, 48, 49, 55, 57–61, 64, 68]. The correspondence model can be formulated as a linear multivariate regression problem:

$$\mathbf{m}_t = \mathbf{C}\mathbf{s}_t \tag{9.5}$$

where $\mathbf{C}$ contains the correspondence model parameters, which can be found from the training data using ordinary least squares by minimising the squared difference between $\mathbf{M}$ and $\mathbf{CS}$, i.e.

$$\arg\min \left(\mathbf{M} - \mathbf{CS}\right)^2 \tag{9.6}$$

this is done by:

$$\mathbf{C} = \mathbf{M}\mathbf{S}^T \left(\mathbf{S}\mathbf{S}^T\right)^{-1} = \boldsymbol{\Sigma}_{\mathbf{MS}} \boldsymbol{\Sigma}_{\mathbf{SS}}^{-1} \tag{9.7}$$

where $\boldsymbol{\Sigma}_{\mathbf{SS}}$ is the covariance matrix of $\mathbf{S}$ and $\boldsymbol{\Sigma}_{\mathbf{MS}}$ the cross-covariance matrix of $\mathbf{M}$ and $\mathbf{S}$.

A motion estimate, $\mathbf{m}_{est}$, can then be made from new surrogate signal values, $\mathbf{s}_{new}$, using the fitted correspondence model parameter, $\mathbf{C}$:

$$\mathbf{m}_{est} = \mathbf{C}\mathbf{s}_{new} \tag{9.8}$$

Note, linear least squares can be used for polynomial models and B-spline models as well as the linear models by considering simple functions of the surrogate signals (such as raising to a power or calculating the B-spline basis functions) as just another surrogate signal. Also, if an additional 'surrogate signal' with a constant value of 1 is used when fitting the linear model this will allow the constant terms $\mathbf{C_0}$ to be fit as well. Example to fit a second order polynomial correspondence model with one surrogate signal, s_1, the surrogate signal vector for each sample, t, will be $\mathbf{s}_t = \left[s_{1,t}^2, s_{1,t}, 1\right]^T$.

9.4.2.2 Principal Component Analysis

Principal Component Analysis (PCA) is a mathematical technique which can be used to help analyse and interpret multi-variate data [30]. PCA is performed by finding the eigenvectors of the data covariance matrix. The result of PCA is a set of linearly uncorrelated variables, the principal components. These are ordered such that the first principal component has the largest possible variance (i.e. accounts for the most variation in the data possible), and each successive component has the highest possible variance while being orthogonal to the previous principal components. The total number of principal components will be the same as the number of variables in the data. However, it is usually possible to represent the majority of the variance in the data using substantially fewer principal components than there were original variables. Therefore PCA can be used as a dimensionality reduction tool. The original data can be re-expressed in terms of the PCA weights, that is the values by which each principal component is multiplied to approximate the original data. If all the principal components are used then the principal components multiplied by the PCA weights will equal the original data exactly. If fewer principal components are used this will approximate the original data, although a good approximation will often be achieved if a sufficient amount of the variance (usually 90-95 %) is included in the principal components that are used.

PCA has been utilised in a number of different ways when fitting respiratory motion models.

Applied to Internal Motion Data

It has been applied to the internal motion data prior to fitting a correspondence model [20, 69]. This can help remove unwanted noise from the motion data due to imaging

artefacts and/or registration errors. First the mean motion vector, $\overline{\mathbf{m}}$, is subtracted from each motion vector to give the mean centred motion vectors, $\widetilde{\mathbf{m}}_t = \mathbf{m}_t - \overline{\mathbf{m}}$, and these are concatenated to give the mean centred motion matrix $\widetilde{\mathbf{M}}$. This is then approximated using K_m principal components:

$$\widetilde{\mathbf{M}} \approx \mathbf{E}_m \mathbf{W}_m \tag{9.9}$$

where the matrix $\mathbf{E}_m = \left[\mathbf{e}_1, \ldots, \mathbf{e}_{K_m}\right]$ consists of the first K_m principal components and matrix $\mathbf{W}_m$ of size $K_m \times N_t$ gives the principal component weights for each of the training motion samples.

The correspondence model now relates the surrogate signal(s) to the principal component weights rather than to the motion vectors themselves. Ordinary least squares can be used as above to fit the correspondence model [69]:

$$\mathbf{C} = \mathbf{W}_m \mathbf{S}^T \left(\mathbf{S}\mathbf{S}^T\right)^{-1} = \boldsymbol{\Sigma}_{\mathbf{W}_m \mathbf{S}} \boldsymbol{\Sigma}_{\mathbf{S}\mathbf{S}}^{-1} \tag{9.10}$$

where $\boldsymbol{\Sigma}_{\mathbf{W}_m \mathbf{S}}$ is the cross-covariance matrix of $\mathbf{W}_m$ and $\mathbf{S}$.

A motion estimate can be made from new surrogate signals values by first estimating the principal component weights, $\mathbf{w}_{m\_est}$:

$$\mathbf{w}_{m\_est} = \mathbf{C}\mathbf{s}_{new} \tag{9.11}$$

and then multiplying by the principal components and adding the mean motion vector to get the motion estimate:

$$\mathbf{m}_{est} = \overline{\mathbf{m}} + \mathbf{E}_m \mathbf{w}_{m\_est} = \overline{\mathbf{m}} + \mathbf{E}_m \mathbf{C}\mathbf{s}_{new} \tag{9.12}$$

Note, alternative fitting methods, such as canonical correlation analysis [20, 40], can be used instead of ordinary least squares to calculate the model parameters, $\mathbf{C}$, which relate the principal component weights to the surrogate signals.

Applied to Surrogate Signal Data

PCA has also been applied to the surrogate signal data before fitting a correspondence model [33]. The correspondence model then relates the PCA weights (which now represent the surrogate signals) to the internal motion data. This approach is known as principal component regression (PCR) and it can help provide a more stable and robust fit by removing co-linearities in the surrogate data. This can be particularly useful if there are a large number of surrogate signals that are highly correlated with each other, e.g. when the surrogate signals are from points on an organ/skin surface, and can help prevent over-fitting in such circumstances. The mean centred surrogate signals, $\widetilde{\mathbf{S}}$ are represented using K_s principal components:

$$\widetilde{\mathbf{S}} \approx \mathbf{E}_s \mathbf{W}_s \tag{9.13}$$

where the matrix $\mathbf{E}_s$ contains the first K_s principal components and matrix $\mathbf{W}_s$ the principal component weights for each of the training surrogate samples.

Ordinary least squares is then used to fit the correspondence model relating the internal motion to the principal component weights:

$$\mathbf{C} = \mathbf{M}\mathbf{W}_s^T \left(\mathbf{W}_s \mathbf{W}_s^T\right)^{-1} = \boldsymbol{\Sigma}_{\mathbf{M}\mathbf{W}_s} \boldsymbol{\Sigma}_{\mathbf{W}_s\mathbf{W}_s}^{-1} \tag{9.14}$$

where $\boldsymbol{\Sigma}_{\mathbf{W}_s\mathbf{W}_s}$ is the covariance matrix of $\mathbf{W}_s$ and $\boldsymbol{\Sigma}_{\mathbf{M}\mathbf{W}_s}$ the cross-covariance matrix of $\mathbf{M}$ and $\mathbf{W}_s$. A motion estimate is made from new surrogate signal values by first calculating the corresponding principal component weights, $\mathbf{w}_{s\_new}$:

$$\mathbf{w}_{s\_new} = \mathbf{E}_s^T \left(\mathbf{s}_{new} - \bar{\mathbf{s}}\right) \tag{9.15}$$

where $\bar{\mathbf{s}}$ is the mean of the training surrogate vectors, and then estimating the motion using the correspondence model:

$$\mathbf{m}_{est} = \mathbf{C}\mathbf{w}_{s\_new} = \mathbf{C}\mathbf{E}_s^T \left(\mathbf{s}_{new} - \bar{\mathbf{s}}\right) \tag{9.16}$$

Applied to Motion and Surrogate Data

PCA can also be applied to both the motion data and the surrogate data separately, before fitting a correspondence model relating the motion PCA weights to the surrogate data PCA weights [40]. This should both help to remove noise from the motion data and remove co-linearities from the surrogate data. The motion estimate is then made using:

$$\mathbf{m}_{est} = \overline{\mathbf{m}} + \mathbf{E}_m \mathbf{C}\mathbf{E}_s^T \left(\mathbf{s}_{new} - \bar{\mathbf{s}}\right) \tag{9.17}$$

Used to Fit the Correspondence Model

PCA has also been used to actually fit the correspondence model $\mathbf{C}$ [6, 7, 15, 17, 19, 32, 70]. All the mean centred motion vectors and surrogate vectors are combined into a single data vector, $\mathbf{z}_t = \left[\widetilde{\mathbf{m}}_t^T, \widetilde{\mathbf{s}}_t^T\right]^T$ with length $N_m + N_s$. PCA is then performed on the $(N_m + N_s) \times N_t$ matrix $\mathbf{Z}$ which contains all the combined data vectors from all the N_t training samples.

$$\mathbf{Z} \approx \mathbf{E}_z \mathbf{W}_z \tag{9.18}$$

where the matrix $\mathbf{E}_z$ consists of the first K_z principal components. This equation can be split into two separate equations:

$$\widetilde{\mathbf{M}} \approx \mathbf{E}_{zm}\mathbf{W}_z \tag{9.19}$$

$$\widetilde{\mathbf{S}} \approx \mathbf{E}_{zs}\mathbf{W}_z \tag{9.20}$$

where $\mathbf{E}_{zm}$ and $\mathbf{E}_{zs}$ are constructed from the upper N_m and lower N_s rows of $\mathbf{E}_z$ respectively. Assuming the inverse matrix $\mathbf{E}_{zs}^{-1}$ exists $\mathbf{W}_z$ can be eliminated from the equations:

$$\widetilde{\mathbf{M}} \approx \mathbf{E}_{zm}\mathbf{E}_{zs}^{-1}\widetilde{\mathbf{S}} \tag{9.21}$$

and a motion estimate can be made from new surrogate signal values using:

$$\mathbf{m}_{est} = \overline{\mathbf{m}} + \mathbf{E}_{zm}\mathbf{E}_{zs}^{-1}\left(\mathbf{s}_{new} - \overline{\mathbf{s}}\right) \tag{9.22}$$

Note, for $\mathbf{E}_{zs}^{-1}$ to exist there must be at least as many rows as columns in $\mathbf{E}_{zs}$, i.e. the number of principal components used, K_z, cannot exceed the number of surrogate signals, N_s.

9.4.2.3 Other Fitting Methods

There have been a number of other fitting methods proposed in the literature. These include: ridge regression [32], canonical correlation analysis [20, 40], support vector regression [13, 14], multi-level B-spline approximation [18], Nelder-Mead optimisation [71], the Levenberg-Marquardt algorithm [29, 64], Fuzzy logic methods [64], and digital filtering [65]. Some of these fitting methods are general methods that can be used with many different correspondence models, and others are specialised methods designed for specific correspondence models. However, they have not been widely used and will not be discussed in detail. Interested readers should refer to the papers referenced above for more detail on these methods.

9.4.2.4 Fitting the Model Directly to the Imaging Data

Some authors have proposed methods which iterate between fitting the correspondence model directly to the (raw) imaging data and performing a motion compensated image reconstruction. This approach was originally proposed for MR imaging [52], where the correspondence model is fitted directly to the k-space data. The approach has also been used for 4D CT imaging [21, 23], where the model is fitted to the unsorted Cine CT volumes, and for CBCT imaging [44], where the model is fitted directly to the CBCT projection data.

For example, in the case of CBCT it can take a minute or more to acquire all the projections images that are required to reconstruct a full 3D volume. This means that the reconstructed volume will contain artefacts due to the respiratory motion, e.g. the tumour can appear blurred. If a surrogate signal is simultaneously acquired with the projection data then a correspondence model can be used to estimate the motion that

occurred when each projection was acquired. This can be used to perform a motion compensated image reconstruction which should not contain any motion artefacts (cf. Sect. 14.4). The correspondence model can be fitted using prior imaging data [37, 54, 69], but this assumes that the motion is the same during the CBCT acquisition as it was when the prior imaging data was acquired. Alternatively an iterative method can be used which fits the correspondence model directly to the CBCT projection data [44]. In this case a image reconstruction is first performed assuming no motion. This reconstructed volume can then be 'animated' according to the correspondence model, and projections can be simulated from the animated reconstructed volume and compared to the original projections. The correspondence model parameters are optimised to give the best match between the simulated projections and the original projections. The correspondence model can then be used to perform a motion compensated image reconstruction. This whole procedure can then be iterated, using the motion compensated image reconstruction to get a better estimate of the correspondence model parameters, and then using the better estimate of the correspondence model to improve the motion compensated image reconstruction.

9.4.2.5 Adaptive Fitting

If extra images of the internal motion can be acquired during a fraction of RT treatment then they can be used for 'adaptive fitting' [9–11, 25, 29, 57–61, 64]. For example the Cyberknife system (Accuray, Sunnyvale, California, USA) can acquire x-ray images of the patient in the treatment position, allowing images to be acquired during treatment as well as prior to treatment (for building the initial correspondence model). In theory x-ray images could be acquired continuously throughout treatment, removing the need for a correspondence model, but this would greatly increase the radiation dose to the patient due to imaging. Adaptive fitting means that the correspondence model is intermittently updated as new data becomes available. This allows the model to adapt to gradual changes in the relationship between the internal motion and the surrogate. This is usually done by discarding the oldest data in favour of the newly acquired sample and re-fitting the model. The newly acquired sample can also be used to check the accuracy of the current model, and if it drops below a predetermined tolerance the treatment can be paused while the model is completely rebuilt using new data. This approach can help the model react to more sudden changes in the motion-surrogate relationship.

9.4.3 Indirect Correspondence Models

Unlike the correspondence models described in the previous sections, indirect correspondence models do not directly relate the motion to the surrogate data. Instead, they parameterise the motion using one or more internal variables, and make estimates of the surrogate data as well as the motion data. When surrogate data is acquired during a procedure the internal variables are optimised to give the best match

between the estimated surrogate data and the measured surrogate data. This can be expressed as:

$$\mathbf{x} = \phi(\mathbf{v}) \tag{9.23}$$

$$\mathbf{v} = \arg\max_{\mathbf{v}} \; Sim\left(F\left(T\left(I, \mathbf{x}\right)\right), \mathbf{s}\right) \tag{9.24}$$

where $\phi(\mathbf{v})$ is an indirect correspondence model that estimates the motion, $\mathbf{x}$, from some internal variables, $\mathbf{v}$. I is a reference image, T is a function that transforms the reference image according to the motion estimate $\mathbf{x}$, F is a function which simulates the surrogate data from the transformed reference image, and *Sim* is a measure of similarity between the simulated surrogate data and the measured surrogate data, $\mathbf{s}$. The function F can vary: for the RT related models in the literature [36, 65] the function F simulates a CBCT projection from CT data, but for other applications F can simulate different types of data (e.g. an Ultrasound slice from MR data for cardiac interventions[31]).

The model $\phi(\mathbf{v})$ can also vary. Two models have been used in the literature: a linear model [36], and a B-spline model which incorporates an additional linear scaling of the motion estimates to allow for variations in the depth of breathing [65]. The linear model is fit to the motion data using PCA and the internal variables, $\mathbf{v}$, are the principal component weights. For the B-spline model the internal variables represent the respiratory phase and the depth of breathing. The B-spline model is fit to the motion data using digital filtering.

At treatment time when the surrogate data is available the internal variables are optimised to estimate the motion that best matches the CBCT projections. The two papers use different strategies to help the optimisation. Li et al. [36] use a prediction model (cf. Chap. 12) to obtain good initial guesses for the internal variables. Vandemeulebroucke et al. [65] assume the respiratory phase and depth of breathing vary smoothly with time, and then optimise their values for the CBCT projections from an entire breath cycle simultaneously.

9.5 Discussion and Conclusions

This chapter has reviewed the various different options that have been used in the literature for constructing respiratory motion model that relate the motion of the internal anatomy to one or more easily measured surrogate signals. There are a number of issues that should be considered when designing and using such models which will now be discussed.

9.5.1 Intra-Fraction Variation

If the models will be used to estimate the respiratory motion during a fraction of RT treatment then the models needs to be able to account for intra-fraction variations in the motion. The model can try and estimate the variations in the internal motion from variations in the surrogate signals. This can potentially be done by using two or more surrogate signals (one of which may be a derived surrogate signal such as the temporal derivative or a time delayed copy of a measured surrogate signal). However, the ability of such models to accurately estimate the motion and its variation over a time frame corresponding to a fraction of treatment has yet to be demonstrated.

The models can also be made to adapt to the intra-fraction variations by using an adaptive fitting approach as described in Sect. 9.4.2.5. This requires intermittent measurements of the internal motion during treatment, which may be difficult to acquire. An adaptive fitting approach is used in the Cyberknife system from Accuray, one of the only commercial products currently in routine clinical use that utilises correspondence models to estimate the internal respiratory motion. The fact that the accuracy of the models can be verified and the models can be updated during treatment may be one of the main reasons that the models are considered accurate and robust enough to be used in a clinical setting. However, it should be noted that in order to acquire intermittent measurements of the internal motion it is usually necessary to implant internal markers in or around the tumours so that they can be imaged during treatment.

9.5.2 Inter-Fraction Variation

If the models will be used to estimate the respiratory motion during different fractions of RT treatment then the models need to be able to account for inter-fraction variations. As with intra-fraction variation, the models could try and estimate the inter-fraction variations from variations in the surrogate signals. However, this could be very challenging as between different fractions of treatment there can be anatomical changes such as weight loss/gain and growing/shrinking tumour, and the patient can change the way that they breathe (e.g. from chest breathing to abdominal breathing). These inter-fraction variations can effect the relationship between the surrogate signal(s) and the internal motion, and can invalidate models built during a previous fraction of RT or from data acquired at planning [48].

Another approach for dealing with inter-fraction variations is to check the validity of the correspondence model prior to each fraction of treatment, and if necessary update or rebuild the model. This requires measurements of the internal motion just prior to each fraction of treatment, which may be difficult or impractical to acquire. Additionally, if the anatomy and/or motion have changed considerably from that seen during planning then the treatment plan may no longer be suitable and a new

plan may be required. This approach of 'Adpative RT' is an active area of research [63], and correspondence models that can be updated to account for inter-fraction variations could be a valuable tool for this work.

9.5.3 Reducing Variations

Breath-coaching and audio and/or visual feedback can be used to try and reduce intra- and inter-fraction variations in the respiratory motion. A number of methods have been presented in the literature [22, 26], and although they have generally shown promising results, they have only entered limited clinical use. The methods have usually been assessed using surrogate data, and it has been shown that they can reduce the variation of the surrogate signals. However, the effects of these methods on the internal motion, (and on the stability of the correspondence models) has not been fully assessed. The studies also show that using feedback is not beneficial for all patients, and in some cases the feedback can make the variation worse. Additionally, these methods will be of limited or no help with inter-fraction variations due to anatomical changes, as these cannot be accounted for just by having the patient breathing in a reproducible way. In conclusion, breath-coaching and feedback methods could potentially be very useful, particularly for gated or tracked treatments, but more work is required before firm conclusions can be drawn.

9.5.4 Amount of Data Used to Build and Validate Models

Ideally the internal motion data used to fit the motion model would sample all the types of variation that the model will be used to estimate (i.e. intra-fraction and inter-fraction variation). However, if ionising radiation is used for the imaging then this limits the number of images that can be acquired. Even if dose is not an issue (e.g. if MRI used) it may not be practical or possible to acquire data over the time frames required to sample all of the variation. The amount of data required will also be affected by the use of adaptive fitting methods. If extra data is acquired to update the models to adapt to intra- or inter-fraction variation then it is not necessary to sample all the variation in the initial data. More studies are required to determine the optimal amount of data to acquire in different circumstances in order to find a good trade off between scanning time and resources and model accuracy.

The data used to validate the models should also sample all expected types of variations in the motion. But, as with the data used to build the models it is often difficult to acquire sufficient data to thoroughly validate the models. When designing and investigating models they can be validated using retrospectively acquired data. However, if the models are to be used clinically then it is desirable to have some way of validating them prior to and during use. The difficulty in acquiring good validation data, and hence the lack of confidence in the accuracy of models,

could be one of the main reasons that such models have not yet been more adopted in clinical use.

9.5.5 Computation Time

The computation time required to build the motion models can vary greatly. It will depend heavily on the way the motion is measured from the imaging data and represented in the models, e.g. if deformable registrations of several large 3D volumes is required this can take from a few minutes to several hours depending on the algorithms and implementations used. The model fitting itself is generally quite fast but obviously depends on the method used and the amount of data being fit. Often in the literature the imaging data used to build the models is acquired several days before the model is needed (i.e. at treatment time), so the time required to build the models is not a major concern. However, if the models are to be updated or rebuilt for every fraction of treatment in order to account for inter-fraction variations then the time required to construct the models will be an important factor.

If the models are to be used to guide gated or tracked treatments then the motion estimates are required in 'real-time' so the computation time required to calculate them from the surrogate data will be important. Generally this can be done in a fraction of a second for most models, even if estimating a dense deformation field. Indirect models (see Sect. 9.4.3) may take longer as they need to optimise the motion estimate to best match the surrogate data. However, even if the motion estimates can be calculated quickly they do require some time, as does acquiring and processing the surrogate data and determining how to modify the treatment, so there will always be some degree of latency to treatment which will negatively affect the accuracy. To account for this latency methods that can predict the surrogate signals or the internal motion a short time in the future based on current and past measurements need to be used. These are discussed in detail in Chap. 12. One interesting approach is to combine the predict ahead method and the correspondence model into a single model which can predict the motion estimate a short time in the future from the current and past surrogate signals [29].

9.5.6 Conclusion

In conclusion respiratory motion models that can estimate the internal respiratory motion from easily acquired surrogate signals clearly have many potential uses. There have been a large number of different but closely related methods presented in the literature. This chapter has detailed and discussed the most commonly used methods from the literature, and considered some of the issues relevant to designing and using such motion models for RT. At the time of writing these models remain very much as research proposals, with relatively little clinical use or commercial

products. The continued output of research papers proposing or using such models, both for radiotherapy and other applications, would indicate that the models hold some promise, but more work is required to establish the accuracy and robustness of the models in clinical circumstances before they become more widely adopted.

References

1. Ahn, S., Yi, B., Suh, Y., Kim, J., Lee, S., Shin, S., Shin, S., Choi, E.: A feasibility study on the prediction of tumour location in the lung from skin motion. Br. J. Radiol. **77**, 588–596 (2004)
2. Beddar, A.S., Kainz, K., Briere, T.M., Tsunashima, Y., Pan, T., Prado, K., Mohan, R., Gillin, M., Krishnan, S.: Correlation between internal fiducial tumor motion and external marker motion for liver tumors imaged with 4D-CT. Int. J. Radiat. Oncol. Biol. Phys. **67**, 630–638 (2007)
3. Benchetrit, G.: Breathing pattern in humans: diversity and individuality. Respir. Physiol. **122**, 123–129 (2000)
4. Berbeco, R.I., Nishioka, S., Shirato, H., Chen, G.T.Y., Jiang, S.B.: Residual motion of lung tumours in gated radiotherapy with external respiratory surrogates. Phys. Med. Biol. **50**, 3655–3667 (2005)
5. Blackall, J.M., Ahmad, S., Miquel, M.E., McClelland, J.R., Landau, D.B., Hawkes, D.J.: MRI-based measurements of respiratory motion variability and assessment of imaging strategies for radiotherapy planning. Phys. Med. Biol. **51**, 4147–4169 (2006)
6. Cervino, L.I., Chao, A.K.Y., Sandhu, A., Jiang, S.B.: The diaphragm as an anatomic surrogate for lung tumor motion. Phys. Med. Biol. **54**, 3529–3541 (2009)
7. Cervino, L.I., Jiang, Y., Sandhu, A., Jiang, S.B.: Tumor motion prediction with the diaphragm as a surrogate: a feasibility study. Phys. Med. Biol. **55**, N221–N229 (2010)
8. Chi, P.C.M., Balter, P., Luo, D., Mohan, R., Pan, T.: Relation of external surface to internal tumor motion studied with cine CT. Med. Phys. **33**, 3116–3123 (2006)
9. Cho, B., Poulsen, P.R., Keall, P.J.: Real-time tumor tracking using sequential kV imaging combined with respiratory monitoring: a general framework applicable to commonly used IGRT systems. Phys. Med. Biol. **55**, 3299–3316 (2010)
10. Cho, B., Poulsen, P.R., Sawant, A., Ruan, D., Keall, P.J.: Real-time target position estimation using stereoscopic kilovoltage/megavoltage imaging and external respiratory monitoring for dynamic multileaf collimator tracking. Int. J. Radiat. Oncol. Biol. Phys. **79**, 269–278 (2011)
11. Cho, B., Suh, Y., Dieterich, S., Keall, P.J.: A monoscopic method for real-time tumour tracking using combined occasional x-ray imaging and continuous respiratory monitoring. Phys. Med. Biol. **53**, 2837–2855 (2008)
12. Colgan, R., McClelland, J., McQuaid, D., Evans, P.M., Hawkes, D., Brock, J., Landau, D., Webb, S.: Planning lung radiotherapy using 4D CT data and a motion model. Phys. Med. Biol. **52**, 5815–5830 (2008)
13. Ernst, F., Bruder, R., Schlaefer, A., Schweikard, A.: Correlation between external and internal respiratory motion: a validation study. Int. J. Comput. Assist. Radiol. Surg. **6**(5), 601–607 (2011)
14. Ernst, F., Martens, V., Schlichting, S., Beširević, A., Kleemann, M., Koch, C., Petersen, D., Schweikard, A.: Correlating chest surface motion to motion of the liver using ε-SVR—a porcine study. In: Proceedings of Medical Image Computing and Computer-Assisted Interventions (MICCAI), pp. 356–364 (2009)
15. Fayad, H., Clement, J.F., Pan, T., Roux, C., Rest, C.C.L., Pradier, O., Visvikis, D.: Towards a generic respiratory motion model for 4D CT imaging of the thorax. In: IEEE Nuclear Science Symposium Conference Record (2009)
16. Fayad, H., Pan, T., Clement, J.F., Visvikis, D.: Technical note: correlation of respiratory motion between external patient surface and internal anatomical landmarks. Med. Phys. **38**, 3157–3164 (2011)

17. Fayad, H., Pan, T., Roux, C., Rest, C.C.L., Pradier, O., Clement, J.F., Visvikis, D.: A patient specific respiratory model based on 4D CT data and a time of flight camera (TOF). In: IEEE Nuclear Science Symposium Conference Record (2009)
18. Fayad, H., Pan, T., Roux, C., Rest, C.C.L., Pradier, O., Visvikis, D.: A 2D-spline patient specific model for use in radiation therapy. In: Proceedings of the International Symposium on Biomedical Imaging (ISBI), pp. 590–593 (2009)
19. Fayad, H., Pan, T., Roux, C., Visvikis, D.: A generic respiratory motion model for motion correction in PET/CT. In: IEEE Nuclear Science Symposium Conference, Record, pp. 2455–2458 (2010)
20. Gao, G., McClelland, J., Tarte, S., Blackall, J., Hawkes, D.: Modelling the respiratory motion of the internal organs by using canonical correlation analysis and dynamic MRI. In: The First International Workshop on Pulmonary Image Analysis held at MICCAI 2008 (2008)
21. Geneser, S., Hinkle, J., Kirby, R., Wang, B., Salter, B., Joshi, S.: Quantifying variability in radiation dose due to respiratory-induced tumor motion. Med. Image Anal. **15**, 640–649 (2011)
22. George, R., Chung, T.D., Vedam, S.S., Ramakrishnan, V., Mohan, R., Weiss, E., Keall, P.J.: Audio-visual biofeedback for respiratory-gated radiotherapy: Impact of audio instruction and audio-visual biofeedback on respiratory-gated radiotherapy. Int. J. Radiat. Oncol. Biol. Phys. **65**(3), 924–933 (2006)
23. Hinkle, J., Fletcher, P.T., Wang, B., Salter, B., Joshi, S.: 4D MAP image reconstruction incorporating organ motion. In: Proceedings of the International Conference on Information Processing in Medical Imaging (IPMI), pp. 676–687 (2009)
24. Hoisak, J.D.P., Sixel, K.E., Tirona, R., Cheung, P.C.F., Pignol, J.P.: Correlation of lung tumour motion with external surrogate indicators of respiration. Int. J. Radiat. Oncol. Biol. Phys. **60**, 1298–1306 (2004)
25. Hoogeman, M., Prévost, B.J., Nuyttens, J., Levendag, J.P.P., Heijmen, B.: Clinical accuracy of the respiratory tumor tracking system of the cyberknife: assessment by analysis of log files. Int. J. Radiat. Oncol. Biol. Phys. **74**, 297–303 (2009)
26. Hughes, S., McClelland, J., Tarte, S., Blackall, J., Liong, J., Ahmad, S., Hawkes, D., Landau, D.: Assessment of respiratory cycle variability with and without training using a visual guide. Cancer Ther. **6**, 945–954 (2008)
27. Hughes, S., McClelland, J., Tarte, S., Lawrence, D., Ahmad, S., Hawkes, D., Landau, D.: Assessment of two novel ventilatory surrogates for use in the delivery of gated/tracked radiotherapy for non-small cell lung cancer. Radiother. Oncol. **91**, 336–341 (2009)
28. Ionascu, D., Jiang, S.B., Nishioka, S., Shirato, H., Berbeco, R.I.: Internal-external correlation investigations of respiratory induced motion of lung tumors. Med. Phys. **34**, 3893–3903 (2007)
29. Isaksson, M., Jalden, J., Murphy, M.J.: On using an adaptive neural network to predict lung tumor motion during respiration for radiotherapy applications. Med. Phys. **32**, 3801–3809 (2005)
30. Jolliffe, I.T.: Principal Component Analysis (Springer Series in Statistics). Springer, New York (2002)
31. King, A.P., Rhode, K.S., Ma, Y., Yao, C., Jansen, C., Razavi, R., Penney, G.P.: Registering preprocedure volumetric images with intraprocedure 3-D ultrasound using an ultrasound imaging model. IEEE Trans. Med. Imaging **29**(3), 924–937 (2010)
32. Klinder, T., Lorenz, C., Ostermann, J.: Free-breathing intra- and intersubject respiratory motion capturing, modeling, and prediction. In: Proceedings of SPIE Medical Imaging 2009: Image Processing (2009)
33. Klinder, T., Lorenz, C., Ostermann, J.: Prediction framework for statistical respiratory motion modelling. In: Proceedings of Medical Image Computing and Computer-Assisted Interventions (MICCAI) 2010, pp. 327–334 (2010)
34. Koch, N., Liu, H.H., Starkschall, G., Jacobson, M., Forster, K., Liao, Z., Komaki, R., Stevens, C.W.: Evaluation of internal lung motion for respiratory-gated radiotherapy using MRI: part I correlating internal lung motion with skin fiducial motion. Int. J. Radiat. Oncol. Biol. Phys. **60**, 1459–1472 (2004)

35. Li, G., Arora, N.C., Xie, H., Ning, H., Lu, W., Low, D., Citrin, D., Kaushal, A., Zach, L., Camphausen, K., Miller, R.W.: Quantitative prediction of respiratory tidal volume based on the external torso volume change: a potential volumetric surrogate. Phys. Med. Biol. **54**, 253–267 (2009)
36. Li, R., Lewis, J.H., Jia, X., Gu, X., Folkerts, M., Men, C., Song, W.Y., Jiang, S.B.: 3D tumor localization through real-time volumetric x-ray imaging for lung cancer radiotherapy. Med. Phys. **38**, 2783–2794 (2011)
37. Li, T., Schreibmann, E., Yang, Y., Xing, L.: Motion correction for improved target localization with on-board cone-beam computed tomography. Phys. Med. Biol. **51**, 253–267 (2006)
38. Li, T., Thorndyke, B., Schreibmann, E., Yang, Y., Xing, L.: Model-based image reconstruction for four-dimensional PET. Med. Phys. **33**(5), 1288–1298 (2006)
39. Liu, H.H., Koch, N., Starkschall, G., Jacobson, M., Forster, K., Liao, Z., Komaki, R., Stevens, C.W.: Evaluation of internal lung motion for respiratory-gated radiotherapy using MRI: part II—margin reduction of internal target volume. Int. J. Radiat. Oncol. Biol. Phys. **60**, 1473–1483 (2004)
40. Liu, X., Oguz, I., Pizer, S.M., Mageras, G.S.: Shape-correlated deformation statistics for respiratory motion prediction in 4D lung. In: Proceedings of SPIE Medical Imaging 2010 (2010)
41. Low, D.A., Parikh, P., Lu, W., Dempsey, J., Wahab, S., Hubenschmidt, J., Nystrom, M., Handoko, M., Bradley, J.: Novel breathing motion model for radiotherapy. Int. J. Radiat. Oncol. Biol. Phys. **63**, 921–929 (2005)
42. Low, D.A., Zhao, T., White, B., Yang, D., Mutic, S., Noel, C.E., Bradley, J.D., Parikh, P.J., Lu, W.: Application of the continuity equation to a breathing motion model. Med. Phys. **37**, 1360–1364 (2010)
43. Lu, W., Low, D.A., Parikh, P.J., Nystrom, M.M., El Naqa, I.M., Wahab, S.H., Handoko, M., Fooshee, D., Bradley, J.D.: Comparison of spirometry and abdominal height as four-dimensional computed tomography metrics in lung. Med. Phys. **32**, 2351–2357 (2005)
44. Martin, J., McClelland, J., Thomas, C., Wildermuth, K., Landau, D., Ourselin, S., Hawkes, D.: Motion modelling and motion compensated reconstruction of tumours in cone-beam computed tomography. In: Proceedings IEEE Workshop on Mathematical Methods in Biomedical Image Analysis (MMBIA) (2012)
45. McClelland, J.R., Chandler, A.G., Blackall, J.M., Ahmad, S., Landau, D., Hawkes, D.J.: 4D motion models over the respiratory cycle for use in lung cancer radiotherapy planning. In: Proceedings of SPIE Medical Imaging 2005: Visualization, Image-Guided Procedures, and Display (2005)
46. McClelland, J.R., Chandler, A.G., Blackall, J.M., Tarte, S., Hughes, S., Ahmad, S., Landau, D., Hawkes, D.J.: A continuous 4D motion model from multiple respiratory cycles for use in lung radiotherapy. Med. Phys. **33**, 3348–3358 (2006)
47. McClelland, J.R., Hawkes, D.J., Schaeffter, T., King, A.P.: Respiratory motion models: a review. Med. Image Anal. **16**(3), 642–661 (2012)
48. McClelland, J.R., Hughes, S., Modat, M., Qureshi, A., Ahmad, S., Landau, D.B., Ourselin, S., Hawkes, D.J.: Inter-fraction variations in respiratory motion models. Phys. Med. Biol. **56**, 251–272 (2011)
49. McClelland, J.R., Webb, S., McQuaid, D., Binnie, D.M., Hawkes, D.J.: Tracking differential organ motion with a breathing multileaf collimator: magnitude of problem assessed using 4D CT data and a motion-compensation strategy. Phys. Med. Biol. **52**, 4805–4826 (2007)
50. de Mey, J., de Steene, J.V., Vandenbroucke, F., Verellen, D., Trappeniers, L., Meysman, M., Everaert, H., Noppen, M., Storme, G., Bossuyt, A.: Percutaneous placement of marking coils before stereotactic radiation therapy of malignant lung lesions. J. Vasc. Interv. Radiol. **16**(1), 51–56 (2005)
51. Mori, S., Kanematsu, N., Mizuno, H., Sunaoka, M., Endo, M.: Physical evaluation of CT scan methods for radiation therapy planning: comparison of fast, slow and gating scan using the 256-detector row CT scanner. Phys. Med. Biol. **51**, 587–600 (2006)
52. Odille, F., Vuissoz, P.A., Marie, P.Y., Felblinger, J.: Generalized reconstruction by inversion of coupled systems (GRICS) applied to free-breathing MRI. Magn. Reson. Med. **60**(1), 146–157 (2008)

53. Plathow, C., Zimmermann, H., Fink, C., Umathum, R., Schbinger, M., Huber, P., Zuna, I., Debus, J., Schlegel, W., Meinzer, H.P., Semmler, W., Kauczor, H.-U., Bock, M.: Influence of different breathing maneuvers on internal and external organ motion: use of fiducial markers in dynamic MRI. Int. J. Radiat. Oncol. Biol. Phys. **62**, 238–245 (2005)
54. Rit, S., Wolthaus, J.W.H., van Herk, M., Sonke, J.J.: On-the-fly motion-compensated cone-beam CT using an a priori model of the respiratory motion. Med. Phys. **36**, 2283–2296 (2009)
55. Ruan, D., Fessler, J.A., Balter, J.M., Berbeco, R.I., Nishioka, S., Shirato, H.: Inference of hysteretic respiratory tumour motion from external surrogates: a state augmentation approach. Phys. Med. Biol. **53**, 2923–2936 (2008)
56. Rueckert, D., Sonoda, L.I., Hayes, C., Hill, D.L.G., Leach, M.O., Hawkes, D.J.: Non-rigid registration using free-form deformations: application to breast MR images. IEEE Trans. Med. Imaging **18**(8), 712–721 (1999)
57. Schweikard, A., Glosser, G., Bodduluri, M., Murphy, M.J., Adler, J.R.: Robotic motion compensation for respiratory movement during radiosurgery. Comput. Aided Surg. **5**, 263–277 (2000)
58. Schweikard, A., Shiomi, H., Adler, J.: Respiration tracking in radiosurgery. Med. Phys. **31**, 2738–2741 (2004)
59. Schweikard, A., Shiomi, H., Adler, J.: Respiration tracking in radiosurgery without fiducials. Int. J. Med. Robot. Comput. Assist. Surg. **1**, 19–27 (2005)
60. Schweikard, A., Shiomi, H., Fisseler, J., Dötter, M., Berlinger, K., Gehl, H.B., Adler, J.: Fiducial-less respiration tracking in radiosurgery. In: Proceedings of Medical Image Computing and Computer-Assisted Interventions (MICCAI) 2004, pp. 992–999 (2004)
61. Seppenwoolde, Y., Berbeco, R.I., Nishioka, S., Shirato, H., Heijmen, B.: Accuracy of tumour motion compensation algorithm from a robotic respiratory tracking system: a simulation study. Med. Phys. **34**, 2774–2784 (2007)
62. Shirato, H., Harada, T., Harabayashi, T., Hida, K., Endo, H., Kitamura, K., Onimaru, R., Yamazaki, K., Kurauchi, N., Shimizu, T., et al.: Feasibility of insertion/implantation of 2.0-mm-diameter gold internal fiducial markers for precise setup and real-time tumor tracking in radiotherapy. Int. J. Radiat. Oncol. Biol. Phys. **56**(1), 240–247 (2003)
63. Sonke, J.J., Belderbos, J.: Adaptive radiotherapy for lung cancer. Semin. Radiat. Oncol. **20**(2), 94–106 (2010) (Adaptive Radiotherapy)
64. Torshabi, A.E., Pella, A., Riboldi, M., Baroni, G.: Targeting accuracy in real-time tumor tracking via external surrogates: a comparative study. Technol. Cancer Res. Treat. **9**, 1–11 (2010)
65. Vandemeulebroucke, J., Kybic, J., Clarysse, P., Sarrut, D.: Respiratory motion estimation from cone-beam projections using a prior model. In: Proceedings of Medical Image Computing and Computer-Assisted Interventions (MICCAI), 2009 (2009)
66. Vedam, S.S., Kini, V.R., Keall, P.J., Ramakrishnan, V., Mostafavi, H., Mohan, R.: Quantifying the predictability of diaphragm motion during respiration with a noninvasive external marker. Med. Phys. **30**, 505–513 (2003)
67. Xu, Q., Hamilton, R.: A novel respiratory detection method based on automated analysis of ultrasound diaphragm video. Med. Phys. **33**, 916–921 (2006)
68. Yang, D., Lu, W., Low, D.A., Deasy, J.O., Hope, A.J., Naqa, I.E.: 4D-CT motion estimation using deformable image registration and 5D respiratory motion modeling. Med. Phys. **35**, 4577–4590 (2008)
69. Zhang, Q., Hu, Y.C., Liu, F., Goodman, K., Rosenzweig, K.E., Mageras, G.S.: Correction of motion artifacts in cone-beam CT using a patient-specific respiratory motion model. Med. Phys. **37**, 2901–2909 (2010)
70. Zhang, Q., Pevsner, A., Hertanto, A., Hu, Y.C., Rosenzweig, K.E., Ling, C.C., Mageras, G.S.: A patient-specific respiratory model of anatomical motion for radiation treatment planning. Med. Phys. **34**, 4772–4781 (2007)
71. Zhao, T., Lu, W., Yang, D., Mutic, S., Noel, C.E., Parikh, P.J., Bradley, J.D., Low, D.A.: Characterization of free breathing patterns with 5D lung motion model. Med. Phys. **36**, 5183–5189 (2009)

Chapter 10
Computational Motion Phantoms and Statistical Models of Respiratory Motion

Jan Ehrhardt, Tobias Klinder and Cristian Lorenz

Abstract Breathing motion is not a robust and 100 % reproducible process, and inter- and intra-fractional motion variations form an important problem in radiotherapy of the thorax and upper abdomen. A widespread consensus nowadays exists that it would be useful to use prior knowledge about respiratory organ motion and its variability to improve radiotherapy planning and treatment delivery. This chapter discusses two different approaches to model the variability of respiratory motion. In the first part, we review computational motion phantoms, i.e. computerized anatomical and physiological models. Computational phantoms are excellent tools to simulate and investigate the effects of organ motion in radiation therapy and to gain insight into methods for motion management. The second part of this chapter discusses statistical modeling techniques to describe the breathing motion and its variability in a population of 4D images. Population-based models can be generated from repeatedly acquired 4D images of the same patient (intra-patient models) and from 4D images of different patients (inter-patient models). The generation of those models is explained and possible applications of those models for motion prediction in radiotherapy are exemplified. Computational models of respiratory motion and motion variability have numerous applications in radiation therapy, e.g. to understand motion effects in simulation studies, to develop and evaluate treatment strategies or to introduce prior knowledge into the patient-specific treatment planning.

J. Ehrhardt (✉)
University of Lübeck, Lübeck, Germany
e-mail: ehrhardt@imi.uni-luebeck.de

T. Klinder · C. Lorenz
Philips Research Laboratories, Hamburg, Germany

J. Ehrhardt and C. Lorenz (eds.), *4D Modeling and Estimation of Respiratory Motion for Radiation Therapy*, Biological and Medical Physics, Biomedical Engineering,
DOI: 10.1007/978-3-642-36441-9_10,

10.1 Introduction

In radiation therapy, spatiotemporal 4D imaging opens up the possibility to identify respiratory induced tumor and organ motion of the thorax and upper abdomen (see Chaps. 2 and 3). The acquired 4D CT images and motion estimates are used to optimize radiotherapy plans in order to compensate for tumor and organ motion by (a) including the range of motion of the tumor by adding margins around the target volume or by (b) using prediction models together with respiratory gating or tumor tracking techniques. Different approaches for respiratory motion management during radiotherapy planning and treatment are discussed in detail in Chap. 11.

Deformable image registration (DIR) plays a central role in the developing of predictive 4D RT planning and treatment techniques. As shown in Chaps. 5–7, a variety of deformable registration algorithms have been used for respiratory motion estimation in recent years, and many of these algorithms have been shown to be accurate and robust (see Chap. 8). Registration algorithms can be used for the automatic contouring in 4D images [44, 57, 85, 86], the generation of surrogate-based models for motion prediction (see Chap. 9) or for the verification and optimization of treatment plans by 4D dose accumulation [1, 22, 62, 63, 88].

The motion of tumor and inner organs compromises highly target-conformal treatments in radiation therapy such as intensity-modulated radiotherapy (IMRT). Although different approaches for motion-adapted 4D treatment planning and 4D radiation dose delivery have been reported in the last years [1, 33, 35, 60, 72], the clinical implementation of 4D RT is currently still in its infancy. Besides a qualitative and quantitative understanding of the effects of tumor and organ motion, an essential question in the development of 4D RT systems is, how variations in depth and frequency of breathing effect the irradiation dose delivered. Simulation studies with flexible and realistic models of the human anatomy and physiology of respiratory motion have the potential to deliver valuable insights into respiration-related effects in radiation therapy. Such computerized anatomical and physiological models offer the possibility to investigate motion-related effects for variable anatomies, e.g. male, female, different body sizes etc., and for different motion patterns, e.g. changes in depth and frequency of breathing.

However, a major issue in 4D RT are day-to-day (inter-fractional) as well as breath-to-breath (intra-fractional) changes of the breathing. 4D CT images and the computed motion estimates are confined to the individual patient data and the breathing cycles represented in the 4D image data. This limitation leads to the presupposition that the breathing motion is reproducible throughout image acquisition, radiotherapy planning and the delivery process of treatment. However, it has been shown that breathing motion is not a robust and 100% reproducible process [50, 81]. A number of motion modeling approaches have been proposed to deal with these variations during the treatment process [34, 35, 64]. Because the direct imaging of the tumor motion during treatment is often not possible or laborious, many of these approaches use a surrogate signal, e.g. skin motion or spirometry measurements, that can be easily acquired during image acquisition and treatment, and relate this signal to the

internal respiratory motion. These techniques were discussed in detail in Chap. 9 and it was shown that motion variability can be modeled up to a certain amount. However, these modeling approaches are based on the individual 4D image data only, and the model will be confined by the motion present in these 4D images.

To improve the robustness of 4D RT systems with respect to possible motion variations, prior knowledge about the respiratory motion and its variabilities is needed. The aim of this chapter is to discuss the generation, representation and possible applications of such prior knowledge. We will discuss two different approaches: The first part of this chapter (Sect. 10.2) reviews mathematical and geometrical defined models of the human anatomy and physiology, commonly termed as software phantoms, and their applications in the context of 4D radiation therapy and beyond. Motion phantoms, like 4D MCAT, 4D XCAT or 4D VIP, are characterized with respect to different criteria, and we try to formulate limitations, requirements and future needs of these models.

The second part of this chapter is focused on statistical motion models generated from a population of 4D images acquired from one or several individuals. Sect. 10.3 details the main steps for the generation of such motion models and in Sect. 10.4 two different approaches for statistical modeling of organ motion are presented. In this context, representations of organ motion are discussed and the impact of motion representation on the statistical analysis. Methods for utilization of statistical motion models to predict breathing motion and evaluation methods are presented and first results for applications in radiation therapy are shown. The results are discussed in Sect. 10.5 and chances and limitations of statistical anatomical motion models are summarized.

10.2 Computational Motion Phantoms in Radiation Therapy

Computerized anatomical and physiological models play an important role in many areas of medical imaging and image processing. On the one hand, these models are used to evaluate, analyze, and tune image processing algorithms, on the other hand image processing algorithms make use of the anatomical prior-knowledge represented in the model. For example, computerized models and atlas-matching are already used in some commercial up-to-date radiation treatment planning systems (e.g. *Pinnacle*^{3} by Philips Healthcare to support the delineation of structures of interest, i.e. the organs at risk [32]).

Computational anatomical phantoms have been reported in the literature since the 1960s. In combination with Monte Carlo methods these computational models are used to simulate complex radiation interactions and energy depositions in the human body. Xu et al. [91] reported 121 different computational phantoms used in radiation protection dosimetry, imaging, radiotherapy etc. until 2009. A general overview of computational phantoms used in radiation dosimetry can be found in [94].

10.2.1 Characterization of Computational Motion Phantoms

Since the late 1990s the incorporation of physiology-dependent organ deformations, like heart-beat or respiratory motion, in computational phantoms is an active and growing area of research. The advantages of computational phantoms in contrast to physical phantoms are realism, flexibility and precision. Computational phantoms provide a ground truth to assess and validate medical image processing algorithms with respect to anatomical variations and with respect to respiration- or heart-beat-driven organ deformations. Furthermore, the models of physiological organ motions in the phantoms can be used as prior knowledge for motion estimation algorithms provided that these models are realistic and general.

Regarding the representation of anatomical structures, computational phantoms can be categorized into three types:

(1) In **stylized mathematical representations** the organ geometries are represented by simple geometrical shapes. Due to the mathematical definition, these models can easily be manipulated to reflect anatomical variations and organ motion. However the lack of realism makes these models unsuitable for applications in radiotherapy planning. An early model of this type is the mathematical Medical Internal Radiation Dosimetry (MIRD) phantom developed at the Oak Ridge National Laboratory (ORNL) in the 1960s [74] (see Fig. 10.1a). In the following

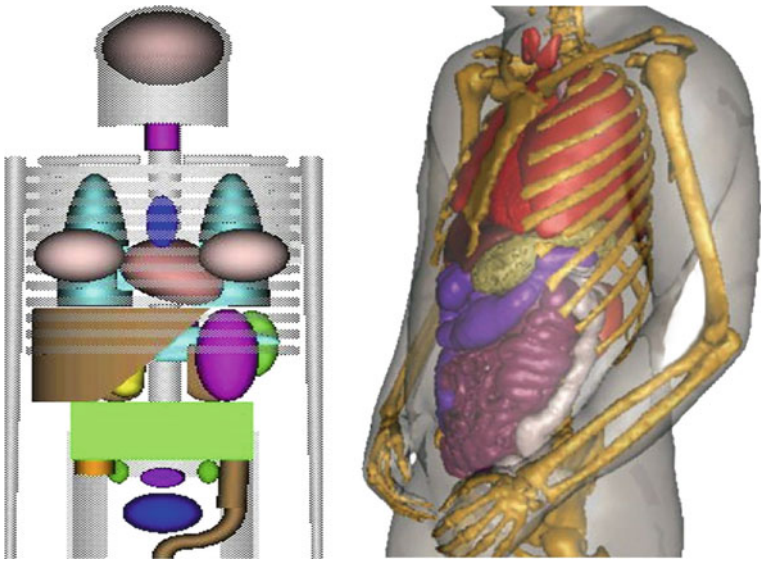

(a) stylized MIRD phantom **(b)** voxelbased VIP phantom

Fig. 10.1 Examples for different representation types of computational phantoms: **a** stylized mathematical representation in the MIRD phantom [13] and **b** voxel-based representation in the VIP-Man phantom [93]

decades a number of gender-, age-, and race-spezific stylized phantoms were developed by different groups in the world [13, 40, 96]. A prominent example of such a model for applications in medical imaging is the 3D and 4D mathematical cardiac torso phantom (MCAT) with gated patient organ information [66].

(2) **Voxel-based representations** are based on tomographic images acquired from real individuals. These models consist of segmented images with each voxel labeled with tissue type (e.g. air, bone, soft tissue) and/or anatomical information (lung, leg, liver). Xu [91] reported a total number of 74 phantoms constructed from tomographic data. One of the most detailed and well-known models is the VIP-Man phantom [93] generated from cross sectional photographs of the Visible Human Male cadaver [75] (see Fig. 10.1b). Voxel-based phantoms are very realistic, but they are limited in their abilities to model anatomical variations and organ motion. Furthermore, the necessary segmentation of anatomical structures takes a great amount of work.

(3) In **boundary representation models** (**BREPs**) the outer surface of the anatomical structures are represented by NURBS surfaces or polygon meshes. BREP models are generated from tomographic image data by transforming the voxel representations into smooth surface models. BREPs are able to provide more realistic models of the anatomy and cardiac and respiratory motions than stylized mathematical models, and on the the other hand they offer more flexibility than voxel representations by enabling analytical descriptions of organ deformations and variations. Consequently, most prominent examples of 4D computational phantoms, as the 4D NCAT, 4D XCAT and 4D VIP-Man phantoms [66, 70, 97], belong to this category of representations (see Fig. 10.2).

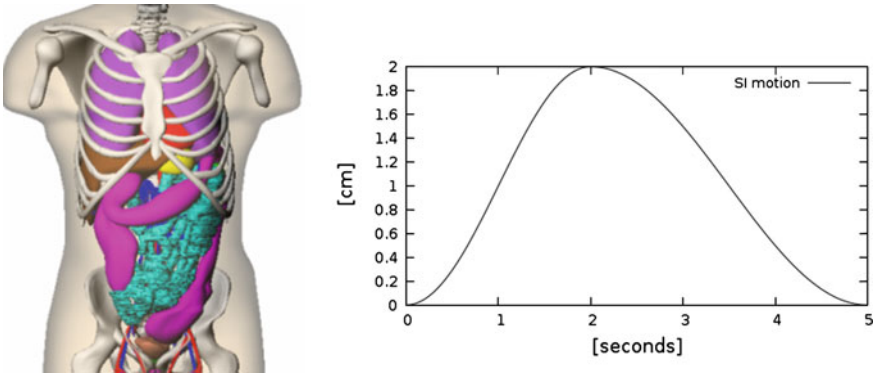

Fig. 10.2 Surface rendering of the NCAT phantom[1] [66] (*left*) and time-dependent motion of the diaphragm in z-direction (*right*)

[1] http://dmip1.rad.jhmi.edu/xcat/

10.2.1.1 Representation of Respiratory Motion in Computational Phantoms

While organ motion became a critical issue in medical imaging research and radiation therapy, the incorporation of motion information into the computational phantoms was forced. An example for including motion information into stylized phantoms is the 4D MCAT phantom developed for nuclear imaging research, specifically to study the effects of involuntary motion on SPECT and PET [55]. Besides a higher level of realism compared to the MIRD phantom, 4D MCAT models the beating heart and respiration. In this phantom, respiration was modeled by altering the parameters of the geometric models defining diaphragm, lungs, and ribs combined with a translation of heart, liver, stomach, spleen, and kidney.

Examples for BREP motion models are the 4D NCAT phantom, 4D XCAT phantom and 4D VIP phantoms [66–68, 90]. These phantoms consist of NURBS-based descriptions of organ surfaces and a software tool to convert the surfaces back to voxelized representations (e.g. simulated CT or SPECT images). NURBS are a very flexible mathematical description and the shape of the NURBS surface can be altered by applying transformations to the associated control points. The modeling of the respiratory motion is based on a respiratory gated 4D CT data set of a normal volunteer. A general motion model for each organ was formulated by tracking landmark points in different regions in the 4D CT data and the derived transformations are applied to the control points of the organ surfaces. By using transformation parameters that are functions of the time t, the control points are extended from 3D to 4D space. For example, in the 4D XCAT and 4D NCAT phantom the motion amplitude of the diaphragm is defined by the function:

$$\Delta^{z}_{dia}(t) = \begin{cases} 1.0 - \cos\left(\frac{\pi}{2}t\right) & 0 \leq t < 2 \\ 1.0 - \cos\left(\frac{\pi}{3}(5-t)\right) & 2 \leq t < 5 \end{cases} \tag{10.1}$$

for a respiratory phase of 5 s (2 s inhale, 3 s exhale) and a motion amplitude of 2 mm (see Fig. 10.2). By altering the parameters of this function, duration and amplitude of respiratory motion can be changed. Due to missing biophysical mechanics in the surface-based modeling approach, the organ transformations are adjusted laboriously to reflect motion dependencies, to avoid surface intersections and to work in concert. For example, the deformation of the lung surface depends on the motion of diaphragm and ribs, or the motion of sternum and skin depends on the rib motion.

10.2.2 Applications of Computational Motion Phantoms in Radiation Therapy

Early developments in computational phantoms (in the 1960s–1980s) are mostly related to health care physics with the goal to provide recommendations and guidance on radiation protection. So, many stylized and voxel-based phantoms were generated

according to the definition of the *reference man* by the International Commission on Radiological Protection (ICRP) [41]. Mostly, these phantoms are integrated with Monte Carlo methods to simulate radiation transport inside the body and to analyze the energy and patterns of radiation interactions.

In medical radiological imaging applications of computational phantoms are related to the evaluation of image reconstruction algorithms [58, 98], and image quality optimization [24, 31]. 4D motion phantoms were used for the demonstration of imaging artifacts related to cardiac and respiratory organ motions [71] and for the development of reconstruction techniques in 4D PET [42, 87] and 4D CBCT [7].

In radiation therapy, computational motion phantoms were used for the investigation of the spatial and temporal distribution of radiation in the patient body and to gain insight into methods for the management of organ motions. Three effects play a major role in radiation delivery to moving organs: *dose blurring*, *interplay effects* and *dose deformation* [10]. Dose blurring (or smearing) takes place at the field edges where the dose delivered to a point in the patient is smeared or reduced by the motion of this point in and out of the radiation beam resulting in an enlarged beam penumbra. It should be noted that the blurring results as a consequence of both intra- and inter-fractional movements. The interplay effect can occur if the treatment delivery involves moving parts, such as multileaf collimators in IMRT. The third motion effect, dose deformation, is related to the variation of the spatial dose distribution due to the motion of interfaces between structures of different densities. Simulation studies based on computational motion phantoms integrated with 4D Monte Carlo methods [47, 59] have been used for the investigation of these effects because they provide a precise and realistic ground truth with varying motion parameters, like lesion localization, amplitude or frequency of breathing. Zhang et al. [97] used the 4D VIP phantom to study the dosimetric effects of respiratory gating and 4D motion tracking for conformal treatment and IMRT treatment. McGurk et al. [47] investigated IMRT dose distributions as a function of diaphragm motion, lesion size and lung density using the 4D NCAT phantom.

Examples for other applications of computational phantoms in radiation therapy are risk assessment for RT-induced secondary cancer [61, 92], optimal selection of external beam directions [84], or assessment of organ doses in IGRT due to the use of kilovoltage cone-beam computed tomography (kV CBCT) and mega-voltage computed tomography (MV CT) [21].

10.2.3 Limitations of Computational Motion Phantoms

As shown in the last sections, computational phantoms designed to investigate the interaction of radiation with the human body have a remarkable long way. Numerous anatomically realistic computational phantoms were generated since the 1980s, however, the number of realistic computational phantoms incorporating organ motion is limited.

Computational motion phantoms developed so far suffer from limitations that degrade the applicability of these models in radiotherapeutic scenarios. First, the generation of these models is very time-consuming, requiring laborious steps for segmentation, surface modeling and incorporation of organ motion. Then, anatomy and motion information of these models are based on example data. Although some phantoms allow to alter parameters like body size and weight [24], an adaptation of these models to the individual patient anatomy is laborious and time-consuming. Furthermore, they do not have the ability to realistically simulate motion variations that may occur within the same individual or within a population [95]. Third, the motion-related deformation, displacement and interaction of organs is defined geometrically. This geometric definition does not fully take into account inner-organ deformations and the biophysical organ contact mechanics. For example, the respiration-related motion of abdominal organs is represented by a translation in the 4D NCAT phantom and the inner-lung deformation appears to be simplified (see Fig. 10.3).

In this context, Xu et al. identified two main directions in future research related to computational motion phantoms [95]: (1) the efficient generation of individual, patient-specific models and (2) the incorporation of biophysical modeling techniques to allow for realistic physics-based organ deformations. First steps to generate patient-specific computerized phantoms were presented by Segars et al. and Tward et al. by applying diffeomorphic registration algorithms to map a computational phantom to patient-specific data sets [69, 79]. Using this technique it is possible to create a detailed patient-specific model within 1–2 days. Biophysical modeling techniques were discussed in Chap. 4. As pointed out there, biophysical models provide powerful tools to simulate respiratory mechanics, however, recent studies show that in terms of accuracy and applicability these models were outperformed by DIR algorithms in motion estimation for individual 4D image data.

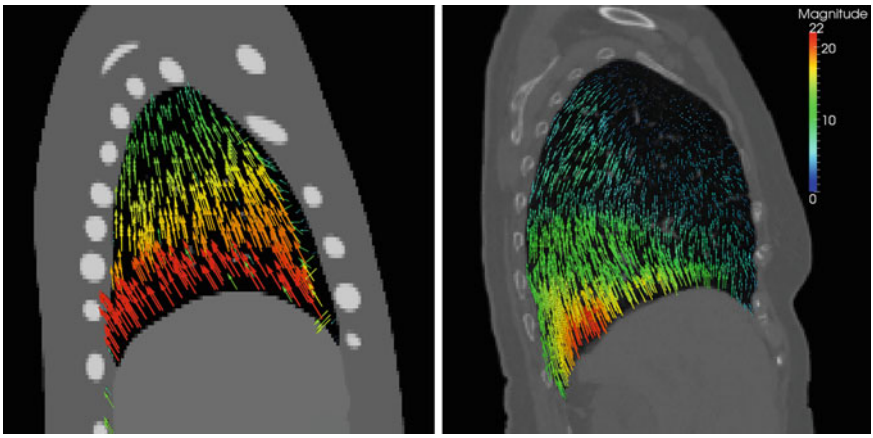

Fig. 10.3 Visualization of deformation fields showing the lung motion between end-inspiration and end-expiration. *Left* deformation field generated with the 4D NCAT phantom. *Right* deformation field estimated with DIR based on patient-specific 4D CT data (*right*)

In the rest of this chapter, we will discuss an alternative approach to generate respiratory motion models that have the potential to overcome some limitations of classical computerized anatomical phantoms.

10.3 Generation of Population-Based Motion Models

Computational motion phantoms discussed in Sect. 10.2 consist of a single reference data set or a small number of reference data sets build from example image data. In contrast, population-based motion models aim to represent anatomical variations and motion variations in a population of 4D images. These models consist of a "mean" representation and a variation model describing variations in the population. In medical image processing, this concept is used commonly for image segmentation and classification with statistical shape models [26].

By the increasing accessibility of 4D imaging techniques in the clinic, 4D patient data is more and more available, and the generation of population-based models of organ motion becomes feasible. As shown in Sect. 10.2, the generation of a single full-body motion model with a high level of anatomical detail is a time-consuming and laborious work. Population-based models rely on automatic algorithms to process a considerable amount of image data in the patient pool. With the availability of automatic segmentation and registration algorithms in the last years, the generation of such models was possible at least for a fraction of the body and a small number of organs, e.g. lung and/or liver [18, 38, 73].

Four steps are needed to generate population-based motion models: (1) acquisition of a set of 4D images, (2) the motion information is extracted from the 4D images, and (3) correspondence between the different images is established to (4) compute a statistical model of motion information in the data sets.

The 4D images can be acquired from different patients or from the same patient in repeated sessions. Figure 10.4 visualizes the principal idea of statistical inter-patient models. For intra-patient models the same four steps have to be performed and the correspondence model has to account for pose variations of the patient in the scanner.

In contrast to the geometrical definition of organ motion in stylized or BREP-based phantoms (see Sect. 10.2.1.1), the population-based approach generates a statistical description of the organ motion including a mean and variance. In the context of radiation therapy, such a model has the potential to allow for the estimation of uncertainties introduced by inter- and intra-fractional respiratory motion variability (see Sect. 10.4.3).

10.3.1 Variability of Respiratory Motion

Day-to-day and breath-to-breath variations of respiratory motion form an important problem in RT. To cope with such inter- and intra-fractional motion variations, a

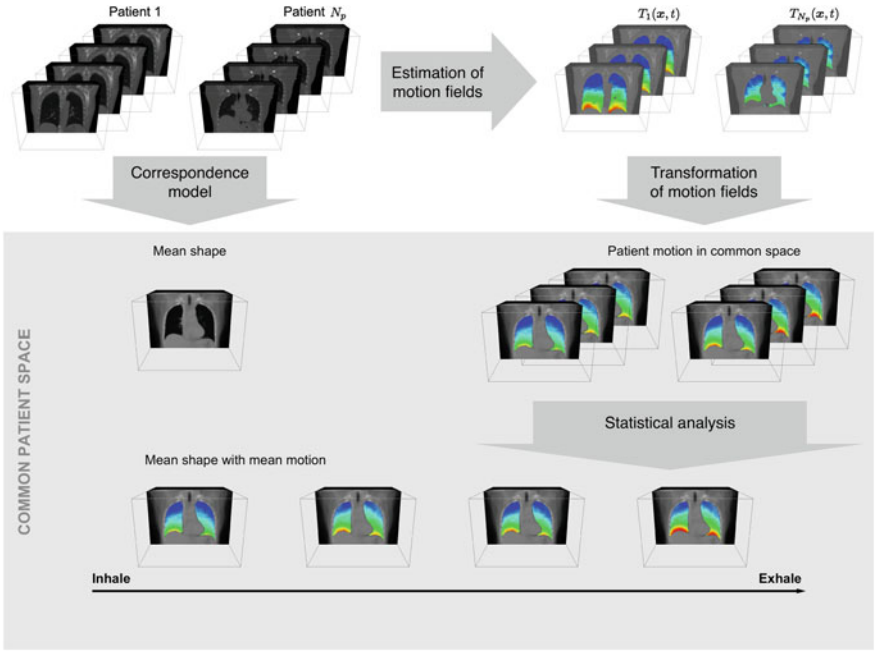

Fig. 10.4 Principal idea of statistical inter-patient models: Given is a set of 4D images from different patients, the motion information is extracted from the 4D images, and correspondence between the different patient anatomies is established to define a common coordinate space. The computed motion fields are transformed into the common coordinate space and a statistical model of the motion information in the data sets is computed

number of approaches were developed to relate internal motion to external surrogate signals, as skin motion (e.g. [65, 82]) or tidal volume and air-flow [43]. Those models were discussed in Chap. 9 in detail. The majority of these models use a single 4D data set representing a single breathing cycle and therefore, the representation of intra- and inter-fractional variations is limited. If repeatedly acquired 4D images are available for the patient, a population-based intra-patient model can be build from the ensemble of motion data sets and can therefore cover a broader range of motion patterns.

However, the availability of multiple 4D image data sets for a single patient is very limited, and the questions raises whether motion information of different patients can be combined to generate prior knowledge about respiratory lung motion. In Fig. 10.5, the magnitude of respiratory lung motion between maximum inhale and maximum exhale is visualized color-coded for different patients. As shown in this figure, there is an anatomical variation regarding shape and size of the lungs and a variation in magnitude and pattern of respiratory motion, but the overall pattern of respiratory motion of different patient is similar: large deformations near diaphragm and small deformations near the tip of the lung. Thus, inter-patient population-based modeling

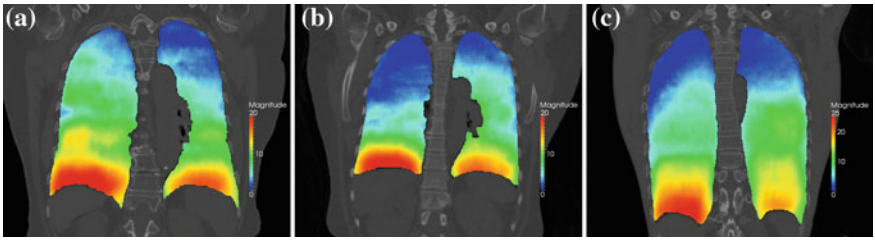

Fig. 10.5 Examples of computed breathing motion displacement fields. The magnitude of the estimated lung motion between end expiration and end inspiration is visualized color coded (in mm). The lung geometry and motion amplitude differ between patients, motion patterns appear to be similar

approaches rely on the assumption, that breathing dynamics works similarly for all patients and useful statistical information can be generated.

Accordingly, population-based models can be roughly divided into models derived from ensembles of 4D images of the same patient or from ensembles of 4D images from different patients. For models of the first category, 4D images have to be acquired repeatedly for one patient, for example 4D CT data set repeatedly acquired during the course of treatment were used in [38], or 4D CT images and additional 4D MR images can be acquired before the treatment alternatively [8, 14, 36]. For models of the second category, 4D images of different patients are combined to one motion model with the advantage that no additional effort, costs and irradiation dose is needed for each patient, and the pool of available data for model generation growth continuously. All steps shown in Fig. 10.4 have to be performed for both types of models. However, in the case of subject-specific models rigid or affine transformations can be used to compensate for different positions of the subject in the CT or MR scanner, whereas establishing correspondence between different subjects is a challenging task due to anatomical variations and missing correspondences in the presence of pathological structures.

10.3.2 Estimation of Motion Fields

Given is a pool of N_p 4D images (from one or different patients) to generate the population-based motion model. Each 4D image in the pool consists of a sequence of N_j 3D images $I_{p,j} : \Omega_p \rightarrow \mathbb{R}$ $(p = 1, \ldots, N_p)$ acquired at different phases $j = 0, \ldots, N_j - 1$ of the breathing cycle, as introduced in Chap. 2.

For each 4D data set, the motion represented in the images has to be estimated. Registration-based algorithms for motion estimation are discussed in Chaps. 4–7. Depending on the choice of registration method, different representations of the motion information are generated. Intensity-based registration approaches (Chaps. 6 and 7) compute **dense motion fields** where deformations are given for each voxel.

Surface- and feature-based registration approaches as introduced in Chap. 5 generate **point-based representations** where displacements are given for distinct feature-points or sampled points on the organ surface only. However, both representations can be transferred into each other by sampling the dense motion field at a subset of voxels or by an interpolation of sparse motion fields (see Chap. 5.4).

The computed motion fields for the p-th 4D image define transformations $T_p(\boldsymbol{x}, t) : \Omega_p \times \mathbb{R} \to \Omega_p$ of the specific coordinate system Ω_p modeling the motion-related organ deformation for a time t. In most approaches, these transformations are given only for discrete time-points t_j associated with a state $j = 0, \ldots, N_j - 1$ in the breathing cycle. In surface- or landmark-based representations, the deformations are known only for distinct points.

As discussed in Chap. 9, in most approaches, the organ deformations are expressed with respect to a baseline image for a reference point in the breathing cycle, e.g. with respect to $I_{p,0}$, and $T_p(\boldsymbol{x}, t_j)$ describes the organ deformation between breathing phase 0 and phase j. The transformation $T_p(\boldsymbol{x}, t)$ is usually represented by displacement vectors $T_p(\boldsymbol{x}, t) = \boldsymbol{x} + \boldsymbol{u}_p(\boldsymbol{x}, t)$ (defined voxel-wise or for distinct points only) and the statistical analysis of organ deformations is based on the displacement vectors $\boldsymbol{u}_p(\boldsymbol{x}, t_j)$ at discrete phases j. Other representations of organ deformations are possible. McClelland et al. presents a time-continuous motion representation of $T_p(\boldsymbol{x}, t)$ based on a B-spline approximation [46]. Ehrhardt et al. proposes the use of diffeomorphisms for motion representation and statistics [18], and Klinder et al. compares the application of explicit point coordinates, displacements, and fourier descriptors for motion modeling [39]. The different representations have different advantages and disadvantages and at present, it is not known in advance which is the most suitable representation for a given problem. We will discuss the differences in point-based representations by displacement vectors and voxel-based representations by diffeomorphisms in more detail in Sects. 10.4.1 and 10.4.2. Examples for population-based motion models and their applied motion estimation algorithms and motion representations are summarized in Table 10.1.

10.3.3 The Correspondence Problem

The motion-related organ deformation of each subject (data set) is described within its own reference frame. This reference frame is defined by the imaging process, i.e. the computed transformations T_p and T_q of two subjects p and q are defined with respect to the underlying image spaces Ω_p and Ω_q. This is the case too, if the same subject is imaged twice due to the different positions of the subject in the CT or MR scanner.

To analyze the spatiotemporal variability in a population, we need to compare the deformation of organ-shapes over time and across subjects. In order to compare two deformation functions T_p and T_q *anatomical correspondence* between the organ shapes has to be defined, i.e. the comparison of $T_p(\boldsymbol{x}_p, t)$ and $T_q(\boldsymbol{x}_q, t)$ only makes sense if $\boldsymbol{x}_p$ and $\boldsymbol{x}_q$ refer to identical anatomical localizations. Furthermore,

Table 10.1 Population-based respiratory motion models used for applications in radiation therapy

Year	Reference	Organ and data	Motion estimation algorithm	Motion representation	Correspondence model	Statistical model
2004	Sundaram et al. [76]	Lung (2D+t MR)	Intensity-based registration	Voxel-based, displacement vectors	Explicit, non-linear registration between all subjects	Average lung motion model
2007	von Siebenthal et al. [73]	Liver (4D MRI)	Intensity-based registration	Point-based, displacement vectors at landmarks inside liver	Implicit, manual fitting of a liver model and landmark extraction, rigid alignment of all data sets before statistical analysis	PCA (liver drift model)
2008	Ehrhardt et al. [19]	Lung (4D CT)	Intensity-based registration	Voxel-based, displacement vectors	Explicit, non-linear registration to an atlas, affine alignment of motion vectors	Mean motion
2009	Klinder et al. [38]	Lung (4D CT)	Surface-based registration	Point-based, displacement vectors at mesh positions	Implicit, fitting a surface mesh to all data sets, affine alignment of motion vectors	PCA (intra- and inter-patient)
2009	Nguyen et al. [51]	Liver (4D CT)	FEM-based registration (MORFEUS)	Point-based, displacement vectors at the nodes of FE mesh	Implicit, fitting a FE mesh to all subjects, rigid alignment of motion vectors	Mean motion
2010	He et al. [25]	Lung (4D CT)	Joint segmentation and registration framework	Point-based, displacement vectors at landmark positions	Explicit, non-linear registration to a template image, affine alignment of motion vectors	K-PCA
2011	Ehrhardt et al. [18]	Lung (4D CT)	Diffeomorphic, intensity-based registration	Voxel-based, diffeomorphism represented by static velocity field	Explicit, diffeomorphic registration to an atlas, non-linear alignment of motion vectors	Mean motion (diffeomorphic)
2012	Preiswerk et al. [54]	Liver (4D MRI)	Intensity-based registration	Point-based, displacement vectors at feature points inside the liver	Implicit, manual fitting of a liver model and landmark extraction, rigid alignment of motion vectors	PCA

a *temporal correspondence* is needed this means $T_p(\boldsymbol{x}_p, t_j)$ and $T_q(\boldsymbol{x}_q, t_j)$ have to refer to the same breathing state for given t_j. Several choices can be made to define temporal consistency, e.g. by (i) mapping selected time points in the breathing cycle (e.g. end-expiration) and regular partitioning in between (phase-based sorting), or by (ii) mapping according to the percentage lung volume change (amplitude-based sorting), or by (iii) mapping according to a morphological configuration, e.g. diaphragm position. The choice depends on the application purpose of the breathing model and on quantities that can be measured during application. Here, we assume that the temporal consistency is ensured during the image acquisition, e.g. by sorting into corresponding bins for all subjects (see Chaps. 1–3), or in a preprocessing step, e.g. by using a method described by Sundaram et al. [76, 77].

Anatomical Correspondence

Statistical motion analysis in a pool of N_p 4D data sets necessitate to establish correspondence between all subjects. One approach is to extract corresponding landmark positions in all subjects, as proposed by Siebenthal et al. and Arnold et al. for a liver motion model [2, 73]. Klinder et al. propagate a structurally identical deformable surface mesh to all patient data sets [38]. This surface mesh was generated by averaging lung segmentations of training data sets [9] and is used for lung segmentation and motion estimation simultaneously. Nguyen et al. generate a finite element mesh of the liver from combined binary mask of training data sets. The finite element mesh is fitted to each patient data sets using a FEM-based deformable surface registration [51]. We refer to those approaches by *implicit correspondence*, because identical sets of features (landmarks or surface meshes) are propagated to each 4D data set in the population, and correspondence is given by the mapping of corresponding features. But implicit correspondence alone is not sufficient for a statistical analysis. As shown in Fig. 10.6, the orientation of structures inside the image space influences the direction of the displacement vectors. Therefore, it is necessary to bring the 4D images in the population into a common coordinate system before a statistical analysis.

In contrast, *explicit correspondence* is defined by mapping functions $\Psi_{p\to q}$ and $\Psi_{q\to p} = \Psi_{p\to q}^{-1}$ between the reference frames Ω_p and Ω_q computed by registra-

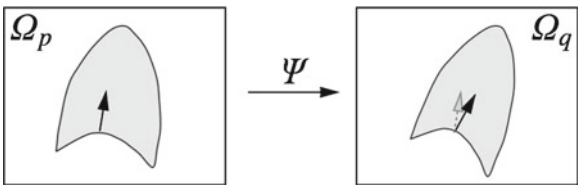

Fig. 10.6 Transformation of motion fields between two patient coordinate systems Ω_p and Ω_q. Beside the anatomical correspondence, an adjustment and reorientation of the motion vectors is performed with Eq. (10.2) to account for position, size, and shape variations

tion algorithms. Because deformations in 4D image sequences are often expressed with respect to the baseline image $I_{p,0}$, several approaches applying correspondence between 4D image sequences of different subjects by a 3D registration of baseline images $I_{p,0}$ and $I_{q,0}$ [12, 18, 56]. Some explicit correspondence methods select one target to which all other subjects are registered or deformed, e.g. [25]. This, however biases the registration result to the selected shape. Different strategies were proposed to minimize this bias, e.g. by selecting a subject that lies closest to the mean shape [52], or by evolving a mean shape [23, 29]. Other explicit approaches aim to take into account the full temporal information to register two 4D image sequences. Peyrat et al. [53] proposes a 4D–4D registration by computing deformations between any pair of scans of two different subjects at the same time-point simultaneously via a multi-channel co-registration. A more general approach proposed by Durrleman et al. does not require that subjects are scanned the same number of times or at the same time points, and computes spatial and temporal correspondences simultaneously [16].

It is obvious that anatomical correspondence for intra-patient models is easier to define, whereas inter-patient registration has to deal with high-dimensional transformations and varying anatomies. A further shortcoming of current methods for inter-subject correspondences is that the accuracy of these methods is widely unknown. Although, a number of attempts exists to assess accuracy and robustness of registration techniques for intra-patient registration and motion estimation, e.g. the MIDRAS and EMPIRE10 studies [11, 49] (see Chap. 8), similar evaluation studies for inter-subject registration are missing. One reason is the difficulty to define an accurate ground truth: due to the anatomical variability, definition of a sufficiently large number of corresponding landmarks between subjects is a challenging task. The assessment of inter-patient registration methods is an ongoing topic of research, but available evaluations suggest an accuracy in the order of the inter-observer variability [27, 37].

Transformation of the Motion Fields T_p

The computed motion fields have to be transformed into a common coordinate system before a statistical analysis to eliminate subject-specific orientation information (see Fig. 10.6). A general formulation is given as follows: Given a transformation $T_p : \Omega_p \rightarrow \Omega_p$ and a homeomorphism $\Psi_{p\rightarrow q} : \Omega_p \rightarrow \Omega_q$ between the coordinate systems Ω_p and Ω_q, then $T_{p\rightarrow q} : \Omega_q \rightarrow \Omega_q$ is the topologically conjugate of T_p, if

$$T_{p\rightarrow q} = \Psi_{p\rightarrow q} \circ T_p \circ \Psi^{-1}_{p\rightarrow q}. \tag{10.2}$$

Equation (10.2) is used to transfer the deformation T_p from image space Ω_p to image space Ω_q. If $\boldsymbol{y} = T_p(\boldsymbol{x}) \in \Omega_p$ and $\boldsymbol{y}', \boldsymbol{x}'$ are the corresponding points in Ω_q, then $\boldsymbol{x}'$ is mapped to $\boldsymbol{y}'$ by the transformation $T_{p\rightarrow q}$: $\boldsymbol{y}' = T_{p\rightarrow q}(\boldsymbol{x}')$. The necessary inter-subject transformation $\Psi_{p\rightarrow q}$ can be any invertible (diffeomorphic) transformation. A schematic sketch to clarify this transformation is shown in Fig. 10.6.

A common solution for the transformation of motion fields T_p is to compute an affine alignment of the organ shapes to eliminate differences in orientation and size [19, 25, 38], other approaches only eliminate orientation information using rigid transformations [51, 73]. Although this is an adequate approach for intra-patient models, anatomical variances between subjects are not adequately represented by affine transformations and the resulting statistical deformation models will be influenced by local anatomical variations in cases of population-based inter-subject models. If explicit correspondences were computed by deformable registration, the resulting transformations can be used in Eq. (10.2) to transform the motion fields, too [18].

10.3.4 Model Computation

Assuming a common reference coordinate system Ω_{ref} for spatial correspondence and a temporal correspondence of all subjects in the data pool, statistics of the deformations can be computed. The aim of the statistical analysis is to generate a model capturing the mean and the variability in the pool of training data sets. Most approaches use a principal component analysis (PCA) to generate such a model.

PCA-Based Modeling

Suppose that a set of N_p subject-specific motion fields mapped into the reference coordinate system are given: $T_{p\to ref}(\boldsymbol{x}, t) : \Omega_{ref} \times \mathbb{R} \to \Omega_{ref}, (p = 1, \ldots, N_p)$, where $T_{p\to ref}(\boldsymbol{x}, t) = \boldsymbol{x} + \boldsymbol{u}_{p\to ref}(\boldsymbol{x}, t)$ is defined by displacement fields. For PCA the motion fields have to be converted into a vectorial representation, therefore, a spatial and temporal discretization is necessary. Assuming N_j respiratory phases besides the reference phase t_0 and N_m defined sampling positions, a vectorial representation of $T_{p\to ref}$ for a phase j is given by sampling the displacement fields and concatenating the sample positions:

$$\boldsymbol{U}_{p,j} = [\boldsymbol{u}_{p\to ref}(\boldsymbol{x}_1, t_j), \cdots, \boldsymbol{u}_{p\to ref}(\boldsymbol{x}_i, t_j), \cdots, \boldsymbol{u}_{p\to ref}(\boldsymbol{x}_{N_m}, t_j)]^{\mathrm{T}},$$

where each $\boldsymbol{u}_{p\to ref}(x_i, t_j) = [u_{x,p\to ref}(\boldsymbol{x}_i, t_j), u_{y,p\to ref}(\boldsymbol{x}_i, t_j), u_{z,p\to ref}(\boldsymbol{x}_i, t_j)]$ is the vector of its components. The phase-specific vectors can now be arranged in a $3N_mN_j$-dimensional motion vector for each of the N_p 4D images

$$\boldsymbol{U}_p = [\boldsymbol{U}_{p,1}, \cdots, \boldsymbol{U}_{p,j}, \cdots, \boldsymbol{U}_{p,N_j}]^{\mathrm{T}}. \tag{10.3}$$

The intra-subject modeling approaches discussed in Chap. 9 reflect the variability in the motion fields between different phases of the respiratory cycle. In contrast, the modeling approach discussed here aims to reflect the variability of the respiratory

motion (in all phases) between individuals. Given N_p vectors $\boldsymbol{U}_p$, $p = 1, \ldots, N_p$, a population mean is computed by averaging the displacements at each landmark position

$$\bar{\boldsymbol{U}} = \frac{1}{N_p} \sum_{p=1}^{N_p} \boldsymbol{U}_p, \tag{10.4}$$

and a PCA is performed by computing eigenvalues and eigenvectors of the sample covariance matrix

$$\boldsymbol{\Sigma} = \frac{1}{N_p - 1} \sum_{p=1}^{N_p} (\boldsymbol{U}_p - \bar{\boldsymbol{U}})(\boldsymbol{U}_p - \bar{\boldsymbol{U}})^{\mathrm{T}}. \tag{10.5}$$

The eigenvectors represent the principal modes of variation $\boldsymbol{\phi}_k$ and intuitively, each eigenvalue λ_k represents how much variation or variance in the data is captured by the corresponding eigenvector. In practice, the eigenvalues usually decrease very fast, and a given motion vector $\boldsymbol{U}_p$ can be approximated by a linear combination of the eigenvectors corresponding to the largest eigenvalues (e.g. $\kappa = 0.9$):

$$\boldsymbol{U}_p \approx \bar{\boldsymbol{U}} + \sum_{k=1}^{K} w_k \boldsymbol{\phi}_k, \quad \text{with} \quad \sum_{k=1}^{K} \lambda_k \geq \kappa \sum_{k=1}^{\operatorname{rank} \boldsymbol{\Sigma}} \lambda_k.$$

The size of the vectors $\boldsymbol{U}_p$ depends on the number of breathing phases and sampled point landmarks, this means the covariance matrix $\boldsymbol{\Sigma}$ can be very large with dimensions $3N_m N_j \times 3N_m N_j$. However, the eigenvectors $\boldsymbol{\phi}_k$ of $\boldsymbol{\Sigma}$ can be computed efficiently, see e.g. [17], allowing for a large set of landmarks or yet to use voxel-based representations with every image voxel as sampling point. The mean lung motion generated from a voxel-based representation is shown in Fig. 10.7. As

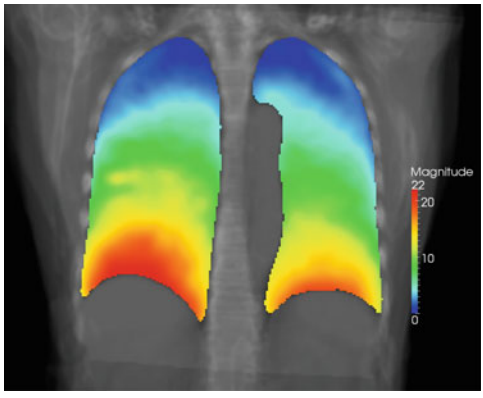

Fig. 10.7 Visualization of the mean lung motion from 12 subjects. The magnitude of the mean deformation between maximum inhalation and maximum exhalation is shown *color-coded* inside the lung. The mean deformation model shows a typical respiratory motion pattern. See [18] for details

discussed in Sect. 10.3.2, other representations of motion information are possible, and $\boldsymbol{U}_p$ is composed of the chosen representatives in these cases, e.g. absolute point coordinates or fourier coefficients [39].

Other Approaches

A number of population-based approaches are restricted to the computation of the mean motion [18, 19, 51, 76]. Motion variabilities are represented by scaled versions of this mean motion model. Interestingly, desirable accuracies were achieved using those models for patient motion prediction [18, 51]. A continuous formulation of the mean motion computation for diffeomorphic transformations was recently given by Ehrhardt et al. [18] (see Sect. 10.4.2). In contrast to the PCA-based approach, spatial discretization and vectorial representation can be renounced, and diffeomorphic representations avoid the possibilities of singularities in the model-generated motion fields.

Recently, He et al. presented the generation of a population-based model based on Kernel Principal Component Analysis (K-PCA) [25]. This motion model was used to estimate the lung motion from the motion of fiducial for patients during an image-guided lung intervention.

An overview of population-based models of respiratory motion with applications in radiation therapy is given in Table 10.1.

10.4 Applications of Population-Based Models

Statistical modeling of respiratory motion based on populations of 4D images is capable of providing valuable prior knowledge in many fields of applications. In this section, two examples of such models with possible applications in the fields of radiation therapy are discussed. We present two conceptually different modeling approaches and debate their applications for patient-specific motion prediction in the radio-therapeutic context.

10.4.1 Statistical Modeling of Organ Motion Using Surface-Based Registration

In this section, registration for both motion field estimation as well as for inter-patient registration relies on surface-based registration. Sparse correspondences are at first established by adapting a deformable surface mesh to the images. As the mesh topology is preserved during adaptation, anatomical point correspondences are assumed to be preserved. A dense motion field is finally obtained by thin-plate

spline interpolation. The calculated registrations are then used to build a statistical model. The general workflow follows the concept from Sect. 10.3.

10.4.1.1 Motion Estimation

Lung motion fields are derived from the 4D-CT images using the surface-based tracking technique proposed in [6] which is also explained in Chap. 5. For each 4D-CT image, the lungs are at first segmented in one selected reference phase and a patient-specific lung surface mesh is obtained by triangulating the thresholded image (cf. in Sect. 5.3.5). The meshes cover the outer border of the lungs but also inside structures as the surfaces of the pulmonary vessel tree and potential tumor surfaces. The surface mesh is then tracked through all phases of the 4D-CT data set using deformable mesh adaptation as described in Sect. 5.3.5. By propagating a topologically identical patient-specific lung surface mesh through all phases, anatomical point correspondences are assumed to be preserved. The trajectories of corresponding points of the adapted meshes thus provide a sparse motion field, which is finally interpolated using thin-plate-splines.

The method has been intensively validated, e.g. in [30], and shown to provide plausible motion fields with a similar accuracy compared to other registration schemes. Furthermore, as the tracking scheme allows for tangential motion, sliding at the rib-lung interface can be handled. The output are continuous motion fields $T_p(\boldsymbol{x}_p, t_j)$ between a selected reference phase q and all other phases $j \in \{1, 2, \ldots, N_j\}$.

10.4.1.2 Establishing Correspondences

To express the motion fields from different patients in one common reference system, inter-patient correspondences need to be defined between the selected reference phases of the various patients. However, establishing a dense anatomical correspondence of the lungs between patients is difficult as inside structures like the airways or the vessel tree show varying topologies across patients. For this reason, we estimate the inter-patient correspondences on the basis of the outer surface of the lungs. In each selected reference phase of each patient, an average shape model covering the outer lung surfaces [9] is adapted. As the mesh is restricted during adaptation to be most similar to the initial model, we again assume that vertex correspondences provide sparse anatomical correspondences. Based on corresponding vertices on the outer surface, a thin-plate spline interpolation provides dense transformations. Knowing the N_P continuous transformations $\Psi_{p \to ref}$ $p \in \{1, 2, \ldots, N_P\}$ from N_P patients to the shape model space allows for representing the motion fields in one common reference space.

10.4.1.3 Statistical Motion Model Representation

For statistical modeling, a vectorial representation is chosen. Prerequisite is a set of motion fields expressed in the common model space. In order to reduce the computational effort, we subsample the model space by considering a reduced set of vertices on the outer surface and a regular grid inside the lung model space sampled by 5 mm isotropically. In total, we only consider the motion at around 1000 locations per lung. Figure 10.8 illustrates the representation. To re-estimate the continuous transformation, thin-plate spline interpolation based on the subset is again chosen. The displacement of a set of N_m locations in model space can now be expressed as defined in Eq. (10.3) resulting in a vector $\boldsymbol{U}_p$ for patient p. This representation can be considered as a deformation model that gives the deformation of a set of landmarks over the breathing cycle. The set of N_p corresponding vectors $\boldsymbol{U}_p$ can then combined in a matrix $\boldsymbol{U} = [\boldsymbol{U}_1|\boldsymbol{U}_2|\ldots|\boldsymbol{U}_{N_p}]$ and statistical analysis, as, e.g. principal component analysis (PCA) can be applied on the covariance matrix (see Eq. (10.5)).

The statistics covered in $\boldsymbol{U}$ can finally be used to predict a motion field of a new patient q. In order to perform motion prediction, the transformations from the model space to the new patient and vice versa have to be known. A common assumption is that a static CT of the new patient is given. After performing adaptation of the average shape model to the new CT image, the necessary transformations can be calculated as described above. Knowing the transformations allows for transforming the statistical model into the new patient space. If no further information is known, the best prediction that can then be made is to use the mean motion field calculated from the statistical model. However, one could also assume that some sparse information at a few locations is given, e.g. the diaphragm motion, and the rest of lung motion is supposed to be predicted. In that case, we partition the vector $\boldsymbol{U}_q$ into two parts $\boldsymbol{U}_q = [\frac{\mathbf{y}_q}{\mathbf{x}_q}]$, where $\mathbf{y}_q$ gives the motion to be predicted and the $\mathbf{x}_q$ gives the information available during application to drive the model. Motion prediction

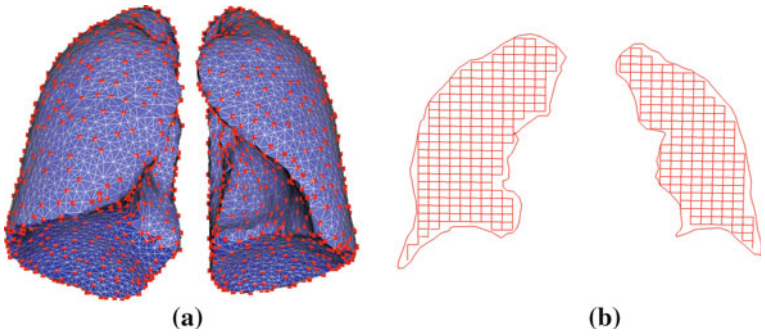

Fig. 10.8 Locations used for the representation of the motion model. To reduce the computational effort, locations are taken from a selected subset on outer surface (**a**) as well as locations inside the lungs on a regular grid sampled by 5 mm isotropically. In total, 1000 locations per lung are chosen

based on a vectorial representation can formulated as a linear multivariate regression problem

$$\mathbf{y}_{\text{pred},q} = \mathbf{B} \cdot \mathbf{x}_q \,, \tag{10.6}$$

where $\mathbf{B}$ can be learned from the statistical model and different methods can be used to solve this problem, e.g. ridge regression, partial least squares or principal component regression.

10.4.2 Statistical Modeling of Organ Motion Using Diffeomorphic Image Registration

The model generation process described in this section follows the approach presented in [17, 18]. A statistical inter-subject model is generated, i.e. the population of 4D images was acquired from different patients, the transformations are represented by dense vector fields, more specifically by velocity fields parameterizing diffeomorphisms, and the correspondence problem is solved explicitly by a deformable registration between the subjects in the population.

A central part of this section is the discussion of approaches for diffeomorphic image registration (Sect. 10.4.2.1) and statistics on diffeomorphic transformations (Sect. 10.4.2.2). The workflow for the generation of the statistical motion model follows the central steps discussed in Sect. 10.3.

10.4.2.1 Motion Estimation Using Diffeomorphic Transformations

Diffeomorphisms are globally one-to-one and differentiable mappings with a differentiable inverse. Constraining transformations to be diffeomorphisms maintains the topology of structures and is therefore a natural choice for motion estimation as the smoothness of anatomical features is preserved and connected structures remain connected [5]. Diffeomorphisms prove their profitableness in the EMPIRE10 study for motion estimation, where 3 out of the 10 best registration algorithms were diffeomorphic, including the 1st placed approach. Further advantages of diffeomorphic transformations arise in the statistical analysis of deformations which will be discussed in the next sections.

Diffeomorphic transformations can be modeled as arising from an evolution over unit time $\tau \in [0, 1]$, corresponding to the transport equations from continuum mechanics [78]. If $\boldsymbol{v} : \Omega \times [0, 1] \to \mathbb{R}^d$ is a time–dependent velocity field, then the diffeomorphism ϕ is initialized with the identity transform and evolves by:

$$\frac{\partial}{\partial \tau}\phi(\boldsymbol{x}, \tau) = \boldsymbol{v}(\phi(\boldsymbol{x}, \tau), \tau), \quad \phi(\boldsymbol{x}, 0) = \boldsymbol{x}. \tag{10.7}$$

This term has a physical interpretation: If $\phi(\boldsymbol{x}, \tau) = \boldsymbol{y}$ then a particle placed at $\boldsymbol{x}$ at time 0 ends at $\boldsymbol{y}$ at time τ subject to the vector field $\boldsymbol{v}$ which represents the time and position dependent velocity of this particle. Given two images $I_1 : \Omega \to \mathbb{R}$ and $I_2 : \Omega \to \mathbb{R}$, the diffeomorphic registration problem can be phrased as minimization problem with cost function $\mathcal{E}(\boldsymbol{T})$ [5]:

$$\begin{aligned} \mathcal{E}(\boldsymbol{T}) &= \alpha S(I_1, I_2, \boldsymbol{T}) + \int_0^1 \|\boldsymbol{v}_\tau\|_V^2 \, d\tau \\ \text{s.t. } \boldsymbol{T}(\boldsymbol{x}) &= \int_0^1 \boldsymbol{v}(\phi(\boldsymbol{x}, \tau), \tau) \, d\tau, \end{aligned} \tag{10.8}$$

where $\|\boldsymbol{v}_\tau\|_V^2$ is an appropriate norm on the velocity field $\boldsymbol{v}(\cdot, \tau)$, and $S(I_1, I_2, \boldsymbol{T})$ is an arbitrary (dis)similarity metric which evaluates the correspondence between the two images, as introduced in Chap. 6. The registration approach in Eq. (10.8) is called Large Deformation Diffeomorphic Metric Mapping (LDDMM) and has proven its applicability for different image registration problems.

In recent works [3, 4], diffeomorphisms are parameterized by *stationary* vector fields $\boldsymbol{v}(\boldsymbol{x}, \tau) = \boldsymbol{v}(\boldsymbol{x})$, i.e. the velocity fields remain constant over time. This approach still results in deformations that are diffeomorphic and has the advantage over the non-stationary setting that the resulting deformations can be computed rapidly and memory efficiently. The solution of Eq. (10.7) for stationary velocity fields is given by the group exponential map of the Lie group of diffeomorphisms: $T(x) = \phi(\boldsymbol{x}, 1) = Exp(\boldsymbol{v}(\boldsymbol{x}))$. The exponential map can be computed efficiently by the scaling-and-squaring algorithm [3]. Only a subgroup of diffeomorphisms can be parametrized in this way, however, diffeomorphisms parameterized by stationary vector fields have been shown to be versatile enough to describe the anatomical variability in different applications [4, 28, 83].

The registration algorithm defined in Eq. (10.8) (restricted to static velocity fields) is now used to compute the transformations $T_p(\boldsymbol{x}, t_j)$ for all subjects $p = 1, \ldots, N_p$ and respiratory phases $j = 1, \ldots, N_j$.

10.4.2.2 Establishing Correspondences

The central problem of inter-patient models is establishing the correspondence between the different subjects. First, an appropriate reference frame is needed. Because selecting one of the patient data sets induces a bias toward this anatomy, an average shape atlas of the lung is generated by a common atlas generation method [23]. Then, the diffeomorphic mappings $\Psi_{p \to ref}$, $p = 1, \ldots, N_p$, are computed by registering patient images representing the reference breathing phase $I_{p,0}$ to the atlas image $I_{ref,0}$. Because inner lung structures show a high anatomical variability and pathological structures are present in patient data sets, e.g. lesions, the outer lung surfaces and major vessels are used to guide the registration. The smoothness con-

strain of the non-linear registration propagate the transformation to the whole lung area.

The resulting patient-to-atlas transformations $\Psi_{p\to ref}$ are used to transform the estimated patient-specific motion fields to the atlas coordinate system by generating the topological conjugate transformations $T_{p\to ref}(\boldsymbol{x}, t_j)$ with Eq. (10.2).

10.4.2.3 Statistical Motion Model Representation

Statistics of transformations defining motion related organ deformations are necessary to generate a statistical motion model. The representation of the transformation has a decisive influence on the results of the statistical analysis. Many approaches use a small deformation model, in which the spatial transformation is parametrized by a displacement field $\boldsymbol{u}$ (see Sect. 10.3.4): $T(\boldsymbol{x}) = \boldsymbol{x} + \boldsymbol{u}(\boldsymbol{x})$. Although this additive model is applied successfully for statistical model computation in many applications [19, 38, 73] and efficient algorithms were developed, this parametrization has several disadvantages. Applying vectorial statistics on displacement fields, i.e. assuming a vector space with the usual additive structure, leads to inconsistencies, since e.g. the inverse of $\boldsymbol{x} + \boldsymbol{u}(\boldsymbol{x})$ cannot be approximated by $\boldsymbol{x} - \boldsymbol{u}(\boldsymbol{x})$ for larger deformations (see [4] for a detailed discussion). As a consequence, for example the mean of a sample of invertible transformations is not necessarily invertible, or the mean of the two transformations T and T^{-1} is not the identity.

Research in the field of Computational Anatomy has shown that diffeomorphisms provide an excellent tool to analyze and quantify shape differences and to characterize the biological variability of human anatomy [15, 20, 48], and some work has been done in the last years to define the methodology for a statistical computation framework on the manifold of diffeomorphic transformations [45, 80]. Recently, Arsigny et al. [3] presented an efficient framework for computing statistics on diffeomorphisms parametrized by stationary velocity fields, commonly termed as *Log-Euclidean framework*. Static velocity fields form a linear space, therefore the distance between two transformations $T_1(x) = Exp(\boldsymbol{v}_1(\boldsymbol{x}))$ and $T_2(x) = Exp(\boldsymbol{v}_2(\boldsymbol{x}))$ can be defined as the Euclidean distance between the associated velocity fields: $d(T_1, T_2) = \|\boldsymbol{v}_1 - \boldsymbol{v}_2\|$, and statistics on this subgroup of diffeomorphic transformations can be computed by Euclidean statistics on the associated static velocity fields. Contrary to Euclidean statistics on displacement fields, the Log-Euclidean framework always preserve the invertibility constraint, and is invariant with respect to inversion, since $T(x) = Exp(\boldsymbol{v}(\boldsymbol{x})) \Leftrightarrow T^{-1}(x) = Exp(-\boldsymbol{v}(\boldsymbol{x}))$. On the other hand, some theoretical problems exists, e.g. the metric linked to this distance is not translation invariant, and only a subgroup of diffeomorphisms can be parametrized in this way. However, experiments show satisfying results in different applications [3, 18] and statistics can be computed efficiently.

Using the Log-Euclidean framework the mean of transformations $T_{p\to ref}(\boldsymbol{x}, t_j) = Exp(\boldsymbol{v}_{p\to ref}(\boldsymbol{x}, t_j))$[2] is given by:

$$\bar{\boldsymbol{T}}(\boldsymbol{x}, t_j) = Exp\left(\frac{1}{N_p}\sum_{i=1}^{N_p}\boldsymbol{v}_{p\to ref}(\boldsymbol{x}, t_j)\right). \tag{10.9}$$

Ehrhardt et al. applied a scaling to the mean motion to represent motion variations caused by the depth of breathing. Here a scaled version of the average velocity field $\bar{\boldsymbol{v}}$ is used to compute the transformation $\tilde{T} = Exp(\lambda \cdot \bar{\boldsymbol{v}})$, where the scaling factor λ is related to a one-dimensional surrogate signal, i.e. the tidal volume.

For a more detailed representation of the motion variability, a PCA can be applied by sampling the velocity fields, assembling in the vectors

$$\boldsymbol{V}_{p,j} = [\boldsymbol{v}_{p\to ref}(\boldsymbol{x}_1, t_j), \ldots, \boldsymbol{v}_{p\to ref}(x_i, t_j), \ldots, \boldsymbol{v}_{p\to ref}(\boldsymbol{x}_{N_m}, t_j)]^{\mathrm{T}},$$

and using the methods described in Sect. 10.3.4 for model computation. Because an integration of the velocity field is necessary for the calculation of a transformation (see Eq. (10.8)), the sampling of the velocity fields must be adequately dense, e.g. at each voxel position, to allow for the reconstruction of the vector fields. Given a set of weights w_k for the first K principal components, a new transformation can be computed using:

$$\tilde{T} = Exp\left(\bar{V} + \sum_{k=1}^{K} w_k \phi_k\right). \tag{10.10}$$

If surrogate signals are available for the data sets in the patient pool, the methods presented in Sect. 9.4.2 can be used to relate the motion model to acquired surrogate signals and to compute the weights w_k depending on new surrogate signals. In this case, the number of principal components used, K, cannot exceed the number of available surrogate signals.

It should be mentioned, that the statistical modeling of shapes and shape changes has undergone significant development over the past twenty years, and diffeomorphic transformations play a central role in this research during the past few years. Because of the availability of time-resolved medical imaging data, the study of time dependent data of biological shapes has become an emerging question of interest. However, a variety of open problems—regarding theoretical and practical aspects—exist and significant development in these fields can be expected in the future.

[2] Note that in general iterative optimization methods are used to compute the static velocity field of the composition $T_{p\to ref} = \Psi_{p\to ref} \circ T_p \circ \Psi^{-1}_{p\to ref}$.

10.4.3 Applications of Statistical Motion Models

Population-based models have been already designed for a number of applications. In this context, motion compensation during radiotherapy has gained lots of attraction to define accurate treatment margins, to calculate dose distributions and to plan and guide gated or tracked treatments. Both models introduced in the previous section have been designed for these purposes and can be used to predict the lung motion including the tumor movement over the breathing cycle. After learning the model from a set of training images, the model can be adapted to a new patient to predict the patient specific motion. The first step is thereby to adapt the model to the patient-specific anatomy and to transfer the motion model to the patient space (see Sect. 10.3.3). For this purpose, a static three-dimensional CT or MR scan is assumed to be given that covers the patient's anatomy. In order to predict to the patient-specific motion, a surrogate signal is furthermore needed to drive the model, e.g. volume curve provided by a spirometer or motion information at some selected locations, e.g. provided by a navigator. The motion indicator allows for taking into account variations in motion amplitude and frequency, and techniques to predict internal motion by considering the information obtained from a surrogate signal are explained in Chap. 9. The principal idea of model-based motion prediction is sketched in Fig. 10.9.

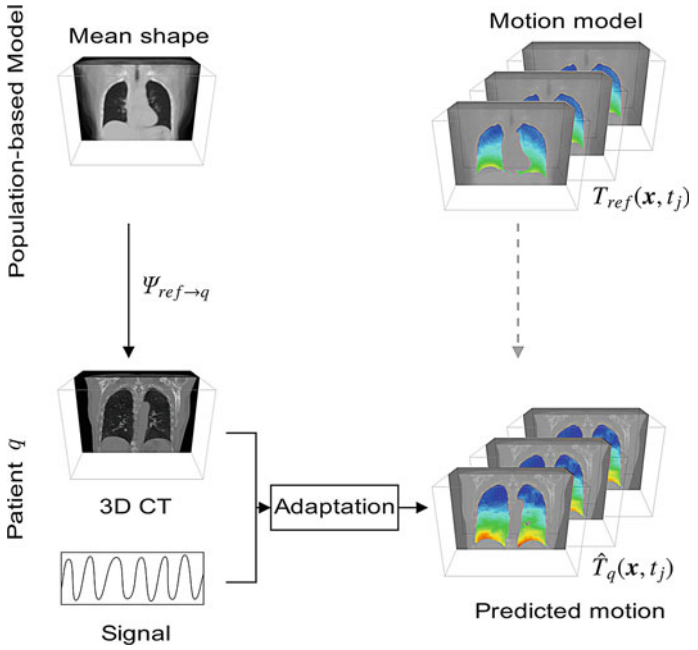

Fig. 10.9 Utilization of population-based models for motion prediction: The model is adapted to the patient-specific anatomy (provided by a static three-dimensional CT or MR scan), and the motion model is transferred to the patient space. A surrogate signal is used to drive the motion model and to adapt the model to the individual breathing-state and amplitude

While first approaches indicate the benefit of motion models for motion prediction, it has to be noted that to the best of our knowledge motion models have not been integrated into current clinical applications. This is due to several reasons. The most important one is probably the lack of thorough validation. Current evaluation is usually performed in a rather synthetic set-up where the motion model is applied to 4D CT or 4D MR images. Although this allows for detailed quantification by comparing the predicted motion against the extracted motion fields from the 4D image data, this can only be seen as a first proof of concept. The translation into the clinical practice will most likely introduce several additional challenges, e.g. that the prediction has to be performed over several breathing cycles with varying breathing patterns or that the model-based prediction has to deal with different pathologies and image protocols. Another drawback is that the integration of motion models may change the clinical workflow, e.g. by acquiring additional data, which is difficult to achieve. Finally, as prediction results have to be available in real-time, current motion models have to be significantly improved in performance.

Although a thorough validation of population-based models is missing, first studies exist to assess the prediction accuracies. Klinder et al. [38] applied population-based motion models to retrospectively predict lung motion and to compare intra- and inter-patient models. Using 267 4D CT data sets acquired from 36 patients, the intra-patient model was build from repeated CT scans of the same patient, and the inter-patient model was build from CT scans of different patients using the methods described in Sect. 10.4.1. To drive the motion model during prediction the diaphragm motion is assumed to be known. The study found that "intra-patient models outperformed the inter-patient models in all cases although much less samples were used for training than in the inter-patient case". The mean error of predicted inner-lung landmarks between end expiration and end insparation was reported as 3.4mm for the intra-patient and 4.2mm for the inter-patient study.

Similar error values were reported by Ehrhardt et al. [18] for an inter-patient lung motion model build with the methods described in Sect. 10.4.2. The generated model achieved mean landmark prediction error of 3.0 mm between EE and EI for lungs with intact respiratory dynamics. It was further shown that the model-based prediction precision is significantly lower for lungs affected by large tumors (4.0 mm). In a second application, the model was applied to predict patient-specific lung tumor motion and shows that prediction accuracy is degraded for tumors adhering to non-lung structures. The authors suppose that population-based inter-patient models are applicable only in cases of small lung tumors, non-adhering to outer-lung structures (see Fig. 10.10). However, the number of 4D CT data sets used for model-building and evaluation was small (17 4D CT data sets acquired from different patients), and more substantial evaluation is necessary. Though, Werner et al. showed in a preliminary study that this model can be used for model-based risk assessment in RT [89].

Other applications for population-based motion models were proposed for the prediction of respiratory liver motion [51, 54] and liver drift [73] in image-guided liver radiation therapy. The landmark-based prediction accuracy for such models

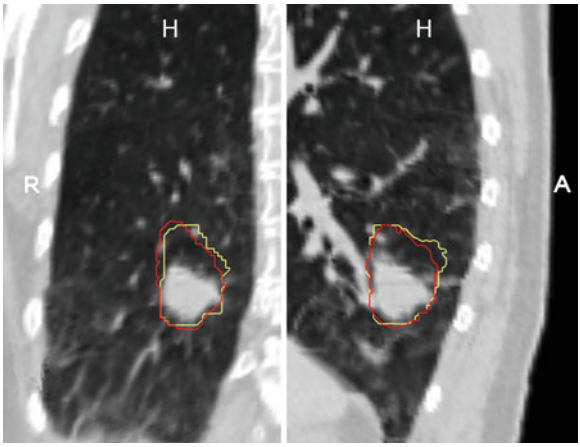

Fig. 10.10 Visualization of the internal target volume (ITV) of a patient with small non-adhering lung tumor in a coronal (*left*) and sagittal (*right*) CT slice. The ITV was calculated from expert-defined tumor segmentations in EI, EE, ME and MI (*yellow contour*) and from tumor positions predicted by the average motion model (*red contour*) [18]

were specified in the range from 1.2 [54] to 3.3 mm [51] for respiratory liver motion and between 0.6 and 2.3 mm [73] for liver drift models.

10.5 Summary and Discussion

Computational models of respiratory motion have numerous applications in radiation therapy, e.g. to understand motion effects in simulation studies, to develop and evaluate treatment strategies or to introduce prior knowledge into the patient-specific treatment planning. In this chapter, we discussed two types of respiratory motion models: mathematical and geometrical defined motion phantoms based on example data, and population-based statistical motion models. An advantage of population-based models is that the modeled motion information describes directly the motion variability in a training data set. However, these models rely on automatic motion estimation algorithms and automatic registration methods to establish intra- or inter-patient correspondences. Therefore, the accuracy and reliability of those methods has to be investigated. Although some efforts were made to evaluate motion estimation and intra-patient registration, inter-patient registration is still afflicted with uncertainties and the accuracy is widely unknown. On the other hand, statistical intra-patient models rely on repeatedly acquired 4D images increasing efforts and costs in the clinical workflow.

In order to incorporate model-based prediction into the clinical practice, physicians need to know the suitability and precision of a certain model for the concrete patient depending on diagnosis, treatment strategy, tumor location etc. Therefore,

one ongoing focus of research is the development of patient-tailored motion models and the adaptation of these models to the specific breathing motion during treatment. Here, the development of reliable non-linear registration algorithms plays a central role.

References

1. Admiraal, M.A., Schuring, D., Hurkmans, C.W.: Dose calculations accounting for breathing motion in stereotactic lung radiotherapy based on 4D-CT and the internal target volume. Radiother Oncol **86**(1), 55–60 (2008)
2. Arnold, P., Preiswerk, F., Fasel, B., Salomir, R., Scheffler, K., Cattin, P.C.: 3D organ motion prediction for MR-guided high intensity focused ultrasound. Med Image Comput Comput Assist Interv **14**(Pt 2), 623–630 (2011)
3. Arsigny, V., Commowick, O., Pennec, X., Ayache, N.: A log-euclidean framework for statistics on diffeomorphisms. In: Larsen R., Nielsen M., Sporring J. (eds.) Medical Image Computing and Computer-Assisted Intervention, MICCAI 2006. Lecture Notes in Computer Science, vol. 4190, pp. 924–931. Springer (2006) PMID: 17354979
4. Ashburner, J.: A fast diffeomorphic image registration algorithm. Neuroimage **38**(1), 95–113 (2007)
5. Beg, M.F., Miller, M.I., Trouvé, A., Younes, L.: Computing large deformation metric mappings via geodesic flows of diffeomorphisms. Int J Comput Vis **61**(2), 139–157 (2005)
6. von Berg, J., Barschdorf, H., Blaffert, T., Kabus, S., Lorenz, C.: Surface based cardiac and respiratory motion extraction motion extraction for pulmonary structures from multi-phase CT. In: Proceeding of SPIE Medical Imaging, vol. 6511, pp. 65, 110Y1-11 (2007)
7. Bergner, F., Berkus, T., Oelhafen, M., Kunz, P., Pan, T., Grimmer, R., Ritschl, L., Kachelriess, M.: An investigation of 4D cone-beam CT algorithms for slowly rotating scanners. Med Phys **37**(9), 5044–5053 (2010)
8. Blackall, J.M., Ahmad, S., Miquel, M.E., McClelland, J.R., Landau, D.B., Hawkes, D.J.: MRI-based measurements of respiratory motion variability and assessment of imaging strategies for radiotherapy planning. Phys Med Biol **51**(17), 4147 (2006)
9. Blaffert, T., Barschdorf, H., von Berg, J., Dries, S., Franz, A., Klinder, T., Lorenz, C., Renisch, S., Wiemker, R.: Lung lobe modeling and segmentation with individualized surface meshes. In: SPIE: medical imaging, society of photo-optical instrumentation engineers (SPIE) conference series, vol. 6914 (2008)
10. Bortfeld, T., Jiang, S., Rietzel, E.: Effects of motion on the total dose distribution. Semin Radiat Oncol **14**(1), 41–51 (2004)
11. Brock, K.K., Consortium, D.R.A.: Results of a multi-institution deformable registration accuracy study (MIDRAS). Int J Radiat Oncol Biol Phys **76**(2), 583–596 (2010)
12. Chandrashekara, R., Rao, A., Sanchez-Ortiz, G., Mohiaddin, R., Rueckert, D.: Construction of a statistical model for cardiac motion analysis using nonrigid image registration. In: Goos G., Hartmanis J., van Leeuwen J. (eds.) Proceeding of the Information Processing in Medical Imaging, Lecture Notes in Computer Science, vol. 2732, pp. 599–610. Springer (2003)
13. Cristy, M., Eckerman, K.: Specific absorbed fractions of energy at various ages from internal photon sources: 7, adult male. Technical report. Oak Ridge National Laboratory, TN (1987)
14. Dinkel, J., Hintze, C., Tetzlaff, R., Huber, P.E., Herfarth, K., Debus, J., Kauczor, H.U., Thieke, C.: 4D-MRI analysis of lung tumor motion in patients with hemidiaphragmatic paralysis. Radiother Oncol **91**(3), 449–454 (2009)
15. Dupuis, P., Grenander, U.: Variational problems on flows of diffeomorphisms for image matching. Q Appl Math **LVI**(3), 587–600 (1998)

16. Durrleman, S., Pennec, X., Trouvé, A., Gerig, G., Ayache, N.: Spatiotemporal atlas estimation for developmental delay detection in longitudinal datasets. Med Image Comput Comput Assist Interv **12**(Pt 1), 297–304 (2009)
17. Ehrhardt, J., Werner, R., Schmidt-Richberg, A., Handels, H.: A statistical shape and motion model for the prediction of respiratory lung motion. In: Dawant B.M., Haynor D.R. (eds.) Medical Imaging 2010: Image Processing, vol. 7623, pp. 53–62. SPIE (2010)
18. Ehrhardt, J., Werner, R., Schmidt-Richberg, A., Handels, H.: Statistical modeling of 4D respiratory lung motion using diffeomorphic image registration. IEEE Trans Med Imaging **30**(2), 251–265 (2011, in press)
19. Ehrhardt, J., Werner, R., Schmidt-Richberg, A., Schulz, B., Handels, H.: Generation of a mean motion model of the lung using 4D CT data. In: Botha, C., Kindlmann, G., Niessen, J., Preim, B. (eds.) Visual Computing for Biomedicine, pp. 69–76. Eurographics Association, Delft (2008)
20. Grenander, U., Miller, M.I.: Computational anatomy: an emerging discipline. Q Appl Math **LVI**(4), 617–694 (1998)
21. Gu, J., Bednarz, B., Xu, X.G., Jiang, S.B.: Assessment of patient organ doses and effective doses using the vip-man adult male phantom for selected cone-beam CT imaging procedures during image guided radiation therapy. Radiat Prot Dosim **131**(4), 431–443 (2008)
22. Guckenberger, M., Wilbert, J., Krieger, T., Richter, A., Baier, K., Meyer, J., Flentje, M.: Four-Dimensional treatment planning for stereotactic body radiotherapy. Int J Radiat Oncol Biol Phys **69**(1), 276–285 (2007)
23. Guimond, A., Meunier, J., Thirion, J.P.: Average brain models: A convergence study. Comput Vis Image Underst **77**(2), 192–210 (2000)
24. He, B., Du, Y., Segars, W.P., Wahl, R.L., Sgouros, G., Jacene, H., Frey, E.C.: Evaluation of quantitative imaging methods for organ activity and residence time estimation using a population of phantoms having realistic variations in anatomy and uptake. Med Phys **36**(2), 612–619 (2009)
25. He, T., Xue, Z., Xie, W., Wong, S.T.C.: Online 4-D CT estimation for patient-specific respiratory motion based on real-time breathing signals. Med Image Comput Comput Assist Interv **13**(Pt 3), 392–399 (2010)
26. Heimann, T., Meinzer, H.P.: Statistical shape models for 3D medical image segmentation: A review. Med Image Anal **13**(4), 543–563 (2009)
27. Hellier, P., Barillot, C., Corouge, I., Gibaud, B., Le Goualher, G., Collins, D., Evans, A., Malandain, G., Ayache, N., Christensen, G., Johnson, H.: Retrospective evaluation of intersubject brain registration. IEEE Trans Med Imaging **22**(9), 1120–1130 (2003)
28. Hernandez, M., Bossa, M.N., Olmos, S.: Registration of anatomical images using paths of diffeomorphisms parameterized with stationary vector field flows. Int J Comput Vis **85**, 291–306 (2009)
29. Joshi, S., Davis, B., Jomier, M., Gerig, G.: Unbiased diffeomorphic atlas construction for computational anatomy. Neuroimage **23**(Suppl 1), S151–S160 (2004)
30. Kabus, S., Klinder, T., Murphy, K., Ginneken, B.v., Lorenz, C., Pluim, J.: Evaluation of 4D-CT lung registration. In: MICCAI, vol. 5761, pp. 747–54 (2009)
31. Karakatsanis, N., Loudos, G., Nikita, K.: A methodology for optimizing the acquisition time of a clinical PET scan using GATE. In: IEEE Nuclear Science Symposium Conference Record (NSS/MIC), pp. 2896–2901 (2009)
32. Kaus, M.R., McNutt, T., Shoenbill, J.: Model-based segmentation for treatment planning with Pinnacle3. philips white paper. Techncal report. Philips Healthcare, Andover (2006)
33. Keall, P.: 4-dimensional computed tomography imaging and treatment planning. Semin Radiat Oncol **14**(1), 81–90 (2004)
34. Keall, P.J., Joshi, S., Vedam, S.S., Siebers, J.V., Kini, V.R., Mohan, R.: Four-dimensional radiotherapy planning for DMLC-based respiratory motion tracking. Med Phys **32**(4), 942–951 (2005)
35. Keall, P.J., Mageras, G., Balter, J.M., et al.: The management of respiratory motion in radiation oncology report of AAPM task group 76. Med Phys **33**(10), 3874–3900 (2006)

36. King, A., Buerger, C., Tsoumpas, C., Marsden, P., Schaeffter, T.: Thoracic respiratory motion estimation from MRI using a statistical model and a 2-D image navigator. Med Image Anal **16**(1), 252–264 (2012)
37. Klein, A., Andersson, J., Ardekani, B.A., Ashburner, J., Avants, B., Chiang, M.C.C., Christensen, G.E., Collins, D.L., Gee, J., Hellier, P., Song, J.H.H., Jenkinson, M., Lepage, C., Rueckert, D., Thompson, P., Vercauteren, T., Woods, R.P., Mann, J.J., Parsey, R.V.: Evaluation of 14 nonlinear deformation algorithms applied to human brain mri registration. NeuroImage **46**(3), 786–802 (2009)
38. Klinder, T., Lorenz, C., Ostermann, J.: Free-breathing intra- and intersubject respiratory motion capturing, modeling, and prediction. In: Pluim J.P.W., Dawant B.M. (eds.) Medical Imaging 2009: Image Processing, vol. 7259, p. 72590T. SPIE (2009)
39. Klinder, T., Lorenz, C., Ostermann, J.: Prediction framework for statistical respiratory motion modeling. Med Image Comput Comput Assist Interv **13**(Pt 3), 327–334 (2010)
40. Kramer R. an Zankl, M., Williams, G., Drexler, G.: The calculation of dose from external photon exposures using reference human phantoms and monte carlo methods. Part I: The male (ADAM) and female (EVA) adult mathematical phantoms. Technical Report. GSF-Report S-885, Institut fuer Strahlenschutz, GSF-Forschungszentrum fuer Umwelt und Gesundheit, Neuherberg (1982)
41. Kramer, R., Khoury, H.J., Vieira, J.W., Lima, V.J.M.: Max06 and fax06: update of two adult human phantoms for radiation protection dosimetry. Phys Med Biol **51**(14), 3331–3346 (2006)
42. Lamare, F., Cresson, T., Savean, J., Rest, C.C.L., Reader, A.J., Visvikis, D.: Respiratory motion correction for PET oncology applications using affine transformation of list mode data. Phys Med Biol **52**(1), 121–140 (2007)
43. Low, D.A., Parikh, P.J., Lu, W., Dempsey, J.F., Wahab, S.H., Hubenschmidt, J.P., Nystrom, M.M., Handoko, M., Bradley, J.D.: Novel breathing motion model for radiotherapy. Int J Radiat Oncol Biol Phys **63**(3), 921–929 (2005)
44. Lu, W., Olivera, G.H., Chen, Q., Chen, M.L., Ruchala, K.J.: Automatic re-contouring in 4D radiotherapy. Phys Med Biol **51**(5), 1077 (2006)
45. Marsland, S., Twining, C.J.: Constructing an atlas for the diffeomorphism group of a compact manifold with boundary, with application to the analysis of image registrations. J Comput Appl Math **222**(2), 411–428 (2008)
46. McClelland, J.R., Blackall, J.M., Tarte, S., Chandler, A.C., Hughes, S., Ahmad, S., Landau, D.B., Hawkes, D.J.: A continuous 4D motion model from multiple respiratory cycles for use in lung radiotherapy. Med Phys **33**(9), 3348–3358 (2006)
47. McGurk, R., Seco, J., Riboldi, M., Wolfgang, J., Segars, P., Paganetti, H.: Extension of the NCAT phantom for the investigation of intra-fraction respiratory motion in IMRT using 4D monte carlo. Phys Med Biol **55**(5), 1475–1490 (2010)
48. Miller, M.I.: Computational anatomy: shape, growth, and atrophy comparison via diffeomorphisms. Neuroimage **23**(Suppl 1), S19–S33 (2004)
49. Murphy, K., van Ginneken, B., Reinhardt, J.M., et al.: Evaluation of registration methods on thoracic CT: the EMPIRE10 challenge. IEEE Trans Med Imaging **30**(11), 1901–1920 (2011)
50. Nehmeh, S.A., Erdi, Y.E., Pan, T., Yorke, E., Mageras, G.S., Rosenzweig, K.E., Schoder, H., Mostafavi, H., Squire, O., Pevsner, A., Larson, S.M., Humm, J.L.: Quantitation of respiratory motion during 4D-PET/CT acquisition. Med Phys **31**(6), 1333–1338 (2004)
51. Nguyen, T.N., Moseley, J.L., Dawson, L.A., Jaffray, D.A., Brock, K.K.: Adapting liver motion models using a navigator channel technique. Med Phys **36**(4), 1061–1073 (2009)
52. Park, H., Bland, P.H., Hero, A.O., Meyer, C.R.: Least biased target selection in probabilistic atlas construction. Med Image Comput Comput Assist Interv **8**(Pt 2), 419–426 (2005)
53. Peyrat, J.M., Delingette, H., Sermesant, M., Pennec, X., Xu, C., Ayache, N.: Registration of 4D time-series of cardiac images with multichannel diffeomorphic demons. Med Image Comput Comput Assist Interv **11**(Pt 2), 972–979 (2008)
54. Preiswerk, F., Arnold, P., Fasel, B., Cattin, P.C.: Robust tumour tracking from 2D imaging using a population-based statistical motion model. In: IEEE Computer Society Workshop on Mathematical Methods in Biomedical Image Analysis (MMBIA). Breckenridge (2012)

55. Pretorius, P.H., King, M.A., Tsui, B.M., LaCroix, K.J., Xia, W.: A mathematical model of motion of the heart for use in generating source and attenuation maps for simulating emission imaging. Med Phys **26**(11), 2323–2332 (1999)
56. Qiu, A., Albert, M., Younes, L., Miller, M.I.: Time sequence diffeomorphic metric mapping and parallel transport track time-dependent shape changes. Neuroimage **45**(1 Suppl), S51–S60 (2009)
57. Ragan, D.: Semiautomated four-dimensional computed tomography segmentation using deformable models. Med Phys **32**, 2254 (2005)
58. Reyes, M., Malandain, G., Koulibaly, P.M., González-Ballester, M.A., Darcourt, J.: Model-based respiratory motion compensation for emission tomography image reconstruction. Phys Med Biol **52**(12), 3579 (2007)
59. Riboldi, M., Chen, G.T.Y., Baroni, G., Paganetti, H., Seco, J.: Design and testing of a simulation framework for dosimetric motion studies integrating an anthropomorphic computational phantom into four-dimensional monte carlo. Technol Cancer Res Treat **7**(6), 449–456 (2008)
60. Rietzel, E., Chen, G.T.Y., Choi, N.C., Willet, C.G.: Four-dimensional image-based treatment planning: Target volume segmentation and dose calculation in the presence of respiratory motion. Int J Radiat Oncol Biol Phys **61**(5), 1535–1550 (2005)
61. Rijkee, A.G., Zoetelief, J., Raaijmakers, C.P.J., Marck, S.C.V.D., Zee, W.V.D.: Assessment of induction of secondary tumours due to various radiotherapy modalities. Radiat Prot Dosim **118**(2), 219–226 (2006)
62. Rosu, M., Hugo, G.D.: Advances in 4D radiation therapy for managing respiration: Part II - 4D treatment planning. Z Med Phys **22**, 272–280 (2012)
63. Sarrut, D.: Deformable registration for image-guided radiation therapy. Z Med Phys **16**(4), 285–297 (2006)
64. Schweikard, A., Glosser, G., Bodduluri, M., Murphy, M.J., Adler, J.R.: Robotic motion compensation for respiratory movement during radiosurgery. Comput Aided Surg **5**(4), 263–277 (2000)
65. Schweikard, A., Shiomi, H., Adler, J.: Respiration tracking in radiosurgery. Med Phys **31**(10), 2738–2741 (2004)
66. Segars, W., Lalush, D., Tsui, B.: Modeling respiratory mechanics in the MCAT and spline-based MCAT phantoms. IEEE Trans Nucl Sci **48**(1), 89–97 (2001)
67. Segars, W., Mahesh, M., Beck, T., Frey, E., Tsui, B.: Realistic ct simulation using the 4D XCAT phantom. Med Phys **35**(8), 3800–3808 (2008)
68. Segars, W.P.: Development and application of the new dynamic nurbs-based cardiac-torso (ncat) phantom. Ph.D. thesis, University of North Carolina (2001)
69. Segars, W.P., Sturgeon, G., Li, X., Cheng, L., Ceritoglu, C., Ratnanather, J.T., Miller, M.I., Tsui, B.M.W., Frush, D., Samei, E.: Patient specific computerized phantoms to estimate dose in pediatric ct. In: Samei E., Hsieh J. (eds.) Medical Imaging 2009: Physics of Medical Imaging, vol. 7258, pp. 0H1-0H8. SPIE (2009)
70. Segars, W.P., Sturgeon, G., Mendonca, S., Grimes, J., Tsui, B.M.W.: 4D XCAT phantom for multimodality imaging research. Med Phys **37**(9), 4902–4915 (2010)
71. Segars, W.P., Tsui, B.M.W.: Study of the efficacy of respiratory gating in myocardial SPECT using the new 4-D NCAT phantom. IEEE Trans Nucl Sci **49**, 675–679 (2002)
72. Shirato, H., Shimizu, S., Kitamura, K., Nishioka, T., Kagei, K., Hashimoto, S., Aoyama, H., Kunieda, T., Shinohara, N., Dosaka-Akita, H., Miyasaka, K.: Four-dimensional treatment planning and fluoroscopic real-time tumor tracking radiotherapy for moving tumor. Int J Radiat Oncol Biol Phys **48**(2), 435–442 (2000)
73. von Siebenthal, M., Székely, G., Lomax, A., Cattin, P.: Inter-subject modelling of liver deformation during radiation therapy. Med Image Comput Comput Assist Interv **10**(Pt 1), 659–666 (2007)
74. Snyder, W.S., Fisher, H.L., Ford, M.R., Warner, G.G.: Estimates of absorbed fractions for monoenergetic photon sources uniformly distributed in various organs of a heterogeneous phantom. J Nucl Med **10**(Suppl 3), 7–52 (1969)

75. Spitzer, V., Ackerman, M.J., Scherzinger, A.L., Whitlock, D.: The visible human male: a technical report. J Am Med Inform Assoc **3**(2), 118–130 (1996)
76. Sundaram, T.A., Avants, B.B., Gee, J.C.: A dynamic model of average lung deformation using capacity-based reparameterization and shape averaging of lung MR images. In: Barillot C., Haynor D.R., Hellier P. (eds.) Medical Image Computing and Computer-Assisted Intervention, MICCAI 2004. Lecture Notes in Computer Science, vol. 3217, pp. 1000–1007. Springer (2004)
77. Sundaram, T.A., Avants, B.B., Gee, J.C.: Towards a dynamic model of pulmonary parenchymal deformation: evaluation of methods for temporal reparameterization of lung data. In: Med Image Comput Comput Assist Interv Int Conf Med Image Comput Comput Assist Interv **8**, 328–335 (2005)
78. Trouve, A.: Diffeomorphisms groups and pattern matching in image analysis. Int J Comput Vis **28**(3), 213–221 (1998)
79. Tward, D.J., Ceritoglu, C., Kolasny, A., Sturgeon, G.M., Segars, W.P., Miller, M.I., Ratnanather, J.T.: Patient specific dosimetry phantoms using multichannel lddmm of the whole body. J Biomedical Imaging **3**(1—-3), 9 (2011)
80. Vaillant, M., Miller, M.I., Younes, L., Trouvé, A.: Statistics on diffeomorphisms via tangent space representations. Neuroimage **23**(Suppl 1), S161–S169 (2004)
81. Vedam, S.S., Keall, P.J., Docef, A., Todor, D.A., Kini, V.R., Mohan, R.: Predicting respiratory motion for four-dimensional radiotherapy. Med Phys **31**(8), 2274–2283 (2004)
82. Vedam, S.S., Keall, P.J., Kini, V.R., Mostafavi, H., Shukla, H.P., Mohan, R.: Acquiring a four-dimensional computed tomography dataset using an external respiratory signal. Phys Med Biol **48**(1), 45–62 (2003)
83. Vercauteren, T., Pennec, X., Perchant, A., Ayache, N.: Diffeomorphic demons: efficient non-parametric image registration. Neuroimage **45**(1 Suppl), S61–S72 (2009)
84. Wang, B., Goldstein, M., Xu, X.G., Sahoo, N.: Adjoint monte carlo method for prostate external photon beam treatment planning: an application to 3D patient anatomy. Phys Med Biol **50**(5), 923–935 (2005)
85. Wang, H., Dong, L., O'Daniel, J., Mohan, R., Garden, A.S., Ang, K.K., Kuban, D.A., Bonnen, M., Chang, J.Y., Cheung, R.: Validation of an accelerated 'demons' algorithm for deformable image registration in radiation therapy. Phys Med Biol **50**(12), 2887 (2005)
86. Wang, H., Garden, A.S., Zhang, L., Wei, X., Ahamad, A., Kuban, D.A., Komaki, R., O'Daniel, J., Zhang, Y., Mohan, R., Dong, L.: Performance evaluation of automatic anatomy segmentation algorithm on repeat or four-dimensional computed tomography images using deformable image registration method. Int J Radiat Oncol Biol Phys **72**(1), 210–219 (2008)
87. Wang, J., Byrne, J., Franquiz, J., McGoron, A.: Evaluation of amplitude-based sorting algorithm to reduce lung tumor blurring in PET images using 4D NCAT phantom. Comput Methods Programs Biomed **87**(2), 112–122 (2007)
88. Werner, R., Ehrhardt, J., Schmidt-Richberg, A., Albers, D., Frenzel, T., Petersen, C., Cremers, F., Handels, H.: Towards accurate dose accumulation for step-&-shoot IMRT: Impact of weighting schemes and temporal image resolution on the estimation of dosimetric motion effects. Z Med Phys **22**, 109–122 (2012)
89. Werner, R., Ehrhardt, J., Schmidt-Richberg, A., Handels, H.: Model-based risk assessment for motion effects in 3D radiotherapy of lung tumors. In: III D.R.H., Wong K.H. (eds.) Medical Imaging 2012: Image-Guided Procedures, Robotic Interventions, and Modeling, vol. 8316, pp. 0C1-0C8. SPIE (2012)
90. Xu, X., Chao, T.C., Bozkurt, A., Shi, C., Zhang, J.: The 3D and 4D VIP-man computational phantoms. In: Handbook of Anatomical Models for Radiation Dosimetry, pp. 135–162. Taylor & Francis (2009)
91. Xu, X.G.: Handbook of Anatomical Models for Radiation Dosimetry, Chap. Computational Phantoms for Radiation Dosimetry: A 40-year history of evolution, pp. 3–41. Taylor & Francis, London (2009)
92. Xu, X.G., Bednarz, B., Paganetti, H.: A review of dosimetry studies on external-beam radiation treatment with respect to second cancer induction. Phys Med Biol **53**(13), R193–R241 (2008)

93. Xu, X.G., Chao, T.C., Bozkurt, A.: VIP-man:An image-based whole-body adult male model constructed from color photographs of the visible human project for multi-particle monte carlo calculations. Health Phys **78**(5), 476–486 (2000)
94. Xu, X.G., Eckerman, K.F. (eds.): Handbook of anatomical models for radiation dosimetry. Taylor & Francis, London (2009)
95. Xu, X.G., Stabin, M.G., Bolch, W.E., Segars, W.P.: Summary and future needs related to computational phantoms. In: Handbook of Anatomical Models for Radiation Dosimetry, pp. 679–683. Taylor & Francis (2009)
96. Zankl, M., Veit, R., Williams, G., Schneider, K., Fendel, H., Petoussi, N., Drexler, G.: The construction of computer tomographic phantoms and their application in radiology and radiation protection. Radiat Environ Biophys **27**, 153–164 (1988). doi:10.1007/BF01214605
97. Zhang, J., Xu, G.X., Shi, C., Fuss, M.: Development of a geometry-based respiratory motion-simulating patient model for radiation treatment dosimetry. J Appl Clin Med Phys **9**(1), 2700 (2008)
98. Zhang, Q., Hu, Y.C., Liu, F., Goodman, K., Rosenzweig, K.E., Mageras, G.S.: Correction of motion artifacts in cone-beam CT using a patient-specific respiratory motion model. Med Phys **37**(6), 2901–2909 (2010)

Part IV
Applications of Motion Estimation Algorithms

Chapter 11
4-Dimensional Imaging for Radiation Oncology: A Clinical Perspective

Max Dahele and Suresh Senan

Abstract This chapter is concerned with tumor and organ motion. It is written from a clinical perspective. It starts by putting motion into context and describing some of the fundamentals of contemporary radiotherapy. Subsequent sections focus on the use of imaging to detect motion (4-dimensional [4D] imaging), strategies to incorporate 4D imaging into radiotherapy treatment (4D radiotherapy) and ways in which motion can be managed and verified. It highlights a number of practical clinical issues and touches on the impact of 4D technology on treatment outcomes. The content is naturally selective and so the reader is provided with an extensive list of references.

11.1 Introduction

Tumors and organs can be broadly divided into those that move and those that do not, a distinction that is increasingly important for radiation dose escalation and high-precision image-guided radiotherapy (IGRT). One of the most common reasons for tumor and organ motion is breathing (respiration). Table 11.1 and Table 1.2 illustrate respiration-induced organ and tumor motion in the thoracic and abdominal regions.

A tenet of modern RT is that the target should be accurately identified, following which the high-dose treatment volume may be expanded into the surrounding tissues in order to create the clinical and planning target volumes (CTV and PTV). In Fig. 11.1 the different treatment-related volumes recommended by the International Commission on Radiation Units and Measurements (ICRU) are illustrated. Although the accurate identification of the gross tumor volume (GTV) is essential, it remains a weak link in the radiotherapy treatment planning (RTP) process. Defining the GTV is often difficult due to the lack of a sharply demarcated tumor boundary and it is subject

M. Dahele (✉) · S. Senan
Department of Radiation Oncology, VU University Medical Center, Amsterdam, The Netherlands
e-mail: m.dahele@vumc.nl

J. Ehrhardt and C. Lorenz (eds.), *4D Modeling and Estimation of Respiratory Motion for Radiation Therapy*, Biological and Medical Physics, Biomedical Engineering,
DOI: 10.1007/978-3-642-36441-9_11,

Table 11.1 Examples of mobility of selected tumors and organs

Tumor or organ	Motion and comments	Reference
Lung tumor	4D CT studies show that the majority of lung tumors move less than 1 cm in the cranio-caudal direction	[71]
Mediastinal lymph nodes	On 4D CT scans, nodes had a mean 3D motion of 0.68 cm (0.17–1.64 cm). No association was observed between 3D primary tumor and nodal motion	[94]
Pancreatic tumor / pancreas	On 4D CT scans the mean motion observed was 0.55 cm (±0.23 cm) in supero-inferior direction. Addition of a 1 cm margin accounted for all GTV motion in 97 % of patients	[35]
Liver tumor	On cine MRI mean liver tumor motion in patients without abdominal compression was 11.7 mm (range 4.8–23.3 mm) in the cranio-caudal direction	[25]
Kidney	4D CT studies have shown that motion is predominantly cranio-caudal and that there can be large inter-patient variation. Mean mobility in one study was 9.8 mm (2.5–30 mm) and 9 mm (2.5–20 mm) for the left and right kidney, respectively	[136]
Esophagus	In one 4D CT study, margins of 9 and 8 mm, respectively, were needed to account for all medio-lateral and dorso-ventral motion of the distal esophagus. The corresponding values for the proximal and mid-esophagus were 5/5 and 7/6 mm, respectively	[23]

to inter-observer variation (Fig. 11.2). Tumor motion creates additional challenges, and an important component of 4D RTP for motion-affected tumors is the definition of an appropriate internal target volume (ITV). The ITV is then typically expanded to create the planning target volume (PTV) which accounts for all uncertainties in the treatment delivery process.

In this paradigm, the more uncertainty there is, the more expansion will be necessary, with a corresponding increase in risk of damage to surrounding normal tissues and decrease in the therapeutic ratio, where the therapeutic ratio is defined as:

$$\frac{\text{Tumor control probability (TCP)}}{\text{Normal tissue complication probability (NTCP)}}.$$

It is therefore necessary to control and where possible reduce uncertainty in target designation and treatment delivery at the level of the individual patient.

Historically, RTP in the thoracic and abdominal regions has used 2- or 3-dimensional images acquired under uncoached free-breathing conditions,

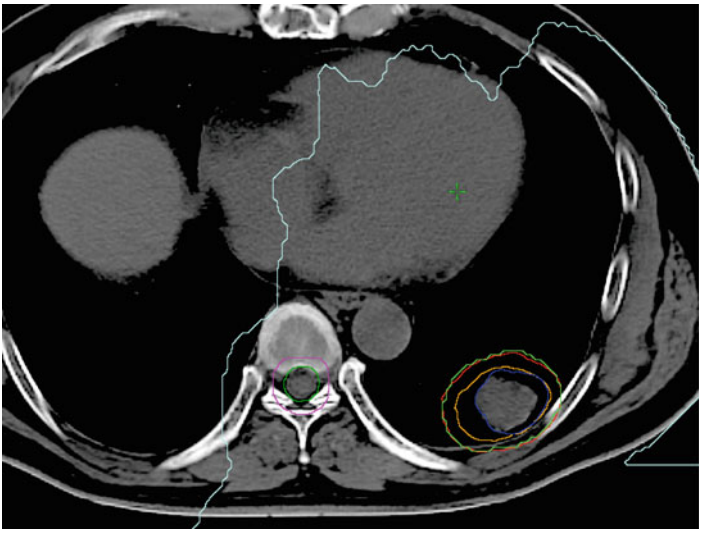

ICRU volume	Description	Illustration
Gross tumor volume (GTV)	Gross extent of tumor on imaging and possibly also using additional information such as clinical examination or direct visualization (e.g. bronchoscopy)	The dark blue contour illustrates the GTV in phase 0 of the 4D CT scan acquired for treatment planning (the lesion shown is as it appears on the average intensity projection dataset, not phase 0).
Clinical target volume (CTV)	CTV = GTV + margin for microscopic disease. This margin may be informed by radiology-pathology correlation studies. The margin may be asymmetrical and there may be more than one CTV in a plan	In this case, the lesion is being treated with high-precision, high-dose stereotactic body radiotherapy (SBRT) and no CTV margin has been added (i.e. GTV = CTV).
Internal target volume (ITV)	ITV = Internal margin (IM) + CTV, where the IM includes variation in shape, size and position of the CTV due to motion (e.g. as a result of breathing)	The orange contour represents the ITV, which in this case is the contour encompassing the position of the GTV in all 10 phases of the 4D CT scan.
Planning target volume (PTV)	PTV = ITV + margin for uncertainty in treatment delivery (e.g. variation in patient position, accuracy of treatment machine hardware and imaging apparatus).	The red contour is the PTV, in this case a 5mm isotropic expansion of the ITV.
Treated volume	Volume enclosed by the dose considered necessary to achieve the aim of the treatment	The light green contour represents 100% of the prescription dose, in this case 55Gy delivered in 5 fractions.
Irradiated volume	Volume receiving a dose that is significant to normal tissues	The light blue contour represents the 5Gy isodose, in this case considered clinically relevant for lung toxicity.
Organ at risk (OAR)	Normal organ whose radiation tolerance influences the treatment plan	The dark green contour has been used to denote the spinal canal which contains the spinal cord.
Planning organ at risk volume (PRV)	PRV = OAR + margin to account for variation in spatial location of the OAR, including positioning uncertainty during treatment	The pink contour represents a 5mm margin around the spinal canal.

Fig. 11.1 Illustration and description of treatment volumes and concepts described in ICRU Report 62 [48]

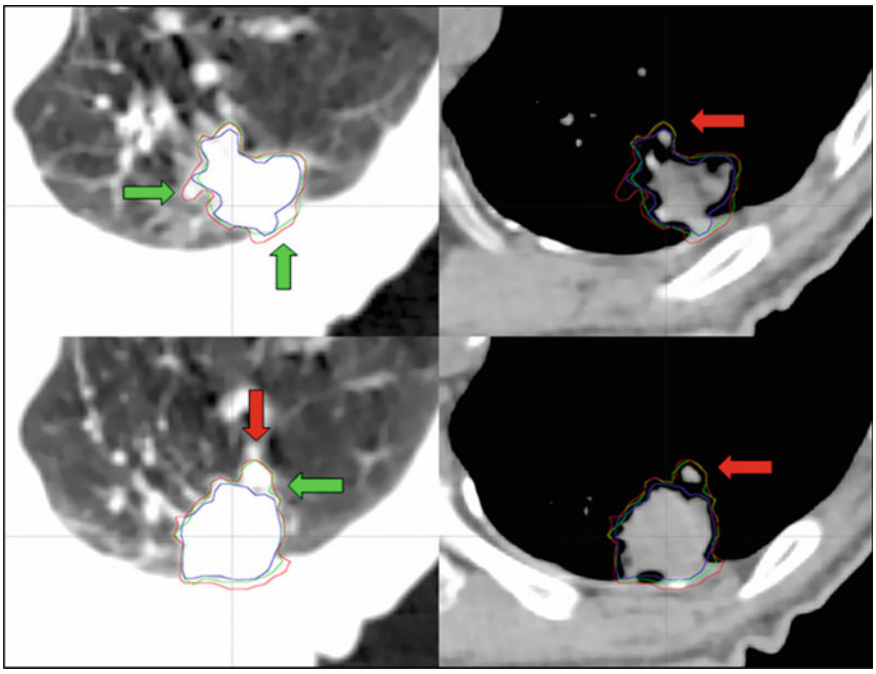

Fig. 11.2 An example of contouring variations by 3 clinicians who delineated a peripheral lung tumor on a single phase from a 4D CT (*red*, *green* and *blue contours*) using information from lung (*left panel*) and mediastinal (*right panel*) window/level settings. Illustrative differences in interpretation of anatomical data are highlighted (*green arrows*). Blood vessels (*red arrow*) are among the normal structures that can contribute to such inter-clinician variation

irrespective of whether the target tumor is moving or not. Once the GTV has been delineated, standard margins are commonly added in order to account for motion. However, the use of such generic margins does not usually take into account the location of the target in its motion trajectory, and furthermore might under, or over-estimate motion in individual patients with subsequent risks of missing the target during treatment, or irradiating excessive normal tissue [4]. RTP based on the use of conventional 'fast' CT images acquired at a random phase of the respiratory cycle therefore risks introducing systematic errors into treatment planning and delivery. In lung cancer, for example, such systematic errors may remain undetected if set-up at the treatment unit does not include daily [44] or frequent visualization of the tumor, or a robust surrogate/fidicual marker, and could occur if image-guidance is based solely on orthogonal kilovoltage images of the bony anatomy [103]. This increases the risk that the calculated tumor doses will not correspond to the delivered dose which may impact on both TCP and NTCP. The recent availability of on-line soft-tissue verification of tumor position can reduce the risk of systematic errors arising from a non-representative RTP scan and allow for modification/adaptation in treatment

planning margins. Such strategies also require that attention is paid to the location of critical normal structures.

4-dimensional (4D) imaging permits patient-specific treatment planning by incorporating temporal information about tumor and organ at risk (OAR) motion, thereby allowing for the use of individualized margins. A general approach for integrating 4D image information into the treatment planning workflow can be divided into the following steps:

(i) acquisition of 4D images for radiotherapy planning,
(ii) target and OAR delineation with appropriate use of motion information from 4D imaging data and addition of appropriate margins,
(iii) generating a treatment plan with a dose distribution that adequately treats the volume encapsulating the observed tumor motion, and
(iv) quality assurance to verify that the treatment plan can be robustly delivered.

These steps are discussed in the next sections and strategies to integrate tumor and organ motion are reviewed. Strategies for respiratory motion management during the radiotherapy treatment are reviewed in Sect. 11.6 and methods for imaging-based on-line verification are discussed in Sect. 11.7. The rapid developments in image acquisition and IGRT over recent years means that 4D CT is now widely considered to be the standard for treatment planning in the chest and upper abdomen, and that on-line volumetric positional verification with cone-beam CT (CBCT) is increasingly used for image-guided treatment delivery. Both 4D CT and CBCT can be readily integrated into clinical workflows.

11.2 4D Imaging for Radiotherapy Planning

Individual approaches to 4D imaging are briefly reviewed, and clinical examples will largely focus on lung cancer, in particular early-stage non-small-cell lung cancer (NSCLC), where considerable work has been performed on 4D imaging. The most common contemporary imaging technique for identifying tumor motion is 4D computed tomography (4D CT). In other approaches, additional spatio-temporal images are acquired beside the 3D planning CT to identify the extent of tumor and organ motion. Usually, in these approaches a co-registration of the additional images with the planning CT is necessary either as an integral part of the image acquisition technique (e.g. PET/CT) or by using registration algorithms as described in Chaps. 5 and 6. Note that depending on the 4D imaging strategy used, and the extent of image acquisition, the final set of treatment planning images may or may not include 4D information about organs at risk in addition to the target. In some scenarios this will be an important clinical consideration and if there is no 4D information about OAR motion, then alternative strategies (such as the application of an appropriate PRV margin) may be necessary in order to design an acceptable treatment plan.

11.2.1 Multiple Conventional CT Scans

Acquiring multiple fast CT scans at random during the same session allows for a better assessment of breathing motion than a single scan. There are several possible approaches to this. In breath-hold end tidal CT, 3 fast scans may be acquired, one in free breathing and one each during quiet end inspiratory and expiratory breath-hold [118]. Alternative techniques involve the acquisition of multiple scans at random points in the breathing cycle while the patient is in the treatment position. The initial scan typically includes all of the required cranio-caudal volume for treatment planning purposes, whilst subsequent scans are limited to the region of the tumor. All the scans are co-registered to each other, and the GTV can then be contoured on each scan separately. These contours can be combined on the full-length scan, which is used for treatment planning, to generate an internal target volume (ITV). Underberg et al. compared the ITV from a single respiration-correlated 4D CT scan (ITV_{4DCT}) to one derived from 6 conventional CT scans (ITV_{6CT}) in treatment planning for stereotactic lung RT [128]. This study found that the ITV_{4DCT} was comparable to, or larger than the ITV_{6CT}, suggesting that the former more reliably identified the true extent of tumor motion. The same study also evaluated expansion of the GTV derived from a standard CT scan by an isotropic margin of 10 mm. It found that although this lead to a PTV that was on average twice the size of that formed by a 3 mm expansion of the ITV_{4DCT} and ITV_{6CT} there was nonetheless incomplete geometric coverage of the two tumors showing most mobility. This study highlights the potential benefits of systematically accounting for tumor motion, reducing in some cases both the risk of tumor miss and the volume of normal tissue in the PTV.

11.2.2 Fluoroscopy

Fluoroscopy can allow selected tumors to be imaged in more than one dimension and the data to be used in several different ways. Clinical examples include (1) combining digital fluoroscopy loops with digitally-reconstructed radiographs from a conventional CT scan in order to derive a patient-specific ITV [119], (2) following CT-based RTP using generic treatment planning margins, fluoroscopy can be performed using a conventional simulator in order to verify that the planning margins adequately encompass tumor motion, (3) use of on-line/on-board kilo- or mega-voltage (kV or MV) fluoroscopic imaging to verify tumor motion and the adequacy of the PTV and dosimetric tumor coverage immediately prior to daily treatments. All the above can be performed with or without implanted fiducial markers. Although they may be easier to identify on fluoroscopy than the tumor itself, fiducial markers are not widely used in patient care as they introduce additional risks for the patient and may present logistical and technical challenges [116]. In practice therefore, while selected peripheral lung tumors may be visualised with fiducial-free fluoroscopy, this is less often the case for moving tumors located more centrally in the thorax (which even

if seen, may only be partially visible), and for lesions within the abdomen. This has resulted in guidelines that have cautioned against using fluoroscopy alone as a primary method with which to characterize lung tumor motion for RTP [114].

11.2.3 Slow CT

This technique differs from conventional fast CT in that the period of scanner rotation is slowed down, for example to 4 s, which is often long enough to capture respiratory tumor motion during a full respiratory cycle. This results in a blurred image that can be registered to a conventional CT for RT planning. Lagerwaard et al. compared conventional CT and slow CT scans of peripheral lung tumors and reported that the latter better accounted for motion, generating larger and more reproducible target volumes [60]. A subsequent study evaluated the number of slow CT scans required for treatment planning by comparison with a reference target volume derived from a total of 3 fast and 3 slow CT scans [22]. This found that a single slow CT scan with a 5 mm isotropic expansion was sufficient to cover 99 % of the reference volume. Phantom studies have shown that modern CT scanners with more limited ability to slow down the gantry rotation time (e.g. to 1.5 s) can still be used to capture information about target motion [18]. A drawback of slow CT is the fact that central tumors, and lesions adjacent to the mediastinum and diaphragm may be poorly visualized using this approach.

11.2.4 4-Dimensional CT (4D CT)

While combinations of conventional CT scans can be used to approximate tumor motion, they may be susceptible to motion artifact. Several authors have now described methods for generating 4D CT images that oversample the same anatomical location during respiration and then 'sort' or 'bin' images that have been allocated to the appropriate respiratory phase based, for example, on matching either the internal anatomy or an external respiratory signal (see [92, 109, 137] and Chaps. 2 and 3). 4D CT has now become the preferred modality for imaging tumor motion in routine clinical practice. This approach allows for discrete image sets to be generated for individual respiratory phases, as well as average and maximum intensity projection datasets (AIP, MIP respectively). However, 4D CT images are prone to imaging artifacts (see Chap. 2). These artifacts may arise due to higher motion velocity [84], greater motion amplitude or variations in breathing patterns [61, 97, 112], incorrect binning of images and missing images [1]. Such artifacts can affect the image quality and fidelity of the AIP and MIP and may affect the target delineation [12, 13]. A greater variability in CT number (Hounsfield units) than is seen with conventional CT has also been reported [123]. In 50 patients undergoing 4D CT for thoracic or abdominal radiotherapy, Yamamoto et al. reported artifacts in 90 % in the region of

diaphragm or heart (4.4–56 mm in size), and 6 of 20 patients exhibited at least one artifact in a lung or mediastinal tumor. They concluded that significant improvement was still needed in 4D CT imaging [147].

It is important, therefore, that 4D CT workflows should include an evaluation of the respiratory signal at the time of imaging and also the quality of the 4D CT images (see Fig. 11.3). This should ideally be performed prior to the patient coming off the CT couch and leaving the facility, so that they can be rescanned if excessive artifacts are observed.

Strategies to reduce the variability in breathing pattern include respiratory coaching. Combined audio-visual (AV) signals are one way of trying to regularize breathing however not all patients may be able to comply with this. Indeed Neicu et al. found that approximately half of the patients studied could not simultaneously follow audio and visual prompts [86]. For those patients that are coached, differences in breathing amplitude can be expected between coached and free-breathing conditions [98] indicating that if it is used for 4D CT planning then coaching should also be used during treatment. In an early study on AV coaching, Kini et al. found that audio coaching tended to improve the breathing frequency and visual coaching the amplitude, although each was somewhat at the expense of the other [54]. Audio coaching has also been shown to improve the correlation, reproducibility and phase shift between lung tumor motion and abdominal marker displacement, again perhaps at the expense of an increase in the depth of breathing and absolute tumor motion [82]. Differences in ITV position exceeding 5 mm between coached and uncoached 4D CT scans have been detected in up to 56 % of mobile lung tumors, with both end-inspiration and end-expiration positions susceptible to displacements [40]. In practice, the requirement for consistent coaching between 4D CT and treatment delivery [40], time, complexity and equipment has probably reduced the widespread uptake of this technique.

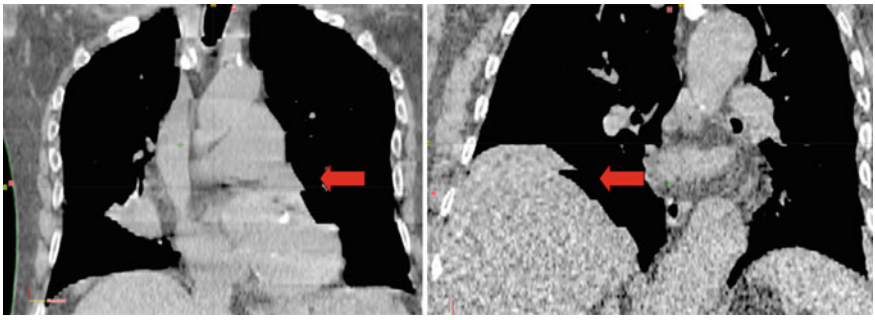

Fig. 11.3 4D CT images of the thorax acquired under uncoached, free-breathing conditions using a 16-slice CT scan and a cine CT technique. Typical artifacts (*arrows*) are seen in the region of the mediastinum (*left*) and diaphragm (*right*)

11.2.5 Positron Emission Tomography (PET)

PET imaging often involves the acquisition of data over several minutes in the same position, which means that a moving tumor will produce a blurred image. It has been postulated that PET images may define the motion envelope of the tumor. Identifying this envelope with a high degree of certainty and spatial confidence is an ongoing challenge in PET imaging. An early paper on this topic described a phantom study of moving spheres imaged with conventional CT and PET [14]. Uniform PTV margins added were 7.5 mm to the PET-based target and 7.5, 10 and 15 mm to the CT-based target. The CT images were prone to distortion and underestimated the motion envelope while the PET targets reflected the shape of the spheres and overestimated the true envelope. The 7.5 mm PET margin was reported to be adequate to avoid a geographic miss, whereas the CT-target required 15 mm margin that would have translated into more normal tissue being treated in-vivo. A key drawback of PET is that it suffers from limited spatial resolution and there is persisting uncertainty in how to segment the motion envelope of the tumor. Not surprisingly therefore, a great variety of approaches have been described for PET-based contouring [88, 144]. The challenges of knowing what represents the ground truth and in establishing appropriate segmentation parameters for mobile and non-mobile tumors, has led to an increasing interest in radiology-pathology correlation studies for PET and other imaging modalities [21, 77]. Many tumors have dominant motion in one direction (e.g. cranio-caudal) and it has been demonstrated that the size of the target, extent of motion, velocity and background activity may all affect PET images [107]. Despite this, most PET segmentation algorithms use isotropic segmentation methods to segment moving targets on 3D PET images, which it has been demonstrated can 'lose' PET data when the target is moving [27, 70]. We feel that anisotropic segmentation merits further evaluation as a means of detecting motion envelopes.

Key limitations of PET imaging must be acknowledged in order to ensure appropriate clinical use of this modality. The ability of PET to be used to guide biological sub-volume boosting or dose-painting has been studied by Perrin et al. who felt that with the available imaging quality 'simple' techniques seemed possible at intermediate contrast levels, which they defined as a tumor-background ratio of about 10 [96]. The advent of 4D PET [85] with attenuation maps derived from 4D CT has made it possible to recover some of the 'lost' metabolic information from a moving tumor. However, several issues remain unresolved such as the optimum number of phases to use, which represents a balance between reducing the amount of motion in any given phase by increasing the number of phases, at the expense of an increased signal to noise ratio [8, 85, 95]. The optimum integration of 3 and 4D PET-CT imaging into radiation treatment planning is still uncertain, and the specific role of metabolic imaging is likely to vary between tumor sites and whether they are mobile or not. At the present time, PET cannot be recommended as a primary modality for the routine identification of tumor motion in RTP.

11.2.6 4D Cine Magnetic Resonance Imaging (MRI)

Cine MRI has been used by a number of authors to image tumor motion at anatomical sites including pancreas, liver, bladder, cervix and prostate [16, 33, 75]. 4D 1.5 Tesla (1.5 T) fast low angle shot (FLASH) MRI has also been used to characterize complex breathing motion in patients with diaphragmatic paralysis due to lung cancer [24]. A recent investigation studied the ability of 4D CT, 4D MRI and 4D CBCT to detect nodule size and displacement in a dynamic ex-vivo lung model [9]. All modalities were found to have underestimated lesion displacement, and both 4D MRI and 4D CBCT overestimated lesion size. Kirilova et al. used T2-weighted single shot fast spin echo MRI sequences to image liver tumor motion in 3 dimensions, but this approach did not correlate well with fluoroscopic images of cranio-caudal diaphragmatic motion [55]. This, together with other studies, highlights the challenges of integrating multi-modal imaging studies acquired at different time points under different conditions, and in determining tumor motion with high levels of certainty. In terms of the relationship of tumor motion to anatomical surrogates, 3T cine MRI imaging of the pancreas has shown that the position of the tumor correlates poorly with that of the diaphragm (and abdominal wall), which can lead to inadequacies with gating based on these structures [30]. This study also demonstrated that tumor motion was greater than expected, requiring margins of 20, 7, 10 and 4 mm in inferior, superior, anterior and posterior directions to achieve 99 % geometric target coverage. Cine fast gradient echo MRI has also been used to show that lung blood vessels (used an internal surrogate for lung structures) have a variable correlation with different skin surface sites. The strength of correlation was influenced by the locations of the internal and external surrogates and the breathing pattern [57].

11.2.7 Comparison of 4D Imaging Methods

Multiple methods of imaging tumor motion have been described prompting several questions including (1) are there cautionary notes with any of these imaging modalities and (2) is one of them superior to the others?

When tumor motion in all directions on 4D CT in 29 patients was compared with motion assessed in antero-posterior projection using fluoroscopy, the latter method resulted in a mean ITV that was 52 % larger, with 4D CT generating a larger ITV in only 3 patients [134]. This study again demonstrated some of limitations of fluoroscopy, which did not allow motion to be evaluated in at least one direction in 8 of 29 patients. Underberg et al. found that a single 4D CT produced a PTV (ITV + 3 mm) that was comparable to or larger than that derived from a combination of 6 conventional fast CT scans (again with a 3 mm PTV margin) in patients with stage I NSCLC, indicating that the 4D CT more completely accounted for tumor motion [128]. This study highlighted the potential of 4D CT to simultaneously account for tumor motion and, in some patients, also reduce normal tissue irradiation. Nakamura et al. have

looked at whether slow CT captures 4D CT motion, finding that even when tumor motion is less than 8 mm, it may not be able to do so [83]. In situations where no 4D CT is available a combination of end-tidal breath-hold images may best describe tumor motion [118]. In relation to this, Hunjan et al. have evaluated the accuracy of end-tidal image acquisition when guided by the location of an external abdominal marker and concluded that relying solely on an external abdominal marker as a surrogate for the extremes of free breathing may be subject to error [47]. The same group have recently reported that the absolute difference between mean free breathing and breath hold marker displacement did not correlate well with the absolute difference between GTV centroid positions on free breathing 4D CT and breath-hold images, again highlighting the potential limitations of using external surrogates of tumor motion [46]. Although they represent an improvement over conventional fast CT and generic margins, some uncertainty still needs to be assumed when imaging tumor motion with current methods including 4D CT.

There are currently no clinical outcome data to indicate the superiority of one method of imaging motion over another. Lung stereotactic body radiotherapy often involves treating relatively small tumors in patients who are unfit to undergo surgery because of medical morbidity including chronic obstructive pulmonary disease (COPD) [59]. High radiation doses are used (e.g. 3 fractions of 18 Gy or 5 fractions of 11 Gy), which indicates a need for precise and accurate treatment in order to limit the dose to organs at risk (OAR) and reduce the likelihood of geographic miss. The information from selected publications on the treatment planning methods and motion management strategy can be contrasted with reported clinical outcomes (see Table 11.2). In summary, local control rates in excess of 90 % have been reported after stereotactic lung RT for relatively small, early-stage lung tumors, and control rates are comparable across a variety of treatment planning and delivery methods, including those that use generic planning margins and image-guidance based on surrogate anatomy. This therefore makes it difficult to currently ascribe superiority to one technical approach over another on the basis of clinical outcome. Possible responses to this could include (1) differences in the rates of local recurrences were masked by the high rates of non-cancer mortality due to extensive co-morbidity in treated patients, (2) the studies were not designed to detect gains from using a specific technology, or (3) the use of very high doses may have been forgiving of any imperfection in accounting for motion or inaccuracy in treatment delivery, which could mask the benefit from individual technologies.This final point contrasts with some reports suggesting that at lower biological doses, the transition from 2D RT to 3D conformal RT (CRT), while using similar conventional dose-fractionation schedules for stage I non-small cell lung cancer (NSCLC), and from 3D CRT to 4D CT/intensity modulated RT (IMRT) in locally advanced NSCLC, may be associated with improvements in clinical outcome, including patient survival [29, 66].

In contrast, review of non-clinical end-points suggest an apparent advantage to specific technologies frequently used in lung SBRT, such as the use of tumor-based matching for on-line volumetric guidance, or treatment planning with heterogeneity correction [121, 146]. Determining the contribution of technological advances, such as optimal motion management, to clinical outcomes can therefore be difficult. One

Table 11.2 Treatment planning, image-guidance strategies and local control in selected stereotactic lung radiotherapy series'

Reference	Treatment planning and margins	Image-guidance strategy	Patients (n) and follow up (FU)	Local control (LC)
Grills et al. JCO, 2010 (abstract) [36]	Not specified	On-line CBCT	n = 434, mean FU 1.3 years	Kaplan Meier estimated 92 % LC at 2 years
Timmerman et al. JAMA 2010 [127]	CT plus fluoroscopy, or 4D CT, no CTV expansion maximum 5 mm axial and 10 mm cranio-caudal PTV margins, motion control if it exceeds these margins	'Image-guidance capable of confirming the position of the target'	n = 59, median FU 34.4 months	Kaplan Meier estimated 97.6 % LC at 3 years
Baumann et al. JCO, 2009 [5]	CT, 1–2 mm GTV-CTV margin, 5–10 mm transversal and 10 mm longitudinal CTV-PTV margins	CT before treatment to verify reproducibility of target within the stereotactic system	n = 57, median FU 35 months	Kaplan Meier estimated 92 % LC at 3 years
Lagerwaard et al. IJROBP, 2008 [59]	4D CT derived ITV with 3 m ITV-PTV margin	Stereoscopic x-rays with match on spine	n = 206, median FU 12 months	Kaplan Meier estimated 93 % LC at 2 years

view is that the paradigm shift in radiation treatment is primarily radiobiological or related to improvements in combined modality therapies, and that one of the real (although perhaps less tangible) benefits of technological advances has been to enhance the confidence of the clinical team in delivering such treatments and increase their uptake into mainstream clinical practice as well as helping to extend the application of effective dose-fractionation schedules to ever more challenging situations (e.g. where the tumor is in closer proximity to critical structures) [34].

11.3 Target Delineation in 4D RTP

In this section, we discuss target delineation (GTV and ITV) in 4D RTP based on 4D CT images. In many of the the following examples relating to studies carried out for the treatment of early stage lung cancer, no CTV margin is used, and so the ITV contour represents the GTV plus an internal margin.

A number of approaches are in use for contouring the target volume [120], including

(1) contouring a GTV in all 10 phases, and then combining contours of all phases to define the ITV,
(2) contouring of only end-inspiration and end-expiration images in order to derive a motion encompassing volume,
(3) presenting the 4D CT images as a maximum intensity projections image (MIP), reflecting the maximum data value for a given pixel in all phases of the 4D CT and then contouring the tumor edge as it appears on the MIP, and
(4) a modified MIP approach that involves modifying the ITV contour derived from the tumor edge as it appears on the MIP images, with information from all 4D CT phases, or selected phases that represent extremes of motion.

Note that these methods cannot all be considered equal. For example, it is important to note that the extremes of motion may not be represented by extremes of the breathing cycle, and that the maxima of cranio-caudal, medio-lateral and antero-posterior motion may be located in different phases. Evaluating early stage lung tumors in different 4D CT phases, Wu et al. concluded that the major effect of respiration on lung tumors was translational, as the addition of rotation or deformation had little impact on registration metrics such as the overlap index [143].

The increased anatomical detail provided by 4D CT imaging also allows the mobility of mediastinal lymph nodes and organs at risk such as the esophagus and kidneys to be identified and where necessary taken into account during treatment planning [23, 94, 136]. Although the use of a planning organ at risk volume (PRV) was conceptualized in ICRU report 62 to incorporate uncertainties in OAR localization and shape, it is currently less clear how best to evaluate and trade-off dose-volume histograms predicated on constructs such as the PRV and OAR volumes defined using 4D CT imaging, for example if the time spent by an OAR at the extreme of motion is very short, or there is uncertainty over the consequences of partial organ irradiation [104].

Can MIP images adequately reproduce the ITV from all 10 phases of the breathing cycle? This issue was addressed using 4D CT images from 12 patients with stage I lung cancer and a phantom study which reported a ratio between 10-phase GTV and MIP of 1.04 [130]. The former study was in early-stage NSCLC and suggested that the MIP was a quick and fairly reliable way to identify tumor motion. For more advanced tumors and in patients with irregular breathing, however, the MIP may be less reliable and risks underestimating the ITV defined by using all 10-phases [80]. In practice, the MIP may be viewed as a way of approximating the motion envelope that can subsequently be refined by incorporating additional information from individual respiratory phases. This is consistent with the findings of Rietzel et al. [108] and Ezhil et al. [28]. The latter found that in 27 patients with stage I or III NSCLC the ITV derived from the MIP and modified by using all 10 phases of the 4D CT agreed most closely with the ITV defined from all 10 respiratory phases, which was underestimated by using the MIP or the 0 and 50 % respiratory phases alone. The MIP may be unreliable for example where the tumor is close to chest wall, blood vessels, diaphragm or mediastinal structures (denser, mobile structures). Although an ITV derived from MIP-modified identifies an approximate motion envelope, it does not help to identify microscopic disease, which means that in some instances an additional margin for the CTV may be considered desirable. In addition there is no guarantee that the motion of the tumor during treatment will be the same as it was when the planning 4D CT was acquired.

Inter-observer variations and reproducibility of target volume delineation are key factors contributing to overall quality of treatment [115], and this remains the case in the 4D CT era [72]. This provides an impetus to the development of automated contouring for target volume delineation. The use of deformable registration as introduced in Chaps. 5–7 to auto-propagate a single GTV may reduce inter-clinician variations in generating ITV's for peripheral lung tumors [132]. Automated contouring or registration-based contour propagation is impeded by the aforementioned possible imaging artifacts in 4D CT datasets. Ehler et al. presented a system to auto-segment the GTV using 4D CT with up to 15 % phase binning errors [26]. Further, challenges for auto-segmentation include identifying structures when they have inherently indistinct boundaries or the imaging modality used for treatment planning has low resolving power for the structure in question and cannot differentiate it well from surrounding tissues. This means that such contours still need to be verified by the clinician (see Fig. 11.4).

With the variation in patient breathing and localisation, can a single planning study adequately describe tumor motion? Studies addressing this point have reached varying conclusions. For example, a study on the motion of implanted fiducial markers in 20 patients undergoing single fraction stereotactic RT for pancreatic cancer found that neither the mean, nor the maximum motion during treatment was predicted by the 4D CT planning study [78]. When 4 separate 4D CT studies, one every 10 min, were performed in 10 patients with lung metastases, increased uncertainty in tumor location was observed in patients with poor respiratory function, and lower lobe tumors [38]. Van der Geld et al. evaluated the reproducibility of 4D CT by comparing 2 uncoached scans acquired during quiet breathing at the same session

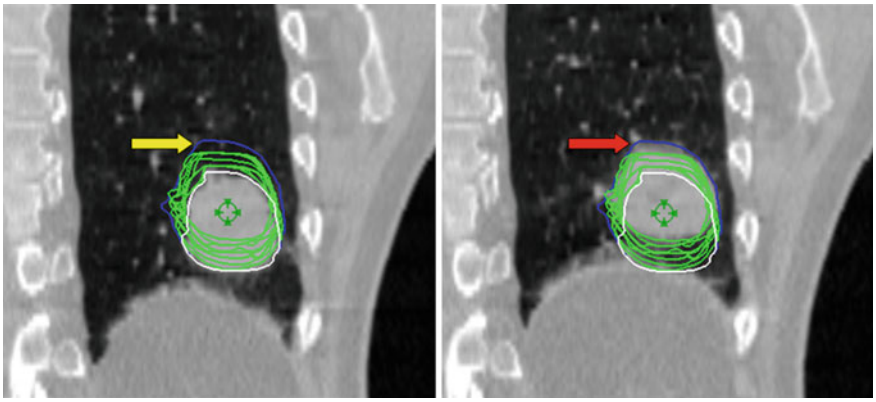

Fig. 11.4 Example showing the use of deformable registration for tumor segmentation. A single manual GTV contour at end inspiration (*white contour*) was successfully deformed to each of the other phases of 4D CT (*green contours*). The *blue contour* encompasses the manual contours of a single observer who has delineated the GTV on all 10 phases of the same 4D CT. Differences between the *green* and *blue contours* (*yellow arrow*) are seen on the end-inspiration data set (*left panel*) at the cranial extent of contours propagated using deformable registration and the manually derived contour. Inspection of the end-exhale image of 4D CT (*right panel*) shows a region of increased CT density (*red arrow*) which was incorporated by the clinician, but not by the software-based registration. This highlights the need for clinicians to verify all automated contours

in 26 patients with stage I lung cancer [133]. In 19 % of their patients, the centre of mass of PTV was displaced by at least 2 mm, but a treatment plan optimized for one PTV provided at least 90 % coverage of the other in all but one patient, which led to the conclusion that a single 4D CT scan was sufficient for lung tumors. A study evaluating the centre of mass displacement of the PTV using repeat, uncoached 4D CT for small, stage I tumors, reported an average 3-dimensional displacement of 2 mm, with 98 % of the PTV on repeat 4D CT covered by the initial prescription isodose [39]. It is clear that motion during treatment may vary from that at planning which makes tools that image true intrafraction motion desirable. This is especially so if they can be combined with intuitive user-interfaces that identify when tumor coverage is no longer adequate.

11.4 Generation of Treatment Plans

While a detailed discussion of treatment planning is beyond the scope of this chapter, selected considerations follow. External beam treatment planning using simple conformal fields, or static field or volumetric IMRT is concerned with the design of dose distributions to adequately cover the PTV and (relatively) spare OARs (Fig. 11.1). The trade off between target coverage and OAR dose will largely be determined by the geometry of these structures, the prescribed dose/fractionation and desired

PTV coverage, and the dose limits that are placed on the OARs. In some cases it may be necessary to define OAR volumes using 4D CT motion information and so if the excursion is large (such as can happen for example with the stomach) then the volume to be avoided during RTP may be substantially more than appreciated on a single 4D CT phase. In practice while 4D CT can be used to delineate OARs, determining dose-volume constraints for 4D OAR volumes is subject to uncertainty. When calculating the dose to the PTV or OARs, current treatment planning systems in common use do not explicitly account for the effects of motion during the dose calculation and optimization process (e.g. dose blurring or interplay—see below). The dose distribution of the plan can affect the positioning tolerance during treatment. It is necessary therefore to take into account the treatment delivery process during planning. For example, if the patient will be positioned on the basis of the tumor, then if tumor position is variable relative to a given OAR (such as can occur with a mobile lung tumor and the spinal cord), then a safety margin (PRV) needs to be included in the treatment planning process and the appropriate OAR dose constraint applied to this structure. This means that if the OAR is located within the PRV at the time of treatment, then it will receive an acceptable dose. For this to be determined there needs to be an on-line check of the OAR as well as the tumor position. The design of high quality treatment plans often relies on experienced planners. However, what constitutes and optimal plan and establishing whether such a plan has been delivered by the planning system, remains the subject of ongoing research. There is increasing interest in planning automation and in designing 'intelligent' approaches to treatment planning that exploit the experience acquired from prior plans and in some cases clinical outcome data.

11.5 4D Dose and Quality Assurance (QA)

The above-mentioned examples illustrate how treatment volumes derived using 4D CT are often smaller and reduce the dose delivered to normal organs. Use of 4D imaging should in theory translate into an improved therapeutic ratio but clinical data to support this are currently rather limited [66]. In connection with this, fully 4D treatment planning software is not commercially available at present. However, a common clinical approach of using the 4D CT-derived average intensity projection (AIP) for planning lung stereotactic body radiotherapy (SBRT) with conventional planning software has been shown to agree with the cumulative tumor dose from 10 individual breathing phases suggesting that current treatment planning methods are reasonably accurate [3]. Nonetheless, verifying dose delivery in 4D and accounting for the effects of blurring, interplay and changes in the shape of the dose distribution that can occur during treatment (see below), is typically not a feature of current approaches to routine clinical QA.

With increasing use of IMRT technologies, including volumetric modulated arc therapy (VMAT), there has been some concern over the possibility of dosimetric uncertainty when applying treatments that contain spatio-temporal variations in

dose-delivery to a target that is itself mobile. The impact of motion on dose distribution depends on several factors including the type of dose distribution and delivery method, for example an open field, conformal plan with relatively homogeneous dose or an intensity modulated radiotherapy (IMRT) plan with a more heterogenous distribution and the amount of motion (dose blurring); the interaction between target motion and changes in the size and location of the beam aperture (interplay); and differences in the internal anatomy between treatment planning and delivery (which can alter the shape of the dose distribution). Current limitations in dosimetry make these challenging issues to resolve.

Court et al. used a novel IMRT quality assurance (QA) method to evaluate the interplay between RapidArc volumetric modulated arc therapy (Varian Medical Systems, Palo Alto, CA, USA) and tumor motion [20]. They found that when motion was limited to $\leq$1 cm fewer than 15 % of pixels had a daily dose error of more than 5 % whereas for 2 cm motion the error could be more than 5 % for 40 % of pixels. It is relevant that by using a combination of logfile analysis and Monte Carlo simulation, calculated and measured RapidArc doses have been demonstrated to agree to within 2.1 % [126].

Motion interplay has also been identified as a potential issue with helical tomotherapy [17]. Using GafChromic EBT film and the Quasar phantom (Modus Medical Devices Inc., London, ON, Canada) our group has studied the interplay effect for high dose per fraction stereotactic lung radiotherapy delivered with RapidArc and found in a phantom study that under sinusoidal conditions, within the limitations of film dosimetry, interplay did not appear to significant when treatment was delivered with 2 arcs and collimator rotation [42, 91, 131]. In this study the number of breathing cycles per arc was 16–20, leading to the suggestion that in this aspect, RT delivery over many breaths may be analogous to conventional treatments with many shorter fractions, and therefore also associated with a possible averaging out of spatial differences in dosimetry. How sensitive this is to the increased dose rates now possible with next-generation linear accelerators, and potential for reduced delivery times, remains to be seen.

It is appropriate to acknowledge that some uncertainty in delivered dose to the tumor and OAR is always accepted in radiation oncology. This is implicit for example when using a gamma factor analysis (representing a quantitative comparison of two dose distributions) with 3 % dose and 2 mm distance to agreement criteria or using 4D CT in which phase assignment discrepancies have been observed in about 40 % of scans [81]. From the available data the uncertainty in dose delivery might be increased when using highly modulated treatment plans to treat mobile targets over a small number of fractions [56]. This dosimetric uncertainty also applies to normal tissue dosimetry which might be just as, or even more important than tumor doses in certain clinical situations, especially as new technologies are being used to treat ever more challenging tumor-OAR geometries [31]. In clinical practice end-to-end QA and summary evaluations of uncertainty in delivered dose and treatment accuracy may be valuable to the user and may make it possible to express the expected tumor and critical OAR dose as a more meaningful probabilistic range, rather than a single

figure and then often to decimal places, that gives an overly precise impression of the treatment process.

Quality assurance plays a critical role in the successful implementation of new technologies [6, 69]. Specific methods are now commercially available for 4D QA and it is likely that these will be increasingly applied to technologies such as 4D CT and IMRT-type delivery to moving targets [135, 148]. Recognizing the importance of overall treatment quality to outcome, standardized QA metrics could be an advantage and they are also likely to become an important factor whenever there is a need to compare images taken on different machines, or when using different image sets for treatment planning, including for example when conducting multi-centre clinical trials that incorporate 4D CT imaging, this is analogous with recent work on PET-CT [11, 45, 50, 65, 84, 99].

11.6 Motion Management

Various approaches to studying tumor motion in the thorax and upper abdomen indicate that respiration is largely responsible for mobility (see Table 11.1), but other contributors include peristalsis and the heart beat. While the motion of most tumors is relatively limited encompassing all motion during target delineation and treatment planning may be acceptable. However, it is important to note that in some patients a motion-encompassing protocol can generate a large PTV, which may be associated with a higher risk of normal tissue toxicity. Although it is then reasonable to consider other respiratory motion management strategies, reasons for not using these include (1) the perception of marginal improvements in therapeutic index, (2) patients being unable to tolerate certain available interventions, (3) potential for significant impact on patient and departmental workflow, and (4) the lack of tools for verifying the accuracy of active interventions, which might increase the risk of geographic miss during delivery.

The threshold above which additional interventions for tumor motion should be considered will depend in any given patient on factors such as the available technologies and tools for motions management, anatomic tumor location, proximity to critical structures, risk of complications and treatment intent. Although this was not specifically defined in the European Organization for the Research and Treatment of Cancer (EORTC) recommendations for lung cancer [114], American Association of Physicists in Medicine (AAPM) suggests that some form of motion management should be considered for a tumor motion of 5 mm or above [52]. If active intervention is deemed necessary, then there are several categories of technique for mitigating motion, which may broadly be characterized as follows (1) physical motion reduction (e.g. abdominal compression), (2) effective motion reduction (e.g. respiratory gating), (3) motion compensation (e.g. dynamic multi-leaf collimator [MCL] tumor tracking). These have been comprehensively reviewed [52] and some examples are discussed in the following paragraphs.

11.6.1 Physical Motion Reduction

11.6.1.1 Abdominal Compression

Abdominal compression can be applied in several ways, including with an adjustable compression plate, in order to restrict diaphragm motion and limit the depth of breathing. This has been shown to reduce supero-inferior and overall motion of lower lobe lung and liver tumors on 4D CT [43]. The mean overall motion was reduced from 13.6 mm to 8.3 mm and 7.2 mm with medium and high-level compression respectively. Pancreas motion was also controlled by abdominal compression. One study found that the abdominal compression plate was rated more comfortable by patients than the BodyFIX® (Elekta AB), was more effective in reducing lung lesion motion and faster to set up [41]. But both systems reduced motion compared to free breathing. In patients receiving stereotactic lung RT abdominal compression was found to be associated with more variation in time spent on the treatment machine and also with more inter- and intra-fraction variability in changes in tumor amplitude [10].

11.6.1.2 Breath-Hold

Active breathing is suspended during breath-hold, limiting tumor movement. Breath-hold can be voluntary, or performed with mechanical assistance (e.g. Active Breathing Coordinator, Elekta AB) and used with or without monitoring. Breath-hold techniques should be reproducible so that the target and OAR location is predictable, however some residual spatial uncertainty should be anticipated. Active Breathing Coordinator (ABC) was tolerated in 83 % of patients undergoing radical radiotherapy for NSCLC and the reduction in PTV size translated into an 18–25 % reduction in lung metrics that included mean lung dose and V20 [93]. ABC is clinically feasible. It is recommended that potential patients have a minimum breath hold time of 15 s prior to commencement [76].

11.6.1.3 Coached Breathing

Coaching typically uses audio and/or visual prompts to manipulate the breathing pattern. It may improve the relationship between lung tumor and abdominal wall motion, which may be important for some gating methods (see below), but tumor excursion may be increased [82]. The method of coaching should remain consistent throughout treatment [40] and coaching should ideally be combined with (volumetric) image guidance for verification purposes.

11.6.2 Effective Motion Reduction

Respiratory gating aims to synchronize treatment delivery with a specific part of the breathing cycle (the gating window) on the assumption that the tumor will reliably be located within the high-dose treatment volume. Typically the gating window represents a period during breathing when the tumor moves least, and/or the normal anatomy is in a favorable position. The start and finish of the gating window is usually signified by user-defined displacement or respiratory phase parameters (amplitude or phase-based gating respectively). It is apparent that depending on the patient, breathing and tumor motion characteristics, treatment technique and verification, there may be appreciable uncertainty associated with the use of gating. This makes it desirable to be able to verify target position during, or at the beginning/end of the gating window. The reduction in lung irradiation achieved with respiratory gating in patients with early stage NSCLC may be most apparent in those tumors with 3D mobility of $\geq$1 cm [129]. More effective reduction in PTV margins and optimal target coverage are achieved by combining respiratory gating with image-guided set-up [51, 87]. Gated delivery alone cannot be used to advocate margin reduction [58]. The relationship between tumor motion and surrogates may be unreliable. There is a growing body of literature on temporo-spatial tumor surrogates. A specific combination of surrogate anatomical markers identified on 4D CT may be advantageous [73] however the integrity of the tumor-surrogate relationship needs to be monitored during treatment as there are data showing that the phase relationship between the tumor and marker may vary on a daily basis [53]. Phase-based gating may be more susceptible to variation in the breathing pattern than displacement gating [111].

11.6.3 Motion Compensation

This section briefly discusses motion compensation by tracking. The essence is that if a tumor moves, then provided that the motion can be accurately tracked, directly or indirectly, then it is possible to begin to investigate whether the delivery of radiation can be 'slaved' to the tumor. Strategies being investigated for this include dynamically changing the aperture in the multi-leaf collimator to account for tumor location, moving the treatment couch that the patient is lying on, relative to the treatment beam, in order to account for tumor motion, and moving the beam delivery system in a manner that is synchronized with target motion and location. Accurately identifying the motion of targets within the body, in real-time, is challenging. Implanting fiducial markers to aid tracking is in clinical use, but ultimately, non-invasive strategies are inherently more attractive.

Tracking with implanted fiducials may be prone to uncertainty if the location of the markers is suboptimal, for example too far away from the tumor [49], or they are in place for too long a period [145]. Marker design needs to be tailored to the host tissue to minimize the risk of displacement and maximize the accuracy of

the guidance system. Systems that require the implantation of only a single fiducial for accurate tracking would be preferable to multiple markers and these are being evaluated [117].

Fiducial-free tracking requires that the tumor is visible. Lung tumor tracking using an electronic portal imaging device (EPID) was possible in only 47 % of treatment beams used in patients undergoing stereotactic body radiotherapy, demonstrating one of the challenges with this approach [106]. Cone beam CT may improve tumor visualization and can be used to reconstruct the tumor trajectory [64]. The potential of other technologies, including digital tomosynthesis (DTS) is being investigated.

Although IMRT treatment plans incorporating 4D CT volumes and sensitive to changes in tumor position can be designed [124] such plans are based on treatment planning, rather than real-time tumor motion data. Because these may be different, this runs the risk that there will be differences between the planned and delivered dose. The ability to respond to real-time tumor tracking is one response to this. Although this is a feature of the Cyberknife system [2], various strategies are being evaluated for application on conventional linear accelerators, including motion compensation with a robotic treatment couch [142] and dynamic multi-leaf collimator (DMLC) tracking. A research system has been reported that combines electromagnetic marker tracking with DMLC tracking, it has a reported target-MLC response latency of 220 ms, sub-2 mm accuracy for lung motion and sub 1 mm accuracy for prostate motion in phantom studies [113].

11.7 On-line 4D Verification

Given the potential for time-related patient or organ-specific motion and the uncertainty that surrounds the use of surrogates (as discussed in Chap. 9), intra-fraction monitoring becomes an important part of the treatment process when highly conformal techniques and small uncertainty margins are used. A reliable imaging of the tumor location and motion during treatment would be desirable as it could provide an opportunity to respond to differences in planning and real-time displacement. This may range for example from interrupting treatment until the correct conditions are re-instated, to real-time adaptation of treatment delivery. Again, while the focus has been on tumor identification and motion, any real-time 'on-the-fly' intervention or change in the treatment plan would need to ensure that normal tissue constraints and cumulative dose limits were not violated.

Most treatment units in routine clinical use are currently not able to directly image tumor motion during beam-on time (either with or without fiducial markers). The Cyberknife is an exception in that it is a commercially available treatment unit that does possess the capability to perform real-time tumor tracking [2]. Several strategies are being explored that could be applied to a conventional linear accelerator to deliver real-time tumor tracking during radiation beam-on with the aim of increasing the accuracy of treatment delivery. It is noted that to date there is an absence of clinical data to show that such an approach is associated with an improvement in clinical

outcome over other motion management strategies (Table 11.2). At the present time therefore postulated improvements in clinical outcome due to a specific technology may be predicated on dosimetric or theoretical evaluations, which may be more or less appropriate depending on the claims being made.

Although the duration of treatment has been considered a risk factor for intra-fraction organ/target or patient motion [103], some recent data offer an alternative view. For a mobile target represented by a hepatic tumor, a study of 29 patients undergoing stereotactic liver RT found that the change in liver motion amplitude based on repeated end-inhale/end-exhale kilovoltage cone beam CT images, showed no obvious relationship with treatment time for most patients [15]. For a relatively immobile target such as spinal vertebra, pre-, mid- and post-treatment cone beam CT imaging from 31 single fraction stereotactic spine treatments revealed found that intra-fraction motion was unrelated to the total treatment time [32].

Most treatment plans assume that the tumor motion trajectory will remain the same throughout treatment without explicitly quantifying patient-specific variability in breathing pattern, or assigning a specific margin for this purpose [19]. Rather, it becomes one of possible sources of uncertainty in treatment delivery that are accounted for by the overall PTV margin. The creation of robust intensity-modulated treatment plans that are more resistant to the effects of motion is one practical response to tumor motion, such techniques, however, are still in development [89, 138, 139].

11.7.1 Imaging Techniques for Advanced On-line Treatment Verification

The development of on-board, on-line imaging tools that will quantify and verify 4D intra-fraction tumor and patient motion is an active area of research [141]. Ideally, the tumor itself will be imaged during beam delivery, given the uncertainty of surrogates and a desire to avoid implanting markers. Future developments will perhaps involve the use of software that will rapidly evaluate the discrepancies and determine whether conditions are acceptable to continue with beam delivery or not. Some techniques for real-time acquisition of positional and motion data are discussed further in the final section of this chapter.

11.7.1.1 Cone Beam CT (CBCT)

On-line set-up using CBCT-based tumor match has been shown to be more accurate than using bony anatomy as a surrogate [74] (see Fig. 11.5). The tumor volume on CBCT was shown to localize the 4D CT-derived ITV within 1 mm and 8.7 % in a phantom study [140]. Tumor motion results in CBCT artifacts and 4D CBCT has been developed and validated in order to improve imaging of mobile tumors [122]. Improved image quality [63] means that CBCT can be used for dose

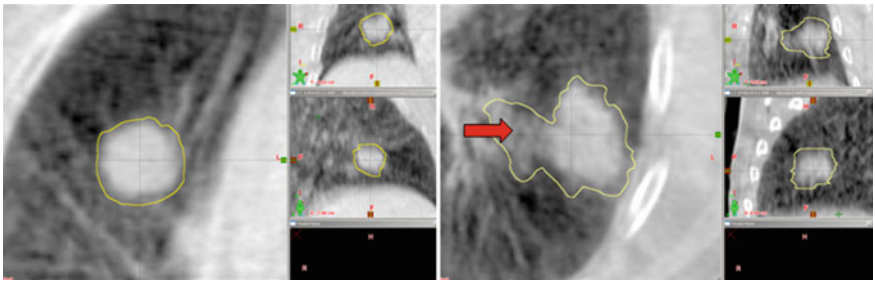

Fig. 11.5 On-line imaging with cone-beam CT (CBCT) captures information about tumor motion. In these two examples (*left* and *right*), the apparent extent of the tumor on CBCT is shown to be in good visual agreement with the extent of tumor and high risk region (*red arrow*) identified on the 10 phase 4D CT that was used for treatment planning (*yellow contour*)

calculation/treatment planning [105] and deformable image registration can be used to further enhance the application of CBCT to high precision image-guided therapeutics [90]. Megavoltage CT (MVCT) is more resistant to streak artifact and can also be used for dose calculation/treatment planning [100, 102]. Both CBCT and MVCT, have been used to reconstruct and estimate the delivered dose, which may be useful for example, in calculating doses to tumor and organs at risk and for performing adaptive RT [62, 79].

11.7.1.2 Digital Tomosynthesis (DTS)

DTS acquires volumetric images using data from a limited arc of, for example, 30°. 4D capability has been added to DTS to improve the visualization of moving targets and aid in imaging the tumor trajectory and quantifying tumor displacement during the respiratory cycle. On-line DTS is not yet in routine clinical use. It has been reported that 4D DTS agreed with 4D CBCT to within about 2–3 mm, the same order of magnitude as the inter-observer repeatability of the measurements [110].

11.7.1.3 Fluoroscopy

Markerless fluoroscopic tracking has been further refined in response to the limitations of indistinct tumor boundaries, external surrogates and a desire to avoid implanting fiducial markers (see Fig. 11.6). Recent work has used methods such as principle component analysis, regression models, artificial neural networks and support vector machine, for example to evaluate and use the optimum anatomic surrogates [67, 68]. Although fluoroscopy has not been considered an optimal modality with which to establish tumor motion for the purpose of treatment planning, it is nonetheless being used or evaluated as a tool for on-board treatment verification. Rigorous evaluation will be needed to ensure that it is able to perform this task with sufficient accuracy.

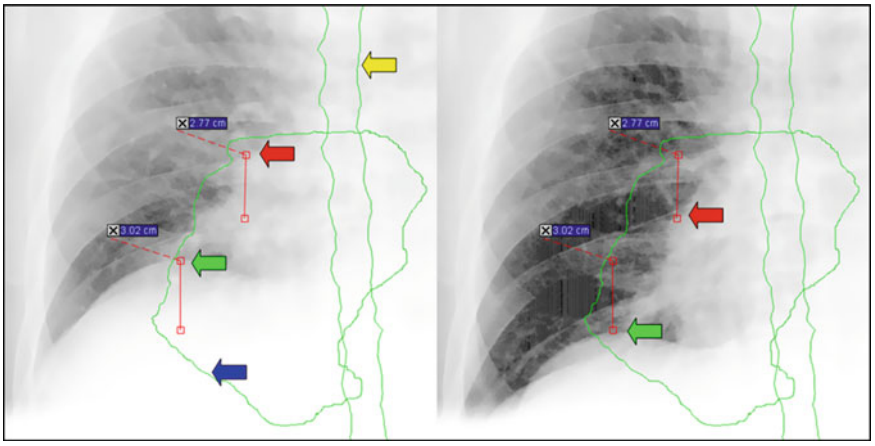

Fig. 11.6 On-line kilovoltage fluoroscopy showing displacement between end-expiration (*left*) and end-inspiration (*right*) of the diaphragm (*green arrow*, in this case measured at ~3 cm) and a point on the fluoroscopic tumor edge (e.g. *red arrow*, ~2.8 cm). Contours of the spinal canal (*yellow arrow*) and the motion-encompassing 4D CT tumor volume (*blue arrow*) have been superimposed, showing that not all the tumor is visualised on fluoroscopy

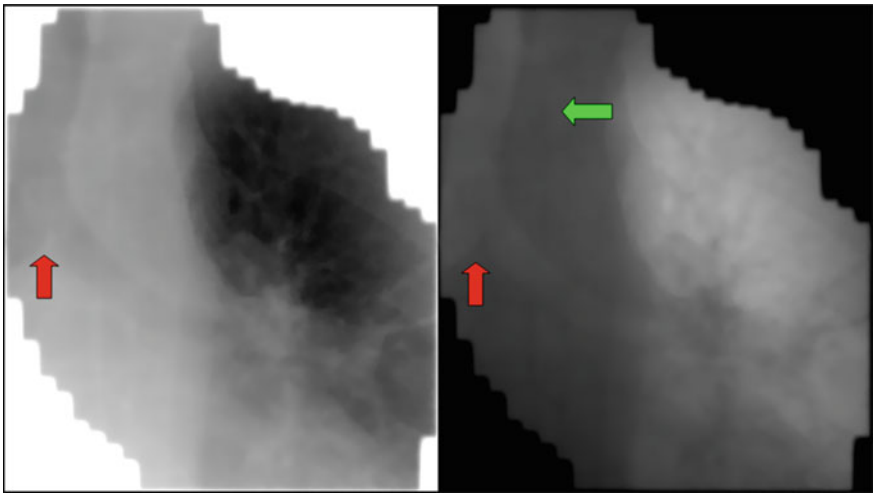

Fig. 11.7 A megavoltage fluoroscopy image showing sufficient contrast to identify different structures. In this case, the *left* and *right* pictures have had the contrast inverted and landmarks such as the spinous processes of vertebrae (*green arrow*) and surrogates for tumor motion, for example the carina (*red arrow*), can be seen

On-line megavoltage (MV) fluoroscopy has been developed to the point that it can be used in the clinic to evaluate tumor motion and verify the adequacy of ITV/PTV constructs [125] (see Fig. 11.7).

11.8 Conclusions

Recent developments have reduced the uncertainty around target identification, localization and dosimetry, even though clinical data showing the contribution of any specific development to individual or group patient outcome is limited. 4D imaging of mobile tumors in the chest and upper abdomen is now widely considered to be preferable to conventional scans. Nonetheless, there is still significant work to be done to improve target designation, real-time target visualization/positional verification during radiation delivery, minimizing OAR doses and accurately quantifying the delivered dose to both the tumor and OAR. The successful implementation of 4D imaging into routine clinical treatment requires workflows that acknowledge and deal with possible motion artifacts, and an approach to evaluating the optimum combination of different imaging strategies [37]. Patients who stand to benefit most from specific imaging modalities need to be identified in order to better manage clinical workloads. Improved physical and functional integration of different imaging modalities is necessary, for example to have concordance of multiple isocentres including that of the treatment beam. Similarly, it is essential to have improved display of multi-modal images, and a clinical operating environment that is conducive to on-line decision making. As technologies are being developed and refined, robust, transparent and consistent means of evaluation are required and although it often represents a significant challenge, reliable impact analysis is also desirable. Relying on phase III studies to provide the necessary 'gold-standard' data to support a technology may not be optimal, given for example, the challenges of patient accrual to such studies, and the probability of further technological advances during their course, rendering the technology under evaluation obsolete [7, 101].

Acknowledgments J van Sörnsen de Koste for his assistance with illustrations for this chapter.

Conflicts of Interest statement: VUmc has research collaborations with Varian Medical Systems, Palo Alto, CA, USA; BrainLAB AG, Feldkirchen, Germany; Velocity Medical Solutions, Atlanta, GA, USA.

References

1. Abdelnour, A., Nehmeh, S., Pan, T., Humm, J., Vernon, P., Schöder, H., Rosenzweig, K., Mageras, G., Yorke, E., Larson, S., Erdi, Y.: Phase and amplitude binning for 4D-CT imaging. Phys. Med. Biol. **52**(12), 3515–3529 (2007)
2. Adler, J.J., Chang, S., Murphy, M., Doty, J., Geis, P., Hancock, S.: The cyberknife: a frameless robotic system for radiosurgery. Stereotact. Funct. Neurosurg. **69**, 1–4 (1997)
3. Admiraal, M., Schuring, D., Hurkmans, C.: Dose calculations accounting for breathing motion in stereotactic lung radiotherapy based on 4D-CT and the internal target volume. Radiother. Oncol. **86**(1), 55–60 (2008)
4. Allen, A., Siracuse, K., Hayman, J., Balter, J.: Evaluation of the influence of breathing on the movement and modeling of lung tumors. Int. J. Radiat. Oncol. Biol. Phys. **58**(4), 1251–1257 (2004)

5. Baumann, P., Nyman, J., Hoyer, M., Wennberg, B., Gagliardi, G., Lax, I., Drugge, N., Ekberg, L., Friesland, S., Johansson, K., Lund, J., Morhed, E., Nilsson, K., Levin, N., Paludan, M., Sederholm, C., Traberg, A., Wittgren, L., Lewensohn, R.: Outcome in a prospective phase II trial of medically inoperable stage I non-small-cell lung cancer patients treated with stereotactic body radiotherapy. J. Clin. Oncol. **27**(20), 3290–3296 (2009)
6. Bedford, J., Warrington, A.: Commissioning of volumetric modulated arc therapy (VMAT). Int. J. Radiat. Oncol. Biol. Phys. **73**(2), 537–545 (2009)
7. Bentzen, S.: Randomized controlled trials in health technology assessment: overkill or overdue? Radiother. Oncol. **86**(2), 142–147 (2008)
8. Bettinardi, V., Rapisarda, E., Gilardi, M.: Number of partitions (gates) needed to obtain motion-free images in a respiratory gated 4D-PET/CT study as a function of the lesion size and motion displacement. Med. Phys. **36**(12), 5547–5558 (2009)
9. Biederer, J., Dinkel, J., Remmert, G., Jetter, S., Nill, S., Moser, T., Bendl, R., Thierfelder, C., Fabel, M., Oelfke, U., Bock, M., Plathow, C., Bolte, H., Welzel, T., Hoffmann, B., Hartmann, G., Schlegel, W., Debus, J., Heller, M., Kauczor, H.: 4D-imaging of the lung: reproducibility of lesion size and displacement on helical CT, MRI, and cone beam CT in a ventilated ex vivo system. Int. J. Radiat. Oncol. Biol. Phys. **73**(3), 919–926 (2009)
10. Bissonnette, J., Franks, K., Purdie, T., Moseley, D., Sonke, J., Jaffray, D., Dawson, L., Bezjak, A.: Quantifying interfraction and intrafraction tumor motion in lung stereotactic body radiotherapy using respiration-correlated cone beam computed tomography. Int. J. Radiat. Oncol. Biol. Phys. **75**(3), 688–695 (2009)
11. Boellaard, R., O'Doherty, M., Weber, W., Mottaghy, F., Lonsdale, M., Stroobants, S., Oyen, W., Kotzerke, J., Hoekstra, O., Pruim, J., Marsden, P., Tatsch, K., Hoekstra, C., Visser, E., Arends, B., Verzijlbergen, F., Zijlstra, J., Comans, E., Lammertsma, A., Paans, A., Willemsen, A., Beyer, T., Bockisch, A., Schaefer-Prokop, C., Delbeke, D., Baum, R., Chiti, A., Krause, B.: FDG PET and PET/CT: EANM procedure guidelines for tumour PET imaging: version 1.0. Eur. J. Nucl. Med. Mol. Imaging **37**(1), 181–200 (2010)
12. Cai, J., Read, P., Baisden, J., Larner, J., Benedict, S., Sheng, K.: Estimation of error in maximal intensity projection-based internal target volume of lung tumors: a simulation and comparison study using dynamic magnetic resonance imaging. Int. J. Radiat. Oncol. Biol. Phys. **69**(3), 895–902 (2007)
13. Cai, J., Read, P., Sheng, K.: The effect of respiratory motion variability and tumor size on the accuracy of average intensity projection from four-dimensional computed tomography: an investigation based on dynamic MRI. Med. Phys. **35**(11), 4974–4981 (2008)
14. Caldwell, C., Mah, K., Skinner, M., Danjoux, C.: Can PET provide the 3D extent of tumor motion for individualized internal target volumes? A phantom study of the limitations of CT and the promise of PET. Int. J. Radiat. Oncol. Biol. Phys. **55**(5), 1381–1393 (2003)
15. Case, R., Moseley, D., Sonke, J., Eccles, C., Dinniwell, R., Kim, J., Bezjak, A., Milosevic, M., Brock, K., Dawson, L.: Interfraction and intrafraction changes in amplitude of breathing motion in stereotactic liver radiotherapy. Int. J. Radiat. Oncol. Biol. Phys. **77**(3), 918–925 (2010)
16. Chan, P., Dinniwell, R., Haider, M., Cho, Y., Jaffray, D., Lockwood, G., Levin, W., Manchul, L., Fyles, A., Milosevic, M.: Inter- and intrafractional tumor and organ movement in patients with cervical cancer undergoing radiotherapy:a cinematic-MRI point-of-interest study. Int. J. Radiat. Oncol. Biol. Phys. **70**(5), 1507–1515 (2008)
17. Chaudhari, S., Goddu, S., Rangaraj, D., Pechenaya, O., Lu, W., Kintzel, E., Malinowski, K., Parikh, P., Bradley, J., Low, D.: Dosimetric variances anticipated from breathing- induced tumor motion during tomotherapy treatment delivery. Phys. Med. Biol. **54**(8), 2541–2555 (2009)
18. Chinneck, C., McJury, M., Hounsell, A.: The potential for undertaking slow CT using a modern CT scanner. Br. J. Radiol. **83**(992), 687–693 (2010)
19. Coolens, C., Webb, S., Shirato, H., Nishioka, K., Evans, P.: A margin model to account for respiration-induced tumour motion and its variability. Phys. Med. Biol. **53**(16), 4317–4330 (2008)

20. Court, L., Wagar, M., Berbeco, R., Reisner, A., Winey, B., Schofield, D., Ionascu, D., Allen, A., Popple, R., Lingos, T.: Evaluation of the interplay effect when using RapidArc to treat targets moving in the craniocaudal or right-left direction. Med. Phys. **37**(1), 4–11 (2010)
21. Dahele, M., Hwang, D., Peressotti, C., Sun, L., Kusano, M., Okhai, S., Darling, G., Yaffe, M., Caldwell, C., Mah, K., Hornby, J., Ehrlich, L., Raphael, S., Tsao, M., Behzadi, A., Weigensberg, C., Ung, Y.: Developing a methodology for three-dimensional correlation of PET-CT images and whole-mount histopathology in non-small-cell lung cancer. Curr. Oncol. **15**(5), 62–69 (2008)
22. de Koste, J., Lagerwaard, F., de Boer, H., Nijssen-Visser, M., Senan, S.: Are multiple CT scans required for planning curative radiotherapy in lung tumors of the lower lobe? Int. J. Radiat. Oncol. Biol. Phys. **55**(5), 1394–1399 (2003)
23. Dieleman, E., Senan, S., Vincent, A., Lagerwaard, F., Slotman, B., van Sörnsen de Koste, J.: Four-dimensional computed tomographic analysis of esophageal mobility during normal respiration. Int. J. Radiat. Oncol. Biol. Phys. **67**(3), 775–780 (2007)
24. Dinkel, J., Hintze, C., Tetzlaff, R., Huber, P., Herfarth, K., Debus, J., Kauczor, H., Thieke, C.: 4D-MRI analysis of lung tumor motion in patients with hemidiaphragmatic paralysis. Radiother. Oncol. **91**(3), 449–454 (2009)
25. Eccles, C., Patel, R., Simeonov, A., Lockwood, G., Haider, M., Dawson, L.: Comparison of liver tumor motion with and without abdominal compression using cine-magnetic resonance imaging. Int. J. Radiat. Oncol. Biol. Phys. **79**(2), 602–608 (2011)
26. Ehler, E., Bzdusek, K., Tom, W.: A method to automate the segmentation of the GTV and ITV for lung tumors. Med. Dosim. **34**(2), 145–153 (2009)
27. Erdi, Y., Nehmeh, S., Pan, T., Pevsner, A., Rosenzweig, K., Mageras, G., Yorke, E., Schoder, H., Hsiao, W., Squire, O., Vernon, P., Ashman, J., Mostafavi, H., Larson, S., Humm, J.: The CT motion quantitation of lung lesions and its impact on PET-measured SUVs. J. Nucl. Med. **45**(8), 1287–1292 (2004)
28. Ezhil, M., Vedam, S., Balter, P., Choi, B., Mirkovic, D., Starkschall, G., Chang, J.: Determination of patient-specific internal gross tumor volumes for lung cancer using four-dimensional computed tomography. Radiat. Oncol. **4**, 4 (2009)
29. Fang, L., Komaki, R., Allen, P., Guerrero, T., Mohan, R., Cox, J.: Comparison of outcomes for patients with medically inoperable stage I non-small-cell lung cancer treated with two-dimensional versus three-dimensional radiotherapy. Int. J. Radiat. Oncol. Biol. Phys. **66**(1), 108–116 (2006)
30. Feng, M., Balter, J., Normolle, D., Adusumilli, S., Cao, Y., Chenevert, T., Ben-Josef, E.: Characterization of pancreatic tumor motion using cine MRI: surrogates for tumor position should be used with caution. Int. J. Radiat. Oncol. Biol. Phys. **74**(3), 884–891 (2009)
31. Gagne, I., Ansbacher, W., Zavgorodni, S., Popescu, C., Beckham, W.: A monte carlo evaluation of RapidArc dose calculations for oropharynx radiotherapy. Phys. Med. Biol. **53**(24), 7167–7185 (2008)
32. Gerszten, P., Monaco, E.R., Quader, M., Novotny, J.J., Kim, J., Flickinger, J., Huq, M.: Setup accuracy of spine radiosurgery using cone beam computed tomography image guidance in patients with spinal implants. J. Neurosurg. Spine **12**(4), 413–420 (2010)
33. Ghilezan, M., Jaffray, D., Siewerdsen, J., Van Herk, M., Shetty, A., Sharpe, M., Zafar Jafri, S., Vicini, F., Matter, R., Rabbins, D., Martinez, A.: Prostate gland motion assessed with cine-magnetic resonance imaging (cine-MRI). Int. J. Radiat. Oncol. Biol. Phys. **62**(2), 406–417 (2005)
34. Glatstein, E.: Distinguishing "controversy" from conflict of interest: the wrong image for radiation oncology. Int. J. Radiat. Oncol. Biol. Phys. **76**(5), 1283–1284 (2010)
35. Goldstein, S., Ford, E., Duhon, M., McNutt, T., Wong, J., Herman, J.: Use of respiratory-correlated four-dimensional computed tomography to determine acceptable treatment margins for locally advanced pancreatic adenocarcinoma. Int. J. Radiat. Oncol. Biol. Phys. **76**(2), 597–602 (2010)
36. Grills, I.S., Hope, A.J., Guckenberger, M., Kestin, L.L., Werner-Wasik, M., Yan, D., Sonke, J., Bissonnette, J., Xiao, Y., Belderbos, J.: A multinational pooled analysis of 434 cases of stage

I non-small cell lung cancer (NSCLC) treated with volumetrically image-guided (VIGRT) stereotactic lung radiotherapy (SBRT): results from the Elekta Collaborative Lung Research Group. J. Clin. Oncol. **28**(15s), abstr 7015 (2010)
37. Guckenberger, M., Krieger, T., Richter, A., Baier, K., Wilbert, J., Sweeney, R., Flentje, M.: Potential of image-guidance, gating and real-time tracking to improve accuracy in pulmonary stereotactic body radiotherapy. Radiother. Oncol. **91**(3), 288–295 (2009)
38. Guckenberger, M., Wilbert, J., Meyer, J., Baier, K., Richter, A., Flentje, M.: Is a single respiratory correlated 4D-CT study sufficient for evaluation of breathing motion? Int. J. Radiat. Oncol. Biol. Phys. **67**(5), 1352–1359 (2007)
39. Haasbeek, C., Lagerwaard, F., Cuijpers, J., Slotman, B., Senan, S.: Is adaptive treatment planning required for stereotactic radiotherapy of stage I non-small-cell lung cancer? Int. J. Radiat. Oncol. Biol. Phys. **67**(5), 1370–1374 (2007)
40. Haasbeek, C., Spoelstra, F., Lagerwaard, F., van Sörnsen de Koste, J., Cuijpers, J., Slotman, B., Senan, S.: Impact of audio-coaching on the position of lung tumors. Int. J. Radiat. Oncol. Biol. Phys. **71**(4), 1118–1123 (2008)
41. Han, K., Cheung, P., Basran, P., Poon, I., Yeung, L., Lochray, F.: A comparison of two immobilization systems for stereotactic body radiation therapy of lung tumors. Radiother. Oncol. **95**(1), 103–108 (2010)
42. Hartmann, B., Martisiková, M., Jäkel, O.: Homogeneity of Gafchromic EBT2 film. Med. Phys. **37**(4), 1753–1756 (2010)
43. Heinzerling, J., Anderson, J., Papiez, L., Boike, T., Chien, S., Zhang, G., Abdulrahman, R., Timmerman, R.: Four-dimensional computed tomography scan analysis of tumor and organ motion at varying levels of abdominal compression during stereotactic treatment of lung and liver. Int. J. Radiat. Oncol. Biol. Phys. **70**(5), 1571–1578 (2008)
44. Higgins, J., Bezjak, A., Hope, A., Panzarella, T., Li, W., Cho, J., Craig, T., Brade, A., Sun, A., Bissonnette, J.: Effect of image-guidance frequency on geometric accuracy and setup margins in radiotherapy for locally advanced lung cancer. Int. J. Radiat. Oncol. Biol. Phys. **80**(5), 1330–1337 (2011)
45. Huang, L., Park, K., Boike, T., Lee, P., Papiez, L., Solberg, T., Ding, C., Timmerman, R.: A study on the dosimetric accuracy of treatment planning for stereotactic body radiation therapy of lung cancer using average and maximum intensity projection images. Radiother. Oncol. **96**(1), 48–54 (2010)
46. Hunjan, S., Starkschall, G., Prado, K., Dong, L., Balter, P.: Lack of correlation between external fiducial positions and internal tumor positions during breath-hold CT. Int. J. Radiat. Oncol. Biol. Phys. **76**(5), 1586–1591 (2010)
47. Hunjan, S., Starkschall, G., Rosen, I., Prado, K., Tolani, N., Balter, P.: Comparison of breath-hold and free-breathing positions of an external fiducial by analysis of respiratory traces. J. Appl. Clin. Med. Phys. **9**(3), 2768 (2008)
48. ICRU: ICRU report 62: prescribing, recording and reporting photon beam therapy (supplement to ICRU report 50). In: International Commission on Radiation Units and Measurements (ICRU), Bethesda, USA (1999). Technical report
49. Imura, M., Yamazaki, K., Shirato, H., Onimaru, R., Fujino, M., Shimizu, S., Harada, T., Ogura, S., Dosaka-Akita, H., Miyasaka, K., Nishimura, M.: Insertion and fixation of fiducial markers for setup and tracking of lung tumors in radiotherapy. Int. J. Radiat. Oncol. Biol. Phys. **63**(5), 1442–1447 (2005)
50. Jiang, S., Wolfgang, J., Mageras, G.: Quality assurance challenges for motion-adaptive radiation therapy: gating, breath holding, and four-dimensional computed tomography. Int. J. Radiat. Oncol. Biol. Phys. **71**(1 Suppl), S103–S107 (2008)
51. Juhler-Nttrup, T., Korreman, S., Pedersen, A., Persson, G., Aarup, L., Nyström, H., Olsen, M., Tarnavski, N., Specht, L.: Interfractional changes in tumour volume and position during entire radiotherapy courses for lung cancer with respiratory gating and image guidance. Acta Oncol **47**(7), 1406–1413 (2008)
52. Keall, P., Mageras, G., Balter, J., Emery, R., Forster, K., Jiang, S., Kapatoes, J., Low, D., Murphy, M., Murray, B., Ramsey, C., Van Herk, M., Vedam, S., Wong, J., Yorke, E.: The

management of respiratory motion in radiation oncology report of AAPM Task Group 76. Med. Phys. **33**(10), 3874–3900 (2006)
53. Killoran, J., Allen, A., Kann, B., Lyatskaya, Y.: Inter fractional variability of breathing phase definition as determined by fiducial location. Med. Phys. **35**(2), 753–763 (2008)
54. Kini, V., Vedam, S., Keall, P., Patil, S., Chen, C., Mohan, R.: Patient training in respiratory-gated radiotherapy. Med. Dosim. **28**(1), 7–11 (2003)
55. Kirilova, A., Lockwood, G., Choi, P., Bana, N., Haider, M., Brock, K., Eccles, C., Dawson, L.: Three-dimensional motion of liver tumors using cine-magnetic resonance imaging. Int. J. Radiat. Oncol. Biol. Phys. **71**(4), 1189–1195 (2008)
56. Kissick, M., Boswell, S., Jeraj, R., Mackie, T.: Confirmation, refinement, and extension of a study in intrafraction motion interplay with sliding jaw motion. Med. Phys. **32**(7), 2346–2350 (2005)
57. Koch, N., Liu, H., Starkschall, G., Jacobson, M., Forster, K., Liao, Z., Komaki, R., Stevens, C.: Evaluation of internal lung motion for respiratory-gated radiotherapy using MRI: Part I-correlating internal lung motion with skin fiducial motion. Int. J. Radiat. Oncol. Biol. Phys. **60**(5), 1459–1472 (2004)
58. Korreman, S., Juhler-Nttrup, T., Boyer, A.: Respiratory gated beam delivery cannot facilitate margin reduction, unless combined with respiratory correlated image guidance. Radiother. Oncol. **86**(1), 61–68 (2008)
59. Lagerwaard, F., Haasbeek, C., Smit, E., Slotman, B., Senan, S.: Outcomes of risk-adapted fractionated stereotactic radiotherapy for stage I non-small-cell lung cancer. Int. J. Radiat. Oncol. Biol. Phys. **70**(3), 685–692 (2008)
60. Lagerwaard, F., van Sornsen de Koste, J., Nijssen-Visser, M., Schuchhard-Schipper, R., Oei, S., Munne, A., Senan, S.: Multiple "slow" CTscans for incorporating lung tumor mobility in radiotherapy planning. Int. J. Radiat. Oncol. Biol. Phys. **51**(4), 932–937 (2001)
61. Langner, U., Keall, P.: Accuracy in the localization of thoracic and abdominal tumors using respiratory displacement, velocity, and phase. Med. Phys. **36**(2), 386–393 (2009)
62. Lee, L., Le, Q., Xing, L.: Retrospective IMRT dose reconstruction based on cone-beam CT and MLC log-file. Int. J. Radiat. Oncol. Biol. Phys. **70**(2), 634–644 (2008)
63. Leng, S., Tang, J., Zambelli, J., Nett, B., Tolakanahalli, R., Chen, G.: High temporal resolution and streak-free four-dimensional cone-beam computed tomography. Phys. Med. Biol. **53**(20), 5653–5673 (2008)
64. Lewis, J., Li, R., Watkins, W., Lawson, J., Segars, W., Cervi, L., Song, W., Jiang, S.: Markerless lung tumor tracking and trajectory reconstruction using rotational cone-beam projections: a feasibility study. Phys. Med. Biol. **55**(9), 2505–2522 (2010)
65. Li, J., Yan, G., Liu, C.: Comparison of two commercial detector arrays for IMRT quality assurance. J. Appl. Clin. Med. Phys. **10**(2), 2942 (2009)
66. Liao, Z., Komaki, R., Thames, H.J., Liu, H., Tucker, S., Mohan, R., Martel, M., Wei, X., Yang, K., Kim, E., Blumenschein, G., Hong, W., Cox, J.: Influence of technologic advances on outcomes in patients with unresectable, locally advanced non-small-cell lung cancer receiving concomitant chemoradiotherapy. Int. J. Radiat. Oncol. Biol. Phys. **76**(3), 775–781 (2010)
67. Lin, T., Cervi, L., Tang, X., Vasconcelos, N., Jiang, S.: Fluoroscopic tumor tracking for image-guided lung cancer radiotherapy. Phys. Med. Biol. **54**(4), 981–992 (2009)
68. Lin, T., Li, R., Tang, X., Dy, J., Jiang, S.: Markerless gating for lung cancer radiotherapy based on machine learning techniques. Phys. Med. Biol. **54**(6), 1555–1563 (2009)
69. Ling, C., Zhang, P., Archambault, Y., Bocanek, J., Tang, G., Losasso, T.: Commissioning and quality assurance of RapidArc radiotherapy delivery system. Int. J. Radiat. Oncol. Biol. Phys. **72**(2), 575–581 (2008)
70. Liu, C., Pierce, L.N., Alessio, A., Kinahan, P.: The impact of respiratory motion on tumor quantification and delineation in static PET/CT imaging. Phys. Med. Biol. **54**(24), 7345–7362 (2009)
71. Liu, H., Balter, P., Tutt, T., Choi, B., Zhang, J., Wang, C., Chi, M., Luo, D., Pan, T., Hunjan, S., Starkschall, G., Rosen, I., Prado, K., Liao, Z., Chang, J., Komaki, R., Cox, J., Mohan, R., Dong, L.: Assessing respiration-induced tumor motion and internal target volume using

four-dimensional computed tomography for radiotherapy of lung cancer. Int. J. Radiat. Oncol. Biol. Phys. **68**(2), 531–540 (2007)
72. Louie, A., Rodrigues, G., Olsthoorn, J., Palma, D., Yu, E., Yaremko, B., Ahmad, B., Aivas, I., Gaede, S.: Inter-observer and intra-observer reliability for lung cancer target volume delineation in the 4D-CT era. Radiother. Oncol. **95**(2), 166–171 (2010)
73. Malinowski, K., Pantarotto, J., Senan, S., McAvoy, T., D'Souza, W.: Inferring positions of tumor and nodes in stage III lung cancer from multiple anatomical surrogates using four-dimensional computed tomography. Int. J. Radiat. Oncol. Biol. Phys. **77**(5), 1553–1560 (2010)
74. Masi, L., Casamassima, F., Menichelli, C., Pasciuti, K., Doro, R., Polli, C., D'imporzano, E., Bonucci, I.: On-line image guidance for frameless stereotactic radiotherapy of lung malignancies by cone beam CT: comparison between target localization and alignment on bony anatomy. Acta Oncol. **47**(7), 1422–1431 (2008)
75. McBain, C., Khoo, V., Buckley, D., Sykes, J., Green, M., Cowan, R., Hutchinson, C., Moore, C., Price, P.: Assessment of bladder motion for clinical radiotherapy practice using cine-magnetic resonance imaging. Int. J. Radiat. Oncol. Biol. Phys. **75**(3), 664–671 (2009)
76. McNair, H., Brock, J., Symonds-Tayler, J., Ashley, S., Eagle, S., Evans, P., Kavanagh, A., Panakis, N., Brada, M.: Feasibility of the use of the active breathing co ordinator (ABC) in patients receiving radical radiotherapy for non-small cell lung cancer (NSCLC). Radiother. Oncol. **93**(3), 424–429 (2009)
77. Milot, L., Guindi, M., Gallinger, S., Moulton, C., Brock, K., Dawson, L., Haider, M.: Mr imaging correlates of intratumoral issue types within colorectal liver metastases: a high-spatial-resolution fresh ex vivo radiologic-pathologic correlation study. Radiology **254**(3), 747–754 (2010)
78. Minn, A., Schellenberg, D., Maxim, P., Suh, Y., McKenna, S., Cox, B., Dieterich, S., Xing, L., Graves, E., Goodman, K., Chang, D., Koong, A.: Pancreatic tumor motion on a single planning 4D-CT does not correlate with intrafraction tumor motion during treatment. Am. J. Clin. Oncol. **32**(4), 364–368 (2009)
79. Morin, O., Chen, J., Aubin, M., Gillis, A., Aubry, J., Bose, S., Chen, H., Descovich, M., Xia, P., Pouliot, J.: Dose calculation using megavoltage cone-beam CT. Int. J. Radiat. Oncol. Biol. Phys. **67**(4), 1201–1210 (2007)
80. Muirhead, R., McNee, S., Featherstone, C., Moore, K., Muscat, S.: Use of maximum intensity projections (MIPs) for target outlining in 4DCT radiotherapy planning. J. Thorac. Oncol. **3**(12), 1433–1438 (2008)
81. Mutaf, Y., Antolak, J., Brinkmann, D.: The impact of temporal inaccuracies on 4DCT image quality. Med. Phys. **34**(5), 1615–1622 (2007)
82. Nakamura, M., Narita, Y., Matsuo, Y., Narabayashi, M., Nakata, M., Sawada, A., Mizowaki, T., Nagata, Y., Hiraoka, M.: Effect of audio coaching on correlation of abdominal displacement with lung tumor motion. Int. J. Radiat. Oncol. Biol. Phys. **75**(2), 558–563 (2009)
83. Nakamura, M., Narita, Y., Matsuo, Y., Narabayashi, M., Nakata, M., Yano, S., Miyabe, Y., Matsugi, K., Sawada, A., Norihisa, Y., Mizowaki, T., Nagata, Y., Hiraoka, M.: Geometrical differences in target volumes between slow CT and 4D CT imaging in stereotactic body radiotherapy for lung tumors in the upper and middle lobe. Med. Phys. **35**(9), 4142–4148 (2008)
84. Nakamura, M., Narita, Y., Sawada, A., Matsugi, K., Nakata, M., Matsuo, Y., Mizowaki, T., Hiraoka, M.: Impact of motion velocity on four-dimensional target volumes: a phantom study. Med. Phys. **36**(5), 1610–1617 (2009)
85. Nehmeh, S., Erdi, Y., Pan, T., Pevsner, A., Rosenzweig, K., Yorke, E., Mageras, G., Schoder, H., Vernon, P., Squire, O., Mostafavi, H., Larson, S., Humm, J.: Four-dimensional (4D) PET/CT imaging of the thorax. Med. Phys. **31**(12), 3179–3186 (2004)
86. Neicu, T., Berbeco, R., Wolfgang, J., Jiang, S.: Synchronized moving aperture radiation therapy (SMART): improvement of breathing pattern reproducibility using respiratory coaching. Phys. Med. Biol. **51**(3), 617–636 (2006)
87. Nelson, C., Balter, P., Morice, R., Bucci, K., Dong, L., Tucker, S., Vedam, S., Chang, J., Starkschall, G.: Evaluation of tumor position and PTV margins using image guidance and respiratory gating. Int. J. Radiat. Oncol. Biol. Phys. **76**(5), 1578–1585 (2010)

88. Nestle, U., Kremp, S., Schaefer-Schuler, A., Sebastian-Welsch, C., Hellwig, D., Rübe, C., Kirsch, C.: Comparison of different methods for delineation of 18F-FDG PET-positive tissue for target volume definition in radiotherapy of patients with non-small cell lung cancer. J. Nucl. Med. **46**(8), 1342–1348 (2005)
89. Ngwa, W., Meeks, S., Kupelian, P., Schnarr, E., Langen, K.: Validation of a computational method for assessing the impact of intra-fraction motion on helical tomotherapy plans. Phys. Med. Biol. **54**(21), 6611–6621 (2009)
90. Nithiananthan, S., Brock, K., Daly, M., Chan, H., Irish, J., Siewerdsen, J.: Demons deformable registration for CBCT-guided procedures in the head and neck: convergence and accuracy. Med. Phys. **36**(10), 4755–4764 (2009)
91. Ong, C., Verbakel, W., Cuijpers, J., Slotman, B., Senan, S.: Dosimetric impact of interplay effect on RapidArc lung stereotactic treatment delivery. Int. J. Radiat. Oncol. Biol. Phys. **79**(1), 305–311 (2011)
92. Pan, T., Lee, T., Rietzel, E., Chen, G.: 4D-CT imaging of a volume influenced by respiratory motion on multi-slice CT. Med. Phys. **31**(2), 333–340 (2004)
93. Panakis, N., McNair, H., Christian, J., Mendes, R., Symonds-Tayler, J., Knowles, C., Evans, P., Bedford, J., Brada, M.: Defining the margins in the radical radiotherapy of non-small cell lung cancer (NSCLC) with active breathing control (ABC) and the effect on physical lung parameters. Radiother. Oncol. **87**(1), 65–73 (2008)
94. Pantarotto, J., Piet, A., Vincent, A., van Sörnsen de Koste, J., Senan, S.: Motion analysis of 100 mediastinal lymph nodes: potential pitfalls in treatment planning and adaptive strategies. Int. J. Radiat. Oncol. Biol. Phys. **74**(4), 1092–1099 (2009)
95. Park, S., Ionascu, D., Killoran, J., Mamede, M., Gerbaudo, V., Chin, L., Berbeco, R.: Evaluation of the combined effects of target size, respiratory motion and background activity on 3D and 4D PET/CT images. Phys. Med. Biol. **53**(13), 3661–3679 (2008)
96. Perrin, R., Evans, P., Webb, S., Partridge, M.: The use of PETimages for radiotherapy treatment planning: an error analysis using radiobiological endpoints. Med. Phys. **37**(2), 516–531 (2010)
97. Persson, G., Nygaard, D., Brink, C., Jahn, J., Rosenschöld, P., Specht, L., Korreman, S.: Deviations in delineated GTV caused by artefacts in 4DCT. Radiother. Oncol. **96**(1), 61–66 (2010)
98. Persson, G., Nygaard, D., Olsen, M., Juhler-Nttrup, T., Pedersen, A., Specht, L., Korreman, S.: Can audio coached 4D CT emulate free breathing during the treatment course? Acta Oncol. **47**(7), 1397–1405 (2008)
99. Peters, L., O'Sullivan, B., Giralt, J., Fitzgerald, T., Trotti, A., Bernier, J., Bourhis, J., Yuen, K., Fisher, R., Rischin, D.: Critical impact of radiotherapy protocol compliance and quality in the treatment of advanced head and neck cancer: results from TROG 02.02. J. Clin. Oncol. **28**(18), 2996–3001 (2010)
100. Petit, S., van Elmpt, W., Nijsten, S., Lambin, P., Dekker, A.: Calibration of megavoltage cone-beam CT for radiotherapy dose calculations: correction of cupping artifacts and conversion of CT numbers to electron density. Med. Phys. **35**(3), 849–865 (2008)
101. Ploquin, N., Dunscombe, P.: A cost-outcome analysis of image-guided patient repositioning in the radiation treatment of cancer of the prostate. Radiother. Oncol. **93**(1), 25–31 (2009)
102. Pouliot, J., Bani-Hashemi, A., Chen, J., Svatos, M., Ghelmansarai, F., Mitschke, M., Aubin, M., Xia, P., Morin, O., Bucci, K., Roach, M.R., Hernandez, P., Zheng, Z., Hristov, D., Verhey, L.: Low-dose megavoltage cone-beam CT for radiation therapy. Int. J. Radiat. Oncol. Biol. Phys. **61**(2), 552–560 (2005)
103. Purdie, T., Bissonnette, J., Franks, K., Bezjak, A., Payne, D., Sie, F., Sharpe, M., Jaffray, D.: Cone-beam computed tomography for on-line image guidance of lung stereotactic radiotherapy: localization, verification, and intrafraction tumor position. Int. J. Radiat. Oncol. Biol. Phys. **68**(1), 243–252 (2007)
104. Purdy, J.: Current ICRU definitions of volumes: limitations and future directions. Semin. Radiat. Oncol. **14**(1), 27–40 (2004)
105. Richter, A., Hu, Q., Steglich, D., Baier, K., Wilbert, J., Guckenberger, M., Flentje, M.: Investigation of the usability of conebeam CT data sets for dose calculation. Radiat. Oncol. **3**, 42 (2008)

106. Richter, A., Wilbert, J., Baier, K., Flentje, M., Guckenberger, M.: Feasibility study for markerless tracking of lung tumors in stereotactic body radiotherapy. Int. J. Radiat. Oncol. Biol. Phys. **78**(2), 618–627 (2010)
107. Riegel, A., Bucci, M., Mawlawi, O., Johnson, V., Ahmad, M., Sun, X., Luo, D., Chandler, A., Pan, T.: Target definition of moving lung tumors in positron emission tomography: correlation of optimal activity concentration thresholds with object size, motion extent, and source-to-background ratio. Med. Phys. **37**(4), 1742–1752 (2010)
108. Rietzel, E., Liu, A., Chen, G., Choi, N.: Maximum-intensity volumes for fast contouring of lung tumors including respiratory motion in 4DCT planning. Int. J. Radiat. Oncol. Biol. Phys. **71**(4), 1245–1252 (2008)
109. Rietzel, E., Pan, T., Chen, G.: Four-dimensional computed tomography: image formation and clinical protocol. Med. Phys. **32**(4), 874–889 (2005)
110. Santoro, J., Kriminski, S., Lovelock, D., Rosenzweig, K., Mostafavi, H., Amols, H., Mageras, G.: Evaluation of respiration-correlated digital tomosynthesis in lung. Med. Phys. **37**(3), 1237–1245 (2010)
111. Santoro, J., Yorke, E., Goodman, K., Mageras, G.: From phase-based to isplacement-based gating: a software tool to facilitate respiration-gated radiation treatment. J. Appl. Clin. Med. Phys. **10**(4), 2982 (2009)
112. Sarker, J., Chu, A., Mui, K., Wolfgang, J., Hirsch, A., Chen, G., Sharp, G.: Variations in tumor size and position due to irregular breathing in 4D-CT: a simulation study. Med. Phys. **37**(3), 1254–1260 (2010)
113. Sawant, A., Smith, R., Venkat, R., Santanam, L., Cho, B., Poulsen, P., Cattell, H., Newell, L., Parikh, P., Keall, P.: Toward submillimeter accuracy in the management of intrafraction motion: the integration of real-time internal position monitoring and multileaf collimator target tracking. Int. J. Radiat. Oncol. Biol. Phys. **74**(2), 575–582 (2009)
114. Senan, S., de Ruysscher, D., Giraud, P., Mirimanoff, R., Budach, V.: Radiotherapy group of european organization for research and treatment of cancer literature-based recommendations for treatment planning and execution in high-dose radiotherapy for lung cancer. Radiother. Oncol. **71**(2), 139–146 (2004)
115. Senan, S., van Sörnsen de Koste, J., Samson, M., Tankink, H., Jansen, P., Nowak, P., Krol, A., Schmitz, P., Lagerwaard, F.: Evaluation of a target contouring protocol for 3D conformal radiotherapy in non-small cell lung cancer. Radiother. Oncol. **53**(3), 247–255 (1999)
116. Senan, S., Palma, D.: Stereotactic lung radiotherapy: Do we need fiducial markers? Ann. Thorac. Surg. **91**(1), 335–336 (2011)
117. Shchory, T., Schifter, D., Lichtman, R., Neustadter, D., Corn, B.: Tracking accuracy of a real-time fiducial tracking system for patient positioning and monitoring in radiation therapy. Int. J. Radiat. Oncol. Biol. Phys. **78**(4), 1227–1234 (2010)
118. Shih, H., Jiang, S., Aljarrah, K., Doppke, K., Choi, N.: Internal target volume determined with expansion margins beyond composite gross tumor volume in three-dimensional conformal radiotherapy for lung cancer. Int. J. Radiat. Oncol. Biol. Phys. **60**(2), 613–622 (2004)
119. Sixel, K., Ruschin, M., Tirona, R., Cheung, P.: Digital fluoroscopy to quantify lung tumor motion: potential for patient-specific planning target volumes. Int. J. Radiat. Oncol. Biol. Phys. **57**(3), 717–723 (2003)
120. Slotman, B., Lagerwaard, F., Senan, S.: 4D imaging for target definition in stereotactic radiotherapy for lung cancer. Acta Oncol. **45**(7), 966–972 (2006)
121. Sonke, J., Rossi, M., Wolthaus, J., van Herk, M., Damen, E., Belderbos, J.: Frameless stereotactic body radiotherapy for lung cancer using four-dimensional cone beam CT guidance. Int. J. Radiat. Oncol. Biol. Phys. **74**(2), 567–574 (2009)
122. Sonke, J., Zijp, L., Remeijer, P., van Herk, M.: Respiratory correlated cone beam CT. Med. Phys. **32**(4), 1176–1186 (2005)
123. Starkschall, G., Desai, N., Balter, P., Prado, K., Luo, D., Cody, D., Pan, T.: Quantitative assessment of four-dimensional computed tomography image acquisition quality. J. Appl. Clin. Med. Phys. **8**(3), 2362 (2007)

124. Suh, Y., Sawant, A., Venkat, R., Keall, P.: Four-dimensional IMRTtreatment planning using a DMLC motion-tracking algorithm. Phys. Med. Biol. **54**(12), 3821–3835 (2009)
125. Tai, A., Christensen, J., Gore, E., Khamene, A., Boettger, T., Li, X.: Gated treatment delivery verification with on-line megavoltage fluoroscopy. Int. J. Radiat. Oncol. Biol. Phys. **76**(5), 1592–1598 (2010)
126. Teke, T., Bergman, A., Kwa, W., Gill, B., Duzenli, C., Popescu, I.: Monte carlo based, patient-specific RapidArc QA using Linac log files. Med. Phys. **37**(1), 116–123 (2010)
127. Timmerman, R., Paulus, R., Galvin, J., Michalski, J., Straube, W., Bradley, J., Fakiris, A., Bezjak, A., Videtic, G., Johnstone, D., Fowler, J., Gore, E., Choy, H.: Stereotactic body radiation therapy for inoperable early stage lung cancer. JAMA **303**(11), 1070–1076 (2010)
128. Underberg, R., Lagerwaard, F., Cuijpers, J., Slotman, B., van Sörnsen de KostE, J., Senan, S.: Four-dimensional CT scans for treatment planning in stereotactic radiotherapy for stage I lung cancer. Int. J. Radiat. Oncol. Biol. Phys. **60**(4), 1283–1290 (2004)
129. Underberg, R., Lagerwaard, F., Slotman, B., Cuijpers, J., Senan, S.: Benefit of respiration-gated stereotactic radiotherapy for stage I lung cancer: an analysis of 4DCT datasets. Int. J. Radiat. Oncol. Biol. Phys. **62**(2), 554–560 (2005)
130. Underberg, R., Lagerwaard, F., Slotman, B., Cuijpers, J., Senan, S.: Use of maximum intensity projections (MIP) for target volume generation in 4DCT scans for lung cancer. Int. J. Radiat. Oncol. Biol. Phys. **63**(1), 253–260 (2005)
131. van Battum, L., Hoffmans, D., Piersma, H., Heukelom, S.: Accurate dosimetry with Gafchromic EBT film of a 6 MV photon beam in water: what level is achievable? Med. Phys. **35**(2), 704–716 (2008)
132. van Dam, I., van Sörnsen de Koste, J., Hanna, G., Muirhead, R., Slotman, B., Senan, S.: Improving target delineation on 4-dimensional CT scans in stage I NSCLC using a deformable registration tool. Radiother. Oncol. **96**(1), 67–72 (2010)
133. van der Geld, Y., Lagerwaard, F., van Sörnsen de Koste, J., Cuijpers, J., Slotman, B., Senan, S.: Reproducibility of target volumes generated using uncoached 4-dimensional CT scans for peripheral lung cancer. Radiat. Oncol. **1**, 43 (2006)
134. van der Geld, y, Senan, S., van Sörnsen de Koste, J., van Tinteren, H., Slotman, B., Underberg, R., Lagerwaard, F.: Evaluating mobility for radiotherapy planning of lung tumors: a comparison of virtual fluoroscopy and 4DCT. Lung Cancer **53**(1), 31–37 (2006)
135. van Dyk, J.: Quality assurance of radiation therapy planning systems: current status and remaining challenges. Int. J. Radiat. Oncol. Biol. Phys. **71**, 23–27 (2008)
136. van Sörnsen de Koste, J., Senan, S., Kleynen, C., Slotman, B., Lagerwaard, F.: Renal mobility during uncoached quiet respiration: an analysis of 4DCT scans. Int. J. Radiat. Oncol. Biol. Phys. **64**(3), 799–803 (2006)
137. Vedam, S., Keall, P., Kini, V., Mostafavi, H., Shukla, H., Mohan, R.: Acquiring a four-dimensional computed tomography dataset using an external respiratory signal. Phys. Med. Biol. **48**(1), 45–62 (2003)
138. Vrancić, C., Trofimov, A., Chan, T., Sharp, G., Bortfeld, T.: Experimental evaluation of a robust optimization method for IMRT of moving targets. Phys. Med. Biol. **54**(9), 2901–2914 (2009)
139. Waghorn, B., Shah, A., Ngwa, W., Meeks, S., Moore, J., Siebers, J., Langen, K.: A computational method for estimating the dosimetric effect of intra-fraction motion on step-and-shoot IMRT and compensator plans. Phys. Med. Biol. **55**(14), 4187–4202 (2010)
140. Wang, Z., Wu, Q., Marks, L., Larrier, N., Yin, F.: Cone-beam CT localization of internal target volumes for stereotactic body radiotherapy of lung lesions. Int. J. Radiat. Oncol. Biol. Phys. **69**(5), 1618–1624 (2007)
141. Wertz, H., Stsepankou, D., Blessing, M., Rossi, M., Knox, C., Brown, K., Gros, U., Boda-Heggemann, J., Walter, C., Hesser, J., Lohr, F., Wenz, F.: Fast kilovoltage/megavoltage (kV/MV) breathhold cone-beam CT for image-guided radiotherapy of lung cancer. Phys. Med. Biol. **55**(15), 4203–4217 (2010)
142. Wilbert, J., Baier, K., Richter, A., Herrmann, C., Ma, L., Flentje, M., Guckenberger, M.: Influence of continuous table motion on patient breathing patterns. Int. J. Radiat. Oncol. Biol. Phys. **77**(2), 622–629 (2010)

143. Wu, J., Lei, P., Shekhar, R., Li, H., Suntharalingam, M., D'Souza, W.: Do tumors in the lung deform during normal respiration? An image registration investigation. Int. J. Radiat. Oncol. Biol. Phys. **75**(1), 268–275 (2009)
144. Wu, K., Ung, Y., Hornby, J., Freeman, M., Hwang, D., Tsao, M., Dahele, M., Darling, G., Maziak, D., Tirona, R., Mah, K., Wong, C.: PET CT thresholds for radiotherapy target definition in non-small-cell lung cancer: how close are we to the pathologic findings? Int. J. Radiat. Oncol. Biol. Phys. **77**(3), 699–706 (2010)
145. Wunderink, W., Mndez Romero, A., Seppenwoolde, Y., de Boer, H., Levendag, P., Heijmen, B.: Potentials and limitations of guiding liver stereotactic body radiation therapy set-up on liver-implanted fiducial markers. Int. J. Radiat. Oncol. Biol. Phys. **77**(5), 1573–1583 (2010)
146. Xiao, Y., Papiez, L., Paulus, R., Timmerman, R., Straube, W., Bosch, W., Michalski, J., Galvin, J.: Dosimetric evaluation of heterogeneity corrections for RTOG 0236: stereotactic body radiotherapy of inoperable stage I-II non-small-cell lung cancer. Int. J. Radiat. Oncol. Biol. Phys. **73**(4), 1235–1242 (2009)
147. Yamamoto, T., Langner, U., Loo, B.J., Shen, J., Keall, P.: Retrospective analysis of artifacts in four-dimensional CT images of 50 abdominal and thoracic radiotherapy patients. Int. J. Radiat. Oncol. Biol. Phys. **72**(4), 1250–1258 (2008)
148. Yan, G., Lu, B., Kozelka, J., Liu, C., Li, J.: Calibration of a novel four-dimensional diode array. Med. Phys. **37**(1), 108–115 (2010)

Chapter 12
Respiratory Motion Prediction in Radiation Therapy

Sastry Vedam

Abstract Active respiratory motion management has received increasing attention in the past decade as a means to reduce the internal margin (IM) component of the clinical target volume (CTV)—planning target volume (PTV) margin typically added around the gross tumor volume (GTV) during radiation therapy of thoracic and abdominal tumors. Engineering and technical developments in linear accelerator design and respiratory motion monitoring respectively have made the delivery of motion adaptive radiation therapy possible through real-time control of either dynamic multileaf collimator (MLC) motion (gantry based linear accelerator design) or robotic arm motion (robotic arm mounted linear accelerator design).

12.1 Necessity for Respiratory Motion Prediction

The accuracy and precision of radiation delivery with either system is directly dependent on the ability of the system to "adapt" to the constantly changing relationship between target position and beam position. Success of such adaptation depends on the nature of the typical time delay between sensing a change in target position and actuating a system response to such a change. Linear accelerators (both gantry and robotic arm based); being complex systems, require a finite amount of time for adaptation, referred to as latency. During such time, the target continues to move, thereby causing a perennial lag in the system response to change in the target position, as seen in Fig. 12.1.

Predicting the position of the target in advance is therefore considered as an approach to minimize positioning errors due to the lag in system response. The ultimate goal of prediction is to ensure that the radiation beam encompasses the target

S. Vedam (✉)
Department of Radiation Physics, University of Texas M. D. Anderson Cancer Center, Houston, TX, USA
e-mail: svedam@mdanderson.org

J. Ehrhardt and C. Lorenz (eds.), *4D Modeling and Estimation of Respiratory Motion for Radiation Therapy*, Biological and Medical Physics, Biomedical Engineering,
DOI: 10.1007/978-3-642-36441-9_12,

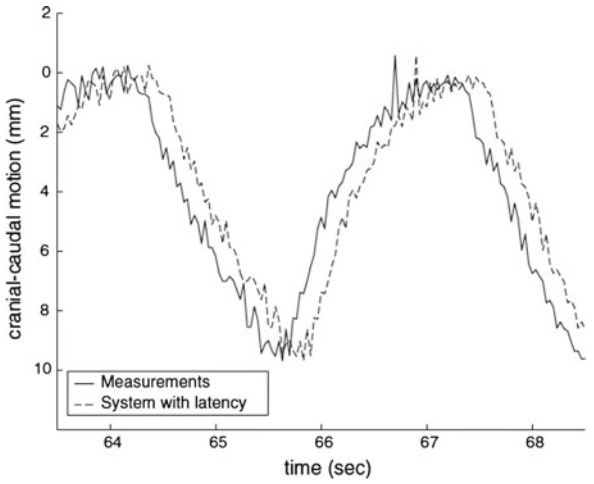

Fig. 12.1 Illustration of the effect of system latency on the target localization accuracy (from Sharp et al. [13])

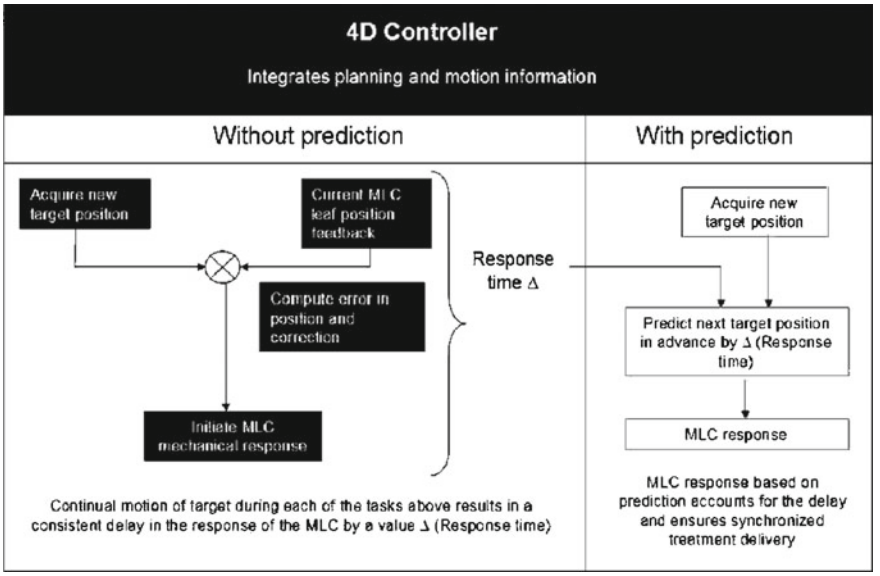

Fig. 12.2 Necessity for predicting respiratory motion, illustrated in the framework of a MLC based linear accelerator design (from Vedam et al. [15])

as it moves throughout the respiratory cycle. Figure 12.2 illustrates the necessity for predicting respiratory motion within the framework of an MLC based gantry mounted linear accelerator design.

12.2 Understanding Respiratory Motion Prediction

Respiratory motion in radiation therapy is typically monitored through mainly two approaches: (a) Direct tumor tracking or (b) Indirect tumor surrogate tracking. Direct tumor tracking is usually implemented through on board imaging systems that track the position of the tumor through radiographic/fluoroscopic imaging or electromagnetic transponder tracking. Such approaches, more often than not, involve implantation of fiducials into or in the vicinity of the tumor volume. Indirect tumor surrogate tracking involves monitoring the position of internal or external anatomy based surrogates that have an established position correlation with respect to the actual tumor motion throughout the respiratory cycle. An example of an external surrogate is chest/abdominal wall motion. The lung/diaphragm interface is considered a good internal surrogate for certain thoracic and abdominal tumors. All of the above approaches provide the input data necessary for predicting respiratory motion.

In order to understand the concepts behind respiratory motion prediction, it is useful to introduce and define some basic terminology. The following terms represent the various parameters that will find mention in all of the predictive models that will be discussed henceforth.

Sampling Rate

Sampling rate refers to the frequency at which respiratory motion data is sensed or acquired. It is usually quantified in terms of samples/sec or Hz. Faster sampling rates result in greater resolution of respiratory motion, thereby inspiring higher confidence in the accuracy/precision of respiratory motion monitoring. Direct tumor tracking, being a typically resource intensive process yields slower sampling rates (of the order of 10 samples/sec) as compared to indirect tumor surrogate tracking, which can yield near real time (30 samples/sec) sampling rates.

Latency

Adaptive systems require a finite amount of time to sense and react to changes in the sensed parameter, which presently, is respiratory motion. Such a time interval is usually indicative of the lag in the response of the system to the change in respiratory tumor position, and is therefore defined as latency. It is usually quantified in milliseconds or seconds.

Signal History/Training Length

Predicting respiratory tumor position at a future time instant is always based on respiratory motion information collected from the past. The duration of such past

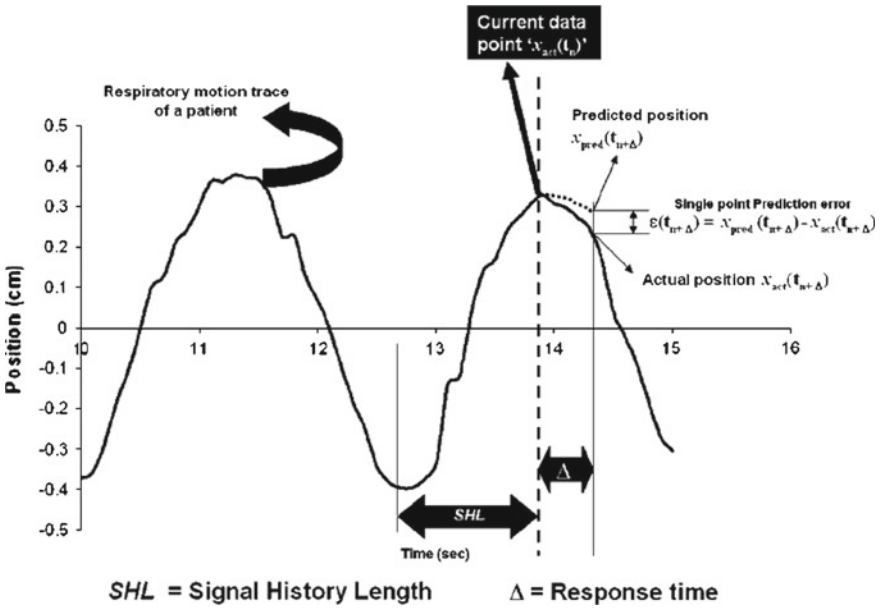

Fig. 12.3 Illustration of the prediction parameters, signal history length and response time relative to the current data point in the respiratory motion trace (from Vedam et al. [15])

motion history used for prediction is referred to as signal history length or training length. It is usually quantified in milliseconds or seconds.

Response Time

The time interval in advance for which the prediction of respiratory tumor position is made is referred to as response time. It is usually quantified in milliseconds.

Figure 12.3 provides an illustration of the above parameters in the context of respiratory motion prediction.

12.3 Respiratory Motion Prediction Models

In increasing order of complexity, predictive filter algorithms span the range from the simpler stationary linear filter models to the highly complex adaptive nonlinear filter models [15]. Several predictive models have been studied recently for the purpose of image guided and adaptive radiotherapy. The following sections provide a brief insight into some of these predictive models.

For any given random sequence $\{x\} = x_{act}(t_n)_{n=1,m}$ at a given time instant t_n, prediction provides an estimate $x_{pred}(t_n + \Delta)$of $\{x\}$, ahead by an interval Δ. The prediction $x_{pred}(t_n + \Delta)$is based on a number of previous values of the sequence, referred to as signal history window; the length of which is referred to as signal history length SHL, as seen in the equation below:

$$x_{pred}(t_n + \Delta) = f\{x_{act}(t_n), x_{act}(t_{n-1}), ..., x_{act}(t_{n-SHL})\} \tag{12.1}$$

Depending on how one employs the chosen signal history for prediction, several different approaches are available to obtain the predicted position at a time instance in the future.

12.3.1 Parametric Models

If one makes assumptions about the functional form of the respiratory signal, these functions can be used to guide a prediction algorithm. This approach has been studied by Vedam et al. [15]; employing a sinusoidal model to predict external chest wall position. They found that the sinusoidal model did reduce the geometric error introduced by the response time compared with no prediction; adaptive prediction models performed better in reducing the geometric uncertainty.

12.3.2 Empirical Algorithms

In this approach, the prediction is based on a combination (linear/non linear) of prior inputs from some past history of the respiratory motion signal, as shown below:

$$x_{pred}(t_n + \Delta) = \sum_{i=1}^{SHL} c_i x_{t_{n-i}} \tag{12.2}$$

where $x_{pred}(t_n + \Delta)$is the predicted position in advance by a time Δ, $\{c\}$ is the vector of filter coefficients and $x_{t_{n-i}}$ represents a vector of past respiratory motion signal inputs. In such a formulation, the problem of optimal prediction is essentially a problem of optimization of the filter coefficient vector $\{c\}$. For stationary input signals with known statistics, the optimal $\{c\}$ values are given by the Yule-Walker equations [1], or a least mean squares algorithm approach, resulting in what is referred to as linear filtering/prediction.

In the case of real-time respiratory motion, such statistics may not be completely available. Therefore, linear adaptive filtering is employed for determining optimal values of $\{c\}$, which are further used for prediction, according to Eq. (12.2). In adaptive filtering, coefficient vector $\{c\}$ is updated after each prediction $x_{pred}(t_n+\Delta)$

through a correction term that is proportional to the prediction error $\varepsilon(t_n + \Delta)$ of the most recent prediction, thereby introducing a feedback that attempts to minimize prediction error $\varepsilon(t_n)$. Linear prediction and adaptive linear prediction methods have been studied by Sharp et al. [13], Vedam et al. [15] and Murphy et al. [5].

Other increasingly complex approaches to empirical algorithms have been examined. McCall et al. [4], have employed a dual component model to separate the respiratory motion pattern into periodic and non periodic components. The periodic component is usually a representative mean respiratory motion trace, estimated from a set of recent respiratory motion data. The non periodic component, which is the difference in between the respiratory signal and the magnitude of its corresponding periodic component, is described as an auto regressive moving average (ARMA) model. Ren et al. [8], have also employed a variation of the above ARMA model to predict respiratory motion. To account for instability inherent in respiratory motion patterns, they have employed an iterative least mean squares approach to adapt the ARMA coefficients in order to minimize prediction errors.

Ruan et al. [10], have reported on a comprehensive approach to respiratory motion prediction based on local regression models. Their approach addresses the problem in three stages. These include (a) capturing representative system dynamics or determine a representative state of a portion of the input respiratory motion data, (b) developing a local regression based training model to train the predictor from previous observations of respiratory motion and (c) iteratively adjusting the weights of coefficients in the training model to incorporate any residual fading temporal correlations.

12.3.3 Kernel Density Approximation (KDE)

KDE [9] is essentially a probabilistic approach to address the problem of respiratory motion prediction. A simplistic description of KDE is as follows. In this statistical method, the PDF of the input respiratory motion data is considered. Each training sample for the model is therefore an output in the PDF. The problem of prediction in this case is to estimate a conditional distribution of outputs for a given set of inputs and then apply the conditional distribution to predict the output for subsequent input respiratory motion data points. Ruan et al. [11], further improved on the above work to address the problem of predicting in three dimensions. Prinicpal component analysis was applied to construct a low dimensional feature space to enable KDE with limited training data. This is useful especially in situations where there is a limited training data set and prediction is still necessary along multiple co-ordinate dimensions, as is seen for example with the Cyberknife robotic arm mounted linear accelerator system during tumor tracking delivery.

12.3.4 Kalman Filtering

Another approach, based on a combination of using source models and empirical sampling, is referred to as Kalman filtering. In other words, it is a method to estimate the internal state of a linear dynamic system. As an example, Sharp et al. [13] have used Kalman filtering to generate an optimal estimate for the current state of the system by combining a previous estimate, its covariance, and the current measurement. From such an estimated state, the future value of the input signal was predicted. This predicted value was then used to constantly update the internal state of the dynamic system. Murphy et al. [5] have also reported on nonlinear Kalman filtering in their work on predicting respiratory motion. Putra et al. [7], have presented an interacting multiple model (IMM) filter that employs Kalman filtering as the basis for two individual models that characterize respiratory tumor motion based on constant velocity and constant acceleration. The IMM filter then combines the predictions of the individual Kalman filters to predict respiratory tumor motion.

12.3.5 Neural Network Models

Artificial neural networks have the unique feature that allows them to modify their response to their environment [2]. The networks are usually made aware of their environment through an initial training process. Once trained, the response is fairly insensitive to minor variations (usually noise and distortion) in the input and, therefore, can better adapt and respond to the actual patterns of the input. Another advantage of developing such a neural network framework is its adaptability to function as both a linear and nonlinear filter, thus providing us with an integrated approach that is inclusive of all classes of predictive filters. A schematic of the various building blocks of an artificial neural network are as shown in Fig. 12.4.

The training algorithm updates the weight matrix iteratively during each epoch or instance of training to minimize a network performance function. Performance functions can range from simple mean square error (average squared error between the network and the target-training outputs) to more complex algorithms such as the Levenberg-Marquardt algorithm that can increase the speed of convergence.

Activation functions alter the output from the neuron layer to provide a final network output. These functions may be simple linear functions or complex nonlinear functions. One may think of an activation function as defining a gain (linear/nonlinear) for the artificial neuron.

Isaksson et al. [3] have developed and compared the performance of an artificial neural network trained using the Levenberg-Marquardt method, combined with a sigmoid activation function, with a least mean squares-based adaptive filtering approach. Yan et al. [16] have also used neural networks to predict internal positions from a combination of internal markers and external respiratory signals.

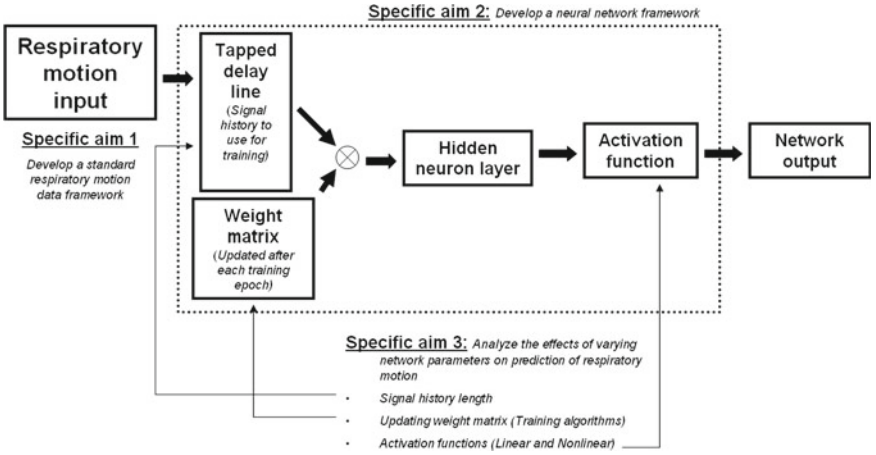

Fig. 12.4 Schematic illustration of the building blocks of an artificial neural network

12.4 Quantifying Errors in Respiratory Motion Prediction

The prediction process, irrespective of the actual predictive filter algorithms mentioned above, is not always perfect. Consequently, tumor/surrogate positions predicted by the prediction algorithm do not always match the corresponding actual anticipated positions. Such a discrepancy in position due to imperfect prediction leads to geometric errors. Geometric errors further lead to discrepancies in dose delivered to the tumor, thus leading to dosimetric errors.

It is therefore important to establish a framework to understand and evaluate geometric errors from prediction for all of the models described in sections above.

12.4.1 Simple Standard Deviation (1σ)

Prediction error can be quantified by obtaining the standard deviation of the instantaneous differences between the predicted and actual respiratory motion position of the tumor within a respiratory motion monitoring session.

Thus, for a prediction time series

$x_{pred}(t_n + \Delta) = f\{x_{act}(t_n), x_{act}(t_{n-1}), ..., x_{act}(t_{n-SHL})\}$, the instantaneous error in prediction is given by [15]

$$\varepsilon(t_n + \Delta) = x_{pred}(t_n + \Delta) - x_{act}(t_n + \Delta). \tag{12.3}$$

The inherent assumption here though is that both the prediction error and the respiratory motion pattern for which such prediction is made are approximately normally distributed.

12.4.2 Normalized Root Mean Square Error (nRMSE)

nRMSE represents, as it states, the normalized root mean square error between the predicted and actual respiratory motion position of the tumor within a respiratory motion monitoring session. The normalization ensures that the output of the prediction process scales with the input, or in other words, the performance of the prediction algorithm should be independent of absolute magnitude of the input respiratory motion signal. Thus,

$$nRMSE = \sqrt{\frac{\sum_i (D_i - P_i)^2}{\sum_i (D_i - \mu_z)^2}} \tag{12.4}$$

where D_i is the ith observation of respiratory position, P_i is the prediction estimate of the ith observation and μ_z is the mean of all observations [3].

12.5 Effect of Sampling Interval, Signal History Length and Response Time on Prediction Error

Regardless of the type of prediction model being used, a finite prediction error always exists. The objective of all prediction models is however to minimize the prediction error when compared to errors that could arise due to system latencies during real time tracking without any prediction. Shirato et al. [14] have reported a latency of 0.09 s between fiducial recognition and initiation of respiratory gated irradiation for a gantry mounted MLC based linear accelerator. Schweikard et al. [12], have reported a corresponding latency on the order of 0.3 s for a robotic arm mounted linear accelerator. Poulsen et al. [6], in their detailed analysis of system latency for a gantry mounted MLC based linear accelerator have reported latencies ranging from 350 to 1400 ms for sampling intervals ranging from 150 to 1000 ms. Thus, the choice of prediction model should be based on the specific system latency that requires attention.

Indirect tumor/surrogate tracking systems typically have a significantly smaller sampling interval than direct tumor tracking systems that usually employ some form of medical imaging. Therefore, it can be said that indirect tumor tracking systems could benefit from simpler predictive algorithms while direct tumor tracking systems require the more complex predictive models to reduce system latencies.

Sharp et al. [13] investigated the effect of sampling interval on prediction error and found that in general prediction error decreased with reduced sampling interval. In almost all predictive models, prediction errors either increase or reach a plateau the further ahead in time that the prediction is made for. The gradient of the magnitude of increase in prediction error with respect to the response time is usually steeper for simpler predictive models that do not properly account for the non stationary nature of respiratory motion. As seen in Fig. 12.5, Vedam et al. [15], have reported prediction errors of <2 mm for response times <0.4 s for adaptive linear prediction.

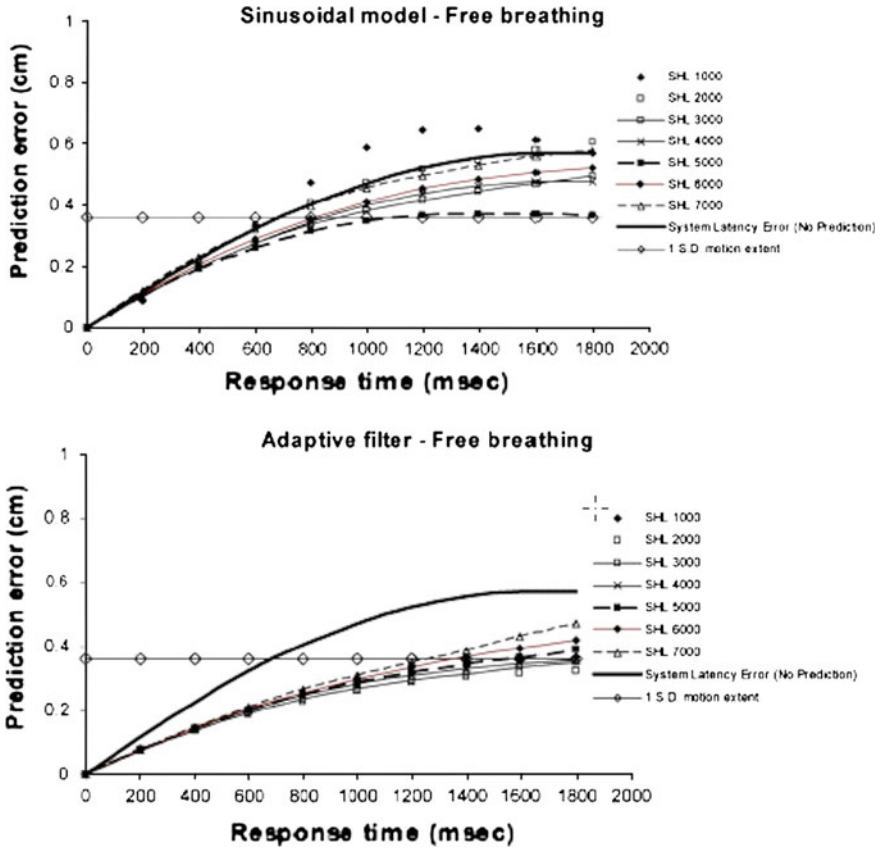

Fig. 12.5 Illustration of the impact of response time and signal history length on prediction error for a simple parametric (sinusoidal) model based filter and a more complex adaptive filter (from Vedam et al. [15])

However, for response times >0.4 s, these models prove to be progressively less accurate.

Isaksson et al. [3], have been able to achieve a nRMSE value of <60 % for response times as further into the future as 0.8 s, using adaptive neural networks. Putra et al. [7], have reported similar results of prediction error on the order of 2 mm for response times of around 0.6 s, with their IMM approach. Ruan et al. [9], were able to achieve nRMSE values of ranging from 0.6 to 0.4 for sampling rates ranging from 5 to 30 Hz and also for response times up to 1 s in the future using the KDE approach.

The effect of signal history length on the prediction error on the other hand is not entirely straight forward. The manner in which data from the signal history is applied in any given predictive model has a bearing on its effect on prediction error. Longer signal history lengths typically imply that more of the signal history is considered for modeling the prediction. However, this also could include more noise (especially in

the case of highly irregular respiratory motion), thereby resulting in greater prediction error. Another effect is that, with longer signal history lengths, the response of the system to high frequency changes in respiratory motion (irregular motion in other words) could be delayed. It can also be appreciated that the more complex predictive models do address such instability in the respiratory motion, thereby yielding robust predictive models that minimize uncertainties during dynamic tumor tracking delivery.

12.6 Summary

Respiratory motion management in general and tumor tracking delivery in particular have received increased attention as viable modes of radiation delivery for thoracic and abdominal tumors that exhibit significant respiratory tumor motion. Advances in on board imaging and respiratory motion monitoring technology have signaled the potential for such approaches to track moving targets. Respiratory motion prediction is a critical component that ensures the accuracy of dynamic delivery of radiation for real time tracking applications. Initial predictive approaches, such as the ones based on parametric modeling and empirical filters, were made simplistic assumptions of the characteristics of underlying respiratory motion patterns. As a result, their resultant prediction accuracy was found to be acceptable only within a limited "look ahead" or response time into the future. This greatly limited the applicability of such models in online prediction applications. Further advances through approaches such as Kalman filtering and adaptive neural networks brought about better prediction accuracy over a longer range of "look ahead" or response times into the future. Despite such advances, most of these approaches did not explicitly account for the temporally stochastic nature of human respiratory motion; a phenomenon described as non-stationarity. Such non-stationarity introduced instabilities in the prediction model, thereby reducing prediction accuracy in certain situations where sudden changes in respiratory motion patterns occurred. The advent of approaches such as KDE and empirical modeling with explicit accounting of non-stationarity has currently yielded reliably accurate models of respiratory motion prediction for "look ahead" or response times that are practically reasonable (>1 s into the future). Typical system latencies encountered during dynamic target tracking based radiation delivery are estimated to be of the order of 300 ms. It is evident that sufficient technology exists currently for implementing respiratory motion prediction during online target/tumor tracking based radiation delivery. Such advances have also therefore greatly improved the robustness of dynamic delivery of radiation through real time tracking.

References

1. Hayes, M.H.: Statistical digital signal processing and modeling. Wiley (1996)
2. Haykin, S.: Neural Networks: a Comprehensive Foundation. MacMillan, New York (1994)
3. Isaksson, M., Jalden, J., Murphy, M.J.: On using an adaptive neural network to predict lung tumor motion during respiration for radiotherapy applications. Med. Phys. **32**(12), 3801–3809 (2005)
4. McCall, K.C., Jeraj, R.: Dual-component model of respiratory motion based on the periodic autoregressive moving average (periodic ARMA) method. Phys. Med. Biol. **52**(12), 3455–3466 (2007)
5. Murphy, M.J., Dieterich, S.: Comparative performance of linear and nonlinear neural networks to predict irregular breathing. Phys. Med. Biol. **51**(22), 5903–5914 (2006)
6. Poulsen, P.R., Cho, B., Sawant, A., Ruan, D., Keall, P.J.: Detailed analysis of latencies in image-based dynamic MLC tracking. Med. Phys. **37**(9), 4998–5005 (2010)
7. Putra, D., Haas, O.C., Mills, J.A., Burnham, K.J.: A multiple model approach to respiratory motion prediction for real-time IGRT. Phys. Med. Biol. **53**(6), 1651–1663 (2008)
8. Ren, Q., Nishioka, S., Shirato, H., Berbeco, R.I.: Adaptive prediction of respiratory motion for motion compensation radiotherapy. Phys. Med. Biol. **52**(22), 6651–6661 (2007)
9. Ruan, D.: Kernel density estimation-based real-time prediction for respiratory motion. Phys. Med. Biol. **55**(5), 1311–1326 (2010)
10. Ruan, D., Fessler, J.A., Balter, J.M.: Real-time prediction of respiratory motion based on local regression methods. Phys. Med. Biol. **52**(23), 7137–7152 (2007)
11. Ruan, D., Keall, P.: Online prediction of respiratory motion: multidimensional processing with low-dimensional feature learning. Phys. Med. Biol. **55**(11), 3011–3025 (2010)
12. Schweikard, A., Glosser, G., Bodduluri, M., Murphy, M.J., Adler, J.R.: Robotic motion compensation for respiratory movement during radiosurgery. Comput. Aided Surg. **5**(4), 263–277 (2000)
13. Sharp, G.C., Jiang, S.B., Shimizu, S., Shirato, H.: Prediction of respiratory tumour motion for real-time image-guided radiotherapy. Phys. Med. Biol. **49**(3), 425–440 (2004)
14. Shirato, H., Shimizu, S., Kunieda, T., Kitamura, K., van Herk, M., Kagei, K., Nishioka, T., Hashimoto, S., Fujita, K., Aoyama, H., Tsuchiya, K., Kudo, K., Miyasaka, K.: Physical aspects of a real-time tumor-tracking system for gated radiotherapy. Int. J. Radiat. Oncol. Biol. Phys. **48**(4), 1187–1195 (2000)
15. Vedam, S.S., Keall, P.J., Docef, A., Todor, D.A., Kini, V.R., Mohan, R.: Predicting respiratory motion for four-dimensional radiotherapy. Med. Phys. **31**(8), 2274–2283 (2004)
16. Yan, H., Yin, F.F., Zhu, G.P., Ajlouni, M., Kim, J.H.: Adaptive prediction of internal target motion using external marker motion: a technical study. Phys. Med. Biol. **51**(1), 31–44 (2006)

Chapter 13
Estimation of Lung Ventilation

Kai Ding, Kunlin Cao, Kaifang Du, Ryan Amelon, Gary E. Christensen, Madhavan Raghavan and Joseph M. Reinhardt

Abstract Since the primary function of the lung is gas exchange, ventilation can be interpreted as an index of lung function in addition to perfusion. Injury and disease processes can alter lung function on a global and/or a local level. MDCT can be used to acquire multiple static breath-hold CT images of the lung taken at different lung volumes, or with proper respiratory control, 4DCT images of the lung reconstructed at different respiratory phases. Image registration can be applied to this data to estimate a deformation field that transforms the lung from one volume configuration to the other. This deformation field can be analyzed to estimate local lung tissue expansion, calculate voxel-by-voxel intensity change, and make biomechanical measurements. The physiologic significance of the registration-based measures of respiratory function can be established by comparing to more conventional measurements, such as nuclear medicine or contrast wash-in/wash-out studies with CT or MR. An important emerging application of these methods is the detection of pulmonary function change in subjects undergoing radiation therapy (RT) for lung cancer. During RT, treatment is commonly limited to sub-therapeutic doses due to unintended toxicity to normal lung tissue. Measurement of pulmonary function may be useful as a planning tool during RT planning, may be useful for tracking the progression of toxicity to nearby normal tissue during RT, and can be used to evaluate the effectiveness of a treatment post-therapy. This chapter reviews the basic measures to estimate regional ventilation from image registration of CT images, the comparison of them to the existing golden standard and the application in radiation therapy.

K. Ding · K. Du · R. Amelon · G. E. Christensen · M. Raghavan · J. M. Reinhardt (✉)
The University of Iowa, Iowa, USA
e-mail: joe-reinhardt@uiowa.edu

K. Cao
Biomedical Image Analysis Lab, GE Global Research Center, Niskayuna, USA

J. Ehrhardt and C. Lorenz (eds.), *4D Modeling and Estimation of Respiratory Motion for Radiation Therapy*, Biological and Medical Physics, Biomedical Engineering,
DOI: 10.1007/978-3-642-36441-9_13,

13.1 Introduction

Regional lung ventilation is the term used to characterize the volume of fresh gas per unit time that enters or exits the lung at the acinar (gas exchange) level. Disruption of regional ventilation can reflect alterations to airways (physiological or pathological), alterations in parenchymal mechanics, changes to the muscles of respiration, body posture effects and inhaled gas properties. Thus, measures of regional lung mechanics may serve as a sensitive test of the major status of the respiratory system and may be considerably more sensitive and informative than a global pulmonary function tests (PFTs) such as spirometry testing, diffusion studies and body plethysmography. PFTs provide a global measure of airflow obstruction and/or restriction but provide no regional information about the lung function. In addition, they are known to be relative insensitive to early lung disease and to small changes in the severity of lung disease [1] since they are essentially an integral of the regional changes. To study the regional lung function, various imaging modalities have been developed. Positron emission tomography (PET) and single photon emission CT (SPECT) can provide regional ventilation assessment [15] or even local ventilation/perfusion ratio (V'/Q'), but their application is constrained by low spatial resolution. Hyperpolarized helium-3 or xenon-129 MR has been developed for functional imaging of pulmonary ventilation and it avoids the concern about ionizing radiation [2, 16, 23]. Xe-enhanced CT (Xe-CT) measures regional ventilation by observing the gas wash-in and wash-out rate on serial CT images [3]. Xe-CT time series are usually acquired at the same phase over several respiratory cycles with switching from room air to xenon (wash-in) or from xenon to room air (wash-out). By fitting the lung density increase (wash-in) or decrease (wash-out) over the time to single compartment exponential model, one can measure the time constant (the inverse of specific ventilation) required to reach the lung density equilibrium. But both the helium-3 and xenon gas based imaging modalities require expensive and complex equipments to either hyperpolarize or harvest the gas, which are only available in few medical centers.

Recent advances in multi-detector-row CT (MDCT), 4D CT respiratory gating methods, and image processing techniques enable us to study pulmonary function at the regional level with high resolution anatomical information compared to other methods. As discussed in Chaps. 2 and 3, MDCT can be used to acquire multiple static breath-hold CT images of the lung taken at different lung volumes, or to acquire 4DCT images of the lungs with spiral scanning using a low pitch and retrospectively reconstructed at different respiratory phases with proper respiratory control [18, 20, 24]. Image registration can be applied to these data to estimate a deformation field that transforms the lung from one volume configuration to the other. This deformation field can be analyzed to estimate local lung tissue expansion, calculate voxel-by-voxel intensity change, and make biomechanical measurements. When combined with image segmentation algorithms [8, 9, 11, 25], functional and biomechanical measurements can be reported on a lung, lobe, and sublobar basis, and can be used to interpret regional lung function relative to specific segments of bronchial tree. Such measurements of pulmonary function have proven useful as a planning

tool during RT planning [31] and may be useful for tracking the progression of toxicity to nearby normal tissue during RT and can be used to evaluate the effectiveness of a treatment post-therapy [6].

Early studies using CT to study regional air volume changes have proved to enhance our understanding of normal lung function. Several groups have proposed methods that couple image registration and CT imaging to study regional lung function. Guerrero et al. have used optical-flow based registration to compute lung ventilation from 4DCT [13, 14] with intensity-based ventilation measure. Christensen et al. used image registration to match images across cine-CT sequences and estimate rates of local tissue expansion and contraction [5] using a Jacobian-based ventilation measure. In addition, as shown in Sect. 13.2, the intensity-based and Jacobian-based ventilation measures are based on the assumption that the regional lung volume change is due solely to air content change, which may not always be a valid assumption [7]. Other factors, such as blood volume change, may also contribute to the regional lung volume change.

Radiation induced pulmonary diseases can change the tissue material properties of lung parenchyma and the mechanics of the respiratory system. In patients such as lymphoma, esophageal and breast cancer with reasonable functional reserve, this damage is often insignificant. However, lung cancer patients with marginal pulmonary function are at increased risk for developing symptomatic pulmonary dysfunction secondary to radiation [22]. The regional functional lung imaging offers the opportunity to optimize the radiation therapy planning that preferentially avoid the functioning lung regions, thus potentially reducing the physiological damage. 3D conformal radiotherapy (3D CRT), intensity modulated radiotherapy (IMRT) and volumetric modulated arc therapy (VMAT) have been previously studied for the functional avoidance and showed less damage to the highly functioning lung regions when appropriate avoidance structures derived from the functional imaging were assigned to the planning system [22, 29, 31]. Furthermore, the functional lung imaging can also be applied during the lung cancer radiation therapy to help the decision for the adaptive radiation therapy.

This chapter reviews the basic measures to estimate regional ventilation from image registration of CT images, the comparison of them to the existing golden standard and the application in radiation therapy.

13.2 Image-Registration-Based Estimates of Regional Lung Ventilation

The lung ventilation (air volume change) and perfusion (blood/tissue volume change) are the two main components of lung volume change. In order to study lung ventilation, which is part of the lung volume change, we wish to find the motion of all tissue inside the lung due to the interactions with each other caused by the change of the transpulmonary pressure. The motion of the lung tissue, can be expressed in the form

of spatial function of each region of the lung if the mapping of the region between different conditions can be found. Therefore, the problem can be stated as: Given images of the lungs in two or more different conditions, find the region mapping between the different conditions.

The problem statement brings us into the realm of image registration. Image registration is the task of finding a spatial transform mapping one image into another. Many image registration algorithms have been proposed and various features such as landmarks, contours, surfaces and volumes have been utilized to manually, semi-automatically or automatically define correspondences between two images as described in Chaps. 5, 6 and 7. The basic components of the registration framework and their interconnections are shown in Fig. 7.1 of Chap. 7. As mentioned in Chap. 7, with the image registration displacement field, functional and mechanical parameters such as the regional volume change and compliance, stretch and strain, anisotropy, and specific ventilation can be evaluated.

Let I_1 and I_2 represent two 3D image volumes to be registered. The vector $\mathbf{x} = (x_1, x_2, x_3)^T$ defines the voxel coordinate within an image. The algorithm finds the optimal transformation $\mathbf{T}$ that maps the (moving image) I_1 to the fixed image I_2 by minimizing the cost function defined by the user such as the combination of the similarity and the regularity. The transformation $\mathbf{T}$ is a (3×1) vector-valued function that maps a point $\mathbf{T}(\mathbf{x})$ in the fixed image to its corresponding location in the moving image.

In X-ray CT based images, because the gray scale is linear between air and lung tissue, the measured Hounsfield units (HU) in the lung CT images can be assumed as a function of tissue and air content. In other words, this assumes that the lung consists only of structures equal in opacity to either air or lung tissue. Following the air-tissue mixture model by Hoffman et al. [17], from the CT value of a given voxel, the tissue volume can be estimated as

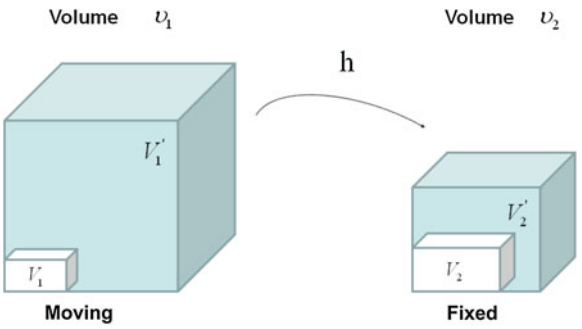

Fig. 13.1 Example of a region under deformation $\mathbf{T}(\mathbf{x})$ from moving image to fixed image. V_1 and V_2 are tissue volumes in the regions. V_1' and V_2' are air volumes in the regions. Region volumes $v_1 = V_1 + V_1'$ and $v_2 = V_2 + V_2'$

$$V(\mathbf{x}) = v(\mathbf{x})\frac{I(\mathbf{x}) - HU_{air}}{HU_{tissue} - HU_{air}} = v(\mathbf{x})\beta(I(\mathbf{x})), \tag{13.1}$$

and the air volume can be estimated as

$$V'(\mathbf{x}) = v(\mathbf{x})\frac{HU_{tissue} - I(\mathbf{x})}{HU_{tissue} - HU_{air}} = v(\mathbf{x})\alpha(I(\mathbf{x})), \tag{13.2}$$

where $v(\mathbf{x})$ denotes the volume of volume element $\mathbf{x}$ and $I(\mathbf{x})$ is the intensity of a voxel at position $\mathbf{x}$. HU_{air} and HU_{tissue} refer to the intensity of air and tissue, respectively. Here, we assume that air is -1000 HU and tissue is 0 HU. $\alpha(I(\mathbf{x})) = \frac{HU_{tissue} - I(\mathbf{x})}{HU_{tissue} - HU_{air}}$ and $\beta(I(\mathbf{x})) = \frac{I(\mathbf{x}) - HU_{air}}{HU_{tissue} - HU_{air}}$ are introduced for notational simplicity. Notice that $\alpha(I(\mathbf{x})) + \beta(I(\mathbf{x})) = 1$.

Figure 13.1 shows an example of a cubic shaped region under deformation $\mathbf{T}$ from moving image to fixed image. The region volumes are v_1 and v_2. The volumes can be decomposed into the tissue volume fraction and air volume fraction based on the mean voxel intensity within the cube. The small white sub volumes inside the cubes represent the tissue volume V_1 and V_2. Air volumes are represented by V_1' and V_2' (in blue). As the ratio of air to tissue decreases, the CT intensity of a voxel increases. The mean cube voxel intensities for the moving, I_1, and fixed images, I_2, are functions of the ratios of air to tissue volumes within the cubes.

13.2.1 Definition of Regional Lung Ventilation

After we obtain the optimal warping function $\mathbf{T}(\mathbf{x})$, we can calculate the regional ventilation, which is equal to the difference in local air volume change per unit time. The commonly-used ventilation measure is the specific ventilation sV which takes the initial air volume into account. The sV is equal to the specific air volume change sVol per unit time. Or in other words, in a unit time,

$$sV = sVol = \frac{V_1'(\mathbf{T}(\mathbf{x})) - V_2'(\mathbf{x})}{V_2'(\mathbf{x})}. \tag{13.3}$$

Three different approaches for estimating (13.3) are described below:

13.2.2 Specific Air Volume Change by Specific Volume Change (SAJ)

The SAJ regional ventilation measure is based on the assumption that there is no tissue volume within the moving or fixed volumes, and thus any local air volume change is equal to the local volume change. Figure 13.2 illustrates such an assumption. Compared with the general condition in Fig. 13.1, the region volume now is pure

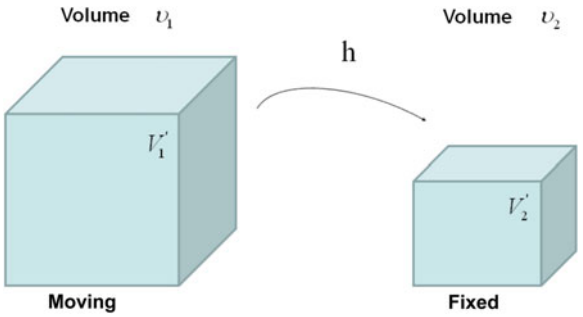

Fig. 13.2 Example of a given region under deformation $\mathbf{T}(\mathbf{x})$ from moving image to fixed image, with the assumption of no tissue volume ($V_1 = V_2 = 0$). V_1' and V_2' are air volumes

air volume, or equivalently, $v_1 = V_1'$ and $v_2 = V_2'$. In this case, the specific air volume change is equal to specific volume change. Since the Jacobian tells us the local volume expansion (or contraction), the regional ventilation can be measured by:

$$SAJ = \frac{v_1(\mathbf{T}(\mathbf{x})) - v_2(\mathbf{x})}{v_2(\mathbf{x})} = J(\mathbf{x}) - 1. \tag{13.4}$$

Previously, SAJ has been used as an index of the regional function and was compared with Xe-CT estimates of regional lung function [25] which is the local ventilation time constants calculated by observing the gas wash-in and wash-out rates on serial CT images. Regional lung expansion, as estimated from the Jacobian of the image registration transformations, was well correlated with xenon CT specific ventilation [8, 25] (linear regression, average $r^2 = 0.73$).

Since the SAJ does not depend on the air-ratio which may not be available in some modalities, it can be applied to non-X-ray CT images, such as hyperpolarized He-3 MRI [10], as long as the regional transformation of the lung tissue is known.

13.2.3 Specific Air Volume Change by Corrected Jacobian (SACJ)

Starting with (13.4) and expressing the air volumes $V_1'(\mathbf{T}(\mathbf{x}))$ and $V_2'(\mathbf{x})$ using the air-tissue mixture model (13.1) and (13.2), we obtain the corrected Jacobian measure of region air volume change, SACJ,

$$SACJ = \frac{V_1'(\mathbf{T}(\mathbf{x})) - V_2'(\mathbf{x})}{V_2'(\mathbf{x})} \tag{13.5}$$

$$= \frac{V_1'(\mathbf{T}(\mathbf{x}))}{V_2'(\mathbf{x})} - 1 \tag{13.6}$$

$$= \frac{v_1(\mathbf{T}(\mathbf{x}))\alpha(I_1(\mathbf{T}(\mathbf{x})))}{v_2(\mathbf{x})\alpha(I_2(\mathbf{x}))} - 1 \tag{13.7}$$

The notation $I_1(\mathbf{T}(\mathbf{x}))$ is interpreted as the image $I_1(\mathbf{x})$ deformed by the transformation $\mathbf{T}(\mathbf{x})$ and is computed using linear interpolation. The deformed volume element $\nu_1(\mathbf{T}(\mathbf{x}))$ is calculated using the Jacobian $J(\mathbf{x})$ times the volume element $\nu_2(\mathbf{x})$, i.e., $\nu_1(\mathbf{T}(\mathbf{x})) = J(\mathbf{x})\nu_2(\mathbf{x})$. The specific air volume change is then

$$SACJ = J(\mathbf{x})\frac{\alpha(I_1(\mathbf{T}(\mathbf{x})))}{\alpha(I_2(\mathbf{x}))} - 1 \tag{13.8}$$

$$= J(\mathbf{x})\frac{HU_{tissue} - I_1(\mathbf{T}(\mathbf{x}))}{HU_{tissue} - I_2(\mathbf{x})} - 1 \tag{13.9}$$

If we assume that pure tissue is 0 HU, then specific air volume change is

$$SACJ = J(\mathbf{x})\frac{I_1(\mathbf{T}(\mathbf{x}))}{I_2(\mathbf{x})} - 1. \tag{13.10}$$

Compared to Eq. 13.4, the term $\frac{I_1(\mathbf{T}(\mathbf{x}))}{I_2(\mathbf{x})}$ is a correction factor that depends on the voxel intensities in the moving and fixed images. The SAJ is a special case of SACJ where tissue volume is assumed to be 0, or the air volume fraction $\alpha(I_1(\mathbf{T}(\mathbf{x}))) = \alpha(I_2(\mathbf{x})) = 1$. The SACJ measure is illustrated in Fig. 13.1, and represents the most general case of where there is both tissue volume and air volume change within the region.

13.2.4 Specific Air Volume Change by Intensity Change (SAI)

The intensity-based measure of regional air volume change SAI can be derived from the SACJ by assuming that tissue volume is preserved during deformation, or equivalently, that the tissue volume difference $\Delta V(\mathbf{x}) = V_1(\mathbf{T}(\mathbf{x})) - V_2(\mathbf{x}) = 0$. Under this assumption, $V_1(\mathbf{T}(\mathbf{x})) = V_2(\mathbf{x})$ and we have

$$\nu_1(\mathbf{T}(\mathbf{x}))\beta(I_1(\mathbf{T}(\mathbf{x}))) = \nu_2(\mathbf{x})\beta(I_2(\mathbf{x})), \tag{13.11}$$

and

$$\nu_1(\mathbf{T}(\mathbf{x})) = \nu_2(\mathbf{x})\frac{\beta(I_2(\mathbf{x}))}{\beta(I_1(\mathbf{T}(\mathbf{x})))}, \tag{13.12}$$

Since $\nu_1(\mathbf{T}(\mathbf{x})) = J(\mathbf{x})\nu_2(\mathbf{x})$, with above equation, we have

$$J(\mathbf{x}) = \frac{\beta(I_2(\mathbf{x}))}{\beta(I_1(\mathbf{T}(\mathbf{x})))} \tag{13.13}$$

$$= \frac{I_2(\mathbf{x}) - HU_{air}}{I_1(\mathbf{T}(\mathbf{x})) - HU_{air}}. \tag{13.14}$$

Substituting the above equation into Eq. 13.9, yields

$$SAI = \frac{I_2(\mathbf{x}) - HU_{air}}{I_1(\mathbf{T}(\mathbf{x})) - HU_{air}} \frac{HU_{tissue} - I_1(\mathbf{T}(\mathbf{x}))}{HU_{tissue} - I_2(\mathbf{x})} - 1 \tag{13.15}$$

$$= \frac{I_2(\mathbf{x})HU_{tissue} + HU_{air}I_1(\mathbf{T}(\mathbf{x})) - I_1(\mathbf{T}(\mathbf{x}))HU_{tissue} - HU_{air}I_2(\mathbf{x})}{(I_1(\mathbf{T}(\mathbf{x})) - HU_{air})(HU_{tissue} - I_2(\mathbf{x}))} \tag{13.16}$$

Finally, if we assume that pure air is -1000 HU and pure tissue is 0 HU, then

$$SAI = 1000\frac{I_1(\mathbf{T}(\mathbf{x})) - I_2(\mathbf{x})}{I_2(\mathbf{x})(I_1(\mathbf{T}(\mathbf{x})) + 1000)} \tag{13.17}$$

which is exactly the result from Simon [26], Guerrero et al. [14], and Fuld et al. [12].

Figure 13.3 illustrates the assumption with no tissue volume change in SAI. In Fig. 13.3 as the region volume changes from v_1 to v_2, the tissue volume inside the cube remains the same ($V_1 = V_2$).

13.2.5 *Difference of Specific Air Volume Change (DSA) and Difference of Tissue Volume (DT)*

To investigate the relationship between the measurements of specific air volume changes and the tissue volume change, we can calculate the difference between Eqs. (13.9) and (13.16) and define the difference of specific air volume change (DSA) between SACJ and SAI, and the difference of tissue volume (DT) as:

$$DSA = |SACJ - SAI| \tag{13.18}$$

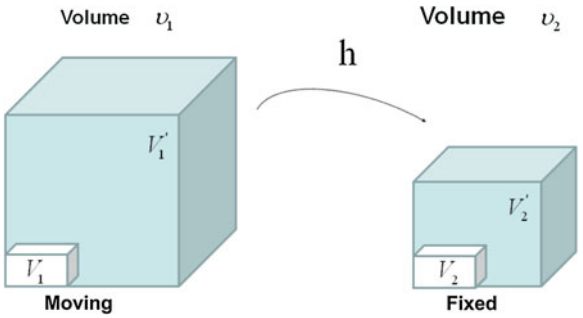

Fig. 13.3 Example of a given voxel under deformation $\mathbf{T}(\mathbf{x})$ from moving image to fixed image, with the assumption of no tissue volume change. Notice the tissue volume $V_1 = V_2$ under this assumption. V_1' and V_2' are air volumes

$$DT = |V_1(\mathbf{T}(\mathbf{x})) - V_2(\mathbf{x})| \tag{13.19}$$

$$= |\nu_1(\mathbf{T}(\mathbf{x}))\beta(I_1(\mathbf{T}(\mathbf{x}))) - \nu_2(\mathbf{x})\beta(I_2(\mathbf{x}))| \tag{13.20}$$

$$= |J(\mathbf{x})\nu_2(\mathbf{x})\beta(I_1(\mathbf{T}(\mathbf{x}))) - \nu_2(\mathbf{x})\beta(I_2(\mathbf{x}))| \tag{13.21}$$

$$= \left|\nu_2(\mathbf{x})\frac{J(\mathbf{x})(I_1(\mathbf{T}(\mathbf{x})) - HU_{air}) - (I_2(\mathbf{x}) - HU_{air})}{HU_{tissue} - HU_{air}}\right| \tag{13.22}$$

Again, if we assume that air is −1000 HU and tissue is 0 HU, then the tissue volume difference is:

$$DT = \left|\nu_2(\mathbf{x})\frac{J(\mathbf{x})(I_1(\mathbf{T}(\mathbf{x})) + 1000) - (I_2(\mathbf{x}) + 1000)}{1000}\right| \tag{13.23}$$

13.3 Compare Registration Based Regional Ventilation with Gold Standard

The physiologic significance of these registration-based measures of respiratory function can be established by comparing to more conventional measurements, such as nuclear medicine or contrast wash-in/wash-out studies with CT or MR. Xenon-enhanced CT (Xe-CT) measures regional ventilation by observing the gas wash-in or wash-out rate on serial CT images [3, 21, 28]. Xe-CT imaging has the advantage of high temporal resolution and spatial resolution and reflects a measure of fresh gas delivery to the gas exchange units of the lung. Although the dynamic Xe-CT method comes along with limited Z-axis coverage, expense of Xe gas, and difficulties of implementation, it serves as the gold standard of regional ventilation and can be used to compare with registration-based measures of regional lung function in animal studies for validation purposes.

Another gold standard is comparing through the registration validation metric. As described in Sect. 8.2.1.1, a registration validation metric such as target registration error (TRE) assess through anatomical landmarks is usually used to measure registration accuracy quantitatively. The registration-based measures of respiratory function introduced are based on the transformation result from the image registration, therefore, registration validation metric can indirectly validate the accuracy of the ventilation measures. In addition to TRE, Jacobian is another important metric that can be used to assess the folding of the transformation of the lung tissue. Any transform indicating local folding is not allowed.

Figure 13.4 shows an example of the distribution of the landmarks in sheep lung for both a volume near end expiration (EE) and a volume near end inspiration (EI) images. The coordinate of each landmark location is recorded for each image data set before and after registration. To locally compare the regional ventilation measures, the corresponding region of Xe-CT image at the initial end expiration scan EE_0 in the EE is divided into approximately 100 non-overlapping cubes with size of $20 \times 20 \times 20$ mm. The average regional ventilation measures (SAJ, SACJ and SAI) are

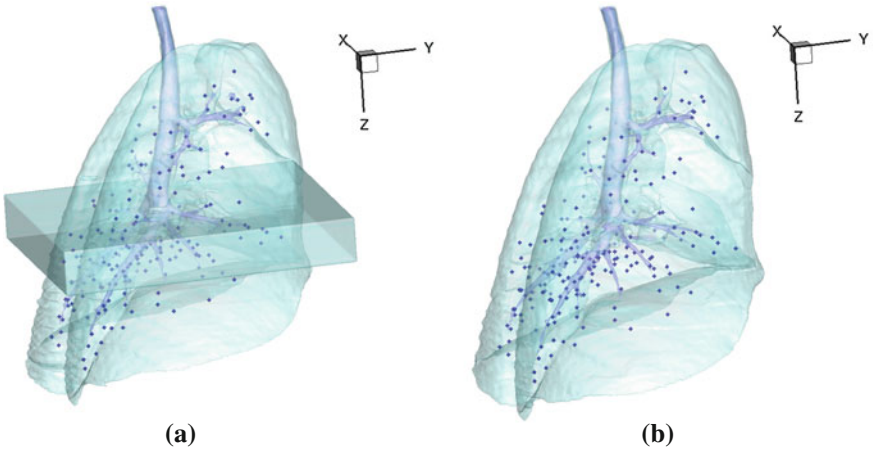

Fig. 13.4 3D view of the landmarks in: **a** EE with EE_0 and **b** EI. The *dark region* below the carina in (**a**) is the EE_0 and the *spheres* are the automatically defined landmarks

compared to the corresponding average sV measurement from Xe-CT images within each cube. Figure 13.4a shows the location of the EE_0 (Xe-CT) slab overlaid on the EE image. The correlation coefficients between any two estimates (SAJ-sV, SACJ-sV or SAI-sV) are calculated by linear regression. Our goal is to validate and compare the measures used to estimate regional lung ventilation from image registration by comparing them to Xe-CT ventilation. Two types of data were acquired for each animal: a 4DCT scan and a Xe-CT scan. In order to make our comparisons under the same physiological conditions, each animal was scanned and mechanically ventilated with the same respiratory rate, tidal volume (TV) and positive end-expiratory pressure (PEEP) during the two types of scans. The data sets from the 4D CT scan were reconstructed in volumes at eight phases of the respiratory cycle. For this study we focus on the data sets from two of the phases, a volume near end expiration (EE) and a volume near end inspiration (EI). For the Xe-CT scan, 45 distinctive partial lung volumetric scans were performed at volume near end expiration, or the initial end expiration scan (EE_0) to the last expiration scan (EE_{44}).

Figure 13.5a shows a comparison between the registration-derived indices of ventilation and the Xe-CT estimated sV in cube-shaped regions of interest for animal D. The corresponding Xe-CT regions in the EE are divided into about 100 cubes. Figure 13.5b is the Xe-CT estimate of sV. Figure 13.5c, d and e are the corresponding registration ventilation measures SAJ, SACJ and SAI. The regions with edema are excluded from the comparison. Figure 13.5b, c and d all show noticeable similar gradient in the ventral-dorsal direction. Notice that the color scales are different in each map and are set based on the range of values from the appropriate plot in Fig. 13.6.

Figure 13.6 shows scatter plots comparing the registration ventilation measures and the Xe-CT ventilation sV in all four animals. The SACJ column shows the strongest correlation with the sV (average $r^2 = 0.82$). The SAJ, which is directly

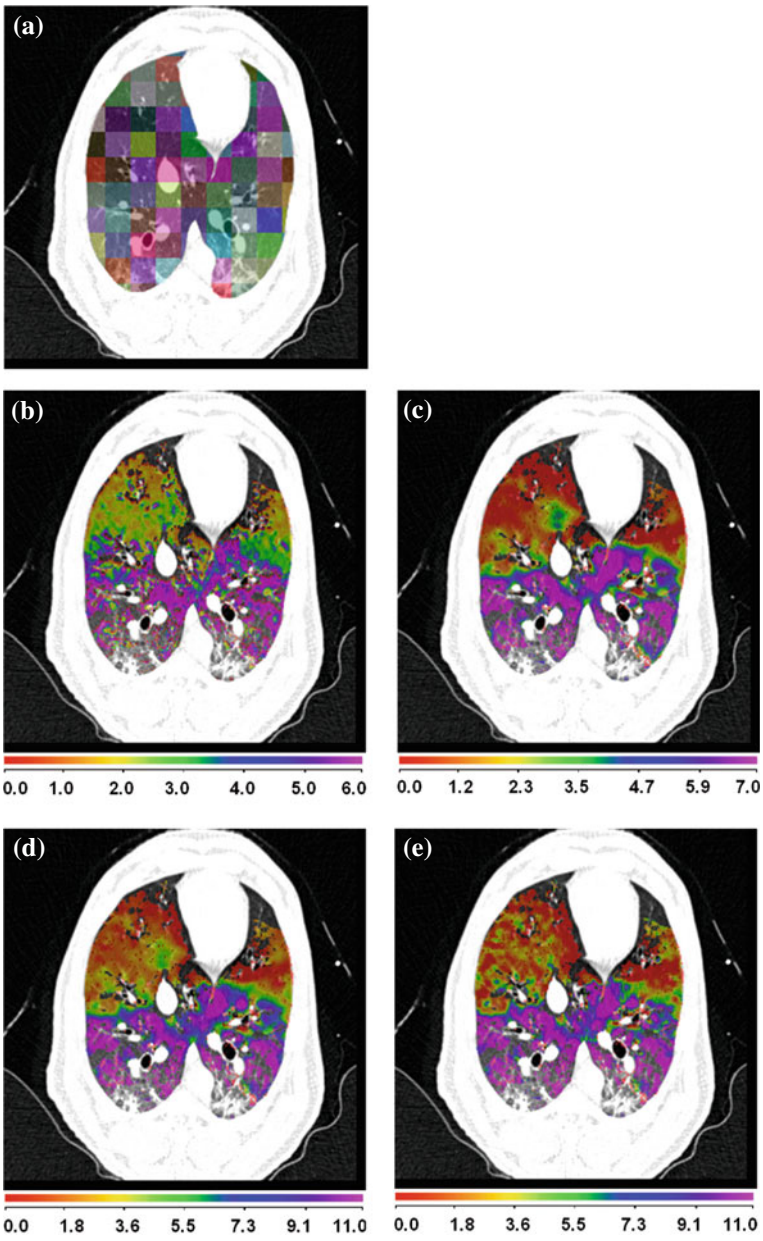

Fig. 13.5 Comparison of the regional ventilation measures for animal D. **a** EE with *color coded cubes* showing the sample region. **b**, **c**, **d** and **e** *color map* of the sV, SAJ, SACJ and SAI. Note that the *color scales* are different for (**b**)–(**e**), and are set based on the range of values from the appropriate plot in Fig. 13.6

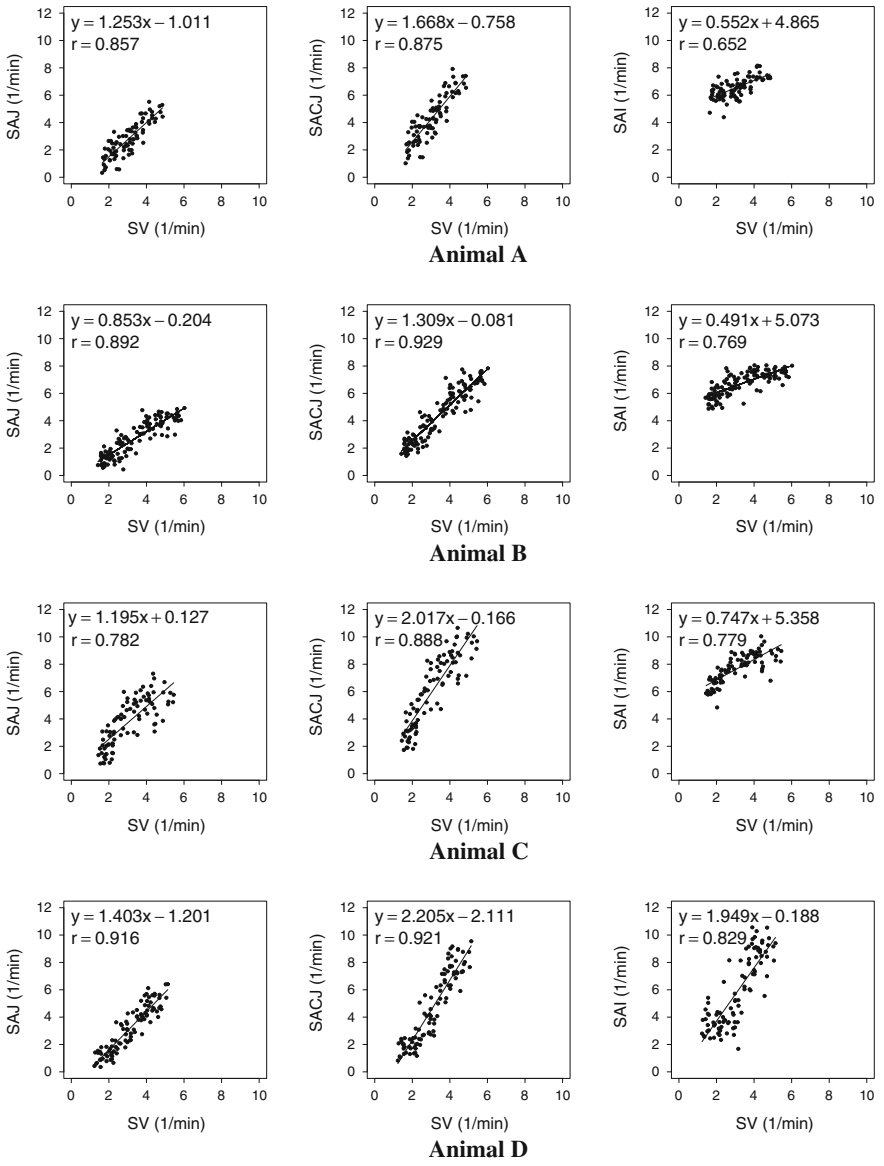

Fig. 13.6 Small cube ROIs with size $20 \times 20 \times 20$ mm results for registration estimated ventilation measures compared to the Xe-CT estimated ventilation sV in scatter plot with linear regression in four animals. The first column is the SAJ versus sV. The second column is the SACJ versus sV. The third column is the SAI versus sV

Table 13.1 Comparison of ventilation measures between SACJ and SAI in small cube ROIs with size $20 \times 20 \times 20$ mm

Animal	Correlation pair	Correlation with sV (r value)	Number of samples	SACJ versus SAI p value
A	SACJ versus sV	0.88	83	$p <= 0.0001$
	SAI versus sV	0.65		
B	SACJ versus sV	0.93	119	$p <= 1.18e^{-6}$
	SAI versus sV	0.77		
C	SACJ versus sV	0.89	86	$p <= 0.0075$
	SAI versus sV	0.78		
D	SACJ versus sV	0.92	110	$p <= 0.0017$
	SAI versus sV	0.83		

Table 13.2 Comparison of ventilation measures between SAJ and SAI in small cube ROIs with size $20 \times 20 \times 20$ mm

Animal	Correlation pair	Correlation with sV (r value)	Number of samples	SAJ versus SAI p value
A	SAJ versus sV	0.86	83	$p <= 0.0005$
	SAI versus sV	0.65		
B	SAJ versus sV	0.89	119	$p <= 0.002$
	SAI versus sV	0.77		
C	SAJ versus sV	0.78	86	$p <= 0.5$
	SAI versus sV	0.78		
D	SAJ versus sV	0.92	110	$p <= 0.0017$
	SAI versus sV	0.83		

related to Jacobian as $\text{SAJ} = \text{J} - 1$, also shows good correlation with the sV (average $r^2 = 0.75$). The intensity-based measure SAI shows the lowest correlation with the sV (average $r^2 = 0.58$).

Table 13.1 shows the results of comparing the r values from SACJ versus sV and SAI versus sV. All four animals show that the correlation coefficient from SACJ versus sV is significantly stronger than it from SAI versus sV. Similarly, Table 13.2 shows the results of comparing the r values from SAJ versus sV and SAI versus sV. The registration ventilation measure SAJ also shows a significantly stronger correlation with sV than SAI. Comparing the r values from SACJ versus sV and SAJ versus sV as in Table 13.3, only animal B and C show that the SACJ has significantly stronger correlation with sV than SAJ. To compare two correlation coefficients, the Fisher Z-transform of the r values is used and the level of significance is determined.

Figure 13.7 shows the scatter plots between DSA (the absolute difference of the value between the SACJ and SAI) and the DT (the absolute difference of the tissue volume) with linear regression in all four animals (average $r^2 = 0.86$). From the Eqs. (13.9) and (13.16), we know that the SAI measurement assumes no tissue volume change in a given region being registered, which may not be valid assumption in all lung regions. Figure 13.7 shows that as the tissue volume change increases, the

Table 13.3 Comparison of ventilation measures between SACJ and SAJ in small cube ROIs with size 20 × 20 × 20 mm

Animal	Correlation pair	Correlation with sV (r value)	Number of samples	SACJ versus SAJ p value
A	SACJ versus sV	0.88	83	$p <= 0.302$
	SAJ versus sV	0.86		
B	SACJ versus sV	0.93	119	$p <= 0.035$
	SAJ versus sV	0.89		
C	SACJ versus sV	0.89	86	$p <= 0.007$
	SAJ versus sV	0.78		
D	SACJ versus sV	0.92	110	$p <= 0.5$
	SAJ versus sV	0.92		

difference between the measures of regional ventilation from SACJ and SAI increases linearly in all four animals. It indicates that the lower correlation of SAI with sV compared with SACJ with sV may be caused by the tissue volume change between two volumes.

13.4 Application: Detecting Changes in Lung Function in Subjects Following Radiation Therapy

Radiation induced pulmonary diseases can change the tissue material properties of lung parenchyma and the mechanics of the respiratory system. In patients such as lymphoma, esophageal and breast cancer with reasonable functional reserve, this damage is often insignificant. However, lung cancer patients with marginal pulmonary function are at increased risk for developing symptomatic pulmonary dysfunction secondary to radiation [22] due to unintended toxicity to normal lung tissue. Reducing the frequency of occurrence and magnitude of normal lung function loss may benefit from treatment plans that incorporate relationships between regional and functional based lung information and the radiation dose. The 3D functional lung imaging offers the opportunity to optimize the radiation therapy planning that preferentially avoid the functioning lung regions, thus potentially reducing the physiological damage. 3D conformal radiotherapy (3D CRT), intensity modulated radiotherapy (IMRT) and volumetric modulated arc therapy (VMAT) have been previously studied for the functional avoidance and showed less damage to the highly functioning lung regions when appropriate avoidance structures derived from the functional imaging were assigned to the planning system [22, 29, 31]. Furthermore, the functional lung imaging can also be applied during the lung cancer radiation therapy to help the decision for the adaptive radiation therapy. During the treatment course, the radiation dose needed to control the tumor is well above that which causes toxicity to the normal lung tissue. Increase of tumor control could be achieved by delivering substantially higher radiation doses to the tumor [19], which is optimally achieved with radiation

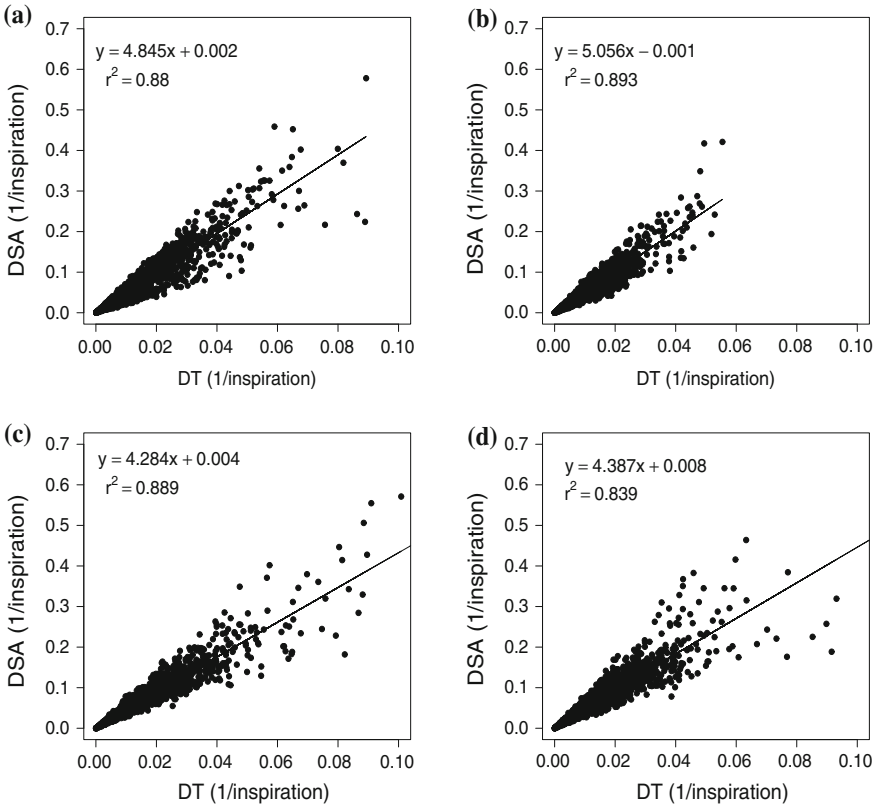

Fig. 13.7 Linear regression analysis between DSA and DT. **a**–**d** DSA (the absolute difference of the value between the SACJ and SAI) compared to DT (the absolute difference of the tissue volume) in animals A, B, C and D

therapy schemes that planned and delivered adaptively during the treatment course to reduce toxicity. Various imaging modalities can be used for functional lung imaging. Positron emission tomography (PET) and single photon emission CT (SPECT) can provide regional assessment [15], but their application is constrained by low spatial resolution. Hyperpolarized helium-3 MR has been developed for functional imaging of pulmonary ventilation and it avoids the concern about ionizing radiation [2, 16, 23]. Xe-enhanced CT (Xe-CT) measures regional ventilation by observing the gas wash-in and wash-out rate on serial CT images [3]. But both the helium-3 and xenon gas based imaging modalities require expensive and complex equipments to either hyperpolarize or harvest the gas, which are only available in few medical centers.

Our goal is to measure changes in lung function by comparing regional lung volumes at end-inspiration and end-expiration before and after treatment. Figure 13.8 shows a block diagram of the entire process. Five image data sets are used in the

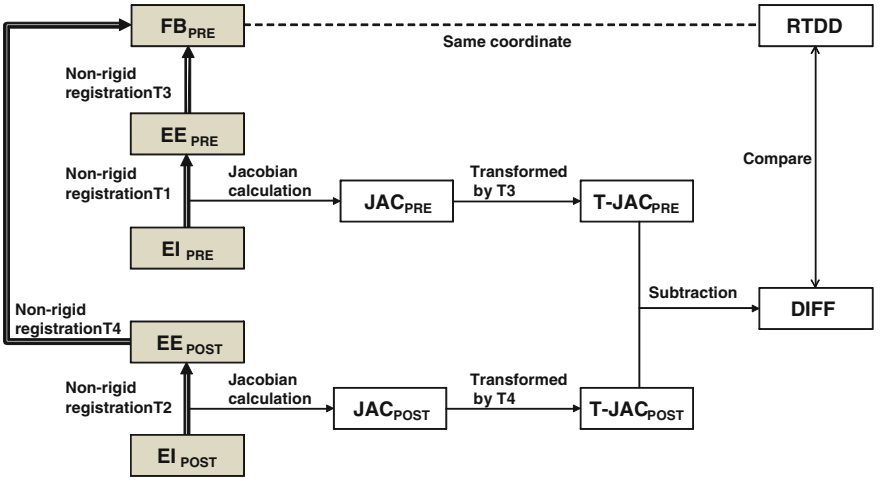

Fig. 13.8 Figure shows the five images (EE_{PRE}, EI_{PRE}, EE_{POST}, EI_{POST}, and FB_{PRE}) that are analyzed during the processing. Transformations T1 and T2 register end inspiration (EI) to end expiration (EE) data and can be used to assess local lung function via the Jacobian (JAC) of the transformations. PRE and POST indicate before and after RT. The difference (DIFF) between the pre- and post-treatment Jacobian data can be used to look for changes in pulmonary function. Transformations T3 and T4 map the Jacobian data into the coordinate system of the FB_{PRE} (planning CT) image, which allows direct comparison with the radiation treatment dose distribution (RTDD). FB_{PRE} and RTDD are in the same coordinate system since the FB_{PRE} scan is used to create the dose plan. (*Shaded boxes* indicate CT image data; *white boxes* indicated derived or calculated data; *thick arrows* indicate image registration transformations being calculated; *thin solid lines* indicate other operations.)

processing. A "free breathing" pretreatment (FB_{PRE}) fan beam CT scan for treatment planning is acquired prior to RT using an ungated protocol with the subject breathing quietly during the scan. The FB_{PRE} image is used during the treatment planning process as the fixed data set; all radiation dose calculations and daily localization procedures are registered to the FB_{PRE} CT coordinate system. A 4DCT scan is also acquired prior to RT, and CT data sets are reconstructed at ten distinct phases of respiration. For this study we focus on the data sets from two of the phases, a volume at end expiration (EE_{PRE}) and a volume at end inspiration (EI_{PRE}). A second 4DCT study was acquired one year after RT and used in this study as "post" RT scans for analysis of post-RT changes (EE_{POST} and EI_{POST}).

Nonlinear image registration is used to define four transformations on these data sets. Table 13.4 summarizes these four transformations. Transformations T1 and T2 are defined between respiratory phase points on the 4DCT, and are used to estimate local lung expansion. Transformations T3 and T4 are used to convert the lung expansion data into same coordinate system as the RT dose map, and are used to compare changes in lung expansion with delivered RT dose.

Since $SAJ = \frac{\nu_1(\mathbf{T}(\mathbf{x}))-\nu_2(\mathbf{x})}{\nu_2(\mathbf{x})} = J(\mathbf{x}) - 1$ and it is independent of potential noise from the CT HU values, here local lung function is assessed via the Jacobian (JAC) of

Table 13.4 Summary of image registrations performed to detect RT-induced changes in lung function. Names of images and transformations refer to those given in Fig. 13.8

Transformation name	Image transformed	Used to	Algorithm used
T1	$EI_{PRE} \rightarrow EE_{PRE}$	Calculate pre-RT lung expansion map (Jacobian of T1)	SICLE [4]
T2	$EI_{POST} \rightarrow EE_{POST}$	Calculate post-RT lung expansion map (Jacobian of T2)	SICLE [4]
T3	$EE_{PRE} \rightarrow FB_{PRE}$	Transform pre-RT Jacobian into RT dose planning system coordinate system for comparison	SICLE [4]
T4	$EE_{POST} \rightarrow FB_{PRE}$	Transform post-RT Jacobian into RT dose planning system coordinate system for comparison	Elastix-NRP [27]

the transformations T1 and T2 which register end inspiration (EI) to end expiration (EE) data.

The Jacobian of the transformation T1 (JAC_{PRE}) describes the volume changes from EI_{PRE} to EE_{PRE} and the Jacobian of transformation T2 (JAC_{POST}) describes the volume changes from EI_{POST} to EE_{POST}. To compare these changes, the Jacobian of T1 and the Jacobian of T2 were mapped to the FB_{PRE} coordinate system with transformations T3 and T4, respectively. Additional details on the registration algorithms and other processing steps are given below.

Figure 13.9 shows the color-coded pulmonary function images and function change image DIFF for two subjects. The first column shows the pulmonary function map before RT. The second column shows the pulmonary function map after RT. Note that the color scales for these images are different for the different subjects because of differences in tidal volume. For example, in subject A, green and blue indicate normally functioning (expanding) lung tissue with a Jacobian value greater than 1.1, while orange and red regions show decreased lung function with a Jacobian value less than 0.95. Both function images are mapped to FB_{PRE} using transformations T3 and T4. The pulmonary function change images are shown in column three. In the difference images, blue regions represent increased pulmonary function and the red regions represent decreased pulmonary function. The rightmost column in the figure is the planned radiation dose distribution, in units of Grays (Gy). The spatial map of functional changes in column three can be visually compared to the regions receiving the highest radiation doses (column four).

For subject A, the most dramatic change in pulmonary function is seen in the treated left lung (right side of figure), demonstrating changes from significant expansion (green and blue) before RT to little or no expansion (orange to red) after RT

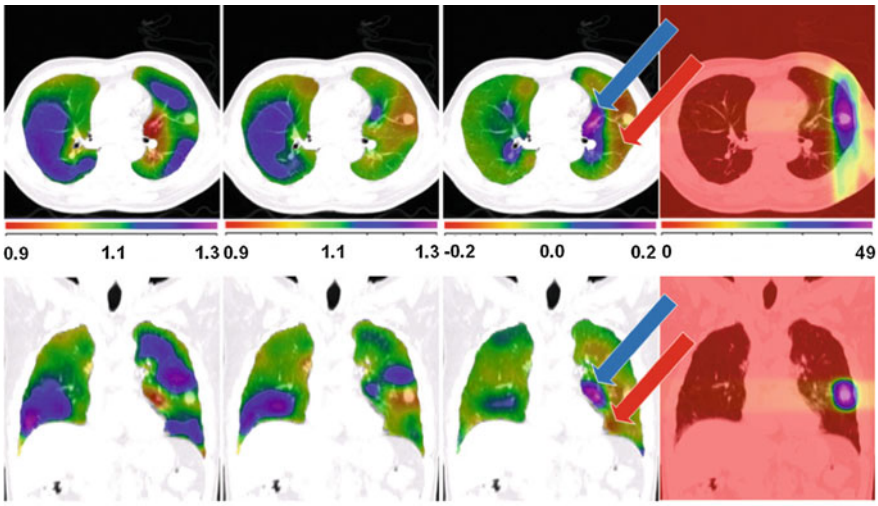

(a) Subject A

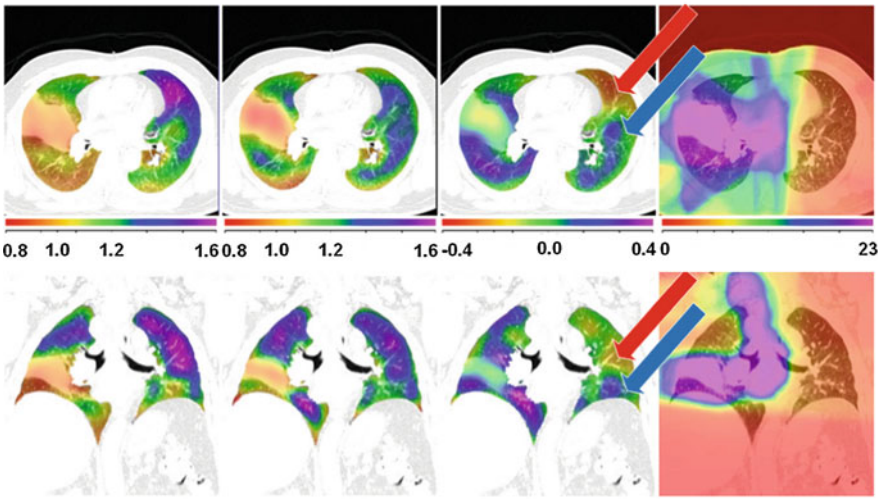

(b) Subject B

Fig. 13.9 The pulmonary function change compare to the planned radiation dose distribution. The dose map, pulmonary function and pulmonary function change are overlaid on the FB_{PRE}. The first column is the pulmonary function before RT. The second column is the pulmonary function after RT. The third column is the pulmonary function change from the subtraction of the previous two images. The fourth column is the planned radiation dose distribution. In the third column, the *red arrows* show regions with decreased pulmonary function and the *blue arrows* show regions with increased pulmonary function

in high dose regions. Notice that more regions in the left lung have increased lung function (blue) following RT than the right lung. However, the right lung (left side of the figure) also shows modest changes in lung function while receiving modest radiation (<8 Gy). The Jacobian change ranges from −0.15 to 0.1 with a mean value of −0.02 in the right lung and from −0.22 to 0.23 with a mean value of −0.02 in the left lung. It is consistent with our expectation that the left lung (ipsilateral lung, where the radiation dose is targeted) has larger change of pulmonary function than the right lung (contralateral lung, where the radiation dose is much lower). The similar mean value of Jacobian change in both lungs may be caused by the small volume of the tumor in subject A. For subject B, the first and second columns show modest changes in pulmonary function before and after RT for the untreated left lung, while there is large increase in pulmonary function in the treated right lung following 13 of 37 fractions of RT. The third column in subject B also indicates that the rim of the tumor shows an increase in lung function induced by the decrease in tumor volume. The Jacobian change ranges from −0.40 to 0.39 with a mean value of −0.03 in the contralateral lung and from −0.25 to 0.50 with a mean value of 0.11 in the ipsilateral lung. This change in function might have been concealed if purely nonrigid image registration algorithms were used to estimate T4. The correlation coefficients (linear regression) for pulmonary function change and the radiation dose were calculated for each patient and each lung. For the subject A, the r value is −0.19 in the ipsilateral lung and −0.14 in the contralateral lung. For subject B, the r value is −0.37 in the ipsilateral lung and 0.25 in the contralateral lung. Therefore, the correlation between the pulmonary function change and radiation dose for the whole lung is very weak and other factors such as treatment location may play a role in this relationship.

Using 4DCT and image registration the regional lung function can be measured by Jacobian before and after radiation therapy. Changes in regional lung function before and after RT can be compared with the radiation dose distribution by transforming the pulmonary function maps into the same coordinate system as that of the computed dose distribution. This provides a framework to examine the relationship between lung function change, delivered dose, and treatment location within the lung. Establishing a quantitative measurement of the pulmonary function change before and after RT may greatly accelerate the studies of the relationship between RT treatment and resultant changes in pulmonary function. Furthermore, this could translate into clinically relevant data for future treatment planning schemes that avoid increased functional injury to the lungs [30].

References

1. Altes, T.A., Eichinger, M., Puderbach, M.: Magnetic resonance imaging of the lung in cystic fibrosis. Proc. Am. Thorac. Soc. **4**(4), 321–327 (2007)
2. van Beek, E.J., Wild, J.M., Kauczor, H.U., Schreiber, W., Mugler, J.P.III., de Lange, E.E.: Functional MRI of the lung using hyperpolarized 3-helium gas. J. Magn. Reson. Imaging **20**(4), 550–554 (2004)

3. Chon, D., Simon, B.A., Beck, K.C., Shikata, H., Saba, O.I., Won, C., Hoffman, E.A.: Differences in regional wash-in and wash-out time constants for xenon-CT ventilation studies. Respir. Physiol. Neurobiol. **148**(1–2), 65–83 (2005)
4. Christensen, G., Johnson, H.: Consistent image registration. IEEE Trans. Med. Imaging **20**(7), 568–582 (2001)
5. Christensen, G.E., Song, J.H., Lu, W., Naqa, I.E., Low, D.A.: Tracking lung tissue motion and expansion/compression with inverse consistent image registration and spirometry. Med. Phys. **34**(6), 2155–2165 (2007)
6. Ding, K., Bayouth, J.E., Buatti, J.M., Christensen, G.E., Reinhardt, J.M.: 4DCT-based measurement of changes in pulmonary function following a course of radiation therapy. Med. Phys. **37**(3), 1261–1272 (2010)
7. Ding, K., Cao, K., Amelon, R.E., Raghavan, M.L., Christensen, G.E., Reinhardt, J.M.: Comparison of intensity- and Jacobian-based estimates of lung regional ventilation. In: Brown, M., de Bruijne, M., van Ginneken, B., Ding, K., Kiraly, A., Kuhnigk, J.M., McClelland, J., Mori, K., Reinhardt, J.M. (eds.) Third International Workshop on Pulmonary Image Analysis, pp. 49–60, Beijing (2010)
8. Ding, K., Cao, K., Christensen, G.E., Hoffman, E.A., Reinhardt, J.M.: Registration-based regional lung mechanical analysis: retrospectively reconstructed dynamic imaging versus static breath-hold image acquisition. In: SPIE, p. 72620D (2009)
9. Ding, K., Cao, K., Christensen, G.E., Raghavan, M.L., Hoffman, E.A., Reinhardt, J.M.: Registration-based lung tissue mechanics assessment during tidal breathing. In: Brown, M., de Bruijne, M., van Ginneken, B., Kiraly, A., Kuhnigk, J.M., Lorenz, C., Mori, K., Reinhardt, J.M. (eds.) First International Workshop on Pulmonary Image Analysis, pp. 63–72, New York (2008)
10. Ding, K., Miller, W., Cao, K., Christensen, G., Reinhardt, J., Benedict, S., Libby, B., Sheng, K.: Quantification of regional lung ventilation from tagged hyperpolarized helium-3 MRI. In: 2011 IEEE International Symposium on Biomedical Imaging: From Nano to Macro, pp. 1074–1077 (2011)
11. Ding, K., Yin, Y., Cao, K., Christensen, G.E., Lin, C.L., Hoffman, E.A., Reinhardt, J.M.: Evaluation of lobar biomechanics during respiration using image registration. In: Proceedings of International Conference on Medical Image Computing and Computer-Assisted Intervention 2009, vol. 5761, pp. 739–746 (2009)
12. Fuld, M.K., Easley, R.B., Saba, O.I., Chon, D., Reinhardt, J.M., Hoffman, E.A., Simon, B.A.: CT-measured regional specific volume change reflects regional ventilation in supine sheep. J. Appl. Physiol. **104**(4), 1177–1184 (2008)
13. Guerrero, T., Sanders, K., Castillo, E., Zhang, Y., Bidaut, L., Komaki, T.P.R.: Dynamic ventilation imaging from four-dimensional computed tomography. Phys. Med. Biol. **51**(4), 777–791 (2006)
14. Guerrero, T., Sanders, K., Noyola-Martinez, J., Castillo, E., Zhang, Y., Tapia, R., Guerra, R., Borghero, Y., Komaki, R.: Quantification of regional ventilation from treatment planning CT. Int. J. Radiat. Oncol. Biol. Phys. **62**(3), 630–634 (2005)
15. Harris, R.S., Schuster, D.P.: Visualizing lung function with positron emission tomography. J. Appl. Physiol. **102**(1), 448–458 (2007)
16. Hoffman, E.A., van Beek, E.: Hyperpolarized media MR imaging—expanding the boundaries? Acad. Radiol. **13**(8), 929–931 (2006)
17. Hoffman, E.A., Ritman, E.L.: Effect of body orientation on regional lung expansion in dog and sloth. J. Appl. Physiol. **59**(2), 481–491 (1985)
18. Keall, P.J., Kini, V.R., Vedam, S.S., Mohan, R.: Potential radiotherapy improvements with respiratory gating. Australas. Phys. Eng. Sci. Med. **25**(1), 1–6 (2002)
19. Kong, F.M., Haken, R.K.T., Schipper, M.J., Sullivan, M.A., Chen, M., Lopez, C., Kalemkerian, G.P., Hayman, J.A.: High-dose radiation improved local tumor control and overall survival in patients with inoperable/unresectable non-small-cell lung cancer: long-term results of a radiation dose escalation study. Int. J. Radiat. Oncol. Biol. Phys. **63**(2), 324–333 (2005)

20. Low, D.A., Nystrom, M., Kalinin, E., Parikh, P., Dempsey, J.F., Bradley, J.D., Mutic, S., Wahab, S.H., Islam, T., Christensen, G., Politte, D.G., Whiting, B.R.: A method for the reconstruction of four-dimensional synchronized CT scans acquired during free breathing. Med. Phys. **30**(6), 1254–1263 (2003)
21. Marcucci, C., Nyhan, D., Simon, B.A.: Distribution of pulmonary ventilation using Xe-enhanced computed tomography in prone and supine dogs. J. Appl. Physiol. **90**(2), 421–430 (2001)
22. Marks, L.B., Spencer, D.P., Sherouse, G.W., Bentel, G., Clough, R., Vann, K., Jaszczak, R., Coleman, R., Prosnitz, L.R.: The role of three dimensional functional lung imaging in radiation treatment planning: the functional dose-volume histogram. Int. J. Radiat. Oncol. Biol. Phys. **33**(1), 65–75 (1995)
23. Moller, H.E., Chen, X.J., Saam, B., Hagspiel, K.D., Johnson, G.A., Altes, T.A., de Lange, E.E., Kauczor, H.U.: MRI of the lungs using hyperpolarized noble gases. Magn. Reson. Med. **47**(6), 1029–1051 (2002)
24. Pan, T.: Comparison of helical and cine acquisitions for 4D-CT imaging with multislice CT. Med. Phys. **32**(2), 627–634 (2005)
25. Reinhardt, J.M., Ding, K., Cao, K., Christensen, G.E., Hoffman, E.A., Bodas, S.V.: Registration-based estimates of local lung tissue expansion compared to xenon CT measures of specific ventilation. Med. Image Anal. **12**(6), 752–763 (2008) (Special issue on information processing in medical, imaging 2007)
26. Simon, B.A.: Non-invasive imaging of regional lung function using X-ray computed tomography. J. Clin. Monit. Comput. **16**(5), 433–442 (2000)
27. Staring, M., Klein, S., Pluim, J.P.W.: A rigidity penalty term for nonrigid registration. Med. Phys. **34**(11), 4098–4108 (2007)
28. Tajik, J.K., Chon, D., Won, C.H., Tran, B.Q., Hoffman, E.A.: Subsecond multisection CT of regional pulmonary ventilation. Acad. Radiol. **9**, 130–146 (2002)
29. Yamamoto, T., Kabus, S., von Berg, J., Lorenz, C., Keall, P.J.: Impact of four-dimensional computed tomography pulmonary ventilation imaging-based functional avoidance for lung cancer radiotherapy. Int. J. Radiat. Oncol. Biol. Phys. **2**, 1–10 (2010)
30. Yamamoto, T., Kabus, S., von Berg, J., Lorenz, C., Keall, P.J.: Impact of four-dimensional computed tomography pulmonary ventilation imaging-based functional avoidance for lung cancer radiotherapy. Int. J. Radiat. Onclol. Biol. Phys. **79**(1), 279–288 (2011)
31. Yaremko, B.P., Guerrero, T.M., Noyola-Martinez, J., Guerra, R., Lege, D.G., Nguyen, L.T., Balter, P.A., Cox, J.D., Komaki, R.: Reduction of normal lung irradiation in locally advanced non-small-cell lung cancer patients, using ventilation images for functional avoidance. Int. J. Radiat. Oncol. Biol. Phys. **68**(2), 562–571 (2007)

Chapter 14
Respiratory Motion Correction in Cone-Beam CT for Image-Guided Radiotherapy

Simon Rit, David Sarrut and Jan-Jakob Sonke

Abstract Cone-beam CT has been integrated with the linear accelerator for image-guided radiotherapy, i.e., the accurate assessment and correction of the target position prior to treatment delivery. The slowness of these cone-beam CT scanners, which rotate at less than 1 rpm, induces respiratory motion artifacts if the patient can breath freely during the acquisition. As in conventional CT, several techniques have been proposed to correct for these artifacts. Respiration-correlated cone-beam CT assumes that respiratory motion is periodic to sort the cone-beam projection images in subsets according to a respiratory signal, and reconstructs from each subset the corresponding phase of the respiratory cycle, resulting in a 4D cone-beam CT image. A more advanced solution is motion-compensated cone-beam CT which necessitates an estimate of the respiratory motion during the cone-beam acquisition to compensate for the respiratory motion during the reconstruction from all the cone-beam projection images. This chapter is an overview of these recent developments for correction of respiratory motion in cone-beam CT for image-guided radiotherapy.

14.1 Introduction

In the past decades, several advances in hardware and software have greatly improved the ability of radiotherapy to conform the dose to the target and to spare organs at risk (OARs) with sharp doses, e.g., intensity modulated radiotherapy (IMRT) and particle therapy. At the same time, these improvements have increased the risk

S. Rit (✉) · D. Sarrut
Université de Lyon, CREATIS, CNRS UMR5220; Inserm U1044, INSA-Lyon, Université Lyon 1, Centre Léon Bérard, Lyon, France
e-mail: simon.rit@creatis.insa-lyon.fr

J.-J. Sonke
Department of Radiation Oncology, The Netherlands Cancer Institute, Amsterdam, The Netherlands

J. Ehrhardt and C. Lorenz (eds.), *4D Modeling and Estimation of Respiratory Motion for Radiation Therapy*, Biological and Medical Physics, Biomedical Engineering,
DOI: 10.1007/978-3-642-36441-9_14,

of treatment errors and pushed for the development of image-guided radiotherapy (IGRT), i.e., guidance in the treatment room by means of imaging.

Many imaging devices have been developed for use in radiation treatment rooms. Currently, the most popular are flat panels mounted in front of the X-ray MV treatment beam or in front of an additional X-ray kV source dedicated to imaging. These X-ray imagers acquire 2D projection images that can be used in several ways. Initially, they have been used as is for setup verification using 2D/3D rigid registration [31]. Subsequently, reconstruction software has been developed to reconstruct a 3D computed tomography (CT) from a sequence of projection images acquired during a gantry revolution [20]. These images are referred to as cone-beam CT images due to the geometry of the X-ray beam.

Cone-beam CT images capture the position and the anatomy of the patient during the treatment fractions which is essential information in many clinical scenarios. Before treatment delivery, it can be used for patient re-positioning in order to accurately treat the target while ensuring that organs-at-risks are spared [58]. Additionally, it can be used to evaluate anatomical deformations between fractions, recalculate and accumulate the delivered dose [19] and adapt the initial treatment plan [51]. In each of these scenarios, 3D/3D rigid or deformable registration is required between the planning CT and the cone-beam CTs. An overview of 3D/3D deformable registrations is available in Part II of this book.

The characteristics of the panels and the X-ray sources may differ between cone-beam CT systems. However, the majority shares two essential characteristics with respect to the problem of respiratory motion. First, the flat panel acquires frames fast enough (a few frames per second) to assume that breathing motion artifacts in projection images are neglectable [47]. Second, the imager is attached to the gantry of the linear accelerator which limits the speed of the rotation to about 1 rpm. Therefore, the acquisition of the projection images lasts a few breathing cycles which produces motion artifacts during the reconstruction of 3D cone-beam CT images.

Respiratory motion artifacts in 3D cone-beam CT images impair the anatomy representation in the thorax and the upper-abdomen which can reduce their clinical value. For example, motion blur hampers accurate tumor localization of lung tumors [42]. With the advent of 4D radiotherapy, described in Chap. 11, it was natural to investigate the management of respiratory motion in cone-beam CT. This chapter summarizes the effect of breathing motion on cone-beam CT and the different solutions that have recently been developed to correct for breathing artifacts.

14.2 Problem Description

The problem explored in this chapter is breathing motion in cone-beam CTs acquired with IGRT scanners attached to the gantry of linear accelerators. The X-ray source follows a circular trajectory parameterized with the gantry angle $\beta(t) \in [0, 2\pi)$ which is a function of the acquisition time $t \in T \subset \mathbb{R}$. One acquisition consists of a

set of projection images $g(\boldsymbol{y}, t)$ with $\boldsymbol{y} \in \mathbb{R}^2$ the coordinates of the 2D flat panel for the projection image acquired at time t.

In dynamic tomography, the spatial distribution of tissues changes during the acquisition due to patient movements so the sought CT f is a function of space and time, i.e., $f : \Omega \times T \rightarrow \mathbb{R}$ with $\Omega \subset \mathbb{R}^3$ the field-of-view and $f(\boldsymbol{x}, t)$ the voxel intensity at point $\boldsymbol{x} \in \Omega$ and time $t \in T$. Assuming a monochromatic beam, no scattering and an ideal flat panel, the relationship between g and f is given by the Beer-Lambert law

$$g(\boldsymbol{y}, t) = I_0 \exp\left(- \int_{L_{y,t}} f(\boldsymbol{x}, t) d\boldsymbol{x} \right) \tag{14.1}$$

with I_0 the intensity of the X-ray source and $L_{y,t}$ the straight line segment going from the X-ray source to the flat panel pixel with coordinates $(\boldsymbol{y}, t)$.

Reconstructing f from an acquisition g is the inverse problem of tomography. Because the dynamic tomography f is a 3D+t function and the set of cone-beam projection images g is a 2D+t function, the reconstruction of f is only possible based on a model of the breathing motion during the cone-beam acquisition.

14.2.1 Static Cone-Beam Reconstruction

The simplest solution is to assume that the scanned object is static during acquisition, i.e., $f(\boldsymbol{x}, t) = f(\boldsymbol{x}, 0),\ \forall \boldsymbol{x} \in \Omega,\ \forall t \in T$. The acquisition protocol is then designed to acquire enough projection images for the reconstruction of the 3D cone-beam CT image from the 2D+t sequence. Many solutions have been proposed to the problem of cone-beam CT reconstruction for circular trajectories but none of them is exact since the acquisition does not satisfy Tuy's data sufficiency condition [57]. So far, the preferred algorithm for circular cone-beam CT has been Feldkamp, Davis and Kress (FDK) algorithm [15], the popularity of which stems from its simplicity and its efficiency. The reader is referred to the extensive literature on the subject for its mathematical description and details on its implementation, e.g., [21]. Briefly, the FDK algorithm is a filtered backprojection algorithm. The filtered projections are obtained with a ramp filter applied to the weighted projection images

$$\tilde{g}(\boldsymbol{y}, t) = \int_{\mathbb{R}} \left(\int_{\mathbb{R}} -\ln\left(\frac{g(\boldsymbol{y}, t)}{I_0} \right) w_{2D}(\boldsymbol{y}) e^{-i2\pi(\boldsymbol{y}\cdot\boldsymbol{u})\rho} d\rho \right) e^{i2\pi(\boldsymbol{y}\cdot\boldsymbol{u})\nu} |\nu| d\nu$$

where $w_{2D} : \mathbb{R}^2 \rightarrow \mathbb{R}$ is a 2D weighting function which depends on the scanner geometry, $\boldsymbol{u} \in \mathbb{R}^2$ is the unit vector of the flat panel coordinate system orthogonal to the rotation axis of the scanner and $\cdot$ is the dot product. This formula converts the measured projection values $g(\boldsymbol{y}, t)$ to attenuation values using Eq. 14.1, weights the attenuation images with a 2D function w_{2D} and applies a ramp filter in the direction $\boldsymbol{u}$. The two integrals correspond to the Fourier transform and its inverse in

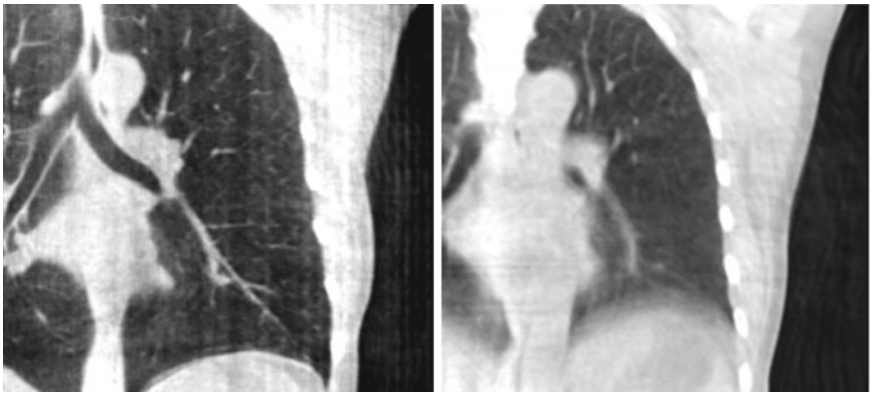

Fig. 14.1 Cone-beam CT images of the same patient using static cone-beam CT image reconstruction. *Left* Reconstruction from breath-hold acquisition of 95 projection images. *Right* Reconstruction from free-breathing acquisition of 670 projection images

the direction $\boldsymbol{u}$. The final solution is obtained with the weighted backprojection of the filtered projections

$$f(\boldsymbol{x}) \approx \int_0^{2\pi} w_{3D}(\boldsymbol{x}, \beta)\tilde{g}\left(\boldsymbol{y}'(\boldsymbol{x}, \beta)\right) d\beta \tag{14.2}$$

where $w_{3D} : \mathbb{R}^3 \times T \rightarrow \mathbb{R}$ is a 3D weighting function which depends on the scanner geometry and $\boldsymbol{y}' : \mathbb{R}^3 \times T \rightarrow \mathbb{R}^3$ the projection function, i.e., $\boldsymbol{y}'(\boldsymbol{x}, \beta)$ are the coordinates of the projection of point $\boldsymbol{x}$ at angle $\beta(t)$ in the coordinate system of the flat panel.

The breathing of lung patients is one of the main sources of motion in the field-of-view, together with cardiac motion [47]. One solution is to ask the patients to hold their breath during acquisition [5, 56, 60] (Fig. 14.1). However, the rotation speed of cone-beam CT scanners attached to the gantry of linear accelerators is at maximum 1 rpm which generally requires interrupted acquisitions for lung cancer patients. Moreover, in the context of IGRT, this solution is only useful when the breath-hold is reproduced during the radiation delivery. It is often preferred to let the patient breath freely during treatment and, consequently, during the cone-beam CT acquisition as well for consistency of tumor position between image guidance and treatment.

14.2.2 Breathing Artifacts

Breathing motion impacts static cone-beam CT reconstruction because projection images are not consistent with static objects in the field-of-view. The backprojection

of FDK algorithm (Eq. 14.2) implies that the impacted region encompasses every part of the field-of-view which superimposed on a part that moved during cone-beam acquisition in one or more projection images. The movement results in streaks tangential to the moving object in the X-ray directions which are typical of inconsistent or missing data. The periodicity of breathing motion tends to blur out the streaks near the moving parts, resulting in blurred moving objects, e.g., the diaphragm in Fig. 14.1.

The consequences of breathing artifacts in cone-beam CT for IGRT have not been fully investigated yet. In [17], the authors argue that blurred cone-beam CT images are generally sufficient for the localization of the tumor when registered on a corresponding reference image, e.g., the blurred 3D CT average computed from a conventional 4D CT. Another contradictory study [42] has obtained a significant difference between static and motion-corrected cone-beam CT with up to 5 mm difference on average between tumor localization with static and motion-corrected cone-beam CT. Moreover, improved image quality is beneficial for adaptive RT requiring (automatic) segmentation, deformable registration and dose accumulation. Anyhow, breathing artifacts were deemed preoccupying enough to trigger many investigations in the past few years on respiratory motion correction techniques for cone-beam CT. Two of them are described in the following: respiration-correlated cone-beam CT and motion-compensated cone-beam CT.

14.3 Respiration-Correlated Cone-Beam CT

Respiration-correlated cone-beam CT is very similar to conventional respiration-correlated CT described in Part I of the book. It is assumed that breathing motion is periodic, i.e., that the patient regularly recovers the same position during data acquisition. This periodicity is described with the phase or the amplitude of a respiratory signal which is typically one-dimensional. Respiration-correlated cone-beam CT consists in selecting projection images acquired at corresponding positions in the respiratory cycle using the respiratory signal. The selected subset of projection images is then used to reconstruct the 3D cone-beam CT image of the respiratory phase using a static reconstruction algorithm (Sect. 14.2.1). Repetition of the process at successive respiratory phases results in a 4D cone-beam CT image describing the respiratory motion of the patient over one respiratory cycle (see Sect. 14.5.1 for its estimation). Table. 14.1 provides an overview of the literature on respiration-correlated cone-beam CT.

The respiratory signal is a key component of respiration-correlated cone-beam CT which varies between studies (Table. 14.1). As in conventional CT, external devices can be used to record a signal which must be synchronized with the acquisition, e.g., thoracic belts with a pressure sensor or surfacic infrared markers with a dedicated camera. However, cone-beam CT has an advantage over conventional CT: the full field-of-view Ω is covered by the X-ray beam at every projection image. Therefore, the whole sequence of projection images contains distinct motion information

Table 14.1 Overview of the literature on respiration-correlated cone-beam CT with scanners attached to the gantry of a linear accelerator

Author	Year	Respiratory signal	Reconstruction algorithm
Sonke et al. [42, 45, 52–54]	2005	Processing of projection images (Fig. 14.2)	FDK
Li et al. [28, 29]	2006	External radiopaque marker tracked in projection images	FDK
Purdie et al. [38]	2006	Processing of projection images	FDK
Dietrich et al. [14]	2006	Abdominal belt	FDK
Chang et al. [9, 10]	2006	Infrared external marker	FDK
Lu et al. [30]	2007	Infrared external marker	FDK
Leng et al. [24, 25]	2008	Infrared external marker	FDK, MKB, PICCS
Maurer et al. [33, 34]	2008	Infrared external marker	FDK for tomosynthesis
Rit et al. [43]	2009	Processing of projection images	FDK, SART
Bergner et al. [2, 3]	2009	Processing of projection images	FDK, AAPC, MKB, PICCS, ASD-POCS
Chen et al. [11, 12]	2010	Processing of projection images	FDK
Santoro et al. [49]	2010	Infrared external marker	FDK for tomosynthesis
Qi et al. [39, 40]	2011	Infrared external marker	FDK, PICCS, MKB

The reconstruction algorithms refer to Feldkamp, David and Kress (FDK) [15], McKinnon-Bates (MKB) [35], Prior Image Constrained Compressed Sensing (PICCS) [24], Simultaneous Algebraic Reconstruction Technique (SART) [1], AutoAdaptive Phase-Correlation (AAPC) [3], Adaptive Steepest Descent Projection Onto Convex Sets (ASD-POCS) [50]. Note that studies on digital tomosynthesis (DTS) are included in this review because DTS corresponds to the reconstruction from a partial cone-beam acquisition

and it has been proposed to extract the respiratory signal from projection images. The advantage is that the signal is based on the motion of internal structures, it is perfectly synchronized with the projection images and no additional hardware is required.

Among the solutions for the extraction of the respiratory signal from the projection images, the *Amsterdam shroud* [44, 54, 64] is now used clinically for the on-the-fly reconstruction of 4D cone-beam CT images. The method consists in sequentially applying basic processing filters on each 2D cone-beam projection image to obtain the 2D image called the *Amsterdam shroud* by its authors. The axes of the *Amsterdam shroud* are the projection index horizontally, i.e. time, and the cranio-caudal position vertically (Fig. 14.2). This processing allows to highlight the moving structures which are perpendicular to the cranio-caudal axis, mainly the diaphragm domes. The respiratory signal is clearly visible in this image and it can be extracted with a simple correlation between consecutive columns.

The selection of a subset of projection images for static reconstruction poses a data sufficiency problem in respiration-correlated cone-beam CT. Without modification of the acquisition protocol or the reconstruction algorithm, large angular gaps between consecutive projection images of the selected subset produce streak artifacts. The

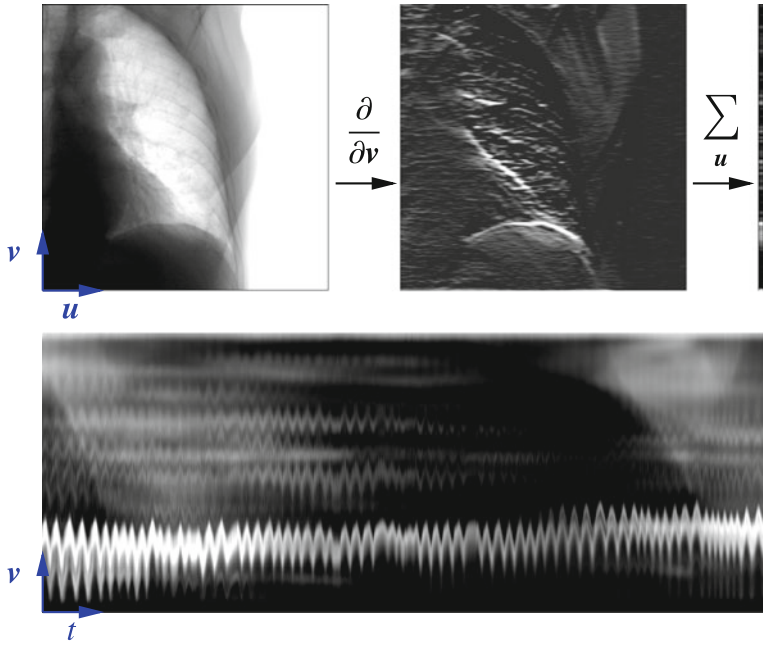

Fig. 14.2 Example of algorithm for respiratory signal extraction from projection images, the *Amsterdam shroud* [54, 64]. *Top* Each projection image is processed with a derivative filter in the ***v*** direction and projected horizontally by taking the sum in the ***u*** direction. *Bottom* The process is repeated for each projection and produces the columns of a 2D image from which the respiratory signal can be extracted

problem lies in the relation between the length of the breathing cycle and the rotation speed, and the frame rate of the flat panel has little influence on this matter. Two solutions have been investigated to handle this problem. First, the angular gaps can be decreased by modifying the acquisition with a slower rotation [30, 34, 54] or multiple rotations [33]. Otherwise, several authors have attempted to develop specific reconstruction algorithms to reduce the amount of artifacts (Table 14.1). A comparative study has recently shown that image improvement must be cautiously analyzed for clinical use [2].

Respiration-correlated imaging enables the estimation of breathing motion during treatment fractions of lung [52, 53] and upper-abdominal targets [7, 8]. The first clinical system for 4D cone-beam CT recommended a gantry rotation speed four times slower than regular 3D cone-beam CT and a dose per projection divided by four to maintain the same total dose per cone-beam acquisition [54]. These settings were a trade-off between acquisition time and image quality (Fig. 14.3). The increase in acquisition time, the decrease in image quality and the residual motion artifacts due to the incorrectness of the periodicity assumption have pushed for the development of motion compensation techniques.

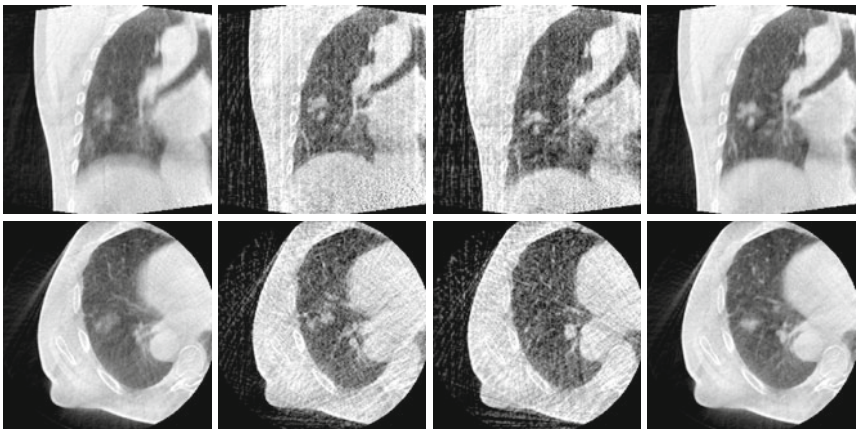

Fig. 14.3 Coronal (*top*) and axial (*bottom*) slices at the isocenter of, from *left* to *right*, the 3D cone-beam CT [15], the end-exhale and the end-inhale frame of the respiration-correlated 4D cone-beam CT [54] and the motion-compensated cone-beam CT [45]. The patient was a lung cancer patient treated with stereotactic body radiotherapy [53]. A sequence of 1318 projection images acquired over 200° in 4 min was used with an imaging dose of about 2 cGy. The average respiratory period of the patient during the acquisition was 3.5 s

14.4 Motion-Compensated Cone-Beam CT

Motion-compensated cone-beam CT is the domain of tomography which aims at finding the dynamic tomography f from the sequence of projection images g using an estimate of the deformation of the objects in the field-of-view during acquisition. There are two challenges in motion-compensated CT reconstruction: (1) to estimate the deformation during the cone-beam acquisition and (2) to incorporate the estimate in the reconstruction. Table 14.2 provides an overview of the state-of-the-art on motion-compensated cone-beam CT for IGRT. The problem of motion estimation is described in the next section. This section briefly summarizes the different solutions to the reconstruction problem assuming a known motion estimate.

Using the dynamic particle model of [16], let $\Phi : \Omega \times T \to \Omega$ be the motion estimate with $\Phi(\boldsymbol{x}, t)$ the spatial position of the particle at time t which was at position $\boldsymbol{x}$ at a chosen reference time $t_r \in T$. The estimation of Φ is discussed in the next section. Motion-compensated reconstruction assumes a link between two instants of the dynamic tomography, e.g.,

$$f(\boldsymbol{x}, t) = f(\Phi(\boldsymbol{x}, t), t_r) = f_r(\Phi(\boldsymbol{x}, t)) \tag{14.3}$$

where $f_r : \Omega \to \mathbb{R}$ is the frame of the dynamic tomography f at instant t_r. Additionally, mass preservation can be enforced using the determinant of the Jacobian

Table 14.2 Overview of the literature on motion-compensated cone-beam CT with scanners attached to the gantry of a linear accelerator

Author	Year	Motion model	Motion estimation	Reconstruction
Zeng et al. [61, 62]	2005	B-splines	2D/3D registration with periodicity constraint	–
Li et al. [26, 27]	2006	B-splines	4D CBCT and 2D/3D registration	FDK
Rit et al. [42, 43, 45]	2009	Optical flow based	4D CT correlated with the *Amsterdam shroud*	FDK, SART
Zhang et al. [63]	2010	Principal component analysis	4D (CB)CT and surrogate signal in projection images	FDK
Pengpan et al. [36, 37]	2011	Translations of large organs	Electrical impedance tomography	SART

The reconstruction algorithms refer to Feldkamp, David and Kress (FDK) [15] and Simultaneous Algebraic Reconstruction Technique (SART)

of the deformation [13, 22] but mass preservation is not always a valid assumption in lungs due to the blood flow (see Chap. 13). Using Eq. 14.3 in Eq. 14.1, we obtain

$$g(\boldsymbol{y}, t) = I_0 \exp\left(- \int_{L_{\boldsymbol{y},t}} f_r(\Phi(\boldsymbol{x}, t)) d\boldsymbol{x} \right). \tag{14.4}$$

Equation 14.4 is the inverse problem of motion-compensated reconstruction, i.e., the reconstruction of the frame f_r at time t_r of the dynamic CT f from a known set of projections images g and the deformation Φ. In contrast to respiration-correlated cone-beam CT, only the single 3D CT f_r is reconstructed, e.g., the time-weighted average in Fig. 14.3. Other instants of the dynamic tomography f can be subsequently obtained by warping f_r at any other time using the motion estimate Φ. Both analytic and iterative algorithms have been proposed to solve this problem.

Analytic reconstruction algorithms are often preferred because they are computationally more efficient than iterative algorithms. However, current analytic algorithms for motion compensated reconstruction can only compensate a limited class of deformations: the deformations that transform the set of convergent lines $L_{\boldsymbol{y},t}$ at each time $t \in T$ (Eq. 14.1) into another set of convergent lines at the reference time t_r [13]. This class of deformations includes time-dependent affine transformations [48] but does not include respiratory motion. Therefore, other approximate algorithms have been proposed [16, 22, 27, 46, 55]. Most of them only modify the backprojection of the FDK algorithm [15] with a warped backprojection, i.e., the composition of the deformation Φ with the backprojection (Eq. 14.2):

$$f_r(\boldsymbol{x}) \approx \int_0^{2\pi} w_{3D}(\Phi(\boldsymbol{x}, t), \beta) \tilde{g}(\boldsymbol{y}'(\Phi(\boldsymbol{x}, t), \beta)) d\beta. \tag{14.5}$$

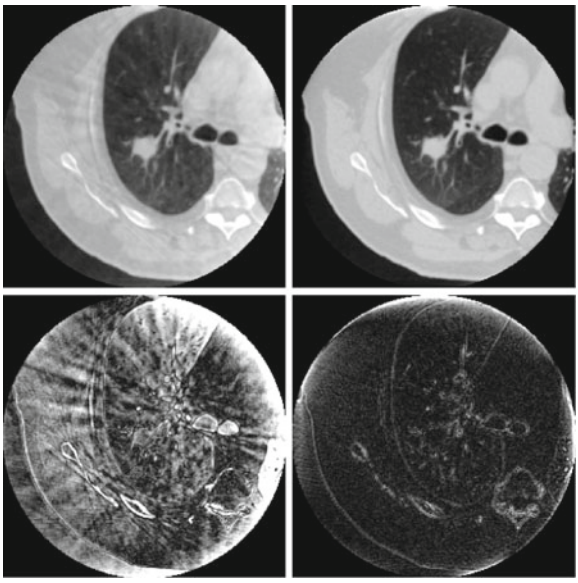

Fig. 14.4 Axial slices (*top*) and difference with the gold standard (*bottom*) of two motion-compensated cone-beam CT reconstruction algorithm applied to the same simulated sequence of projection images. Residual streaks are visible in the motion-compensated FDK algorithm (Eq. 14.5 derived from [15]) whereas motion-compensated Simultaneous Algebraic Reconstruction Technique [1] fully corrects for streak artifacts. From Rit et al. [43]

The motion-compensated reconstruction of a real sequence with an approximate estimate of the deformation is provided in Fig. 14.3.

Alternatively, one can numerically solve the motion-compensated reconstruction problem using iterative algorithms. Typically, one disposes of a vector $\boldsymbol{g}$ of measured samples of $-\ln(g/I_0)$ and seeks for the vector $\boldsymbol{f_r}$ of samples of f_r. Using a forward operator, i.e., a discretization of Eq. 14.1, one links $\boldsymbol{f_r}$ and $\boldsymbol{g}$ with the system of linear equations

$$\boldsymbol{f_r} = \boldsymbol{A}\boldsymbol{g} \tag{14.6}$$

where $\boldsymbol{A}$ is the so-called system matrix. In motion-compensated reconstruction, $\boldsymbol{A}$ accounts for the breathing deformation Φ in addition to the linear attenuation (Eq. 14.1) and, more specifically, for the deformation of the regular lattice of samples $\boldsymbol{f_r}$. Many techniques have been proposed to compute $\boldsymbol{A}$ and solve the system of linear equations from the measurements $\boldsymbol{g}$ for a variety of modalities [6, 18, 41, 43] and it has been observed that, as in many other situations, iterative algorithms benefit from their flexibility. Indeed, contrary to motion-compensated analytic reconstruction, there is no mathematical difficulty in solving Eq. 14.6 as long as there is enough projection images, which explains the better image quality of motion-compensated CT images reconstructed with iterative methods compared to approximate analytic algorithms [43] (Fig. 14.4). However, the computation time is prohibitive for use during the treatment fractions and only approximate analytical solutions are usable for online IGRT [45].

14.5 Motion Estimation for Motion-Compensated Cone-Beam CT

Motion-compensated reconstruction requires an estimate of the respiratory motion Φ during the acquisition. Generally, if one excludes the external respiratory surrogates (Chap. 9) and additional modalities [36, 37], the only images acquired in the treatment room are the cone-beam projection images, in which case the respiratory motion Φ must be estimated from the cone-beam sequence g. However, estimating Φ from g without prior information is very challenging because it mixes an inverse problem (Eq. 14.1) with a registration problem (Eq. 14.3). Use of prior images and/or motion models is mandatory (Table 14.2).

14.5.1 Use of 4D Cone-Beam CT Images

A simple solution is to assume periodicity of breathing and to use the 4D respiration-correlated cone-beam CT images to estimate the respiratory motion. The same algorithms as the ones developed for conventional 4D CT, described in Part II of this book, may be used for this purpose. For example, Li et al. [27] used B-splines deformable registration. However, the quality of 4D cone-beam CT images (Fig. 14.3) necessarily limits the accuracy of the registration. The challenging image quality has lead to the development of more robust models, e.g., the model of Zhang et al. [63] based on Principal Component Analysis (PCA) of deformable registrations correlated to surrogate respiratory signals, similar to those described in Part III of the book. Moreover, the periodicity assumption is known to be partly invalid, causing residual motion artifacts in 4D cone-beam CT images, and it is preferable to estimate pseudo-periodic motion.

14.5.2 Use of Prior 3D CT Images

Another solution is to use other images of the same patient acquired prior to treatment, e.g., a 3D CT image without breathing artifact such as a breath-hold CT image [62] or a phase of a 4D CT image [59], and to handle the problem as a 2D/3D deformable image registration problem [31].

The similarity measure of 2D/3D deformable registration is generally defined in the 2D space between the measured projection images and the *Digitally Computed Radiographs* (DRRs) of the prior CT, i.e., the digital computation of projections g from the prior CT f in Eq. 14.1. In theory, this is a unimodal problem and one could use the Sum of Squared Differences (SSD) [26, 32, 61]. However, it is usually preferred to use more robust similarity measures, e.g., the normalized correlation coefficient [59, 62], due to imaging artifacts such as scatter and beam-hardening.

The parametrization of the deformation is an essential component of 2D/3D deformable registration. In theory, spatio-temporal free form transformations can be used without any modeling specific to breathing [61] but only a rough estimate of a full 3D+t deformation Φ can be computed from a 2D+t sequence g. It is therefore preferable to use a better modeling of the motion. For example, Zeng et al. [62] have used 4D B-splines registration with an additional pseudo-periodicity assumption.

14.5.3 Use of Prior 4D CT Images

4D respiration-correlated CT images are routinely acquired for treatment planning in most 4D treatment strategies [23]. As it has been described in this book, 4D CT allows patient-specific modeling of the breathing motion. Therefore, it has been proposed to use a prior model of breathing to estimate the respiratory motion. Ideally, the model is tailored to have an adequate number of degrees of freedom for the amount of input projection images g. For example, it has been proposed to assume similar motion during cone-beam CT acquisition as during planning CT acquisition and to use the phase of the respiratory signal to correlate the breathing motion with the prior estimate on-the-fly, i.e., during cone-beam acquisition [45]. This solution allows online motion-compensated cone-beam CT reconstruction (Fig. 14.3) which is attractive for IGRT. In [59], these strong assumptions have been relaxed by registering a phase/amplitude model using a 2D/3D deformable image registration technique. Better modeling and more precise registration are still under investigation.

14.6 Discussion and Conclusion

This chapter was a summary of the state-of-the-art in the handling of respiratory motion in cone-beam CT for IGRT. The field is relatively new since cone-beam CT scanners have been integrated to linear accelerators in the early two thousands [20]. Mainly two directions have been investigated so far, respiration-correlated and motion-compensated cone-beam CT.

Respiration-correlated is a pragmatic solution which had already proven efficient for 4D CT (Part I) although it is inherently limited by the periodicity assumption of the breathing cycle. One difficulty is its need to acquire more data than static cone-beam CT to obtain similar image quality, but adapted acquisition protocols are already in clinical use and new reconstruction algorithms for handling the problem of the undersampling of projection images might further improve image quality (Table 14.1).

Motion-compensation is a seducing alternative solution which accounts for the fact that all acquired projection images are a representation of the same patient and can therefore be used together in the reconstruction of a higher quality 3D cone-beam CT image. But we have pointed out the difficulties in estimating the respiratory

motion and in reconstructing the image. Among the proposed solutions (Table 14.2), an approximate solution was deemed sufficiently efficient for clinical use [42, 45]. This book, which has covered the problem of motion modeling and estimation in many aspects along its chapters, could be a source of inspiration for improving motion estimation during cone-beam CT acquisition.

Clinical use of 4D cone-beam CT has already found several applications. On the one hand, it allows evaluating the evolution of breathing motion during the course of the radiation treatment which has already been investigated for both lung [4, 52] and liver targets [7]. But, more importantly at first, it allows accurate measurement of the time average position of the target, the variability of which would require large margins without image guidance [52, 53]. In the future, 4D cone-beam CT will also find applications in adapting the treatment when the patient breathing has evolved during the course of the treatment with a significant impact on the delivered dose.

References

1. Andersen, A., Kak, A.: Simultaneous algebraic reconstruction technique (SART): a superior implementation of the art algorithm. Ultrason. Imaging **6**(1), 81–94 (1984)
2. Bergner, F., Berkus, T., Oelhafen, M., Kunz, P., Pan, T., Grimmer, R., Ritschl, L., Kachelriess, M.: An investigation of 4D cone-beam CT algorithms for slowly rotating scanners. Med. Phys. **37**(9), 5044–5053 (2010)
3. Bergner, F., Berkus, T., Oelhafen, M., Kunz, P., Pan, T., Kachelriess, M.: Autoadaptive phase-correlated (AAPC) reconstruction for 4D CBCT. Med. Phys. **36**(12), 5695–5706 (2009)
4. Bissonnette, J.P., Franks, K., Purdie, T., Moseley, D., Sonke, J.J., Jaffray, D., Dawson, L., Bezjak, A.: Quantifying interfraction and intrafraction tumor motion in lung stereotactic body radiotherapy using respiration-correlated cone beam computed tomography. Int. J. Radiat. Oncol. Biol. Phys. **75**(3), 688–695 (2009)
5. Blessing, M., Stsepankou, D., Wertz, H., Arns, A., Lohr, F., Hesser, J., Wenz, F.: Breath-hold target localization with simultaneous kilovoltage/megavoltage cone-beam computed tomography and fast reconstruction. Int. J. Radiat. Oncol. Biol. Phys. **78**(4), 1219–1226 (2010)
6. Blondel, C., Vaillant, R., Malandain, G., Ayache, N.: 3D tomographic reconstruction of coronary arteries using a precomputed 4D motion field. Phys. Med. Biol. **49**(11), 2197–2208 (2004)
7. Case, R., Moseley, D., Sonke, J.J., Eccles, C., Dinniwell, R., Kim, J., Bezjak, A., Milosevic, M., Brock, K., Dawson, L.: Interfraction and intrafraction changes in amplitude of breathing motion in stereotactic liver radiotherapy. Int. J. Radiat. Oncol. Biol. Phys. **77**(3), 918–925 (2010)
8. Case, R., Sonke, J.J., Moseley, D., Kim, J., Brock, K., Dawson, L.: Inter- and intrafraction variability in liver position in non-breath-hold stereotactic body radiotherapy. Int. J. Radiat. Oncol. Biol. Phys. **75**(1), 302–308 (2009)
9. Chang, J., Mageras, G., Yorke, E., De Arruda, F., Sillanpaa, J., Rosenzweig, K., Hertanto, A., Pham, H., Seppi, E., Pevsner, A., Ling, C., Amols, H.: Observation of interfractional variations in lung tumor position using respiratory gated and ungated megavoltage cone-beam computed tomography. Int. J. Radiat. Oncol. Biol. Phys. **67**(5), 1548–1558 (2007)
10. Chang, J., Sillanpaa, J., Ling, C., Seppi, E., Yorke, E., Mageras, G., Amols, H.: Integrating respiratory gating into a megavoltage cone-beam CT system. Med. Phys. **33**(7), 2354–2361 (2006)
11. Chen, M., Siochi, R.: Diaphragm motion quantification in megavoltage cone-beam CT projection images. Med. Phys. **37**(5), 2312–2320 (2010)

12. Chen, M., Siochi, R.: Feasibility of using respiratory correlated mega voltage cone beam computed tomography to measure tumor motion. J. Appl. Clin. Med. Phys. **12**(2), 3473 (2011)
13. Desbat, L., Roux, S., Grangeat, P.: Compensation of some time dependent deformations in tomography. IEEE Trans. Med. Imaging **26**(2), 261–269 (2007)
14. Dietrich, L., Jetter, S., Tücking, T., Nill, S., Oelfke, U.: Linac-integrated 4D cone beam CT: first experimental results. Phys. Med. Biol. **51**(11), 2939–2952 (2006)
15. Feldkamp, L., Davis, L., Kress, J.: Practical cone-beam algorithm. J. Opt. Soc. Am. A **1**(6), 612–619 (1984)
16. Grangeat, P., Koenig, A., Rodet, T., Bonnet, S.: Theoretical framework for a dynamic cone-beam reconstruction algorithm based on a dynamic particle model. Phys. Med. Biol. **47**(15), 2611–2625 (2002)
17. Hugo, G., Liang, J., Campbell, J., Yan, D.: On-line target position localization in the presence of respiration: a comparison of two methods. Int. J. Radiat. Oncol. Biol. Phys. **69**(5), 1634–1641 (2007)
18. Isola, A., Ziegler, A., Koehler, T., Niessen, W., Grass, M.: Motion-compensated iterative cone-beam CT image reconstruction with adapted blobs as basis functions. Phys. Med. Biol. **53**(23), 6777–6797 (2008)
19. Jaffray, D., Lindsay, P., Brock, K., Deasy, J., Tomé, W.: Accurate accumulation of dose for improved understanding of radiation effects in normal tissue. Int. J. Radiat. Oncol. Biol. Phys. **76**(3), S135–S139 (2010)
20. Jaffray, D., Siewerdsen, J., Wong, J., Martinez, A.: Flat-panel cone-beam computed tomography for image-guided radiation therapy. Int. J. Radiat. Oncol. Biol. Phys. **53**(5 Suppl), 1337–1349 (2002)
21. Kak, A., Slaney, M.: Principles of Computerized Tomographic Imaging. IEEE Press, New York (1988)
22. Katsevich, A.: An accurate approximate algorithm for motion compensation in two-dimensional tomography. Inverse Prob. **26**(6), 065,007 (2010)
23. Keall, P., Mageras, G., Balter, J., Emery, R., Forster, K., Jiang, S., Kapatoes, J., Low, D., Murphy, M., Murray, B., Ramsey, C., van Herk, M., Vedam, S., Wong, J., Yorke, E.: The management of respiratory motion in radiation oncology report of AAPM task group 76. Med. Phys. **33**(10), 3874–3900 (2006)
24. Leng, S., Tang, J., Zambelli, J., Nett, B., Tolakanahalli, R., Chen, G.H.: High temporal resolution and streak-free four-dimensional cone-beam computed tomography. Phys. Med. Biol. **53**(20), 5653–5673 (2008)
25. Leng, S., Zambelli, J., Tolakanahalli, R., Nett, B., Munro, P., Star-Lack, J., Paliwal, B., Chen, G.H.: Streaking artifacts reduction in four-dimensional cone-beam computed tomography. Med. Phys. **35**(10), 4649–4659 (2008)
26. Li, T., Koong, A., Xing, L.: Enhanced 4D cone-beam CT with inter-phase motion model. Med. Phys. **34**(9), 3688–3695 (2007)
27. Li, T., Schreibmann, E., Yang, Y., Xing, L.: Motion correction for improved target localization with on-board cone-beam computed tomography. Phys. Med. Biol. **51**(2), 253–267 (2006)
28. Li, T., Xing, L.: Optimizing 4D cone-beam CT acquisition protocol for external beam radiotherapy. Int. J. Radiat. Oncol. Biol. Phys. **67**(4), 1211–1219 (2007)
29. Li, T., Xing, L., Munro, P., McGuinness, C., Chao, M., Yang, Y., Loo, B., Koong, A.: Four-dimensional cone-beam computed tomography using an on-board imager. Med. Phys. **33**(10), 3825–3833 (2006)
30. Lu, J., Guerrero, T.M., Munro, P., Jeung, A., Chi, P.C., Balter, P., Zhu, X., Mohan, R., Pan, T.: Four-dimensional cone beam CT with adaptive gantry rotation and adaptive data sampling. Med. Phys. **34**(9), 3520–3529 (2007)
31. Markelj, P., Tomaževič, D., Likar, B., Pernuš, F.: A review of 3D/2D registration methods for image-guided interventions. Med. Image Anal. **16**(3), 642–661 (2012)
32. Martin, J., McClelland, J., Thomas, C., Wildermuth, K., Landau, D., Ourselin, S., Hawkes, D.: Motion modelling and motion compensated reconstruction of tumours in cone-beam computed tomography. In: Proceedings of the IEEE Workshop on Mathematical Methods in Biomedical Image Analysis (2012)

33. Maurer, J., Godfrey, D., Wang, Z., Yin, F.F.: On-board four-dimensional digital tomosynthesis: first experimental results. Med. Phys. **35**(8), 3574–3583 (2008)
34. Maurer, J., Pan, T., Yin, F.F.: Slow gantry rotation acquisition technique for on-board four-dimensional digital tomosynthesis. Med. Phys. **37**(2), 921–933 (2010)
35. Mc Kinnon, G., Bates, R.: Towards imaging the beating heart usefully with a conventional CT scanner. IEEE Trans. Biomed. Eng. **28**(2), 123–127 (1981)
36. Pengpan, T., Qiu, W., Smith, N., Soleimani, M.: Cone beam CT using motion-compensated algebraic reconstruction methods with limited data. Comput. Methods Programs Biomed. **105**(3), 246–256 (2012)
37. Pengpan, T., Smith, N., Qiu, W., Yao, A., Mitchell, C., Soleimani, M.: A motion-compensated cone-beam CT using electrical impedance tomography imaging. Physiol. Meas. **32**(1), 19–34 (2011)
38. Purdie, T., Moseley, D., Bissonnette, J.P., Sharpe, M., Franks, K., Bezjak, A., Jaffray, D.: Respiration correlated cone-beam computed tomography and 4DCT for evaluating target motion in stereotactic lung radiation therapy. Acta Oncol. **45**(7), 915–922 (2006)
39. Qi, Z., Chen, G.H.: Extraction of tumor motion trajectories using PICCS-4DCBCT: a validation study. Med. Phys. **38**(10), 5530–5538 (2011)
40. Qi, Z., Chen, G.H.: Performance studies of four-dimensional cone beam computed tomography. Phys. Med. Biol. **56**(20), 6709–6721 (2011)
41. Reyes, M., Malandain, G., Koulibaly, P., Gonzàlez-Ballester, M., Darcourt, J.: Model-based respiratory motion compensation for emission tomography image reconstruction. Phys. Med. Biol. **52**(12), 3579–3600 (2007)
42. Rit, S., Nijkamp, J., van Herk, M., Sonke, J.J.: Comparative study of respiratory motion correction techniques in cone-beam computed tomography. Radiother. Oncol. **100**(3), 356–359 (2011)
43. Rit, S., Sarrut, D., Desbat, L.: Comparison of analytic and algebraic methods for motion-compensated cone-beam CT reconstruction of the thorax. IEEE Trans. Med. Imaging **28**(10), 1513–1525 (2009)
44. Rit, S., van Herk, M., Zijp, L., Sonke, J.J.: Quantification of the variability of diaphragm motion and implications for treatment margin construction. Int. J. Radiat. Oncol. Biol. Phys. **82**(3), e399–e407 (2012)
45. Rit, S., Wolthaus, J., van Herk, M., Sonke, J.J.: On-the-fly motion-compensated cone-beam CT using an a priori model of the respiratory motion. Med. Phys. **36**(6), 2283–2296 (2009)
46. Ritchie, C., Crawford, C., Godwin, J., King, K., Kim, Y.: Correction of computed tomography motion artifacts using pixel-specific back-projection. IEEE Trans. Med. Imaging **15**(3), 333–342 (1996)
47. Ritchie, C., Godwin, J., Crawford, C., Stanford, W., Anno, H., Kim, Y.: Minimum scan speeds for suppression of motion artifacts in CT. Radiology **185**(1), 37–42 (1992)
48. Roux, S., Desbat, L., Koenig, A., Grangeat, P.: Exact reconstruction in 2D dynamic CT: compensation of time-dependent affine deformations. Phys. Med. Biol. **49**(11), 2169–2182 (2004)
49. Santoro, J., Kriminski, S., Lovelock, D., Rosenzweig, K., Mostafavi, H., Amols, H., Mageras, G.: Evaluation of respiration-correlated digital tomosynthesis in lung. Med. Phys. **37**(3), 1237–1245 (2010)
50. Sidky, E., Pan, X.: Image reconstruction in circular cone-beam computed tomography by constrained, total-variation minimization. Phys. Med. Biol. **53**(17), 4777–4807 (2008)
51. Sonke, J.J., Belderbos, J.: Adaptive radiotherapy for lung cancer. Semin. Radiat. Oncol. **20**(2), 94–106 (2010)
52. Sonke, J.J., Lebesque, J., van Herk, M.: Variability of four-dimensional computed tomography patient models. Int. J. Radiat. Oncol. Biol. Phys. **70**(2), 590–598 (2008)
53. Sonke, J.J., Rossi, M., Wolthaus, J., van Herk, M., Damen, E., Belderbos, J.: Frameless stereotactic body radiotherapy for lung cancer using four-dimensional cone beam CT guidance. Int. J. Radiat. Oncol. Biol. Phys. **74**(2), 567–574 (2009)
54. Sonke, J.J., Zijp, L., Remeijer, P., van Herk, M.: Respiratory correlated cone beam CT. Med. Phys. **32**(4), 1176–1186 (2005)

55. Taguchi, K., Kudo, H.: Motion compensated fan-beam reconstruction for nonrigid transformation. IEEE Trans. Med. Imaging **27**(7), 907–917 (2008)
56. Thompson, B., Hugo, G.: Quality and accuracy of cone beam computed tomography gated by active breathing control. Med. Phys. **35**(12), 5595–5608 (2008)
57. Tuy, H.: An inversion formula for cone-beam reconstruction. SIAM J. Appl. Math. **43**, 91–100 (1983)
58. van Herk, M.: Different styles of image-guided radiotherapy. Semin. Radiat. Oncol. **17**(4), 258–267 (2007)
59. Vandemeulebroucke, J., Kybic, J., Clarysse, P., Sarrut, D.: Respiratory motion estimation from cone-beam projections using a prior model. Med. Image Comput. Comput. Assist. Interv. **12**(Pt 2), 365–372 (2009)
60. Wertz, H., Stsepankou, D., Blessing, M., Rossi, M., Knox, C., Brown, K., Gros, U., Boda-Heggemann, J., Walter, C., Hesser, J., Lohr, F., Wenz, F.: Fast kilovoltage/megavoltage (kVMV) breathhold cone-beam CT for image-guided radiotherapy of lung cancer. Phys. Med. Biol. **55**(15), 4203–4217 (2010)
61. Zeng, R., Fessler, J., Balter, J.: Respiratory motion estimation from slowly rotating X-ray projections: theory and simulation. Med. Phys. **32**(4), 984–991 (2005)
62. Zeng, R., Fessler, J., Balter, J.: Estimating 3-D respiratory motion from orbiting views by tomographic image registration. IEEE Trans. Med. Imaging **26**(2), 153–163 (2007)
63. Zhang, Q., Hu, Y.C., Liu, F., Goodman, K., Rosenzweig, K., Mageras, G.: Correction of motion artifacts in cone-beam CT using a patient-specific respiratory motion model. Med. Phys. **37**(6), 2901–2909 (2010)
64. Zijp, L., Sonke, J.J., van Herk, M.: Extraction of the respiratory signal from sequential thorax cone-beam X-ray images. In: International Conference on the Use of Computers in Radiation Therapy (ICCR), pp. 507–509. Jeong Publishing, Seoul (2004)

Index

J. Ehrhardt and C. Lorenz (eds.), *4D Modeling and Estimation of Respiratory Motion for Radiation Therapy*, Biological and Medical Physics, Biomedical Engineering,
DOI: 10.1007/978-3-642-36441-9, © Springer-Verlag Berlin Heidelberg 2013